Characterisation of the structure and self-assembly of a small cyclic peptide.

An analysis using NMR spectroscopy, diffusion and heteronuclear relaxation measurements.

Davy Sinnaeve

Proefschrift voorgelegd aan de Faculteit Wetenschappen
tot het behalen van de graad van
Doctor in de Wetenschappen: Chemie

Gent, mei 2010

Promotor:

Prof. Dr. J. C. Martins	Universiteit Gent

Examencommissie:

Prof. Dr. Katrien Strubbe (voorzitter)	Universiteit Gent
Prof. Dr. Bruno Kieffer	Université de Strasbourg
Prof. Dr. Guy Lippens	Université Lille 1
Prof. Dr. Rudolph Willem	Vrije Universiteit Brussel
Prof. Dr. Savvas N. Savvides	Universiteit Gent
Prof. Dr. Zeger Hens	Universiteit Gent

Table of contents

List of publications and conferences

List of peer reviewed papers

Reporting on results presented in this work

1. D. Sinnaeve, C. Michaux, J. Van hemel, J. Vandenkerckhove, E. Peys, F.A.M. Borremans, B. Sas, J. Wouters, and J.C. Martins
   "Structure and X-ray conformation of pseudodesmins A and B, two new cyclic lipodepsipeptides from *Pseudomonas* bacteria"*.*
   Tetrahedron, **2009**, 65(21) 4173-4181.

2. D. Sinnaeve, P.M.S. Hendrickx, J. Van hemel, E. Peys, B. Kieffer, and J.C. Martins,
   "The Solution Structure and Self-Association Properties of the Cyclic Lipodepsipeptide Pseudodesmin A Support Its Pore-Forming Potential"*.*
   Chemistry-a European Journal, **2009**, 15(46) 12653-12662.

Reporting on results not presented in this work

3. P. Saveyn, E. Cocquyt, D. Sinnaeve, J.C. Martins, D. Topgaard, and P. Van der Meeren
   “NMR study of the sorption behavior of benzyl alcohol derivatives into sonicated and extruded dioctadecyldimethylammonium chloride (DODAC) dispersions: The relevance of membrane fluidity”.
   Langmuir, **2008**, 24(7) 3082-3089.

4. T. De Meyer, D. Sinnaeve, B. Van Gasse, E. Tsiporkova, E.R. Rietzschel, M.L. De Buyzere, T.C. Gillebert, S. Bekaert, J.C. Martins, and W. Van Criekinge
   "NMR-based characterization of metabolic alterations in hypertension using an adaptive, intelligent binning algorithm".
   Analytical Chemistry, **2008**, 80(10) 3783-3790.

5. P. Saveyn, E. Cocquyt, W. Zhu, D. Sinnaeve, K. Haustraete, J.C. Martins, and P. Van der Meeren
   "Solubilization of flurbiprofen within non-ionic Tween 20 surfactant micelles: a ^{19}F and ^{1}H NMR study".
   Physical Chemistry Chemical Physics, **2009**, 11(26) 5462-5468.

6. P. Saveyn, J. De Geeter, D. Sinnaeve, P. Van der Meeren, and J.C. Martins
   "Influence of the Vesicular Bilayer Structure on the Sorption of Ethylbenzyl Alcohol".
   Langmuir, **2009**, 25(19) 11322-11327.

7. M. Verbrugghe, E. Cocquyt, P. Saveyn, P. Sabatino, D. Sinnaeve, J.C. Martins, and P. Van der Meeren
   "Quantification of hydrophilic ethoxylates in polysorbate surfactants using diffusion ^{1}H NMR spectroscopy".
   Pharmaceutical and Biomedical Analysis, **2010**, 51(3) 583-589.

List of oral communications presented at conferences and symposia

1. D. Sinnaeve, P.M.S. Hendrickx, F.A.M. Borremans, J. Van hemel, B. Sas, and J.C. Martins
   "Conformation and self-association of a cyclic lipodepsipeptide investigated by NMR spectroscopy".
   5th Young Belgian Magnetic Resonance Scientists symposium
   17th November 2006, Brussels, Belgium

2. D. Sinnaeve, B. Kieffer, and J.C. Martins
   "Characterizing the self-assembly of a natural cyclic lipodepsipeptide in solution with NMR diffusion and heteronuclear relaxation measurements".
   Materials Research Society (MRS) Spring Meeting, Symposium NN: Materials Exploiting Peptide and Protein Self Assembly - Toward Design Rules,
   5th–9th April 2010, San Francisco, California, United States of America

List of posters presented at conferences and symposia

1. D. Sinnaeve, J. Van hemel, B. Sas, and J.C. Martins
   "Structure Elucidation of a new Cyclic Lipodepsipeptide and Determination of its Self-associating Properties by Diffusion NMR".
   French-Benelux Meeting on Magnetic Resonance
   19th-22nd March 2006, Blankenberge, Belgium

2. D. Sinnaeve, P.M.S. Hendrickx, C. Michaux, J. Van hemel, B. Sas, J. Wouters, F.A.M. Borremans, and J.C. Martins
   "Conformation and Self-association of a Cyclic Lipodepsipeptide Investigated by NMR Spectroscopy".
   Doctoraatssymposium Faculteit Wetenschappen 2007 (UGent)
   24th April 2007, Gent, Belgium

3. D. Sinnaeve, P.M.S. Hendrickx, C. Michaux, J. Van hemel, B. Sas, J. Wouters, F.A.M. Borremans, and J.C. Martins
   "Conformation and Self-association of a cyclic lipodepsipeptide investigated by NMR spectroscopy".
   Euromar 2007 Magnetic Resonance Conference
   1st-5th July 2007, Tarragona, Spain

4. D. Sinnaeve, P.M.S. Hendrickx, C. Michaux, J. Van hemel, B. Sas, J. Wouters, F.A.M. Borremans, and J.C. Martins
   "Conformation and Self-association of a cyclic lipodepsipeptide investigated by NMR spectroscopy".
   Small Molecule NMR conference (SMASH)
   16th-19th September 2007, Chamonix, France

5. D. Sinnaeve, P.M.S. Hendrickx, C. Michaux, J. Van hemel, B. Sas, J. Wouters, B. Kieffer, and J.C. Martins
   "Conformation and self-association of a cyclic lipodepsipeptide investigated by NMR spectroscopy".
   9e Vlaamse Jongeren Congres van de Chemie
   4th April 2008, Antwerpen, Belgium
   Winner of the poster price in the section Medicinal chemistry and Biochemistry

6. D. Sinnaeve, B. Kieffer, and J.C. Martins
   "Characterization of the self-association of a cyclic lipodepsipeptide using NMR diffusion and relaxation measurements".
   EMBO Course "Multidimensional NMR in Structural Biology"
   3rd-8th August 2008, Il Ciocco, Castelvecchio Pascoli, Lucca, Italy

7. D. Sinnaeve, B. Kieffer, and J.C. Martins
   "Combining NMR Diffusion and Relaxation Measurements to Characterize the Self-association of a Cyclic Lipodepsipeptide".
   Experimental Nuclear Magnetic Resonance Conference (ENC)
   29th March – 3rd April 2009, Asilomar Conference Grounds, Pacific Grove, California, United States of America

8. D. Sinnaeve, B. Kieffer, and J.C. Martins
   "Combining NMR Diffusion and Relaxation Measurements to Characterize the Self-association of a Cyclic Lipodepsipeptide".
   Doctoraatssymposium Faculteit Wetenschapppen 2009 (UGent)
   28th April 2009, Gent, Belgium

9. D. Sinnaeve, B. Kieffer, and J.C. Martins
   "Combining NMR diffusion and relaxation measurements to gain insight into the supramolecular structure of a pore forming cyclic lipodepsipeptide".
   Hydroprot 09: Macromolecular hydrodynamics from aqueous solutions to living cells
   29th–30th June 2009, Institut Pasteur, Paris, France

List of conferences and symposia attended without contribution

- *3rd Young Belgian Magnetic Resonance Scientists symposium*
  26th November 2004, Brussels, Belgium
- *"The Future of NMR" Symposium*
  10th November 2005, Nijmegen, The Netherlands

- *4th Young Belgian Magnetic Resonance Scientists symposium*
  25th November 2005, Brussels, Belgium
- *Metabolomics Society's 3rd Annual International Conference*
  11th-14th June 2007, Manchester, United Kingdom
- *6th Young Belgian Magnetic Resonance Scientists symposium*
  30th November 2007, Brussels, Belgium
- *NMR: a tool for biology VIII*
  28th-30th January 2008, Institut Pasteur, Paris, France
- *7th Young Belgian Magnetic Resonance Scientists symposium*
  21st November 2008, Brussels, Belgium
- *8th Young Belgian Magnetic Resonance Scientists symposium*
  27th November 2009, Brussels, Belgium

List of abbreviations

AFM	atomic force microscopy
AMP	antimicrobial peptide
CLP	cyclic lipodepsipeptide
COSY	correlation spectroscopy
CPMG	Carr-Purcell-Meiboom-Gill
CSA	chemical shift anisotropy
CTP	coherence transfer pathway
DECRA	direct exponential curve resolution algorithm
DMF	N,N-dimethyl formamide
DMSO	dimethyl sulfoxide
DOSY	diffusion ordered spectroscopy
ELISE	experimental liquid sealing
EM	energy minimisation
ERETIC	electronic reference to access *in vivo* concentrations
FID	free induction decay
FT	Fourier transform
gHSQC	gradient enhanced heteronuclear single quantum coherence
GRAM	generalized rank annihilation method
HDA	3-hydroxydecanoic acid
HMQC	heteronuclear multiple quantum coherence
HSQC	heteronuclear single quantum coherence
ILT	inverse Laplace transform
INEPT	insensitive nuclei enhancement by polarisation transfer
LED	longitudinal eddy current delay
LT	Laplace transform
MaxEnt	maximum entropy
MCR	multivariate curve resolution
MD	molecular dynamics
NMR	nuclear magnetic resonance
nOe	nuclear Overhauser enhancement
NOESY	nuclear Overhauser enhancement spectroscopy
PEG	polyethylene glycol
PFG	pulsed field gradient
RMSD	root mean square difference
rOe	rotating frame nuclear Overhauser enhancement
ROESY	rotating frame nuclear Overhauser enhancement spectroscopy
rRNA	ribosomal ribonucleic acid
SDS	sodium dodecyl sulfate
SEM	scanning electron microscopy
SERF	selective refocusing
SS	sum of square difference
STE	stimulated echo
TMS	tetramethyl silane
TOCSY	total correlation spectroscopy
rf	radio frequency
WLIP	White Line Inducing Principle

List of letter codes for the standard amino acids used in this work

name	three letter code	one letter code
Alanine	Ala	A
Asparagine	Asn	N
Aspartic acid	Asp	D
Glutamic acid	Glu	E
Glutamine	Gln	Q
Glutamine or Glutamic acid	Glx	
Glycine	Gly	G
Isoleucine	Ile	I
Leucine	Leu	L
Phenylalanine	Phe	F
Proline	Pro	P
Serine	Ser	S
Threonine	Thr	T
Valine	Val	V

List of constants and their values

name	symbol	value
Boltzmann constant	k_b	1.381×10^{-21} J/K
Planck's constant	h	6.626×10^{-34} J·s
Permeability of the vacuum	μ_0	$4\pi\times10^{-7}$ T·m·A^{-1}
$^{13}C^{\alpha}$ – ^{1}H distance in a peptide backbone	r_{CH}	1.07 Å
^{15}N – ^{1}H distance in a peptide backbone amide	r_{NH}	1.02 Å
CSA for a $^{13}C^{\alpha}$ nucleus	$\Delta\sigma_C$	25 ppm
CSA for a ^{15}N peptide backbone nucleus	$\Delta\sigma_N$	–160 ppm
Gyromagnetic ratio of the ^{1}H nucleus	γ_H	2.675×10^{8} T^{-1}s^{-1}
Gyromagnetic ratio of the ^{13}C nucleus	γ_C	6.728×10^{7} T^{-1}s^{-1}
Gyromagnetic ratio of the ^{15}N nucleus	γ_N	-2.712×10^{7} T^{-1}s^{-1}

Voorwoord

Beste lezer,

Wat u hier in uw handen houdt (of voor u ziet op een scherm) is het resultaat van een vier jaar lange investering van mijn tijd en energie in een wetenschappelijke studie van een klein cyclisch peptide met behulp van NMR spectroscopie. Indien u verder leest dan enkel dit voorwoord, zult u hopelijk tot de vaststelling komen dat het resultaat eigenlijk al bij al wel meevalt. U zult zien dat ik een poging heb gewaagd om de intrigerende wereld van NMR te doorgronden, dat ik mijn best heb gedaan om het gedrag van één relatief kleine molecule te begrijpen en hiervoor trachtte een nieuwe aanpak uit te werken. Wat u misschien niet zo heel duidelijk te zien zult krijgen, behalve indien u zeer getalenteerd bent in het tussen de regels door lezen, zijn de lange, eenzame avonden op het labo, de ettelijke tegenslagen, de om soms niet verklaarbare redenen compleet mislopen van experimenten, de frustraties wanneer het eens niet wilde vlotten, maar ook de vele eurekamomenten, het enthousiasme wanneer er een verrassend mooi spectrum of experimentele curve tevoorschijn komt, de voldoening om de puzzelstukken langzaam in mekaar te zien vallen en de motivatie dat daaruit voortvloeit om door te gaan. En wat er misschien ook niet op het eerste zicht naar boven komt, doch niet voldoende in de verf kan worden gezet, zijn de directe of indirecte bijdragen van al die mensen die mij hebben begeleid, verder hebben geholpen of gewoon het leven een stuk aangenamer hebben gemaakt. Dit is dan ook het gedeelte van dit boekje waar ik toch even heel duidelijk mijn appreciatie hiervoor wil laten blijken.

De eerste persoon die ik wens te bedanken is Prof. J. C. Martins, bij ons op het labo beter bekend als gewoonweg José. Ik dank hem vooreerst om mij, na mijn licentiaatsthesis, de kans te geven om mijn doctoraat aan te vatten in zijn onderzoeksgroep. Alhoewel ik een zekere vrijheid heb ervaren, zou dit onderzoek nooit in de juiste richting gegaan zijn zonder zijn begeleiding. De vele discussies die wij hielden over de laatste wetenschappelijke resultaten of over vroege versies van geschreven teksten bleken van onschatbare waarde te zijn. Mijn ervaring was ook dat hij heel bereikbaar is voor problemen van allerlei niveaus en dat zijn deur dan ook altijd open stond. Ook ben ik zeer dankbaar voor de meerdere malen dat ik mocht erop uit mocht gaan naar congressen, cursussen of andere instellingen om mijn werk te presenteren of om nieuwe kennis op te doen. Op persoonlijk vlak ben ik hem eeuwig dankbaar om mij de aandacht te doen vestigen op wat waarschijnlijk één van de beste science fiction programma's ooit is: Doctor Who.

Een tweede persoon die een zeer grote impact op dit werk heeft gehad is Prof. Dr. Bruno Kieffer van de Université de Strasbourg. Als expert op het vlak van NMR relaxatiemetingen en dynamiekstudies was zijn inbreng en enthousiasme cruciaal om het relaxatiegedeelte in dit werk op te starten en tot een goed einde te brengen. Het is ook dankzij zijn stimulans dat ik heb geprobeerd om zo diepgaand de theorie van relaxatie te doorgronden. Ook voelde ik mij zeer hartelijk ontvangen door hem en de andere leden van zijn groep tijdens mijn twee korte

verblijven in Straatsburg. Dr. Marc-André Delsuc, die gedurende mijn doctoraat de transitie maakte van Montpellier naar Straatsburg, dien ik te bedanken voor zijn hulp in het gebruik van zijn MaxEnt methode en later voor zijn interesse in het translationele diffusieluik van dit werk.

Ik wens ook het Fonds Wetenschappelijk Onderzoek Vlaanderen (FWO) te bedanken voor het toekennen van een aspirantenmandaat in de periode oktober 2005 tot en met september 2009. De Facultaire Commissie voor Wetenschappelijk Onderzoek (FCWO) dank ik voor het mij tweemaal toekennen van een kostenvergoeding voor het bijwonen van congressen in de Verenigde Staten.

De leden van de examencommissie wens ik te bedanken voor het doornemen van dit werk en hun kritische commentaren.

Het natuurproduct waar dit doctoraatswerk om draait, pseudodesmine A, werd ons toevertrouwd door Kemin Pharma. Ik wens hierbij dan ook Dr. Johan Van hemel en Dr. Benedikt Sas (ondertussen werkzaam bij de Universiteit Gent) te bedanken voor de blijvende samenwerking en de steun van dit project. Dr. Jan Vandenkerckhove en Dr. Eric Peys worden bedankt voor het uitvoeren van de biologische essays en de initiële massaspectrometrische analyse van het product.

Dr. Catherine Michaux en Prof. Dr. Johan Wouters van de Laboratoire de Chimie Biologique Structurale van de Universite´ de Namur kunnen niet voldoende worden bedankt voor de succesvolle kristallisatie van pseudodesmine A en de daaropvolgende X-stralen diffractie analyse. Dit was voor mij het eerste grote keerpunt van mijn doctoraat, aangezien het probleem van de onvolledig gekende stereochemie hierdoor eindelijk van de baan was.

Ik wens ook Prof. Dr. Pat Sandra en Dr. Alberto dos Santos Pereira van het Research Institute for Chromatography te Kortrijk te bedanken voor het uitvoeren van een hoge resolutie massaspectrometrische analyse van pseudodesmine A.

Prof. Dr. Gareth Morris van de University of Manchester ben ik zeer dankbaar voor de discussies die hij met mij heeft willen aangaan in verband met DOSY en de hulp die hij bood om de problemen die wij hadden met de convectiegecompenseerde sequenties op te lossen. Dr. Mathias Nilsson, ook van de University of Manchester, dank ik voor de discussies over DOSY en voor het toestaan van het gebruik van zijn DOSY Toolbox.

*Het dagelijkse leven als doctoraatsstudent zou maar zeer saai zijn zonder collega-doctoraatsstudenten. Vooreerst Katelijne, mijn bureaugenoot van in het begin. We zaten op dezelfde golflengte en vaak werden er dan ook onderwerpen aangesneden die weinig met wetenschap te maken hebben. Als ik Katelijne zeg, dien ik natuurlijk onmiddellijk over te gaan naar David. Wat ik altijd van David zal onthouden is zijn enorme gave om mensen te plagen en meer specifiek om ze te doen schrikken. In mijn hoofd is het woordje '**boe!**'*

onlosmakelijk met hem verbonden. Katelijne en David wens ik enorm veel geluk toe samen, zeker nu ze samen succesvol hun DNA hebben gekloond. In Pieter vond ik dan weer een geestesgenoot in het bediscussiëren van totaal nutteloze onderwerpen met een wiskundig, fysisch of chemisch kantje, al verloren we wel eens daarmee de aandacht van omstaanders. Ik ben hem ook dankbaar voor de onmisbare hulp bij de moleculaire modellering, het overweg gaan met Linux PC's, MATLAB en wat nog allemaal, zolang het maar software is. Dan is er Bjorn, altijd bereid voor een gesprekje over politiek en actualiteit. Altijd goedgeluimd, een eigenschap dat ik ten zeerste apprecieer. Paolo bedank ik om mijn DOSY scripts te gebruiken en de resultaten ervan aan een kritische blik te onderwerpen. Tenslotte Peter, waarvan ik vooral zijn talent om gevatte opmerkingen te maken zal onthouden. Ik ben hem vooral dankbaar om mij bij te staan bij de eerste practica die ik moest begeleiden.

Naast doc's waren er ook postdoc's. Eerst en vooral Agnieszka, werkelijk een droom om mee samen te werken. Hardwerkend, intelligent, heel enthousiast en een zeer goed gevoel voor humor. Er kon duidelijk een onderscheid gemaakt worden tussen de dagen dat ze bij ons op het lab, dan wel bij Agfa Gevaert was. De andere postdoc, Bernd, bedank ik om altijd paraat te staan wanneer er weer eens problemen waren met de 700 of min of meer alles waar een computer aan hangt. Ook mijn eerste stappen in het leren pulsprogramma's schrijven valt hem toe te schrijven. Het feit dat ik dankzij hem zeker nooit alleen moest gaan eten 's middags werd geapprecieerd.

De laatste onmisbare schakels in de groep zijn uiteraard de ATP leden. Katrien maakt ons het leven een stuk gemakkelijker door de administratie van bestellingen e.d. op haar te nemen. Ik heb graag met haar samengewerkt op enkele wetenschappelijke projecten en zeker genoten van de vele babbels. Tim dank ik voor alle keren waar hij te hulp schoot bij computer- en printerproblemen en voor de soms afschuwelijke taak om de posters af te drukken; toch steeds met een lach. Ook aan hun voorgangers, Georges en Roland, hou ik zeker goeie herinneringen over.

Ook de Master en Bachelor studenten die door onze groep passeerden wil ik zeker ook niet vergeten. Lien wil ik bedanken voor de toffe sfeer die ze meebracht en voor het spontaan nemen van initiatief voor het kerstfeestje. Ook aan de (toenmalige) 3^{e} Bachelorstudenten die ik heb begeleid gedurende hun project van vier weken houd ik tevreden herinneringen over: Roel, Stijn en Sigelinde. Het DOSY spectrum dat te zien is in Figuur 2.2 verder in dit werk werd door hen gemeten op een staal dat zij ook hebben bereid, wat hier ook zeker mag vermeld worden.

Ook vele anderen binnen de S4 bedank ik voor de vele bewezen diensten. Veerle en Jan Verstraete voor de bestellingen; Tom Parlevliet, Freddy en Carine voor de administratie; Ingrid voor de onkostennota's en het posten van brieven; Paul, Tom Debruyne en hun voorgangers Hector en Dirk voor de practica en voor wanneer er eens een klusje diende opgeknapt te worden; Prof. Dr. Frans Borremans voor zijn advies en interesse in mijn werk; Prof. Dr. Dirk Tavernier voor de enorme vriendelijkheid en sfeer dat hij schiep toen hij nog bij

ons op gang vertoefde. Jan Goeman, Frank en Jos verdienen allen ook een speciale vermelding voor de hulp bij talrijke meer labogerichte of chemische probleemstellingen. Ook Lolita, onze eeuwig goedlachse, vriendelijke en zeer efficiënte schoonmaakster, verdient hier zeker een vermelding!

Ook vele andere mensen van buiten de vakgroep wens ik te vermelden om allerlei redenen, te veel om allemaal in detail op in te gaan. De nanomensen, Iwan en Antti, de metabo-dames uit Antwerpen, Kim en Isabelle, de VUB'ers, Luk, Vanja en Ingrid. Camelia verdient een speciale vermelding, omdat ze altijd koeken of ander lekkers meebracht en er voor zorgde dat de gezelligheidsgraad plots met een factor tien steeg. Ook de mensen waar we mee samenwerkten om NMR binnen hun onderzoeksdomein toe te passen: Pieter Saveyn en later Maarten Verbrugghe uit de groep van Prof. Dr. Paul Van der Meeren; Tim De Meyer en Dr. Sofie Bekaert uit de groep van Prof. Dr. Wim Van Criekinge.

Annelies verdient hier ook een plaats in deze lange lijst dankbetuigingen, om het leven op de S4 een stukje aangenamer te maken. Hoe vaak hebben we niet aan elkaars bureau staan kletsen, of in de gang tot men kwam vragen of we misschien een kopje koffie wilden? Ook Jelle, met wie ik zo vaak samen naar Gent spoorde op zondagavond, een traditie ontstaan van voor onze doctoraatsjaren die we flink hebben voortgezet. Zowel Annelies als Jelle moet ik ook bedanken voor de meerdere malen dat ik iets uit hun labo mocht komen 'lenen' (vaak iets niet herbruikbaars).

Zo zijn er nog vele mensen, zowel binnen als buiten de S4, die mij op een of andere manier hebben verder geholpen. Dit varieert van het uitleggen van de werking van een speedvac, tot het mij vermaken door het uitwisselen van leuke mails vanuit het verre zuiden tijdens het schrijven van dit boek. Een volledige opsomming van dit alles is jammer genoeg niet haalbaar.

Als laatste doch zeker niet in het minste bedank ik mijn ouders, Kathleen en Wim, mijn zus, Evelyn, en de rest van mijn familie voor de onophoudelijke steun en het geduld die ze hebben uitgeoefend.

En u, beste lezer, bedank ik alvast voor uw blijk van interesse in dit werk, of dit nu omwille van wetenschappelijke redenen, sympathie, nieuwsgierigheid of per vergissing is. In ieder geval hoop ik dat u er iets aan heeft.

Davy, 7 mei 2010

Foreword

Dear Reader,

What you are holding in your hands right now (or are reading from a screen) is the result of four years of investment of my time and energy in the scientific study of a small cyclic peptide by means of NMR spectroscopy. If you would read further than this foreword, you will hopefully come to the conclusion that the result is in fact not that bad. You will see that I attempted to comprehend the intriguing world of NMR, that I have done my best to understand the behaviour of one relatively small molecule and that I have tried to develop a new methodology. What you may not be able to see very clearly, except if you are very talented in reading stuff between lines, are the long, lonely nights at the lab, the many setbacks, the experiments gone completely wrong sometimes for no apparent reason at all, the frustrations when things didn't go as swiftly as desired, but also the many moments of eureka, the enthusiasm when a surprisingly beautiful spectrum or experimental curve came up, the satisfaction when the pieces of the puzzle slowly came together and the motivation to go on that it created. And what may also not be clear at a first glance, though cannot be emphasised enough, are the direct or indirect contributions of all those people that have guided me or helped me or simply made life somewhat more pleasant. Therefore, this part of this little book is the place where I would like to make very clear how much I appreciate all this.

The first person that I wish to thank is Prof. Dr. J. C. Martins, better known in our lab simply as José. I wish to thank him in the first place because – after I already did my Licentiate (Master) degree with him – he gave me the opportunity to start my PhD in his research group. Although I have enjoyed a certain degree of freedom, this research would never have had the right direction without his guidance. The many discussions that we shared concerning the latest scientific results or early draft versions of papers, turned out to be invaluable. My experience was that he is very reachable for many issues of different levels and that his door was always open. I am also very grateful for the many times that I was allowed to go to conferences, courses or another institution to either present my work or to delve into new knowledge. On a personal level, I am eternally grateful that he has brought to my attention something that must be one of the best science fiction shows ever: Doctor Who.

A second person who had a very large impact on this work is Prof. Dr. Bruno Kieffer from the Université de Strasbourg. An expert in the field of NMR relaxation measurements and dynamics studies, his contribution and enthusiasm were crucial to start up the relaxation part of this work and to bring it to a good end. It is also under his impulse that I have attempted to thoroughly comprehend the theory concerning relaxation. I also felt that I was welcomed very warmly by him and the other members of his group during my two short stays in Strasbourg. Dr. Marc-André Delsuc, who during the period of my PhD made the transition

from Montpellier to Strasbourg, I have to thank for his help in using his MaxEnt method and later on for his interest in the translational diffusion part of this work.

I also wish to acknowledge the Fund for Scientific Research Flanders (FWO) to grant a bursary in the period from October 2005 until September 2009. The Faculty Commission for Scientific Research (FCWO) should be thanked to grant me the reimbursement of the expenditures of my attendance at two conferences in the United States.

I wish to thank the members of the exam commission for the thorough reading of this work and their comments and criticism.

The natural product that is the centre of attention of this work, pseudodesmin A, was entrusted to us by Kemin Pharma. I hereby wish to show my gratitude to Dr. Johan Van hemel and Dr. Benedikt Sas (who currently works at Ghent University) for their continuing cooperation and support to this project. Dr. Jan Vandenkerckhove en Dr. Eric Peys are thanked to perform the biological essays and initial mass spectrometry analysis of the compound.

Dr. Catherine Michaux and Prof. Dr. Johan Wouters of the Laboratoire de Chimie Biologique Structurale of the Université de Namur cannot be sufficiently acknowledged for the successful crystallisation of pseudodesmin A and the subsequent X-ray diffraction analysis. This was for me the first big turning point of my PhD, since the problem of not knowing the complete stereochemistry was finally resolved thanks to this.

I wish to thank Prof. Dr. Pat Sandra and Dr. Alberto dos Santos Pereira from the Research institute for Chromatography in Kortrijk as well for performing a high resolution mass spectrometry analysis of pseudodesmin A.

I am most grateful to Prof. Dr. Gareth Morris or the University of Manchester for the discussions we had concerning DOSY and the help he offered to solve the problems we experienced with the convection compensated sequences. Dr. Mathias Nilsson, also from the University of Manchester, I thank for the discussions we had about DOSY and for allowing us the use of his DOSY Toolbox.

*The daily life of a graduate student would be very dull if there were no graduate student colleagues. Firstly Katelijne, with whom I shared an office since the very beginning. We communicated on the same wavelength and therefore we often discussed topics that did not have much to do with science anymore. When I say Katelijne, I of course should proceed immediately to David. What I always will remember from David is his enormous gift to tease people and more specifically to scare them. In my head, the word '**boe!**' is inextricably connected to him. I wish Katelijne and David a lot of happiness together, especially now that they have successfully cloned their DNA. Pieter was for me a kindred spirit when it came to discussing totally useless subjects with a mathematical, physical or chemical connotation,*

even if like this we lost the attention of the people around us now and then. I am also most grateful to him for the vital help with the molecular modelling, working with Linux PCs, MATLAB and whatever, as long as it was software. Then there is Bjorn, always willing to start a conversation about politics and current events. He always is in a good mood, a characteristic that I appreciate very much. Paolo I thank for using my DOSY scripts and subject their results to criticism. Finally, Peter, from whom I will especially remember his talent to make witty remarks. I am particularly thankful to him for guiding me during the first practicals I had to supervise.

Besides doc's there were also postdoc's. First and foremost Agnieszka, who is truly a dream to work with. Hardworking, very clever, very enthusiastic and a very good sense of humor. There was clearly a difference between the days that she was with us at the lab and those where she would be in Agfa Gevaert. The other postdoc, Bernd, I thank for always standing ready when there were once again some problems with the 700 or about anything else where a computer is involved with. Also he is credited for my first steps in learning how to do pulse programming. The fact that thanks to him I certainly never had to go out eating alone at noon was much appreciated.

The last vital part of the group is of course the technical personnel. Katrien made our lives a lot easier by taking upon her all the administration of the orders. I liked to work with her on some scientific projects and certainly enjoyed our conversations. Tim I thank for all those times where he came to the rescue for all computer and printer problems and for the sometimes horrible task of printing the posters; nevertheless always with a smile. Also from their predecessors, Georges and Roland, I keep good memories.

Also I certainly do not wish to forget the Master and Bachelor students that passed through our group. Lien I would like to thank for the fun atmosphere she brought with her and for taking spontaneously the initiative for the Christmas party. Also from the (at the time) 3rd Bachelor students that I have supervised during their four-week project I keep satisfying memories: Roel, Stijn and Sigelinde. The DOSY spectrum of Figure 2.2 further in this book was measured by them on a sample they prepared themselves, something that certainly should be mentioned here.

Also to the many others within the S4 I express my gratitude for their many services. Veerle and Jan Verstraete for the orders; Tom Parlevliet, Freddy and Carine for the administration; Ingrid for the notes of expenses and posting letters; Paul, Tom Debruyne and their predecessors Hector and Dirk for the practicals and whenever there needed to be done some small jobs; Prof. Dr. Frans Borremans for his advice and interest in my work; Prof. Dr. Dirk Tavernier for the enormous kindliness and good atmosphere he created when he was still stationed in our hall. Jan Goeman, Frank and Jos all deserve a special mention for their help with numerous laboratory or chemically related issues. Also Lolita, the cleaning lady who is eternally full of laughter, very friendly and very efficient, certainly deserves to be mentioned!

Also many people outside the department I would like to mention for various reasons that are simply too numerous to talk about in detail. The nanofolks, Iwan and Antti, the metabo-ladies from Antwerp, Kim and Isabelle, the VUB-people, Luk, Vanja and Ingrid. Camelia deserves a special mention, as she always brought cookies or other sweets and made sure that the degree of cosiness increased tenfold. Also the people with whom we cooperated to apply NMR in their research domains: Pieter Saveyn and later Maarten Verbrugghe from the group of Prof. Dr. Paul Van der Meeren; Tim De Meyer and Dr. Sofie Bekaert from the group of Prof. Dr. Wim Van Criekinge.

Annelies also deserves a spot in this long list of acknowledgements, as she did make life on the S4 still a bit more pleasant even. How many times could we be found chatting at each other's desk, or in the hallway until someone came by to ask if we perhaps would like to have a cup of coffee? Also Jelle, with whom I have travelled to Ghent by train so many times on Sunday evenings, a tradition that began from before we started our PhD and that we firmly continued. Both Annelies and Jelle I should thank for the multiple times that I was allowed to 'lend' something from their lab (most often something that couldn't be reused).

There are still so many people, both from the S4 and outside, that have helped in some way or another. This varies from explaining how to work with a speedvac, to entertaining me by exchanging fun mails from the distant south during the writing of this book. A full listing of all of this is sadly not feasible.

Last but not least I thank my parents, Kathleen and Wim, my sister, Evelyn, and the rest of the family for the everlasting support and patience they have showed.

And you, dear reader, I thank you in advance for showing your interest in this work, if this either is for scientific reasons, sympathy, curiosity or because you took the wrong book from the shelf. In any case, I do hope you find something useful.

Davy, May 7th 2010

Introduction and dissertation outline

This work concerns the study of the structure and self-association properties of pseudodesmin A, a cyclic lipodepsipeptide (CLP) produced by *Pseudomonas* bacteria. Pseudodesmin A, previously referred to as KMCP-1, is of pharmaceutical interest since it shows potential antimicrobial activity. It was isolated by Plethodon Research (Georgia, USA) and further distributed to the NMR and Structure analysis group of prof. J. Martins at Ghent University by Kemin Pharma, with the purpose of determining the – at that time still unknown – molecular structure of the compound using NMR spectroscopy. The structure elucidation was successful (Davy Sinnaeve, Licentiaatsthesis 2005, Universiteit Gent), while the stereochemistry was fully determined by using both total hydrolysis followed by LC-MS analysis and later X-ray diffraction analysis in the course of this work. During the NMR analysis, it became clear that pseudodesmin A behaved differently depending on which solvent was used. The solvents screened were chloroform, dioxane, benzene and DMSO. It was concluded that it self-associates in the non-polar solvents, while it did not in polar DMSO. This conclusion was based on the observed change in line widths in the ^{1}H NMR spectra, the magnitude of the nOe in the non-polar solvents and an initial translational diffusion NMR study (Davy Sinnaeve, Licentiaatsthesis 2005, Universiteit Gent).

Pseudodesmin A appeared to be a new member of the viscosin group, a collection of CLPs that shares similarity both in oligopeptide chain length and in amino acid sequence. For some of the members of the viscosin group, it had already been hypothesised or established that they are capable of forming ion pores in cellular membranes. This can be linked to their biological activity, as such pores could allow

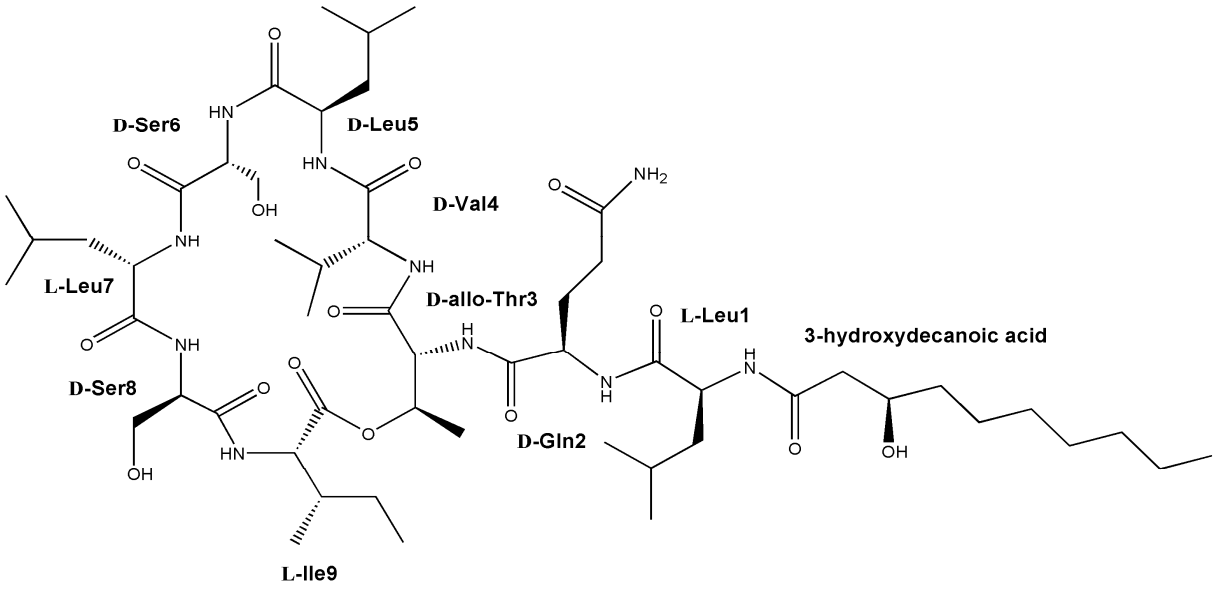

Molecular structure of pseudodesmin A.

passive transport of ions across the membrane, impacting the inner cellular ion concentrations. However, an investigation into the structure and molecular mechanism of such ion pores had never been performed. The conformations of some members of the viscosin group were already described, mainly through X-ray crystal structures. There exists some debate concerning the conformation of these molecules in solution however. Before now, the only member of the viscosin group for which a solution conformation had been determined was WLIP, which was studied in DMSO and found to be different from its crystal structure (see Chapters 4 and 5). This fact made it even more complicated to come up with a structure-function relationship for this group of compounds.

Although organic solvents are a poor mimic of cellular membrane bilayers, the low polarity that induces the self-association is common to both environments. Therefore, the self-association of pseudodesmin A in non-polar solvents can directly be linked with the ability to form ion pores. Because of this, the study of the self-association in organic solvents may provide insight into the pore forming mechanism of pseudodesmin A and the viscosin group in general.

The goal of the work presented in this dissertation is to investigate this self-association and the structure-function relationship of pseudodesmin A using NMR spectroscopic methods. A conformational analysis of pseudodesmin A in acetonitrile solution is performed based on NMR distance restraints. This provides for the first time an unambiguous result for the solution conformation of a viscosin group member. A study in DMSO solution is performed as well, which provides answers to the issues described above concerning the solution conformation previously reported for WLIP. The self-association of pseudodesmin A is investigated using translational diffusion measurements in non-polar chloroform and polar acetonitrile solutions, allowing the concentration and solvent polarity dependence of the self-association to be established. In addition, structural information on the supramolecular assemblies is obtained by studying both the chemical shift variations as a function of the degree of self-association and an off-resonance ROESY spectrum in chloroform solution that allows the identification of intermolecular rOe contacts. All of this information leads to the proposition of a model describing both the supramolecular organisation of the assemblies and their expected function as ion pores. Finally, an analysis of heteronuclear relaxation data in both acetonitrile and various concentrations in chloroform allows to independently confirm several aspects of the proposed model, including the orientation of the monomers within the supramolecular assembly, its shape and its dimensions.

In what follows, an outline is given of this dissertation. It is divided into two separate parts. In the first part, ***Diffusion and NMR***, the theoretical background of the physical phenomenon diffusion and its relevance to NMR are explored.

In the first chapter, ***Diffusion***, both translational and rotational diffusion are introduced. The relevant theoretical basis for the following two chapters is surveyed and the relation between the diffusion coefficient and the molecular size and shape is outlined.

The second chapter, ***Impact of translational diffusion in NMR: diffusion NMR – DOSY***, provides an overview of the impact of translational diffusion on the NMR signal intensity during experiments that apply magnetic field gradient pulses. How this can be exploited to determine the translational diffusion coefficient of molecules in solution is explained in detail. The chapter begins with an introduction of the basic principles and applications of this technique. This should allow readers that wish to skip the theoretical and technical parts to gain sufficient appreciation of this technique to understand the results presented in this dissertation.

The third chapter, ***Impact of rotational diffusion in NMR: relaxation***, provides a discussion of heteronuclear relaxation in a two spin system (*e.g.* ^{13}C-^{1}H or ^{15}N-^{1}H) and how relaxation can be linked to the rotational diffusion properties of the molecular object. The principles of longitudinal, transverse and cross-relaxation are introduced, the latter leading to the well-known nuclear Overhauser enhancement or nOe. Expressions are derived for the rate constants in terms of values sampled from the spectral density function at certain frequencies. The spectral density function itself is then examined and its relation to rotational diffusion and to internal motion is presented. How the size, the shape (anisotropy) and the presence of fast internal motion (on a time scale shorter than the global correlation time) then influence the relaxation rate constants will be reviewed. Besides this, the effect of conformational exchange processes on a time scale of the order of milliseconds is investigated as well. The chapter concludes with an overview of the experiments used to measure the $^{13}C^{\alpha}$ or ^{15}N relaxation rate constants.

In the second part of the dissertation, ***Pseudodesmin A***, the compound of interest is introduced and its conformation and self-association is investigated.

The fourth chapter, ***Antimicrobial peptides, cyclic lipodepsipeptides and the viscosin group***, provides an overview of the group of compounds that pseudodesmin A belongs to. The observed behaviour of pseudodesmin A in different solvents is introduced.

In the fifth chapter, ***Conformational analysis of pseudodesmin A***, the results of the conformational analysis of pseudodesmin A, both by X-ray diffraction and solution NMR, are presented. Both the crystal and acetonitrile solution conformations are compared to one another and to the structures of the close analogues of pseudodesmin A described in literature. An investigation of the behaviour of

pseudodesmin A in DMSO is performed, as this differs from other polar solvents. These results are relevant to WLIP, another member of the viscosin group, since its DMSO solution structure, reported previously in literature, is effectively invalidated by the results presented in this dissertation. The chapter concludes with an examination of the monomer conformation within the supramolecular structure in chloroform, where it is shown to remain unaltered.

The sixth chapter, ***Self-association of pseudodesmin A***, investigates the self-association of pseudodesmin A in chloroform by means of translational diffusion NMR measurements. The effects of varying concentration and solvent polarity are investigated. Changes in chemical shift and information obtained from a 2D off-resonance ROESY spectrum are used to find intermolecular contacts between the individual molecules in the supramolecular assembly. These results, together with those obtained in the previous chapter, are then used to hypothesise a model for the structure and organisation of the supramolecular assembly. The model takes into account the expected biological mechanism of this group of CLP molecules, namely the formation of ion pores in cellular membrane bilayers.

The seventh chapter, ***Heteronuclear relaxation study of pseudodesmin A***, mainly $^{13}C^{\alpha}$ relaxation is used to study both the monomer (acetonitrile solution) and oligomer forms (chloroform solution at different concentrations) of pseudodesmin A. The obtained relaxation rate constants allow an assessment to be made of the size and anisotropy of the supramolecular structure. The strategy that is employed to achieve this is described in detail. The results provide strong arguments in favour of the previously proposed model.

In the eighth and final chapter, ***Relaxation rate constant behaviour under self-association conditions***, the impact of the self-association on the behaviour of the relaxation rate constants is explored using simulations. These provide a qualitative explanation of apparent discrepancies between the different experimental relaxation rate constants that were observed for pseudodesmin A in chloroform. Some theory is provided concerning indefinite self-association models, which is then subsequently used in the simulations. An attempt is made to find a self-association model that explains the data quantitatively and provides an idea of the distribution of oligomer sizes at each concentration.

Finally, the main results of this work are reiterated in the ***General conclusion*** section.

Part 1:

Diffusion and NMR

1 Diffusion

1.1. Introduction

The physical phenomenon of diffusion plays an important role in solution NMR spectroscopy. Rotational diffusion is the main driving force to relaxation, the process with which the NMR signal disappears and the thermodynamic equilibrium is restored. The rotational diffusion properties of a molecular species therefore strongly influence the efficiency of this process. On the other hand, translational diffusion can have a strong impact on the NMR signal intensity when magnetic field gradients are present. As such, NMR spectroscopy provides the possibility to study both these diffusion processes in detail. In turn, studying diffusion leads to information concerning the size and shape of the molecular species through the diffusion coefficient, which reflects the ease with which diffusion takes place.

In this chapter, the physical phenomenon of diffusion will be discussed, both translational (section 1.2) and rotational (section 1.3). The diffusion coefficient and how it is linked to the molecular dimensions is the subject of section 1.4. In the chapters that follow, the concepts that were introduced here will be used to show how diffusion affects NMR spectroscopy, both by translational diffusion (chapter 2) and rotational diffusion (chapter 3).

1.2. Brownian motion and translational diffusion

Brownian motion is a natural phenomenon where particles or molecules without any external force exerted upon them experience a seemingly random (or stochastic) movement. This happens spontaneously to any molecule or particle that is dissolved or suspended in a liquid, a gas and even within a solid phase. The first independent reports of this observation occurred between the late 18^{th} and early 19^{th} century. However, it is the Scottish botanist Robert Brown in 1827 whom is generally credited

for the discovery of the phenomenon that now carries his name. While studying the structure of grains of pollen with a microscope[1], he noticed the pollen changed their relative positions and even turned over their own axis. He performed several experiments, where he confirmed that the motion was an inherent property of the particle and that the same motions occurred on any particle that he was able to suspend in water. He did not only study organic particles, but also inorganic powders of glass, metals and minerals (even a fragment of the Sphinx was included in his study). He estimated that the diameter of all these particles ranged between 1/30,000 to 1/20,000 of an inch (about 0.85 – 1.27 µm).

The mathematics of Brownian motion was described later in the 19th century (*cf*. the random walk), but it was Albert Einstein[2] whom in 1905 convincingly showed that this motion is a consequence of the molecular kinetic theory of heat, which at the time was still under debate. This theory predicts that the small solvent molecules are moving randomly through space due to their translational thermal energy, possessing a distribution of velocities. The solute particles randomly experience collisions with these solvent molecules, effectively creating a motion in a random direction. In other words, the particles are being pushed around. Einstein was also able to link the root mean square displacement of the particles to the frictional drag they experience within the solution (via the diffusion coefficient, see section 1.4).

When by means of Brownian motion the movement of several solute molecules is considered, it is generally called diffusion. When the distribution of solute molecules is non-uniform over a certain range of space, *i.e.* concentration differences exist over the sample, diffusion will cause a spontaneous net transport of the solute molecules from the higher towards the lower concentration regions until the concentration is uniform. Even before it was fully understood that the molecular mechanism of this process is in fact linked to Brownian motion, the theory of diffusive transport processes was already developed in 1855 by physiologist Aldolf Fick, the key aspects of which will be given here.

Define the flux $\mathbf{J}$ as the number of solute molecules that pass through a unit surface area during a unit time. This can also be expressed as the product of the concentration c and the particle velocity $\mathbf{v}$:

$$\mathbf{J}(x,y,z) = \mathrm{c}(x,y,z)\,\mathbf{v}(x,y,z) \tag{1.1}$$

Fick established an empirical relation between this flux and the gradient of the concentration (the degree and direction in which the concentration changes). This is known as Fick's first law[3]:

$$\mathbf{J}(x,y,z) = -D_t \nabla \mathrm{c}(x,y,z) = -D_t \left(\frac{\partial}{\partial x}\mathbf{e}_x + \frac{\partial}{\partial y}\mathbf{e}_y + \frac{\partial}{\partial z}\mathbf{e}_z \right) \mathrm{c}(x,y,z) \tag{1.2}$$

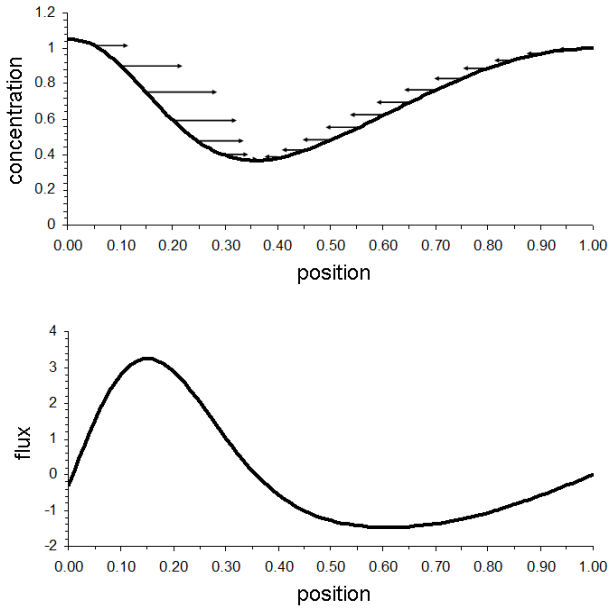

Figure 1.1: The upper graph shows an example of a one dimensional concentration profile that undergoes diffusion. The flux (lower graph) is proportional to the first derivative of this profile. The arrows in the first graph indicate the size and direction of the flux at each position, clearly showing how diffusion attempts to flatten the concentration profile over time.

with ∇ the gradient operator. This equation shows that the net movement (flux) of solute molecules at a certain position will be in the direction where the concentration is the most strongly decreasing and that the size of the flux is proportional to the degree in which the concentration decreases in this direction. This is illustrated in Figure 1.1 for the case of diffusion in only one dimension. D_t is the translational diffusion coefficient, a proportionality constant that depends on the size and shape of the solute molecule and on the temperature and viscosity of the solution (see section 1.4).

It is already clear from Fick's first law that diffusion will ensure that over time the concentration differences will fade away as solute molecules are transported from high concentration regions to lower concentration regions, spreading the molecules evenly over the available space. The concentration gradient is thus the driving force of the diffusion transport process, driving the molecules towards an evenly distributed situation and thus a thermodynamic state of maximum entropy. How exactly the concentration at a certain position changes over time is described in Fick's second law, which follows easily from the first law combined with the principle of conservation of number of molecules[3]:

$$\frac{\partial \mathrm{c}(x,y,z,t)}{\partial t} = D_t \nabla^2 \mathrm{c}(x,y,z,t) = D_t \left(\frac{\partial^2}{\partial x^2} + \frac{\partial^2}{\partial y^2} + \frac{\partial^2}{\partial z^2} \right) \mathrm{c}(x,y,z,t) \tag{1.3}$$

with ∇^2 the Laplacian operator. A similar result was also found by Einstein for the Brownian motion of one particle[2], where $\mathrm{c}(x,y,z)$ would then represent the probability distribution of finding the particle at a position (x,y,z) at time t. The solution to this partial differential equation provides the concentration as a function of both position and time if sufficient boundary conditions are imposed. Alternatively, if the concentration profile at one certain time is known, then through this equation the

evolution of this profile over time can be calculated[4]. This can be shown by use of a known mathematical property of the Fourier transformation applied on any continuous function $\mathrm{H}(x)$ for which $\mathrm{H}(\pm\infty) = 0$:

$$\mathrm{FT}\left[\frac{d\mathrm{H}(x)}{dx};\omega\right] = i\omega\,\mathrm{FT}\left[\mathrm{H}(x);\omega\right] \tag{1.4}$$

Where $\mathrm{FT}[\mathrm{H}(x);\omega]$ denotes the Fourier transform operation from the x domain to the ω domain applied on $\mathrm{H}(x)$. Assume for simplicity a concentration distribution along only one spatial dimensional $\mathrm{c}(x,t)$ and assume that the molecules are able to diffuse without restriction (*cf.* within the spatial interval $[-\infty,+\infty]$), then Fick's second law (1.3) is reduced to:

$$\frac{\partial\,\mathrm{c}(x,t)}{\partial t} = D_t\,\frac{\partial^2\,\mathrm{c}(x,t)}{\partial x^2} \tag{1.5}$$

Assuming $\mathrm{k}(\omega,t)$ to be the Fourier transform of $\mathrm{c}(x,t)$, and using (1.4), (1.5) can be rewritten as:

$$\frac{\partial\,\mathrm{k}(\omega,t)}{\partial t} = -\omega^2 D_t\,\mathrm{k}(\omega,t) \tag{1.6}$$

The solution to this differential equation is straightforward, assuming that $\mathrm{c}(x,t_0)$ is known (and thus also $\mathrm{k}(\omega,t_0)$):

$$\mathrm{k}(\omega,t) = \mathrm{k}(\omega,t_0)\,e^{-D_t\omega^2(t-t_0)} \tag{1.7}$$

Applying the inverse Fourier transform operation IFT to this equation an expression for $\mathrm{c}(x,t)$ is obtained:

$$\begin{aligned}\mathrm{c}(x,t) &= \mathrm{IFT}\left[\mathrm{k}(\omega,t)\right]\\ &= \mathrm{IFT}\left[\mathrm{FT}\left[\mathrm{c}(x,t_0)\right]e^{-D_t\omega^2(t-t_0)}\right]\\ &= \frac{1}{2\pi}\int_{-\infty}^{+\infty}\left(\int_{-\infty}^{+\infty}\mathrm{c}(x,t_0)\,e^{-i\omega x}dx\right)e^{-D_t\omega^2(t-t_0)}e^{i\omega x}d\omega\end{aligned} \tag{1.8}$$

So if at any time t_0 the concentration distribution is exactly known, the concentration distribution at any other time is easily calculated. As a side note, consider the physical meaning of the Fourier transform of a function. It is the distribution of the weights that is put on a continuous set of cosine and sine functions with frequencies

ω whose sum perfectly describes the original function (*cf.* Fourier expansion). Equation (1.7) then shows that diffusion in fact first attenuates the higher frequency components of the concentration distribution, as the attenuation exponential term in (1.7) contains ω^2. One could say that the most detailed or "fine structured" aspects of a distribution, which are described by these higher frequency components, are removed the earliest by diffusion. Thus diffusion progressively makes the distribution smoother over time. This idea is similar and thus relevant to understand the "ill-posed problem" concept in diffusion NMR data processing later on[4] (see section 2.5.1)

As an example, assume that at a time $t_0 = 0$ all molecules are located at the same position $x = x_0$. To put it in mathematical terms, the concentration distribution is a delta function:

$$\mathrm{c}(x,0) = C_0\delta(x - x_0) \tag{1.9}$$

In which C_0 is the total analytical concentration. The concentration distribution at any time $t > 0$ can then be calculated using (1.8):

$$\begin{aligned}\mathrm{c}(x,t) &= \frac{1}{2\pi}\int_{-\infty}^{+\infty}\left(\int_{-\infty}^{+\infty} C_0\delta(x - x_0)e^{-i\omega x}dx\right)e^{-D_t\omega^2 t}e^{i\omega x}d\omega \\ &= \frac{C_0}{2\pi}\int_{-\infty}^{+\infty} e^{-D_t\omega^2 t}e^{i\omega(x-x_0)}d\omega \\ &= \frac{C_0}{\sqrt{4\pi t}}e^{-\frac{(x-x_0)^2}{4D_t t}}\end{aligned} \tag{1.10}$$

This shows that the molecules will diffuse from x_0 according to a Gaussian distribution (Figure 1.2). The average position of the molecules remains constant, always remaining x_0, however the root mean square displacement from their initial position is proportional to the square root of time:

$$\sqrt{\left\langle (x - x_0)^2 \right\rangle} = \sqrt{2D_t t} \tag{1.11}$$

In the general case for three dimensions this becomes, with R the displacement of a molecule from its initial position:

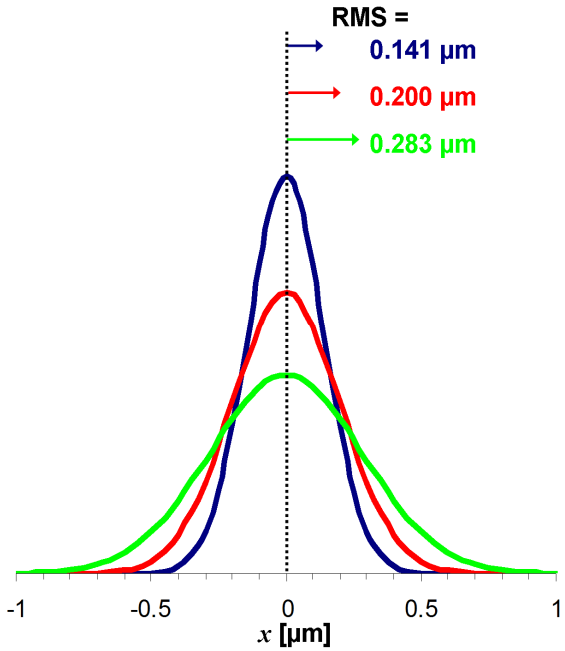

Figure 1.2: Illustration of free translational diffusion according to equation (1.10). All molecules start out at $x = 0$ µm at time $t = 0$ and have a diffusion coefficient of 100 µm^2/s. The diffusion concentration profiles are shown after a time of 100 µs (blue), 200 µs (red) and 400 µs (green). The corresponding root mean square (RMS) displacement is indicated.

coefficient and the time t in the same way.

$$\sqrt{\langle R^2 \rangle} = \sqrt{6D_t t} \tag{1.12}$$

Note that this result is valid independent of the initial distribution. The proportionality with $t^{1/2}$ and not with t is a consequence of the stochastic nature of the Brownian motion. Because the molecule is moving in several directions and velocities during a time t, it will on average have displaced less far than would have been expected if it moved in one direction and at its average velocity only.

As a final note, for the Brownian movement of one particle, a similar result as (1.10) is found by Einstein[2], where the probability distribution of finding the particle at a position x at time t is also a Gaussian, related to the diffusion

1.3. Brownian rotational and rotational diffusion

Until now, only translational Brownian motion and diffusion has been considered. However, also rotational Brownian motion exists: collisions of a molecule with other molecules will also change the velocity and direction of its rotational movement. After a certain time, a molecule will have assumed a new, random orientation. A collection of molecules will therefore assume a distribution of orientations relative to their initial orientation. This is then called rotational diffusion. Because of its impact on NMR relaxation and its importance in the rest of this dissertation, this phenomenon will be described further in detail.

For an anisotropic molecule, rotations about different axes generally do not proceed with the same moment of inertia. To account for this, rotational diffusion needs to be described by use of a rotational diffusion tensor:

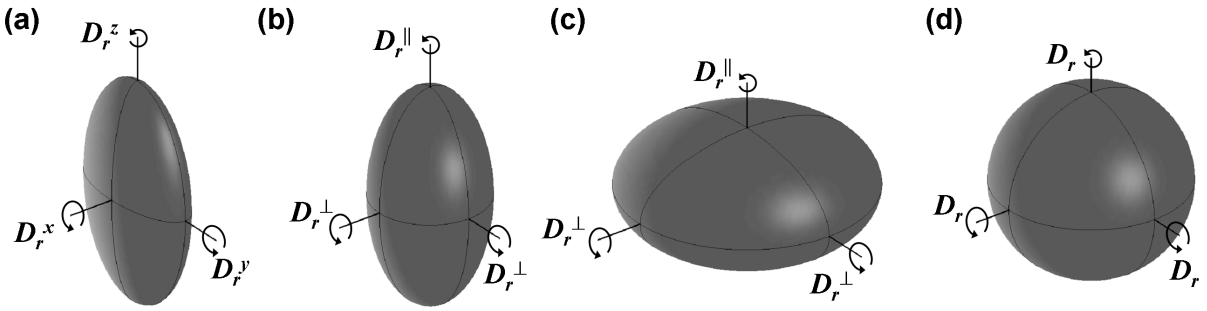

Figure 1.3: Illustration of the different possible situations for rotational diffusion. (a) Full anisotropy with three unique rotational diffusion coefficients, represented by an ellipsoid with three different semiaxes. (b) Axial symmetric anisotropy with two unique rotational diffusion coefficients, represented by a prolate ellipsoid. (c) Same as in (b), but now an oblate ellipsoid. (d) Isotropic object with only one unique rotational diffusion coefficient, represented by a sphere.

$$\mathbf{D_r} = \begin{bmatrix} D_{xx} & D_{xy} & D_{xz} \\ D_{yx} & D_{yy} & D_{yz} \\ D_{zx} & D_{zy} & D_{zz} \end{bmatrix} \tag{1.13}$$

The eigenvectors of this tensor form the frame of reference in which the tensor is reduced to a diagonal matrix. These eigenvectors constitute the principal axes of the molecule. The rotational diffusion around one of these principal axes is then determined by a single rotational diffusion coefficient, given by the corresponding eigenvalue of the tensor. Therefore, the rotational diffusion of a full anisotropic molecule can be described by rotations about only these three principal axes, each with a unique rotational diffusion coefficient (here labelled as D_r^x, D_r^y and D_r^z). When the molecular shape possesses an axial symmetry (*e.g.* a prolate or oblate ellipsoid, a cylinder, a disc), one of the principal axes will be oriented along this symmetry axis, while the direction of the two other axes will no longer be uniquely defined. Consequently only two unique rotational diffusion coefficients are required. These are labelled $D_r^{\parallel}$ for rotation around the axial symmetry axis and $D_r^{\perp}$ for rotation around an axis perpendicular to the axial symmetric axis. When the shape of the molecule has a spherical symmetry, there are no unique principal axes (the tensor is diagonal within each reference frame), and only one rotational diffusion coefficient D_r is needed. In this case, the rotational diffusion is said to be isotropic. These different cases are illustrated in Figure 1.3.

The properties of rotational diffusion are similar as for translational diffusion. The root mean square angular displacements around each principal axis are given by:

$$\sqrt{\left\langle (\alpha-\alpha_0)^2 \right\rangle} = \sqrt{2D_r^x t}$$
$$\sqrt{\left\langle (\beta-\beta_0)^2 \right\rangle} = \sqrt{2D_r^y t} \qquad (1.14)$$
$$\sqrt{\left\langle (\gamma-\gamma_0)^2 \right\rangle} = \sqrt{2D_r^z t}$$

with α, β and γ the Euler angles, which represent the amount of rotation around each principle axis. Also these displacements are uncorrelated with each other

$$\left\langle (\alpha-\alpha_0)(\beta-\beta_0) \right\rangle = \left\langle (\alpha-\alpha_0)(\gamma-\gamma_0) \right\rangle = \left\langle (\beta-\beta_0)(\gamma-\gamma_0) \right\rangle = 0 \qquad (1.15)$$

In what follows, a derivation will be done of the probability distribution P of the new orientation at a time t of a particle undergoing rotational Brownian motion, given its original orientation. This will be done for the simple isotropic case, while afterwards the anisotropic case will be briefly discussed. For the isotropic case, Fick's second law (1.3) can be rewritten in spherical coordinates[5], with the laplacian ∇^2 only containing its angular part:

$$\frac{\partial \mathrm{P}(\theta,\phi,t)}{\partial t} = D_r \nabla^2 \mathrm{P}(\theta,\phi,t) = D_r \left[\frac{\partial^2}{\partial \theta^2} + \frac{1}{\tan\theta}\frac{\partial}{\partial \theta} + \frac{1}{\sin^2\theta}\frac{\partial^2}{\partial \phi^2} \right] \mathrm{P}(\theta,\phi,t) \qquad (1.16)$$

Here θ and ϕ are respectively the polar and azimuth angles of a vector (for example a CH bond) attached to the isotropic molecule. These angles fully represent the orientation of the vector, and will be written as $(\theta,\phi) = \Omega$. Assume that $\mathrm{P}(\Omega,t)$ can be split into a spatial and a time dependent function

$$\mathrm{P}(\Omega,t) = \mathrm{g}(t)\,\mathrm{h}(\Omega) \qquad (1.17)$$

It is assumed that $\mathrm{P}(\Omega,0) = \mathrm{h}(\Omega)$, so that $\mathrm{g}(0) = 1$. Then (1.16) can be rearranged to achieve a separation of variables:

$$\frac{1}{D_r\,\mathrm{g}(t)}\frac{\partial \mathrm{g}(t)}{\partial t} = \frac{1}{\mathrm{h}(\Omega)}\nabla^2 \mathrm{h}(\Omega) = \lambda \qquad (1.18)$$

with λ a constant, since the equality must hold for every value of Ω and t. This results in two separate differential equations:

$$\frac{\partial \mathrm{g}(t)}{\partial t} = \lambda D_r\,\mathrm{g}(t) \qquad (1.19)$$
$$\nabla^2 \mathrm{h}(\Omega) = \lambda\,\mathrm{h}(\Omega) \qquad (1.20)$$

The possible solutions to (1.20) are the eigenfunctions of ∇^2, which are the well known spherical harmonic functions $\mathrm{Y}_l^m(\Omega)$, and λ the corresponding eigenvalues:

$$\begin{aligned} \mathrm{h}(\Omega) &= \mathrm{Y}_l^m(\Omega) \\ \lambda &= -l(l+1) \end{aligned} \tag{1.21}$$

with:

$$\begin{aligned} l &= 0,1,2,3,... \\ m &= -l,-l+1,...,l-1,l \end{aligned} \tag{1.22}$$

Expressions for the spherical harmonic functions are included in appendix A. The solution to (1.19) is straightforward, taking into account the result for λ from (1.21):

$$\mathrm{g}(t) = \mathrm{g}(0)e^{\lambda D_r t} = e^{-l(l+1)D_r t} \tag{1.23}$$

The general solution for $\mathrm{P}(\Omega,t)$ is then given by a linear combination of all possible solutions for $\mathrm{h}(\Omega)$ (for every value of l and m) combined with $\mathrm{g}(t)$.

$$\begin{aligned} \mathrm{P}(\Omega,t) &= \sum_{l=0}^{+\infty}\left[\sum_{m=-l}^{l} c_{lm}\,\mathrm{Y}_l^m(\Omega)\right]e^{-l(l+1)D_r t} \\ &= c_{00}\,\mathrm{Y}_0^0(\Omega) \\ &+\left[c_{1-1}\,\mathrm{Y}_1^{-1}(\Omega)+c_{10}\,\mathrm{Y}_1^0(\Omega)+c_{11}\,\mathrm{Y}_1^1(\Omega)\right]e^{-2D_r t} \\ &+\left[c_{2-2}\,\mathrm{Y}_2^{-2}(\Omega)+c_{2-1}\,\mathrm{Y}_2^{-1}(\Omega)+c_{20}\,\mathrm{Y}_2^0(\Omega)+c_{21}\,\mathrm{Y}_2^1(\Omega)+c_{22}\,\mathrm{Y}_2^2(\Omega)\right]e^{-6D_r t} \\ &+... \end{aligned} \tag{1.24}$$

The coefficients c_{lm} are defined by the initial distribution function $\mathrm{P}(\Omega,0)$ and can be obtained by using the orthogonal properties of the spherical harmonics together with (1.24) (with the integral taken over all values of Ω):

$$c_{lm} = \int \mathrm{Y}_l^{m*}(\Omega)\,\mathrm{P}(\Omega,0)\,d\Omega \tag{1.25}$$

The interpretation of (1.24) is similar to the case of translational diffusion. In equation (1.8), the initial distribution function is first expanded into sine and cosine functions with a continuous distribution of different frequencies (Fourier transform) and afterwards the different functions (frequency components) decay with time with different rates (expressed in the $e^{-D_t\omega^2 t}$ term). Here, the initial distribution function is again first expanded in terms of a set of basis functions (the spherical harmonics)

which then decay with different rates (the $e^{-l(l+1)D_r t}$ term). Note that the first term in (1.24) represents a uniform distribution over all orientations (since $\mathrm{Y}_0^0(\Omega) = (4\pi)^{-1/2}$), while all other terms represent the deviation from this uniform distribution. Only the latter terms decay over time and thus the rotational Brownian motion has the effect of removing this deviation in favour of a uniform distribution.

It was assumed that the initial orientation of the molecule is at $\Omega = \Omega_0$, and therefore $\mathrm{P}(\Omega,0)$ is defined by the delta function $\delta(\Omega-\Omega_0)$, providing the coefficients c_{lm}:

$$\begin{aligned} c_l^m &= \int \mathrm{Y}_l^{m*}(\Omega)\,\delta(\Omega-\Omega_0)\,d\Omega \\ &= \mathrm{Y}_l^{m*}(\Omega_0) \end{aligned} \tag{1.26}$$

$$\Rightarrow \mathrm{P}(\Omega,t) \equiv \mathrm{P}(\Omega_0,\Omega,t) = \sum_{l=0}^{+\infty}\left[\sum_{m=-l}^{l} \mathrm{Y}_l^{m*}(\Omega_0)\,\mathrm{Y}_l^m(\Omega)\right] e^{-l(l+1)D_r t}$$

It is this function which will later be required to understand the impact of rotational diffusion in NMR relaxation. As shall be discussed later (section 3.3.3), for the NMR relaxation mechanisms that will be discussed, only the spherical harmonics with $l = 2$ are important, and thus only the decay rate of $6D_r$. The correlation time constant is defined as:

$$\tau = \frac{1}{6D_r} \tag{1.27}$$

These results represent the case of isotropic rotational diffusion. For completeness, and because the rotational diffusion of anisotropic molecules play an important role in this dissertation, the partial differential equations describing anisotropic Brownian rotational motion are provided, as derived by Francis Perrin[6]. Here, the orientation of the molecule is described in terms of the Euler angles α, β and γ:

$$\begin{aligned} \frac{\partial \mathrm{P}(\alpha,\beta,\gamma,t)}{\partial t} &= \left(D_r^x \cos^2\gamma + D_r^y \sin^2\gamma\right)\frac{\partial^2 \mathrm{P}}{\partial \alpha^2} \\ &\quad + \left(D_r^x \sin^2\gamma + D_r^y \cos^2\gamma\right)\left(\frac{1}{\tan\alpha}\frac{\partial \mathrm{P}}{\partial \alpha} + \frac{1}{\sin^2\alpha}\frac{\partial^2 \mathrm{P}}{\partial \beta^2}\right. \\ &\quad \left. + \frac{1}{\tan^2\alpha}\frac{\partial^2 \mathrm{P}}{\partial \gamma^2} - 2\frac{\cos\alpha}{\sin^2\alpha}\frac{\partial^2 \mathrm{P}}{\partial \beta \partial \gamma}\right) + D_r^z \frac{\partial^2 \mathrm{P}}{\partial \gamma^2} \end{aligned} \tag{1.28}$$

When an axial symmetric molecule is considered, $D_r^x = D_r^y = D_r^\perp$ and $D_r^z = D_r^\parallel$. In addition, the probability of a rotation β and a rotation γ becomes equivalent, so that with $\nu = \beta + \gamma$, (1.28) simplifies to:

$$\frac{\partial \mathrm{P}(\alpha,\nu,t)}{\partial t} = D_r^\perp \left(\frac{\partial^2 \mathrm{P}}{\partial \alpha^2} + \frac{1}{\tan\alpha}\frac{\partial \mathrm{P}}{\partial \alpha} \right) + \left(D_r^\perp \frac{1-\cos\alpha}{1+\cos\alpha} + D_r^\parallel \right) \frac{\partial^2 \mathrm{P}}{\partial \nu^2} \tag{1.29}$$

The latter equation was solved by Perrin[6], yielding the result:

$$\mathrm{P}(\alpha,\nu,t) = \frac{1}{4\pi} \sum_{m=0}^{\infty} \sum_{n=0}^{\infty} \mathrm{Q}_{mn}(\alpha,\nu)\, e^{-\left[(m+n(2m+n+1))D_r^\perp + m^2 D_r^\parallel\right]t} \tag{1.30}$$

with Q_{mn} a rather complex function:

$$\begin{aligned} Q_{mn}(\alpha,\nu) = {} & \frac{q_m (-1)^n (2n+2m+1)}{2^n n!} \frac{\cos(m\nu)\cos^{2m}\left(\frac{\alpha}{2}\right)}{(1+\cos\alpha)^{2m}} \\ & \times \left\{ \frac{d^n}{d(\cos\alpha)^n} \left[(1+\cos\alpha)^{2m} \left(1+\cos^2\alpha\right)^n \right] \right\} \end{aligned} \tag{1.31}$$

and $q_m = 1$ for $m = 0$ and $q_m = 2$ otherwise. Again, the distribution function is expressed as a superposition of several base functions each decaying with separate rates. For NMR relaxation, only the decay rates with $m + n = 2$ are relevant. Thus, in the case of axial symmetric rotational diffusion, there are in fact three NMR correlation time constants, defined by:

$$\tau_A = \frac{1}{6D_r^\perp} \tag{1.32}$$

$$\tau_B = \frac{1}{5D_r^\perp + D_r^\parallel} \tag{1.33}$$

$$\tau_C = \frac{1}{2D_r^\perp + 4D_r^\parallel} \tag{1.34}$$

1.4. The diffusion coefficient

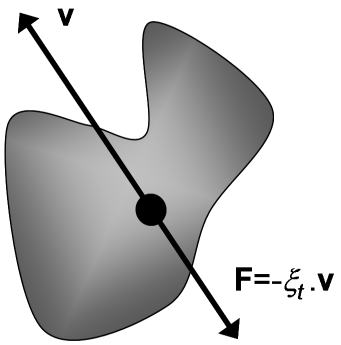

Figure 1.4: When an object moves with a speed **v** through a medium, it experiences a frictional force **F** in the opposite direction with a proportionality constant ξ_t.

The diffusion coefficient determines the rate at which the Brownian motion takes place, and were introduced earlier as proportionality constants in the equation that describe translational (1.2) and rotational diffusion (1.16). What determines their value? An expression for the translational diffusion coefficient was derived independently by Albert Einstein[2] and Marian Smoluchowski[7]. They derived that there is a simple relationship with the friction coefficient ξ_t of the molecule in the solvent (Figure 1.4):

$$D_t = \frac{k_B T}{\xi_t} \tag{1.35}$$

where k_B is the Boltzmann constant. The friction coefficient depends on the size and shape of the molecule, and on the solvent viscosity. For example, George Gabriel Stokes showed that the friction coefficient for translational motion of a sphere with radius R in a fluid with dynamic viscosity η is given by:

$$\xi_t = 6\pi\eta R \tag{1.36}$$

The combination of (1.35) and (1.36) is known as the Stokes-Einstein relation:

$$D_t = \frac{k_B T}{6\pi\eta R} \tag{1.37}$$

Stokes' derivation assumed that the interaction with the solvent is sufficiently strong so that the layer of fluid at the surface of the sphere moves with the same speed as the sphere, the so-called stick boundary condition[8]. When this assumption does not hold, the friction coefficient will be lower. In the most extreme case of no interaction with the solvent (the fluid 'slips' along the sphere), the friction coefficient becomes

$$\xi_t = 4\pi\eta R \tag{1.38}$$

This is known as the slip boundary condition. In this dissertation, the stick boundary condition will always be assumed. The Stokes-Einstein relation is very often used to get an idea of the size of a molecule through its experimentally measured translational diffusion coefficient. The value for the radius obtained is then called the Stokes radius or hydrodynamic radius R_H:

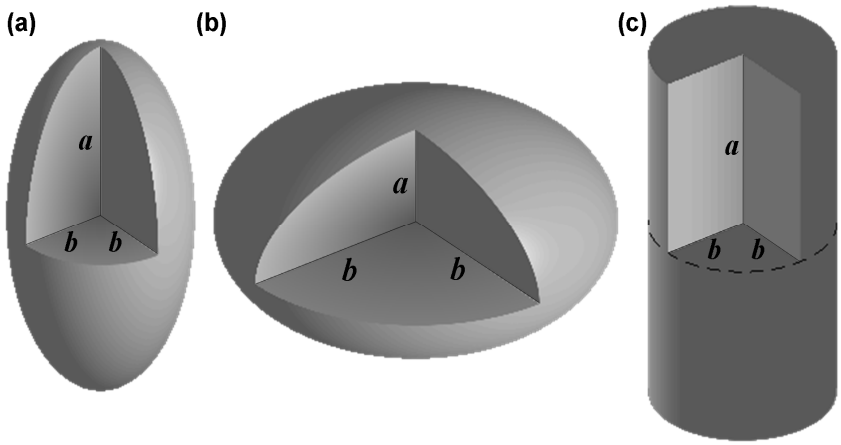

Figure 1.5: Definitions of the a and b semiaxes in axially symmetric objects: (a) prolate ellipsoid ($a/b > 0$); (b) oblate ellipsoid ($a/b < 0$); (c) cylinder.

$$R_H = \frac{k_B T}{6\pi\eta D_t} \tag{1.39}$$

However, for significantly anisotropic molecules the shape is badly approximated by a sphere. In such cases, the friction coefficient will generally be higher than that of a sphere with the same volume, thus leading to an overestimation of the molecular size when (1.39) is used.

Another shape often assumed for a (macro)molecule is that of an axially symmetric ellipsoid. Francis Perrin has derived the frictional coefficients of both prolate and oblate ellipsoids[9, 10]. With a and b being the semiaxes directed along and perpendicular to the axial symmetry axis respectively (Figure 1.5), and p the axial ratio ($p = a/b$), the friction coefficients are given by:

$$\begin{aligned} \xi &= \xi_{t0} \frac{\sqrt{p^2-1}}{p^{1/3} \ln\left(p+\sqrt{p^2-1}\right)} \\ &= \frac{6\pi\eta a \sqrt{p^2-1}}{p \ln\left(p+\sqrt{p^2-1}\right)} \end{aligned} \tag{1.40}$$

(for a prolate ellipsoid, $p > 1$)

$$\xi = \xi_{t0} \frac{\sqrt{1-p^2}}{p^{1/3} \arctan\left(\frac{\sqrt{1-p^2}}{p}\right)} = \frac{6\pi\eta a\sqrt{1-p^2}}{p \arctan\left(\frac{\sqrt{1-p^2}}{p}\right)} \quad \text{(for an oblate ellipsoid, } p < 1\text{)} \tag{1.41}$$

In these equations, ξ_{t0} is the friction coefficient of a sphere with the same volume as the ellipsoid, given by:

$$\xi_{t0} = 6\pi\eta\left(\frac{3V}{4\pi}\right)^{1/3} = 6\pi\eta\left(ab^2\right)^{1/3} = \frac{6\pi\eta a}{p^{2/3}} \tag{1.42}$$

The ratio ξ_t/ξ_{t0} represents the effect of the anisotropy on the translational friction coefficient and depends only on p. This is shown in Figure 1.6a. For small degrees of anisotropy the effect on the friction coefficient is limited, being for example only about 4% for axial ratios of 0.5 or 2. However, when comparing the actual size of the molecule (taken as the longest semiaxis) and the Stokes radius calculated through (1.39) for varying p values as shown in Figure 1.7, it is clear that a significant inaccuracy is introduced by the anisotropy, especially for prolate shapes. For example an ellipsoid with $p = 2$ and $a = 15.9$ Å (and thus $b = 7.9$ Å) leads to a Stokes radius of only 10.4 Å.

It should be noted that in fact the friction of translational movement for axially symmetric ellipsoids depends along which axis the movement occurs. However, since in solution the molecules are distributed evenly over all possible orientations, only a single averaged out diffusion coefficient is measured in all directions unless some form of alignment is present. This is the reason why anisotropy does not have such a strong effect in translational diffusion as in rotational diffusion. Also, information concerning the shape of a molecule cannot be obtained from the translational diffusion coefficient alone, as a larger D_t can be interpreted as either an increased size or a more anisotropic structure. Even if it is known that the molecule is anisotropic, the information the diffusion coefficient provides is insufficient as two semiaxes (or three in the case of full anisotropy) cannot be acquired out of a single experimental value. When rotational diffusion is studied on the other hand, it is possible to directly make the connection to anisotropy, since multiple experimental rotational diffusion coefficients can be obtained, for example from NMR relaxation data.

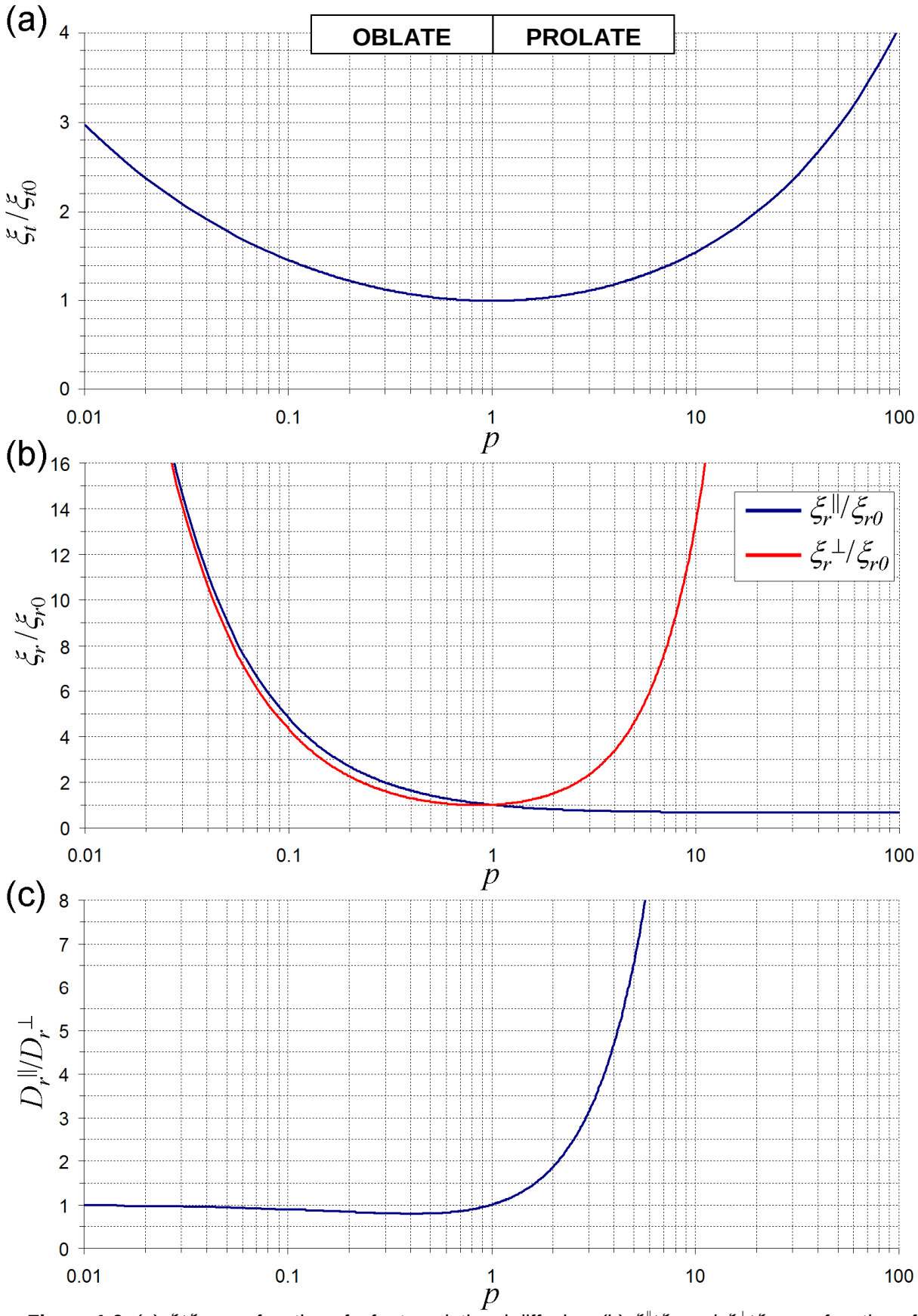

Figure 1.6: (a) ξ_t/ξ_{r0} as a function of p for translational diffusion. (b) $\xi_r^{\parallel}/\xi_{r0}$ and $\xi_r^{\perp}/\xi_{r0}$ as a function of p for axially symmetric rotational diffusion. (c) $D_r^{\parallel}/D_r^{\perp}$ (= $\xi_r^{\perp}/\xi_r^{\parallel}$) as a function of p for axially symmetric rotational diffusion; note that this ratio allows to obtain p independent of the total volume of the molecule (reflected in ξ_{r0})

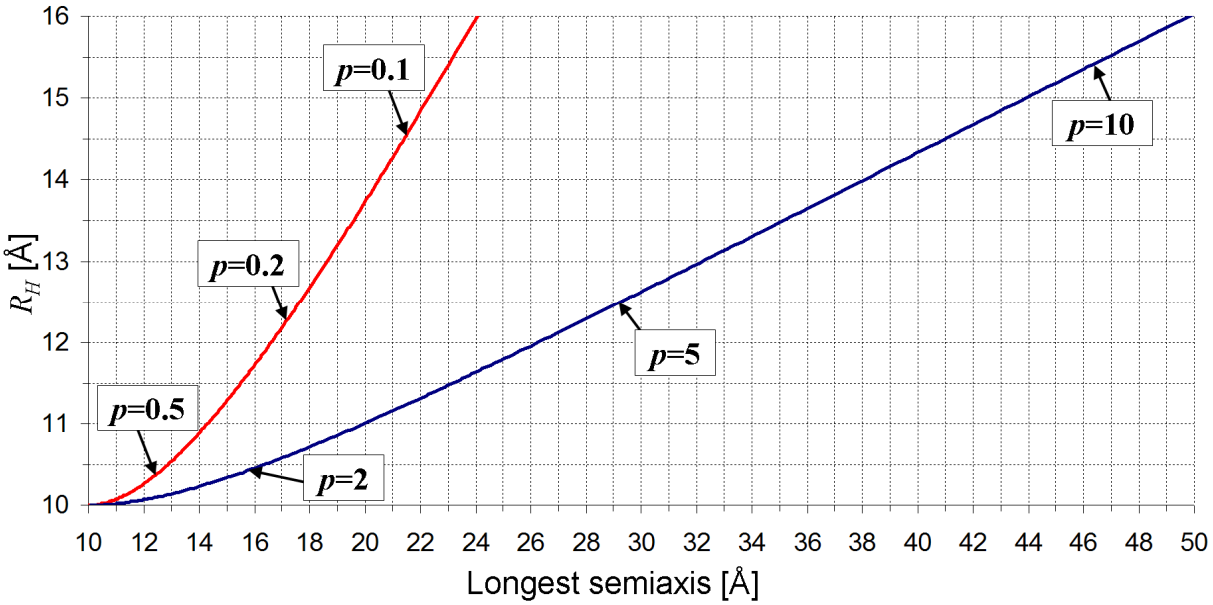

Figure 1.7: Stokes radius as a function of the longest semiaxis in a prolate (blue) or oblate (red) ellipsoid for varying values of p and constant volume. At p = 1, a sphere is assumed with 10 Å radius.

Rotational diffusion coefficients are linked to the friction coefficient of rotation ξ_r in exactly the same way as the translational diffusion coefficients were in equation (1.35). Peter Debye was the first to present the expression for the rotational diffusion coefficient of a spherical object[11], which is known as the Debye-Einstein relation:

$$D_r = \frac{k_B T}{\xi_r} = \frac{k_B T}{8\pi\eta R^3} = \frac{k_B T}{6\eta V} \tag{1.43}$$

The main difference with the Stokes-Einstein relation for translational diffusion coefficients is the dependence on R^3 and thus on the volume V of the sphere rather than R. Again this assumes the stick boundary condition. For slip boundary conditions, the rotational friction coefficient approaches 0. Just as for translational diffusion coefficients, Francis Perrin has derived the expressions for the two rotational friction coefficients of oblate and prolate ellipsoids[9, 10]:

$$\xi_r^{\parallel} = \xi_{r0}\frac{4\left(p^2-1\right)}{3\left(2p^2-S\right)} = \frac{32\pi\eta a^3\left(p^2-1\right)}{3p^2\left(2p^2-S\right)} \tag{1.44}$$

$$\xi_r^{\perp} = \xi_{r0}\frac{4\left(p^4-1\right)}{3\left(S\left(2p^2-1\right)-2p^2\right)} = \frac{32\pi\eta a^3\left(p^4-1\right)}{3p^2\left(S\left(2p^2-1\right)-2p^2\right)} \tag{1.45}$$

in which S is a function of p and ξ_{r0} is the friction coefficient of a sphere with the same volume as the ellipsoids:

$$S = \frac{2p}{\sqrt{p^2 - 1}} \ln\left(p + \sqrt{p^2 - 1}\right) \tag{1.46}$$

(for a prolate ellipsoid, $p > 1$)

$$S = \frac{2p}{\sqrt{1 - p^2}} \arctan\left(\frac{\sqrt{1 - p^2}}{p}\right) \tag{1.47}$$

(for an oblate ellipsoid, $p < 1$)

$$\xi_{r0} = 8\pi\eta\left(\frac{3V}{4\pi}\right) = 8\pi\eta ab^2 = 8\pi\eta\frac{a^3}{p^2} \tag{1.48}$$

The effect of varying p on the ratios $\xi_r^{||}/\xi_{r0}$, $\xi_r^{\perp}/\xi_{r0}$ and $D_r^{||}/D_r^{\perp}$ (= $\xi_r^{\perp}/\xi_r^{||}$) is shown in Figure 1.6b and c. In the case of oblate ellipsoids, both friction coefficients increase quite strongly upon decreasing p when compared to ξ_{r0}. $\xi_r^{||}$ is always slightly larger than $\xi_r^{\perp}$, however this difference is only significant for axial ratios between 0.1 and 0.9, with an optimum around 0.4 at which $\xi_r^{\perp}/\xi_r^{||} \approx 0.8$. In the case of prolate ellipsoids, $\xi_r^{\perp}/\xi_{r0}$ increases very strongly with p, while $\xi_r^{||}/\xi r_0$ decreases only slightly and then stays levelled.

Just as for translational diffusion, molecular anisotropy has a strong effect on the values of the rotational diffusion coefficients. However, because both rotational friction coefficients vary differently with p, it is possible to unambiguously identify anisotropy by use of the ratio $D_r^{||}/D_r^{\perp}$ (except for oblate ellipsoids with $p << 1$) and obtain the lengths of both semiaxes using the absolute values of the diffusion coefficients.

An alternative for axially symmetric ellipsoids are cylinders. Ortega and de la Torre have calculated the translational and rotational properties of such shapes using a bead shape model treatment[12]. They fitted the numerical results to a set of expressions which are valid for p values in the range of 0.1 – 20. The translational friction coefficient was found to be described by the expression:

$$\xi_t = \xi_{t0}\left[1.009 + 0.01395\ln p + 0.07880\left(\ln p\right)^2 + 0.00640\left(\ln p\right)^3\right] \tag{1.49}$$

in which ξ_{t0} is the friction coefficient of a sphere with the same volume, given by:

$$\xi_{t0} = 6\pi\eta a\left(\frac{3}{2p^2}\right)^{1/3} \tag{1.50}$$

The rotational diffusion coefficients were not calculated directly, but expressions were given for the three NMR relaxation correlation times, previously defined by equations (1.32), (1.33) and (1.34):

$$\tau_A = \tau_0 \times \begin{cases} \left[1.18 + 0.1744\left(\ln p + 0.2877\right)^2 - 0.2417\left(\ln p + 0.2877\right)^3 \right. \\ \left. -0.03882\left(\ln p + 0.2877\right)^4\right] \text{.....if } p < 0.75 \\ \left[1.18 + 1.116\left(\ln p + 0.2877\right)^2 - 0.9729\left(\ln p + 0.2877\right)^3 \right. \\ \left. -0.4954\left(\ln p + 0.2877\right)^4\right] \text{.....if } p > 0.75 \end{cases} \tag{1.51}$$

$$\tau_B = \tau_0 \left[1.183 + 0.2902 \ln p + 0.4406\left(\ln p\right)^2 - 0.05850\left(\ln p\right)^3 - 0.009544\left(\ln p\right)^4\right] \tag{1.52}$$

$$\tau_C = \tau_0 \left[0.9833 + \frac{0.06532}{p} + \frac{0.05168}{p^2} - \frac{0.003234}{p^3}\right] \tag{1.53}$$

With τ_0 the correlation time of a sphere with the same volume:

$$\tau_0 = \frac{2\pi\eta a^3}{k_B T p^2} \tag{1.54}$$

The behaviour of all these diffusion coefficients with p is similar to that of ellipsoids.

In conclusion, for both the translational and rotational diffusion coefficients a clear link has been now established with the dimensions of the molecule. These relations will be important to interpret the results from experimental diffusion coefficients later on. Next to that, the mathematical descriptions for both the translational and rotational diffusion processes form the basis to understanding their impact in NMR spectroscopy. This will be the subject of the next two chapters.

1.5. References

[1] R. Brown, "A brief account of microscopical observations made in the months of June, July and August, 1827, on the particles contained in the pollen of plants; and on the general existence of active molecules in organic and inorganic bodies". *Edinburgh new Philosophical Journal*, **1828**(July-September) 358-371.

[2] A. Einstein, "Über die von der molekularkinetischen Theorie der Wärme geforderte Bewegung von in ruhenden Flüssigkeiten suspendierten Teilchen". *Annalen der Physik*, **1905**, *17* 549-560.

[3] K. A. Dill and S. Bromberg, "Molecular Driving Forces: Statistical Thermodynamics in Chemistry and Biology", **2003**, New York, Garland Science.

[4] I. J. D. Craig and A. M. Thompson, "Why Laplace Transforms are Difficult to Invert Numerically". *Computers in Physics*, **1994**, *8*(6) 648-654.

[5] A. Abragam, "The Principles of Nuclear Magnetism", **1961**, Oxford, Oxford University Press.

[6] F. Perrin, "Mouvement brownien d'un ellipsoide (II). Rotation libre et dépolarisation des fluorescences. Translation et diffusion de molécules ellipsoidales". *Journal de Physique et le Radium*, **1936**, *7* 1-11.

[7] M. Smoluchowski, "Zur kinetischen Theorie der Brownschen Molekularbewegung und der Suspensionen". *Annalen der Physik* **1906**, *21* 756-780.

[8] C. R. Cantor and P. R. Schimmel, "Biophysical Chemistry: Part II: Thechniques for the study of biological structure and function", **1980**, New York, W.H. Freeman and Company.

[9] S. H. Koenig, "Brownian-Motion of an Ellipsoid - Correction to Perrins Results". *Biopolymers*, **1975**, *14*(11) 2421-2423.

[10] F. Perrin, "Mouvement brownien d'un ellipsoide (I). Dispersion diélectrictrique pour des molécules ellipsoidales". *Journal de Physique et le Radium*, **1934**, *5* 497-511.

[11] P. Debye, "Polar Molecules", **1945**, New York, Dover Publications.

[12] A. Ortega and J. G. de la Torre, "Hydrodynamic properties of rodlike and disklike particles in dilute solution". *Journal of Chemical Physics*, **2003**, *119*(18) 9914-9919.

2

Impact of translational diffusion in NMR: diffusion NMR – DOSY

2.1 Introduction

The principle and applications of NMR translational diffusion measurements and DOSY will be given in this section, while a more detailed explanation of the theory and practice will be provided in the following sections. This allows readers unfamiliar with this technique to gain a quick insight into its principles and applications while at the same time allowing them to skip the more in depth treatment of the next sections.

Diffusion NMR experiments in their most common form involve the application of linear magnetic field gradients along the longitudinal axis of the sample (discussed in section 2.2). The experiment provides a series of 1D NMR spectra in which the intensity I of each signal is attenuated upon increasing the magnetic field gradient strength g, according to the Stejskal-Tanner equation (discussed in section 2.3):

$$I = I_0 e^{-D_t \gamma^2 (\varsigma g)^2 \delta^2 \Delta'} \tag{2.1}$$

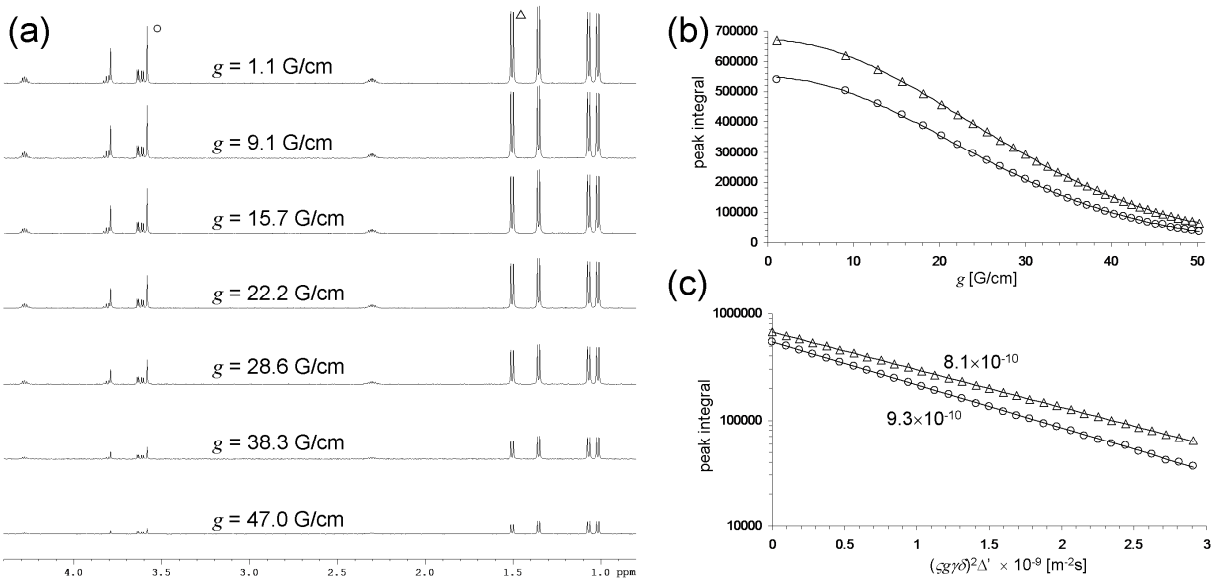

Figure 2.1: (a) The intensities of all resonances in the 1D ^{1}H spectrum decrease as the gradient strength is increased. The resonances seen originate from 1,4-dioxane and the amino acids glycine, alanine, threonine and valine. (b) The signal intensities that are obtained (examples are the CH_2^{α} of glycine (○) and the CH_3^{β} of alanine (△)) decay to the gradient strength according to equation (2.1). (c) A plot of the logarithm of the intensity vs. the squared gradient strength provides a linear curve, the slope of which depends on the diffusion coefficient. It can be clearly seen that the glycine resonance decays slightly faster and has thus a higher diffusion coefficient than alanine.

in which I_0 is the signal intensity in the absence of diffusion attenuation, D_t is the translational diffusion coefficient of the molecule to which the signal belongs, γ is the gyromagnetic ratio of the nucleus studied, ς is a gradient shape factor and δ is the gradient duration (*i.e.* the time during which the gradients were switched on). The diffusion delay Δ is the time during which the molecular diffusion can induce its effect, while Δ' is this same delay corrected with a value that depends on the specific pulse sequence and gradient shape used. To measure the translational diffusion coefficient, several 1D spectra are recorded at variable gradient strength g so as to obtain an intensity decay for each signal (Figure 2.1). Fitting equation (2.1) to these decays then provides the diffusion coefficients of the molecules associated with these signals (as discussed in section 2.5).

With the advent and the wide spread use of NMR probes capable of applying magnetic pulsed field gradients (PFGs) of moderate amplitude, translational diffusion measurements with NMR have found extensive application and methodological development. The ability to measure the diffusion coefficient in a relatively fast manner in combination with all other structural information NMR can provide simultaneously, creates a large potential for mixture analysis, the study of hydrodynamic properties and molecular interactions[2].

In a 2D DOSY plot (diffusion ordered spectroscopy), the chemical shift information, represented on the horizontal axis, is correlated to the translational diffusion

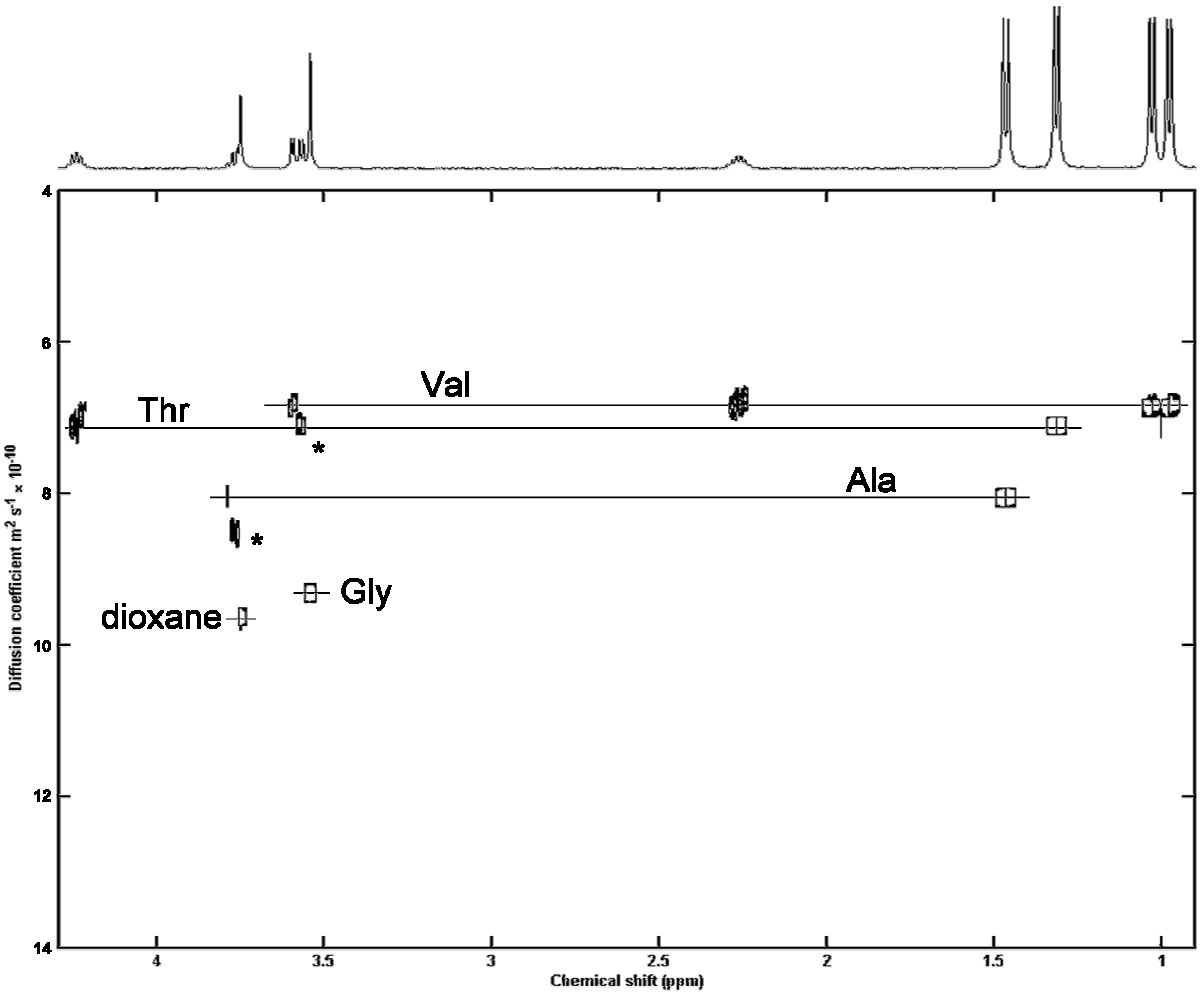

Figure 2.2: A DOSY plot of the mixture seen in Figure 2.1. All resonances belonging to the same molecule are lie on a horizontal line perpendicular to the diffusion coefficient axis, allowing easy assignments of all peaks to a given species. The width of the peaks along the diffusion axis represents the error of fitting. The peaks indicated by an asterisk (*) are the result of overlap between resonances of different molecules, resulting in an averaged (and erroneous) diffusion coefficient (see section 2.5). The 2D plot was obtained by use of the DOSY Toolbox[1].

coefficient, represented by the vertical axis. All signals from the 1D spectrum are thus spread across a 2D plot, where those originating from the same molecule will correlate to the same diffusion coefficient, thus allowing to quickly identify the components in the mixture and to separate their individual NMR spectra[3], provided the diffusion coefficients are sufficiently different. This is illustrated in Figure 2.2 for a mixture of amino acids. Some examples of applications of this technique can be found in combinatorial chemistry[4, 5], analysis of biological fluids[2, 4, 6], food science[7, 8] and polymer mixtures[2, 9] to name a few.

Besides the ability of DOSY to resolve resonances along the diffusion dimension, the diffusion coefficient by itself can of course provide invaluable information. Its dependence on size and shape as discussed in chapter 1 can for example provide insight into the nature and molar mass of supramolecular complexes formed[[5, 10-13], or indicate whether a protein has folded[14]. The diffusion spectrum is also sensitive to chemical exchange[15-17]. When a molecule undergoes a fast chemical exchange

between two or multiple states compared to the diffusion delay Δ, an averaged value for the diffusion coefficient will be measured. When the diffusion coefficients of both two states are sufficiently different (*e.g.* protein ligand interactions), both a qualitative and quantitative assessment of the binding interaction can be obtained[18-20]. Typical examples are the determination of the critical micellar concentration (CMC) of surfactants[21, 22] or the binding of small molecules with micelles or vesicles[[23-27]. Finally, diffusion NMR has also been applied to the study of reaction kinetics.[28, 29].

In the following sections, an overview of both theory and experimental methodology of diffusion NMR will be given. Good reviews on the subject have been written over the years by Johnson, Price and Antalek [15, 30-32].

2.2 Magnetic field gradients

When describing the ideal NMR experiment, the static magnetic field B_0 is assumed to be homogeneous over the entire sample. In reality however, this is not the case. As a consequence, the coherence (the extent to which the different spins add up constructively to the total signal) of the signal to be detected will disappear much faster. This is because spins at different positions in the sample will no longer precess with the same angular velocity around the magnetic field and thus develop a different phase relative to each other over time. Fortunately, a homogenous magnetic field can be achieved to a reasonable extent with modern NMR instruments. There are however many NMR experiments[33] that benefit from temporarily destroying the homogeneity of the magnetic field in a controlled manner by applying a linear magnetic field gradient created by a specially designed coil[32]. In what follows, the effect on the detected signal of such a gradient will be discussed.

Assume a linear magnetic field gradient along the z-axis, with a strength g (*i.e.* the magnetic field varies with a slope g). The total precession angular frequency of the magnetisation (the net sum of all spin magnetic dipoles in the sample at a position z originating from a certain nucleus) during this gradient is given by:

$$\begin{aligned}\omega_{tot}(z) &= -\gamma B_{tot}(z) \\ &= -\gamma B_0 - \gamma B_{grad}(z) \\ &= -\gamma B_0 - \gamma g z \\ &= \omega_0 + \Omega(z)\end{aligned} \tag{2.2}$$

If a rotating frame with angular frequency ω_0 is considered, only the gradient induced precession $\Omega(z)$ needs to be taken into account. When applying the gradient for a time δ, the total angle with which the magnetisation will have precessed within the

rotating frame will be $\Omega(z)\delta$. Assuming the magnetisation is rotated from the z-axis to the y-axis after excitation by a 90°$_x$ pulse, it will evolve as:

$$M_y \rightarrow M_y \cos\left(\Omega(z)\delta\right) - M_x \sin\left(\Omega(z)\delta\right) \tag{2.3}$$

The projection of the magnetisation vectors on the x and y axes will thus depend on its position along the z-axis. When the entire sample length along the z-axis is considered, the end result is a helix structure as illustrated in Figure 2.3. The pitch P of this helix (the displacement along z by a full turn) and the number of turns NT for a given sample length L is given by:

$$P = \frac{2\pi}{\gamma g \delta} \tag{2.4}$$

$$NT = \frac{L}{P} = \frac{\gamma g \delta L}{2\pi} \tag{2.5}$$

The total detectable magnetisation can be found by integration of (2.3) over the sample length L:

$$\begin{aligned}\int_{-L/2}^{L/2}\left[M_y \cos\left(\Omega(z)\delta\right) - M_x \sin\left(\Omega(z)\delta\right)\right]dz &= M_y \int_{-L/2}^{L/2}\left[\cos\left(\gamma g z \delta\right)\right]dz + M_x \int_{-L/2}^{L/2}\left[\sin\left(\gamma g z \delta\right)\right]dz \\ &= M_y \frac{\sin\left(\frac{\gamma g L \delta}{2}\right)}{\gamma g \delta} \\ &= M_y \frac{2}{\mathrm{L}} \mathrm{sinc}\left(\frac{\gamma g L \delta}{2}\right)\end{aligned} \tag{2.6}$$

The detectable magnetisation will remain along the y-axis while its intensity experiences a dampened oscillation under the form of a sinc function with increasing gradient strength g (Figure 2.3). The detected signal will change sign each time the number of helix turns NT becomes an integer number. When the gradient strength is sufficiently strong, the number of helix turns will have increased so much that the relative amount of the magnetisation that does not form a complete helix turn will be insufficient to give rise to a detectable signal.

Because the magnetisation vectors have dephased in a controlled manner, they can be rephased to again give a detectable signal. If a second gradient is applied with the same length δ, but an opposite strength $-g$, then the magnetisation at every position z in (2.3) will be refocused to its original orientation:

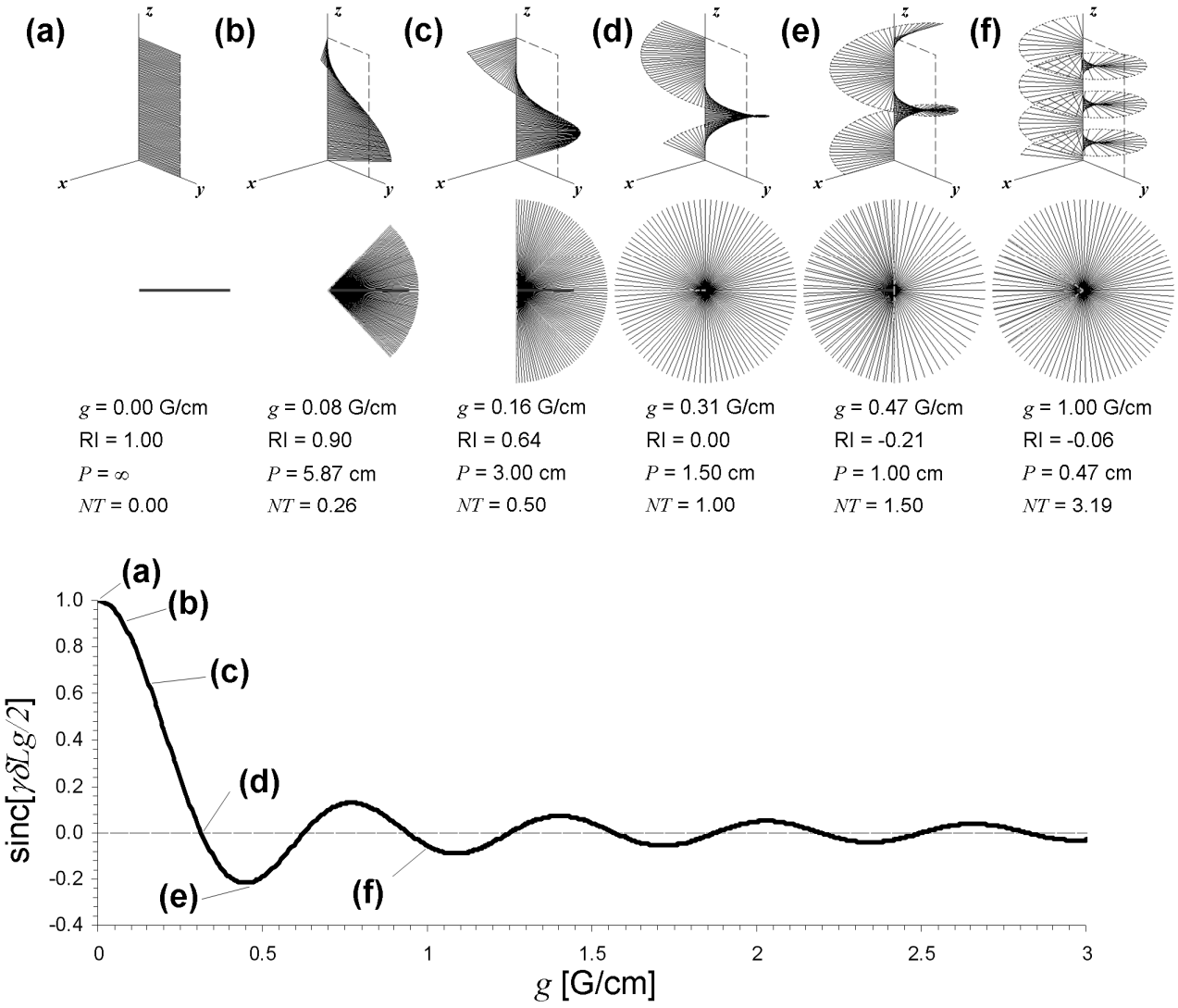

Figure 2.3: Illustration of the effect of a magnetic field gradient on the magnetisation. ^{1}H magnetisation over a 15 mm sample length is subjected to a magnetic field gradient during a 500 µs period for several gradient strengths. The initial magnetisation is along the *y*-axis as in (a) and precesses around the *z*-axis depending on its position along this axis. As the gradient strength increases from (b) to (f), the magnetisation precesses over larger phase angles and a helical structure forms. The dephasing of the magnetisation over the sample is demonstrated by the top views. The vector sum of all the magnetisation vectors, and thus the total detectable magnetisation and the relative intensity of the peak (RI) will decrease with *g* under the form of a sinc function.

$$\begin{aligned} M_y\cos\left(\Omega(z)\delta\right)-M_x\sin\left(\Omega(z)\delta\right) \rightarrow{}& \cos\left(\Omega(z)\delta\right)\left[M_y\cos\left(-\Omega(z)\delta\right)-M_x\sin\left(-\Omega(z)\delta\right)\right] \\ &-\sin\left(\Omega(z)\delta\right)\left[M_x\cos\left(-\Omega(z)\delta\right)+M_y\sin\left(-\Omega(z)\delta\right)\right] \\ \rightarrow{}& M_y \end{aligned} \quad (2.7)$$

Magnetic field gradients during NMR experiments typically find application as a tool to select the desired magnetisation (or, more generally, the coherence transfer pathway) while eliminating the unwanted magnetisation (or coherence). This is achieved by getting it dephased at the end of the pulse sequence, while the desired magnetisation is never dephased or is refocused by the gradients[33]. Alternatively,

the correct magnetisation can be selected by use of phase cycling the rf-pulses. Usually, a combination of both is performed for optimal performance of the pulse sequence.

2.3 Effect of translational diffusion during gradient echoes and the STE experiment

When Erwin L. Hahn reported in 1950 the first spin echo NMR experiments[34], which he used to remove the effects of static magnetic field inhomogeneity in T_2 relaxation measurements, he noted that the signal decayed faster than expected and interpreted this to be due to the translational diffusion of the molecules bearing the nuclear spins during the experiment. A spin echo refocuses magnetisation under the condition that each spin experiences the same magnetic field before and after the refocusing pulses. If the spins have randomly moved during the echo to other regions where the magnetic field is different due to its inhomogeneity, the refocusing will no longer be complete, resulting in a loss of signal (Figure 2.5). Note that the field inhomogeneity can be regarded as a magnetic field gradient. Later, Torrey incorporated the effect of diffusion into the Bloch equations[35], which already described the evolution of the magnetisation under the influence of the magnetic field and relaxation. The so-called Bloch-Torrey equations are given by the general expression (assuming no rf-pulses and a linear magnetic field gradient only along the z axis):

$$\begin{aligned}\frac{\partial}{\partial t}\begin{bmatrix}\mathrm{M}_z(t,z)\\ \mathrm{M}^+(t,z)\\ \mathrm{M}^-(t,z)\end{bmatrix} = \left(\omega_0-\Omega(z)\right)\begin{bmatrix}0\\ -i\,\mathrm{M}^+(t,z)\\ i\,\mathrm{M}^-(t,z)\end{bmatrix} - R_2\begin{bmatrix}0\\ \mathrm{M}^+(t,z)\\ \mathrm{M}^-(t,z)\end{bmatrix}\\ -R_1\begin{bmatrix}\mathrm{M}_z(t,z)-M_0\\ 0\\ 0\end{bmatrix} + D_t\frac{\partial^2}{\partial z^2}\begin{bmatrix}\mathrm{M}_z(t,z)\\ \mathrm{M}^+(t,z)\\ \mathrm{M}^-(t,z)\end{bmatrix}\end{aligned} \tag{2.8}$$

with M_0 the magnitude of the equilibrium magnetisation and $\mathrm{M}^{\pm} = \mathrm{M}_\mathrm{x} \pm i\,\mathrm{M}_\mathrm{y}$. Note that the final term in the equation resembles Fick's second law for translational diffusion along one dimension (equation (1.5)), which links the change in concentration over time with the variation of the concentration along this dimension. In this case, the concentration variation is replaced by the spin phase variation created by the magnetic field gradients. The solution of the Bloch-Torrey equation is derived in appendix B. The final result is presented here:

$$\mathrm{I}(t) = \mathrm{I}_0(t)\,e^{-D_t\int_0^t \mathrm{q}^2(t)dt} \tag{2.9}$$

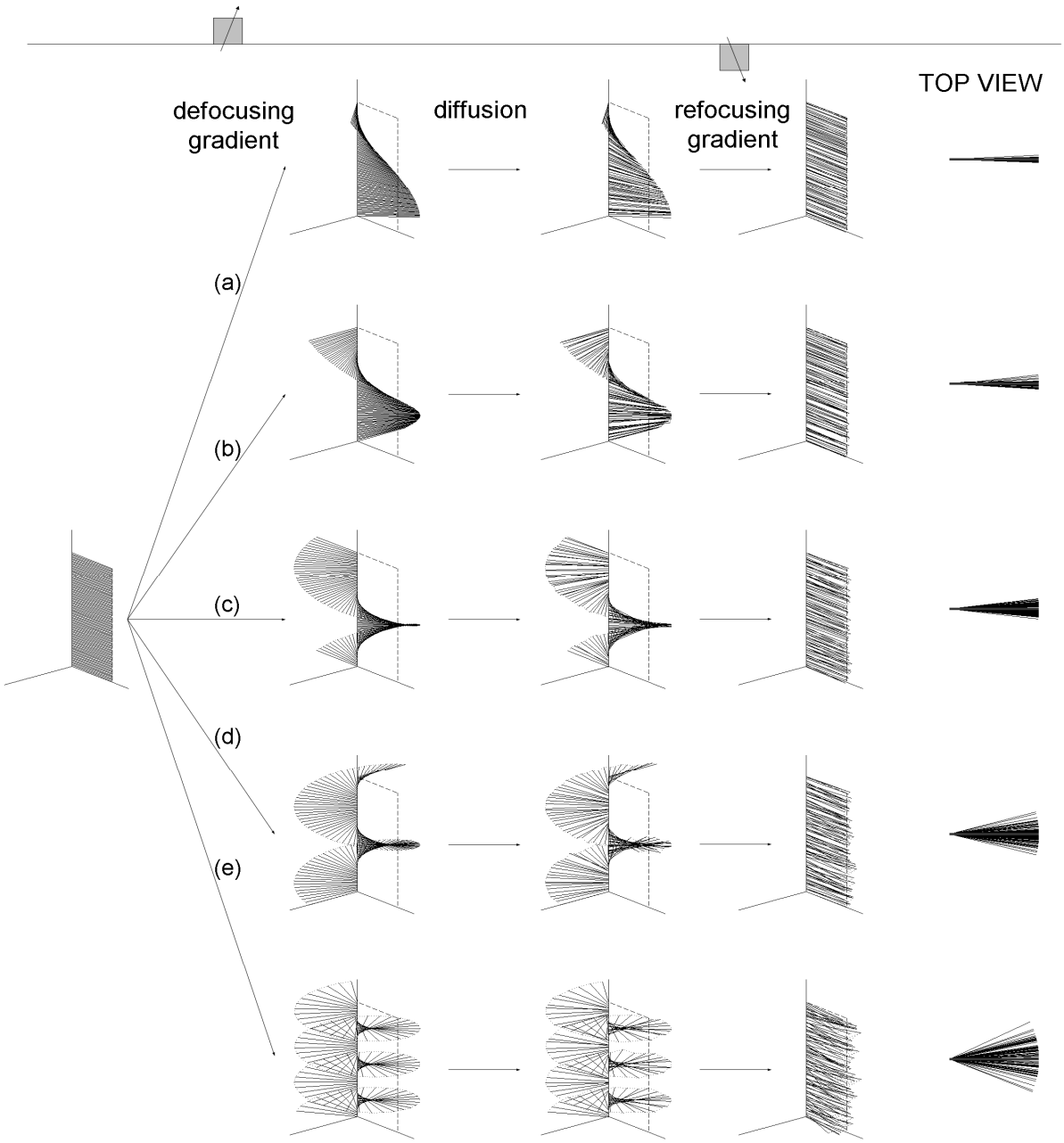

Figure 2.5: Simulation of the effect of translational diffusion. The ^{1}H magnetisation over a length of 15 mm is dephased into a helical structure by a 500 µs gradient with a strength of (a) 0.08 G/cm, (b) 0.16 G/cm, (c) 0.31 G/cm, (d) 0.47 G/cm and (e) 1.00 G/cm. In the second step, Brownian motion is allowed to take its effect during 10 seconds (chosen so long for the purpose of illustration) with a diffusion coefficient of 10^{-9} m^2/s, displacing each vector a random distance along the z-axis. After a second gradient of opposite direction, the magnetisation is no longer perfectly refocused, leading to a partial loss of phase coherence and signal attenuation. As the gradient strength increases, this effect will increase and the helix will have more turns.

in which:

$$\mathrm{q}(t) = \int_0^t \mathrm{p}(t)\,\gamma \mathrm{G}(t)\,dt \tag{2.10}$$

$\mathrm{I}(t)$ is the intensity of the detected signal at time t, $\mathrm{I}_0(t)$ is the signal intensity if no diffusion had taken place, while $\mathrm{p}(t)$ and $\mathrm{G}(t)$ are respectively the coherence order

active during the gradient and the gradient strength as a function of time t. The function $\mathrm{q}(t)$ represents the extent to which the magnetisation has become dephased along the z-axis.

Stejskal and Tanner[36] were the first to apply this phenomenon as a fully developed method to measure diffusion coefficients. Instead of using steady gradients that were active during the whole experiment, they used pulsed field gradients. They used the adapted Bloch equations from Torrey to mathematically derive the effect of diffusion for their experiments, the general result of which (equation (2.1)) is now know as the Stejskal-Tanner equation. Here, equation (2.9) will be evaluated for a monopolar stimulated echo (STE) sequence with rectangular gradients. Figure 2.6 shows the convention of the delays in a standard PFG pulse sequence: δ is the length of the diffusion encoding and decoding gradient pulses and Δ is the time between the starts of both gradients. The phase cycling of the rf-pulses (assisted by the gradients) is chosen as such that the selected coherence transfer pathway (CTP) turns out as shown in Figure 2.6. Note that the gradient applied after the second 90° pulse is a spoil gradient to purge all transverse coherences with non-zero order. It will therefore have no effect on the function $\mathrm{q}(t)$, since the coherence order of the wanted magnetisation is zero at that time. The integral in (2.10) is best evaluated in several steps:

<u>During the encoding gradient, in the time range $0 < t < \delta$:</u>

$$\gamma \mathrm{p}(t)\mathrm{G}(t) = \gamma g \tag{2.11}$$

$$\mathrm{q}(t) = \int_0^t \gamma \mathrm{p}(t)\mathrm{G}(t)\,dt = \gamma g t \tag{2.12}$$

$$\mathrm{q}^2(t) = \gamma^2 g^2 t^2 \tag{2.13}$$

$$\int_0^\delta \mathrm{q}^2(t)\,dt = \frac{\gamma^2 g^2 \delta^3}{3} \tag{2.14}$$

<u>Between the encoding and decoding gradients, in the time range $\delta < t < \Delta$:</u>

$$\gamma \mathrm{p}(t)\mathrm{G}(t) = 0 \tag{2.15}$$

$$\mathrm{q}(t) = \mathrm{q}(\delta) + \int_\delta^t \gamma \mathrm{p}(t)\mathrm{G}(t)\,dt = \gamma g \delta \tag{2.16}$$

$$\mathrm{q}^2(t) = \gamma^2 g^2 \delta^2 \tag{2.17}$$

$$\int_\delta^\Delta \mathrm{q}^2(t)\,dt = \gamma^2 g^2 \delta^2 (\Delta - \delta) \tag{2.18}$$

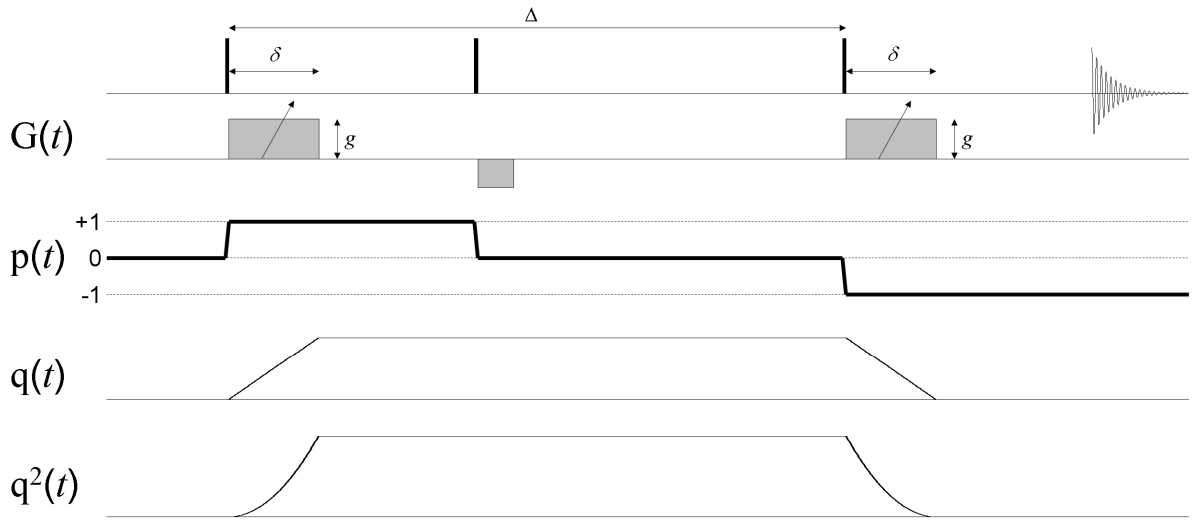

Figure 2.6: STE sequence with illustration of the convention of the symbols used for the delays. The gradient strength as a function of time $\mathrm{G}(t)$ is shown, as well as the coherence order $\mathrm{p}(t)$. The coherence pathway shown is selected by applying the standard Bruker phase cycle. The squared of the function $\mathrm{q}(t)$ illustrates the degree with which the magnetisation is dephased at a certain time. Its squared $q^2(t)$ determines the degree with which diffusion will cause a loss of signal coherence at the time t.

<u>During the decoding gradient, in the time range $\Delta < t < \Delta+\delta$:</u>

$$\gamma \mathrm{p}(t)\mathrm{G}(t) = -\gamma g \tag{2.19}$$

$$\mathrm{q}(t) = \mathrm{q}(\Delta) + \int_{\Delta}^{t} \gamma \mathrm{p}(t)\mathrm{G}(t)\,dt = \gamma g\left(\delta + \Delta - t\right) \tag{2.20}$$

$$\mathrm{q}^2(t) = \gamma^2 g^2\left(\delta^2 + \Delta^2 + t^2 + 2\delta\Delta - 2\delta t - 2\Delta t\right) \tag{2.21}$$

$$\begin{aligned}\int_{\Delta}^{\Delta+\delta} \mathrm{q}^2(t)\,dt &= \gamma^2 g^2 \delta^2 \left[\delta^2 t + \Delta^2 t + \frac{t^3}{3} + 2\delta\Delta t - \delta t^2 - \Delta t^2\right]_{\Delta}^{\Delta+\delta} \\ &= \frac{\gamma^2 g^2 \delta^3}{3}\end{aligned} \tag{2.22}$$

The complete integral of $\mathrm{q}^2(t)$ is then:

$$\begin{aligned}\int_{0}^{\Delta+\delta} \mathrm{q}^2(t)\,dt &= \int_{0}^{\delta} \mathrm{q}^2(t)\,dt + \int_{\delta}^{\Delta} \mathrm{q}^2(t)\,dt + \int_{\Delta}^{\Delta+\delta} \mathrm{q}^2(t)\,dt \\ &= \gamma^2 g^2 \delta^2 \left(\Delta - \frac{\delta}{3}\right)\end{aligned} \tag{2.23}$$

Therefore, the solution to (2.9) becomes:

$$I = I_0 e^{-D_t \gamma^2 g^2 \delta^2 \left(\Delta - \frac{\delta}{3}\right)} \tag{2.24}$$

This is the most commonly known form of the Stejskal-Tanner equation. This equation requires slight modification when different pulse sequences or non-rectangular gradient shapes are used. These modified equations can be derived as discussed in appendix B. Irrespective of this, the general form of the $q^2(t)$ term is always the same, with a squared dependence on the gradient strength g, the gyromagnetic ratio γ and the gradient duration δ and a linear dependence on the diffusion delay Δ. The latter is however always 'corrected' by a small term dependent on the duration and shape of the gradient, which finds its origin in the fact that during the gradient the diffusion that takes place has a lesser impact than the diffusion after the gradient.

Equation (2.24) illustrates that the different parameters can limit the possibility to measure diffusion. For accurate diffusion measurements, it is important to be able to let the signal intensity I drop to about 10% or lower of the original intensity I_0. The parameters in Equation (2.24) put a strong limitation up to which degree this is achievable. The values of δ should not be set too high, since letting the high electrical current flow through the gradient coils might damage the equipment. In addition, long δ or Δ values reduce the signal-to-noise due to relaxation of the magnetisation that takes place during the pulse sequence. For the STE sequence, the pre-exponential term I_0 is dependent on these values according to:

$$I_0 \propto e^{-\frac{\Delta-\delta}{T_1}-\frac{2\delta}{T_2}} \tag{2.25}$$

If δ or Δ are set too high compared to the longitudinal and transverse relaxation time constants T_1 and T_2, the signal-to-noise ratio will be too low for the signal to be detectable at the desired attenuation. The choice of nucleus is also a determining factor through the gyromagnetic ratio. For example, γ_{13C} is about 4 times smaller than γ_{1H}, meaning that the factor within the exponential will be 16 times lower, severely limiting the lowest diffusion coefficient measurable. The maximum achievable gradient strength is something that is dependent on the NMR probe and is typically of the order of 50 G/cm. Special probes for diffusion measurements, which can achieve gradients of more than 2000 G/cm, are commercially available however. A non-rectangular gradient shape (see the following section) can also significantly reduce the effect that the gradient strength has on the diffusion attenuation.

Several modifications exist on the simple STE experiment of Figure 2.6, usually to alleviate technical problems. A short overview of these problems and how the STE sequence is adapted to deal with them will be discussed in the next section.

2.4 Modifications to the STE experiments

2.4.1 Gradient shapes and bipolar gradients

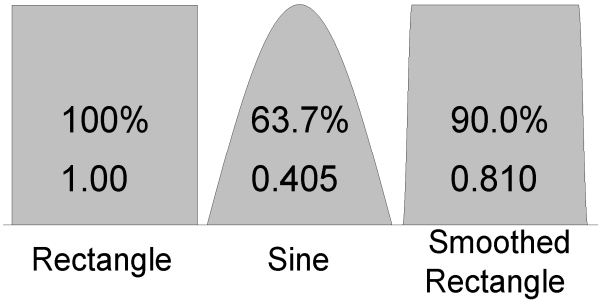

Figure 2.7: Three common gradient shapes with their relative area to the rectangular shapes (in %) and their shape factor. The sine and smoothed rectangle shapes are the only shapes used through this dissertation.

A common modification is the way the gradients are implemented (Figure 2.7). For example, the gradient strength as a function of time during the δ delay (the 'shape' of the gradient) is often changed to a non-rectangular function that has a more gradual increase at the beginning and decrease at the end[37]. The advantage is that the assumed shape of the gradients will correspond better to the actual one, since technically it is not evident to create a rectangular gradient which switching instantaneously from 0 to a relatively large and stable value g. The disadvantage is that any non-rectangular shape will introduce a shape factor into equation (2.24), which is lower than the shape factor 1 of a rectangular gradient, thus reducing the effectiveness of the gradients. Shaped gradients also have positive effect in reducing eddy currents, see section 2.4.2.

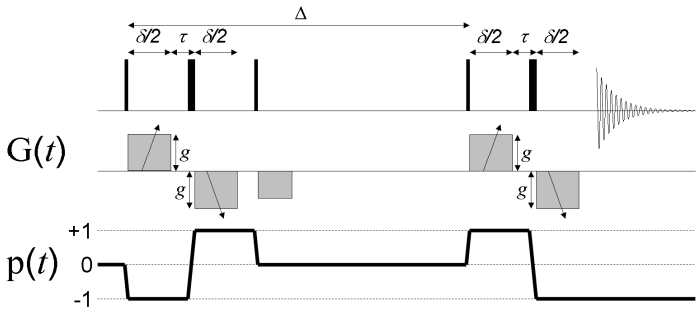

Figure 2.8: STE pulse sequences using bipolar pulsed field gradients. The coherence pathway shown is selected by applying the standard Bruker phase cycle.

Another common modification is the use of so-called bipolar pulsed field gradients[38, 39] (Figure 2.8). In stead of a single (monopolar) gradient with duration δ , these consist of two gradients of duration $\delta/2$ of opposite polarity with a 180° rf-pulse in between. Due to the 180° pulse between the gradients, the sign of the coherence order p is inverted which effectively makes the gradients dephase the magnetisation in the same direction. There are several advantages to this. First, the implementation of two pulsed gradients with opposite sign immediately after each other will have a much reduced effect on the deuterium lock signal. Since the deuterium magnetisation is also dephased by a gradient, the lock signal will momentarily disappear until it has recovered through relaxation. During this time, the field lock cannot be applied. This can possibly increase the amount of small frequency shift artefacts if the static magnetic field fluctuations are sufficiently fast or if the frequency with which gradients are switched on and off is relatively fast (short delays between scans for example).

With bipolar gradients however, the deuterium signal will be immediately refocused by the second gradient, since it of course does not experience the effect of the 180° pulse at the frequency of the observe nucleus. A second advantage is that it greatly reduces the effects from background gradients (field inhomogeneity), which influence the signal decay by creating cross-terms with the pulsed field gradients in the Stejskal-tanner equation[39].

Another advantage arises when slow chemical exchange processes on the frequency time scale occur[40]. Assume a nucleus exchanges between two sites A and B with chemical shifts ω_A and ω_B. If during the delay between the first two 90° pulses of a monopolar gradient STE the nucleus is at site A, then a phase factor will develop through chemical shift evolution (ignoring the gradient effect for simplicity):

$$M^+ \xrightarrow{\omega_A M_z T} M^+ e^{-i\omega_A T} \tag{2.26}$$

with T the time between the 90° pulses, on the order of δ. If at some point during the (much longer) delay between the second and third 90° pulses the nucleus jumps from site A to B, the chemical shift evolution during the time T after the third 90° pulse and before the start of acquisition will be:

$$M^- e^{-i\omega_A T} \xrightarrow{\omega_B M_z T} M^- e^{i(\omega_B - \omega_A)T} \tag{2.27}$$

It is clear that, if ω_A and ω_B are not equal, the phase factors that develop during the two delays will not vanish. If the exchange rate is such that a significant number of spins will make the jump between the sites during the time delay, the end result will be that both resonances at ω_A and ω_B become phase distorted up to a degree depending on the difference in frequency and the exchange rate. In addition, the signal intensity will have decreased because of the loss of coherence created by the distribution of phase factors. When using bipolar PFGs, the 180° pulse acts as a spin echo, refocusing the chemical shift evolution during the time T. The time interval during which chemical exchange would need to occur in order for a chemical shift phase factor to hold on is thus much shorter in the bipolar gradient experiment (T) than in the monopolar experiment ($\Delta + T$). Therefore the bipolar PFG STE sequence is much less sensitive to peak shape artefacts due to chemical exchange. An example of this is shown in Figure 2.9.

A significant disadvantage of bipolar PFGs, however, is the introduction of the additional 180° rf-pulses, which require additional coherence selection through phase cycling (making the duration of the experiment considerably longer) or gradients pulses (which is not always achievable). This is particularly tedious in convection compensated experiments (*vide infra*), which already possess a significantly long

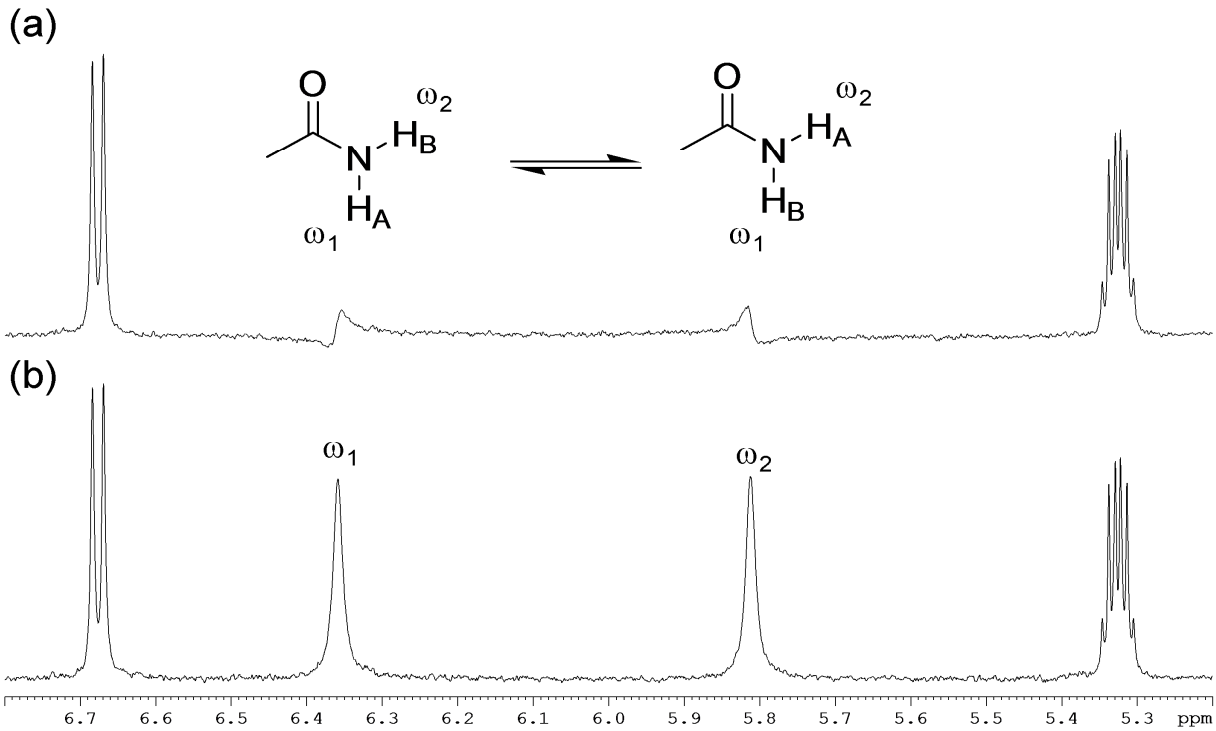

Figure 2.9: Illustration of the effect of exchange on the signal phase in an STE experiment. The two central resonances represent the NH_2 group of a glutamine residue in pseudodesmin A in acetonitrile solution at measured at 25℃ and 16.4 T (see chapter 4), which are in slow exchange on the frequency time scale due to due to the process shown above. (a) Monopolar gradient STE experiment, demonstrating that the exchange is sufficiently fast so that it occurs during Δ. Note the exact opposite phase distortion of both peaks. (b) Same δ and Δ durations, but with bipolar gradients. The phase distortion is no longer present and the signal intensity has been restored.

phase cycle, and would need no less than three additional 180° pulses for the introduction of bipolar gradient pulses. A solution to this problem was proposed by Gareth Morris *et al* under the form of the so-called one-shot pulse sequence[41]. They used gradients of unequal strength (unbalanced gradients) before and after the 180° pulse to select the correct coherence transfer during these pulses.

2.4.2 Modifications to avoid eddy current artefacts

A known source of peak shape distortions during gradient NMR experiments are eddy currents. These are electrical currents caused by the gradients in the conducting metals of the NMR equipment itself by induction. The currents then again create time dependent magnetic fields within the sample, which can distort the spectrum if they are still present during the acquisition time. Both shaped and bipolar gradient pulses can help to alleviate these problems. It has been shown that the slower rise and fall times of shaped gradients can help reduce the eddy currents from occurring[37]. Bipolar PFGs also significantly reduce the duration that eddy currents remain, since the two opposite gradients partially cancel out the effect of each other's eddy currents[42].

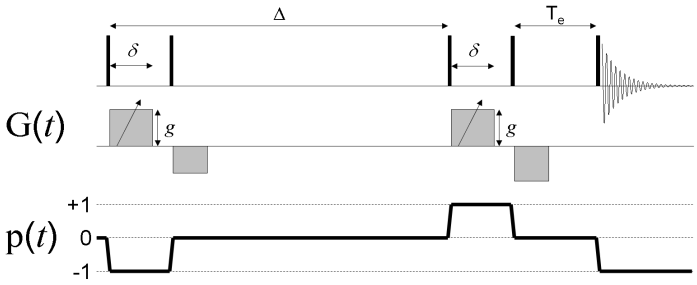

Figure 2.10: STE sequence with a Longitudinal Eddy current Delay (LED) incorporated at the end, storing the magnetisation for a time T_e along the *z*-axis. The coherence pathway shown is selected by applying the standard Bruker phase cycle.

A different measure against eddy currents is the introduction of a delay at the end of the sequence to allow the eddy currents to decay before acquisition commences. This is usually done with two 90° pulses that shortly store the magnetisation along the z-axis, which is favourable in terms of relaxation (since $T_1 \geq T_2$) and brings it back afterwards (Figure 2.10). A spoil gradient is usually applied between the two gradient pulses for coherence selection. This sequence is called the Longitudinal Eddy current Delay (LED). The disadvantage of this approach is that the introduction of two extra 90° pulses requires coherence selection through phase cycling. In addition, in the case of scalar coupled systems the LED can introduce additional artefacts through the generation of zero quantum coherence that is indistinguishable from *z*-magnetisation. Therefore, the LED sequence is best avoided when not needed.

2.4.3 Convection compensation: the double STE experiment

A number of very important variants to the STE experiment has been designed to compensate for convection. Convection is a process where flows are created within the solution under the influence of mechanical disturbances or temperature gradients that induce unequal fluid density over the sample. This will severely interfere with the measurement of diffusion, since now two processes that change the position of the spins will be active during the gradient experiment. The smaller the diffusion coefficient to be measured, the stronger the interference of convection, since the effect of convection is on the whole solution and thus the same for all molecules. Longer sample length and diameter and lower solution viscosity and density all will increase the likelihood of convection occurring and will increase the flow velocity[43]. Therefore convection can be avoided or its effects minimised by using smaller diameter NMR tubes, not filling the sample unnecessarily high with liquid or using more viscous solvents. Of course, in practice this is not always sufficient or feasible. It is however possible to cancel out the convection contribution directly during the NMR experiment, as described hereafter.

Convection[44, 45] can be divided into laminar and turbulent flow convection. In the former case, the solution will move in relatively ordered parallel flows with near

constant velocity over time. This typically happens under the influence of a temperature gradient over the sample[43, 44], creating a convection cell in which part of the fluid moves upwards and another part downwards. In the case of turbulent convection, the solution moves in an incoherent, disordered way. The transition between laminar and turbulent convection occurs when the velocity of the flow reaches a critical value, which is determined by parameters such as sample length, sample diameter, temperature, solution viscosity and solution density. It is important to note that only laminar convection can be compensated by use of special NMR pulse sequences. These are based on the assumption that the molecules flow with a constant speed in a constant direction during the NMR experiment, which is certainly not true for the incoherent movements of turbulent convection.

To comprehend how laminar convection can be compensated, it must first be understood how flow in general affects the magnetisation[46]. When a flow along the z-axis takes place, the degree to which the concentration of a compound at a position z changes over time will be proportional to the concentration gradient along the z-axis and the velocity v_z with which this concentration gradient is shifting over the z-axis. This corresponds to the following relation:

$$\frac{\partial \mathrm{c}(z,t)}{\partial t} = -v_z \frac{\partial \mathrm{c}(z,t)}{\partial z} \tag{2.28}$$

Just as in the case of diffusion, this equation can be implemented into the Bloch equations:

$$\begin{aligned}\frac{\partial}{\partial t}\begin{bmatrix} \mathrm{M}_z(t,z) \\ \mathrm{M}^+(t,z) \\ \mathrm{M}^-(t,z) \end{bmatrix} = (\omega_0 - \Omega(z))\begin{bmatrix} 0 \\ -i\,\mathrm{M}^+(t,z) \\ i\,\mathrm{M}^-(t,z) \end{bmatrix} - R_2\begin{bmatrix} 0 \\ \mathrm{M}^+(t,z) \\ \mathrm{M}^-(t,z) \end{bmatrix} \\ -R_1\begin{bmatrix} \mathrm{M}_z(t,z) - M_0 \\ 0 \\ 0 \end{bmatrix} + D_t\frac{\partial^2}{\partial z^2}\begin{bmatrix} \mathrm{M}_z(t,z) \\ \mathrm{M}^+(t,z) \\ \mathrm{M}^-(t,z) \end{bmatrix} - v_z\frac{\partial}{\partial z}\begin{bmatrix} \mathrm{M}_z(t,z) \\ \mathrm{M}^+(t,z) \\ \mathrm{M}^-(t,z) \end{bmatrix}\end{aligned} \tag{2.29}$$

The solution of (2.29) is derived in appendix B. The effect of flow on the NMR signal I turns out to be:

$$I = I_0 e^{iv_z \int_0^t \mathrm{q}(t)dt} \tag{2.30}$$

Here, I_0 is the magnetisation in the absence of flow (which still can contain the effects of diffusion). Because flow does not destroy the magnetisation helix as with diffusion, but merely shifts it along the z-axis, its effect is the introduction of a phase factor

instead of an attenuation factor. In addition, the effect is dependent on the integral of the function $\mathrm{q}(t)$ instead of $\mathrm{q}^2(t)$. When applying this to the regular STE experiment using equations (2.12), (2.16) and (2.20):

$$\begin{aligned}\int_0^{\Delta+\delta} \mathrm{q}(t)\,dt &= \int_0^{\delta} \mathrm{q}(t)\,dt + \int_{\delta}^{\Delta} \mathrm{q}(t)\,dt + \int_{\Delta}^{\Delta+\delta} \mathrm{q}(t)\,dt \\ &= \gamma g \delta \Delta\end{aligned} \tag{2.31}$$

Combined with (2.30) this yields:

$$M = M_0 e^{i v_z \gamma g \delta \Delta} \tag{2.32}$$

In the case of laminar convection, however, there is not just one velocity present, but a distribution of velocities in both up and down directions. When assuming for simplicity that a uniform velocity distribution[46] is present along the diameter of the sample ranging between $-v_z^{max}$ and v_z^{max} (see the paper of Jershow[44] for a more realistic velocity distribution), the total signal intensity will be proportional to the average of the phase factors:

$$\begin{aligned}I &= I_0 \int_{-v_z^{\max}}^{v_z^{\max}} \frac{1}{2v_z^{\max}} e^{i v_z \gamma g \delta \Delta} dv_z \\ &= I_0 \frac{e^{i v_z^{\max} \gamma g \delta \Delta} - e^{-i v_z^{\max} \gamma g \delta \Delta}}{2 i v_z^{\max} \gamma g \delta \Delta} \\ &= I_0 \,\mathrm{sinc}\left(v_z^{\max} \gamma g \delta \Delta\right)\end{aligned} \tag{2.33}$$

In the presence of convection, the signal will thus experience a damped oscillation as a function of the gradient strength g. This means that convection, when sufficiently strong, can be unambiguously detected by observing a change of signal intensity sign with increasing g. This is often the case in low viscous solvents such as chloroform. However, convection is the most troublesome when it is present to a very low extent so that $v_z^{max} \gamma g \delta \Delta << 1$, since then its effect does not deviate much from Gaussian behaviour:

$$\begin{aligned}\frac{\sin\left(v_z^{\max} \gamma g \delta \Delta\right)}{v_z^{\max} \gamma g \delta \Delta} &\approx \frac{v_z^{\max} \gamma g \delta \Delta - \frac{\left(v_z^{\max} \gamma g \delta \Delta\right)^3}{6}}{v_z^{\max} \gamma g \delta \Delta} \\ &= 1 - \left(\frac{v_z^{\max} \gamma g \delta \Delta}{\sqrt{6}}\right)^2 \\ &\approx e^{-\frac{\left(v_z^{\max}\right)^2 \gamma^2 g^2 \delta^2 \Delta^2}{\sqrt{6}}}\end{aligned} \tag{2.34}$$

in which the Taylor series approximations of the sine and exponential functions were used. When combining this result with the Stejskal-Tanner equation:

$$\begin{aligned} I &= I_0 e^{-D_t \gamma^2 g^2 \delta^2 \Delta'} e^{-\frac{\left(v_z^{\max}\right)^2 \gamma^2 g^2 \delta^2 \Delta^2}{\sqrt{6}}} \\ &= I_0 e^{-\left(D_t \Delta' + \frac{\left(v_z^{\max}\right)^2 \Delta^2}{\sqrt{6}}\right) \gamma^2 g^2 \delta^2} \\ &\approx I_0 e^{-\left(D_t + \frac{\left(v_z^{\max}\right)^2 \Delta}{\sqrt{6}}\right) \gamma^2 g^2 \delta^2 \Delta'} \end{aligned} \tag{2.35}$$

In the last step it was assumed that $\Delta \approx \Delta'$. The above reasoning is based on several approximations (including the uniform velocity distribution) so that the experimental decay may not match equation (2.35). It is clear however that the functional form of the intensity decay will be close to that of the Gaussian functional form as would have been expected when only taking diffusion taking into account, masking the convection's presence[47]. However, the apparent diffusion coefficient will be increased by an amount proportional to both the square of the convection velocity and the diffusion delay Δ. Therefore, the unsuspecting experimentalist can significantly overestimate the diffusion coefficient, especially for slowly diffusion species and long diffusion delays. If the purpose of the diffusion experiment is simply to make a distinction between different components by use of a DOSY plot, a slight convection effect may be acceptable. However, when it is the value of the diffusion coefficient as a physical quantity that is important, or when D_t as a function of Δ is studied for the purpose of studying chemical exchange, the effect of convection must be minimised.

Convection is most often caused by temperature gradients along the sample, caused by the spectrometer temperature control blowing heated or cooled air along the sample, which typically does not heat or cool the sample uniformly along its length. Therefore one way to avoid convection is to simply uncouple the spectrometer temperature control, which avoids the temperature gradient to be created. The obvious disadvantage is then of course that sample temperature cannot be properly set and stabilized. Also, the indirect heating of the sample caused by the Joule effect from the electrical currents through the gradient coils, will not be properly compensated for and thus the sample temperature will increase as the gradient strength is increased.

A more elegant way therefore is to use the pulse sequence shown in Figure 2.10[48]. Here, the magnetisation is led through two subsequent STE sequences, each having

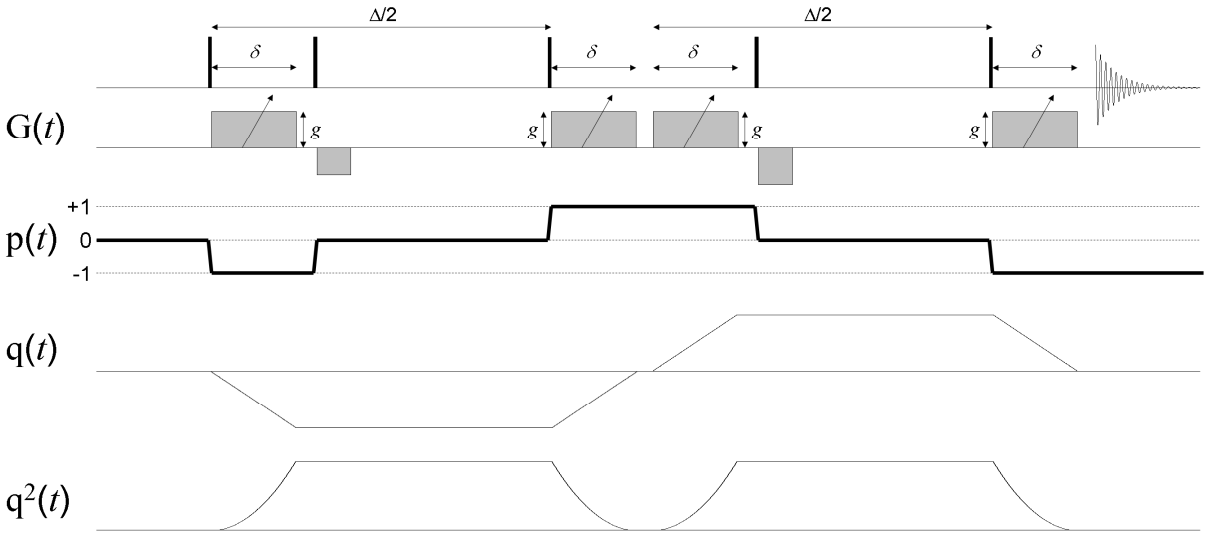

Figure 2.10: Double STE sequence for convection compensated diffusion measurements. The coherence pathway shown is selected by applying the phase cycle described in reference [90]. The integral of $q^2(t)$ determines the signal attenuation due to diffusion, while the integral over $q(t)$ determines the effect of convection. The double STE sequence is constructed in such way that the latter is zero.

a diffusion delay of $\Delta/2$. The only difference is that their CTPs are exactly opposite in sign. The total diffusion attenuation is then given by (see also appendix B):

$$\begin{aligned} I &= I_0 \underbrace{e^{-D_t\gamma^2 g^2\delta^2\left(\frac{\Delta}{2}-\frac{\delta}{3}\right)}}_{\text{STE 1}} \underbrace{e^{-D_t\gamma^2 g^2\delta^2\left(\frac{\Delta}{2}-\frac{\delta}{3}\right)}}_{\text{STE 2}} \\ &= I_0 e^{-D_t\gamma^2 g^2\delta^2\left(\Delta-\frac{2\delta}{3}\right)} \end{aligned} \tag{2.36}$$

This equation is thus practically equivalent as before. However, assuming that v_z remains constant during the pulse sequence, the total phase term because of flow will be:

$$\underbrace{e^{-iv_z\gamma g\delta\Delta}}_{\text{STE 1}} \underbrace{e^{iv_z\gamma g\delta\Delta}}_{\text{STE 2}} = 1 \tag{2.37}$$

The double STE sequence exploits the previously derived fact that flow introduces a phase factor depending on the sign of the gradient strength and thus allows cancelation of this phase factor by applying both STEs with CTPs of opposite signs. This method is very effective in removing the effects of convection as long as it is laminar and that the velocity fluctuations during the experiment time are negligible. It has two distinct disadvantages though. First, an STE sequence inherently reduces the signal by a factor of 2 since only half of the magnetisation helix is transferred to the z-axis by the second 90° pulse and the other half is purged by the spoil gradient. Since in a convection compensated sequence two subsequent STEs are applied, the total inherent signal reduction will be a factor of 4 compared to a 1D spectrum without

taking relaxation into account. This can significantly increase the required measurement time to achieve an adequate signal-to-noise ratio throughout the attenuation profile. In addition, the many rf-pulses required necessitate an extensive phase cycle, making the experiment inherently long even when signal-to-noise ratio does not require that many scans.

2.4.4 Other STE modifications and experiments

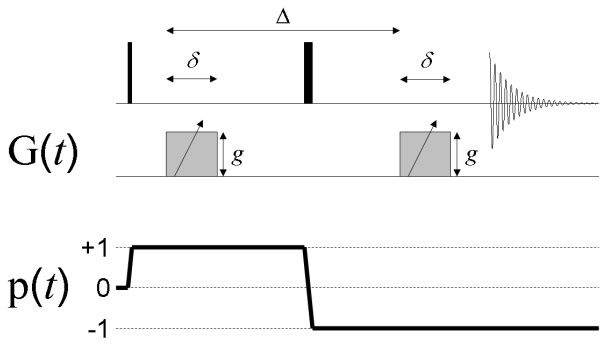

Figure 2.11: Spin echo sequence

An alternative for the STE experiment is the spin echo or Hahn echo, where the echo is formed by a 180° rf-pulse instead of two 90° pulses (Figure 2.11). The advantage of this sequence is that there is no inherent loss of signal with a factor of 2 as in the STE sequence. Indeed, this advantage becomes even more pronounced in its convection compensated version, since then it has an inherent four fold signal-to-noise advantage above the double STE. Another advantage is that the phase cycling of a spin echo is less extensive due to the fewer rf-pulses. The main disadvantage is that during the diffusion delay the magnetisation will be subject to T_2 relaxation instead of T_1 relaxation, which for large molecules is a major issue. Another disadvantage is that homonuclear scalar coupling evolution has much more time to develop during the spin echo sequence (*ca.* $\Delta+\delta$ vs. only *ca.* 2δ in the STE), leading to stronger antiphase distortions of multiplets because of J-modulation.

The relative signal-to-noise ratio between the STE and the spin echo sequences can be compared by considering the time the magnetisation spends longitudinal or transverse, while taking into account the inherent signal-to-noise loss by a factor of two in the STE:

$$\frac{(S/N)_{STE}}{(S/N)_{SE}} = \frac{0.5e^{-(\Delta-\delta)R_1-2\delta R_2}}{e^{-(\Delta+\delta)R_2}} = \frac{1}{2}e^{-(\Delta-\delta)R_1-(\delta-\Delta)R_2} = \frac{1}{2}e^{-(\Delta-\delta)(R_1-R_2)} \qquad (2.38)$$

with R_1 (= $1/T_1$) and R_2 (= $1/T_2$) the relaxation rates. To decide whether to use the STE over the spin echo for reasons of signal-to-noise, one should therefore know the difference in relaxation rates and make the following evaluation:

$$R_2 - R_1 \overset{?}{<} \frac{\ln 2}{\Delta - \delta} \tag{2.39}$$

For larger molecules where $R_2 >> R_1$, this relation will usually favour the STE sequence. Together with the less significant J-modulation, this makes the STE sequence the preferred experiment in most cases.

Several other modifications to both the STE and spin echo sequences exist. For example, experiments which compensate for the effect of background magnetic field gradients[49, 50]. Indeed, the above derivation of the Stejskal-Tanner equation assumed that the static B_0 magnetic field was perfectly homogenous. If this is not the case, it will lead to gradient-B_0 cross-terms in the equation, biasing the results.

Other modifications include, but are not limited to: the insertion of a multiple quantum coherence order step to make the gradients more effective[51]; the inclusion of purge pulses or z-filters to remove the lineshape distortion effects of homonuclear scalar coupling[52]; removal of the multiplet structure by homonuclear decoupling, strongly increases the resolution of the spectra[53]; and several implementations of water suppression[54-56].

DOSY experiments can also be combined with other multidimensional NMR experiments to yield so-called 3D-DOSY spectra. Reported experiments which have been successfully combined with DOSY include 2D J resolved [57, 58], COSY [6, 45], NOESY [59], TOCSY [60] and HMQC spectra[61, 62]. The most interesting advantage of these experiments is that they increase the resolution of the chemical shift information by spreading the information over two dimensions. As discussed in the next section, signal overlap very strongly reduces the extent up to which peaks can be resolved in a DOSY experiment, and thus increasing the resolution will reduce this problem. A great disadvantage is the long experiment time, as two indirect dimensions need to be sampled and the phase cycling can be extensive. The latter problem has been addressed upon by use of so-called internal DOSY (IDOSY) sequences[58, 63] where the diffusion encoding and delay is included within the parent 2D pulse sequence itself instead of before or afterwards. It has also been demonstrated that it is possible to implement convection compensation very efficiently into these IDOSY sequences without any loss of signal-to-noise ratio as in the double STE sequence[45].

2.5 Processing diffusion NMR spectra

2.5.1 Introduction: the ill-posed problem

DOSY is often regarded as a form of two-dimensional NMR spectroscopy along the line of classic experiments as COSY, NOESY, HSQC, etc. However, the mathematics of converting the exponential decays to diffusion coefficients is very different from converting oscillations in a time dimension to frequencies. For the latter, the experimental time function needs to be decomposed into sine and cosine functions of different frequencies, which have the interesting property of being orthogonal with respect to each other. This means that an experimental function over time will be described by only one unique distribution of sine and cosine functions; since each frequency component ω can be extracted by an orthogonal projection out of the function $\mathrm{f}(t)$. This is in fact how the mechanism of the Fourier transform (FT) can be interpreted, generating a function of frequency components $\mathrm{F}(\omega)$ that describe the function $\mathrm{f}(t)$:

$$\mathrm{F}(\omega) = \mathrm{FT}\left[\mathrm{f}(t)\right] = \frac{1}{\sqrt{2\pi}} \int_{-\infty}^{+\infty} \mathrm{f}(t) e^{-i\omega t} dt \tag{2.40}$$

The inverse Fourier transform (IFT) does exactly the opposite: it takes the frequency components and rebuilds the function $\mathrm{f}(t)$:

$$\mathrm{f}(t) = \mathrm{IFT}\left[\mathrm{F}(\omega)\right] = \frac{1}{\sqrt{2\pi}} \int_{-\infty}^{+\infty} \mathrm{F}(\omega) e^{i\omega t} d\omega \tag{2.41}$$

In NMR, the Fourier transform is widely used to analyse the frequencies that are present in the time domain data. The Fourier transform can relatively easy be performed numerically. When noise is present in experimental time function, it will be converted into noise in the frequency function without any change in its magnitude; it will be uniformly spread across all frequencies.

DOSY would require a similar transformation from a signal decay function $\mathrm{F}(s)$ into a decay rate distribution function $\mathrm{f}(D)$; where s is then equivalent with $g^2\gamma^2\delta^2\Delta$'. The Laplace transform (LT) is very similar to the Fourier transform, and can be seen as to convert the decay rate distribution function $\mathrm{f}(D)$ into the decay function $\mathrm{F}(s)$:

$$\mathrm{F}(s) = \mathrm{LT}\left[\mathrm{f}(D)\right] = \frac{1}{\sqrt{2\pi}} \int_{-\infty}^{+\infty} \mathrm{f}(D) e^{-qs} dD \tag{2.42}$$

For example, if two decay rates D_1 and D_2 are present (*i.e.* a signal in the DOSY spectrum which is the result of two overlapping resonances of two distinctly diffusion species), the decay rate distribution function $\mathrm{f}(D)$ is the sum of two delta functions, and the decay function becomes a biexponential:

$$\begin{aligned} \mathrm{F}(s) &= \frac{1}{\sqrt{2\pi}} \int_{-\infty}^{+\infty} \left(\delta(D - D_1) + \delta(D - D_2) \right) e^{-Ds} dD \\ &= \frac{1}{\sqrt{2\pi}} \left(e^{-D_1 s} + e^{-D_2 s} \right) \end{aligned} \tag{2.43}$$

An inverse Laplace transform (ILT) exists as well[64], which converts the decay function into the decay rate distribution function (with c a real number, whose implications fall outside the scope of this text):

$$\mathrm{f}(D) = \mathrm{ILT}\left[\mathrm{F}(s) \right] = \frac{1}{i\sqrt{2\pi}} \int_{c-i\infty}^{c+i\infty} \mathrm{F}(s) e^{Ds} ds \tag{2.44}$$

This is what would be required for the DOSY analysis. However, the discrete experimental data would need to be treated numerically by the ILT, and this is where things go wrong! In the case of the Laplace transform, it is not true that the magnitude of the noise is retained by the transform. Consider the Laplace transform of the sine and cosine functions:

$$\begin{aligned} \int_{-\infty}^{+\infty} \sin(\omega D) e^{-Ds} dD &= \frac{\omega}{\omega^2 + s^2} \\ \int_{-\infty}^{+\infty} \cos(\omega D) e^{-Ds} dD &= \frac{s}{\omega^2 + s^2} \end{aligned} \tag{2.45}$$

It is seen that as the frequency ω increases, the less intense the transformed sine or cosine function will be. Any function can be described by a continuous distribution of frequencies by an integral sum of sine and cosine functions (*cf.* Fourier transform), the higher frequencies describing the 'fine structure' or the 'high resolution part' of the function. Since the Laplace transform reduces the presence of the higher frequencies, it effectively acts as a smoothening operation. The inverse Laplace transform will essentially do the opposite, intensifying the higher frequency components. The problem now arises if an experimentally obtained decay function $\mathrm{F}(s)$ that contains experimental noise is subjected to the ILT. As noted above, noise possesses a more or less uniform distribution in its frequency components. The high frequency noise components will therefore be strongly amplified, quickly dominating the total signal at the higher frequencies.

Another way of looking at this issue is illustrated by the following reasoning[65]. The ILT of an experimental decay $G(s)$ can be solved by finding a trial function $g(D)$ that minimises χ^2, which is defined as the Euclidean distance between the Laplace transform of $g(D)$ and the experimental decay $G(s)$:

$$\chi^2 = \left\| \mathrm{LT}\left[g(D)\right] - G(s) \right\| \tag{2.46}$$

Since the Laplace transform strongly attenuates the higher frequency components, it can be assumed that the Fourier transform of $\mathrm{LT}[g(D)]$ is below the noise level starting from a frequency $\omega_{\max}$ and can thus be considered to be near zero:

$$\mathrm{FT}\left[\mathrm{LT}\left[g(D)\right]\right](\omega) \begin{cases} \neq 0 & \omega \leq \omega_{\max} \\ \approx 0 & \omega > \omega_{\max} \end{cases} \tag{2.47}$$

Consider a function $g^0(q)$ which has the following properties:

$$\mathrm{FT}\left[g^0(D)\right](\omega) \begin{cases} = 0 & \omega \leq \omega_{\max} \\ \neq 0 & \omega > \omega_{\max} \end{cases} \tag{2.48}$$

And therefore:

$$\mathrm{FT}\left[\mathrm{LT}\left[g^0(D)\right]\right](\omega) \begin{cases} = 0 & \omega \leq \omega_{\max} \\ \approx 0 & \omega > \omega_{\max} \end{cases} \tag{2.49}$$

This implies that there is no unique solution to the ILT, since $g(D) + g^0(D)$ will give the same value for χ^2 in (2.46) as would $g(D)$. For this reason the ILT is said to be an ill-posed problem and is therefore not at all so straightforward to implement as the Fourier transform.

2.5.2 Regularisation of the Inverse Laplace transform

As was discussed in the previous section, there exists a whole range of solutions to the ILT. How can one select from these different solutions the one which is most reliable? This selection is called regularisation of the ILT problem[65], and can be achieved by inserting prior knowledge about the system (for example the average of the diffusion coefficient distribution) or physical common sense (*e.g.* non-negativity: no negative diffusion coefficients allowed) into the fitting condition (2.46). When there is insufficient prior knowledge concerning the functional form of the solution (*e.g.* a sample of polydisperse polymers is studied without any knowledge concerning the

distribution of the diffusion coefficients, or the number of discrete components at one frequency in the spectrum), many solutions to the ILT will still remain. At that point, it is necessary to consider the so-called principle of parsimony, which states that the 'simplest' solution should be selected. This means the one distribution which reveals the least amount of detail that is not directly implied by the prior knowledge. Within the frame of reasoning of the previous section, this principle can be roughly understood as selecting the solution with the lowest contribution of high frequency components, which were the ones that are making the ILT ill-posed in the first place. In practice, it comes down to increasing the accuracy of the solution by decreasing the resolution.

Multiple algorithms that attempt to regularize the ILT have been applied in the case of DOSY. One of the earliest is CONTIN, written by Stephen Provencher[66, 67]. It has mainly been used to study polydisperse systems such as polymer mixtures[9], large unilamellar phospholipids[68] or humic and fulvic acids[69]. The program uses the integral of the squared of the second derivative of the function g(D) as an indicator for the smoothness of the function. The program attempts to find a solution $\mathrm{g}(D)$ which agrees to the given prior knowledge and which minimises χ^{*2}, which is a compromise (reflected in the regularisation parameter λ) between minimising (2.46) and minimising this smoothness indicator:

$$\chi^{*2} = \chi^2 + \lambda\left(\int_a^b \left(\frac{d^2\,\mathrm{g}(D)}{dD^2}\right)^2 dD\right) \tag{2.50}$$

with the range of diffusion coefficients assumed to fall in the interval [a,b]. Another method that has found application for the analysis of DOSY spectra is the maximum entropy (MaxEnt) method[70]. The Shannon entropy S in the context of information theory is used here. The entropy of a chance distribution $\mathrm{f}(x)$ is a measure of the uncertainty of the outcome of an experiment subjected to this distribution, and is defined as:

$$S = -\int_{-\infty}^{-\infty} \mathrm{f}(x)\ln\left(\mathrm{f}(x)\right)dx \tag{2.51}$$

The MaxEnt method can be interpreted as finding the distribution having the greatest entropy, and thus uncertainty, given the known information. For example, when it is known that a distribution has a certain mean and standard deviation, but the exact form of the distribution is unknown, then there is in principle an infinite amount of possible distributions. When a prediction needs to be made on the outcome of an experiment however, it is desirable that this prediction is based on the distribution that, besides the given facts of the mean and standard deviation, leaves the greatest

uncertainty. If this would not be the case, the prediction would be biased ('prejudiced') since assumptions would be made that cannot be substantiated from the given knowledge. In this particular example of knowing only the mean and the standard deviation of a distribution, it can be shown that the Gaussian distribution is the one with that maximises entropy. Entropy can be applied as a regularisation function to the ILT[65]. Again χ^{*2} needs to be minimised, which is a compromise between minimising the fitting the distribution via χ^2 and maximising the entropy:

$$\chi^{*2} = \chi^2 - \lambda\left(\int_a^b \mathrm{g}(D)\ln\left(\frac{1}{\mathrm{g}(D)}\right)dD\right) \tag{2.52}$$

λ is again a regularisation parameter. The choice of its value is very important and is controlled by the MaxEnt algorithm[70].

As a final note, a regularisation method using Hopfield neural networks has been described as well[71], but will not be discussed here.

2.5.3 Data fitting using regression analysis

Both CONTIN and MaxEnt are good methods to deal with polydisperse components, as both methods do not necessarily require any input on the exact functional form of the diffusion coefficient distribution in the signal decay. Even in the case of discrete components, both methods are useful to get insight into how many different components are present at each frequency, since the methods are non-parametric in nature. When it is known how many components are present in the signal decay at a certain frequency, the number of possible solutions to the ILT becomes very restricted. If, for example, it is known (or assumed) that only two components are present in the decaying signal (a biexponential decay), the solution should be a sum of two delta functions, and (2.46) becomes:

$$\begin{aligned}\chi^2 &= \left\|\mathrm{LT}\left[A_1\delta(D-D_1)+A_2\delta(D-D_2)\right]-\mathrm{G}(s)\right\| \\ &= \left\|\left(A_1e^{-D_1s}+A_2e^{-D_2s}\right)-\mathrm{G}(s)\right\|\end{aligned} \tag{2.53}$$

This leaves only four parameters to be fitted (A_1, D_1, A_2 and D_2). There is no guarantee however that the assumption of a biexponential decay is correct, as sometimes the presence of another component can be obscured by a similar diffusion coefficient when compared to another other component or when it arises from a relatively small intensity contribution.

Typically, the non-linear regression analysis is performed using the Levenberg-Marquart method[72]. In the work presented in this dissertation, the errors on the fitted parameters were assessed using a Monte Carlo procedure[73], as explained in appendix C. In general, the uncertainty of the fitted parameters increases upon increase of the number of components that needs to be fitted, not only due to the decreased statistical degrees of freedom, but also due to the covariance that exists between the parameters. In the case of multiexponential decays, it is necessary to sample the decay far enough so that the ratios between the different exponentials of the decay have sufficiently decreased[65, 74]. When this is not the case, it won't be possible to separate the components out of the decay with sufficient precision. The lower the relative difference between the diffusion coefficients in the multiexponential decay, the further down the decay will need to be sampled by increasing the maximum gradient strength, the gradient duration δ or the diffusion delay Δ. Therefore, the successfulness of multiexponential analysis of diffusion data is very dependent on the signal-to-noise ratio of the NMR spectra, as the level at which the signal would need to attenuate to must be above the noise level. In any case, when signals of different species overlap in NMR spectra and multiexponential fitting is required, the diffusion analysis becomes much more involved.

2.5.4 Multivariate processing techniques

Several methods have been proposed for the multivariate analysis of diffusion spectra. The idea of these techniques is to take advantage of the fact that all resonances in an NMR spectrum that belong to the same species should theoretically provide the same diffusion coefficient. The dataset obtained from the diffusion NMR experiment can be represented by a matrix $\mathbf{M}$, each row representing a 1D spectrum (consisting out of N_S data points) recorded at one particular gradient strength (N_g increments in total). This matrix can be decomposed into a matrix $\mathbf{C}$ that in each column contains the attenuation decay of a component and a matrix $\mathbf{S}^T$ that contains in each row the 'pure' spectrum of each component[75]:

$$\underbrace{\mathbf{M}}_{(N_g \times N_S)} = \underbrace{\mathbf{C}}_{(N_g \times n)} \times \underbrace{\mathbf{S}^T}_{(n \times N_S)} \tag{2.54}$$

with n the number of components in the spectrum. Mathematically, the matrix $\mathbf{M}$ is not uniquely linked to the matrices $\mathbf{C}$ and $\mathbf{S}$, since a random non-singular matrix $\mathbf{A}$ of size $n \times n$ can convert them into a new pair of matrices that also agrees to equation (2.54):

$$\begin{aligned}\mathbf{M} &= \mathbf{C}\mathbf{S}^T \\ &= \mathbf{C}\mathbf{A}^{-1}\mathbf{A}\mathbf{S}^T \\ &= \left(\mathbf{C}\mathbf{A}^{-1}\right)\left(\mathbf{A}\mathbf{S}^T\right) \\ &= \mathbf{C'}\mathbf{S'}^T\end{aligned} \tag{2.55}$$

The multivariate technique is successful when it is able to fit the physically correct matrices **C** and **S** out of **M**. To do so, restrictions have to be imposed on the properties of the matrices **C** and **S** so that the possible solutions become limited. This can be nonnegativity, for example, or the constraint that the decays in the matrix **C** must have an exponential form.

One of the first methods proposed was CORE[76] (Component resolved NMR spectroscopy), which performs a global least square fitting over the entire spectrum, providing n diffusion coefficients and the intensity of each component at each frequency. The method does suffer from long computation time, although recently an improved time-efficient algorithm has been proposed[77]. Another method is DECRA[78, 79] (Direct Exponential Curve Resolution Algorithm), which further builds on a technique developed by Stilbs[80]. It is based on the Generalised Rank Annihilation (GRAM) method, which states that when two datasets $\mathbf{M}_1$ and $\mathbf{M}_2$ are obtained that are correlated, there exists only one unique solution for **C** and **S** that decomposes both datasets:

$$\begin{aligned}\mathbf{M}_1 &= \mathbf{C}\mathbf{S}^T \\ \mathbf{M}_2 &= \mathbf{C}\boldsymbol{\beta}\mathbf{S}^T\end{aligned} \tag{2.56}$$

with **β** a diagonal matrix establishing the correlation between both datasets. DECRA cleverly uses only one DOSY experiment of N_g increments, splitting into two datasets of N_g-1 increments in accordance with equation (2.56). The advantage of the method is that it is extremely fast in computation and easily implemented, requiring no initial guesses. The disadvantage is that the experiment must be sampled in such a fashion that the squared of the gradient strength is incremented with constant intervals and that the decays are pure exponential. Another method is MCR[75, 81-85] (Multivariate Curve Resolution), which finds the matrices **C** and **S** by starting from an initial guess of one of the two matrices and then through an iterative procedure finds a pair of matrices that fits the data matrix **M**. The method heavily relies on a good choice of the initial guess, and many chemometric methods have been used to achieve this. The advantage of this method is that it does not require the decays to have an exponential form. This is of interest for diffusion analysis of samples with a continuous distribution of sizes, such as polymers. The method can be further improved by forcing the decays to be exponential (or to obey any other functional form), further ensuring that the results are the physically correct ones[83].

Finally, a more recent improvement on multivariate DOSY processing is T_1-DOSY[86], which combines the diffusion measurement with T_1 relaxation measurements. This method effectively creates a dataset M which is trilinear (*i.e.* it can be written as an array with three dimensions instead of a matrix of two dimensions as in equation (2.54)). The contrast added to the dataset by the third dimension has been shown to strongly increase the possibility of separating the component spectra[86].

In general, the advantage of multivariate analysis of DOSY data is that it helps improving the resolution in the diffusion dimension at places in the spectrum where univariate methods would get into trouble. If the component has signals in the spectrum that are isolated and can thus be fitted with good confidence, this will help improve – through the global aspect of the method – the quality of resolution in the diffusion dimension for signals that suffer from spectral overlap and thus behave multiexponentially (section 2.5.3). Also, the signals with low signal-to-noise ratios will provide improved results. The multivariate techniques are thus better in dealing with low signal-to-noise DOSY spectra[76]. A disadvantage is that at certain frequencies the algorithms might predict contributions from components that in reality are not present in that spectral region. This can occur when the algorithm attempts to explain deviations in the exponential behaviour of the decay (*e.g.* non-uniform gradients, see next section) by 'mixing in' the other components. This phenomenon is known as cross-talk and provides confusing results.

2.5.5 Correction for experimental imperfections

As a final note, it should be mentioned that several techniques have been proposed to improve the quality of the data and the fitting itself. Reference Deconvolution[87, 88] is a post-acquisition technique that is capable of correcting for imperfections in the spectra as long as they are present on every single peak. These imperfections include varying line shapes or peak positions over time[89], for example due to temperature fluctuations in aqueous samples. Another example is the correction for gradient non-uniformity. The DOSY experiment assumes that the gradient creates a linearly varying magnetic field over the sample. However, in practice this not perfectly the case. The gradient strength typically slightly varies along the sample, especially along the edges of the detection volume. This leads to probe and pulse sequence dependent small deviations from the Gaussian form of the signal intensity decay. Not only does this lead to small systematic errors in the diffusion coefficients, it further complicates multiexponential analysis. Methods that compensate this problem have been proposed[90, 91], all involving a modification of the Stesjkal-Tanner equation. Such methods have shown to improve the quality of univariate biexponential fitting methods[74] and to reduce the amount of cross-talk in multivariate techniques[89]. In principle, a modification of the Stesjkal-Tanner equation can be applied to all

mentioned multivariate techniques, including DECRA[92]. Though these techniques all improve the results of the diffusion analysis, they will not be applied during this dissertation as mainly monoexponential fitting suffices.

2.6 References

[1] M. Nilsson, "The DOSY Toolbox: A new tool for processing PFG NMR diffusion data". *Journal of Magnetic Resonance*, **2009**, *200*(2) 296-302.

[2] C. S. Johnson, "Diffusion ordered nuclear magnetic resonance spectroscopy: principles and applications". *Progress in Nuclear Magnetic Resonance Spectroscopy*, **1999**, *34*(3-4) 203-256.

[3] K. F. Morris and C. S. Johnson, "Diffusion-Ordered 2-Dimensional Nuclear-Magnetic-Resonance Spectroscopy". *Journal of the American Chemical Society*, **1992**, *114*(8) 3139-3141.

[4] M. F. Lin and M. J. Shapiro, "Mixture analysis in combinatorial chemistry. Application of diffusion-resolved NMR spectroscopy". *Journal of Organic Chemistry*, **1996**, *61*(21) 7617-7619.

[5] Y. Cohen, L. Avram and L. Frish, "Diffusion NMR spectroscopy in supramolecular and combinatorial chemistry: An old parameter - New insights". *Angewandte Chemie-International Edition*, **2005**, *44*(4) 520-554.

[6] D. H. Wu, A. D. Chen and C. S. Johnson, "Three-dimensional diffusion-ordered NMR spectroscopy: The homonuclear COSY-DOSY experiment". *Journal of Magnetic Resonance Series A*, **1996**, *121*(1) 88-91.

[7] M. Nilsson, I. F. Duarte, C. Almeida, I. Delgadillo, B. J. Goodfellow, A. M. Gil and G. A. Morris, "High-resolution NMR and diffusion-ordered spectroscopy of port wine". *Journal of Agricultural and Food Chemistry*, **2004**, *52*(12) 3736-3743.

[8] T. Gostan, C. Moreau, A. Juteau, E. Guichard and M. A. Delsuc, "Measurement of aroma compound self-diffusion in food models by DOSY". *Magnetic Resonance in Chemistry*, **2004**, *42*(6) 496-499.

[9] A. Jerschow and N. Muller, "Diffusion-separated nuclear magnetic resonance spectroscopy of polymer mixtures". *Macromolecules*, **1998**, *31*(19) 6573-6578.

[10] P. S. Pregosin, "Ion pairing using PGSE diffusion methods". *Progress in Nuclear Magnetic Resonance Spectroscopy*, **2006**, *49*(3-4) 261-288.

[11] D. Y. Li, I. Keresztes, R. Hopson and P. G. Williard, "Characterization of Reactive Intermediates by Multinuclear Diffusion-Ordered NMR Spectroscopy (DOSY)". *Accounts of Chemical Research*, **2009**, *42*(2) 270-280.

[12] D. Y. Li, G. Kagan, R. Hopson and P. G. Williard, "Formula Weight Prediction by Internal Reference Diffusion-Ordered NMR Spectroscopy (DOSY)". *Journal of the American Chemical Society*, **2009**, *131*(15) 5627-5634.

[13] S. Floquet, S. Brun, J. F. Lemonnier, M. Henry, M. A. Delsuc, Y. Prigent, E. Cadot and F. Taulelle, "Molecular Weights of Cyclic and Hollow Clusters Measured by DOSY NMR Spectroscopy". *Journal of the American Chemical Society*, **2009**, *131*(47) 17254-17259.

[14] S. Auge, P. O. Schmit, C. A. Crutchfield, M. T. Islam, D. J. Harris, E. Durand, M. Clemancey, A. A. Quoineaud, J. M. Lancelin, Y. Prigent, F. Taulelle and M. A. Delsuc, "NMR Measure of Translational Diffusion and Fractal Dimension. Application to Molecular Mass Measurement". *Journal of Physical Chemistry B*, **2009**, *113*(7) 1914-1918.

[15] C. S. Johnson, "Effects of Chemical-Exchange in Diffusion-Ordered 2D NMR-Spectra". *Journal of Magnetic Resonance Series A*, **1993**, *102*(2) 214-218.

[16] E. J. Cabrita, S. Berger, P. Brauer and J. Karger, "High-resolution DOSY NMR with spins in different chemical surroundings: Influence of particle exchange". *Journal of Magnetic Resonance*, **2002**, *157*(1) 124-131.

[17] E. J. Cabrita and S. Berger, "HR-DOSY as a new tool for the study of chemical exchange phenomena". *Magnetic Resonance in Chemistry*, **2002**, *40* S122-S127.

[18] L. H. Lucas and C. K. Larive, "Measuring ligand-protein binding using NMR diffusion experiments". *Concepts in Magnetic Resonance Part A*, **2004**, *20A*(1) 24-41.

[19] L. Fielding, "NMR methods for the determination of protein-ligand dissociation constants". *Current Topics in Medicinal Chemistry*, **2003**, *3*(1) 39-53.

[20] L. Fielding, "Determination of association constants (K_a) from solution NMR data". *Tetrahedron*, **2000**, *56*(34) 6151-6170.

[21] O. Soderman, P. Stilbs and W. S. Price, "NMR studies of surfactants". *Concepts in Magnetic Resonance Part A*, **2004**, *23A*(2) 121-135.

[22] U. R. M. Kjellin, J. Reimer and P. Hansson, "An investigation of dynamic surface tension, critical micelle concentration, and aggregation number of three nonionic surfactants using NMR, time-resolved fluorescence quenching, and maximum bubble pressure tensiometry". *Journal of Colloid and Interface Science*, **2003**, *262*(2) 506-515.

[23] M. Schonhoff and O. Soderman, "PFG-NMR diffusion as a method to investigate the equilibrium adsorption dynamics of surfactants at the solid/liquid interface". *Journal of Physical Chemistry B*, **1997**, *101*(41) 8237-8242.

[24] P. Saveyn, J. De Geeter, D. Sinnaeve, P. Van der Meeren and J. C. Martins, "Influence of the Vesicular Bilayer Structure on the Sorption of Ethylbenzyl Alcohol". *Langmuir*, **2009**, *25*(19) 11322-11327.

[25] P. Saveyn, E. Cocquyt, D. Sinnaeve, J. C. Martins, D. Topgaard and P. Van der Meeren, "NMR study of the sorption behavior of benzyl alcohol derivatives into sonicated and extruded dioctadecyldimethylammonium chloride (DODAC) dispersions: The relevance of membrane fluidity". *Langmuir*, **2008**, *24*(7) 3082-3089.

[26] K. I. Momot and P. W. Kuchel, "Pulsed field gradient nuclear magnetic resonance as a tool for studying drug delivery systems". *Concepts in Magnetic Resonance Part A*, **2003**, *19A*(2) 51-64.

[27] K. R. Deaton, E. A. Feyen, H. J. Nkulabi and K. F. Morris, "Pulsed-field gradient NMR study of sodium dodecyl sulfate micelle-peptide association". *Magnetic Resonance in Chemistry*, **2001**, *39*(5) 276-282.

[28] T. Brand, E. J. Cabrita, G. A. Morris, R. Gunther, H. J. Hofmann and S. Berger, "Residue-specific NH exchange rates studied by NMR diffusion experiments". *Journal of Magnetic Resonance*, **2007**, *187*(1) 97-104.

[29] M. Nilsson, M. Khajeh, A. Botana, M. A. Bernstein and G. A. Morris, "Diffusion NMR and trilinear analysis in the study of reaction kinetics". *Chemical Communications*, **2009**(10) 1252-1254.

[30] B. Antalek, "Using pulsed gradient spin echo NMR for chemical mixture analysis: How to obtain optimum results". *Concepts in Magnetic Resonance*, **2002**, *14*(4) 225-258.

[31] W. S. Price, "Pulsed-field gradient nuclear magnetic resonance as a tool for studying translational diffusion .1. Basic theory". *Concepts in Magnetic Resonance*, **1997**, *9*(5) 299-336.

[32] W. S. Price, "Pulsed-field gradient nuclear magnetic resonance as a tool for studying translational diffusion: Part II. Experimental aspects". *Concepts in Magnetic Resonance*, **1998**, *10*(4) 197-237.

[33] J. Keeler, R. T. Clowes, A. L. Davis and E. D. Laue, "Pulsed-Field Gradients - Theory and Practice". *Nuclear Magnetic Resonance, Pt C*, **1994**, *239* 145-207.

[34] E. L. Hahn, "Spin Echoes". *Physical Review*, **1950**, *80*(1) 580-594.

[35] H. C. Torrey, "Bloch Equations with Diffusion Terms". *Physical Review*, **1956**, *104*(3) 563.

[36] E. O. Stejskal and J. E. Tanner, "Spin diffusion measurements: spin echoes in the presence of a time-dependent field gradient". *Journal of Chemical Physics*, **1965**, *42*(1) 288-92.

[37] W. S. Price and P. W. Kuchel, "Effect of Nonrectangular Field Gradient Pulses in the Stejskal and Tanner (Diffusion) Pulse Sequence". *Journal of Magnetic Resonance*, **1991**, *94*(1) 133-139.

[38] R. M. Cotts, M. J. R. Hoch, T. Sun and J. T. Markert, "Pulsed Field Gradient Stimulated Echo Methods for Improved NMR Diffusion Measurements in Heterogeneous Systems". *Journal of Magnetic Resonance*, **1989**, *83*(2) 252-266.

[39] R. F. Karlicek and I. J. Lowe, "Modified Pulsed Gradient Technique for Measuring Diffusion in the Presence of Large Background Gradients". *Journal of Magnetic Resonance*, **1980**, *37*(1) 75-91.

[40] A. D. Chen, C. S. Johnson, M. Lin and M. J. Shapiro, "Chemical exchange in diffusion NMR experiments". *Journal of the American Chemical Society*, **1998**, *120*(35) 9094-9095.

[41] M. D. Pelta, G. A. Morris, M. J. Stchedroff and S. J. Hammond, "A one-shot sequence for high-resolution diffusion-ordered spectroscopy". *Magnetic Resonance in Chemistry*, **2002**, *40* S147-S152.

[42] G. Wider, V. Dotsch and K. Wuthrich, "Self-Compensating Pulsed Magnetic-Field Gradients for Short Recovery Times". *Journal of Magnetic Resonance Series A*, **1994**, *108*(2) 255-258.

[43] W. J. Goux, L. A. Verkruyse and S. J. Salter, "The Impact of Rayleigh-Benard Convection on NMR Pulsed-Field-Gradient Diffusion Measurements". *Journal of Magnetic Resonance*, **1990**, *88*(3) 609-614.

[44] A. Jerschow, "Thermal convection currents in NMR: Flow profiles and implications for coherence pathway selection". *Journal of Magnetic Resonance*, **2000**, *145*(1) 125-131.

[45] M. Nilsson and G. A. Morris, "Improving pulse sequences for 3D DOSY: Convection compensation". *Journal of Magnetic Resonance*, **2005**, *177*(2) 203-211.

[46] N. M. Loening and J. Keeler, "Measurement of convection and temperature profiles in liquid samples". *Journal of Magnetic Resonance*, **1999**, *139*(2) 334-341.

[47] W. S. Price, in *Encyclopedia of Nuclear Magnetic Resonance, Vol. 9* (Eds.: D. M. Grant, R. K. Harris), John Wiley & Sons Ltd., Chichester, UK, **2002**, pp. 364-374.

[48] A. Jerschow and N. Muller, "Suppression of convection artifacts in stimulated-echo diffusion experiments. Double-stimulated-echo experiments". *Journal of Magnetic Resonance*, **1997**, *125*(2) 372-375.

[49] W. S. Price, P. Stilbs, B. Jonsson and O. Soderman, "Macroscopic background gradient and radiation damping effects on high-field PGSE NMR diffusion measurements". *Journal of Magnetic Resonance*, **2001**, *150*(1) 49-56.

[50] G. Zheng and W. S. Price, "Suppression of background gradients in (B_0 gradient-based) NMR diffusion experiments". *Concepts in Magnetic Resonance Part A*, **2007**, *30A*(5) 261-277.

[51] G. Zheng, A. M. Torres and W. S. Price, "MQ-PGSTE: A new multi-quantum STE-based PGSE NMR sequence". *Journal of Magnetic Resonance*, **2009**, *198*(2) 271-274.

[52] A. M. Torres, R. Dela Cruz and W. S. Price, "Removal of J-coupling peak distortion in PGSE experiments". *Journal of Magnetic Resonance*, **2008**, *193*(2) 311-316.

[53] M. Nilsson and G. A. Morris, "Pure shift proton DOSY: diffusion-ordered ^{1}H spectra without multiplet structure". *Chemical Communications*, **2007**(9) 933-935.

[54] S. Balayssac, M. A. Delsuc, V. Gilard, Y. Prigent and M. Malet-Martino, "Two-dimensional DOSY experiment with Excitation Sculpting water suppression for the analysis of natural and biological media". *Journal of Magnetic Resonance*, **2009**, *196*(1) 78-83.

[55] K. I. Momot and P. W. Kuchel, "Convection-compensating PGSE experiment incorporating excitation-sculpting water suppression (CONVEX)". *Journal of Magnetic Resonance*, **2004**, *169*(1) 92-101.

[56] G. Zheng, T. Stait-Gardner, P. G. A. Kumar, A. M. Torres and W. S. Price, "PGSTE-WATERGATE: An STE-based PGSE NMR sequence with excellent solvent suppression". *Journal of Magnetic Resonance*, **2008**, *191*(1) 159-163.

[57] L. H. Lucas, W. H. Otto and C. K. Larive, "The 2D-J-DOSY experiment: Resolving diffusion coefficients in mixtures". *Journal of Magnetic Resonance*, **2002**, *156*(1) 138-145.

[58] M. Nilsson, A. M. Gil, I. Delgadillo and G. A. Morris, "Improving pulse sequences for 3D diffusion-ordered NMR spectroscopy: 2DJ-IDOSY". *Analytical Chemistry*, **2004**, *76*(18) 5418-5422.

[59] E. K. Gozansky and D. G. Gorenstein, "DOSY-NOESY: Diffusion-ordered NOESY". *Journal of Magnetic Resonance Series B*, **1996**, *111*(1) 94-96.

[60] S. A. Bradley, K. Krishnamurthy and H. Hu, "Simplifying DOSY spectra with selective TOCSY edited preparation". *Journal of Magnetic Resonance*, **2005**, *172*(1) 110-117.

[61] H. Barjat, G. A. Morris and G. A. Morris, "A three-dimensional DOSY-HMQC experiment for the high-resolution analysis of complex mixtures". *Journal of Magnetic Resonance*, **1998**, *131*(1) 131-138.

[62] M. J. Stchedroff, A. M. Kenwright, G. A. Morris, M. Nilsson and R. K. Harris, "2D and 3D DOSY methods for studying mixtures of oligomeric dimethylsiloxanes". *Physical Chemistry Chemical Physics*, **2004**, *6*(13) 3221-3227.

[63] M. Nilsson, A. M. Gil, I. Delagadillo and G. A. Morris, "Improving pulse sequences for 3D DOSY: COSY-IDOSY". *Chemical Communications*, **2005**(13) 1737-1739.

[64] I. J. D. Craig and T. A.M., "Why Laplace Transforms are Difficult to Invert Numerically". *Computers in Physics*, **1994**, *8*(6) 648-654.

[65] A. A. Istratov and O. F. Vyvenko, "Exponential analysis in physical phenomena". *Review of Scientific Instruments*, **1999**, *70*(2) 1233-1257.

[66] S. W. Provencher, "A Constrained Regularization Method for Inverting Data Represented by Linear Algebraic or Integral-Equations". *Computer Physics Communications*, **1982**, *27*(3) 213-227.

[67] S. W. Provencher, "CONTIN - a General-Purpose Constrained Regularization Program for Inverting Noisy Linear Algebraic and Integral-Equations". *Computer Physics Communications*, **1982**, *27*(3) 229-242.

[68] D. P. Hinton and C. S. Johnson, "Diffusion Ordered 2D NMR Spectroscopy of Phospholipid-Vesicles - Determination of Vesicle Size Distributions". *Journal of Physical Chemistry*, **1993**, *97*(35) 9064-9072.

[69] K. F. Morris, B. J. Cutak, A. M. Dixon and C. K. Larive, "Analysis of diffusion coefficient distributions in humic and fulvic acids by means of diffusion ordered NMR spectroscopy". *Analytical Chemistry*, **1999**, *71*(23) 5315-5321.

[70] M. A. Delsuc and T. E. Malliavin, "Maximum entropy processing of DOSY NMR spectra". *Analytical Chemistry*, **1998**, *70*(10) 2146-2148.

[71] R. C. O. Sebastiao, C. N. Pacheco, J. P. Braga and D. Pilo-Veloso, "Diffusion coefficient distribution from NMR-DOSY experiments using Hopfield neural network". *Journal of Magnetic Resonance*, **2006**, *182*(1) 22-28.

[72] G. A. F. Seber and C. J. Wild, "Nonlinear regression", **1989**, Hoboken, New Jersey, John Wiley & Sons, Inc.

[73] J. S. Alper and R. I. Gelb, "Standard Errors and Confidence-Intervals in Nonlinear-Regression - Comparison of Monte-Carlo and Parametric Statistics". *Journal of Physical Chemistry*, **1990**, *94*(11) 4747-4751.

[74] M. Nilsson, M. A. Connell, A. L. Davis and G. A. Morris, "Biexponential fitting of diffusion-ordered NMR data: Practicalities and limitations". *Analytical Chemistry*, **2006**, *78*(9) 3040-3045.

[75] R. Huo, R. Wehrens, J. van Duynhoven and L. M. C. Buydens, "Assessment of techniques for DOSY NMR data processing". *Analytica Chimica Acta*, **2003**, *490*(1-2) 231-251.

[76] P. Stilbs, K. Paulsen and P. C. Griffiths, "Global least-squares analysis of large, correlated spectral data sets: Application to component-resolved FT-PGSE NMR spectroscopy". *Journal of Physical Chemistry*, **1996**, *100*(20) 8180-8189.

[77] M. Nilsson and G. A. Morris, "Speedy component resolution: An improved tool for processing diffusion-ordered spectroscopy data". *Analytical Chemistry*, **2008**, *80*(10) 3777-3782.

[78] B. Antalek and W. Windig, "Generalized rank annihilation method applied to a single multicomponent pulsed gradient spin echo NMR data set". *Journal of the American Chemical Society*, **1996**, *118*(42) 10331-10332.

[79] W. Windig and B. Antalek, "Direct exponential curve resolution algorithm (DECRA): A novel application of the generalized rank annihilation method for a single spectral mixture data set with exponentially decaying contribution profiles". *Chemometrics and Intelligent Laboratory Systems*, **1997**, *37*(2) 241-254.

[80] D. Schulze and P. Stilbs, "Analysis of Multicomponent FT-PGSE Experiments by Multivariate Statistical-Methods Applied to the Complete Bandshapes". *Journal of Magnetic Resonance Series A*, **1993**, *105*(1) 54-58.

[81] R. Huo, C. Geurts, J. Brands, R. Wehrens and L. M. C. Buydens, "Real-life applications of the MULVADO software package for processing DOSY NMR data". *Magnetic Resonance in Chemistry*, **2006**, *44*(2) 110-117.

[82] R. Huo, R. A. van de Molengraaf, J. A. Pikkemaat, R. Wehrens and L. M. C. Buydens, "Diagnostic analysis of experimental artefacts in DOSY NMR data by covariance matrix of the residuals". *Journal of Magnetic Resonance*, **2005**, *172*(2) 346-358.

[83] R. Huo, R. Wehrens and L. M. C. Buydens, "Improved DOSY NMR data processing by data enhancement and combination of multivariate curve resolution with non-linear least square fitting". *Journal of Magnetic Resonance*, **2004**, *169*(2) 257-269.

[84] R. Huo, R. Wehrens and L. M. C. Buydens, "Robust DOSY NMR data analysis". *Chemometrics and Intelligent Laboratory Systems*, **2007**, *85*(1) 9-19.

[85] L. C. M. Van Gorkom and T. M. Hancewicz, "Analysis of DOSY and GPC-NMR experiments on polymers by multivariate curve resolution". *Journal of Magnetic Resonance*, **1998**, *130*(1) 125-130.

[86] M. Nilsson, A. Botana and G. A. Morris, "T_1-Diffusion-Ordered Spectroscopy: Nuclear Magnetic Resonance Mixture Analysis Using Parallel Factor Analysis". *Analytical Chemistry*, **2009**, *81*(19) 8119-8125.

[87] A. Gibbs and G. A. Morris, "Reference Deconvolution - Elimination of Distortions Arising from Reference Line Truncation". *Journal of Magnetic Resonance*, **1991**, *91*(1) 77-83.

[88] G. A. Morris, H. Barjat and T. J. Horne, "Reference deconvolution methods". *Progress in Nuclear Magnetic Resonance Spectroscopy*, **1997**, *31* 197-257.

[89] M. Nilsson and G. A. Morris, "Correction of systematic errors in CORE processing of DOSY data". *Magnetic Resonance in Chemistry*, **2006**, *44*(7) 655-660.

[90] M. A. Connell, P. J. Bowyer, P. A. Bone, A. L. Davis, A. G. Swanson, M. Nilsson and G. A. Morris, "Improving the accuracy of pulsed field gradient NMR diffusion experiments: Correction for gradient non-uniformity". *Journal of Magnetic Resonance*, **2009**, *198*(1) 121-131.

[91] P. Damberg, J. Jarvet and A. Graslund, "Accurate measurement of translational diffusion coefficients: A practical method to account for nonlinear gradients". *Journal of Magnetic Resonance*, **2001**, *148*(2) 343-348.

[92] M. Nilsson and G. A. Morris, "Improved DECRA processing of DOSY data: correcting for non-uniform field gradients". *Magnetic Resonance in Chemistry*, **2007**, *45*(8) 656-660.

3

Impact of rotational diffusion in NMR: relaxation

3.1 Introduction

In this chapter, an overview will be given on the theory of heteronuclear NMR relaxation and on how it can be linked to rotational diffusion. In section 3.2, the concepts of longitudinal and transverse relaxation will be introduced. A qualitative view will be given on how the motion of the molecules can cause relaxation by creating local magnetic field variations. The case of a two spin system will be discussed and concepts of cross-relaxation and the nuclear Overhauser enhancement (nOe) effect will be introduced. In section 3.3, the Bloch-Wangsness-Redfield theory will be applied to evaluate the longitudinal, transverse and cross-relaxation rate constants in a two spin system and it will be outlined how they can be related to the spectral density function. The latter describes the extent to which each frequency component of the local magnetic field variations contributes to the relaxation efficiency. Readers that would like to skip the theoretical derivation and see the end result of this section can immediately proceed to section 3.3.5.

The link with rotational diffusion, both isotropic and anisotropic, with the spectral density function is discussed in section 3.4. Readers that would like to skip most of the theoretical part and equations in this chapter and see how in practice the molecular size, molecular anisotropy and fast conformational motions affect the

relaxation rate constants, can proceed to Section 3.6 where this matter will be discussed.

In section 3.5, the effects of conformational or chemical exchange processes on the transverse relaxation rate constant and resonance line width will be discussed. Finally, in section 3.7 it will be discussed how the ^{13}C and ^{15}N relaxation rate constants can be acquired experimentally.

3.2 Concepts of relaxation

3.2.1 Longitudinal and transverse relaxation

A nucleus with a spin angular moment I greater than zero has a magnetic dipole moment $\boldsymbol{\mu}$, which will tend to align itself along a static magnetic field B_0 (conventionally collinear to the z-axis of the reference frame) so as to minimise the interaction energy between the dipole and the field. Quantum mechanics reveals that when the z-component of the dipole moment $\boldsymbol{\mu}_z$ is measured, it will only be able to adopt a limited number of orientations each with its distinct energy level. This is called the Zeeman interaction. When I = ½, only two orientations or states can be adopted, labelled the $|\alpha\rangle$ and $|\beta\rangle$ state. When a collection of many spins is considered, the spins will adopt a distribution of orientations which is skewed slightly along the magnetic field as illustrated in Figure 3.1a[1]. The degree to which the spins are aligned to the magnetic field is determined by the interaction strength between the dipole moment and the magnetic field, which attempts to align the spins along the field's direction, and the thermal motions of the spin nuclei, which try to evenly spread the spins' orientations. From a quantum mechanical viewpoint, the two energy states $|\alpha\rangle$ and $|\beta\rangle$ have a population of a certain number of spins, P_α and P_β respectively, although in this many spin situation, it is usually not possible to state whether one particular spin is in the $|\alpha\rangle$ or $|\beta\rangle$ state. The populations at equilibrium are then of course Boltzmann distributed. The net result is that all spins create a macrodipole that is aligned to the magnetic field. This macrodipole $\mathbf{M}$ is called the magnetisation, and the skewness of the distribution towards one direction is termed the coherence of the spins.

It is an inherent physical property of the spin magnetic dipole to precess around a magnetic field with a frequency proportional to the magnitude of the field. Therefore, all spins in Figure 3.1a are in fact rotating around the static magnetic field with a constant precession velocity. When an oscillating magnetic field B_1 (caused by radio frequency radiation) perpendicular to the main magnetic field is applied to the system, all dipoles will precess around the vector sum of the B_1 and B_0 fields. When the

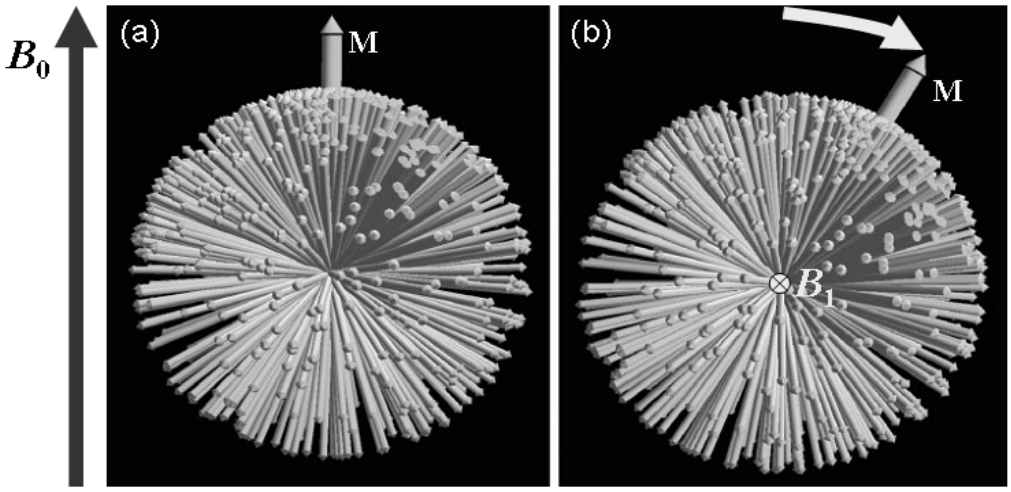

Figure 3.1: (a) At equilibrium, the distribution of nuclear magnetic dipoles is skewed along the magnetic field B_0, creating a macrodipole $\mathbf{M}$. (b) An oscillating magnetic field B_1 (pointing towards the reader) will rotate all spins away from their original position, changing the skewness direction and thus the macrodipole, Original picture copied from the paper of Hanson[1].

frequency of the oscillating field matches the precession frequency of the spins around the B_0 field, the net effect will be that all spins rotate around the oscillating magnetic field when seen in a frame of reference rotating around the B_0 field with this same frequency (Figure 3.1b). All spins will thus change their z-component orientation, disturbing the Boltzmann distribution and reorienting the macrodipole. In addition, after the oscillating field is switched off, the macrodipole will precess around the B_0 field, giving rise to the detectable NMR signal. When the macrodipole is perpendicular to the B_0 field, this corresponds to the $|\alpha\rangle$ or $|\beta\rangle$ states being equally populated.

This new state of the magnetisation does not last forever though. The spin orientation distribution will tend to return to the thermodynamically favoured Boltzmann state. Where the spins' orientation distribution has a skewness along the direction of B_0. This process is called longitudinal relaxation, as it affects the longitudinal (z-axis) part of the magnetisation. This form of relaxation requires that energy be exchanged with the surroundings of the spin (the lattice) and therefore it is often called spin-lattice relaxation. This exchange of energy is mediated by small time dependent local magnetic field variations perpendicular to the static B_0 field.

Another form of relaxation, called transverse or spin-spin relaxation, takes place simultaneously. As noted above, the macrodipole in the Boltzmann state is created by the skewness of the distribution. This skewness was originally created due to the tendency to align the spins with the magnetic field, creating coherence in spin direction. However, in the new state after the radiofrequency pulse, this coherence is now directed perpendicular to the static magnetic field. Since all spins precess around the B_0 field with an angular frequency proportional to this field, the coherence will now precess around this field as well. There is no external driving force that

maintains the skewness in the distribution in the transverse direction as opposed to the longitudinal direction where this driving force was B_0. Small time and space dependent perturbations in the static magnetic field exist however, which will continuously cause, independently for each spin, small time dependent deviations from their angular precession frequency. This adds a random component to the amount each spin will have precessed after a certain amount of time. Therefore, the coherence will slowly and irreversibly be lost over time as the vector sum of the spins will no longer constructively add up to a macrodipole. This process is called spin-spin relaxation or transverse relaxation since it affects only the transverse component of the magnetisation. This form of relaxation does not cause an exchange of energy with the surroundings (it is an adiabatic process). Just as for longitudinal relaxation, it requires time dependent local magnetic field variations, but as opposed to longitudinal relaxation, they need to be parallel with the B_0 field. As a final remark, the lifetime of this coherence is what determines the line width of the resonances in the NMR signal.

3.2.2 Local magnetic field variations

Where do the time dependent local magnetic field variations driving relaxation come from? Multiple mechanisms can contribute[2-6]. In the frame of this dissertation, only two mechanisms are of importance and will be treated in more detail hereafter. The first and most important is the dipole-dipole interaction. Consider for simplicity two nuclear spins (Figure 3.2) that are part of the same molecule and are rigidly attached to each other so that the distance between them remains constant over time (*cf.* there exists a chemical bond between them). Each possesses a magnetic dipole that creates a dipolar magnetic field. The first nucleus (green in the figure) experiences a local magnetic field from the dipole of the second nucleus (blue in the figure). This dipolar magnetic field is anisotropic, and the degree it manifests itself locally at the position of the first nucleus is dependent on the relative orientation of the two spins. When both nuclei change their relative orientation towards each other – either by molecular rotation or conformational motions within the molecule – the orientation of their magnetic dipoles relative to the static magnetic field B_0 will not change. This is illustrated in Figure 3.2, where the reorientation is visualised in such a way that only the second spin appears to have moved. Because of the new relative orientation, the local magnetic field that the first spin now experiences from the dipole of the second spin has changed its direction and amplitude. The same reasoning applies to the local magnetic field experienced by the second (blue) spin by the magnetic dipole of the first (green) spin. Therefore, any process that reorients the two spins relative to the static magnetic field will cause each spin experiencing varying magnetic field over time through their dipole-dipole interactions. The amplitude of this magnetic field variation, and thus the efficiency of the relaxation, will be dependent on the

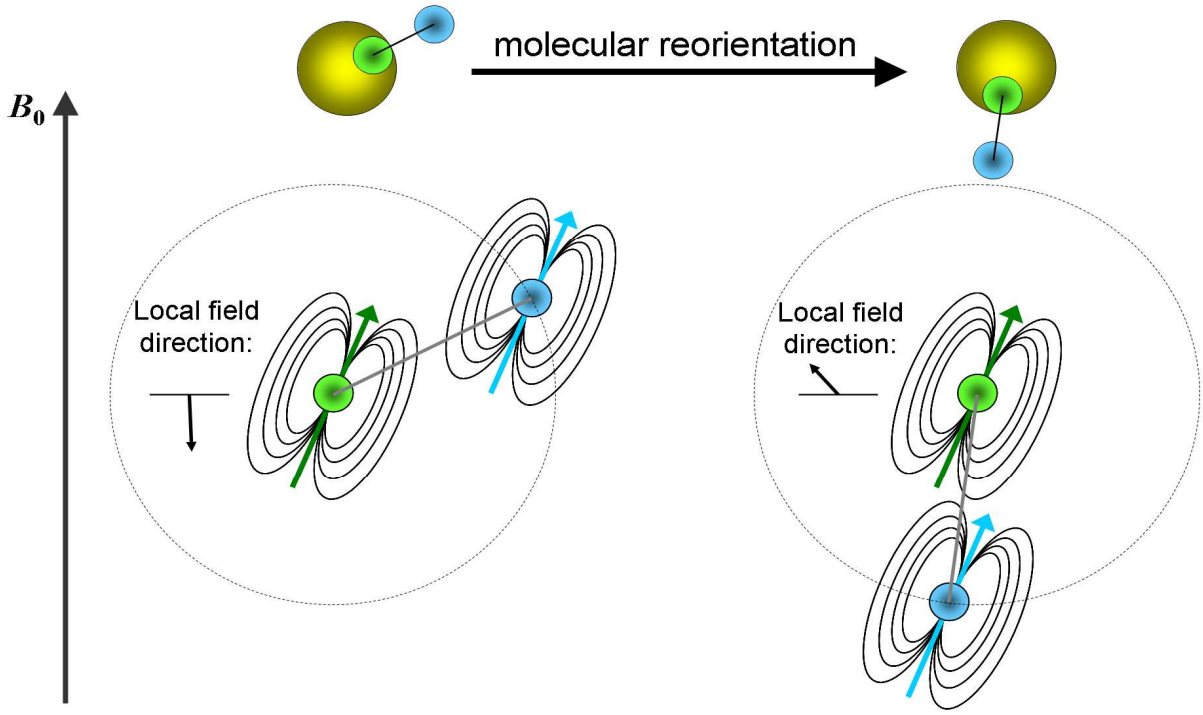

Figure 3.2: Dipolar interaction between two nuclear spins rigidly attached to each other (*cf.* chemical bond). The first (green) spin experiences a local magnetic field from the second (blue) spin. When both spins change their relative orientation (for example, the molecule rotates), the orientation of the dipoles relative to the B_0 field remains the same. Therefore, the local magnetic field experienced by the first spin will have changed.

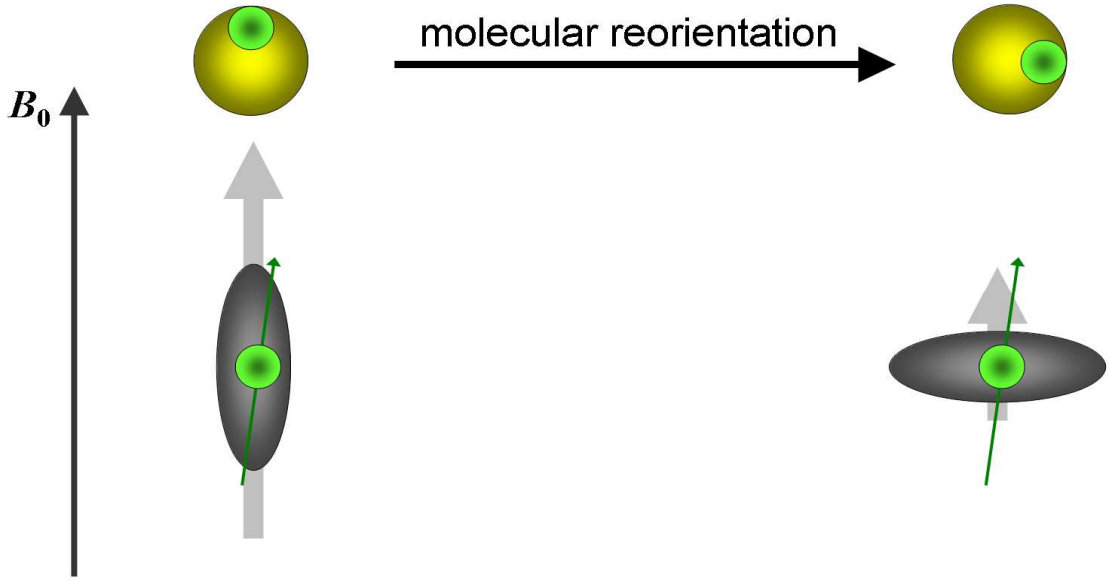

Figure 3.3: Illustration of chemical shift anisotropy. As described in the main text, the electron density around a nuclear spin induces a local magnetic field at the nucleus. When the distribution of electrons is anisotropic, the size and direction of the induced field is dependent on the orientation of the electron density towards the B_0 field. This is described by a chemical shift tensor, which is represented here as a grey ellipse. For simplicity, in the two orientations shown one of the principle components of the tensor is always parallel to the B_0 field. When the molecule varies its orientation, the nuclear spin will experience a varying magnetic field.

magnitude of the dipoles (determined by the nuclear gyromagnetic ratio) and the (average) distance between both dipoles.

A second mechanism of importance is the chemical shift anisotropy (CSA) (Figure 3.3). The NMR chemical shift is caused by the electron density surrounding the nucleus. The static magnetic field induces a circular movement of the charged electrons within this cloud, effectively creating a circular electrical flow. This flow again induces a local magnetic field which affects the total magnetic field experienced by the spin, its magnitude being proportional to the magnitude of the B_0 field. However, this effect is often anisotropic – the chemical shift being represented by a tensor – so that the magnitude and direction of this local magnetic field will also depend on the orientation of the electron density (again by molecular reorientation or by conformational changes) with respect to the B_0 field direction. Reorientation of the electron density relative to the magnetic field will thus cause a varying magnetic field and can thus lead to relaxation. Note that in solution this variation occurs sufficiently fast so that an average chemical shift is observed in the NMR spectrum. The anisotropy of the chemical shift is therefore only expressed in the relaxation rates. The amplitude of the magnetic field variations depends in this case on the degree of anisotropy of the chemical shift tensor and the strength of the static magnetic field B_0.

Dipole-dipole interactions and CSA are the only relaxation mechanisms that are relevant to this work. Other mechanisms include the interaction between electric field gradients (caused by electrons) with the nuclear electric quadrupole moment when the spin magnetic moment $I > ½$ and variations caused by time dependent scalar coupling interactions.

3.2.3 Longitudinal relaxation in a two spin system

When two interacting nuclear spins I and S are considered, the energy diagram representing the transitions between the different spin states is shown in Figure 3.4. Each of the four states has an equilibrium population P^0 imposed by the Boltzmann distribution. At equilibrium, transitions between the states constantly take place by means of the randomly varying magnetic fields, as discussed above, but with such rates so that the populations of each state do not change over time. Each of the transitions is characterised by a first order rate constant representing the efficiency of the transitions. W_I and W_S are the rate constants for transitions that change the state of respectively only the I spin ($|\alpha\alpha\rangle \leftrightarrow |\beta\alpha\rangle$ and $|\alpha\beta\rangle \leftrightarrow |\beta\beta\rangle$) and the S spin ($|\alpha\alpha\rangle \leftrightarrow |\alpha\beta\rangle$ and $|\beta\alpha\rangle \leftrightarrow |\beta\beta\rangle$). These

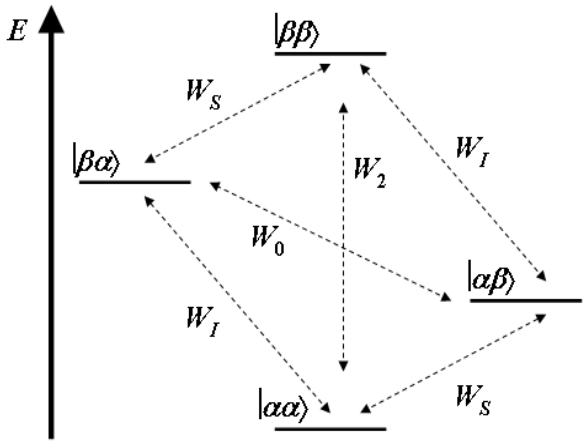

Figure 3.4: Energy diagram and possible transitions for a two spin system.

are the transitions that are also detectable in the NMR spectrum, and imply a change in total magnetic quantum number m_I of ±1 (single quantum transitions). W_0 is the rate constant for the transition which changes the state of both spins at the same time in the case where their relative states are opposite ($|\alpha\beta\rangle \leftrightarrow |\beta\alpha\rangle$), leaving a total change in total magnetic quantum number of zero ($\Delta m_I = 0$; zero quantum transition). The rate constant W_2 represents a similar case, but where their relative states are similar ($|\alpha\alpha\rangle \leftrightarrow |\beta\beta\rangle$), resulting in a change of total magnetic quantum number of ±2 ($\Delta m_I = \pm 2$; double quantum transition). Note that although these zero and double quantum transitions can occur during relaxation processes, they are not visible in the NMR spectrum due to the NMR spectroscopic selection rule of $\Delta m_I = \pm 1$. When the populations at time t are disturbed from their equilibrium values, the differences from the equilibrium value $\Delta\mathrm{P}(t) = \mathrm{P}(t) - P^0$ will develop according to:

$$\begin{aligned}
\frac{d\Delta \mathrm{P}_{\alpha\alpha}(t)}{dt} &= W_I \Delta \mathrm{P}_{\beta\alpha}(t) + W_S \Delta \mathrm{P}_{\alpha\beta}(t) + W_2 \Delta \mathrm{P}_{\beta\beta}(t) - (W_I + W_S + W_2)\Delta \mathrm{P}_{\alpha\alpha}(t) \\
\frac{d\Delta \mathrm{P}_{\beta\alpha}(t)}{dt} &= W_I \Delta \mathrm{P}_{\alpha\alpha}(t) + W_S \Delta \mathrm{P}_{\beta\beta}(t) + W_0 \Delta \mathrm{P}_{\alpha\beta}(t) - (W_I + W_S + W_0)\Delta \mathrm{P}_{\beta\alpha}(t) \\
\frac{d\Delta \mathrm{P}_{\alpha\beta}(t)}{dt} &= W_I \Delta \mathrm{P}_{\beta\beta}(t) + W_S \Delta \mathrm{P}_{\alpha\alpha}(t) + W_0 \Delta \mathrm{P}_{\beta\alpha}(t) - (W_I + W_S + W_0)\Delta \mathrm{P}_{\alpha\beta}(t) \\
\frac{d\Delta \mathrm{P}_{\beta\beta}(t)}{dt} &= W_I \Delta \mathrm{P}_{\alpha\beta}(t) + W_S \Delta \mathrm{P}_{\beta\alpha}(t) + W_2 \Delta \mathrm{P}_{\alpha\alpha}(t) - (W_I + W_S + W_2)\Delta \mathrm{P}_{\beta\beta}(t)
\end{aligned} \tag{3.1}$$

The total longitudinal magnetisation of the I and S spins at time t are given by the difference in population between the energy levels in the diagram:

$$\begin{aligned}
\mathrm{I}_z(t) &= \left(\mathrm{P}_{\beta\alpha}(t) - \mathrm{P}_{\alpha\alpha}(t)\right) + \left(\mathrm{P}_{\beta\beta}(t) - \mathrm{P}_{\alpha\beta}(t)\right) \\
\mathrm{S}_z(t) &= \left(\mathrm{P}_{\alpha\beta}(t) - \mathrm{P}_{\alpha\alpha}(t)\right) + \left(\mathrm{P}_{\beta\beta}(t) - \mathrm{P}_{\beta\alpha}(t)\right)
\end{aligned} \tag{3.2}$$

The deviations from their equilibrium value $\Delta\mathrm{I}_z(t) = \mathrm{I}_z(t) - I_z^0$ and $\Delta\mathrm{S}_z(t) = \mathrm{S}_z(t) - S_z^0$ will then develop as:

$$\begin{aligned}
\frac{d\Delta \mathrm{I}_z(t)}{dt} &= \frac{d\Delta \mathrm{P}_{\beta\alpha}(t)}{dt} - \frac{d\Delta \mathrm{P}_{\alpha\alpha}(t)}{dt} + \frac{d\Delta \mathrm{P}_{\beta\beta}(t)}{dt} - \frac{d\Delta \mathrm{P}_{\alpha\beta}(t)}{dt} \\
\frac{d\Delta \mathrm{S}_z(t)}{dt} &= \frac{d\Delta \mathrm{P}_{\alpha\beta}(t)}{dt} - \frac{d\Delta \mathrm{P}_{\alpha\alpha}(t)}{dt} + \frac{d\Delta \mathrm{P}_{\beta\beta}(t)}{dt} - \frac{d\Delta \mathrm{P}_{\beta\alpha}(t)}{dt}
\end{aligned} \tag{3.3}$$

Substituting equations (3.1) into (3.3) eventually leads to the following set of coupled differential equations, which are known as the Solomon equations for a two spin system:

$$\begin{aligned}\frac{d\Delta \mathrm{I}_z}{dt} &= -\rho_I \Delta \mathrm{I}_z - \sigma_{IS} \Delta \mathrm{S}_z \\ \frac{d\Delta \mathrm{S}_z}{dt} &= -\rho_S \Delta \mathrm{S}_z - \sigma_{IS} \Delta \mathrm{I}_z\end{aligned} \tag{3.4}$$

with ρ_I and ρ_S the auto-relaxation rate constants for spins I and S respectively and σ_{IS} the cross-relaxation rate constant, given by:

$$\begin{aligned}\rho_I &= \left(2W_I + W_0 + W_2\right) \\ \rho_S &= \left(2W_S + W_0 + W_2\right) \\ \sigma_{IS} &= \left(W_2 - W_0\right)\end{aligned} \tag{3.5}$$

The important conclusion from (3.4) is that the rates at which the magnetisation of one spin changes over time is not only dependent on its own deviation from equilibrium, but also on that of the other. It is said that cross-relaxation exists between both spins, which finds its origin in the presence of the double and zero quantum transitions. Both transitions affect the population differences of both spins at the same time. For instance, when the population differences along the transitions of the I spin ($\mathrm{P}_{\beta\alpha} - \mathrm{P}_{\alpha\alpha}$ and $\mathrm{P}_{\beta\beta} - \mathrm{P}_{\alpha\beta}$) are smaller than at equilibrium, a double quantum transition from the $|\beta\beta\rangle$ state to the $|\alpha\alpha\rangle$ state will increase these population differences, but at the same time will increase the population differences of the S spin ($\mathrm{P}_{\alpha\beta} - \mathrm{P}_{\alpha\alpha}$ and $\mathrm{P}_{\beta\beta} - \mathrm{P}_{\beta\alpha}$). Similarly, a zero quantum transition from the $|\beta\alpha\rangle$ state to the $|\alpha\beta\rangle$ state will increase the I spin population differences, but decrease the S spin population differences. The auto-relaxation rate constants contain both W_2 and W_0, since these help to alleviate the deviation from equilibrium population considering only one of both spins. The cross-relaxation rate constant represents to what extent the population deviation of one spin affects the other through W_2 and W_0. Because of the opposite relative effect of W_2 and W_0 on the populations difference of both spins as was just described, it contains the difference between both transition rate constants. The sign of the cross-relaxation rate constant is therefore depends on which of the two transitions gains the upper hand. The solution to the Solomon equations is:

$$\begin{aligned}\Delta \mathrm{I}_z(t) &= a_{II}(t)\Delta \mathrm{I}_z(0) + a_{IS}(t)\Delta \mathrm{S}_z(0) \\ \Delta \mathrm{S}_z(t) &= a_{SS}(t)\Delta \mathrm{S}_z(0) + a_{IS}(t)\Delta \mathrm{I}_z(0)\end{aligned} \tag{3.6}$$

with:

$$
\begin{aligned}
a_{II}(t) &= \frac{1}{2}\left[\left(1-\frac{\rho_I-\rho_S}{\lambda_+-\lambda_-}\right)e^{-\lambda_- t}+\left(1+\frac{\rho_I-\rho_S}{\lambda_+-\lambda_-}\right)e^{-\lambda_+ t}\right] \\
a_{SS}(t) &= \frac{1}{2}\left[\left(1+\frac{\rho_I-\rho_S}{\lambda_+-\lambda_-}\right)e^{-\lambda_- t}+\left(1-\frac{\rho_I-\rho_S}{\lambda_+-\lambda_-}\right)e^{-\lambda_+ t}\right] \\
a_{IS}(t) &= \frac{-\sigma_{IS}}{\lambda_+-\lambda_-}\left(e^{-\lambda_- t}-e^{-\lambda_+ t}\right) \\
\lambda_\pm &= \frac{1}{2}\left[\rho_I+\rho_S \pm \sqrt{(\rho_I-\rho_S)^2+4\sigma_{IS}^2}\right]
\end{aligned}
\tag{3.7}
$$

When the cross-relaxation rate constant is nonzero, these equations show that when the longitudinal magnetisations are disturbed from their equilibrium values in a two spin system, they will generally decay back to the equilibrium biexponentially at rates that are determined by λ_+ and λ_-.

3.2.4 The nuclear Overhauser enhancement

The presence of cross-relaxation has a very interesting consequence. If one of the two spins is selectively excited, the longitudinal magnetisation of the second spin will be affected. When for example the population difference of the I spin is selectively inverted by a 180° pulse so that $\Delta I_z(0) = -2I_z^0$ and $\Delta S_z(0) = 0$, then according to (3.7) the longitudinal magnetisation of the S spin will develop as:

$$
\Delta S_z(t) = \frac{2I_z^0\sigma_{IS}}{\lambda_+-\lambda_-}\left(e^{-\lambda_- t}-e^{-\lambda_+ t}\right) \tag{3.8}
$$

The longitudinal magnetisation of the S spin is increased (or decreased when σ_{IS} is negative) when compared to its equilibrium value, as illustrated in Figure 3.5. Initially, ΔS_z will increasingly deviate from zero with time as a 'side-effect' from the double and zero quantum transitions that attempt to let ΔI_z return to zero. The increase in deviation of ΔS_z levels out as effects of auto-relaxation take over and eventually let both ΔS_z and ΔI_z return to their equilibrium value. The initial slope of ΔS_z is linearly proportional to the cross-relaxation rate:

$$
\begin{aligned}
\Delta S_z(t)\big|_{t\to 0} &\approx \frac{2I_z^0\sigma_{IS}}{\lambda_+-\lambda_-}\left(1+\lambda_+ t-1-\lambda_- t\right) \\
&= 2I_z^0\sigma_{IS}t
\end{aligned}
\tag{3.9}
$$

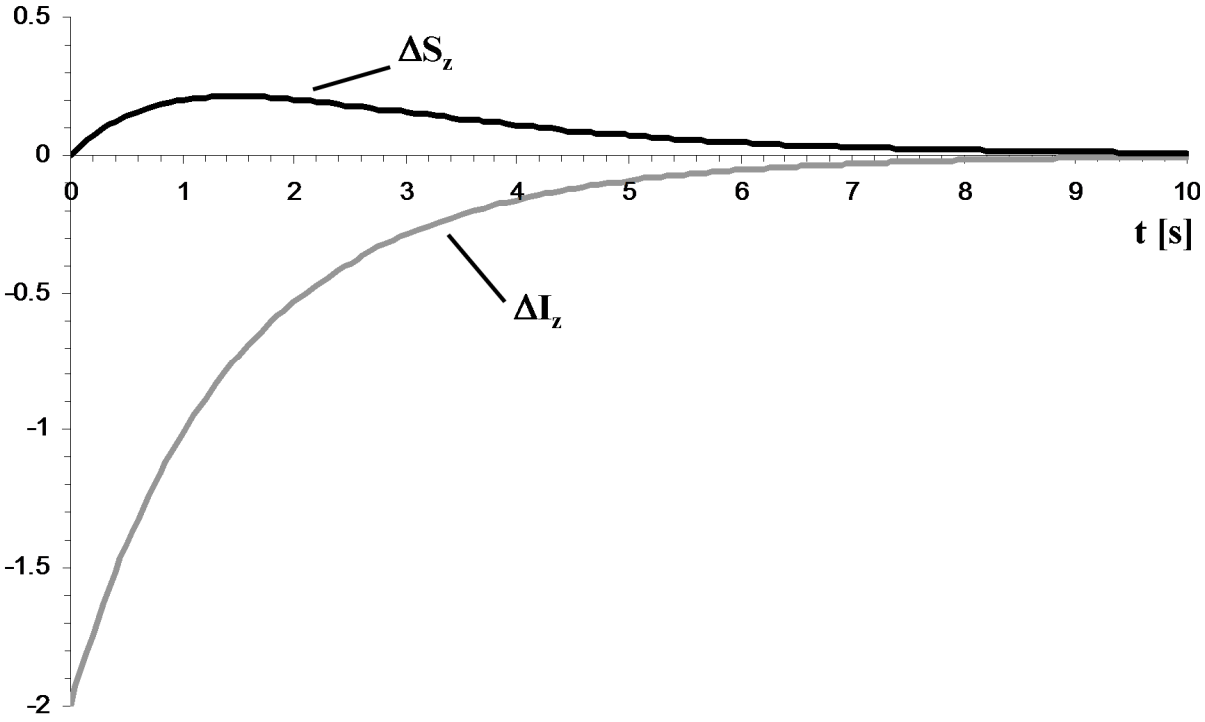

Figure 3.5: Evolution of the deviation from equilibrium magnetisation in a two spin system when applying a selective 180° pulse to spin I so that $\Delta I_z(0) = -2I_z^0$ and $\Delta S_z(0) = 0$. In this simulation, $I_z^0 = 1$, $\rho_I = \rho_S = 0.7\ s^{-1}$ and $\sigma_{IS} = 0.2\ s^{-1}$. Note that since σ_{IS} is positive, ΔS_z initially increases.

The relative increase or decrease of the longitudinal magnetisation of spin S is called the nuclear Overhauser enhancement or nOe[7]:

$$\mathrm{nOe}_S(t) = \frac{\Delta S_z(t)}{S_z^0} \tag{3.10}$$

In this particular example the observed nOe is transient since it eventually dies out due to the auto-relaxation. Remembering that I_z^0 and S_z^0 are proportional to the respective equilibrium population differences and considering that these are proportional to the respective gyromagnetic ratios γ_I and γ_S so that $I_z^0/S_z^0 = \gamma_I/\gamma_S$, combining (3.9) and (3.10) then provides for the initial nOe:

$$\mathrm{nOe}_S(t) = \frac{2\gamma_I}{\gamma_S}\sigma_{IS}t \tag{3.11}$$

This version of the nOe finds important application in the determination of molecular conformation, since the cross-relaxation is inversely proportional to the average of the sixth power of the distance between the spins I and S (see section 3.3.5, equation (3.59)).

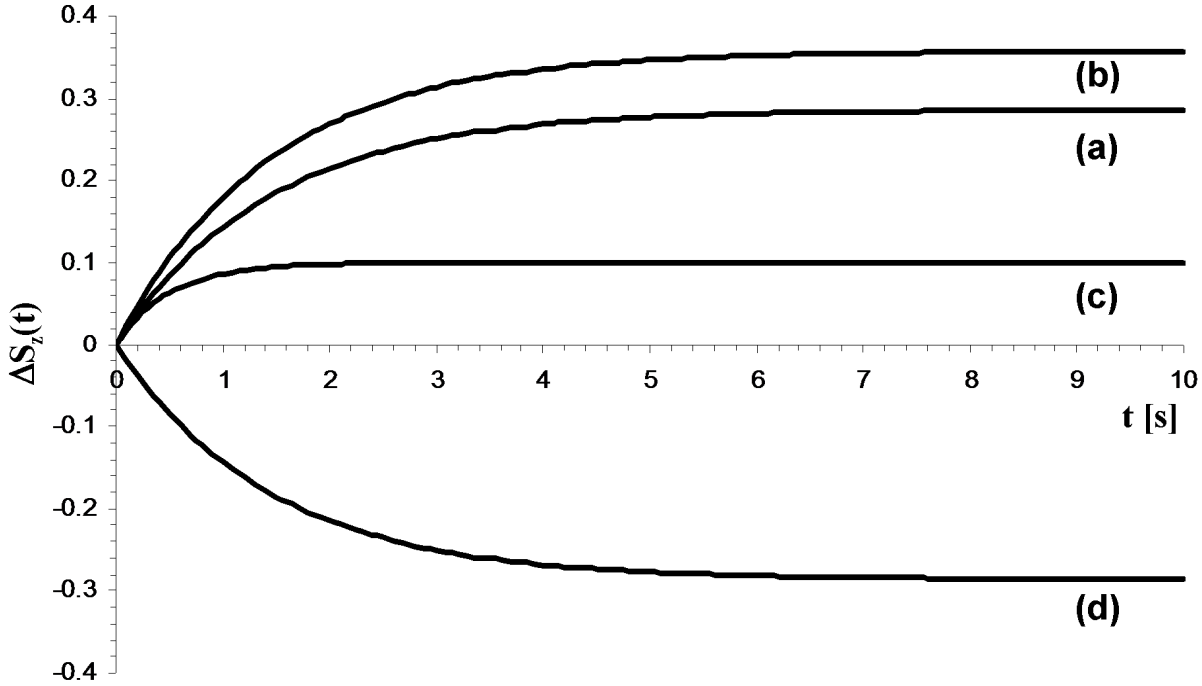

Figure 3.6: Evolution of $\Delta S_z(0)$ according to equation with $I_z^0 = 1$ (3.13). (a) $\rho_S = 0.7\ s^{-1}$ and $\sigma_{IS} = 0.20\ s^{-1}$; (b) $\rho_S = 0.7\ s^{-1}$ and $\sigma_{IS} = 0.25\ s^{-1}$; (c) $\rho_S = 2.0\ s^{-1}$ and $\sigma_{IS} = 0.20\ s^{-1}$; (d) $\rho_S = 0.7\ s^{-1}$ and $\sigma_{IS} = -0.20\ s^{-1}$. Note that the value of the cross-relaxation rate constant σ_{IS} only affects the value of the plateau, while an increasing auto-relaxation rate constant ρ_S decreases the plateau value but increases the rate with which the plateau is reached.

A second relevant example is the case where spin I is continuously irradiated, keeping the populations equalised along its transitions ($P_{\alpha\alpha} - P_{\beta\alpha} = P_{\alpha\beta} - P_{\beta\beta} = 0$) so that $\Delta I_z(t) = -I_z^0$. Inserting this into the differential equations of (3.4) provides:

$$\frac{d\Delta S_z(t)}{dt} = -\rho_S \Delta S_z + \sigma_{IS} I_z^0 \tag{3.12}$$

For which the solution is:

$$\Delta S_z(t) = I_z^0 \frac{\sigma_{IS}}{\rho_S}\left(1 - e^{-\rho_S t}\right) \tag{3.13}$$

When the I spin is irradiated for a time significantly larger than the inverse of the auto-relaxation rate of the S spin, the system will reach a steady state situation (Figure 3.6) and the nOe is given by combining (3.10) with (3.13):

$$nOe_S\big|_{t>>1/\rho_S} = \frac{\gamma_I}{\gamma_S}\frac{\sigma_{IS}}{\rho_S} \tag{3.14}$$

This steady state nOe is independent of the distance between the I and S nuclei. The reason for this is that in the case where dipolar relaxation between the two spins is dominant, both the cross-relaxation and auto-rdelaxation rates depend in the same

way on the internuclear distance and thus cancel each other out (section 3.3.5). When other relaxation mechanisms such as CSA or dipolar relaxation to third party spins contribute to the auto-relaxation rate constant ρ_S, the magnitude of the nOe will be reduced since the cross-relaxation rate constant σ_{IS} depends only on the dipolar relaxation between spins I and S and thus remains the same.

Finally, it should be noted that transverse cross-relaxation also exists, which can be measured when locking the transverse magnetisation along one orientation by use of continuous rf-irradiation[6]. Similarly as for longitudinal relaxation, a rOe (rotating frame nuclear Overhauser enhancement) can be defined. for the conformational analysis and the detection of intermolecular contacts in the system under study in this dissertation, experiments exploiting the transient rOe have several advantages over those that use the transient nOe[7] (see Chapters 4, 5 and 6). In what follows in this chapter, only the theory of the longitudinal cross-relaxation and the nOe will be developed, as only the steady state nOe is of interest in this work to study rotational dynamics.

3.3 Quantitative description of the relaxation rate constants

3.3.1 The spin density operator

Before the Bloch-Wangsness-Redfield theory for relaxation is discussed, brief concepts of the quantum mechanical description of an NMR spin system are introduced[3, 6]. Just like any quantum mechanical system, the state of the spin system is described by the time-dependent Schrodinger equation, with H the Hamiltonian of the system and $\Psi(t)$ the time dependent wave function:

$$\mathrm{H}\Psi(t) = i\frac{\partial\Psi(t)}{\partial t} \tag{3.15}$$

Note that the Planck constant is omitted from this equation for the sake of simplicity. The eigenfunctions of the Hamiltonian of a two-spin system – assuming that both spins they are weakly scalar coupled ($J_{IS} << |\omega_I - \omega_S|$, as is certainly the case for heteronuclear coupling) – are given by $|\alpha\alpha\rangle$, $|\beta\alpha\rangle$, $|\alpha\beta\rangle$ and $|\beta\beta\rangle$ (see also Figure 3.4). These eigenfunctions have the property of being orthonormal:

$$\begin{aligned}&\langle\alpha\alpha|\alpha\alpha\rangle = \langle\beta\alpha|\beta\alpha\rangle = \langle\alpha\beta|\alpha\beta\rangle = \langle\beta\beta|\beta\beta\rangle = 1\\ &\langle\alpha\alpha|\beta\alpha\rangle = \langle\beta\alpha|\alpha\alpha\rangle = \langle\alpha\alpha|\beta\beta\rangle = \ldots = 0\end{aligned} \tag{3.16}$$

Note the use of the Dirac Bra-Ket notation. The time dependent wave function $\Psi(t)$ can be written as a linear combination of these eigenfunctions:

$$\Psi(t) = c_{\alpha\alpha}\left|\alpha\alpha\right\rangle + c_{\beta\alpha}\left|\beta\alpha\right\rangle + c_{\alpha\beta}\left|\alpha\beta\right\rangle + c_{\beta\beta}\left|\beta\beta\right\rangle \tag{3.17}$$

An alternative to the time-dependent Schrodinger equation (3.15) is the Liouville-von Neumann equation[3]:

$$\frac{d\mathrm{P}(\mathrm{t})}{dt} = -i\left[\mathrm{H}, \mathrm{P}(\mathrm{t})\right] \tag{3.18}$$

with […,…] the commutator and $\mathrm{P}(t)$ the projection operator, defined as:

$$\mathrm{P}(t) = \left|\Psi(t)\right\rangle\left\langle\Psi(t)\right| \tag{3.19}$$

This is valid when considering a single two-spin system or an ensemble of two-spin systems that are all in the exact same state $\Psi(t)$. When a realistic ensemble of two-spin systems is considered, these possess, in principle, each a different state, *i.e.* different values of the coefficients $c_{\alpha\alpha}$, $c_{\alpha\beta}$, …[6]. Macroscopic observables, such as the magnetisation or relaxation rate constants, will be determined by the average state over all these spin systems. For this purpose, the spin density operator is defined as:

$$\rho(t) = \overline{\left|\Psi(t)\right\rangle\left\langle\Psi(t)\right|} \tag{3.20}$$

with the overbar indicating the average. Similarly, spin density operator $\rho(t)$ evolves according to the Liouville-von Neumann equation:

$$\frac{d\rho(\mathrm{t})}{dt} = -i\left[\mathrm{H}, \rho(\mathrm{t})\right] \tag{3.21}$$

The state of an ensemble of spin systems is fully described by this spin density operator. Within the basis set, it can be represented in matrix form by using (3.17), which is then called the spin density matrix **ρ**. For this matrix, the 'box notation' introduced by Levitt[6] for a two spin system can also be used:

$$\boldsymbol{\rho}(t)=\begin{bmatrix}\overline{c^*_{\alpha\alpha}c_{\alpha\alpha}} & \overline{c^*_{\alpha\alpha}c_{\alpha\beta}} & \overline{c^*_{\alpha\alpha}c_{\beta\alpha}} & \overline{c^*_{\alpha\alpha}c_{\beta\beta}}\\ \overline{c^*_{\alpha\beta}c_{\alpha\alpha}} & \overline{c^*_{\alpha\beta}c_{\alpha\beta}} & \overline{c^*_{\alpha\beta}c_{\beta\alpha}} & \overline{c^*_{\alpha\beta}c_{\beta\beta}}\\ \overline{c^*_{\beta\alpha}c_{\alpha\alpha}} & \overline{c^*_{\beta\alpha}c_{\alpha\beta}} & \overline{c^*_{\beta\alpha}c_{\beta\alpha}} & \overline{c^*_{\beta\alpha}c_{\beta\beta}}\\ \overline{c^*_{\beta\beta}c_{\alpha\alpha}} & \overline{c^*_{\beta\beta}c_{\alpha\beta}} & \overline{c^*_{\beta\beta}c_{\beta\alpha}} & \overline{c^*_{\beta\beta}c_{\beta\beta}}\end{bmatrix}=\begin{bmatrix}\rho_{\boxed{\alpha\alpha}} & \rho_{\boxed{\alpha+}} & \rho_{\boxed{+\alpha}} & \rho_{\boxed{++}}\\ \rho_{\boxed{\alpha-}} & \rho_{\boxed{\alpha\beta}} & \rho_{\boxed{+-}} & \rho_{\boxed{+\beta}}\\ \rho_{\boxed{-\alpha}} & \rho_{\boxed{-+}} & \rho_{\boxed{\beta\alpha}} & \rho_{\boxed{\beta+}}\\ \rho_{\boxed{--}} & \rho_{\boxed{-\beta}} & \rho_{\boxed{\beta-}} & \rho_{\boxed{\beta\beta}}\end{bmatrix} \tag{3.22}$$

The diagonal elements represent the population of each energy state of the spin system, as represented by Figure 3.4. The non-diagonal elements represent the transitions between the energy states or the coherences. For instance, $\rho_{\boxed{\alpha-}}$ is the single quantum $\alpha\beta\rightarrow\alpha\alpha$ transition where the S spin is flipped while the I spin remains in its α state, while $\rho_{\boxed{+-}}$ is then the zero quantum $\alpha\beta\rightarrow\beta\alpha$ transition. In a state of thermodynamic equilibrium, the matrix is diagonal.

A set of operators X are orthogonal when they obey to the following:

$$\langle \mathrm{X}_n | \mathrm{X}_m \rangle = \delta_{nm} \langle \mathrm{X}_n | \mathrm{X}_n \rangle \tag{3.23}$$

with δ_{nm} the Kronecker delta ($\delta_{nm} = 1$ if $n = m$, otherwise $\delta_{nm} = 0$). The expression $\langle \mathrm{X}_n | \mathrm{X}_m \rangle$ is the trace of the matrix representation of the operator $\mathrm{X}_n^{\dagger}\mathrm{X}_m$, with '$\dagger$' denoting the adjoint of the operator:

$$\begin{aligned}\langle \mathrm{X}_n | \mathrm{X}_m \rangle &= \langle \mathrm{X}_n^{\dagger} \mathrm{X}_m \rangle \\ &= \langle \alpha\alpha | \mathrm{X}_n^{\dagger} \mathrm{X}_m | \alpha\alpha \rangle + \langle \alpha\beta | \mathrm{X}_n^{\dagger} \mathrm{X}_m | \alpha\beta \rangle + \langle \beta\alpha | \mathrm{X}_n^{\dagger} \mathrm{X}_m | \beta\alpha \rangle + \langle \beta\beta | \mathrm{X}_n^{\dagger} \mathrm{X}_m | \beta\beta \rangle\end{aligned} \tag{3.24}$$

The two-spin system spin density operator can at any moment be written as a linear combination of a set of 16 orthogonal base operators, chosen so that each represents some physical meaning. Using these base operators, the spin operator (3.19) can be written as a linear combination of these operators:

$$\rho(t) = \sum_r b_r(t) | \mathrm{B}_r \rangle \tag{3.25}$$

When inserting this into the Liouville-von Neumann equation (3.18) can be rewritten:

$$\sum_r \frac{db_r(t)}{dt} | \mathrm{B}_r \rangle = -i \sum_s b_s(t) [\mathrm{H}, \mathrm{B}_s] \tag{3.26}$$

By multiplying both sides to the left with $\langle \mathrm{B}_r|$ and making use of the orthogonal properties of the base operators, an expression for the individual time-evolution of the coefficients of the linear combination can be found:

$$\frac{db_r(\mathrm{t})}{dt} = \sum_s -i \frac{\langle \mathrm{B}_r | [\mathrm{H}, \mathrm{B}_s] \rangle}{\langle \mathrm{B}_r | \mathrm{B}_r \rangle} b_s(\mathrm{t}) = \sum_s -i\Omega_{rs} b_s(\mathrm{t}) \tag{3.27}$$

The simplest choice of a basis set would be those that are associated with the populations and transitions. The populations:

$$\begin{aligned} \mathrm{I}_\alpha \mathrm{S}_\alpha &= |\alpha\alpha\rangle\langle\alpha\alpha| \\ \mathrm{I}_\alpha \mathrm{S}_\beta &= |\alpha\beta\rangle\langle\alpha\beta| \\ \mathrm{I}_\beta \mathrm{S}_\alpha &= |\beta\alpha\rangle\langle\beta\alpha| \\ \mathrm{I}_\beta \mathrm{S}_\beta &= |\beta\beta\rangle\langle\beta\beta| \end{aligned} \tag{3.28}$$

The single quantum coherences:

$$\begin{aligned} \mathrm{I}^-\mathrm{S}_\alpha &= |\beta\alpha\rangle\langle\alpha\alpha| \quad \mathrm{I}^-\mathrm{S}_\beta = |\beta\beta\rangle\langle\alpha\beta| \\ \mathrm{I}^+\mathrm{S}_\alpha &= |\alpha\alpha\rangle\langle\beta\alpha| \quad \mathrm{I}^+\mathrm{S}_\beta = |\alpha\beta\rangle\langle\beta\beta| \\ \mathrm{I}_\alpha\mathrm{S}^- &= |\alpha\beta\rangle\langle\alpha\alpha| \quad \mathrm{I}_\beta\mathrm{S}^- = |\beta\beta\rangle\langle\beta\alpha| \\ \mathrm{I}_\alpha\mathrm{S}^+ &= |\alpha\alpha\rangle\langle\alpha\beta| \quad \mathrm{I}_\beta\mathrm{S}^+ = |\beta\alpha\rangle\langle\beta\beta| \end{aligned} \tag{3.29}$$

The zero quantum coherences:

$$\mathrm{I}^-\mathrm{S}^+ = |\beta\alpha\rangle\langle\alpha\beta| \quad \mathrm{I}^+\mathrm{S}^- = |\alpha\beta\rangle\langle\beta\alpha| \tag{3.30}$$

The double quantum coherences:

$$\mathrm{I}^-\mathrm{S}^- = |\beta\beta\rangle\langle\alpha\alpha| \quad \mathrm{I}^+\mathrm{S}^+ = |\alpha\alpha\rangle\langle\beta\beta| \tag{3.31}$$

Using equations (3.16) and (3.24), it can be checked that these operators are indeed orthogonal. Note that, with the definition of the Dirac Bra-Ket notation, the complex conjugate of an operator $|\mathrm{X}\rangle\langle\mathrm{Y}|$ is given by $|\mathrm{Y}\rangle\langle\mathrm{X}|$. For our purposes, the most useful operators are the following recombinations, since they can be associated with a physical meaning[3]:

$$
\begin{aligned}
\mathrm{E} &= |\alpha\alpha\rangle\langle\alpha\alpha| + |\alpha\beta\rangle\langle\alpha\beta| + |\beta\alpha\rangle\langle\beta\alpha| + |\beta\beta\rangle\langle\beta\beta| \\
\mathrm{I_z} &= \frac{1}{2}\left[|\alpha\alpha\rangle\langle\alpha\alpha| + |\alpha\beta\rangle\langle\alpha\beta| - |\beta\alpha\rangle\langle\beta\alpha| - |\beta\beta\rangle\langle\beta\beta|\right] \\
\mathrm{S_z} &= \frac{1}{2}\left[|\alpha\alpha\rangle\langle\alpha\alpha| - |\alpha\beta\rangle\langle\alpha\beta| + |\beta\alpha\rangle\langle\beta\alpha| - |\beta\beta\rangle\langle\beta\beta|\right] \\
\mathrm{I_zS_z} &= \frac{1}{4}\left[|\alpha\alpha\rangle\langle\alpha\alpha| - |\alpha\beta\rangle\langle\alpha\beta| - |\beta\alpha\rangle\langle\beta\alpha| + |\beta\beta\rangle\langle\beta\beta|\right]
\end{aligned}
\tag{3.32}
$$

$$
\begin{aligned}
\mathrm{I^-} &= |\beta\alpha\rangle\langle\alpha\alpha| + |\beta\beta\rangle\langle\alpha\beta| \\
\mathrm{I^+} &= |\alpha\alpha\rangle\langle\beta\alpha| + |\alpha\beta\rangle\langle\beta\beta| \\
\mathrm{S^-} &= |\alpha\beta\rangle\langle\alpha\alpha| + |\beta\beta\rangle\langle\beta\alpha| \\
\mathrm{S^+} &= |\alpha\alpha\rangle\langle\alpha\beta| + |\beta\alpha\rangle\langle\beta\beta|
\end{aligned}
\tag{3.33}
$$

$$
\begin{aligned}
\mathrm{I^+S_z} &= \frac{1}{2}\left[|\alpha\alpha\rangle\langle\beta\alpha| - |\alpha\beta\rangle\langle\beta\beta|\right] \\
\mathrm{I^-S_z} &= \frac{1}{2}\left[|\beta\alpha\rangle\langle\alpha\alpha| - |\beta\beta\rangle\langle\alpha\beta|\right] \\
\mathrm{I_z\,S^-} &= \frac{1}{2}\left[|\alpha\beta\rangle\langle\alpha\alpha| - |\beta\beta\rangle\langle\beta\alpha|\right] \\
\mathrm{I_z\,S^+} &= \frac{1}{2}\left[|\alpha\alpha\rangle\langle\alpha\beta| - |\beta\alpha\rangle\langle\beta\beta|\right]
\end{aligned}
\tag{3.34}
$$

$$
\begin{aligned}
\mathrm{I^-S^-} &= |\beta\beta\rangle\langle\alpha\alpha| \\
\mathrm{I^+S^+} &= |\alpha\alpha\rangle\langle\beta\beta| \\
\mathrm{I^-S^+} &= |\beta\alpha\rangle\langle\alpha\beta| \\
\mathrm{I^+S^-} &= |\alpha\beta\rangle\langle\beta\alpha|
\end{aligned}
\tag{3.35}
$$

with $\mathrm{I_z}$ and $\mathrm{S_z}$ representing the total population differences of I and S spin; $2\mathrm{I_zS_z}$ the so-called two spin Zeeman order; $\mathrm{I^+}$, $\mathrm{I^-}$, $\mathrm{S^+}$ and $\mathrm{S^-}$ the in-phase single quantum coherences; $2\mathrm{I^+S_z}$, $2\mathrm{I^-S_z}$, $2\mathrm{I_zS^+}$ and $2\mathrm{I_zS^-}$ the anti-phase single quantum coherences; $2\mathrm{I^+S^+}$ and $2\mathrm{I^-S^-}$ the double quantum coherences; $2\mathrm{I^+S^-}$ and $2\mathrm{I^-S^+}$ the zero quantum coherences and E the unit operator to complete the basis set. It can again be checked that all these operators are orthogonal. Every one of these base operators B_r has an associated frequency, which corresponds to the sum of the individual I and S spin resonance frequencies taking the coherence order into account. These frequencies are given in Table 3.1.

Table 3.1: Associated frequencies of the base operators

Operator	Frequency
I_z, S_z, $2I_zS_z$	0
I^+, I^-	$\pm\omega_I$
$2I^+S_z$, $2I^-S_z$	$\pm\omega_I$
S^+, S^-	$\pm\omega_S$
$2I_zS^+$, $2I_zS^-$	$\pm\omega_S$
$2I^+S^-$, $2I^-S^+$	$\pm(\omega_I-\omega_S)$
$2I^+S^+$, $2I^-S^-$	$\pm(\omega_I+\omega_S)$

3.3.2 Bloch, Wangsness and Redfield theory

What determines the values of the longitudinal auto-relaxation and cross-relaxation rate constants and the transverse relaxation rates? Bloch, Wangsness and Redfield have developed a successful semi-classical theory that answers this question accurately. The theory applies a quantum mechanical description to the spin system itself, but describes the environment (lattice) surrounding the spin system classically. The main drawback of this approach is the inability to predict the Boltzmann distribution for the equilibrium populations, as the population differences are predicted to return zero. This can easily be corrected for *ad hoc* though.

The theory assumes that the Hamiltonian can be written as the sum of a time-independent (in the case when no rf-pulses are applied) part H_0 that acts only on the spin system itself and a stochastic time dependent part $\mathrm{H}_1(t)$ that couples the spin system to the lattice:

$$\mathrm{H}(t) = \mathrm{H}_0 + \mathrm{H}_1(t) \tag{3.36}$$

H_0 contains the effects from the static magnetic field (the Zeeman Hamiltonian) and all other isotropic, local effects (chemical shift, scalar coupling). $\mathrm{H}_1(t)$ is anisotropic (*i.e.* its effects are dependent on the orientation of the molecule) and stochastically time dependent. The average of $\mathrm{H}_1(t)$ over all spins in the ensemble is zero at any time. The Liouville-von Neumann equation can be rewritten:

$$\frac{d\rho(\mathrm{t})}{dt} = -i\left[\mathrm{H}_0, \rho(\mathrm{t})\right] - i\left[\mathrm{H}_1(\mathrm{t}), \rho(\mathrm{t})\right] \tag{3.37}$$

The further derivation of the theory will be omitted here. Good texts which discuss this theory are available[3-5]. During this derivation, some assumptions are made:

1. $\mathrm{H}_1(t)$ and $\rho(t)$ are assumed to be uncorrelated with each other.
2. The time of interest during which the relaxation process occurs satisfies the condition $\tau << t << 1/R$, with τ the correlation time of the stochastic process that drives the relaxation (see section 3.4) and R the relaxation rate constant. This can be extended by defining a time $T = nt$, with t subject to the given condition and n an integer, and performing a piecewise evaluation of T for each of the n intervals[3]. Like this the results are expanded to times $T > 1/R$.
3. $\rho(t)$ can be replaced by $\rho(t) - \rho_0$, with ρ_0 the spin density operator at equilibrium. This ensures that the system evolves back to Boltzmann equilibrium.
4. The Hamiltonian $\mathrm{H}_1(t)$ is expanded into a set of tensor operators T_l^m and stochastic time functions $\mathrm{F}_l^m(t)$ of spatial variables:

$$\mathrm{H}_1(t) = \sum_{m=-l}^{l} (-1)^m \mathrm{F}_l^{-m}(t) \mathrm{T}_l^m \tag{3.38}$$

   The index l denotes the rank of the tensor, and is always 2 for the relaxation mechanisms considered here. The tensor operators are again expanded into the same set of base operators into which the spin density matrix was expanded (thus equations (3.35)):

$$\mathrm{T}_2^m = \sum_p a_p^m \mathrm{B}_p^m \tag{3.39}$$

   These expansions will become more clear when they are applied to specific relaxation mechanisms (see section 3.3.3). The tensor operators and the random functions agree to the following properties:

$$\mathrm{T}_l^{-m} = (-1)^m \mathrm{T}_l^{m\dagger} \tag{3.40}$$

$$\mathrm{F}_l^{-m}(t) = (-1)^m \mathrm{F}_l^{m*}(t) \tag{3.41}$$

   Here, '*' denotes the complex conjugate and '†' denotes the operator (Hermitian) adjoint.
5. Finally, a simplification is assumed known as the secular approximation. Although not necessary, it considerably simplifies the end result. The main consequence of applying this simplification is that cross-relaxation between transverse operators is not considered. This is no issue, as cross-relaxation

between transverse operators is not effective since it is incoherent due to the chemical shift evolution during this process. It only becomes significant when the frequencies of the I and S spins are similar (to within one line width) or are made similar by applying rf-fields (*cf.* ROESY).

After the derivation, the following result is found for (3.37), generally know as the master equation for relaxation:

$$\frac{d\rho(\mathrm{t})}{dt} = -i\left[\mathrm{H}_0, \rho(\mathrm{t})\right] - \Gamma\left(\rho(\mathrm{t}) - \rho_0\right) \tag{3.42}$$

where Γ is the relaxation superoperator, given by:

$$\Gamma = \frac{1}{2}\sum_{m=-2}^{2}\sum_{p}(-1)^m\, a_p^m a_p^{-m}\, \mathrm{j}^m\left(\omega_p^m\right)[\mathrm{B}_p^{-m},[\mathrm{B}_p^m,\ ]] \tag{3.43}$$

Here, $\mathrm{j}^m\left(\omega_p^m\right)$ are the power spectral density function values at the associated frequency of the base operator B_p^m. These represent the contributions of these frequencies to the oscillating magnetic field created by the relaxation mechanisms. They are defined as the real part of the Fourier transform of the correlation functions of the stochastic time functions and will be discussed in detail in sections 3.3.4 and 3.4. Analogous to (3.27), (3.42) can be rewritten:

$$\frac{db_r(\mathrm{t})}{dt} = \sum_s -i\Omega_{rs} b_s(\mathrm{t}) + \sum_s -\Gamma_{rs}\left(b_s(t) - b_{s0}(t)\right) \tag{3.44}$$

with:

$$\Gamma_{rs} = \frac{1}{2}\sum_{m=-2}^{2}\sum_{p}\frac{\left\langle \mathrm{B}_r \middle| [\mathrm{B}_p^{-m},[\mathrm{B}_p^m,\mathrm{B}_s]] \right\rangle}{\left\langle \mathrm{B}_r \middle| \mathrm{B}_s \right\rangle}(-1)^m\, a_p^m a_p^{-m}\, \mathrm{j}^m\left(\omega_p^m\right) \tag{3.45}$$

How this result should be interpreted will now be recapitulated. The state of the two spin system at time t is described by the spin density operator (which can be represented by a $2^2\times2^2 = 4\times4$ matrix), which is a linear combination of $4\times4 = 16$ base operators B_r that are chosen so that they have a physical meaning (*e.g.* z-magnetisation of spin I ($\mathrm{B}_r = \mathrm{I}_z$), double quantum coherence ($\mathrm{B}_r = 2\mathrm{I}^+\mathrm{S}^+$), etc.):

$$\rho(\mathrm{t}) = b_1(t)\mathrm{B}_1 + b_2(t)\mathrm{B}_2 + b_3(t)\mathrm{B}_3 + \ \ldots + b_{16}(t)\mathrm{B}_{16} \tag{3.46}$$

The density operator evolves over time by varying the contribution $b_r(t)$ of each base operator. The degree to which these coefficients change over time is described by the set of differential equations given by (3.44). The first part within the sum of (3.44) describes the evolution due to the static magnetic field (chemical shift), rf-pulses and scalar couplings. The second part describes how the coefficients evolve under the stochastically fluctuating anisotropic interactions with the lattice. The rate at which this occurs is determined by the deviation from the equilibrium values $b_s(t) - b_s^0$ and a rate constant Γ_{rs}, the latter of which is evaluated through (3.46). Note that Γ_{rr} is the auto-relaxation rate constant for B_r, while Γ_{rs} in the case of $r \neq s$ is the cross-relaxation rate constant between B_r and B_s.

All of this is equivalent with the Solomon equations of equation (3.4). The auto-relaxation rate constant ρ_I would for example correspond to the case where $\mathrm{B}_r = \mathrm{B}_s = \mathrm{I}_z$, while the cross-relaxation rate constant would correspond to the case of $\mathrm{B}_r = \mathrm{I}_z$ and $\mathrm{B}_s = \mathrm{S}_z$ or vice versa. It can be shown that cross-relaxation in fact does not occur between base operators of different coherence order; thus not between I_z and I^+ for example. As noted above, cross-relaxation does not occur between transverse operators (of zero, single or double quantum coherence) either, when the condition that the frequencies of the two spins are not too similar is satisfied.

3.3.3 Application on dipolar and CSA relaxation mechanisms

The expressions for the relaxation rate constants Γ_{rs} need to be evaluated for each given relaxation mechanism. For dipolar interaction, the Hamiltonian is given by[5]:

$$\mathrm{H}_1^D(t) = \frac{\mu_0}{8\pi^2}\frac{\gamma_I \gamma_S h}{\mathrm{r}_{IS}^{\,3}(t)}\left(\mathbf{I}\bullet\mathbf{S} - 3\left(\mathbf{I}\bullet\mathbf{e}_{IS}\right)\left(\mathbf{S}\bullet\mathbf{e}_{IS}\right)\right) \tag{3.47}$$

with μ_0 the permeability of vacuum, γ_I and γ_S the gyromagnetic ratios of spin I and S respectively, h the Planck constant, $\mathrm{r}_{IS}(t)$ the time dependent distance between spins I and S, $\mathbf{I}$ and $\mathbf{S}$ the spin angular moments as vector quantities, and $\mathbf{e}_{IS}$ the unit vector along the direction that connects both spins. The decomposition of this Hamiltonian as required by (3.38) and (3.39) is given by:

$$\mathrm{H}_1^D(t) = \sum_{m=-2}^{2} (-1)^m \mathrm{F}_2^{-m}(t) \sum_p a_p^m \mathrm{B}_p^m \tag{3.48}$$

The values for a_p^m and the base operators B_p^m are provided in Table 3.2. For dipole-dipole interaction, the random spatial functions F_p^m are proportional to the second

order spherical harmonic functions $\mathrm{Y}_2^m\left(\Omega(t)\right)$ (appendix A), where its angular variables $\Omega = (\theta,\phi)$ are random functions of time. It will be assumed that the distance between the spins changes much more slowly than does their angular orientation, so that $\mathrm{r}_{IS}(t) \equiv r_{IS}$. This is true when I and S are directly connected through a chemical bond (neglecting the limited effects of bond vibration). The functions F_p^m are then given by:

$$\begin{aligned}\mathrm{F}_2^m(t) &= \frac{\mu_0}{8\pi^2}\frac{\gamma_I\gamma_S h}{{r_{IS}}^3}\sqrt{\frac{4\pi}{5}}\,\mathrm{Y}_2^m\left(\Omega(t)\right)\\ &= K_{DD}\sqrt{\frac{4\pi}{5}}\,\mathrm{Y}_2^m\left(\Omega(t)\right)\end{aligned} \tag{3.49}$$

Table 3.2: Base operators and their coefficients for dipolar relaxation

m	p	a_p^m	B_p^m	$a_p^{-m} = (-1)^m\left(a_p^m\right)^*$	$\mathrm{B}_p^{-m} = \left(\mathrm{B}_p^m\right)^\dagger$
0	-1	$-1/2$	$\mathrm{I}^-\mathrm{S}^+$	$-1/2$	$\mathrm{I}^+\mathrm{S}^-$
0	0	2	$\mathrm{I}_z\mathrm{S}_z$	2	$\mathrm{I}_z\mathrm{S}_z$
0	+1	$-1/2$	$\mathrm{I}^+\mathrm{S}^-$	$-1/2$	$\mathrm{I}^-\mathrm{S}^+$
-1	0	$-\sqrt{6}/2$	$\mathrm{I}_z\mathrm{S}^-$	$\sqrt{6}/2$	$\mathrm{I}_z\mathrm{S}^+$
-1	+1	$-\sqrt{6}/2$	$\mathrm{I}^-\mathrm{S}_z$	$\sqrt{6}/2$	$\mathrm{I}^+\mathrm{S}_z$
+1	0	$\sqrt{6}/2$	$\mathrm{I}_z\mathrm{S}^+$	$-\sqrt{6}/2$	$\mathrm{I}_z\mathrm{S}^-$
+1	+1	$\sqrt{6}/2$	$\mathrm{I}^+\mathrm{S}_z$	$-\sqrt{6}/2$	$\mathrm{I}^-\mathrm{S}_z$
-2	0	$\sqrt{6}/2$	$\mathrm{I}^-\mathrm{S}^-$	$\sqrt{6}/2$	$\mathrm{I}^+\mathrm{S}^+$
+2	0	$\sqrt{6}/2$	$\mathrm{I}^+\mathrm{S}^+$	$\sqrt{6}/2$	$\mathrm{I}^-\mathrm{S}^-$

For chemical shift anisotropy of a spin I, the anisotropic part of the Hamiltonian (the isotropic part is included in H_0), is given by[4]:

$$\mathrm{H}_1^{CSA}(t) = -\gamma_I\frac{\Delta\sigma}{3}\left(B_0\,\mathrm{I}_z - 3\left(\mathbf{B}\bullet\mathbf{e}_{CSA}(t)\right)\left(\mathbf{I}\bullet\mathbf{e}_{CSA}(t)\right)\right) \tag{3.50}$$

B and **I** are respectively the magnetic field and the spin angular moment in vector form. B_0 is the size of the magnetic field. $\mathbf{e}_{\mathrm{CSA}}(t)$ is the unit vector in the direction of the time dependent orientation of the main principal axis of the chemical shift tensor. It is assumed in (3.50) that the chemical shift tensor is axially symmetric, with $\Delta\sigma$ the chemical shift anisotropy expressed by the difference between its two eigenvalues ($\sigma^{\parallel} - \sigma^{\perp}$). This usually is a fair approximation. Decomposition into base operators in a similar fashion as (3.48) leads to the results in Table 3.3 and to the following random

spatial functions, which are also proportional to second order spherical harmonic functions:

$$\begin{aligned} \mathrm{F}_2^m(t) &= \frac{\gamma_I B_0 \Delta\sigma}{\sqrt{3}} \sqrt{\frac{4\pi}{5}}\, \mathrm{Y}_2^m\left(\Omega(t)\right) \\ &= K_{CSA} \sqrt{\frac{4\pi}{5}}\, \mathrm{Y}_2^m\left(\Omega(t)\right) \end{aligned} \tag{3.51}$$

Table 3.3: Base operators and their coefficients for CSA relaxation

m	p	a_p^m	B_p^m	$a_p^{-m} = (-1)^m \left(a_p^m\right)^*$	$\mathrm{B}_p^{-m} = \left(\mathrm{B}_p^m\right)^\dagger$
0	0	$2/\sqrt{6}$	$\mathrm{I_z}$	$2/\sqrt{6}$	$\mathrm{I_z}$
-1	0	$1/2$	$\mathrm{I^-}$	$-1/2$	$\mathrm{I^+}$
1	0	$-1/2$	$\mathrm{I^+}$	$1/2$	$\mathrm{I^-}$
±2	0	—	—	—	—

3.3.4 The spectral density function

The power spectral density functions $\mathrm{j}^m(\omega)$ in (3.45) are defined as the real part of the Fourier transform of the correlation functions of the spatial random functions $\mathrm{F}_2^m(t)$. A correlation function can be defined as the ensemble average of the spatial random function compared to its initial value and can be seen as the correlation between the value of a spatial function at time t and their initial value. It is defined as:

$$\mathrm{C}^m(t) = \overline{\mathrm{F}_2^m(0)\,\mathrm{F}_2^{m*}(t)} \tag{3.52}$$

Both for dipolar and CSA relaxation, the spatial random functions are proportional to the second order spherical harmonics. Using (3.49) or (3.51):

$$\begin{aligned} \mathrm{C}^m(t) &= K^2 \frac{4\pi}{5} \overline{\mathrm{Y}_2^m\left(\Omega(0)\right)\mathrm{Y}_2^{m*}\left(\Omega(t)\right)} \\ &= K^2 \frac{1}{5} \iint \mathrm{Y}_2^m(\Omega_0)\,\mathrm{Y}_2^{m*}(\Omega)\,\mathrm{P}(\Omega_0,\Omega,t)\,d\Omega_0 d\Omega \end{aligned} \tag{3.53}$$

with $\mathrm{P}(\Omega_0,\Omega,t)$ the probability distribution that the internuclear vector between I and S (in the case of dipolar relaxation) or the main principal axis of the chemical shift tensor (in the case of CSA relaxation) was oriented at Ω_0 at time $t = 0$ and is oriented at Ω at time t. The power spectral density function is then the real part of the Fourier transform of the correlation function:

$$\begin{aligned} \mathrm{j}^m(\omega) &= \mathrm{Re}\left[\mathrm{FT}\left[\mathrm{C}^m(t)\right]\right] \\ &= \int_0^{+\infty} \mathrm{C}^m(t)\cos(\omega t)\,dt \end{aligned} \tag{3.54}$$

The imaginary part of the Fourier transform is not considered, as it does not cause relaxation but leads to dynamic frequency shifts and can be safely neglected for this treatment. The proper evaluation of the correlation function and the spectral density function will be discussed in section 3.4. For now it is sufficient to note that the functional form of the power spectral density function (and the correlation function) is invariant under the index m. It can therefore be stated:

$$\begin{aligned} \mathrm{j}^m(\omega) &= K^2\,\mathrm{J}(\omega) \\ C^m(t) &= K^2 C(t) \end{aligned} \tag{3.55}$$

with K^2 a constant dependent on the relaxation mechanism and $\mathrm{J}(\omega)$ the orientational spectral density function which only depends on the time dependent orientation of the spins and not on their relative distance. Similarly, $\mathrm{C}(t)$ is the orientational correlation function. $\mathrm{J}(\omega)$ will from now on simply be referred to as the spectral density function. It is an even function of ω, so that:

$$\mathrm{J}(\omega) = \mathrm{J}(-\omega) \tag{3.56}$$

3.3.5 Evaluation of the relaxation rate constants

For both dipolar and CSA relaxation mechanisms, Γ_{rs} in equation (3.45) needs to be evaluated for each combination of base operators B_r and B_s using the set of operators given in Tables 3.2 and 3.3 respectively. This is done explicitly for one example in appendix D. The following results are found, taking (3.55) into account:

Longitudinal auto-relaxation of spin I: $\mathrm{B}_r = \mathrm{I}_z$ *and* $\mathrm{B}_s = \mathrm{I}_z$

$$\begin{aligned} R_{1,I}^{DD} &= \rho_I^{DD} = \frac{K_{DD}^2}{4}\left[\mathrm{J}(\omega_I - \omega_S) + 3\,\mathrm{J}(\omega_I) + 6\,\mathrm{J}(\omega_I + \omega_S)\right] \\ R_{1,I}^{CSA} &= \rho_I^{CSA} = K_{CSA,I}^2\,\mathrm{J}(\omega_I) \end{aligned} \tag{3.57}$$

Longitudinal auto-relaxation of spin S: $B_r = S_z$ *and* $B_s = S_z$

$$\begin{aligned} R_{1,S}^{DD} &= \rho_S^{DD} = \frac{K_{DD}^2}{4}\left[\mathrm{J}(\omega_I - \omega_S) + 3\mathrm{J}(\omega_S) + 6\mathrm{J}(\omega_I + \omega_S)\right] \\ R_{1,S}^{CSA} &= \rho_S^{CSA} = K_{CSA,S}^2\,\mathrm{J}(\omega_S) \end{aligned} \tag{3.58}$$

Longitudinal cross-relaxation between spins I *and* S: $B_r = I_z$ *and* $B_s = S_z$

$$\begin{aligned} \sigma_{IS}^{DD} &= \frac{K_{DD}^2}{4}\left[-\mathrm{J}(\omega_I - \omega_S) + 6\mathrm{J}(\omega_I + \omega_S)\right] \\ \sigma_{IS}^{CSA} &= 0 \end{aligned} \tag{3.59}$$

Transverse auto-relaxation of spin I: $B_r = I^+$ *and* $B_s = I^+$ *or* $B_r = I^-$ *and* $B_s = I^-$

$$\begin{aligned} R_{2,I}^{DD} &= \frac{K_{DD}^2}{8}\left[4\mathrm{J}(0) + \mathrm{J}(\omega_I - \omega_S) + 3\mathrm{J}(\omega_I) + 6\mathrm{J}(\omega_S) + 6\mathrm{J}(\omega_I + \omega_S)\right] \\ R_{2,I}^{CSA} &= \frac{K_{CSA,I}^2}{6}\left[4\mathrm{J}(0) + 3\mathrm{J}(\omega_I)\right] \end{aligned} \tag{3.60}$$

Transverse auto-relaxation of spin S: $B_r = S^+$ *and* $B_s = S^+$ *or* $B_r = S^-$ *and* $B_s = S^-$

$$\begin{aligned} R_{2,S}^{DD} &= \frac{K_{DD}^2}{8}\left[4\mathrm{J}(0) + \mathrm{J}(\omega_I - \omega_S) + 3\mathrm{J}(\omega_S) + 6\mathrm{J}(\omega_I) + 6\mathrm{J}(\omega_I + \omega_S)\right] \\ R_{2,S}^{CSA} &= \frac{K_{CSA,S}^2}{6}\left[4\mathrm{J}(0) + 3\mathrm{J}(\omega_S)\right] \end{aligned} \tag{3.61}$$

The constants K_{DD}^2 and K_{CSA}^2 are given by:

$$K_{DD}^2 = \left(\frac{\mu_0}{8\pi^2}\right)^2 \frac{\gamma_I^2 \gamma_S^2 h^2}{r_{IS}^{\,6}} \tag{3.62}$$

$$K_{CSA}^2 = \frac{\gamma_I^2 B_0^2 \Delta\sigma^2}{3} \tag{3.63}$$

The internuclear distance r_{IS} will be assumed to be 1.02 Å for a ^{1}H-^{15}N pair in the peptide bond, and 1.07 Å for a ^{1}H-^{13}C$^\alpha$ pair in an amino acid residue. The chemical shift anisotropy $\Delta\sigma$ is assumed to be –160 ppm for a ^{15}N nucleus in a peptide bond and 25 ppm for a ^{13}C$^\alpha$ nucleus in an amino acid residue. The relaxation rate constants are thus linear combinations of values of the spectral density function sampled at different frequencies. When comparing equations (3.57), (3.58) and (3.59) with the expressions of the longitudinal auto- and cross-relaxation rate constants in

terms of the transition rate constants (equations (3.5)), then the following conclusions can be easily made:

$$\begin{aligned} W_I &= \frac{1}{2}\left(\frac{3}{4}K_{DD}^2 + K_{CSA,I}^2\right)\mathrm{J}\left(\omega_I\right) \\ W_S &= \frac{1}{2}\left(\frac{3}{4}K_{DD}^2 + K_{CSA,S}^2\right)\mathrm{J}\left(\omega_S\right) \\ W_0 &= \frac{1}{4}K_{DD}^2\,\mathrm{J}\left(\omega_I - \omega_S\right) \\ W_2 &= \frac{3}{2}K_{DD}^2\,\mathrm{J}\left(\omega_I + \omega_S\right) \end{aligned} \tag{3.64}$$

Each relaxation induced transition rate constant is thus proportional to the degree to which its corresponding frequency is present in the random varying magnetic fields. Note that the zero W_0 and double W_2 quantum transition rate constants are not influenced by CSA relaxation. This is to be expected, since CSA relaxation arises from an interaction between a nuclear spin and the induced magnetic field from the electron environment and not from the interaction between both spins.

Now all that remains is to understand how exactly the motions of the spins influence the spectral density function. This is the subject of the next section.

3.4 Evaluation of the spectral density function: rotational diffusion and internal motion

3.4.1 Effects of isotropic rotational diffusion

The general expression for the correlation functions is provided by equation (3.53). To investigate the impact of any motion that reorients the spins, the probability distribution $\mathrm{P}(\Omega_0,\Omega,t)$ must be evaluated for this motion. The simplest case is that of a two spin system IS that is rigidly attached to a molecule undergoing isotropic rotational diffusion with diffusion coefficient D_r. The probability distribution in this particular case was already derived previously (equation (1.24)):

$$\mathrm{P}\left(\Omega_0,\Omega,t\right) = \sum_{l=0}^{+\infty}\left[\sum_{m=-l}^{l}\mathrm{Y}_l^{m*}\left(\Omega_0\right)\mathrm{Y}_l^{m}\left(\Omega\right)\right]e^{-l(l+1)D_r t} \tag{3.65}$$

Combining this with (3.53) leads to:

$$\begin{aligned}
\mathrm{C}^m(t) &= K^2 \frac{1}{5} \iint \mathrm{Y}_2^m(\Omega_0)\mathrm{Y}_2^{m*}(\Omega) \sum_{l'=0}^{+\infty} \left\{ \left[\sum_{m'=-l'}^{l'} \mathrm{Y}_{l'}^{m'*}(\Omega_0)\mathrm{Y}_{l'}^{m'}(\Omega) \right] e^{-l'(l'+1)D_r t} \right\} d\Omega_0 d\Omega \\
&= K^2 \frac{1}{5} \sum_{l'=0}^{+\infty} \left[e^{-l'(l'+1)D_r t} \sum_{m'=-l'}^{l'} \int \mathrm{Y}_2^m(\Omega_0)\mathrm{Y}_{l'}^{m'*}(\Omega_0) d\Omega_0 \int \mathrm{Y}_2^{m*}(\Omega)\mathrm{Y}_{l'}^{m'}(\Omega) d\Omega \right] \\
&= K^2 \frac{1}{5} \sum_{l=0}^{+\infty} \left[e^{-l(l+1)D_r t} \sum_{m=-l}^{l} \delta_{2l'}\delta_{mm'} \right] \\
&= K^2 \frac{1}{5} \sum_{l=0}^{+\infty} \left[\delta_{2l'} e^{-l(l+1)D_r t} \right] \\
&= K^2 \frac{1}{5} e^{-6D_r t} \\
&= K^2 \frac{1}{5} e^{-t/\tau}
\end{aligned} \tag{3.66}$$

in which the orthonormality of the spherical harmonic functions has been used. In the final step, the NMR correlation time constant $\tau = 1/6D_r$ was introduced. The correlation function in the case of isotropic rotational diffusion is thus a monoexponential decay. The power spectral density function can be calculated using (3.54), and is revealed to be a Lorentzian function:

$$\begin{aligned}
\mathrm{j}^m(\omega) &= K^2 \frac{1}{5} \int_0^{+\infty} e^{-t/\tau} \cos(\omega t)\, dt \\
&= K^2 \frac{2}{5} \frac{\tau}{1+\omega^2\tau^2}
\end{aligned} \tag{3.67}$$

It is clear that the power spectral density function is independent of the index *m* in this particular case, confirming the statement that was made in equation (3.55). The spectral density function is then:

$$\mathrm{J}(\omega) = \frac{2}{5} \frac{\tau}{1+\omega^2\tau^2} \tag{3.68}$$

This also confirms the previous statement that $\mathrm{J}(\omega)$ is an even function (equation (3.56)).

3.4.2 Effects of anisotropic rotational diffusion

As discussed in Chapter 1, anisotropic rotational diffusion is described by the mathematical model proposed by Francis Perrin and requires multiple diffusion coefficients. In 1962, Donald Woessner used Perrin's results to obtain an expression for the NMR correlation function of a two spin system rigidly attached to a fully

anisotropic molecule[8]. The orientational correlation function (invariant of the index m) is given by:

$$\mathrm{C}(t) = \frac{1}{5}\left[c_1 e^{-t/\tau_1} + c_2 e^{-t/\tau_2} + c_3 e^{-t/\tau_3} + c_+ e^{-t/\tau_+} + c_- e^{-t/\tau_-} \right] \tag{3.69}$$

$\mathrm{C}(t)$ is thus a five-exponential decay. Applying (3.54), the spectral density function is given by:

$$\mathrm{J}(\omega) = \frac{2}{5}\left[c_1 \frac{\tau_1}{1+\omega^2\tau_1^2} + c_2 \frac{\tau_2}{1+\omega^2\tau_2^2} + c_3 \frac{\tau_3}{1+\omega^2\tau_3^2} + c_+ \frac{\tau_+}{1+\omega^2\tau_+^2} + c_- \frac{\tau_-}{1+\omega^2\tau_-^2} \right] \tag{3.70}$$

The correlation times are determined by the three rotational diffusion coefficients:

$$\begin{aligned} \tau_1 &= \frac{1}{4D_r^x + D_r^y + D_r^z} & \tau_+ &= \frac{1}{6\left(R + \sqrt{R^2 - L^2}\right)} \\ \tau_2 &= \frac{1}{D_r^x + 4D_r^y + D_r^z} & \tau_- &= \frac{1}{6\left(R - \sqrt{R^2 - L^2}\right)} \\ \tau_3 &= \frac{1}{D_r^x + D_r^y + 4D_r^z} \end{aligned} \tag{3.71}$$

in which R and L^2 are given by:

$$\begin{aligned} R &= \frac{D_r^x + D_r^y + D_r^z}{3} \\ L^2 &= \frac{D_r^x D_r^y + D_r^x D_r^z + D_r^y D_r^z}{3} \end{aligned} \tag{3.72}$$

The pre-exponential coefficients are functions of the orientation of a vector relevant for the relaxation mechanism compared to the principle axes of the rotational diffusion tensor. This orientation is expressed by θ, φ and ψ, the angles between this vector and the three principal axes of the rotational diffusion tensor (associated with D_r^z, D_r^x and D_r^y respectively). For dipolar relaxation, this vector is the internuclear bond vector connecting the I and S spins, while for CSA relaxation this is the main principle axis of the chemical tensor. In the case of peptide $^{15}\mathrm{N}$ and $^{13}\mathrm{C}^{\alpha}$ relaxation, the latter is usually assumed to be colinear with the internuclear vector for simplicity since the exact orientation of the chemical shift tensor is not always accurately known. Because these angles describe the orientation of a vector, the squared of their cosines sum up to 1:

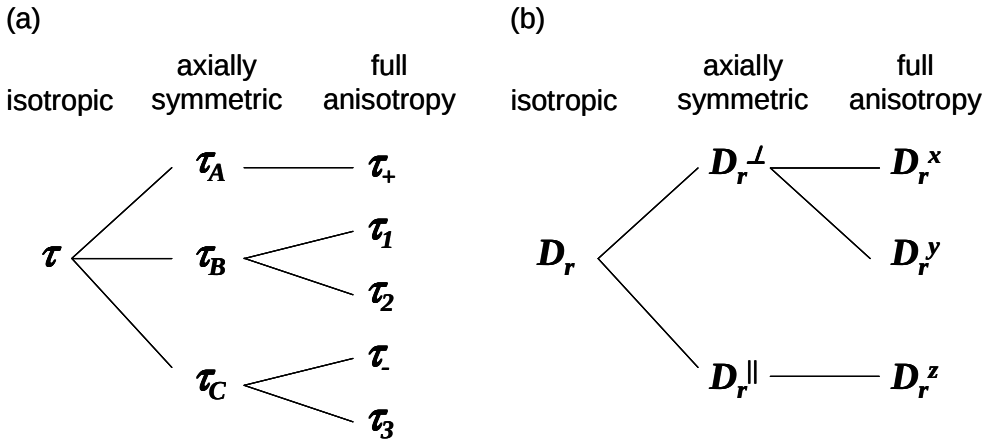

Figure 3.7: Relation between (a) correlation times and (b) rotational diffusion coefficients for isotropic, axially symmetric anisotropic and fully anisotropic molecules.

$$\cos^2\theta + \cos^2\varphi + \cos^2\psi = 1 \tag{3.73}$$

The pre-exponential coefficients are then given by:

$$\begin{aligned} c_1 &= 3\cos^2\psi\cos^2\theta \quad & c_+ &= \frac{d-e}{2} \\ c_2 &= 3\cos^2\varphi\cos^2\theta & & \\ c_3 &= 3\cos^2\varphi\cos^2\psi \quad & c_- &= \frac{d+e}{2} \end{aligned} \tag{3.74}$$

with:

$$\begin{aligned} d &= \frac{1}{2}\left[3\left(\cos^4\theta + \cos^4\varphi + \cos^4\psi\right) - 1\right] \\ e &= \frac{1}{6}\left[\delta_1\left(3\cos^4\varphi + 6\cos^4\theta\cos^4\psi - 1\right) + \delta_2\left(3\cos^4\psi + 6\cos^4\theta\cos^4\varphi - 1\right)\right. \\ &\quad \left. + \delta_3\left(3\cos^4\theta + 6\cos^4\varphi\cos^4\psi - 1\right)\right] \\ \delta_1 &= \frac{D_r^x - R}{\sqrt{R^2 - L^2}}; \quad \delta_2 = \frac{D_r^y - R}{\sqrt{R^2 - L^2}}; \quad \delta_2 = \frac{D_r^z - R}{\sqrt{R^2 - L^2}} \end{aligned} \tag{3.75}$$

These rather extensive expressions for the spectral density function simplify a great deal when the rotational diffusion of an axially symmetric object is considered. Since the rotational diffusion coefficients now reduce from 3 unique values to 2 ($D_r^x = D_r^y = D_r^{\perp}$ and $D_r^z = D_r^{||}$, see section 1.3), some of the correlation time constants of the fully anisotropic object become degenerate:

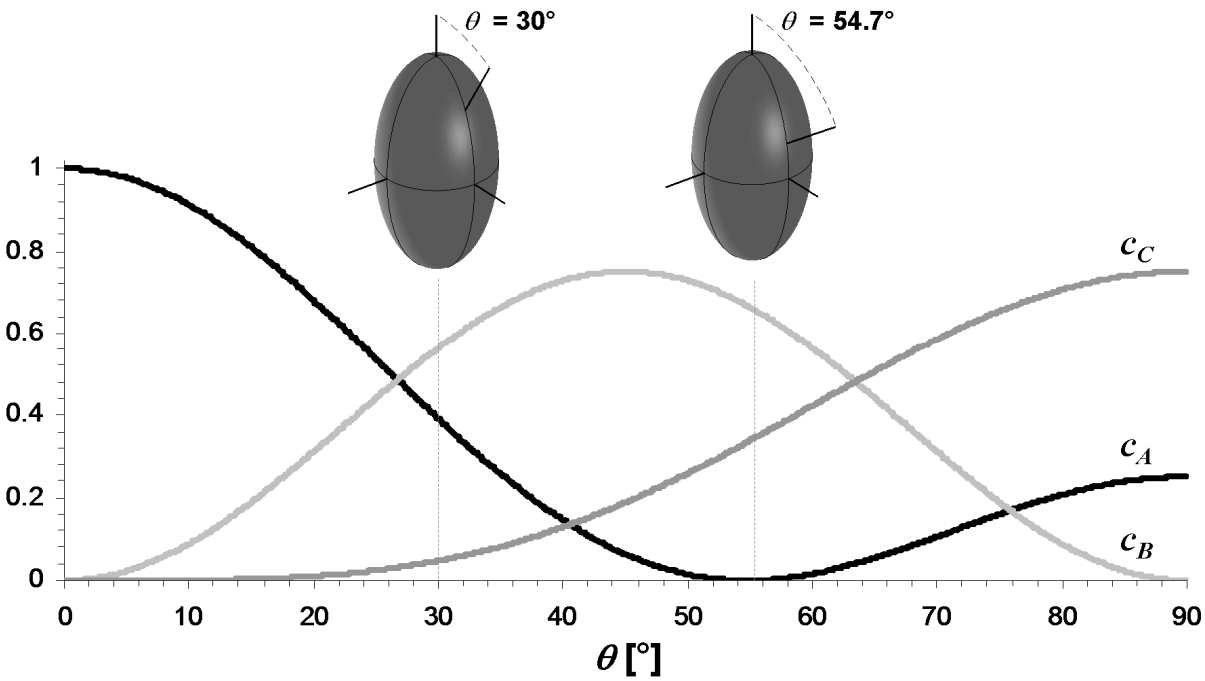

Figure 3.8: Dependence on θ of the coefficients c_A, c_B and c_C according to equations (3.78). If the internuclear vector is parallel to the main principle component of the rotational diffusion tensor ($\theta = 0°$), there is only a contribution to the spectral density function of τ_A, while at the magic angle ($\theta = 54.7°$) there is only a contribution of τ_B and τ_C, and perpendicular to the main axis at ($\theta = 90°$) only there is only a contribution of τ_A and τ_C.

$$\begin{aligned}\tau_+ &= \tau_A = \frac{1}{6D_r^\perp} \\ \tau_1 &= \tau_2 = \tau_B = \frac{1}{5D_r^\perp + D_r^\parallel} \\ \tau_- &= \tau_3 = \tau_C = \frac{1}{2D_r^\perp + 4D_r^\parallel}\end{aligned} \tag{3.76}$$

The relation between the correlation time constants and the rotational diffusion coefficients with the level of anisotropy is shown schematically in Figure 3.7. The correlation function of an axially symmetric object is thus reduced to a three-exponential decay function, and the spectral density function is now given by:

$$\mathrm{J}(\omega) = \frac{2}{5}\left[c_A \frac{\tau_A}{1+\omega^2\tau_A^2} + c_B \frac{\tau_B}{1+\omega^2\tau_B^2} + c_C \frac{\tau_C}{1+\omega^2\tau_C^2} \right] \tag{3.77}$$

The coefficients can be derived from (3.74), taking (3.73) into account:

$$\begin{aligned}c_A &= c_+ = \frac{1}{4}\left(3\cos^2\theta - 1\right)^2 \\ c_B &= c_1 + c_2 = 3\cos^2\theta \sin^2\theta \\ c_C &= c_3 + c_- = \frac{3}{4}\sin^4\theta\end{aligned} \tag{3.78}$$

These coefficients show how the orientation of the I–S bond vector in the anisotropic object determines the contribution of each correlation time to the spectral density, as illustrated in Figure 3.8.

3.4.3 Effects of internal motion

In the previous sections, only the global rotational motion of the molecular object was considered as a source of time dependent variation of the relative orientation of the I and S spins. However, conformational flexibility within the molecular structure can be a very important contributor as well. Lipari and Szabo have developed a very general theory to include fast internal motions (ranging from the picosecond to nanosecond timescale) into the correlation function[9, 10]. They proposed the following expression of the orientational correlation function for internal motion:

$$\mathrm{C}_i(t) = S^2 + \left(1 - S^2\right) e^{-t/\tau_i} \tag{3.79}$$

with S the order parameter and τ_i the correlation time constant associated with the internal motion. The order parameter describes how restricted the internal motion is. The limit value $S^2 = 0$ means that the internal motion allows to sample all spatially possible relative orientations of the I and S spins, while the other limit value $S^2 = 1$ indicates that no internal motion is present. Any value in between indicates a limited range of orientations that can be sampled (for example motion restricted within a cone). After a time much longer than τ_i the internal motion correlation function takes on the value of S^2 (Figure 3.9). When taking the global rotational motion of the molecule into account (assumed here to be isotropic), the total orientational correlation function becomes the product of (3.79) and the orientational correlation function for isotropic rotational diffusion (3.66):

$$\begin{aligned} \mathrm{C}(t) &= \frac{1}{5}\left[S^2 + \left(1 - S^2\right) e^{-t/\tau_i} \right] e^{-t/\tau} \\ &= \frac{1}{5}\left[S^2 e^{-t/\tau} + \left(1 - S^2\right) e^{-t/\tau_{tot}} \right] \end{aligned} \tag{3.80}$$

in which the total correlation time constant is defined as:

$$\tau_{tot} = \left(\tau^{-1} + \tau_i^{-1}\right)^{-1} \tag{3.81}$$

The spectral density function then becomes:

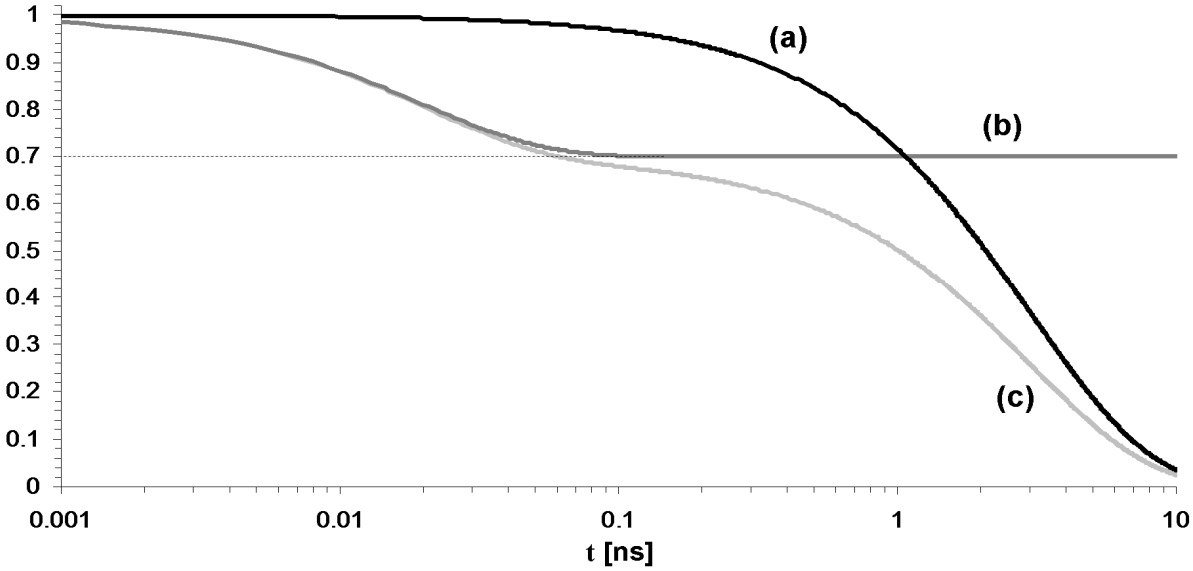

Figure 3.9: Correlation functions as a function of time. (a) Global correlation function of an isotropic molecule with $\tau = 3$ ns, multiplied by 5 for scaling reasons; (b) internal motion correlation function with $\tau_i = 20$ ps and an S^2 value of 0.7; (c) total correlation function multiplied by a factor of 5.

$$\mathrm{J}(\omega) = \frac{2}{5}\left[S^2 \frac{\tau}{1+\omega^2\tau^2} + \left(1-S^2\right)\frac{\tau_{tot}}{1+\omega^2\tau_{tot}^2} \right] \tag{3.82}$$

As the value for S^2 gradually varies from 1 to 0, the spectral density function shifts from a sharp Lorentzian that is dominated by relatively low frequencies due to the slow molecular rotation, to a broad Lorentzian that also covers the higher frequencies caused by the fast internal motions (Figure 3.10). An internal motion influences most the relaxation rates that are influenced by frequency components that reside in the low frequency plateau region of the global rotational spectral density function (Figure 3.10), since these components are scaled down by approximately a factor of S^2. Most notably, the transverse relaxation rate constant R_2 is affected, since it directly depends on the spectral density value at $\omega = 0$.

The advantage of the Lipari-Szabo method is that no model needs to be assumed for the internal motion and is therefore know as the model free method. It is valid when the correlation time associated with the internal motion is much shorter than the global correlation time and is therefore only useful when sufficiently large molecular systems are considered with long global correlation times. This can be understood from equation (3.81). When $\tau_i << \tau$, then $\tau_{tot} \approx \tau_i$, making the two exponentials in (3.80) distinguishable due to dissimilar decay rates. The scaling by S^2 will have an important impact in this case. When τ is of the same order of magnitude as τ_i however, τ_{tot} and τ will not differ so much, giving both exponentials in (3.80) similar decay rates and making the impact of the precise value of S^2 on the total correlation function quite limited. This makes it unfeasible to estimate S^2 from relaxation data in picosecond to nanosecond dynamics studies of molecular systems with large rotational diffusion

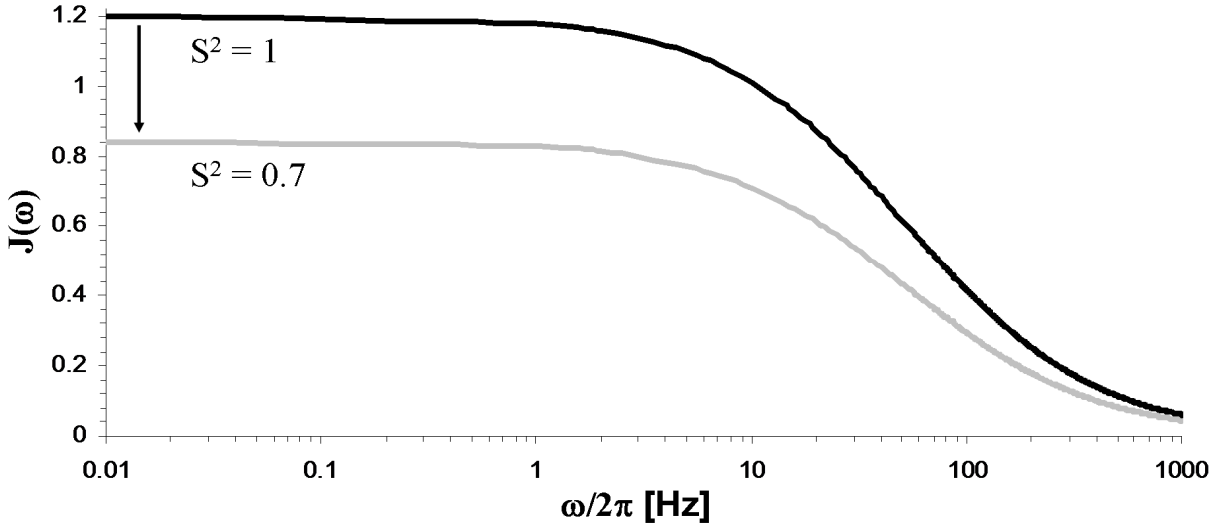

Figure 3.10: Spectral density functions for an isotropically tumbling molecule with $\tau = 3$ ns and no internal motion ($S^2 = 1$) and the same molecule with internal motion ($S^2 = 0.7$ and $\tau_i = 20$ ps). Note that especially the density at low frequencies are reduced strongly with increasing S^2.

coefficients. It should be noted that in fact any internal motion with a correlation time much longer than the global rotational motion has no impact on the spectral density function at all, as the correlation function will have completely decayed to zero before such internal motions have a significant effect.

3.5 Exchange

As mentioned before (section 3.4.3), motions with a correlation time constant larger than that of the global molecular rotation do not contribute to the spectral density function. However, they can have a very strong effect on the resonance line width and on the relaxation measurements. These motions can be considered to make the spins 'jump' between different conformational environments, with in each case a different local magnetic field and thus chemical shift. Such jumping between environments or sites is called an exchange process[11, 12]. If this process is sufficiently fast so that it takes place during the NMR measurement (*i.e.* during the FID), it will have an effect on the observed line width and resonance frequency.

To understand the implications qualitatively, two limit cases will be discussed (Figure 3.11a). Consider a thermodynamic equilibrium situation between two conformations A and B of a molecule and a nuclear spin that is part of this molecule with respective frequencies ω_A and ω_B for each conformation. First assume that the exchange rate is considerably smaller than the difference in frequency between the two states, a situation referenced to as slow exchange. Spins that jump from site B to A will cause an apparent faster decay of the transverse magnetisation of the B site. The magnetisation of A will not be increased by these jumps however, as the spins that

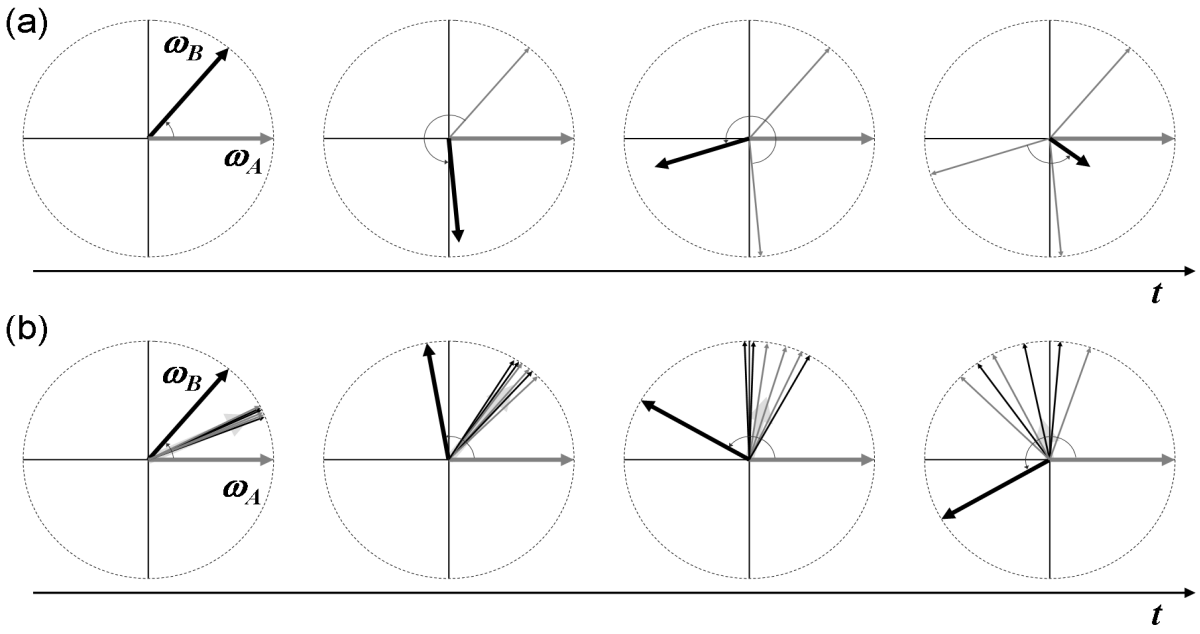

Figure 3.11: Illustration of slow and fast exchange between two sites with frequencies ω_A and ω_B. Equal populations of A and B are assumed. A frame rotating at ω_A is assumed so that A remains stationary and B moves at $\Delta\omega$. (a) At slow exchange, spins jump randomly from site B to site A at rates slower than their precession frequency difference, decreasing the magnetisation of B. The spins that jumped over to A are now static, but do not form a coherent set of spins and thus do not add constructively to the magnetisation of A. (b) At fast exchange, the spins jump from site B to site A and vice versa at rates faster than their precession frequency difference. Each spin will have precessed about the average of ω_A and ω_B, but with a certain variation due to the stochastic nature of the exchange process. This variation increases with time leading to a faster decay of the single observed resonance.

jumped over have done this stochastically at different times and thus at different phase angles and therefore do not add up coherently. The resulting spectrum consists of two resonances at frequencies ω_A and ω_B that are slightly broader than what would be expected from their intrinsic transverse relaxation rate constants. The degree of extra line broadening is only determined by the exchange rate.

In the other limit case of fast exchange (Figure 3.11b), the exchange rate is considerably larger than the difference in resonance frequencies. As the spins jump very fast between each site, the average angle over which they will have precessed after a certain time will be about the average of what the individual magnetisations would have precessed separately. The result is that only one resonance will be present in the spectrum at the averaged frequency. The line width of the resonance will not only be determined by the average of the transverse relaxation rate constants, but by the exchange process as well. Because this process is stochastic, each individual spin will have spent a slightly different time at each site, resulting in a distribution of precession angles which becomes broader as time progresses. Therefore the magnetisation will lose its coherence faster, resulting in a broader line width. As the exchange process becomes faster compared to the frequency difference, this extra line broadening will disappear.

A more quantitative view is achieved when considering the impact of the exchange kinetics on the Bloch equations[12]. It is important to note that the derivation below is only valid for resonances without scalar coupling or with similar scalar coupling in both conformations. If this is not the case, the influence of the exchange on the apparent multiplet structure would need to be considered as well[11]. Assume the equilibrium:

$$A \underset{s_{-1}}{\overset{s_1}{\rightleftharpoons}} B \tag{3.83}$$

The forward and backward rates are given by:

$$\begin{aligned} s_1 &= k_1[A] \\ s_{-1} &= k_{-1}[B] \end{aligned} \tag{3.84}$$

Since chemical equilibrium is assumed, the reaction rates need to be equal. This results in the following, with $C_{tot} = [A] + [B]$ the total concentration:

$$k_1[A] = k_{-1}[B] \Leftrightarrow k_1 \frac{[A]}{C_{tot}} = k_{-1} \frac{[B]}{C_{tot}} \Leftrightarrow k_1 \alpha_A = k_{-1} \alpha_B \tag{3.85}$$

with α_A and α_B the fractions of A and B ($\alpha_A + \alpha_B = 1$). When defining the exchange rate constant k_{ex} as:

$$k_{ex} = k_1 + k_{-1} \tag{3.86}$$

then it is easy to show, using (3.85):

$$k_{ex}\alpha_A = k_1\alpha_A + k_{-1}\alpha_A = k_{-1}\alpha_B + k_{-1}\alpha_A = k_{-1} \tag{3.87}$$

$$k_{ex}\alpha_B = k_1\alpha_B + k_{-1}\alpha_B = k_1\alpha_B + k_1\alpha_A = k_1 \tag{3.88}$$

The Bloch equations that describe the evolution of the transverse magnetisation over time can be extended to include the exchange of magnetisation between A and B. This results in the so-called Bloch-McConnel equations[12] (with $\mathrm{M}^{\pm} = \mathrm{M}^{+} + i\,\mathrm{M}^{-}$):

$$\begin{aligned}\frac{d\,\mathrm{M}_A^+(t)}{dt} &= i\omega_A\,\mathrm{M}_A^+(t) - R_2^A\,\mathrm{M}_A^+(t) - k_1\,\mathrm{M}_A^+(t) + k_{-1}\,\mathrm{M}_B^+(t)\\ &= i\omega_A\,\mathrm{M}_A^+(t) - R_2^A\,\mathrm{M}_A^+(t) - \alpha_B k_{ex}\,\mathrm{M}_A^+(t) + \alpha_A k_{ex}\,\mathrm{M}_B^+(t)\\ \frac{d\,\mathrm{M}_B^+(t)}{dt} &= i\omega_B\,\mathrm{M}_B^+(t) - R_2^B\,\mathrm{M}_B^+(t) - k_{-1}\,\mathrm{M}_B^+(t) + k_1\,\mathrm{M}_A^+(t)\\ &= i\omega_B\,\mathrm{M}_B^+(t) - R_2^B\,\mathrm{M}_B^+(t) - \alpha_A k_{ex}\,\mathrm{M}_B^+(t) + \alpha_B k_{ex}\,\mathrm{M}_A^+(t)\end{aligned} \tag{3.89}$$

The solution of these coupled differential equations is:

$$\begin{aligned}\mathrm{M}_A^+(t) &= c_{AA}(t)\,\mathrm{M}_A^+(0) + c_{AB}(t)\,\mathrm{M}_B^+(0)\\ \mathrm{M}_B^+(t) &= c_{BA}(t)\,\mathrm{M}_A^+(0) + c_{BB}(t)\,\mathrm{M}_B^+(0)\end{aligned} \tag{3.90}$$

in which:

$$\begin{aligned}c_{AA}(t) &= \frac{1}{2}\left[\left(1-\frac{\kappa}{\lambda_+-\lambda_-}\right)e^{-\lambda_- t} + \left(1+\frac{\kappa}{\lambda_+-\lambda_-}\right)e^{-\lambda_+ t}\right]\\ c_{BB}(t) &= \frac{1}{2}\left[\left(1+\frac{\kappa}{\lambda_+-\lambda_-}\right)e^{-\lambda_- t} + \left(1-\frac{\kappa}{\lambda_+-\lambda_-}\right)e^{-\lambda_+ t}\right]\\ c_{AB}(t) &= \frac{k_{ex}\alpha_A}{\lambda_+-\lambda_-}\left[e^{-\lambda_- t} - e^{-\lambda_+ t}\right]\\ c_{BA}(t) &= \frac{k_{ex}\alpha_B}{\lambda_+-\lambda_-}\left[e^{-\lambda_- t} - e^{-\lambda_+ t}\right]\\ \lambda_\pm &= \frac{1}{2}\left[-i(\omega_A+\omega_B) + R_2^A + R_2^B + k_{ex} \pm \sqrt{\kappa^2 + 4\alpha_A\alpha_B k_{ex}^2}\right]\\ \kappa &= -i\Delta\omega + R_2^A - R_2^B + k_{ex}(\alpha_B-\alpha_A)\\ \Delta\omega &= \omega_A - \omega_B\end{aligned} \tag{3.91}$$

The resulting spectrum, given by the Fourier transform of $\mathrm{M}_A^+(t) + \mathrm{M}_B^+(t)$, is shown in Figure 3.12a for different values of k_{ex}. When no exchange is present, $k_{ex} = 0$ and the respective resonance line widths are only determined by R_2^A and R_2^B. In the case of slow exchange ($k_{ex} < \Delta\omega$), the line width of both resonances increases as was predicted from the qualitative picture. The effective relaxation constants are approximated by:

$$\begin{aligned}R_{2tot}^A &= R_2^A + \alpha_B k_{ex}\\ R_{2tot}^B &= R_2^B + \alpha_A k_{ex}\end{aligned} \tag{3.92}$$

The additional line width contribution is thus proportional to the fraction of the other site. This is illustrated in Figure 3.12b, where in the situation of $\alpha_A > \alpha_B$ the line width

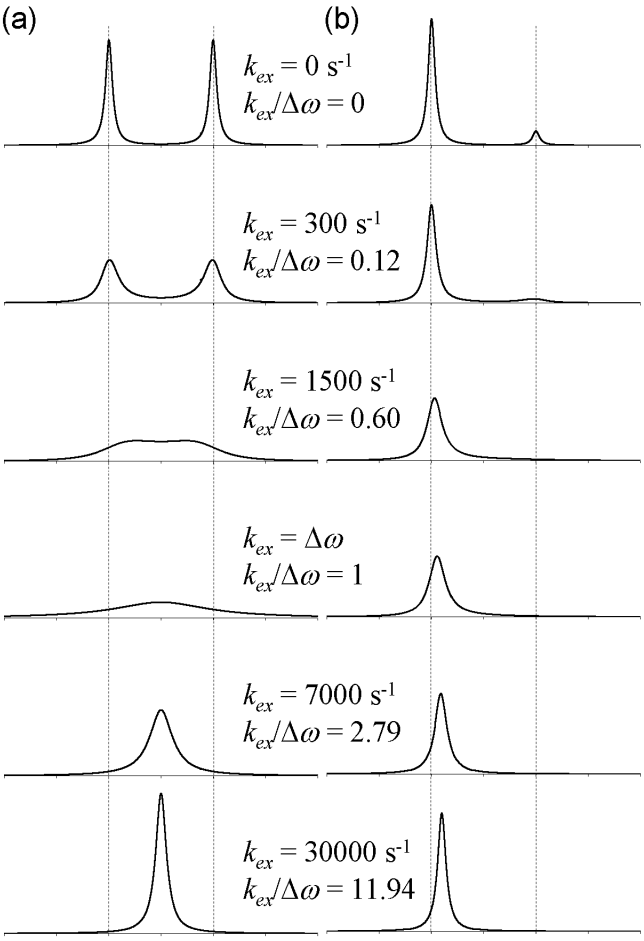

Figure 3.12: Two site exchange for different values of k_{ex}, ranging from slow to fast exchange. The frequency difference between both sites is 400 Hz ($\Delta\omega$ = 2513 rad·s^{-1}). (a) $\alpha_A = 0.5$; (b) $\alpha_A = 0.9$.

of the B resonance increases faster than that of the A resonance as k_{ex} increases. As the exchange rate increases, not only will the line widths increase, but the frequency difference between the maxima of the two resonances will apparently decrease. In the intermediate exchange situation, where $k_{ex} \approx \Delta\omega$, the line width approaches its maximum value and the resonances become practically indistinguishable. The point where $k_{ex} = \Delta\omega/\sqrt{2}$ is identified as the coalescence point in the case of $\alpha_A = \alpha_B$. This is where the second derivative of the spectrum at the mean frequency of the two peaks vanishes[6]. Further increasing the exchange rate brings the system under fast exchange conditions ($k_{ex} > \Delta\omega$) which will decrease line width of the now single resonance and, in the case of unequal equilibrium populations, further move the single resonance towards an average frequency $\omega_{av} = \alpha_A\omega_A + \alpha_B\omega_B$. Eventually, the resonance will reach this frequency and the line width will be determined by both the average transverse relaxation rate $R_{2av} = \alpha_A R_2^A + \alpha_B R_2^B$ and an exchange contribution:

$$R_{2tot} = R_{2av} + \frac{\alpha_A\alpha_B\Delta\omega^2}{k_{ex}} \tag{3.93}$$

In contrast to the slow exchange situation, the exchange contribution under fast exchange depends on the squared frequency difference $\Delta\omega^2$. Since the frequency difference is proportional to the static magnetic field B_0, measuring the exchange contribution as a function of B_0 is a method for identifying the exchange regime[13]. The dependence on B_0 of the exchange contribution will indeed vary from independence under slow exchange conditions to a quadratic proportionality at fast exchange, while intermediate exchange conditions provide a dependence lying somewhere in between. The study of the dependence of the line width on the magnetic field is thus a method to unambiguously establish the exchange regime.

This method is important, as it is possible that a slow exchange situation with $\alpha_A >> \alpha_B$ can cause the resonance of B to be undetectable due to its low signal intensity and the much stronger exchange broadening when compared to A (see equation (3.92)). The observation of only the A resonance would then create the false impression of a fast exchange regime.

Exchange contributions to the transverse magnetisation can thus be used to study molecular motions that are of the same order of magnitude as the difference in frequencies of the different conformations that are sampled. Note that the impact of chemical exchange between two species is treated similarly.

3.6 The relation between relaxation and molecular size, shape and dynamics

3.6.1 Contributions of multiple relaxation mechanisms

Within this dissertation, the relaxation rate constants of peptide backbone $^{13}C^{\alpha}$ and ^{15}N nuclei are of importance. To link the experimental values to theory, the assumption needs to be made that the dipolar relaxation mechanism is dominated by the dipolar interaction with the directly attached proton nucleus. To check the validity of this approximation, the relaxation rate constants of the $^{13}C^{\alpha}$—$^{1}H^{\alpha}$ interaction and the interaction between $^{13}C^{\alpha}$ and the proton attached to the neighbouring amide proton ($^{1}H^{N}$) are compared. The average distance between the first pair of nuclei is assumed to be about 1.1 Å and about 2.1 Å for the latter. Assuming isotropically tumbling molecules, it follows from equations (3.58), (3.61) and (3.49) that (with R_x either R_1 or R_2):

$$\frac{R_x^{DD}\left(^{13}C^{\alpha}\text{-}^{1}H^{N}\right)}{R_x^{DD}\left(^{13}C^{\alpha}\text{-}^{1}H^{\alpha}\right)} = \frac{K_{DD}^2\left(^{13}C^{\alpha}\text{-}^{1}H^{N}\right)}{K_{DD}^2\left(^{13}C^{\alpha}\text{-}^{1}H^{\alpha}\right)} = \frac{r^6\left(^{13}C^{\alpha}\text{-}^{1}H^{\alpha}\right)}{r^6\left(^{13}C^{\alpha}\text{-}^{1}H^{N}\right)} = \left(\frac{1.1}{2.1}\right)^6 = 0.02 \qquad (3.94)$$

The contribution of the dipolar interaction of the $^{13}C^{\alpha}$ nucleus with the H^{N} proton is thus only 2% compared to the dipolar interaction of the H^{α} proton; the inverse sixth power dependence on the internuclear distance is the main reason for this. It is therefore a fair approximation to only consider dipolar relaxation caused by the directly attached proton nucleus. Since the relaxation studies in this dissertation are performed at natural abundance, the impact of dipolar relaxation between the $^{13}C^{\alpha}$ nucleus with the amide ^{15}N or the $^{13}C^{\beta}$ nuclei are negligible and are of no concern in contrast to isotopically enriched proteins.

For both the $^{13}C^{\alpha}$ and amide ^{15}N nuclei, dipolar relaxation is the dominant relaxation mechanism. In addition for $^{13}C^{\alpha}$, CSA relaxation is not that efficient due to the relatively low chemical shift anisotropy ($\Delta\sigma_C$ = *ca.* 25 ppm). CSA relaxation is somewhat more pronounced for the ^{15}N nucleus ($\Delta\sigma_N$ = *ca.* -160 ppm) at higher magnetic fields (since $K_{CSA} \propto B_0$), but even then a comparative calculation at a field strength of 16.4 T shows that it only provides about 1% contribution of the dipolar ^{1}H-^{15}N relaxation. Despite its limited impact, it will always implicitly be taken into account in what follows unless otherwise mentioned.

In what follows, the influence of the global rotational diffusion (molecular size and anisotropy) on the different relaxation parameters will be discussed.

3.6.2 Impact of molecular size

Assuming isotropic rotational motion, how are the relaxation rate constants influenced by the rotational correlation time (and thus the molecular size and solvent viscosity)? When considering a ^{13}C nucleus, the expression for the R_1 relaxation rate constant as a function of the correlation time τ is given by combining equations (3.58) and (3.68):

$$R_1 = \frac{K_{DD}^2}{10}\left[\frac{\tau}{1+(\omega_H-\omega_C)^2\tau^2}+\frac{3\tau}{1+\omega_C^2\tau^2}+\frac{6\tau}{1+(\omega_H+\omega_C)^2\tau^2}\right] + \frac{2K_{CSA,C}^2}{5}\left[\frac{\tau}{1+\omega_C^2\tau^2}\right] \tag{3.95}$$

For small molecules and thus low correlation times, the condition $(\omega_H+\omega_C)^2\tau^2 << 1$ can be assumed, which is known as the extreme narrowing limit. In this case, R_1 is linearly proportional to τ and magnetic field independent when the contribution of CSA relaxation is limited:

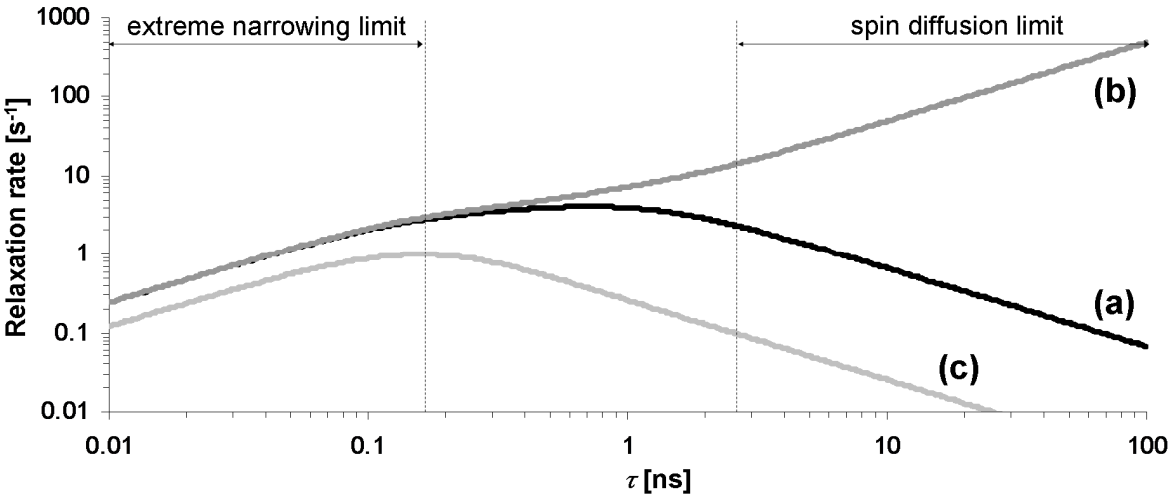

Figure 3.13: Evolution of the $^{1,3}C^{\alpha}$ relaxation rate constants (a) R_1, (b) R_2 and (c) σ_{CH} with the correlation time constant, assuming a magnetic field of 16.4 T. Both dipolar relaxation with the directly attached ^{1}H spin and CSA relaxation are taken into account.

$$R_1 \approx \left(K_{DD}^2 + \frac{2}{5} K_{CSA,C}^2 \right) \tau \tag{3.96}$$

For large molecules, the condition $\omega_C^2 \tau^2 >> 1$ is valid, which is known as the spin diffusion limit. Here, R_1 becomes inversely proportional to the correlation time and to the square of the magnetic field strength (recalling that $\omega_X = -\gamma_X B_0$):

$$R_1 \approx \frac{1}{\tau B_0^2} \left\{ \frac{K_{DD}^2}{10} \left[\frac{1}{\left(\gamma_H - \gamma_C\right)^2} + \frac{3}{\gamma_C^2} + \frac{6}{\left(\gamma_H + \gamma_C\right)^2} \right] + \frac{2K_{CSA,C}^2}{5\gamma_C^2} \right\} \tag{3.97}$$

It is therefore clear that R_1 first increases linearly as a function of τ, eventually reaches a maximum value when $\omega_C^2 \tau^2$ is of the order of 1 and eventually decreases by an inverse relation with τ (Figure 3.13). Since ω_C and ω_H are proportional to B_0, the position of this maximum shifts with B_0. The same exercise can be performed for R_2 by combining equations (3.61) and (3.68):

$$\begin{aligned} R_2 = {} & \frac{K_{DD}^2}{20} \left[4\tau + \frac{\tau}{1+\left(\omega_H - \omega_C\right)^2 \tau^2} + \frac{3\tau}{1+\omega_C^2 \tau^2} + \frac{6\tau}{1+\omega_H^2 \tau^2} + \frac{6\tau}{1+\left(\omega_H + \omega_C\right)^2 \tau^2} \right] \\ & + \frac{K_{CSA,C}^2}{15} \left[4\tau + \frac{3\tau}{1+\omega_C^2 \tau^2} \right] \end{aligned} \tag{3.98}$$

At the extreme narrowing limit where the condition $(\omega_H + \omega_C)^2 \tau^2 << 1$ is satisfied:

$$R_2 \approx \left[K_{DD}^2 + \frac{7K_{CSA,C}^2}{15} \right] \tau \tag{3.99}$$

Besides a small difference in the CSA contribution, R_2 is practically equal to R_1 (equation (3.96)) in this case. At the spin diffusion limit where $\omega_C^2\tau^2 >> 1$ and thus also $\tau >> 1/\omega_C^2\tau$.

$$\begin{aligned} R_2 &\approx \frac{K_{DD}^2}{20}\left[4\tau + \frac{1}{(\omega_H-\omega_C)^2\tau} + \frac{3}{\omega_C^2\tau} + \frac{6}{\omega_H^2\tau} + \frac{6}{(\omega_H+\omega_C)^2\tau}\right] + \frac{K_{CSA,C}^2}{15}\left[4\tau + \frac{3}{\omega_C^2\tau}\right] \\ &\approx \left[\frac{K_{DD}^2}{5} + \frac{4K_{CSA,C}^2}{15}\right]\tau \end{aligned} \quad (3.100)$$

In contrast to R_1, R_2 still increases linearly with τ for large molecules – with a reduced proportionality constant though – and is magnetic field independent when assuming that the CSA relaxation contribution is small (Figure 3.13). Finally, the longitudinal cross-relaxation between the ^{13}C and ^{1}H nuclei is considered by combining (3.59) and (3.68):

$$\sigma_{CH} = \frac{K_{DD}^2}{10}\left(-\frac{\tau}{1+(\omega_H-\omega_C)^2\tau^2} + \frac{6\tau}{1+(\omega_H+\omega_C)^2\tau^2}\right) \quad (3.101)$$

At the extreme narrowing limit:

$$\sigma_{CH} = \frac{K_{DD}^2}{2}\tau \quad (3.102)$$

At the spin diffusion limit:

$$\sigma_{CH} = \frac{1}{\tau B_0^2}\frac{K_{DD}^2}{10}\left(-\frac{1}{(\gamma_H-\gamma_C)^2} + \frac{6}{(\gamma_H+\gamma_C)^2}\right) \quad (3.103)$$

The behaviour of the cross-relaxation is thus quite similar as for R_1 (Figure 3.13). Because of this, the steady state nOe effect on ^{13}C by irradiating ^{1}H (section 3.2.4) becomes independent of the correlation time constant at both extreme narrowing and spin diffusion limits and independent of the magnetic field strength when neglecting the effects of CSA relaxation:

$$\begin{aligned} \mathrm{nOe}\left[(\omega_H+\omega_C)^2\tau^2 << 1\right] &\approx \frac{\gamma_H}{2\gamma_C} \\ \mathrm{nOe}\left[\omega_C^2\tau^2 >> 1\right] &\approx \frac{5\gamma_C^3\gamma_H - 14\gamma_C^2\gamma_H^2 + 5\gamma_C\gamma_H^3}{10\gamma_C^4 + 3\gamma_H^4 - 10\gamma_C^3\gamma_H + \gamma_C^2\gamma_H^2} \end{aligned} \quad (3.104)$$

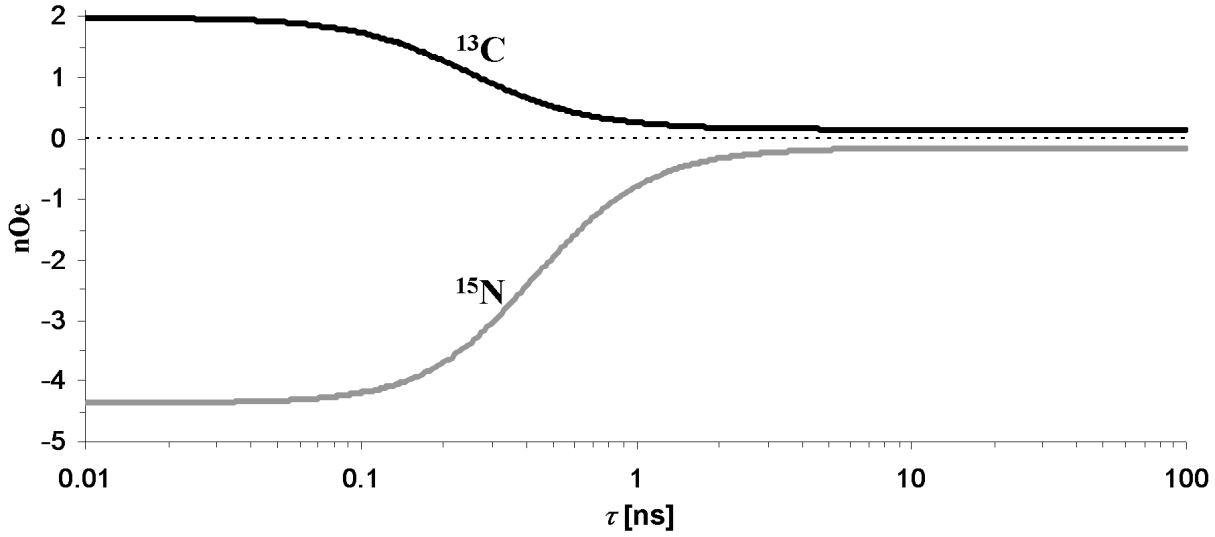

Figure 3.14: ^{1}H-^{13}C and ^{1}H-^{15}N nOe's as a function of the correlation time constant at 16.4 T. Both dipolar and CSA relaxation mechanisms are taken into account.

The evolution of the steady state nOe as a function of the correlation time is illustrated in Figure 3.14 for both the ^{1}H-^{13}C and the ^{1}H-^{15}N cases. Irradiation of the ^{1}H spins will provide a nearly 200% increase in the population difference of the ^{13}C spins at the extreme narrowing limit, while at the spin diffusion limit the increase is limited to about 15%. Due to the negative sign of the gyromagnetic ratio of the ^{15}N spin, the nOe is negative at the extreme narrowing limit and its evolution with the correlation time is opposite compared to that of ^{13}C. At the extreme narrowing limit and taking CSA at 16.4 T into account (Figure 3.14), the nOe is about –4.3, implying that irradiation of the ^{1}H spin will cause the population difference of the ^{15}N spin to be inversed and its magnitude to be 3.3 (=|1-4.3|) times larger than under the Boltzmann equilibrium conditions. At the spin diffusion limit, the ^{1}H-^{15}N nOe is about –0.15, meaning that the ^{15}N population difference won't be inversed anymore but will in fact be reduced to about 0.85 times its original value.

3.6.3 Impact of molecular anisotropy and orientation of the bond vector

As discussed in section 3.4.2, if the global rotational motion of the molecule is anisotropic, the spectral density becomes dependent on the orientation of the I–S bond vector in the molecule. This has the consequence of making all relaxation parameters orientation dependent. This is illustrated in Figure 3.15 for several ellipsoids with constant volume but with axial symmetric anisotropy, as expressed by the ratio of the long and short axes a/b. The increase in anisotropy decreases the absolute values of the rotational diffusion coefficients (and thus increases the values of the correlation time constants) compared to the isotropic case. Therefore all R_1, R_2 and nOe values will be pushed towards values typical for a larger object. In addition, the relaxation values now have a bell-shaped variation as a function of the angle of

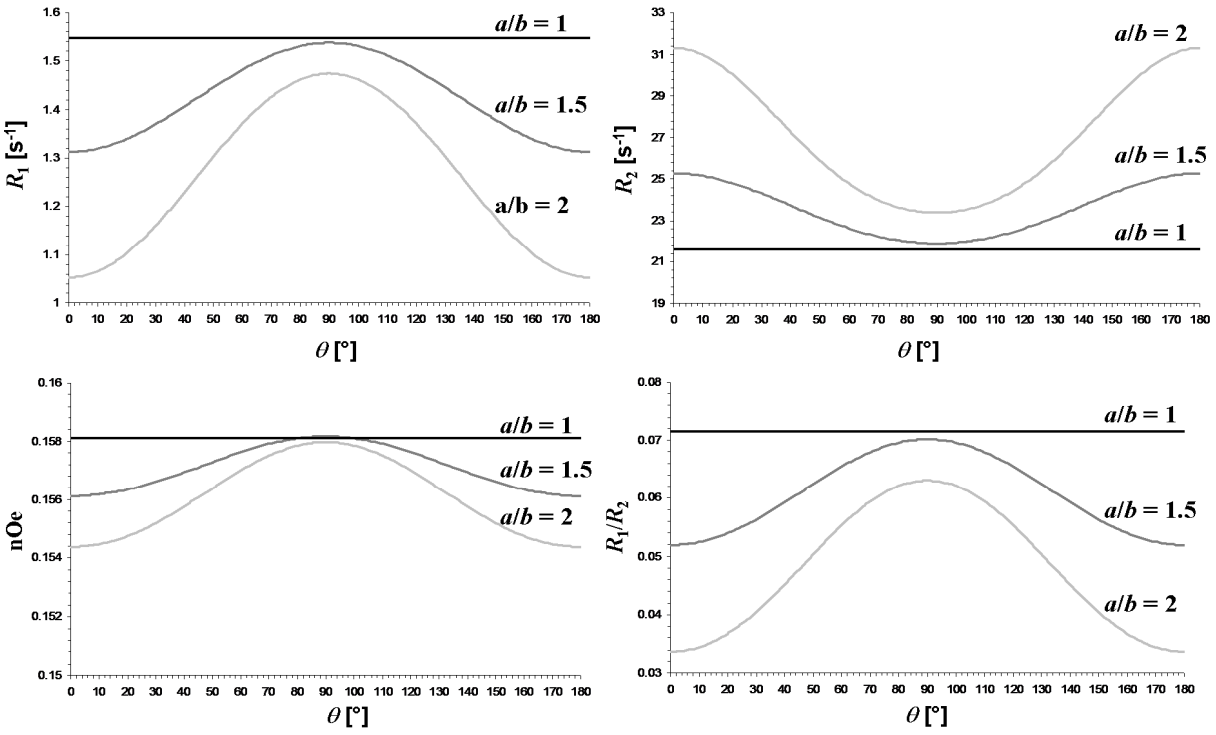

Figure 3.15: Illustration of the impact of axial symmetric anisotropy on the relaxation parameters. A prolate ellipsoid object was assumed with a volume of 17 nm^3, with ratios between the long axis a and short axis b of 1 (isotropic), 1.5 and 2. The rotational diffusion coefficients were calculated using the expressions derived by Perrin (equations (1.44) and (1.45)). The correlation times calculated were: τ_A = τ_B = τ_C = 4.1 ns for a/b = 1; τ_A = 4.9 ns, τ_B = 4.6 ns and τ_C = 3.9 ns for a/b = 1.5; τ_A = 6.2 ns, τ_B = 5.4 ns and τ_C = 3.9 ns for a/b = 2. Note the very limited variation for the nOe value.

the bond vector with the main principle axis of the molecule. In the presence of anisotropy, R_1 can be written as:

$$R_1(\theta) = c_A(\theta) R_{1A} + c_B(\theta) R_{1B} + c_C(\theta) R_{1C} \tag{3.105}$$

with the coefficients c_A, c_B and c_C defined by (3.78) (see also Figure 3.8), and with R_{1A}, R_{1B} and R_{1C} the R_1 relaxation rate constants of an isotropic molecule with correlation time constants of τ_A, τ_B and τ_C respectively (related to $D_r^{\parallel}$ and $D_r^{\perp}$, see equations (3.76)). The effective R_1 can thus be seen as the average of these three R_1 values weighted by the orientation dependent coefficients. The result of the anisotropy is a bell shaped curve with a maximum or a minimum at 90° depending on whether the anisotropy is prolate or oblate respectively. Similar angular dependencies are found for R_2 at low or moderate degrees of anisotropy (for high degrees, see below) and the nOe (Figure 3.15), although for the latter a simple linear combination as in (3.105) between three nOe values cannot be written. For large molecular systems where the nOe as a function of correlation time has reached a plateau, the anisotropy is not visible since all orientations are located within this plateau region and thus have more or less the same value. Therefore the nOe is not useful for detecting anisotropy in systems at the spin diffusion limit. The R_1/R_2 ratio also possesses the same bell

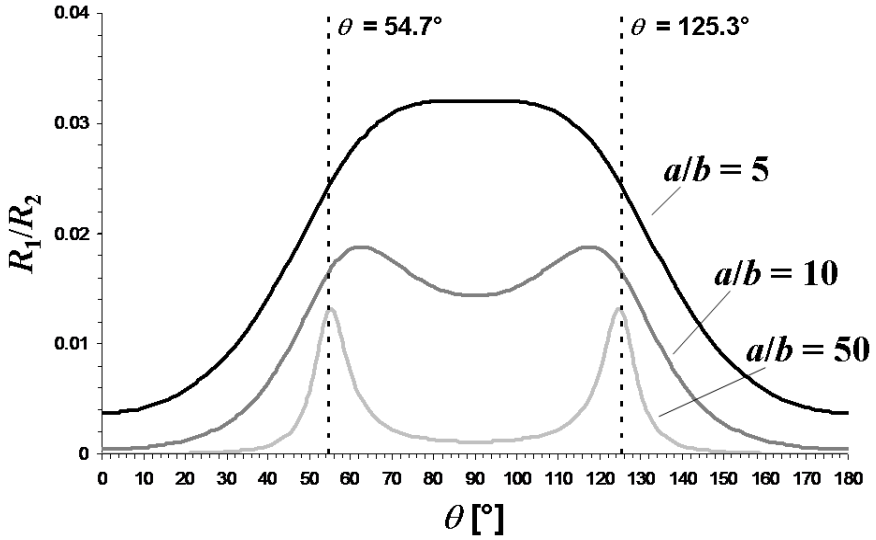

Figure 3.16: Illustration of the impact of axial symmetric anisotropy on the R_1/R_2 ratio for high degrees of anisotropy. A prolate ellipsoid object was assumed with a volume of 17 nm^3, with ratios between the long axis a and short axis b of 5, 10 and 50. The rotational diffusion coefficients were calculated using the expressions derived by Perrin (equations (1.44) and (1.45)). The correlation times calculated were: τ_A = 19.2 ns, τ_B = 9.94 ns and τ_C = 4.07 ns for a/b = 5; τ_A = 55.2 ns, τ_B = 13.4 ns and τ_C = 4.11 ns for a/b = 10; τ_A = 839 ns, τ_B = 16.3 ns and τ_C = 4.13 ns for a/b = 50. The angles where τ_A does not contribute to R_1/R_2 are indicated.

shaped curve at low degrees of anisotropy. This ratio is the most sensitive to the anisotropy since it constructively adds up the angular dependencies of both R_1 and R_2.

At high degrees of anisotropy (a/b >> 1), the angular dependence of R_2 and R_1/R_2 slowly changes to a profile with two extremes, positioned at both magic angle values, as illustrated for R_1/R_2 in Figure 3.16. This is due to the high difference between $D_r^{\perp}$ and $D_r^{\parallel}$ ($D_r^{\parallel}/D_r^{\perp}$ >> 1) that exists under these conditions, resulting in a very large τ_A (=1/6 $D_r^{\perp}$) value as compared to τ_B (≈1/$D_r^{\parallel}$) and τ_C (≈1/4$D_r^{\parallel}$). Since R_2 at the spin diffusion limit depends linearly on the three correlation time constants, τ_A will dominate the relaxation rate constant. At the magic angle (*ca.* 54.7°), the weighting coefficient c_A becomes zero (see equation (3.78) and Figure 3.8), so that here the much lower τ_B and τ_C values determine the R_2 value.

3.6.4 Impact of fast internal motion and estimation of the global correlation time constant

By combining the Lipari-Szabo model free approach for implementing internal motion into the spectral density function for the isotropic case (3.82) with the expressions of R_1 (3.58) and R_2 (3.61), it can be seen that these can be written as a weighted average of the relaxation rate constant in the absence of internal motion and the relaxation rate constant of an isotropic molecule with a correlation time constant of τ_{tot}:

$$\begin{aligned} R_1 &= S^2 R_1[\tau] + (1-S^2) R_1[\tau_{tot}] \\ R_2 &= S^2 R_2[\tau] + (1-S^2) R_2[\tau_{tot}] \end{aligned} \tag{3.106}$$

When only a limited degree of internal motional freedom is present (S^2 is not too far from 1), the global correlation time constant τ is sufficiently large (on the order of nanoseconds) and the internal correlation time constant τ_i (and thus also τ_{tot}) is sufficiently small, so that $(1\text{-}S^2)R_1[\tau_{tot}] << S^2 R_1[\tau]$[14]:

$$\begin{aligned} R_1 &\approx S^2 R_1[\tau] \\ R_2 &\approx S^2 R_2[\tau] \end{aligned} \tag{3.107}$$

$$\Rightarrow \frac{R_1}{R_2} \approx \frac{R_1[\tau]}{R_2[\tau]} \tag{3.108}$$

This means that the R_1/R_2 ratio becomes approximately independent of the internal motion parameters and can be used to obtain an estimation of the global rotational correlation time constant with minimal interference from internal motion. This is illustrated in Figure 3.17, where it can be seen that this method works very well in the case of ^{15}N relaxation. For ^{13}C relaxation, this is much less the case, although this ratio is most often the best choice for estimating the global correlation time constant.

The nOe is a good parameter preliminary assess the presence of a contribution from internal motion. As discussed above (section 3.6.2), at the spin diffusion limit the nOe as a function of correlation time reaches a plateau value upon correlation time constant increase. Therefore, when it is known that the molecule under study is of sufficient size to surely be in the spin diffusion limit, and since the correlation time of the internal motion is usually near to the extreme narrowing limit, any deviating from the expected nOe plateau value indicates the presence of internal motion. The nOe value is proportional to the ratio between the cross-relaxation and R_1:

$$\text{nOe} = \frac{\gamma_I}{\gamma_S} \frac{S^2 \sigma_{IS}[\tau] + (1-S^2)\sigma_{IS}[\tau_{tot}]}{S^2 R_1[\tau] + (1-S^2) R_1[\tau_{tot}]} \tag{3.109}$$

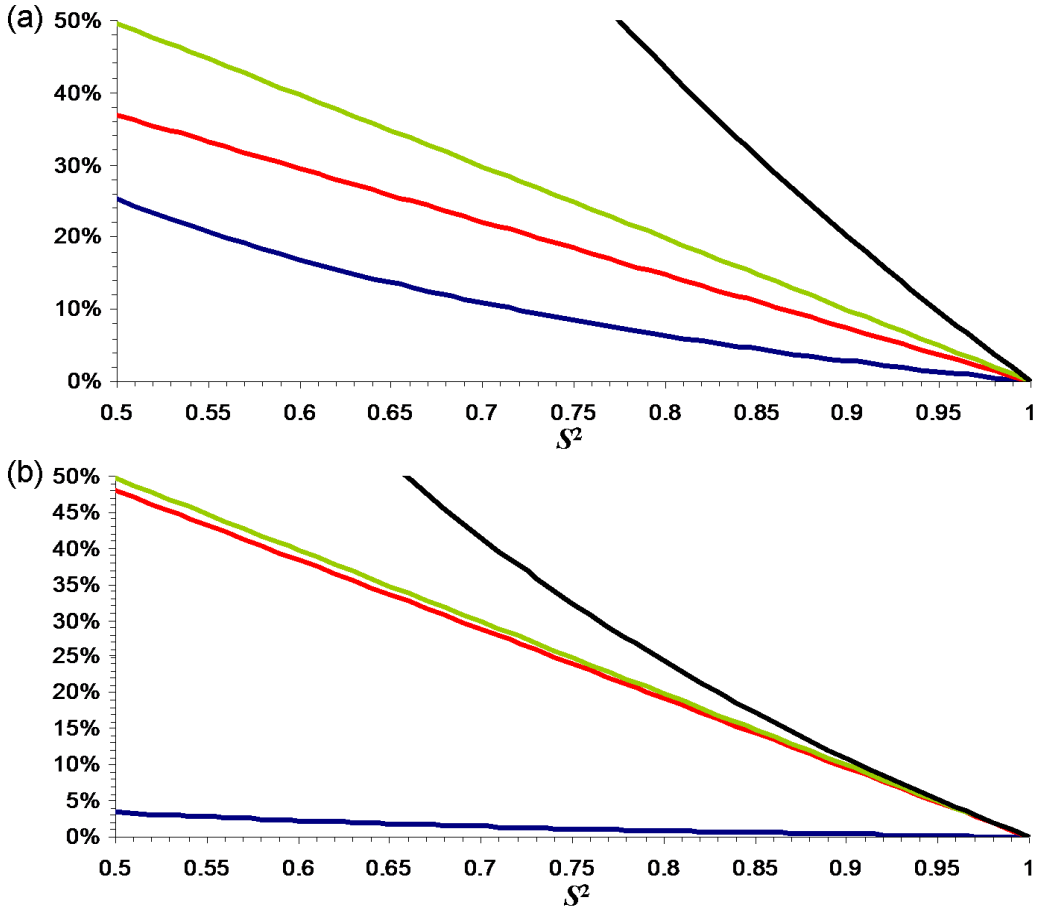

Figure 3.17: Effects of internal motion on the relaxation parameters. The procentual deviation from the $S^2 = 1$ situation is shown for both (a) ^{13}C and (b) ^{15}N nuclei. Isotropic rotational diffusion is assumed with $\tau = 7$ ns and $\tau_i = 10$ ps. The relaxation parameters plotted are R_1 (red), R_2 (green), the nOe (black) and R_1/R_2 (blue).

The same argument as with R_1/R_2 can be invoked to show that the ratio between the cross-relaxation and R_1 is quite independent of S^2 under the right conditions. However, as opposed to R_1/R_2, any deviation will be amplified by the factor γ_I/γ_S, (*ca.* 4 for ^{1}H-^{13}C and *ca.* –10 for ^{1}H-^{15}N). As is illustrated in Figure 3.17, the end effect will be that the nOe is strongly influenced by internal motion for both ^{13}C and ^{15}N. This property of the nOe is useful since it can function as an indicator for whether the conditions to use R_1/R_2 to determine τ are applicable. The nOe thus allows selecting the nuclear probes that are least subjected to internal motion. Note that the plots shown in Figure 3.17 represent a specific case for only one combination of τ and τ_i. Other combinations (with larger τ_i for instance) may provide situations where R_1/R_2 is no longer the least affected by internal motion, especially for ^{13}C. The general trend that the deviation of the nOe is the least affected remains however, making such cases easily identifiable.

When the global correlation time is finally estimated, the values for S^2 and τ_i for each individual ^{13}C or ^{15}N probe can be fitted from the experimental R_1, R_2 and nOe data (measured at one or more magnetic field strengths), providing information on the picosecond timescale dynamics for that particular segment of the molecule.

3.7 Experiments to measure heteronuclear relaxation

3.7.1 Introduction

Direct excitation and detection of the ^{13}C and ^{15}N heteronuclei during a relaxation experiment is in most cases not feasible due to their inherent low sensitivity and low natural abundance. Therefore, the heteronuclear relaxation rates are typically measured by use of a modified 2D HSQC experiment. The advantage is that the sensitivity is inherently boosted by a factor of $(\gamma_H/\gamma_X)^{5/2}$, which is about 32 for ^{13}C and 305 for ^{15}N, not taking into account the losses due to relaxation during the INEPT transfer delays. A schematic overview of how this experiment works is given in Figure 3.18. The ^{1}H spins are first excited, after which the coherence is transferred to the heteronucleus X through the $^{1}J_{HX}$ scalar coupling by use of an INEPT sequence. While the single quantum X-coherence evolves, both the indirect time domain encoding and the appropriate relaxation encoding occur. Afterwards, by use of a second INEPT sequence the coherence is transferred back through the $^{1}J_{HX}$ scalar coupling to the ^{1}H spins and the direct time domain (the FID) can be acquired. This second INEPT sequence can be replaced by a sensitivity improved version[15, 16], which increases the sensitivity by another factor of $2^{1/2}$.

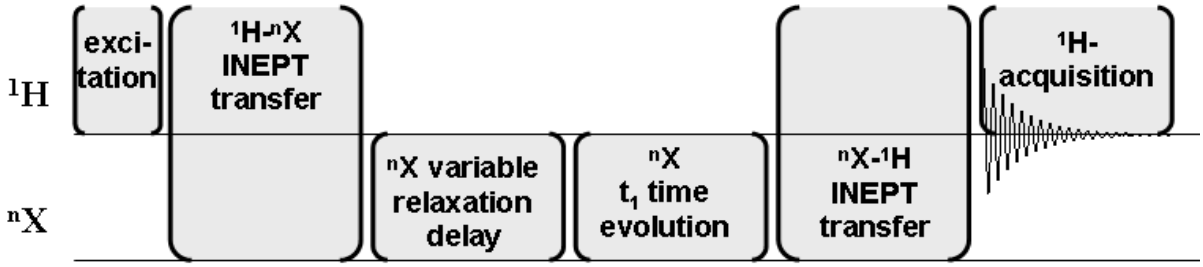

Figure 3.18: Schematic overview of the typical heteronuclear relaxation experiment.

3.7.2 Measurement of R_1

The adapted HSQC pulse sequence for R_1 measurements used in this work is shown in Figure 3.19. The relaxation encoding segment is an inversion recovery type experiment, where the X magnetisation is brought to the z-axis. Since this magnetisation is not at its equilibrium value because the population difference between the $|\alpha\rangle$ and $|\beta\rangle$ states is determined by the polarisation transfer from the ^{1}H spins, it relaxes to equilibrium during the time delay T. The phase ϕ_2 of the 90° pulse in the sequence is inversed every scan, putting the X magnetisation alternately along the $+z$ and $-z$ axis, while the receiver phase is adjusted accordingly. This has the effect to remove both the contribution from the equilibrium X magnetisation, leaving

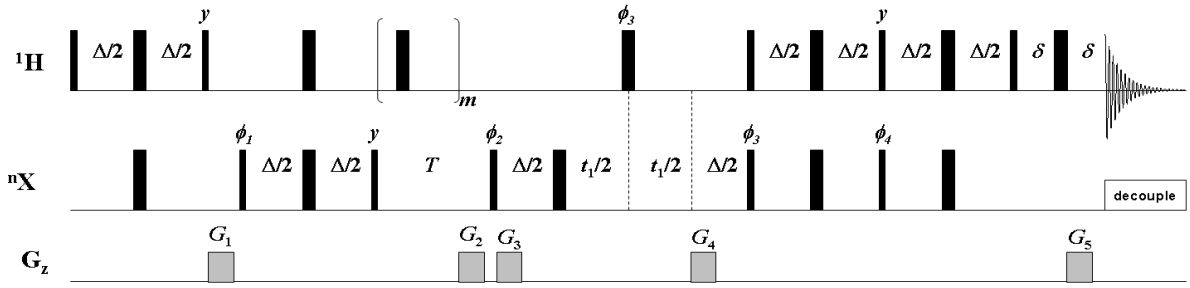

Figure 3.19: Pulse sequence used for heteronuclear R_1 relaxation rate measurements. R_1 relaxation occurs during the delay T, which is an inversion recovery delay, while indirect ^{n}X time domain sampling occurs by incrementing the value of t_1. The delay Δ is set to $1/2^{1}J_{XH}$, or somewhat lower in the case of fast T_2 relaxation for signal-to-noise reasons. The delay δ is set longer than the duration of the G_5 gradient. The phases of the pulses are incremented between scans as: ϕ_1 = *x*, *x*, *x*, *x*, -*x*, -*x*, -*x*, -*x*; ϕ_2 = *y*, -*y*; ϕ_3 = *x*, *x*, -*x*, -*x*; ϕ_4 = -*y*, -*y*, *y*, *y*; ϕ_{rec} = *x*, -*x*, -*x*, *x*, -*x*, *x*, *x*, -*x*. The gradient strengths are chosen to be G_1 = 5%, G_2 = -5%, G_3 = -80%, G_4 = 80%, G_5 = 40% for ^{13}C. For ^{15}N, G_1 = 50, G_2 = 30 and G_5 = 16.2%.. The sign of G_3 and G_4 are alternated for each t_1 increment to obtain an echo-antiecho type signal selection in the indirect dimension.

only the polarisation imposed by the ^{1}H population difference through INEPT, and the impact of steady state magnetisation created by too short interscan delays[17]. Because of this phase alternation, the final signal intensity after the pulse sequence will be an exponential decay as a function of the relaxation delay T:

$$I \propto e^{-R_1 T} \tag{3.110}$$

The saturation of the ^{1}H spins during the relaxation delay (performed by applying 180° pulses with a few milliseconds delay in betwee n) is required to avoid the interference of cross-relaxation and cross-correlated relaxation[18].

R_1 is determined by repeating this experiment several times for different values of T and integrating the HSQC cross-peaks. The exponential intensity decay thus acquired can then be fitted to (3.110) in order to obtain R_1 (Figure 3.20).

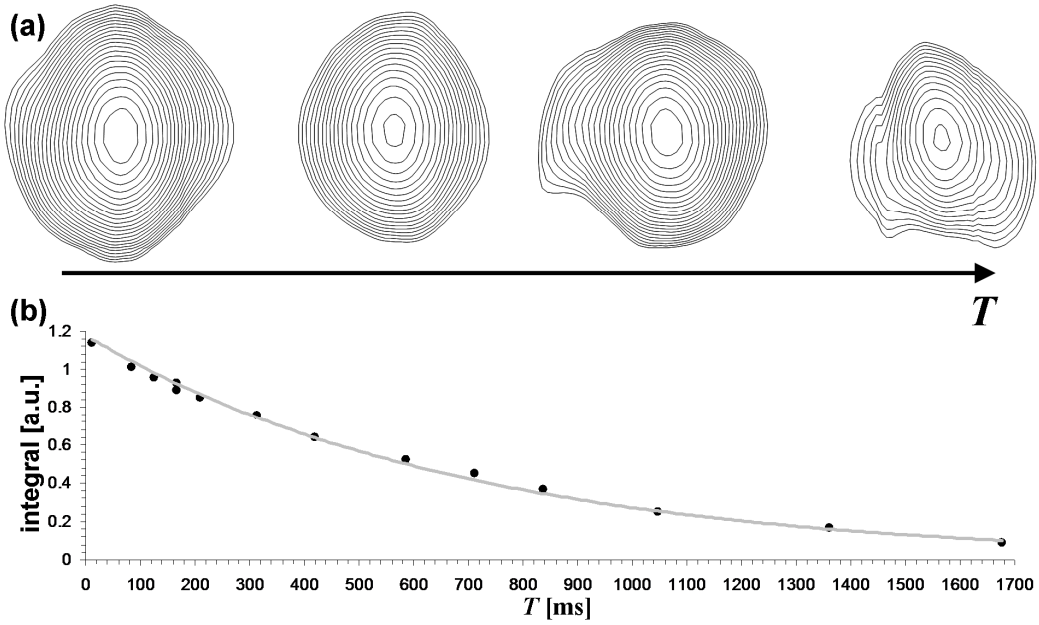

Figure 3.20: (a) The HSQC cross-peaks in the R_1 or R_2 experiment decrease in intensity as the delay T increases. (b) Integration of the cross-peaks for several experiments with varying values of T provides an exponential decay, from which the relaxation rate constant can be extracted through fitting.

3.7.3 Measurement of R_2: CPMG

In this case the relaxation encoding segment uses a CPMG (Carr-Purcell-Meiboom-Gill) pulse train to let the coherence decay with the R_2 relaxation rate constant during the time T (Figure 3.21). The CPMG sequence used in this work consists of a loop of n repeating units of a ^{n}X 180° pulse train with an interpulse delay of τ_{cp} and a ^{1}H 180° degree pulse in the middle of each repeating unit. The variable time T during which the magnetisation is allowed to decay through R_2 relaxation is thus a multiple of the number of repeating units n. R_2 is then obtained similarly as with R_1, as the final signal intensity will be a monoexponential decay according to T:

$$I \propto e^{-R_2 T} \tag{3.111}$$

There are several reasons why multiple ^{n}X 180° pulses are used instead of just a simple spin echo of only one 180° pulse. First, it minimises losses due to translational diffusion in the imperfectly homogenous magnetic field (as described in Chapter 2), which would cause an overestimation of the relaxation rate constant[19]. If τ_{cp} can be made sufficiently short, the CPMG sequence compensates for chemical exchange effects (section 3.7.5). Finally, besides the ^{n}X chemical shift evolution, the ^{n}X 180° pulses also refocus the $^{1}J_{XH}$ scalar coupling evolution and thus minimises the time the ^{n}X magnetisation is in its ^{1}H anti-phase form, which is important since the in-phase and anti-phase product operators have a different relaxation rate constant (section

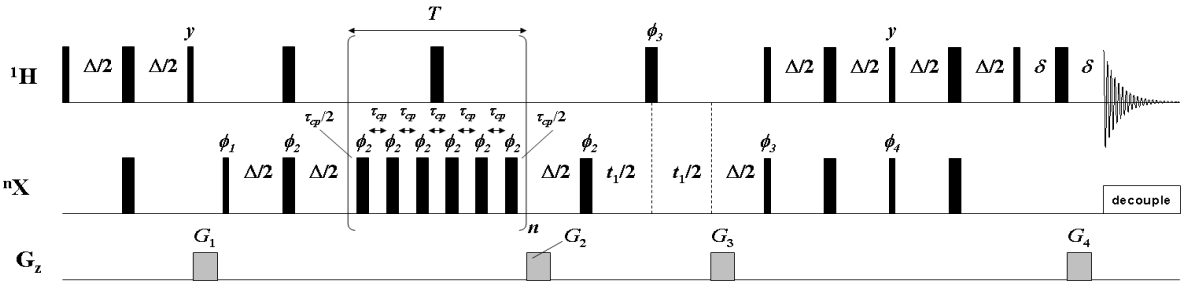

Figure 3.21: Pulse sequence used for heteronuclear R_2 relaxation rate measurements. R_2 relaxation occurs during the delay T, which is a CPMG sequence. The delays Δ, t_1 and δ are set as for the R_1 experiment (Figure 3.19). The phases of the pulses are incremented between scans as: $\phi_1 = x, -x$; $\phi_2 = y, -y$; $\phi_3 = x, x, -x, -x$; $\phi_4 = -y, -y, y, y$; $\phi_{rec} = x, -x, -x, x$. The gradient strengths are chosen to be $G_1 = 5\%$, $G_2 = -80\%$, $G_3 = 80\%$, $G_4 = 40\%$ for ^{13}C. For ^{15}N, $G_1 = 30\%$ and $G_5 = 16.2\%$. The sign of G_2 and G_3 are alternated for each t_1 increment to obtain an echo-antiecho type signal selection in the indirect dimension.

3.7.5)[3]. The ^{1}H 180° pulses need to be applied at a rate that is fast enough to suppress the effects of dipolar-CSA cross-correlated relaxation[20, 21].

3.7.4 Measurement of the steady state nOe

The steady state nOe experiment[3, 14] (Figure 3.22) differs from the R_1 and R_2 experiments in that only two measurements are required and that the initial excitation does not occur on the ^{1}H spins. The latter causes this experiment to be inherently less sensitive. Both experiments first excite the ^{n}X magnetisation. Then the t_1 time domain encoding is performed and finally a ^{n}X-^{1}H INEPT sequence is applied to transfer the magnetisation to the ^{1}H spins to provide a 2D HSQC type spectrum. In one of the two experiments, the ^{1}H spin population difference is initially saturated by use of a 180° pulse train just before the initial excitation to let the ^{1}H-^{n}X cross-relaxation occur. The saturation time must be sufficiently long so that a steady state situation is reached (section 3.2.4). Due to the increased (or decreased) initial ^{n}X z-magnetisation, the final signal strength will be influenced accordingly. The other experiment is performed in identically but without the initial ^{1}H saturation and with the same interscan delay. The nOe can then be calculated by comparing the signal intensities from both experiments:

$$\mathrm{nOe} = \frac{I(\mathrm{sat}) - I(\mathrm{no\ sat})}{I(\mathrm{no\ sat})} \tag{3.112}$$

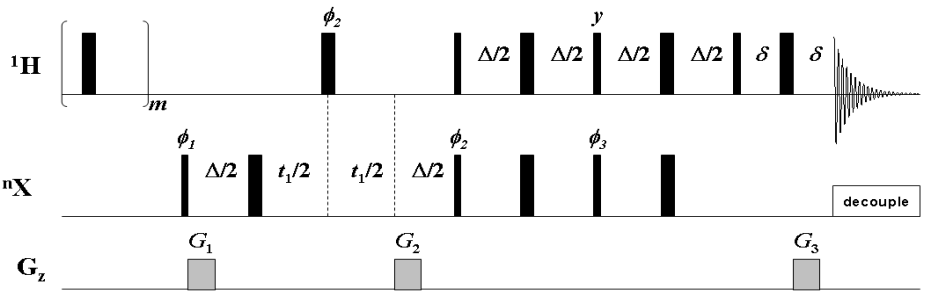

Figure 3.22: Pulse sequence used for steady state ^{1}H-^{n}X nOe measurements. Saturation of the ^{1}H spins occurs by performing a series of 180° pulses before initial excitation of the ^{n}X spins. In a second experiment, this saturation does not occur and a delay with the same duration is put in place of the 180° pulse train. The delays Δ, t_1 and δ are set as for the R_1 experiment (Figure 3.19). The phases of the pulses are incremented between scans as: ϕ_1 = y, $-y$; ϕ_2 = x, x, $-x$, $-x$; ϕ_3 = $-y$, $-y$, y, y; ϕ_{rec} = x, $-x$, $-x$, x. The gradient strengths are chosen to be G_1 = -80%, G_2 = 80%, G_3 = 40% for ^{13}C. For ^{15}N, G_3 = 16.2%. The sign of G_1 and G_2 are alternated for each t_1 increment to obtain an echo-antiecho type signal selection in the indirect dimension.

3.7.5 Effects of exchange during the CPMG and relaxation dispersion

During CPMG type R_2 measurements, the delay between the 180° pulses τ_{cp} strongly influences the degree to which exchange processes affect the apparent R_2 value. When the repetition rate ($1/\tau_{cp}$) of the 180° pulses is much faster than the exchan ge rate k_{ex}, the refocusing rate of the spins will be faster than the rate with which the exchange process dephases them. When on the other hand the repetition rate is much slower than the exchange rate, the full exchange contribution will be able to manifest itself and the equations derived in section 3.5 will hold. For a two spin system experiencing fast exchange (that is $k_{ex} >> \Delta\omega$), an expression for the exchange contribution R_{ex} to R_2 has been derived for any situation in between both described cases[3]:

$$R_{ex} = \frac{p_A p_B \Delta\omega^2}{k_{ex}}\left(1 - \frac{2}{k_{ex}\tau_{cp}}\tanh\left(\frac{k_{ex}\tau_{cp}}{2}\right)\right) \qquad (3.113)$$

A more general expression has also been derived for exchange at any timescale[22]. R_{ex} as a function of τ_{cp} is plotted in Figure 3.23. When it is practically and technically feasible to achieve values of τ_{cp} so that $(k_{ex}\tau_{cp})/2$ is of the order of 1, the presence of the exchange process can be detected by observing the variation of the apparent R_2 with τ_{cp}, at least when the variation is higher than the experimental error. By fitting equation (3.113) to R_{ex} values obtained with different values for τ_{cp}, the exchange rate k_{ex} (and thus the time scale of the conformational motions) can be determined. This method is widely applied to study slow conformational exchange processes and is known as relaxation dispersion[23].

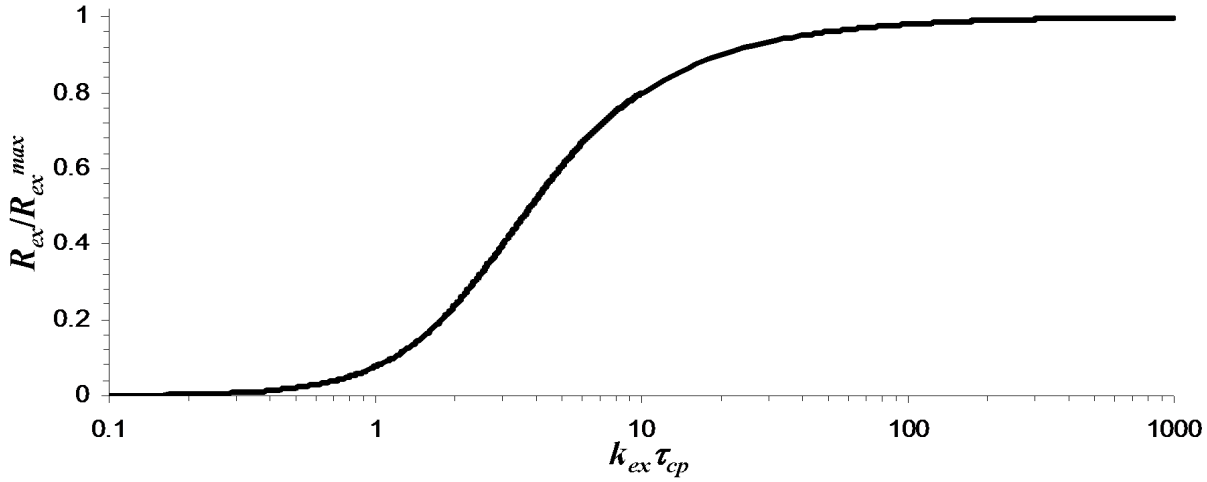

Figure 3.23: Contribution of a fast two site exchange process to the transverse relaxation as a function of $k_{ex}\tau_{cp}$ according to equation (3.113). R_{ex}^{max} is equal to $p_A p_B \Delta\omega^2/k_{ex}$, the exchange contribution in the absence of a CPMG pulse train. When τ_{cp} is sufficiently large so that $k_{ex}\tau_{cp} << 1$, the CPMG sequence nearly completely cancels out the exchange contribution.

In practice, the CPMG experiment as in Figure 3.21 cannot be used. As mentioned before (section 3.6.2), the magnetisation evolves under the $^1J_{XH}$ scalar coupling between the in-phase and the anti-phase states, which have different relaxation rates. The time the magnetisation spends in anti-phase state depends on the duration of τ_{cp}, and therefore a variation in τ_{cp} will also cause a variation in the fraction of total time the magnetisation relaxes with the in-phase or the anti-phase relaxation rate constant. This creates an ambiguous effect, since both the exchange contribution R_{ex} and the non-exchange R_2 value will vary with τ_{cp}[23]:

$$R_2^{tot}\left(\tau_{cp}\right) = a\left(\tau_{cp}\right)R_{2,in} + \left(1 - a\left(\tau_{cp}\right)\right)R_{2,in} + R_{ex}\left(\tau_{cp}\right) \qquad (3.114)$$

A solution to this problem has been presented by Loria *et al*[23]. They presented an experiment where the CPMG sequence was split into equal parts (Figure 3.24). At the start and at the end of the first CPMG sequence, the magnetisation will be anti-phase and exist for a certain fraction of the time as in-phase. After the first CPMG sequence, a segment U is incorporated which converts the anti-phase magnetisation into pure in-phase form, which is then inserted into the second the CPMG sequence. Since during this sequence, the fraction of time the magnetisation will exist as anti-phase is equal to the time it existed as in-phase during the first CPMG sequence, overall it will have spent as much time in both in-phase and anti-phase states. This makes $a(\tau_{cp})$ in equation (3.114) equal to 0.5 for any value of τ_{cp}, resolving the abovementioned ambiguity problem.

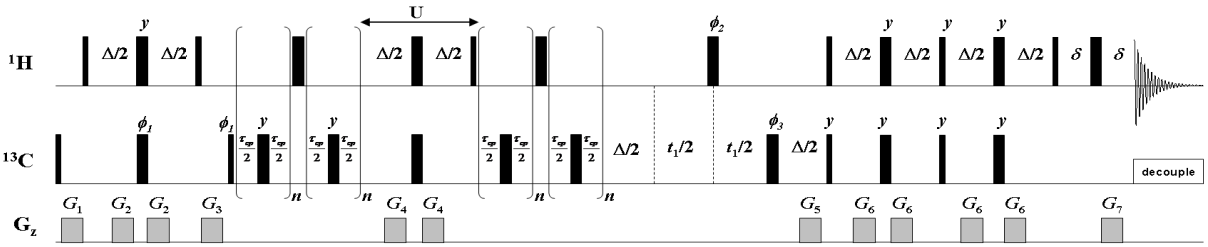

Figure 3.24: Pulse sequence used for ^{13}C relaxation dispersion measurements. The delays Δ, t_1 and δ are set as for the R_1 experiment (Figure 3.19). The phases of the pulses are incremented between scans as: $\phi_1 = x, -x$; $\phi_2 = x, x, x, x, -x, -x, -x, -x$; $\phi_3 = x, x, y, y, -x, -x, -y, -y$; $\phi_{rec} = x, -x, -x, x$. The gradient strengths are chosen to be $G_1 = 20\%$, $G_2 = 5\%$, $G_3 = 50\%$, $G_4 = 10\%$, $G_5 = 80\%$, $G_6 = 24\%$, $G_7 = 20.12\%$. The sign of G_5 is alternated for each t_1 increment to obtain an echo-antiecho type signal selection in the indirect dimension.

3.8 References

[1] L. G. Hanson, "Is quantum mechanics necessary for understanding magnetic resonance?". *Concepts in Magnetic Resonance Part A*, **2008**, *32A*(5) 329-340.

[2] R. A. Atkinson and B. Kieffer, "The role of protein motions in molecular recognition: insights from heteronuclear NMR relaxation measurements". *Progress in Nuclear Magnetic Resonance Spectroscopy*, **2004**, *44*(3-4) 141-187.

[3] J. Cavanagh, W. J. Fairbrother, A. G. Palmer, M. Rance and N. J. Skelton, "Protein NMR Spectroscopy: Principles and Practice, 2nd edition", **2007**, Oxford, Elsevier Academic Press.

[4] M. W. F. Fischer, A. Majumdar and E. R. P. Zuiderweg, "Protein NMR relaxation: theory, applications and outlook". *Progress in Nuclear Magnetic Resonance Spectroscopy*, **1998**, *33*(4) 207-272.

[5] D. M. Korzhnev, M. Billeter, A. S. Arseniev and V. Y. Orekhov, "NMR studies of Brownian tumbling and internal motions in proteins". *Progress in Nuclear Magnetic Resonance Spectroscopy*, **2001**, *38*(3) 197-266.

[6] M. H. Levitt, "Spin Dynamics: Basics of Nuclear Magnetic Resonance 2nd Edition", **2008**, Chichester, John Wiley & Sons, Ltd.

[7] D. Neuhaus and M. P. Williamson, "The Nuclear Overhauser Effect in Structural and Conformational Analysis", 2nd ed., **2000**, New York, John Wiley and Sons Ltd.

[8] D. E. Woessner, "Nuclear spin relaxation in ellipsoids undergoing rotational Brownian motion". *Journal of Chemical Physics*, **1962**, *37* 647-654.

[9] G. Lipari and A. Szabo, "Model-Free Approach to the Interpretation of Nuclear Magnetic-Resonance Relaxation in Macromolecules .1. Theory and Range of Validity". *Journal of the American Chemical Society*, **1982**, *104*(17) 4546-4559.

[10] G. Lipari and A. Szabo, "Model-Free Approach to the Interpretation of Nuclear Magnetic-Resonance Relaxation in Macromolecules .2. Analysis of Experimental Results". *Journal of the American Chemical Society*, **1982**, *104*(17) 4559-4570.

[11] A. D. Bain, "Chemical exchange in NMR". *Progress in Nuclear Magnetic Resonance Spectroscopy*, **2003**, *43*(3-4) 63-103.

[12] A. G. Palmer, C. D. Kroenke and J. P. Loria, "Nuclear magnetic resonance methods for quantifying microsecond-to-millisecond motions in biological macromolecules". *Nuclear Magnetic Resonance of Biological Macromolecules, Pt B*, **2001**, *339* 204-238.

[13] O. Millet, J. P. Loria, C. D. Kroenke, M. Pons and A. G. Palmer, "The static magnetic field dependence of chemical exchange linebroadening defines the NMR chemical shift time scale". *Journal of the American Chemical Society*, **2000**, *122*(12) 2867-2877.

[14] L. E. Kay, D. A. Torchia and A. Bax, "Backbone Dynamics of Proteins as Studied by ^{15}N Inverse Detected Heteronuclear NMR-Spectroscopy - Application to Staphylococcal Nuclease". *Biochemistry*, **1989**, *28*(23) 8972-8979.

[15] L. E. Kay, P. Keifer and T. Saarinen, "Pure Absorption Gradient Enhanced Heteronuclear Single Quantum Correlation Spectroscopy with Improved Sensitivity". *Journal of the American Chemical Society*, **1992**, *114*(26) 10663-10665.

[16] A. G. Palmer, J. Cavanagh, P. E. Wright and M. Rance, "Sensitivity Improvement in Proton-Detected 2-Dimensional Heteronuclear Correlation NMR-Spectroscopy". *Journal of Magnetic Resonance*, **1991**, *93*(1) 151-170.

[17] V. Sklenar, D. Torchia and A. Bax, "Measurement of Carbon-13 Longitudinal Relaxation Using ^{1}H Detection". *Journal of Magnetic Resonance*, **1987**, *73*(2) 375-379.

[18] J. Boyd, U. Hommel and I. D. Campbell, "Influence of Cross-Correlation between Dipolar and Anisotropic Chemical-Shift Relaxation Mechanisms Upon Longitudinal Relaxation Rates of ^{15}N in Macromolecules". *Chemical Physics Letters*, **1990**, *175*(5) 477-482.

[19] H. Y. Carr and E. M. Purcell, "Effects of Diffusion on Free Precession in Nuclear Magnetic Resonance Experiments". *Physical Review*, **1954**, *94*(3) 630.

[20] L. E. Kay, L. K. Nicholson, F. Delaglio, A. Bax and D. A. Torchia, "Pulse Sequences for Removal of the Effects of Cross-Correlation between Dipolar and Chemical-Shift Anisotropy Relaxation Mechanism on the Measurement of Heteronuclear T_1 and T_2 Values in Proteins". *Journal of Magnetic Resonance*, **1992**, *97*(2) 359-375.

[21] A. G. Palmer, N. J. Skelton, W. J. Chazin, P. E. Wright and M. Rance, "Suppression of the Effects of Cross-Correlation between Dipolar and Anisotropic Chemical-Shift Relaxation Mechanisms in the Measurement of Spin Spin Relaxation Rates". *Molecular Physics*, **1992**, *75*(3) 699-711.

[22] D. G. Davis, M. E. Perlman and R. E. London, "Direct Measurements of the Dissociation-Rate Constant for Inhibitor-Enzyme Complexes Via the T-1-Rho and T-2 (Cpmg) Methods". *Journal of Magnetic Resonance Series B*, **1994**, *104*(3) 266-275.

[23] J. P. Loria, M. Rance and A. G. Palmer, "A relaxation-compensated Carr-Purcell-Meiboom-Gill sequence for characterizing chemical exchange by NMR spectroscopy". *Journal of the American Chemical Society*, **1999**, *121*(10) 2331-2332.

Part 2:

Pseudodesmin A

4

Antimicrobial peptides, cyclic lipodepsipeptides and the viscosin group

4.1 Antimicrobial peptides

The increasing resistance of bacteria against antibiotics is one of the important challenges modern medicine faces today[1, 2]. The search for new lead compounds and new molecular mechanisms that tackle bacterial pathogens is therefore more important than ever. In this context, antimicrobial peptides (AMPs) have received considerable attention over the last years[3]. These peptides are produced by a variety of multicellular organisms, including humans, to defend against a broad range of microbes. They are oligopeptide chains of a size ranging between 6 and 60 amino acid residues. Typically they have the property of being amphipathic, *i.e.* in their relevant conformation the hydrophilic and hydrophobic side chains are all grouped to separate sides of the molecular surface. Their conformation is often α-helical or contains a β-sheet like structure, which sometimes will only be adopted in a membrane environment. Several groups of AMPs have been defined, including peptides containing many anionic side chains, cationic side chains or fragments of larger proteins[4].

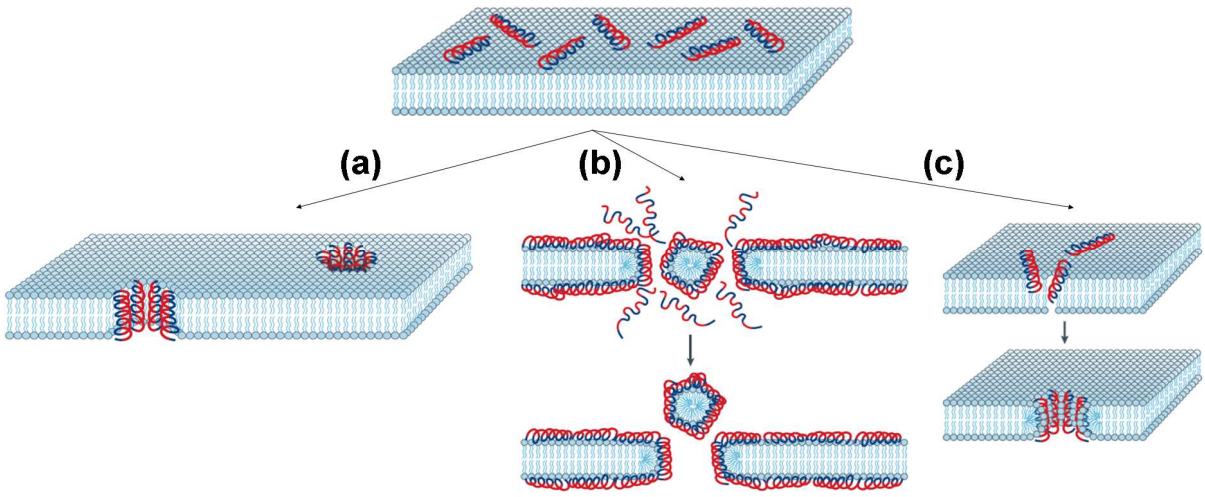

Figure 4.1: AMPs first attach themselves to the membrane. When the local concentration becomes sufficiently high, multiple pore forming model mechanisms have been described (see main text). (a) Barrel-stave model; (b) Carpet model; (c) Toroidal pore model. The hydrophilic parts of the amphipathic peptides are coloured red while the hydrophobic parts are blue. Figure adapted from the review of Brogden[4].

Their most frequently suspected mechanism is a process where they interact with the cellular membrane. In a first step, they orient themselves parallel to the membrane bilayer (perpendicular to the phospholipid chains), where in the case of cationic peptides they interact electrostatically with the phospholipid head groups. Three distinct model mechanisms have been described to explain how the membrane is subsequently disrupted (Figure 4.1)[4]. In the 'barrel-stave' or 'helical-bundle' model, when a critical concentration of AMP at the surface of the membrane is achieved, the AMP helices aggregate to form a barrel like structure with the hydrophobic side chains extending outwards and the hydrophilic side chains directed inwards. The aggregate places itself parallel to the lipid molecules to effectively form a pore structure. A known example of this mechanism is alamethicine[5, 6]. In the carpet model, the AMP molecules align themselves parallel to the surface of the membrane to form an extensive layer (or carpet). They can then act as a detergent and eventually form micelle structures that effectively take out pieces of lipids of the membrane, slowly breaking open the bilayer. The third mechanism is the toroidal pore model, in which the aggregated AMPs effectively push a hole through the membrane. The AMPs are aligned along this hole and the orientation of the lipid chains at the edges of the hole is twisted so that their polar headgroups still interact with the AMPs. Independent of the mechanisms, the creation of a pore structure or opening of the membrane has several lethal effects for the target microorganism. For example, cellular content can leak out of the cell, or ions can pass through which depolarizes the membrane, or water can diffuse in the cell by means of osmotic pressure and cause the cell to lyse.

It is generally assumed that it is improbable for microorganisms to develop resistance against AMPs. This is because developing a resistance would require developing

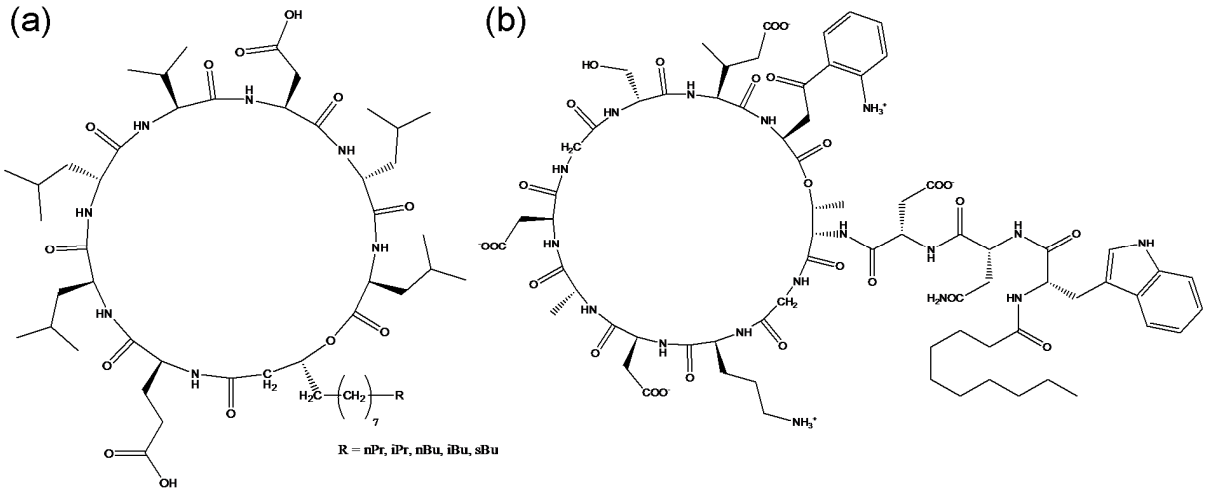

Figure 4.2: (a) Surfactin and (b) Daptomycin.

drastic modifications to the membrane organisation and composition, which would be a costly evolutionary effort. The use of AMPs as systematic therapeutic agents has not gone smoothly however[3]. This would mainly be due to the observation that many naturally occurring AMPs are only active in vitro in animal models at concentrations which are close to their lethal dose. Nevertheless, they have been found to enhance the activity of existing antibiotics, likely because they create a higher accessibility to the bacterial cell. They have also found application as anti-infective agents.

4.2 Cyclic lipodepsipeptides

Cyclic lipodepsipeptides (CLPs) are small molecules that consist of an oligopeptide chain bonded to a long fatty acid moiety. The molecule forms a cyclic structure through a lactone bond, typically involving the C-terminal end of the peptide chain and a hydroxyl group of preceding residue, most often a Ser or Thr residue. A biopolymer involving both amide and ester type bonds is called a depsipeptide[7]. Typically, naturally occurring CLPs are surfactants due to their often amphipathic nature. As a consequence, CLPs are often found to be able to interact or disrupt membrane bilayers, just like AMPs. A different property is their ability to bind metal ions. This has even lead to such applications as removing heavy metals from sediments[8].

A well-known example is surfactin, a naturally occurring CLP produced by *Bacillus subtilis* bacteria (Figure 4.2a). This product has been extensively studied because of its biomedical interest (antibacterial, antiviral and anti-inflammatory activity have among others been observed) and its reputation as being a very strong biosurfactant[9]. It is known to be able to permeabilise membranes, causing lysis of cellular membranes. There is still some debate as to how exactly surfactin disturbs the phospholipid membrane bilayer[9, 10]. Another known example is daptomycin

(Figure 4.2b), a CLP produced by *Streptomyces roseosporus*. This CLP, which was brought on the market under the name cubicin and was approved by the Food and Drug Administration in 2003, is known to be able to bind Ca^{2+} ions and to be able form large aggregates[11, 12].

Production of CLPs does not occur ribosomally, but is facilitated by so-called nonribosomal peptide synthetases[13]. These large enzymes, consisting out of multiple subunit domains, allow the synthesis of oligopeptides that deviate from the classical protein synthesis rulebook. This includes incorporation of unusual amino acids, non-amino acids and, most remarkably, cyclisation of the molecule. The latter has been found to be very important for their function, locking the molecule into a specific conformation. For instance; it has been shown that the non-cyclic form of surfactin is not bio-active[14]. The cyclisation together with the incorporation of unusual amino acids (such as D-amino acids) also make the molecules much harder to tackle by proteases.

Pseudomonas bacteria are a known producer of several CLPs[14, 15] with a diversity of functions. These include a role in plant pathogenesis, antibiotic and antifungal activity, attachment and detachment to natural or synthetic surfaces, and facilitation of movement of the *Pseudomonas* bacteria. Their CLPs have been classified into four groups based on chain length and residue composition (Table 4.1). These include the viscosin group, the amphisin group, the tolaasin group and the syringomycin group. The viscosin and amphisin groups closely resemble each other in terms of amino acid composition, and are discussed more in detail in section 4.3. The tolaasin and syringomycin groups distinguish themselves from the viscosin and amphisin group in that they contain unusual amino acid residues, such as 2,4-diaminobutyric acid (Dab) or 4-chlorothreonine (Thr-4Cl).

The CLPs in the tolaasin group are the largest of all the *Pseudomonas* CLPs present, and include tolaasin itself[16, 17], the fuscopeptins[18], the syringopeptins[19] and the corpeptins[20]. Compared to the other groups, they have only a small ring structure with a very long non-cyclic oligopeptide part at the N-terminus, ending in the lipid tail. In the case of tolaasin itself, it has been shown that the peptide chain is unstructured when dissolved in DMSO[21]. However, when brought in SDS micelles or model membranes[21, 22], the peptide chain adopts a left-handed α-helix and is found to orient itself parallel to the membrane lipid chains as found by studying dichroic spectra from Attenuated Total Reflection (ATR) FT-IR spectroscopy[22]. A similar result was found for the fuscopeptins, which appeared to be unstructured in water solution but become partly helical in a water/trifluoroethanol mixture[23]. It has been found that, in planar lipid membranes, tolaasin forms passive transport, cation selective, ion channels[24, 25], which can be inhibited by Zn^{2+} ions. The pore diameter could be estimated at 21 Å[26] by use of osmotic protectants. These are polyethylene

glycol (PEG) molecules of a certain molecular size that added to a suspension of erythrocytes in a tolaasin solution and are capable of inhibiting the membrane permeability when of sufficient size. By observing how the rate of decrease in suspension turbidity of the solution varies with the PEG molecular size, the pore size estimation can be made.

The CLPs in the syringomycin group[14] consist of nine mainly hydrophilic amino acid residues, all present within the cyclic structure. The group includes syringomycin, syringostatin, syringotoxin, the pseudomycins and the cormycins. The members of this group, especially syringomycin, have been extensively studied for their pore forming capabilities[27, 28]. It was found by Hutchison *et al*[29] that syringomycin causes lysis in erythrocytes, which, just as for tolaasin, can be inhibited by adding PEG osmotic protectants. They measured cation-selective conductivity and capacitance changes when adding syringomycin to artificial planer lipid bilayers. A model was proposed[29] in which syringomycin would aggregate within the cellular membrane, with the hydrophilic peptide ring structures packed towards each other and the hydrophobic fatty acid projecting out into the lipophilic membrane, effectively forming a 'reversed' micelle. It was postulated that this would lead to passive transport of cations such as H^+, K^+ and Ca^{2+}, influencing the cytoplasm pH and causing cellular signalling effects to occur that disturbes the workings of the cell.

4.3 The viscosin and amphisin groups

Viscosin is a CLP consisting of nine amino acid residues, of which seven participate in the cyclic structure (Table 4.1). The C-terminus is esterified with the alcohol group of the threonine side chain at position 3, while the C-terminus is bonded to a 3-hydroxydecanoic acid moiety. The product was first isolated from *Pseudomonas viscosa* in 1951[30] and was initially found to exert a mild antibiotic activity against *Mycobacterium tuberculosis* and an antiviral activity against bronchitis and influenza A[31]. Its complete structure was eventually elucidated in 1970[32]. Later it has been isolated from certain strains of *P. fluorescens*[33], *P. libanesis*[34] and an other as of yet unidentified *Pseudomonas* species[35]. The capacity of viscosin to form complexes with divalent cations, more specifically Cd^{2+}, has also been established[34].

The second member of the viscosin group, the White Line Inducing Principle (WLIP), was first described in 1991[36] as a product isolated from a diverse group of *Pseudomonas* species conveniently known as *P. reactans*. It was found to be the compound responsible for a white line that appears in agar when *P. reactans* is grown in association with *P. tolaasii*. This was relevant at the time, since this white line was used to identify *P. tolaasii*, the cause of the economically significant brown blotch disease in the edible mushrooms *Agaricus bisporus*. It was later reported that

Table 4.1: Primary structure of CLPs produced by *Pseudomonas* bacteria

tolaasin group

	1	2	3	4	5	6	7	8	9	10	11
tolaasin	$CH_3(CH_2)_4CH(OH)CH_2CO$ – z-Dhb	– D-Pro	– D-Ser	– D-Leu	– D-Val	– D-Ser	– D-Leu	– D-Val	– L-Val	– D-Gln	– L--Leu – ⋯→
fuscopeptin A	$CH_3(CH_2)_4CH(OH)CH_2CO$ – z-Dhb	– D-Pro	– L-Leu	– D-Ala	– D-Ala	– D-Ala	– D-Ala	– D-Val	– --Gly	– D-Ala	– D--Val – ⋯→
fuscopeptin B	$CH_3(CH_2)_6CH(OH)CH_2CO$ – z-Dhb	– D-Pro	– L-Leu	– D-Ala	– D-Ala	– D-Ala	– D-Ala	– D-Val	– --Gly	– D-Ala	– D--Val – ⋯→
corpeptin A	$CH_3(CH_2)_6CH(OH)CH_2CO$ – z-Dhb	– ?-Pro	– ?-Ala	– ?-Ala	– ?-Ala	– ?-Val	– ?-Val	– z-Dhb	– ?-Hse	– ?-Val	– ?-aIle – ⋯→
corpeptin B	cis-$CH_3(CH_2)_5CH$=CHCH2$CH(OH)CH_2CO$ – z-Dhb	– ?-Pro	– ?-Ala	– ?-Ala	– ?-Ala	– ?-Val	– ?-Val	– z-Dhb	– ?-Hse	– ?-Val	– ?-aIle – ⋯→
syringopeptin 22A	$CH_3(CH_2)_6CH(OH)CH_2CO$ – z-Dhb	– D-Pro	– D-Val	– L-Val	– D-Ala	– D-Ala	– D-Val	– ———	– ———	– ———	– D--Val – ⋯→
syringopeptin 25A	$CH_3(CH_2)_6CH(OH)CH_2CO$ – z-Dhb	– D-Pro	– D-Val	– L-Ala	– D-Ala	– L-Val	– D-Leu	– D-Ala	– D-Ala	– z-Dhb	– D--Val – ⋯→

	12	13	14	15	16	17	18	19	20	21	22	23	24	25
tolaasin	– ——— – ——— – ——— – ——— – D-Val	– z-Dhb	– D-aThr–	L-Ile	– L-Hse	– D-Dab	– L-Lys							
fuscopeptin A	– D-Ala – ——— – ——— – ——— – D-Val	– z-Dhb	– D-aThr–	L-Ala	– L-Dab	– D-Dab	– L-Phe							
fuscopeptin B	– D-Ala – ——— – ——— – ——— – D-Val	– z-Dhb	– D-aThr–	L-Ala	– L-Dab	– D-Dab	– L-Phe							
corpeptin A	– z-Dhb	– ?-Ala	– ?-Ala	– ?-Ala	– ?-Val	– z-Dhb	– ?-aThr–	?-Ala	– ?-Dab	– ?-Ser	– ?-Ile			
corpeptin B	– z-Dhb	– ?-Ala	– ?-Ala	– ?-Ala	– ?-Val	– z-Dhb	– ?-aThr–	?-Ala	– ?-Dab	– ?-Ser	– ?-Ile			
syringopeptin 22A	– z-Dhb	– D-Ala	– D-Val	– L-Ala	– D-Ala	– z-Dhb	– D-aThr–	D-Ser	– D-Ala	– z-Dhb	– L-Ala	– L-Dab	– D-Dab	– L-Tyr
syringopeptin 25A	– z-Dhb	– D-Ala	– D-Val	– D-Ala	– D-Ala	– z-Dhb	– D-aThr–	D-Ser	– D-Ala	– L-Val	– L-Ala	– L-Dab	– D-Dab	– L-Tyr

syringomycin group

		1	2	3	4	5	6	7	8	9
syringomycin E	$CH_3(CH_2)_8CH(OH)CH_2CO$ –	L-Ser	– D-Ser	– D-Dab	– L-Dab	– L-Arg	– L--Phe	– z-Dhb	– L-Asp(3-OH)	– L-Thr(4-Cl)
syringostatin	$CH_3(CH_2)_8CH(OH)CH_2CO$ –	L-Ser	– D-Dab	– L-Dab	– D-Hse	– L-Orn	– L-aThr	– z-Dhb	– L-Asp(3-OH)	– L-Thr(4-Cl)
syringotoxin	$CH_3(CH_2)_{10}CH(OH)CH_2CO$ –	L-Ser	– D-Dab	– L-Asp	– L-Lys	– L-Dab	– L-aThr	– z-Dhb	– L-Asp(3-OH)	– L-Thr(4-Cl)
pseudomycin A	$CH_3(CH_2)_9CH(OH)CH(OH)CH_2CO$ –	L-Ser	– D-Dab	– L-Asp	– L-Lys	– L-Dab	– L-aThr	– z-Dhb	– L-Asp(3-OH)	– L-Thr(4-Cl)
cormycin A	$CH_3(CH_2)_{11}CH(OH)CH_2CO$ –	L-Ser	– D-Orn	– L-Asn	– D-Hse	– L-His	– L-aThr	– z-Dhb	– L-Asp(3-OH)	– L-Thr(4-Cl)

viscosin group

L-subgroup

		1	2	3	4	5	6	7	8	9
viscosin	$CH_3(CH_2)_6CH(OH)CH_2CO$ –	L-Leu	– D-Glu	– D-aThr	– D--Val	– L-Leu	– D-Ser	– L-Leu	– D-Ser	– L-Ile
viscosinamide	$CH_3(CH_2)_6CH(OH)CH_2CO$ –	L-Leu	– D-Gln	– D-aThr	– D--Val	– L-Leu	– D-Ser	– L-Leu	– D-Ser	– L-Ile
massetolide A	$CH_3(CH_2)_6CH(OH)CH_2CO$ –	L-Leu	– D-Glu	– D-aThr	– D-aIle	– L-Leu	– D-Ser	– L-Leu	– D-Ser	– L-Ile
massetolide B	$CH_3(CH_2)_7CH(OH)CH_2CO$ –	L-Leu	– D-Glu	– D-aThr	– D-aIle	– L-Leu	– D-Ser	– L-Leu	– D-Ser	– L-Ile
massetolide C	$CH_3(CH_2)_8CH(OH)CH_2CO$ –	L-Leu	– D-Glu	– D-aThr	– D-aIle	– L-Leu	– D-Ser	– L-Leu	– D-Ser	– L-Ile
massetolide D	$CH_3(CH_2)_6CH(OH)CH_2CO$ –	L-Leu	– D-Glu	– D-aThr	– D-aIle	– L-Leu	– D-Ser	– L-Leu	– D-Ser	– L-Leu
massetolide E	$CH_3(CH_2)_6CH(OH)CH_2CO$ –	L-Leu	– D-Glu	– D-aThr	– D--Val	– L-Leu	– D-Ser	– L-Leu	– D-Ser	– L-Val
massetolide F	$CH_3(CH_2)_6CH(OH)CH_2CO$ –	L-Leu	– D-Glu	– D-aThr	– D--Val	– L-Leu	– D-Ser	– L-Leu	– D-Ser	– L-Leu
massetolide G	$CH_3(CH_2)_7CH(OH)CH_2CO$ –	L-Leu	– D-Glu	– D-aThr	– D--Val	– L-Leu	– D-Ser	– L-Leu	– D-Ser	– L-Ile
massetolide H	$CH_3(CH_2)_8CH(OH)CH_2CO$ –	L-Leu	– D-Glu	– D-aThr	– D--Val	– L-Leu	– D-Ser	– L-Leu	– D-Ser	– L-Ile

D-subgroup

		1	2	3	4	5	6	7	8	9
pseudodesmin A	$CH_3(CH_2)_6CH(OH)CH_2CO$ –	L-Leu	– D-Gln	– D-aThr	– D--Val	– D-Leu	– D-Ser	– L-Leu	– D-Ser	– L-Ile
pseudodesmin B	$CH_3(CH_2)_6CH(OH)CH_2CO$ –	L-Leu	– D-Gln	– D-aThr	– D--Val	– D-Leu	– D-Ser	– L-Leu	– D-Ser	– L-Val
WLIP	$CH_3(CH_2)_6CH(OH)CH_2CO$ –	L-Leu	– D-Glu	– D-aThr	– D--Val	– D-Leu	– D-Ser	– L-Leu	– D-Ser	– L-Ile
pseudophomin A	$CH_3(CH_2)_6CH(OH)CH_2CO$ –	L-Leu	– D-Glu	– D-aThr	– D--Ile	– D-Leu	– D-Ser	– L-Leu	– D-Ser	– L-Ile
pseudophomin B	$CH_3(CH_2)_8CH(OH)CH_2CO$ –	L-Leu	– D-Glu	– D-aThr	– D--Ile	– D-Leu	– D-Ser	– L-Leu	– D-Ser	– L-Ile

amphisin group

		1	2	3	4	5	6	7	8	9	10	11
amphisin	$CH_3(CH_2)_6CH(OH)CH_2CO$ –	D-Leu	– D-Asp	– D-aThr	– D--Leu	– D-Leu	– D-Ser	– L-Leu	– D-Gln	– L-Leu	– L-Ile	– L--Asp
tensin	$CH_3(CH_2)_6CH(OH)CH_2CO$ –	D-Leu	– D-Asp	– D-aThr	– D--Leu	– D-Leu	– D-Ser	– L-Leu	– D-Gln	– L-Leu	– L-Ile	– L--Glu
pholipeptin A	$CH_3(CH_2)_6CH(OH)CH_2CO$ –	D-Leu	– L-Asp	– L--Thr	– D--Leu	– D-Leu	– D-Ser	– D-Leu	– D-Ser	– D-Leu	– L-Ile	– D-βAsp
Arthrofactin	$CH_3(CH_2)_6CH(OH)CH_2CO$ –	D-Leu	– D-Asp	– D--Thr	– D--Leu	– D-Leu	– D-Ser	– L-Leu	– D-Ser	– L-Ile	– L-Ile	– L--Asp
Lokisin	$CH_3(CH_2)_6CH(OH)CH_2CO$ –	?-Leu	– ?-Asp	– D-aThr	– ?--Leu	– ?-Leu	– D-Ser	– ?-Leu	– D-Ser	– ?-Leu	– L-Ile	– ?--Asp

Dhb: 2,3-dehydro-2-aminobutyric acid, Dab: 2,4-aminobutyric acid, Hse: homoserine, Asp(3-OH): 3-hydroxyapartic acid, Thr(4-Cl): 4-chlorothreonine, Orn: ornithine

WLIP is actually an inhibitor of the effects of the disease[37]. WLIP only differs from viscosin by possessing a D-Leu at position 5 instead of an L-Leu residue. Mortishire-Smith *et al* have performed a conformational analysis in DMSO solution using NMR. The overall conformation was described as resembling the seam of a tennis ball. However, this result was later invalidated as a result of the work described later in the present dissertation[38] and will be discussed in detail in section 5.4. A crystal structure has also been determined[39], showing a significantly different conformation compared to the one found in DMSO by NMR. The pore forming capabilities of WLIP were later demonstrated using PEG osmotic protectants[26], indicating an estimated pore size of 15-17 Å. Shortly thereafter it was demonstrated that WLIP is indeed capable to insert itself within the cellular membrane[22].

The difference in stereochemistry for the conserved Leu at the 5 position observed between viscosin and WLIP divides the rest of the viscosin group in two subgroups. Viscosinamide and the massetolides all possess similar stereochemistry to viscosin and will be referred to as the L-subgroup, while the pseudophomines and the pseudodesmins are similar to WLIP and form the D-subgroup. Only for the latter subgroup have conformational studies been performed, which is unfortunate since a change in stereochemistry at this position should have a very strong impact on the overall conformation, and possibly in the structure-function relation. Crystal structures have been determined for nearly all members of the D-subgroup, all demonstrating practically identical conformations, while solution structures have only been determined for WLIP and pseudodesmin A.

The massetolides A-H have been isolated from two unidentified species of Pseudomonas bacteria living between unidentified marine algae and a tube worm[35]. These compounds differ by the nature of the hydrophobic residue at positions 4 and 9 and by their fatty acid chain length. When feeding to the agar cultures unnatural amino acid residues such as L-butyrine, L-norvaline and L-cyclopropylanaline, it was found that small amounts of massetolide analogues (massetolides I-K) can be isolated with these residues incorporated at the 1 and the 4 position. This indicates that the natural variations between the massetolides may be caused by a certain lack in selectivity of the nonribosomal peptide synthetases involved. An interesting result was that D-butyrine was found at position 4 while only L-butyrine was fed, clearly demonstrating an epimerisation step during the biosynthesis.

Viscosinamide has been isolated from *P. fluorescens* strain DR54, isolated from the sugar beet rhizosphere[40, 41]. It only differs from viscosin in that it features at position 2 a glutamine instead of a glutamate residue. The molecule therefore has no ionisable functional group, which is reflected in its reduced solubility in water when compared to viscosin, reported to be 2 µM and 9 µM respectively[41]. Viscosinamide

has been of interest due to its antifungal activity against *Pythium ultimum* and *Rhizoctonia solani*[42-44].

The pseudophomines A and B were isolated from *P. fluorescens* strain BRG100[45]. Both molecules differ only in their fatty acid chain length, pseudophomin B possessing a 3-hydroxydodecanoic acid instead of 3-hydroxydecanoic acid moiety. Both molecules were screened against a number of fungal plant pathogens. It is noteworthy that pseudophomin B is reported to exhibit a significantly more pronounced inhibitory effect on the tested pathogens. A crystal structure has been determined of pseudophomin A[46].

The pseudodesmins A and B[47], which form the subject of this dissertation, will be discussed in more detail in the next section.

When carefully analysing the sequence of all members of the viscosin group, it becomes apparent that some structural features are conserved. First, the positions and the nature of the hydrophilic residues (Glx and the two serines) always remain. For the hydrophobic residues, only the ones at positions 4 and 9 are seemingly tolerant to variation. With the exception of the Leu5, the stereochemistry is also always preserved between all variants. All of this indicates that the pattern of hydrophobic and hydrophilic residues is very important for the function of this group of CLPs. Indeed, as will become clear for the pseudodesmins later on (Chapter 5), the hydrophilic residues are positioned in such way that the conformation becomes amphipathic, which is a very important structural feature to explain their capability to form ion pores (section 6.5).

The sequence and the conformation of the amphisin group are very similar to the viscosin group. They possess 11 amino acid residues instead of 9, with the two extra residues situated in the cyclic structure. However, the patterns of hydrophobic and hydrophilic residues and the nature of most of the residue side chains are retained compared to the viscosin group. The amphisin group includes amphisin[48], tensin[49], pholipeptin A[50, 51], lokisin[52] and anthrofactin[53]. For both amphisin and tensin, crystal structures have been determined[48, 54]. The conformations adopted by both molecules are very similar to the conformations adopted by WLIP, pseudophomin A and pseudodesmin A in their respective crystal structures (see section 5.2). This further confirms their close relation to the viscosin group and more specifically the D-subgroup. Tensin is produced by *P. fluorescens* strain 96.578 and has showed activity against Rizhoctonia solani, a fungal pathogen of sugar beet seeds. Pholipeptin and anthrofactin differ from the other members of the amphisin group as they both display a different stereochemical pattern. In addition, the C-terminal residue of pholipeptin[50], Asp11, forms an unusual ester bond with Thr3, as it is linked via its side chain carboxylic group. Anthrofactin[53, 55] is produced by

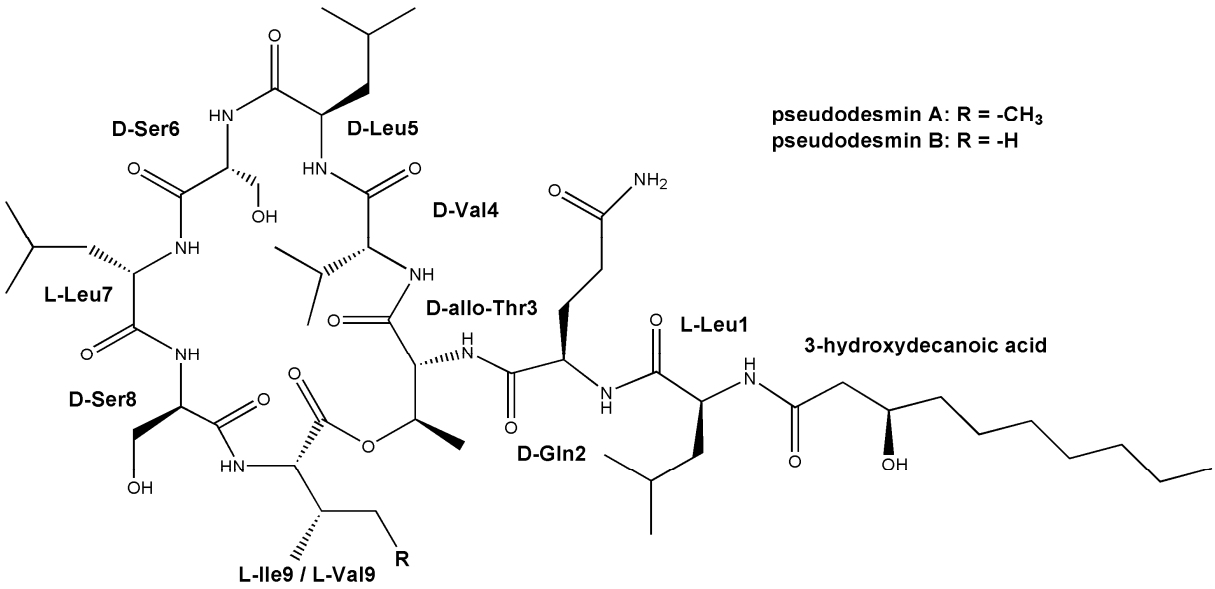

Figure 4.3: Molecular structure of the pseudodesmins.

Arthrobacter species and was found to display up to 5 times higher surfactant activity than surfactin.

4.4 The pseudodesmins

Pseudodesmin A (Figure 4.3) is the main subject of this dissertation and shall here be introduced. The compound and its close analogue, pseudodesmin B (Figure 4.3), are produced by *Pseudomonas* bacteria that can be isolated from the mucus layer on the skin of the black belly salamander (*Desmognathus quadramaculatus*), indigenous to Georgia, USA. The bacterial strain was identified as *P. tolaasii* using rRNA analysis, performed by Dr. R. Austin (Plethodon Inc, Georgia, USA). The isolation, characterization and biological screening are described elsewhere[47, 56]. Initial elucidation of the pseudodesmin A covalent structure and partial determination of the stereochemistry were performed by respectively multidimensional NMR techniques (spectra and assignments are included in appendix E) and LC-MS analysis of a fully hydrolysed pseudodesmin A sample[57]. Later, an X-ray diffraction crystal structure was obtained, allowing the complete stereochemistry to be definitively established[47]. The pseudodesmins are the first viscosin group members in the D-subgroup that possess a glutamine instead of a glutamate residue. Pseudodesmin A can in fact be seen as the amide form of WLIP, or the D-Leu5 epimer of viscosinamide.

NMR was similarly used to determine the covalent structure of pseudodesmin B was determined, while its stereochemistry was assumed to be the same as pseudodesmin A due to the near identical ^{1}H, ^{13}C and ^{15}N chemical shifts and $^{3}J_{HNH\alpha}$ scalar couplings. A difference in stereochemistry would indeed be expected to have a

profound impact on the conformation, and thus on the aforementioned conformation sensitive NMR parameters. In the end, pseudodesmin B only differed from pseudodesmin A by an Ile to Val substitution at position 9, in agreement with a 14 Da mass difference determined via mass spectrometry[47].

Both pseudodesmins were screened against a series of pharmaceutically relevant pathogens[47, 57], including bacteria, fungi and viruses. They were found to be mainly active against Gram positive bacteria, such as methicilin resistant *S. aureus* (MRSA) and vancomycin resistant *Enterococcus* (VRE). However, they are generally less potent and their inhibition spectrum is not as broad as standard antibiotics such as vancomycin. They also do not possess any noteworthy antifungal, antiviral or cytostatic activity. It is interesting to note that pseudodesmin B is generally less active than pseudodesmin A. This would fit an observation that was made for the massetolides[35], which states that the activity seems to correlate with the degree of hydrophobicity of the side chains.

4.5 Solvent dependent behaviour of pseudodesmin A

The appearance of the NMR spectra of pseudodesmin A changes spectacularly depending on the solvent used. Figure 4.4 shows 1D ^{1}H spectra of pseudodesmin A in acetonitrile, acetone, DMF, DMSO, chloroform, dioxane and benzene. The spectra in acetonitrile, acetone and DMF do not show any unexpected features. The spectrum of DMSO however shows several — but not all — resonances to be extensively broadened. The spectra in chloroform and dioxane however also show unexpected line broadening effects, but in this case the effect seems to be present at every resonance. An even more extreme line broadening is observed in benzene.

A second parameter which shows a remarkable solvent dependence is the nOe. The transient ^{1}H-^{1}H nOes in acetonitrile, as measured by a 2D ^{1}H-^{1}H NOESY spectrum (Figure 4.5), again shows nothing out of the ordinary. Since pseudodesmin A is a relatively small molecule and acetonitrile is a low viscous solvent, the ^{1}H-^{1}H cross-correlation rate constants and thus also the nOes are positive (Figure 4.5). In DMSO, the nOe cross-peaks are negative and quite weak. This indicates that the ^{1}H-^{1}H cross-relaxation rate constants are close to the zero-point due to a higher rotational correlation time constant compared to the situation in acetonitrile. This is nothing out of the ordinary since the viscosity at 25℃ in DMSO (1.987 mPa·s) is considerably higher than that of acetonitrile (0.35 mPa·s), effectively reducing the rotational diffusion coefficient (equation (1.43)) and increasing the correlation time constant. The nOe in chloroform is however strongly negative. In addition, a great amount of spin diffusion occurs, which results in every ^{1}H resonance in the spectrum showing a cross-peak with nearly every other ^{1}H resonance. Spin diffusion is a process that

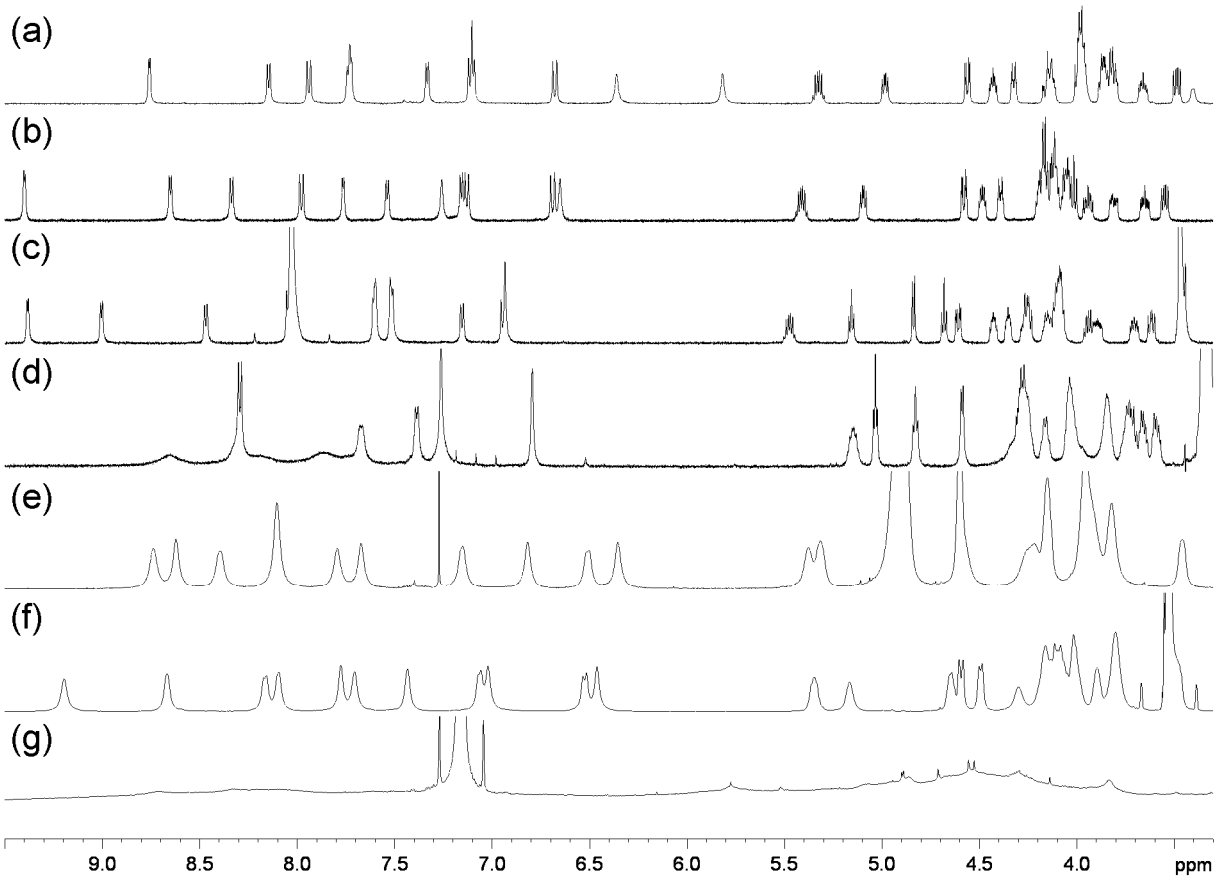

Figure 4.4: 1D ^{1}H spectra of pseudodesmin A in several solvents at 500 MHz and 25℃. (a) acetonitrile; (b) acetone; (c) DMF; (d) DMSO; (e) chloroform; (f) dioxane; (g) benzene (700 MHz).

occurs in a multispin system where the perturbation in magnetisation of spin B through cross-relaxation with spin A occurs so efficiently (equations (3.8)-(3.9)) that it in turn perturbs the magnetisation of spin C through the B-C cross-relaxation[58], which in turn can perturb a fourth spin etc. The effect on the 2D NOESY spectrum is then that the resonance of spin A will not only show cross-peaks with B, but also with C and all other spins the spin diffusion further affects. This is indeed prominently observed for pseudodesmin A in chloroform. Since the cross-relaxation rate constant increases with the correlation time, spin diffusion occurs more efficiently for larger molecular entities. In conclusion, the 2D NOESY spectrum of pseudodesmin A in chloroform suggests a much larger correlation time constant when compared to either acetonitrile or DMSO. This cannot be explained by an effect of viscosity alone, as the viscosity of chloroform (0.537 mPa·s) is not so much higher than that of acetonitrile and quite a bit lower than that of DMSO. The relation between the size of the nOe and the correlation time for all three solvents is summarised in Figure 4.6.

All of this indicates that the line broadening in chloroform is caused by an effective increase in the correlation time constant and this can reasonably only be due to an in size of the molecular entity. The line broadening in DMSO, which is not uniform on all resonances, is not accompanied by an abnormal increase in correlation time. This

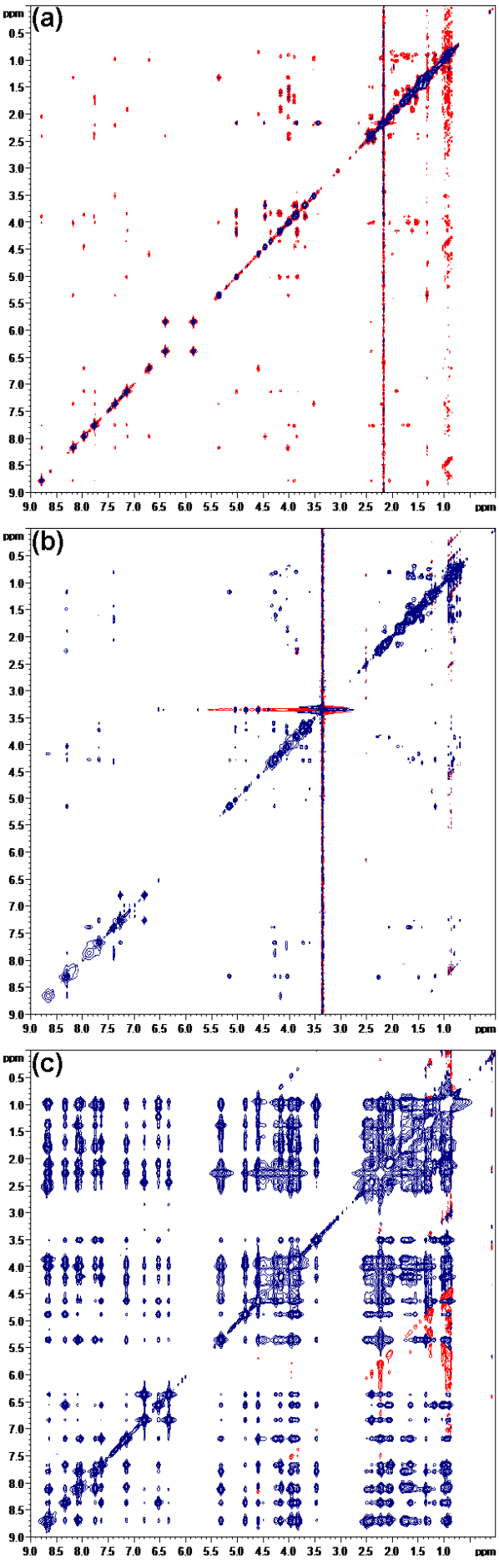

suggests that rather than an increase in apparent molecular size, an exchange broadening occurs tied to conformational processes (see section 5.4 for a more extensive discussion).

It therefore appears that in chloroform, dioxane and benzene, which are non-polar or at most of low polarity and are all low dielectric solvents (Table 4.2), pseudodesmin A must be self-associating to larger complex structures. In the polar solvents (acetonitrile, acetone, DMF and DMSO) this is not the case. It is reasonable to assume that the origin of this self-association in apolar environment can be linked to the formation of transmembrane ion pores in the hydrophobic cellular membrane, which has been hypothesised or observed for several other CLPs, including WLIP.

Table 4.2: Relative dielectric constants and dipole moments of several solvents[59]

solvent	ε_r	μ [D]
DMSO	47	3.96
acetonitrile	37	3.93
acetone	21	2.88
DMF	38	3.82
chloroform	4.8	1.04
dioxane	2.3	0
benzene	2.3	0

The investigation of the nature of the self-association of pseudodesmin A is the main topic of chapters 6 and 7. To be able to gain insight into how the

Figure 4.5: 2D ^{1}H-^{1}H NOESY spectra of pseudodesmin A at 500 MHz and 25℃. (a) acetonitrile, mixing time 200 ms; (b) DMSO, mixing time 300ms; (c) chloroform, between 20-25 mM, mixing time 200 ms. Red cross-peaks represent positive nOes, blue ones are negative.

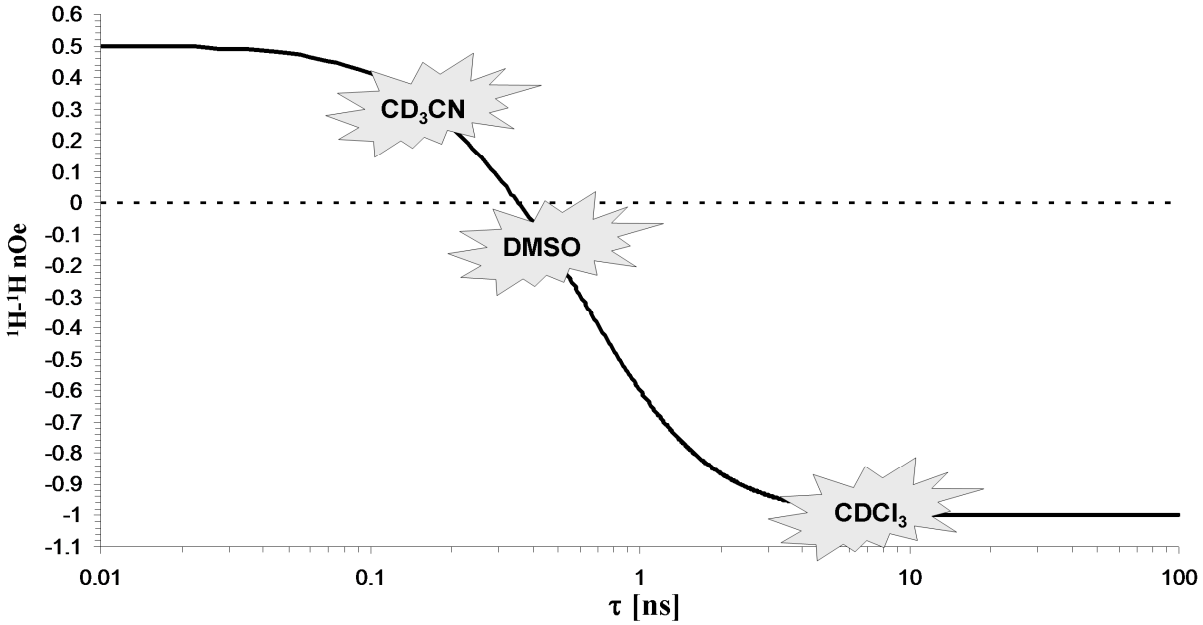

Figure 4.6: The steady state ^{1}H-^{1}H nOe as a function of the correlation time constant at a ^{1}H frequency of 500.13 MHz. The curve can be calculated from equations (3.14), (3.47) and (3.49) by taking $\omega_I = \omega_S = \omega_H$. Although the 2D NOESY spectra use transient nOes, the steady state nOe gives a correct qualitative view. At the low viscosity of acetonitrile, the correlation time constant of pseudodesmin A will be sufficiently small to provide positive nOes. In the viscous DMSO, pseudodesmin A provides small negative nOes due to the increased correlation time constant. In chloroform however, very strongly negative nOes are found, indicating an unexpectedly large correlation time constant.

association occurs molecularly, it is important to establish the conformation of pseudodesmin A in solution, which is presented in Chapter 5.

4.6 References

[1] D. Livermore, "Can better prescribing turn the tide of resistance?". *Nature Reviews Microbiology*, **2004**, *2*(1) 73-78.

[2] J. E. McGowan and F. C. Tenover, "Confronting bacterial resistance in healthcare settings: a crucial role for microbiologists". *Nature Reviews Microbiology*, **2004**, *2*(3) 251-258.

[3] M. Zasloff, "Antimicrobial peptides of multicellular organisms". *Nature*, **2002**, *415*(6870) 389-395.

[4] K. A. Brogden, "Antimicrobial peptides: Pore formers or metabolic inhibitors in bacteria?". *Nature Reviews Microbiology*, **2005**, *3*(3) 238-250.

[5] B. Leitgeb, A. Szekeres, L. Manczinger, C. Vagvolgyi and L. Kredics, "The history of alamethicin: A review of the most extensively studied peptaibol". *Chemistry & Biodiversity*, **2007**, *4*(6) 1027-1051.

[6] A. D. Milov, M. I. Samoilova, Y. D. Tsvetkov, M. Jost, C. Peggion, F. Formaggio, M. Crisma, C. Toniolo, J. W. Handgraaf and J. Raap, "Supramolecular structure of self-assembling alamethicin analog studied by ESR and PELDOR". *Chemistry & Biodiversity*, **2007**, *4*(6) 1275-1298.

[7] C. E. Ballard, H. Yu and B. Wang, "Recent developments in depsipeptide research". *Current Medicinal Chemistry*, **2002**, *9*(4) 471-498.

[8] C. N. Mulligan, R. N. Yong and B. F. Gibbs, "Heavy metal removal from sediments by biosurfactants". *Journal of Hazardous Materials*, **2001**, *85*(1-2) 111-125.

[9] G. Seydlova and J. Svobodova, "Review of surfactin chemical properties and the potential biomedical applications". *Central European Journal of Medicine*, **2008**, *3*(2) 123-133.

[10] C. Carrillo, J. A. Teruel, F. J. Aranda and A. Ortiz, "Molecular mechanism of membrane permeabilization by the peptide antibiotic surfactin". *Biochimica Et Biophysica Acta-Biomembranes*, **2003**, *1611*(1-2) 91-97.

[11] R. Jerala, "Synthetic lipopeptides: a novel class of anti-infectives". *Expert Opinion on Investigational Drugs*, **2007**, *16*(8) 1159-1169.

[12] W. R. P. Scott, S. B. Baek, D. Jung, R. E. W. Hancock and S. K. Straus, "NMR structural studies of the antibiotic lipopeptide daptomycin in DHPC micelles". *Biochimica Et Biophysica Acta-Biomembranes*, **2007**, *1768*(12) 3116-3126.

[13] J. Gewolb, "Bioengineering - Working outside the protein-synthesis rules". *Science*, **2002**, *295*(5563) 2205-2207.

[14] J. M. Raaijmakers, I. de Bruijn and M. J. D. de Kock, "Cyclic lipopeptide production by plant-associated Pseudomonas spp.: Diversity, activity, biosynthesis, and regulation". *Molecular Plant-Microbe Interactions*, **2006**, *19*(7) 699-710.

[15] O. Nybroe and J. Sorensen, "Production of cyclic lipopeptides by fluorescent pseudomonads" in *Pseudomonas Volume III- Macromolecules,* Editor: J.-L. Ramos, Kluwer Academic/Plenum Publishers, New York, **2004**, pp. 147-172.

[16] R. J. Mortishire-Smith, A. F. Drake, J. C. Nutkins and D. H. Williams, "Left-Handed α-Helix Formation by a Bacterial Peptide". *FEBS Letters*, **1991**, *278*(2) 244-246.

[17] J. C. Nutkins, R. J. Mortishiresmith, L. C. Packman, C. L. Brodey, P. B. Rainey, K. Johnstone and D. H. Williams, "Structure Determination of Tolaasin, an Extracellular Lipodepsipeptide Produced by the Mushroom Pathogen Pseudomonas-Tolaasii Paine". *Journal of the American Chemical Society*, **1991**, *113*(7) 2621-2627.

[18] A. Ballio, F. Bossa, L. Camoni, D. DiGiorgio, M. C. Flamand, H. Maraite, G. Nitti, P. Pucci and A. Scaloni, "Structure of fuscopeptins, phytotoxic metabolites of Pseudomonas fuscovaginae". *Febs Letters*, **1996**, *381*(3) 213-216.

[19] A. Ballio, D. Barra, F. Bossa, A. Collina, I. Grgurina, G. Marino, G. Moneti, M. Paci, P. Pucci, A. Segre and M. Simmaco, "Syringopeptins, New Phytotoxic Lipodepsipeptides of Pseudomonas-Syringae Pv Syringae". *FEBS Letters*, **1991**, *291*(1) 109-112.

[20] M. C. Emanuele, A. Scaloni, P. Lavermicocca, N. S. Jacobellis, L. Camoni, D. Di Giorgio, P. Pucci, M. Paci, A. Segre and A. Ballio, "Corpeptins, new bioactive lipodepsipeptides from cultures of Pseudomonas corrugata". *Febs Letters*, **1998**, *433*(3) 317-320.

[21] F. Jourdan, S. Lazzaroni, B. L. Mendez, P. Lo Cantore, M. de Julio, P. Amodeo, N. S. Iacobellis, A. Evidente and A. Motta, "A left-handed α-helix containing both L- and D-amino acids: The solution structure of the antimicrobial lipodepsipeptide tolaasin". *Proteins-Structure Function and Genetics*, **2003**, *52*(4) 534-543.

[22] M. Coraiola, P. Lo Cantore, S. Lazzaroni, A. Evidente, N. S. Lacobellis and M. Dalla Serra, "WLIP and tolaasin I, lipodepsipeptides from Pseudomonas reactans and Pseudomonas tolaasii, permeabilise model membranes". *Biochimica Et Biophysica Acta-Biomembranes*, **2006**, *1758*(11) 1713-1722.

[23] S. Baré, V. M. Coiro, A. Scaloni, A. Di Nola, M. Paci, A. L. Segre and A. Ballio, "Conformations in solution of the fuscopeptins - Phytotoxic metabolites of Pseudomonas fuscovaginae". *European Journal of Biochemistry*, **1999**, *266*(2) 484-492.

[24] C. L. Brodey, P. B. Rainey, M. Tester and K. Johnstone, "Bacterial Blotch Disease of the Cultivated Mushroom Is Caused by an Ion Channel Forming Lipodepsipeptide Toxin". *Molecular Plant-Microbe Interactions*, **1991**, *4*(4) 407-411.

[25] K. H. Cho and Y. K. Kim, "Two types of ion channel formation of tolaasin, a Pseudomonas peptide toxin". *Fems Microbiology Letters*, **2003**, *221*(2) 221-226.

[26] P. Lo Cantore, S. Lazzaroni, M. Coraiola, M. Dalla Serra, C. Cafarchia, A. Evidente and N. S. Iacobellis, "Biological characterization of white line-inducing principle (WLIP) produced by Pseudomonas reactans NCPPB1311". *Molecular Plant-Microbe Interactions*, **2006**, *19*(10) 1113-1120.

[27] M. Dalla Serra, G. Fagiuoli, P. Nordera, I. Bernhart, C. Della Volpe, D. Di Giorgio, A. Ballio and G. Menestrina, "The interaction of lipodepsipeptide toxins from Pseudomonas syringae pv. syringae with biological and model membranes: A comparison of syringotoxin, syringomycin, and two syringopeptins". *Molecular Plant-Microbe Interactions*, **1999**, *12*(5) 391-400.

[28] V. V. Malev, L. V. Schagina, P. A. Gurnev, J. Y. Takemoto, E. M. Nestorovich and S. M. Bezrukov, "Syringomycin E channel: A lipidic pore stabilized by lipopeptide?". *Biophysical Journal*, **2002**, *82*(4) 1985-1994.

[29] M. L. Hutchison, M. A. Tester and D. C. Gross, "Role of Biosurfactant and Ion Channel-Forming Activities of Syringomycin in Transmembrane Ion Flux - a Model for the Mechanism of Action in the Plant-Pathogen Interaction". *Molecular Plant-Microbe Interactions*, **1995**, *8*(4) 610-620.

[30] M. Kochi, D. W. Weiss, L. H. Pugh and V. Groupé, "Viscosin, a new antibiotic". *Bacteriological Proceedings*, **1951**, *1* 29-30.

[31] V. Groupe, L. H. Pugh, D. Weiss and M. Kochi, "Antiviral activity of viscosin". *Proceedings of the Society for Experimental Biology and Medicine*, **1951**, *78*(1) 354-358.

[32] M. Hiramoto, K. Okada and S. Nagai, "Revised structure of viscosin, a peptide antibiotic". *Tetrahedron Letters*, **1970**(13) 1087-90.

[33] M. V. Laycock, P. D. Hildebrand, P. Thibault, J. A. Walter and J. L. C. Wright, "Viscosin, a Potent Peptidolipid Biosurfactant and Phytopathogenic Mediator Produced by a Pectolytic Strain of Pseudomonas-Fluorescens". *Journal of Agricultural and Food Chemistry*, **1991**, *39*(3) 483-489.

[34] H. S. Saini, B. E. Barragan-Huerta, A. Lebron-Paler, J. E. Pemberton, R. R. Vazquez, A. M. Burns, M. T. Marron, C. J. Seliga, A. A. L. Gunatilaka and R. M. Maier, "Efficient purification of the biosurfactant viscosin from *Pseudomonas libanensis* strain M9-3 and its physicochemical and biological properties". *Journal of Natural Products*, **2008**, *71*(6) 1011-1015.

[35] J. Gerard, R. Lloyd, T. Barsby, P. Haden, M. T. Kelly and R. J. Andersen, "Massetolides A-H, antimycobacterial cyclic depsipeptides produced by two pseudomonads isolated from marine habitats". *Journal of Natural Products*, **1997**, *60*(3) 223-229.

[36] R. J. Mortishire-Smith, J. C. Nutkins, L. C. Packman, C. L. Brodey, P. B. Rainey, K. Johnstone and D. H. Williams, "Determination of the Structure of an Extracellular Peptide Produced by the Mushroom Saprotroph Pseudomonas-Reactans". *Tetrahedron*, **1991**, *47*(22) 3645-3654.

[37] C. Soler-Rivas, N. Arpin, J. M. Olivier and H. J. Wichers, "WLIP, a lipodepsipeptide of Pseudomonas 'reactans', as inhibitor of the symptoms of the brown blotch disease of Agaricus bisporus". *Journal of Applied Microbiology*, **1999**, *86*(4) 635-641.

[38] D. Sinnaeve, P. M. S. Hendrickx, J. Van hemel, E. Peys, B. Kieffer and J. C. Martins, "The Solution Structure and Self-Association Properties of the Cyclic Lipodepsipeptide Pseudodesmin A Support Its Pore-Forming Potential". *Chemistry-a European Journal*, **2009**, *15*(46) 12653-12662.

[39] F. S. Han, R. J. Mortishire-Smith, P. B. Rainey and D. H. Williams, "Structure of the White-Line-Inducing Principle Isolated from *Pseudomonas Reactans*". *Acta Crystallographica Section C-Crystal Structure Communications*, **1992**, *48* 1965-1968.

[40] M. N. Nielsen, J. Sorensen, J. Fels and H. C. Pedersen, "Secondary metabolite- and endochitinase-dependent antagonism toward plant-pathogenic microfungi of Pseudomonas fluorescens isolates from sugar beet rhizosphere". *Applied and Environmental Microbiology*, **1998**, *64*(10) 3563-3569.

[41] T. H. Nielsen, C. Christophersen, U. Anthoni and J. Sorensen, "Viscosinamide, a new cyclic depsipeptide with surfactant and antifungal properties produced by Pseudomonas fluorescens DR54". *Journal of Applied Microbiology*, **1999**, *87*(1) 80-90.

[42] M. Hansen, C. Thrane, S. Olsson and J. Sorensen, "Confocal imaging of living fungal hyphae challenged with the fungal antagonist viscosinamide". *Mycologia*, **2000**, *92*(2) 216-221.

[43] C. Thrane, T. H. Nielsen, M. N. Nielsen, J. Sorensen and S. Olsson, "Viscosinamide-producing Pseudomonas fluorescens DR54 exerts a biocontrol effect on Pythium ultimum in sugar beet rhizosphere". *Fems Microbiology Ecology*, **2000**, *33*(2) 139-146.

[44] C. Thrane, S. Olsson, T. H. Nielsen and J. Sorensen, "Vital fluorescent stains for detection of stress in Pythium ultimum and Rhizoctonia solani challenged with viscosinamide from Pseudomonas fluorescens DR54". *FEMS Microbiology Ecology*, **1999**, *30*(1) 11-23.

[45] M. S. C. Pedras, N. Ismail, J. W. Quail and S. M. Boyetchko, "Structure, chemistry, and biological activity of pseudophomins A and B, new cyclic lipodepsipeptides isolated from the biocontrol bacterium Pseudomonas fluorescens". *Phytochemistry*, **2003**, *62*(7) 1105-1114.

[46] J. W. Quail, N. Ismail, M. S. C. Pedras and S. M. Boyetchko, "Pseudophomins A and B, a class of cyclic lipodepsipeptides isolated from a Pseudomonas species". *Acta Crystallographica Section C-Crystal Structure Communications*, **2002**, *58* o268-o271.

[47] D. Sinnaeve, C. Michaux, J. Van hemel, J. Vandenkerckhove, E. Peys, F. A. M. Borremans, B. Sas, J. Wouters and J. C. Martins, "Structure and X-ray conformation of pseudodesmins A and B, two new cyclic lipodepsipeptides from *Pseudomonas* bacteria". *Tetrahedron*, **2009**, *65*(21) 4173-4181.

[48] D. Sorensen, T. H. Nielsen, C. Christophersen, J. Sorensen and M. Gajhede, "Cyclic lipoundecapeptide amphisin from Pseudomonas sp strain DSS73". *Acta Crystallographica Section C-Crystal Structure Communications*, **2001**, *57* 1123-1124.

[49] T. H. Nielsen, C. Thrane, C. Christophersen, U. Anthoni and J. Sorensen, "Structure, production characteristics and fungal antagonism of tensin - a new antifungal cyclic lipopeptide from Pseudomonas fluorescens strain 96.578". *Journal of Applied Microbiology*, **2000**, *89*(6) 992-1001.

[50] H. Ui, T. Miyake, H. Iinuma, M. Imoto, S. Hattori, M. Hamada, T. Takeuchi, S. Umezawa and K. Umezawa, "A Novel Cyclic Lipoundecapeptide, Pholipeptin, Isolated from Pseudomonas Sp". *Tetrahedron Letters*, **1995**, *36*(41) 7479-7480.

[51] H. Ui, T. Miyake, H. Iinuma, M. Imoto, H. Naganawa, S. Hattori, M. Hamada, T. Takeuchi, S. Umezawa and K. Umezawa, "Pholipeptin, a novel cyclic lipoundecapeptide from Pseudomonas fluorescens". *Journal of Organic Chemistry*, **1997**, *62*(1) 103-108.

[52] D. Sorensen, T. H. Nielsen, J. Sorensen and C. Christophersen, "Cyclic lipoundecapeptide lokisin from Pseudomonas sp strain DSS41". *Tetrahedron Letters*, **2002**, *43*(25) 4421-4423.

[53] M. Morikawa, H. Daido, T. Takao, S. Murata, Y. Shimonishi and T. Imanaka, "A New Lipopeptide Biosurfactant Produced by Arthrobacter Sp Strain Mis38". *Journal of Bacteriology*, **1993**, *175*(20) 6459-6466.

[54] A. Henriksen, U. Anthoni, T. H. Nielsen, J. Sorensen, C. Christophersen and M. Gajhede, "Cyclic lipoundecapeptide tensin from Pseudomonas fluorescens strain 96.578". *Acta Crystallographica Section C-Crystal Structure Communications*, **2000**, *56* 113-115.

[55] M. Morikawa, Y. Hirata and T. Imanaka, "A study on the structure-function relationship of lipopeptide biosurfactants". *Biochimica Et Biophysica Acta-Molecular and Cell Biology of Lipids*, **2000**, *1488*(3) 211-218.

[56] R. M. Austin, Jr., J. Van hemel, B. Sas and J. Vanderkerckhove, "Antibiotics from bacteria isolated from amphibian skin". W. I. P. Organization, **2002** Kemin Industries, Inc. & Plethodon Research, L.L.D.

[57] D. Sinnaeve, Licentiaatsthesis, **2005**, "Gevorderde Structuuranalyse van een Recent Geïsoleerd Natuurproduct met Behulp van NMR Spectroscopie" Universiteit Gent (Gent).

[58] D. Neuhaus and M. P. Williamson, "The Nuclear Overhauser Effect in Structural and Conformational Analysis", 2nd ed., **2000**, New York, John Wiley and Sons Ltd.

[59] "Handbook of Chemistry and Physics 90th Edition", Editor: D. R. Lide, CRC Press, Boca Raton, FL., **2009-2010**.

5 Conformational analysis of pseudodesmin A

5.1 Introduction

The conformation of an individual pseudodesmin A molecule is a very relevant piece of information for understanding the origin, the mechanism and ultimately the biological relevance of the self-association. The first conformation that could be obtained for pseudodesmin A was through a crystal structure obtained by X-ray diffraction analysis[1] (section 5.2). The main relevance of the crystal structure was to establish the absolute stereochemistry of pseudodesmin A, which at the time was only partly known[2]. Not surprisingly, the resulting structure closely resembles the previously established crystal structures of WLIP[3] and pseudophomin A[4]. However, it was important to establish the conformation in solution as well, since the only solution structure ever reported of a member of the D-subgroup of the viscosin group, WLIP, was reported to be significantly different from its crystal structure[3, 5]. Since the analysis of WLIP was performed in DMSO solution, this solvent was the first choice for the conformational analysis of pseudodesmin A. There were however several complications when using DMSO (section 5.4). It eventually turned out that in DMSO an exchange process takes place between two or multiple conformations and the use of this solvent was eventually abandoned. Afterwards it was found that this conformational exchange did not take place in other polar, non-self-association inducing solvents. Acetonitrile was eventually the solvent of choice to continue the solution structure determination by NMR, as described in section 5.3. This choice was partly based on the fact that the crystals for the X-ray diffraction study were

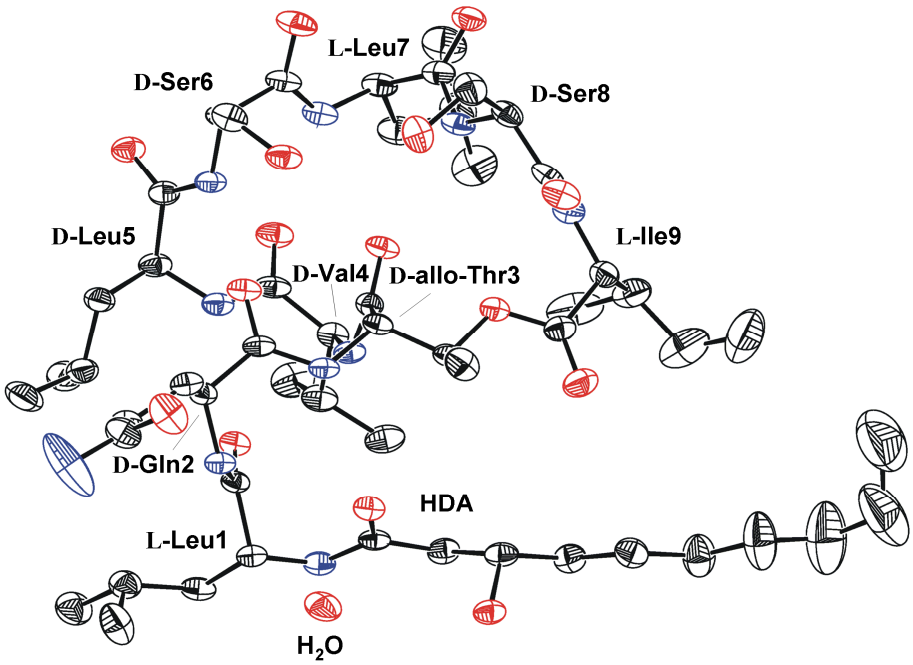

Figure 5.1: Crystal structure of pseudodesmin A with the ellipsoids representing the B-factors. Carbon atoms are coloured black, oxygen atoms red and nitrogen atoms blue.

obtained from an acetonitrile solution. In the end, the obtained acetonitrile solution structure appeared to be similar to the crystal structure. Finally, by comparing the $^{3}J_{HNH\alpha}$ scalar couplings – defining the backbone φ angles – of the monomer form measured in acetonitrile with those of the oligomer form measured in chloroform, it could be established that the monomer conformation in the supramolecular complex is retained (section 5.5). These results have been published as D. Sinnaeve *et al*, *Chemistry-a European Journal*, **2009**, 15(46) 12653-12662.

5.2 Crystal structure

Pseudodesmin A crystals of sufficient quality for X-ray diffraction analysis were obtained by slow evaporation from a concentrated solution in acetonitrile. The crystallisation trials, recording of the X-ray diffraction pattern and crystal structure elucidation were performed by Dr. Catherine Michaux of the Laboratoire de Chimie Biologique, Université de Namur. Details concerning the methods used are described elsewhere[1]. The pseudodesmin A crystal structure with ellipsoids representing the B-factors is presented in Figure 5.1. The crystal system is orthorhombic, having the space group $P2_12_12_1$, with a single water molecule present per unit cell.

The main structural feature of the conformation is a short left-handed α-helix ranging from the D-Gln2 to the D-Leu5 residues (Figure 5.2a). This is confirmed by the main chain φ and ψ torsion angles for these residues (Table 5.1) which are indeed close to the typical left handed α-helix values of about 60° and 45° respectively. In addition,

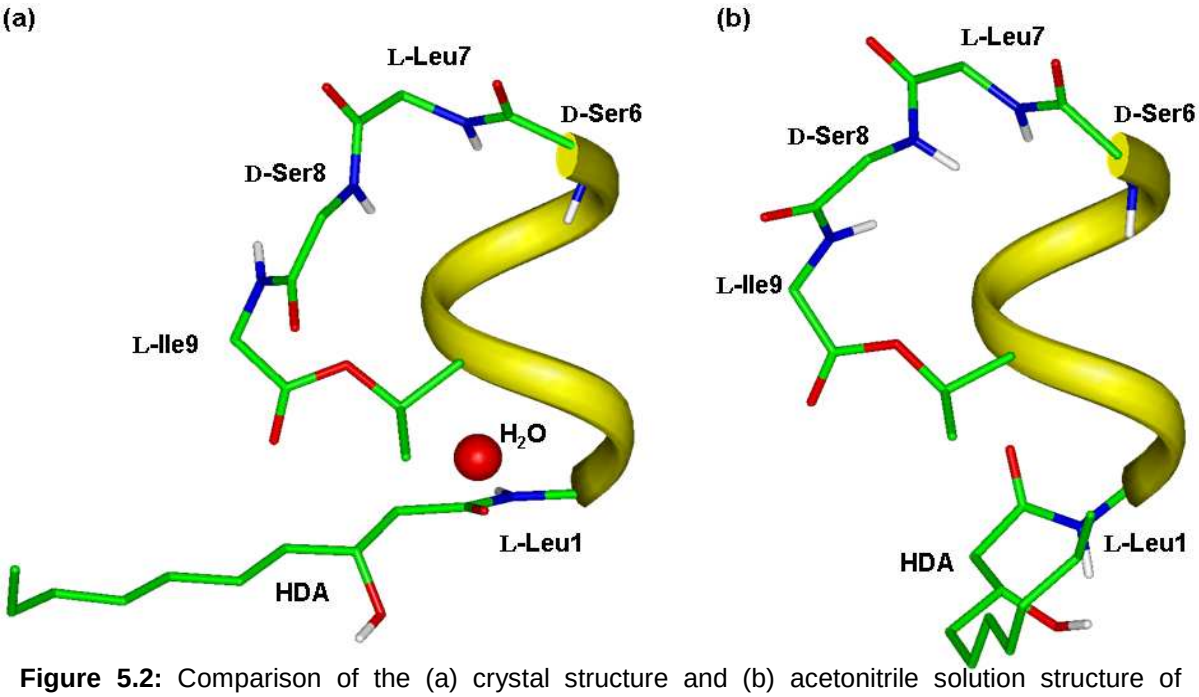

Figure 5.2: Comparison of the (a) crystal structure and (b) acetonitrile solution structure of pseudodesmin A. Only the main chain atoms are shown, while the left-handed α-helix structure is represented by a ribbon. Note the difference in the loop structure at level of Ile9.

the intramolecular hydrogen bonds within this helix structure (Table 5.2) show the typical i+4→i pattern (Leu5 NH → Leu1 CO and Ser6 NH → Gln2 CO). Note that a hydrogen bond is considered to have a donor-acceptor distance of at most 3.4 Å and a bond angle of at least 140°. The helix structure is followed by a type I' β-turn, which possesses its characteristic hydrogen bond (Leu7 NH → Val4 CO). The φ/ψ torsion angles of Leu5/Ser6 indeed fit nicely to the theoretical type I' β-turn (60°, 30°, 90°, 0°) [6]. This reverse turn is possible owing to the L-configuration of Leu7 and it allows to cap one of the free carbonyl groups at the C-terminal side of the helix. Preceding the helix, a type II β-turn is present together with its characteristic hydrogen bond (Thr3 NH → HDA CO). The Leu1/Gln2 φ/ψ torsion angles agree reasonably well with the canonical values of type II β-turn (-60°, 120°, 80°, 0°).

The second structural feature is a three residue loop formed by Leu7-Ser8-Ile9. The alternating L-D-L configuration in this tripeptide segment allows the backbone to loop back and bring the carboxylic end of the main chain in an adequate position to form the lactone bond with the Thr3 side chain. The loop thus locks the N- and C-terminal ends of the α_L-helix together. In addition, this configuration pattern assures that the hydrophilic side chain of Ser8 is directed to the other side of the molecule when compared to the hydrophobic Leu7 and Ile9 side chains. The Ser8 NH group forms a hydrogen bond with the Thr3 CO group, thus capping a second helix C-terminal CO group next to Val4 CO.

Table 5.1: φ and ψ torsion angles of the pseudodesmin A crystal and solution structures

		Leu1	Gln2	Thr3	Val4	Leu5	Ser6	Leu7	Ser8	Ile9
crystal	φ [°]	-60.9	57.09	63.33	61.78	63.12	98.05	-66.43	150.66	-65.99
	ψ [°]	122.69	28.52	40.47	48.59	31.68	1.01	-50.62	-41.21	-6.31
NMR	φ[a] [°]	12.00	61.40	69.47	64.01	55.50	65.15	-66.01	107.00	-118.10
	S^{2}[b]	0.16	0.96	0.97	0.97	0.98	0.97	0.97	0.93	0.92
	Stan. Dev.[c] [°]	73.19	10.57	9.89	9.01	7.87	9.10	9.23	14.01	15.49
	ψ[a] [°]	62.07	38.36	37.90	46.52	45.26	22.38	-24.84	18.65	-4.09
	S^{2}[b]	0.99	0.97	1.00	1.00	1.00	1.00	0.99	0.99	0.99
	Stan. Dev.[c] [°]	6.38	8.62	3.05	2.34	0.78	3.42	4.18	6.18	3.95

[a] Average value of the 40 lowest energy structures. The average of an angle α is defined using the average of the cosine and sine values over all structures: $[\alpha]=\arctan[\langle\sin(\alpha)\rangle/\langle\cos(\alpha)\rangle]+k180°$, with $k=0$ if $\langle\cos(\alpha)\rangle > 0$, $k=1$ if $\langle\cos(\alpha)\rangle < 0$ and $\langle\sin(\alpha)\rangle > 0$ and $k=-1$ if $\langle\cos(\alpha)\rangle < 0$ and $\langle\sin(\alpha)\rangle < 0$.
[b] Squared order parameter according to equation (5.3)
[c] Standard deviation according to equation (5.4)

Table 5.2: Hydrogen bonds in the pseudodesmin A crystal structure

Intramolecular				
Donor		Acceptor	d(D-A) [Å]	angle [°]
Thr3 NH	-	HDA CO	2.95	152.05
Leu5 NH	-	Leu1 CO	3.15	165.35
Ser6 NH	-	Gln2 CO	2.82	149.16
Leu7 NH	-	Val4 CO	3.18	151.21
Ser8 NH	-	Thr3 CO	2.92	168.02
Intermolecular				
Participants			d(D-A) [Å]	angle [°]
HDA OH	-	Ser6 OH[a]	2.85	--
HDA CO	-	Ser8 OH[a]	2.79	160.87
Leu1 NH	-	H_2O[b]	2.83	164.69
Gln2 NH	-	Ser8 CO[a]	2.85	164.38
Val4 CO	-	Gln2 $CONH_2$[c]	2.78	168.51
Leu5 CO	-	Ile9 NH[d]	2.93	139.53
Ser6 CO	-	H_2O[e]	2.77	165.73
Leu7 CO	-	H_2O[e]	2.81	151.60

[a] 2nd participant coordinates are (x-1/2,3/2-y,1-z)
[b] 2nd participant coordinates are (x,y,z)
[c] 2nd participant coordinates are (1/2-x,1-y,z-1/2)
[d] 2nd participant coordinates are (x+1,y,z)

Several intermolecular hydrogen bonds are present in the crystal structure, as listed in Table 5.2. All main chain carbonyl groups from the HDA moiety to the Val4 residue were already involved in intramolecular hydrogen bonds. The Val4 CO is additionally involved in a second hydrogen bond, which is intermolecular and to the Gln2 side chain amide group. The Leu5 CO participates in an intermolecular hydrogen bond with the Ile9 NH of a neighbouring pseudodesmin A molecule. The Ser6 and Leu7 carbonyl groups are hydrogen bonded to the co-crystallised water molecule, while the Ser8 carbonyl group is involved in an intermolecular hydrogen bond with the Gln2 NH.

Only the Ile9 carbonyl group is not involved in any polar contact. Besides acting as a hydrogen bond donor to the Ser6 and Leu7 carbonyl groups, the water molecule is a hydrogen bond acceptor for the Leu1 NH group. Finally, both Ser side chain hydroxyl groups are involved in intermolecular contacts with the HDA moiety.

The organization of the individual molecules is such that the hydrophobic side chains are packed together, delimiting large spaces between different units. The long alkyl chain of the HDA extends out into these spaces, where the high B-factors at the end of this chain indicate a higher degree of motional freedom.

Given the sequence similarity, it is not surprising that the pseudodesmin A crystal structure is nearly identical to those of WLIP[3] and pseudophomin A[4]. The root mean square difference (RMSD) between the pseudodesmin A and both molecules, measured along the oligopeptide backbone and the Thr3 side chain (29 atoms), is in both cases less than 0.03 Å. Although the presence of a Glu instead of a Gln in both WLIP and pseudophomin A implies substitution of a carboxylate by an amide function, two electrostatically different functional groups, it appears to have practically no influence on the orientation of the Glx side chain within the crystal structure. Because of the similarity of the residue sequence, the crystal structures of amphisin[7] and tensin[8] are very comparable. They also possess a left-handed α-helix structure of about as many residues followed by a somewhat longer loop. The RMSD of the backbone of the helix to the pseudodesmin A structure measured starting from the amide group of residue 2 to the carbonyl group of residue 5 (12 atoms) is only 0.15 Å for amphisin and 0.12 Å for tensin.

5.3 Solution structure

5.3.1 Collection of distance restraints

As described in section 3.2.4, the nOe increases linearly with the mixing time before auto-relaxation becomes significant, with a slope proportional to the cross-relaxation rate between both spins. This is also valid for the rOe, which is measured in a ^{1}H-^{1}H 2D ROESY spectrum and is dominated by transverse auto- and cross-relaxation instead of longitudinal relaxation. The cross-relaxation rate constant is inversely proportional to (the average of) the sixth power of the internuclear distance because it is governed by the dipole-dipole relaxation mechanism, which has this dependence; *i.e.* equations (3.59) and (3.62) in the case of longitudinal cross-relaxation. For short mixing times, the nOe (and also rOe) is linearly proportional to the cross-relaxation rate constant and independent of the auto-relaxation rate constant, see equation (3.11). The following relation therefore exists:

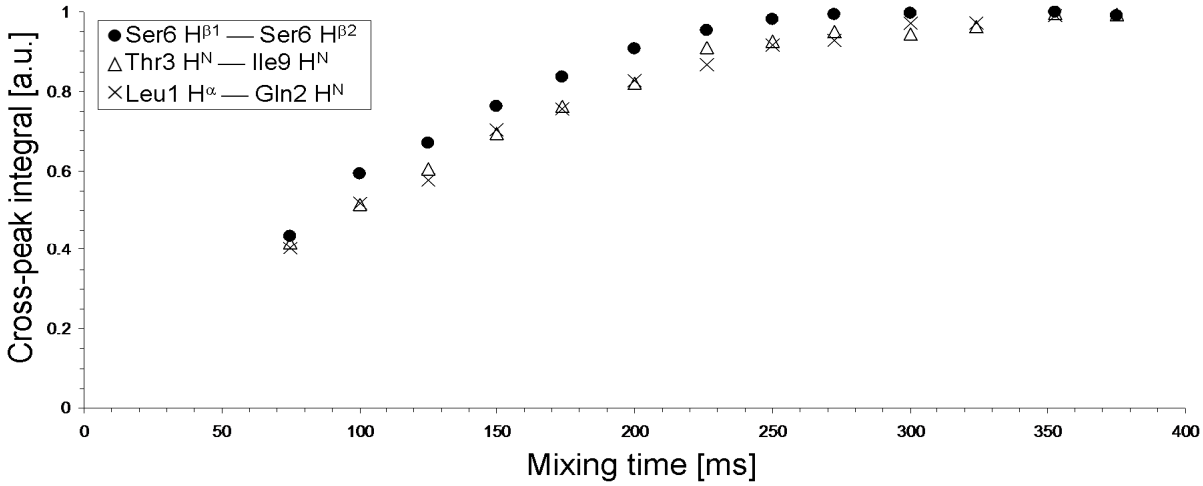

Figure 5.3: Build-up curves for a selected number of ROESY cross-peaks. The build-up curves appear to be linear up to 200 ms.

$$\frac{r_{AB}}{r_{CD}} = \left(\frac{\mathrm{rOe}[\mathrm{C\text{-}D}]}{\mathrm{rOe}[\mathrm{A\text{-}B}]} \right)^{1/6} \tag{5.1}$$

If the distance between the nuclei C and D is known and both rOes can be measured, the internuclear distance between A and B can be calculated. For this to be valid, it is important to be in the initial rate regime where the linear increase of the rOe with the mixing time is well approximated. For this purpose, a series of off-resonance ^{1}H-^{1}H 2D ROESY spectra at 500.13 MHz were recorded, for which the build-up of the integral of a number of selected cross-peaks was monitored as a function of the mixing time (Figure 5.3). Based on these results, a mixing time of 174 ms was chosen, since at this mixing time the rOes are most intense, while still appearing to be within the initial rate regime. A definitive ^{1}H-^{1}H 2D ROESY spectrum was recorded at 700.13 MHz at 25 ℃ to take advantage of the higher resolution. Since the transverse relaxation has a low dependence on field strength, it was assumed that the optimal mixing time does not differ significantly. It is from this 700.13 MHz spectrum that ^{1}H-^{1}H distance restraints for restrained molecular modelling were obtained.

All unambiguously assigned cross-peaks in the ROESY spectrum were integrated using the CCPNMR software[9]. For each ^{1}H-^{1}H pair, both symmetric cross-peaks were integrated and averaged when possible. When a resonance represents equivalent protons (such as in a methyl group), the integral was corrected for the multiplicity (*e.g.* a rOe between two methyl groups would be divided by a factor 9). It was assumed that the interproton distance within a CH_2 group was 1.74 Å[10]. Therefore, the average value of the rOes between the geminal protons in the Leu5 CH_2^{β}, the Leu7 CH_2^{β}, the Ser8 CH_2^{β} and the Ile9 CH_2^{γ} was calibrated to correspond to this value. The Leu1 CH_2^{β} and Ser6 CH_2^{β} rOes deviated significantly from the aforementioned CH_2 groups and were therefore not taken up into the average. Since during the modelling only upper value distance restraints were implemented, the

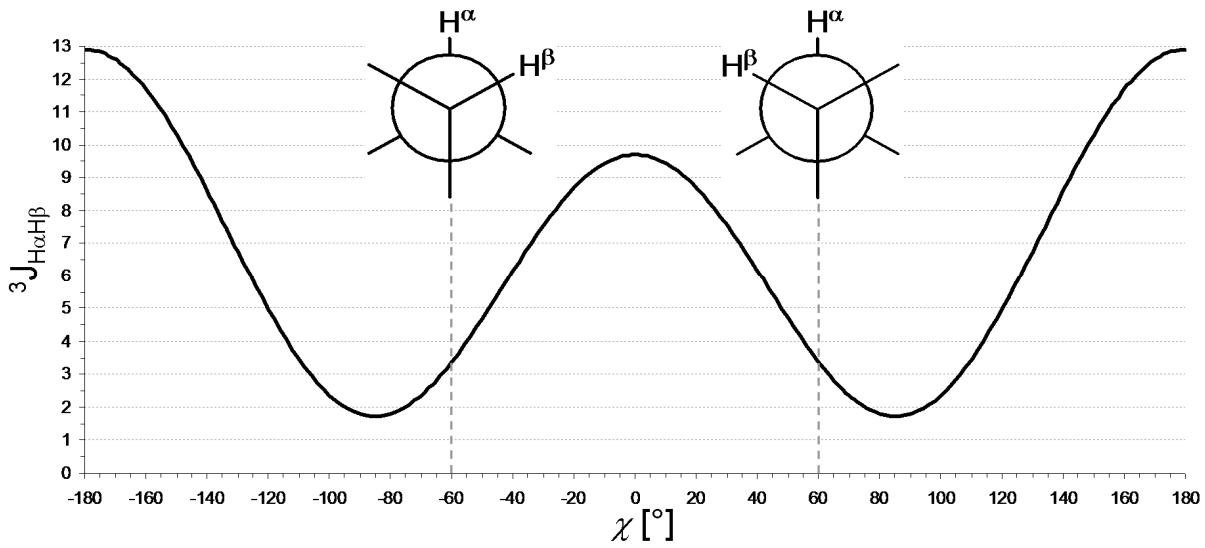

Figure 5.4: Karplus curve by Demarco *et al* (equation (5.2)) for $H^{\alpha}H^{\beta}$ scalar couplings in amino acid residues.

resulting interproton distances were multiplied with a factor 1.1 in order to prevent too tight constraints during the energy minimisation. In the case of equivalent or non-stereospecifically assigned protons, pseudo atom corrections were applied as described in the book of Neuhaus and Williamson [10]. In total, 127 distances were collected (Table 5.3 and appendix G).

Scalar coupling constants between the CH_2^{β} protons and the H^{α} proton, together with the rOe intensity information involving the CH_2^{β} protons, can reveal the diastereospecific resonance assignment of these two geminal protons. These couplings were measured using the SERF experiment[11] (appendix F) and are listed in Table 5.4. The $^3J_{H\alpha H\beta}$ scalar coupling depends on the torsion angle χ between both protons, which is described by a Karplus curve. In this case, a Karplus curve is used with the parameterisation described by Demarco *et al*[12] (Figure 5.4):

$$^3J_{H\alpha H\beta} = 9.5\cos^2\chi - 1.6\cos\chi + 1.8 \qquad (5.2)$$

Table 5.3: Overview of the number of distance restraints

	HDA	Leu1	Gln2	Thr3	Val4	Leu5	Ser6	Leu7	Ser8	Ile9
HDA	4									
Leu1	4	5								
Gln2	1	3	6							
Thr3	1	1	3	3						
Val4	0	2	0	5	7					
Leu5	0	0	0	0	3	11				
Ser6	0	0	0	3	0	4	8			
Leu7	0	0	0	0	3	1	0	6		
Ser8	0	0	0	1	1	0	2	4	8	
Ile9	0	0	0	5	3	0	1	2	4	12
Total	10	15	13	22	24	19	18	16	20	27

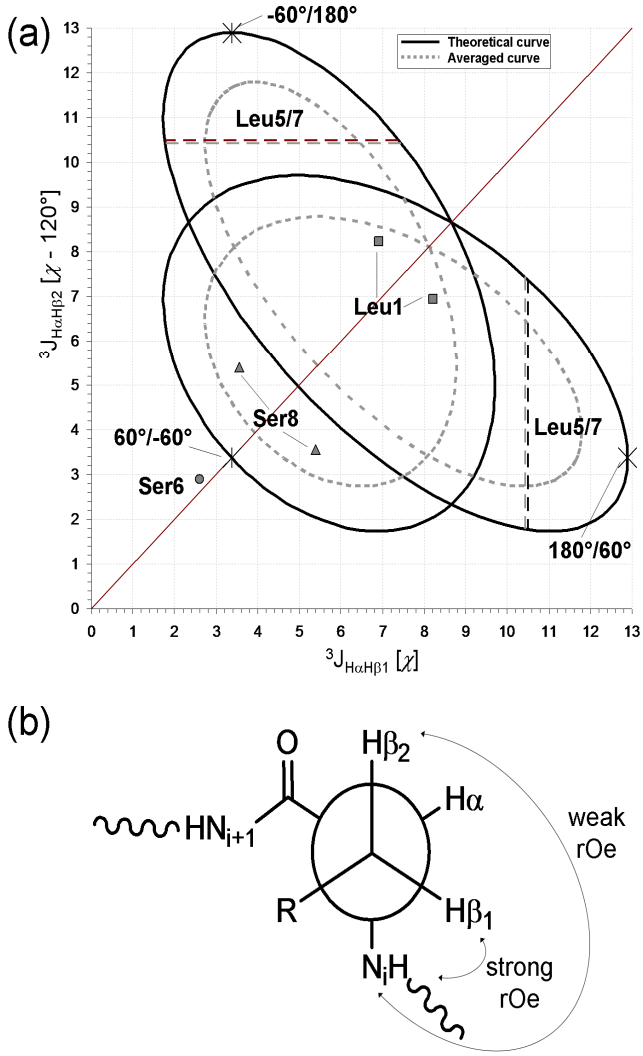

Figure 5.5: (a) The full line in the diagram shows the possible theoretical combinations of $J_{H\alpha H\beta 1}$ and $J_{H\alpha H\beta 2}$ scalar couplings based on the Karplus relation of Demarco *et al* (equation (5.2)). The grey dotted line shows a moving average, weighted using a Gaussian distribution with a standard deviation of 20°. This illustrates the effect of ti me averaged motion on the possible scalar coupling combinations. The diagonal line through the plot illustrates the symmetry of the diagram. The three possible staggered conformations are indicated on the diagram (∗), corresponding with the $H^{\alpha}H^{\beta 1}/H^{\alpha}H^{\beta 2}$ torsion angles of 60°/-60°, 180°/60° and -60°/180° . The experimental scalar couplings for each residue are indicated on the diagram. For all residues except for Ser6, no stereospecific assignment could be made and therefore there are two theoretically possible (symmetric) positions on the diagram. For Leu7 and Leu5, only one of the two scalar couplings could be determined and therefore the theoretically possible second scalar coupling values are indicated by two pairs of symmetric dashed line. (b) Stereospecific assignment for the H^{β} protons in a residue with D configuration, assuming the dominant rotamer having $H^{\alpha}H^{\beta 1}/H^{\alpha}H^{\beta 2}$ torsion angles of 60°/-60°. The Newman projection along the C^{α}-C^{β} bond illustrates how the rOes between H^{α} and the two H^{β} protons should be similar in size, while the rOe with the H^{N} proton is stronger for $H^{\beta 1}$ than for $H^{\beta 2}$ due to the spatial proximity. In the case of Ser6 which in (a) was shown to be in this rotamer, these observations were clearly made and the two H^{β} resonances could be assigned to $H^{\beta 1}$ (3.81 ppm) and $H^{\beta 2}$ (4.15 ppm).

Table 5.4: Overview of the number of the $H^{\alpha}H^{\beta}$ couplings

residue	$^3J_{H\alpha H\beta 1}$ [Hz]	$^3J_{H\alpha H\beta 2}$ [Hz]
Leu1	6.93	8.23
Thr3	10.71	--
Val4	10.65	--
Leu5	10.50	N.D.[a]
Ser6	2.60	2.90
Leu7	10.43	N.D.[a]
Ser8	5.39	3.56

[a] N.D. = not determined

Since there exists a constant phase difference of 120° between the $H^{\alpha}H^{\beta 1}$ and $H^{\alpha}H^{\beta 2}$ torsion angles, the $^3J_{H\alpha H\beta 1}$ can be plotted against $^3J_{H\alpha H\beta 2}$ to provide the diagram represented in Figure 5.5a[13]. When on this diagram the experimental scalar coupling values are plotted, a quick assessment of the rotamer present along the C^{α}-C^{β} bond can be achieved. When this information is combined with rOe intensity information, as illustrated in Figure 5.5b, the diastereotopic identity of the two H^{β} protons can in principle be established. However, when fast rotational flexibility around the C^{α}-C^{β} bond exists, a weighted average will be found for the experimental scalar coupling values. This results in a 'contracted' diagram as seen in Figure 5.5a. From the experimental data points in Figure 5.5a, it can be concluded that fast torsional flexibility exists for Ser8 and especially Leu1. In the case of the latter, this observation completely undermines any possibility to perform the stereospecific methylene assignment, as the experimental values lay far away from the three expected staggered conformations. In the case of Ser8, it can still be safely concluded that the 60°/-60° staggered conformation is dominant. For both Leu5 and Leu7, only one of the two $^3J_{H\alpha H\beta}$ values could be obtained, the other one most likely being too small to be picked up by the SERF experiment. This single value obtained suggests the dominant rotamer to have the -60°/180° or 180°/60° $H^{\alpha}H^{\beta 1}/H^{\alpha}H^{\beta 2}$ torsion angles, but no definite conclusion can be made. The Ser6 scalar couplings on the other hand do indicate a rigid rotamer conformation.

In the end, only for the Ser6 CH_2^{β} protons sufficiently obtained rOe data was available to allow the diastereotopic assigned with good confidence (Figure 5.5b). Also, the diastereotopic methyl groups of the Val4 side chain could be assigned with good confidence, as illustrated and discussed in Figure 5.6.

5.3.2 Molecular modelling

The obtained values were used as upper distance restraints in a molecular modelling procedure using the cff91 force field[14] within DISCOVER 2.98 (Accelrys, San Diego,

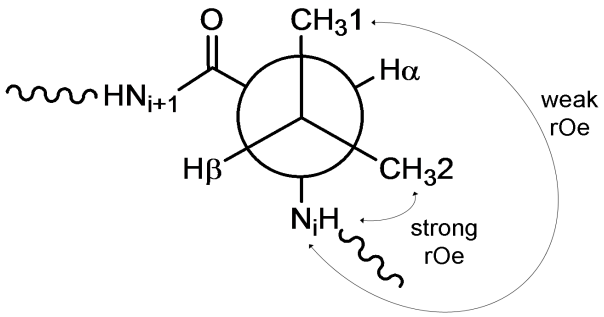

Figure 5.6: Stereospecific assignment of the two methyl groups of Val4. The large experimental $J_{H\alpha H\beta}$ scalar coupling of 10.65 Hz shows that the H^{α} and H^{β} protons to be mostly antiparallel towards each other over time. The Newman projection along the C^{α}-C^{β} bond then illustrates how the two methyl groups should differ in rOe intensity with the H^{N} proton. This was the case for Val4 and the stereospecific assignment for the two methyl groups CH_31 (0.92 ppm) and CH_32 (0.95 ppm) could be performed.

CA, USA) running on an IBM intellisation ZPro under Redhat Linux WS4. The restraints were enforced as a flat-bottomed harmonic potential with a force constant of 10 kcal·mol^{-1}Å^{-2} and a maximum energy penalty of 1000 kcal·mol^{-1}. The peptide bonds were additionally restrained to their trans configuration by adding restraints to the ω torsion angles with a force constant of 100 kcal·mol^{-1}deg^{-2} when the deviation from the ideal 180° exceeded 5°. After building the molecule within the Accelrys Insight II suite, the molecular modelling procedure went as follows. A set of 100 starting structures was obtained by sampling every 5 ps of the last 500 ps of a 50 ps unrestrained molecular dynamics (MD) simulation at 1000 K. Each of these structures were optimized using steepest descents restrained (EM) until the maximum gradient of the total energy was smaller than 2.0 kcal·mol^{-1}Å^{-1}. The weighting factor for the experimental restraints was set to 0.1 during this optimization. This additional step was found necessary for a robust implementation of the simulated annealing protocol. Afterwards, the simulated annealing protocol was performed using a series of 5 consecutive MD simulations at different temperatures (900, 800, 600, 400 and 300K) in which the experimental restraints were gradually enforced. The durations of the initial and final MD simulations at 900K and 300K were set to 5.0 ps and 4.0 ps respectively. For each other temperature a 0.9 ps simulation was performed. The weighting factor for the introduction of the restraints at each temperature was 0.3, 0.7, 1.0, 1.0 and 1.0. Finally, the energy of the obtained structure was optimized by 100 steps of steepest descents restrained EM follow by a conjugate gradients restrained EM until the maximum gradient of the total energy was smaller than 0.0001 kcal·mol^{-1}Å^{-1}, or in other words, a minimum in the potential energy function was reached.

The resulting total energy and restraint energy contribution for each of the 100 structures is shown graphically in Figure 5.7. The graph, which sorts the structures according to the total energy, shows that for both the total energy and the restraint energy the *ca.* 40 lowest energy structures have converged to a plateau value. This is also reflected in the torsion angles φ and ψ of the oligopeptide main chain, which

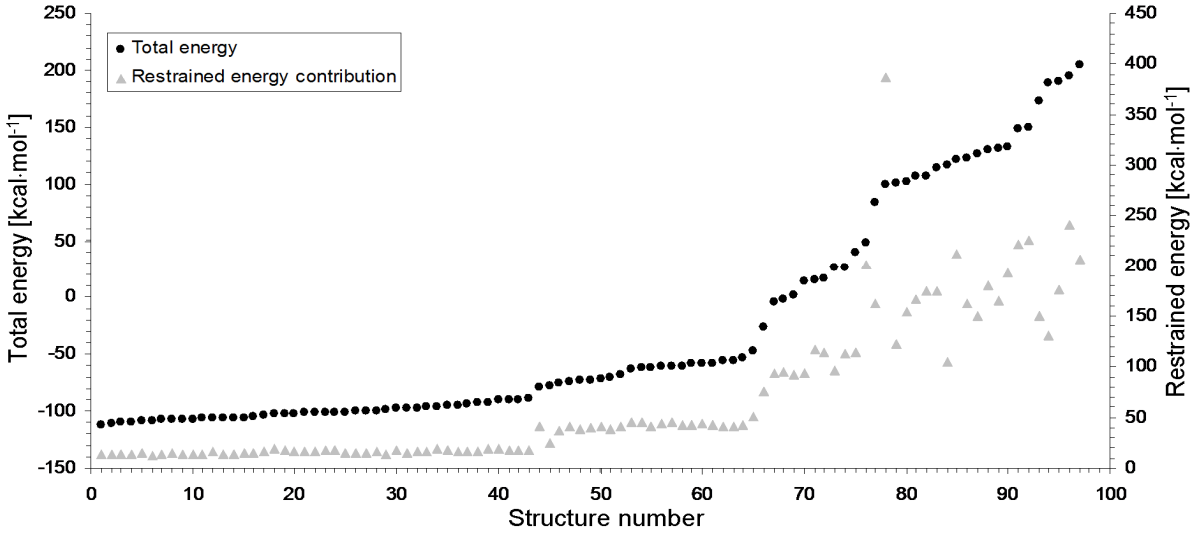

Figure 5.7: Total energy and the energy contribution of the restraints for the obtained structures.

appear to be quite stable for the 40 lowest energy structures. This can be measured by use of the squared dihedral angle order parameter S^2[15], which is defined as the sum of the squared averages of the cosine and sine of the dihedral angle α over N structures:

$$S^2 = \left(\frac{1}{N} \sum_{n=1}^{N} \cos(\alpha_n) \right)^2 + \left(\frac{1}{N} \sum_{n=1}^{N} \sin(\alpha_n) \right)^2 \tag{5.3}$$

Depending on the phase coherence of the dihedral angles between the structures, the value of S^2 will vary between 1 (all α_n are equal) and 0 (perfect uniform distribution in dihedral angles). The value for S^2 is calculated for increasing values of N, starting from 1 (only the lowest energy structure) and subsequently adding the next higher energy structure (Figures 5.8 and 5.9). The S^2 shows that all dihedral angles remain stable over the 40 lowest energy structures (Table 5.1), with the exception of the Leu1 φ angle. That the latter does not converge is hardly surprising since Leu1 lies at the end of the exocyclic chain and thus has more degrees of freedom. The HDA alkyl chain is completely divergent in its orientation, which was to be expected. From the S^2 values, a standard deviation for the torsion angles can also be calculated[15] according to the following expression (see Table 5.1):

$$\text{Stan. Dev.} = 2 \arccos\left(1 + \frac{\log_{10}(S)}{2} \right) \tag{5.4}$$

The 40 lowest energy structures were retained and are shown in Figure 5.10. Statistics concerning the quality of the modelling are presented in Table 5.5. The high precision of the structure is attributed to the high number of restraints imposed on the structure. The violations are not particularly substantial and could perhaps be

attributed to the large number of restraints. They are no reason for concern towards the accuracy of the solution structure. Indeed, as discussed below, the solution structure is very similar to the crystal structure, which in itself is a strong argument in favour of its accuracy.

Table 5.5: Statistics of the 40 lowest energy solution structures

Structure energy [kJ/mol][a]	
Total energy	-427.06±23.28
bond energy	51.56 ± 1.13
Valence angle energy	219.77 ± 6.85
Torsion angle energy	-684.37± 4.73
Improper energy	-74.02 ± 5.08
Cross-term energy	1.84 ± 0.39
van der Waals energy	146.66 ±10.96
Electrostatic energy	-88.50 ±23.10
Coordinate precision [Å][b]	
Heavy atoms (67)[c]	0.91 ± 0.21
Oligopeptide backbone (27)	0.15 ± 0.08
Helix backbone (15)[d]	0.10 ± 0.04
Ring backbone (22)	0.12 ± 0.08
Violations[a]	
Number >= 0.2 Å	11.25 ± 1.81
Sum of violations (Å)	5.48 ± 0.52
Maximum violation (Å)	0.52 ± 0.05

[a]expressed as energy ± standard deviation
[b]expressed as RMSD ± standard deviation; between brackets are the number of atoms
[c]All heavy atoms except the HDA moiety
[d]All backbone atoms from the Leu1 carbonyl C until Ser6 C^{α}

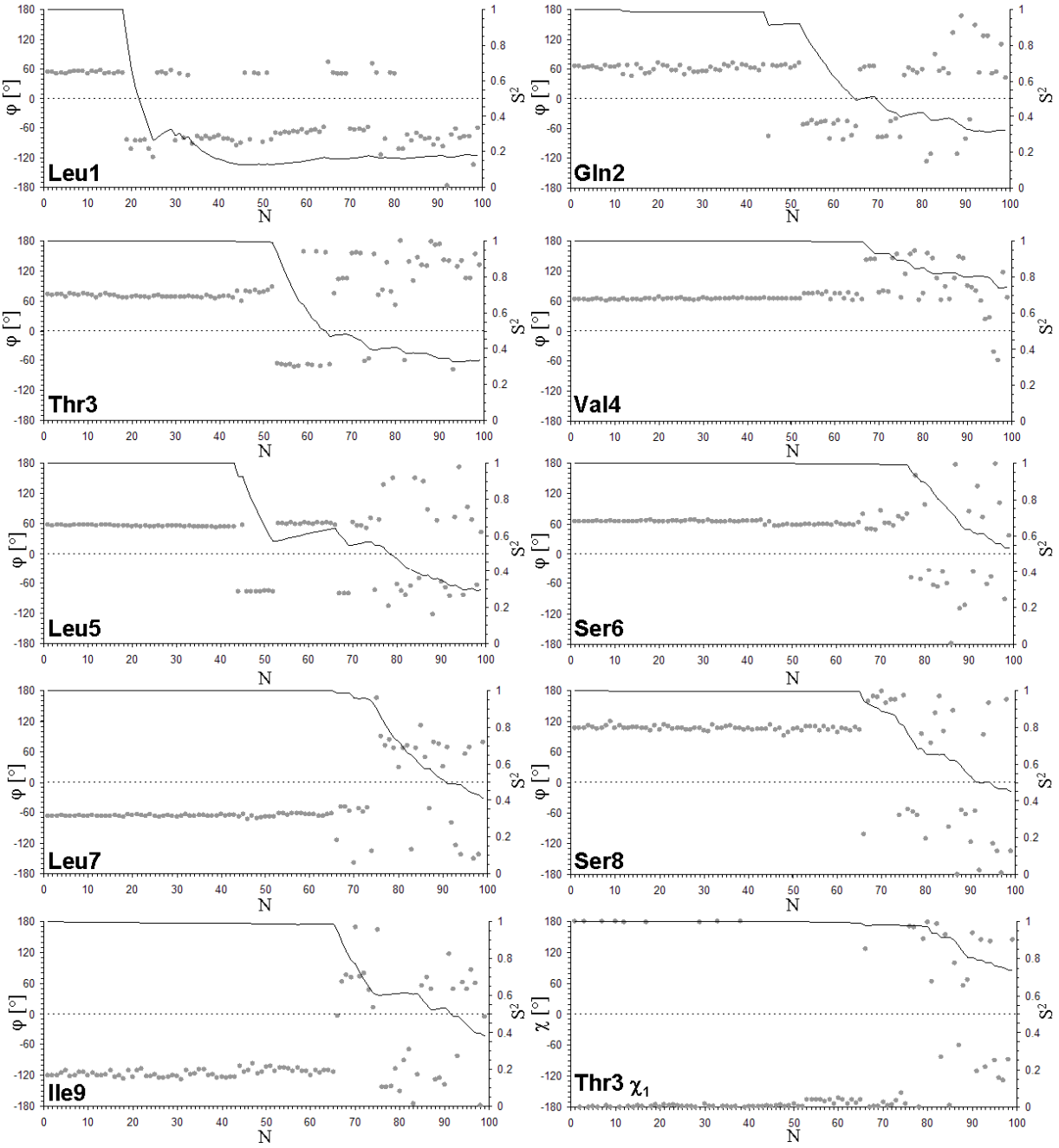

Figure 5.8: Graphical representation of the φ torsion angles and the Thr3 $H^{\alpha}H^{\beta}$ torsion angle for all structures, sorted according to increasing total energy. The S^2 value is calculated according to equation (5.3) and is represented by the solid line.

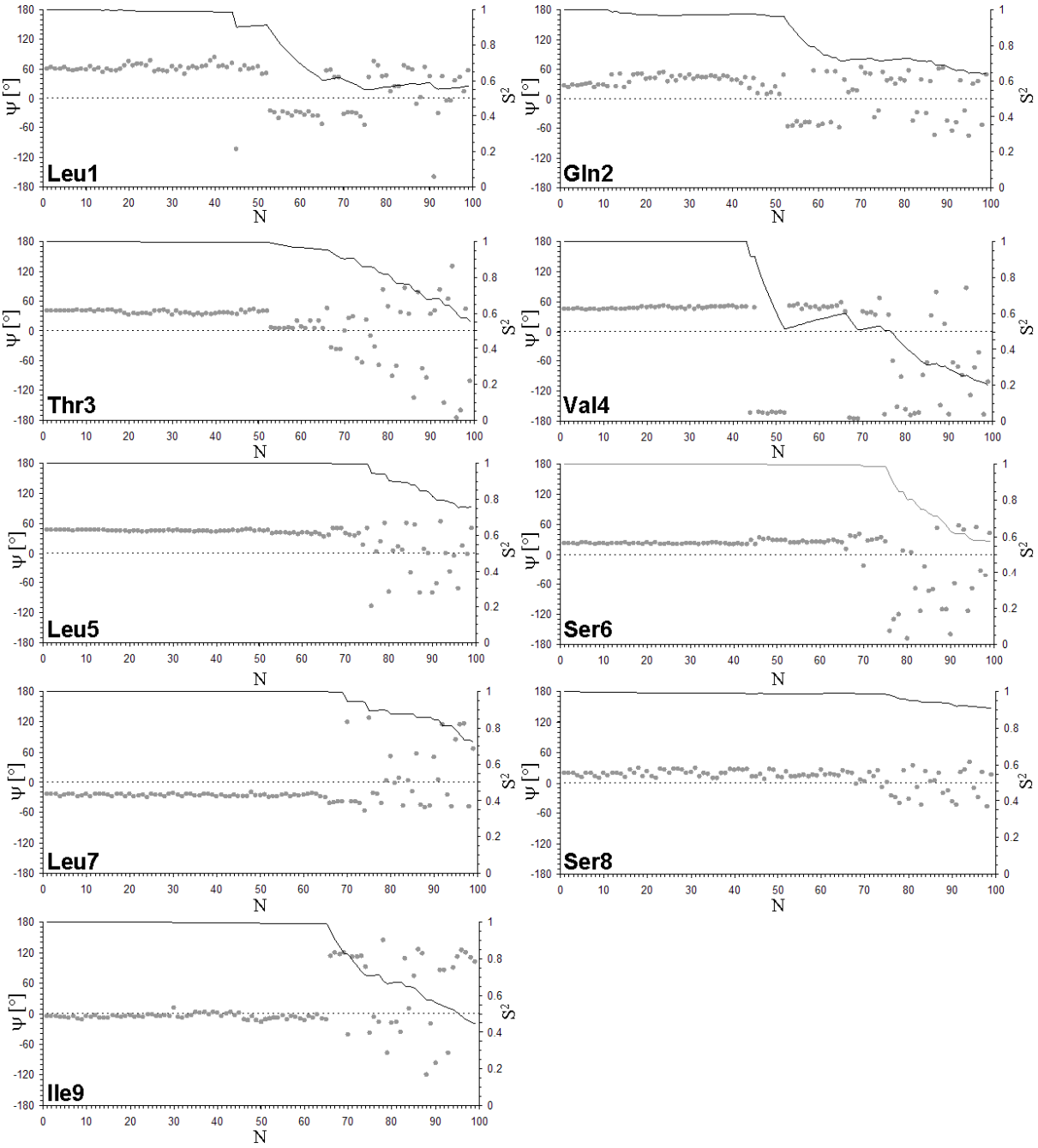

Figure 5.9: Graphical representation of the ψ torsion angles for all structures, sorted according to increasing total energy. The S^2 value is calculated according to equation (5.3) and is represented by the solid line.

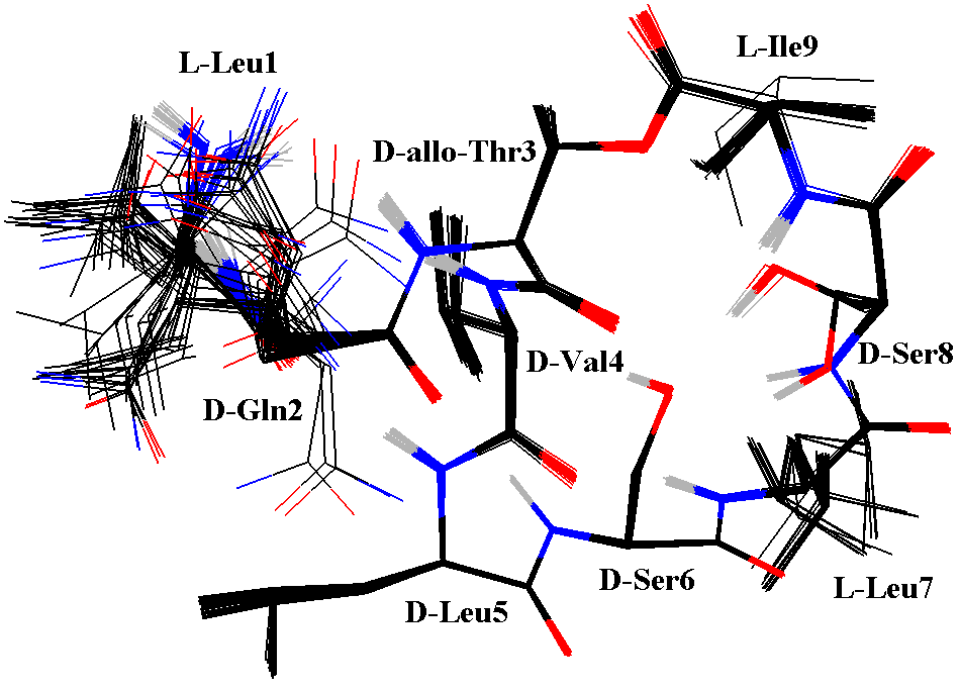

Figure 5.10: Overlay of the 40 lowest energy pseudodesmin A solution structures. The HDA moiety is removed for clarity.

5.3.3 Discussion of the solution structure

The solution structure is very similar to the crystal structure, containing the same main structural features: a short left-handed α-helix followed by a loop structure. A superposition of the backbone atoms of the Leu1-Ser6 peptide segment between the lowest energy solution structure and the crystal structure provides an RMSD value of 0.14 Å. Small differences are also apparent from the individual φ and ψ backbone torsion angles, as listed in Table 5.2. These show that D-Ser6 is now more in line with the α-helix rather than being involved in a type I' β-turn. The Leu5 NH – Leu1 CO and Ser6 NH – Gln2 CO hydrogen bonds that defined the α-helix in the crystal structure are still present (Table 5.6) and have in the lowest energy structure a somewhat improved geometry compared to the crystal structure (Table 5.2). In addition, the Val4 NH group now forms a hydrogen bond with the HDA carbonyl group in about half of the 40 lowest energy structures, extending the left-handed helix at the C-terminal side with the L-Leu1 residue. The hydrogen bond between the Leu7 NH group and the Val4 CO group is still present and has an improved geometry compared to the crystal structure. The Thr3 carbonyl now forms a hydrogen bond with the Ser6 alcohol group rather than with Ser8 NH as was the case in the crystal structure. The loop adopts a somewhat different orientation (Figure 5.2), reflected in the altered φ and ψ torsion angles of D-Ser8 and L-Ile9 (Table 5.1). Careful analysis revealed that these differences can be attributed to the absence of intermolecular contacts that were present in the crystal structure, such as the Ile9 NH – Leu5 CO hydrogen bond.

Table 5.6: Hydrogen bonds in the lowest energy solution structure

Donor	-	Acceptor	$d_{D\text{-}A}$ [Å]	angle [°]
Val4 NH	-	HDA CO	2.88	158.95
Leu5 NH	-	Leu1 CO	2.97	172.42
Ser6 NH	-	Gln2 CO	2.85	158.70
Ser6 OH	-	Thr3 CO	2.71	148.36
Leu7 NH	-	Val4 CO	3.16	154.76
Ser8 NH	-	Ser6 OH	2.92	158.71
Ser8 OH	-	Ser6 OH	2.66	165.77

5.3.4 Validation of the solution structure

The solution structure can be validated against independent experimental information. First, the experimental $^3J_{HNH\alpha}$ scalar coupling constants can be compared with the φ torsion angles to check whether they are in agreement. This can be done by using an appropriate Karplus curve relation. Here, the one by Vuister *et al*[16] is used:

$$^3J_{HNH\alpha} = 6.51\cos^2(\varphi \pm 60°) - 1.76\cos(\varphi \pm 60°) + 1.60 \qquad (5.5)$$

in which the minus sign is for L-residues and the plus sign for D-residues. This curve is plotted in Figure 5.11. The experimental scalar couplings were measured directly from Gaussian resolution enhanced 1D ^1H spectrum and are listed in Table 5.7. These are compared to the calculated couplings based on the average φ torsion angle of the 40 lowest energy structures.

It is however difficult to compare the difference in scalar coupling values between the different residues, since a difference in scalar coupling does not relate to a constant difference in torsion angle. A change in φ torsion angle of 20° for an L-residue will have a larger impact on the scalar coupling around −70° than around −120° for example, as can be seen from Figure 5.11. Therefore φ torsion angles are calculated from the experimental scalar couplings in Table 5.7. Since there are multiple possible solutions for φ in equation (5.5), the value which was the closest to the average solution structure torsion angle was chosen.

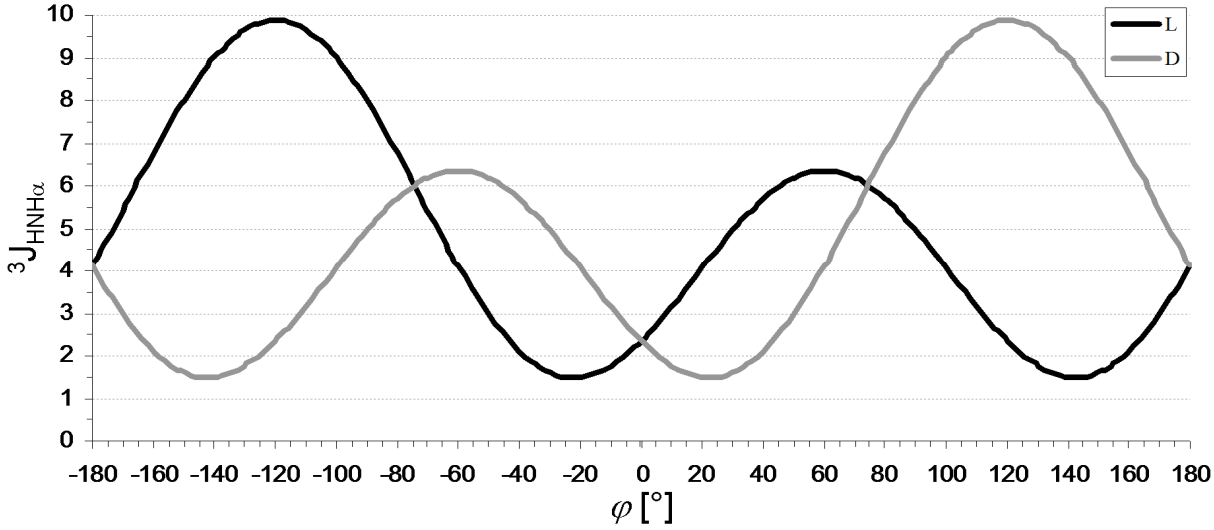

Figure 5.11: Karplus curve by Vuister *et al* (equation (5.5)) for H^NH^α scalar couplings in amino acid residues.

Table 5.7: Comparison between experimental scalar couplings and their corresponding calculated torsion angles and the average values obtained from the 40 lowest energy structures

	Leu1	Gln2	Thr3	Val4	Leu5	Ser6	Leu7	Ser8	Ile9	Thr3 $H^\alpha H^\beta$
$^3J_{HNH\alpha}$ calculated[a] [Hz]	6.74	4.32	5.35	4.62	3.57	4.77	4.89	9.47	9.79	12.89
Standard deviation [Hz]	1.80	1.62	0.71	0.39	0.25	0.27	0.33	0.36	0.21	0.05
$^3J_{HNH\alpha}$ experimental [Hz]	5.67	3.99	7.45	6.30	4.25	8.47	6.53	9.10	10.70	10.71
|difference| [Hz]	**1.06**	**0.33**	**2.10**	**1.68**	**0.68**	**3.70**	**1.64**	**0.37**	**0.91**	**2.17**
φ average torsion angle [°]	12.00	61.40	69.47	64.01	55.50	65.15	-66.01	107.00	-118.10	-178.72
Standard deviation [°]	73.19	10.57	9.89	9.01	7.87	9.10	9.23	14.01	15.49	17.19
φ torsion angle experimental[b] [°]	39.63	59.06	85.32	76.49	61.13	94.30	-78.20	101.20	--[c]	-152.62
|difference| [°]	**27.63**	**2.34**	**15.85**	**12.48**	**5.63**	**29.15**	**12.19**	**5.80**	**--[c]**	**26.09**

[a] Using equation (5.5), except for the Thr3 $H^\alpha H^\beta$ for which equation (5.2) is used.
[b] Using equation (5.5), except for the Thr3 $H^\alpha H^\beta$ for which equation (5.2) is used. Of all possible solutions, the value closest to the solution structure was chosen.
[c] Experimental scalar coupling value falls outside the range of the Karplus curve parameterisation, possibly due to the unusual ester functional group.

From Table 5.7 it can be concluded that overall the experimental scalar couplings are in good agreement with the solution structure. The significance of the larger deviation in φ torsion angle for Leu1 should not be taken too heavily due to the low order parameter observed for the 40 structures (S^2 = 0.16). Only the Ser6 φ angle seems to have a larger discrepancy of about 30° when compared with its expected value from the experimental scalar coupling. The Thr3 $H^\alpha H^\beta$ torsion angle, which is part of the macrocyclic structure, is nearly 180° in the solution structure, which leads to the maximum value for the $^3J_{H\alpha H\beta}$ scalar coupling in equation (5.2) (12.9 Hz). The experimental value (Table 5.7) is somewhat lower however. It is possible that the parameterisation of the Karplus curve of equation (5.2) does not cover this specific structural moiety, which contains an ester group. For all other residues, the deviation

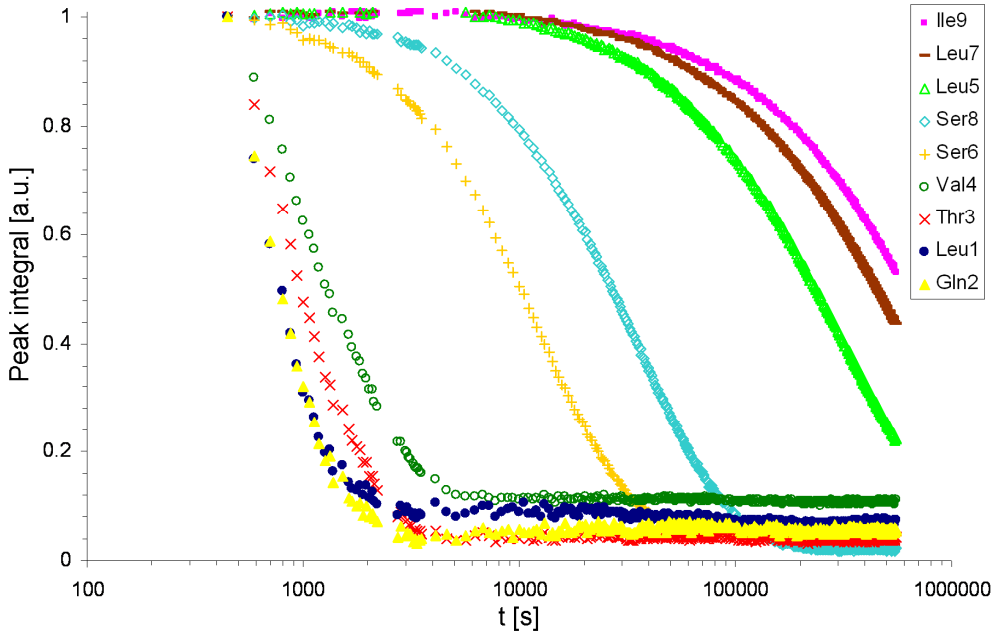

Figure 5.12: Peak integral evolution over time for the H^N protons during the ^1H-^2H exchange experiment in acetonitrile solution.

between φ torsion angle from the solution structure and those calculated from the scalar couplings is within an acceptable level.

Another experiment which reveals structural information is the measurement of ^1H-^2H exchange rates of the amide protons. For this, 61.1 µl D_2O was added to a *ca.* 8 mM solution of pseudodesmin A in 550 µl acetonitrile at 298.0 K. 1D ^1H spectra were then measured over a period of 6 days to monitor the proton signal intensity. All three hydroxyl protons were fully exchanged during the time between the addition of D_2O and the first measurement. The resulting amide signal decay curves are plotted in Figure 5.12. The curves were fitted to the following approximating function:

$$I(t) = I_0\left[(1-\alpha)e^{-kt} + \alpha\right] \tag{5.6}$$

with k the deuterium exchange rate constant, I_0 the signal intensity at time $t = 0$ and α the fraction of remaining protonated amide groups when equilibrium is achieved. From k, the exchange half-life $t_{1/2}$ can be calculated as:

$$t_{1/2} = -\frac{\ln\left[\frac{0.5-\alpha}{1-\alpha}\right]}{k} \tag{5.7}$$

Table 5.8: ^{1}H-^{2}H exchange rate kinetics in acetonitrile solution

Amide resonance	k [s^{-1}]	$t_{1/2}$ [a]
Leu1	2312.2	5m
Gln2	2327.4	5m
Thr3	1366.8	9m
Val4	923.33	14m
Leu5	3.03	2d 18h 8m
Ser6	75.83	2h 39m
Leu7	1.63	5d 2h 57m
Ser8	27.95	7h 6m
Ile9	1.21	6d 22h 12m
Gln2 NH_2 1	836.84	14m
Gln2 NH_2 2	805.75	15m

[a] $t_{1/2}$ expressed in days (d), hours (h) and minutes (m).

The results are listed in Table 5.8. Slow exchange rates on the order of hours to days are found for the amide hydrogens in the Leu5–Ile9 segment. While the Ile9 amide is not involved in any hydrogen bond in the solution structure, its NH bond points inward from the loop to the helix, making it totally solvent inaccessible. The Leu5 until Ser8 amides are all involved in intramolecular hydrogen bonds. The unusually low exchange rate constants shows that this orientation is consistently maintained, indicating conformational rigidity. The higher exchange rates of both Ser amide hydrogens are most probably caused by participation of the side chain hydroxyl groups in the exchange process with the solvent. The relatively fast exchange rates found for the Leu1, Gln2 and Thr3 amide hydrogens agree with their more accessible location at the N-terminal side of the α-helix. Although the solution structure predicts a hydrogen bond involving Val4 NH and HDA CO, the Val4 amide hydrogen exchanges fairly rapidly, but still somewhat slower than Leu1, Gln2 and Thr3. This suggests that this hydrogen bond is not continuously or not at all present due to the higher mobility of the exocyclic part. This is supported by the fact that only about half of the 40 lowest energy structures feature this hydrogen bond. Altogether, the data indicate that the solution structure in acetonitrile is well-defined and considerably rigid.

A DOSY experiment reveals some additional information concerning the relative exchange rates of the three hydroxyl groups. As can be seen in Figure 5.13, both the Ser6 and Ser8 hydroxyl groups provide an apparent diffusion coefficient that is equal to the rest of the pseudodesmin A resonances. The HDA hydroxyl group however provides a diffusion coefficient value equal to that of the H_2O peak. This means that the exchange between the HDA hydroxyl group with water is faster than the diffusion delay set during the experiment (Δ = 250 ms), while the exchange of the Ser hydroxyl groups occur on a time scale which is slower. The latter must therefore be less solvent accessible, indicating that they are either shielded by the adopted molecular conformation or are involved in intramolecular contacts. For Ser6 this is in agreement

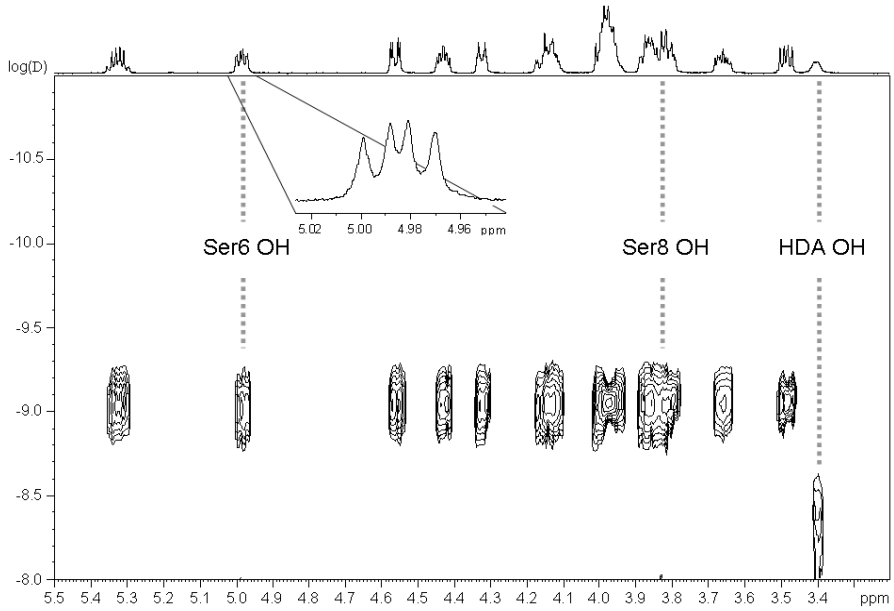

Figure 5.13: 2D DOSY spectrum of pseudodesmin A in acetonitrile solution focusing on the H^{α} spectral region. The DOSY processing was performed using the maximum entropy method (dosym software, NMRtec; section 2.5.2). The Ser6 hydroxyl proton clearly appears to have the same diffusion coefficient as the other pseudodesmin A resonances. The Ser8 hydroxyl proton overlaps with other pseudodesmin A resonances, however visual inspection shows a monoexponential decay for the signal. The HDA hydroxyl group provides a diffusion coefficient similar to that of the H_2O peak (not shown). The inset shows the multiplet structure of the Ser6 hydroxyl proton resonance (see main text).

with the hydrogen bond that the alcohol group makes with the Thr3 carbonyl in the solution structure. This is also supported by observing the multiplet structure of the alcohol proton resonance, which is a doublet of a doublet (Figure 5.13). This also indicates that there is limited rotational freedom along the C^{β}-O^{γ} bond, suggesting a stable hydrogen bond.

5.4 Behaviour in DMSO

The conformational analysis of pseudodesmin A initially occurred in DMSO solution. This was motivated by the fact that the solution structure of WLIP was determined in this solvent as well. It quickly became apparent however that the conformational study in this solvent brought about several complications. It appeared that pseudodesmin A does not adopt a single conformation in DMSO solution and can therefore not be subjected to a restrained molecular modelling procedure in the same way as was done in section 5.3.1. The presence of the different conformations shows itself in the ^{1}H and ^{13}C NMR spectra at 298.0 K under the form of differential line broadening of several resonances caused by an exchange process that is fast on the NMR frequency time scale, but still close to the point of coalescence (Figure 4.4). The broadened resonances arise mainly from the H^{N}, several H^{α} and even ^{13}C carbonyl and C^{α} resonances. Since the line broadening is not present equally on

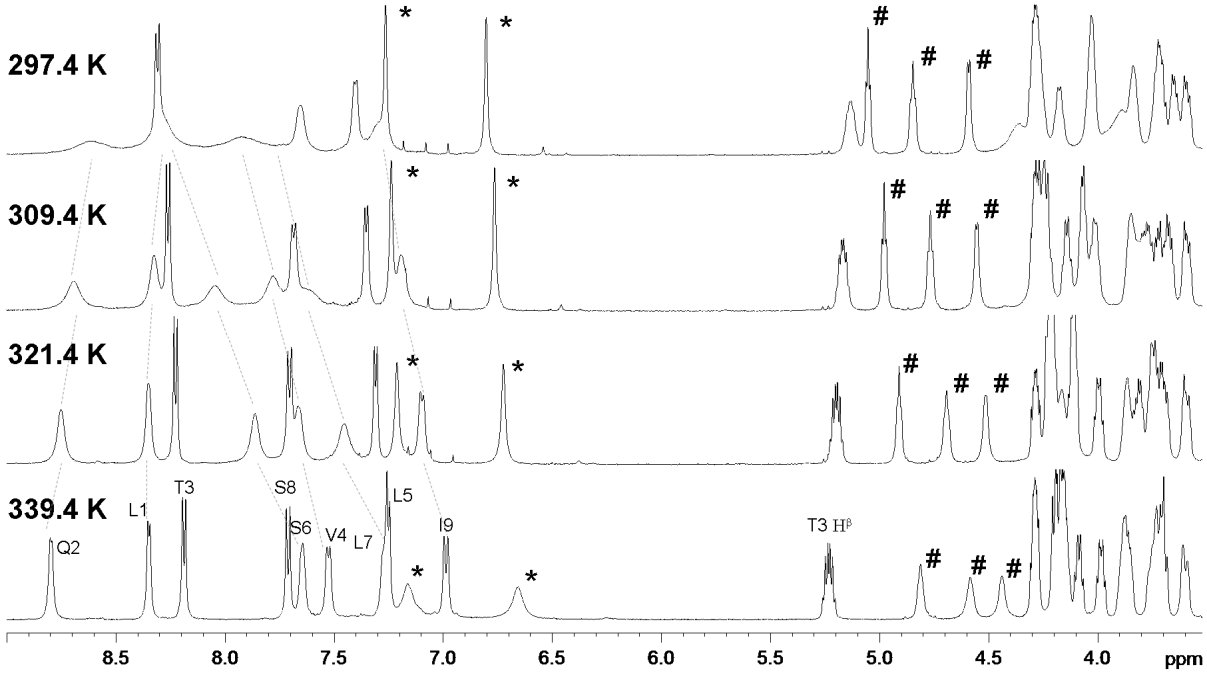

Figure 5.14: Temperature dependence of the pseudodesmin A ^{1}H spectrum in DMSO solution (500.13 MHz). All H^{N} protons are indicated by their corresponding amino acid one letter code and sequence position. Most of the resonances sharpen as the temperature is raised, indicating an intermediate to fast exchange transition. Although the solvent viscosity also drops with elevated temperatures, the dramatic effects seen here cannot possibly be explained by such an effect alone. The two Gln2 amide side chain resonances (*) broaden with increased temperature as the in-plane inversion process of the amide goes from a slow exchange regime to an intermediate exchange. Similarly, the hydroxyl protons (#) broaden with increased temperature due to increased exchange with the water molecules.

each resonance as is the case in the non-polar solvents (section 4.5), self-association to large complexes cannot induce this broadening.

The resonances sharpen as the temperature is increased (Figure 5.14), which can be interpreted as an increase in the exchange kinetics (k_{ex} increases) that drives the exchange more towards the fast exchange regime. In addition, the chemical shifts vary strongly with the temperature, especially when compared to the temperature dependence observed for the corresponding resonances in acetonitrile (Table 5.9). For a stable structure in solution, the chemical shift temperature dependence of hydrogen bond donor protons can often be interpreted in terms of (intra- or intermolecular) hydrogen bond dynamics, which typically provide a negative dependence with temperature. However, the very strong temperature coefficients observed in DMSO are unlikely to be caused by solely this effect (*cf.* the coefficients in acetonitrile), and therefore indicate a conformational exchange between two or multiple conformations of unequal population (section 3.5) in which k_{ex} increases with temperature, or a change in the populations of the different conformations with temperature. Three H^{N} protons (Leu1, Gln2 and Ser8) show non-linear chemical shift temperature dependence, first increasing with temperature and then decreasing after having reached a maximum value. This can be explained as follows. The chemical shift temperature dependence due to the exchange is in the opposite direction when

compared to the chemical shift hydrogen bond dynamics temperature dependence. At lower temperatures the former effect dominates, while as the resonance reaches the fast exchange regime at higher temperature, the latter effect becomes increasingly dominant and changes the sign of the chemical shift variation.

Table 5.9: Temperature coefficients of pseudodesmin A in DMSO and acetonitrile solution

	acetonitrile		DMSO	
Leu1	-3.26	(1.00)	1.27	(0.72)[b]
Gln2	-1.63	(1.00)	4.43	(0.95)[c]
Thr3	-0.41	(0.99)	-2.88	(0.98)
Val4	-0.87	(1.00)	-9.48	(0.99)
Leu5	-4.64	(1.00)	-3.61	(1.00)
Ser6	-0.40	(0.99)	-14.07	(0.99)
Leu7	-0.33	(0.99)	-11.93	(0.99)
Ser8	-1.48	(1.00)	1.34	(0.89)[d]
Ile9	-0.12	(0.97)	-7.39	(0.99)
Gln2 NH_2 1	-2.76	(1.00)	-2.41	(1.00)
Gln2 NH_2 2	-2.62	(1.00)	-3.47	(1.00)

[a] Temperature coefficients in ppb·K^{-1}; in brackets are the R^2 values of the linear regression

[b] Non-linear behaviour, parabolic fit (R^2 = 1.00): $\delta[ppm] = -7.67\times10^{-5}T^2 + 5.06\times10^{-2}T + 0.016$

[c] Non-linear behaviour, parabolic fit (R^2 = 1.00): $\delta[ppm] = -8.02\times10^{-5}T^2 + 5.59\times10^{-2}T - 0.800$

[d] Non-linear behaviour, parabolic fit (R^2 = 1.00): $\delta[ppm] = -3.90\times10^{-5}T^2 + 2.62\times10^{-2}T + 3.317$

A similar result is found when comparing the 1D ^1H spectra measured at different magnetic field strengths (Figure 5.15). All H^N resonances broaden with increased magnetic field strength, except Thr3 H^N, which appears not to be broadened at 700 MHz. In this case, it is the frequency difference $\Delta\nu$ between the different conformational states that increases with the magnetic field, driving the exchange back from fast exchange to the point of coalescence. The strong dependence of the line width with the magnetic field is a strong argument in favour of a fast exchange situation, as slow exchange has nearly no effect on the resonance line width (see section 3.5). Note that the point of coalescence is not reached even at 700 MHz at 298.0 K. Lowering the temperature for this purpose was not an option since DMSO-d6 has its melting point around 18°C. Therefor e a slow exchange regime, in which the different conformations would have been separately observable, cannot be reached. No direct structure determination is therefore possible.

The presence of a different conformation in DMSO as compared to acetonitrile is indicated by the ^1H, ^{13}C and ^{15}N chemical shifts and the $^3J_{HNH\alpha}$ scalar couplings. These all have quite different values in DMSO when compared to what is found in

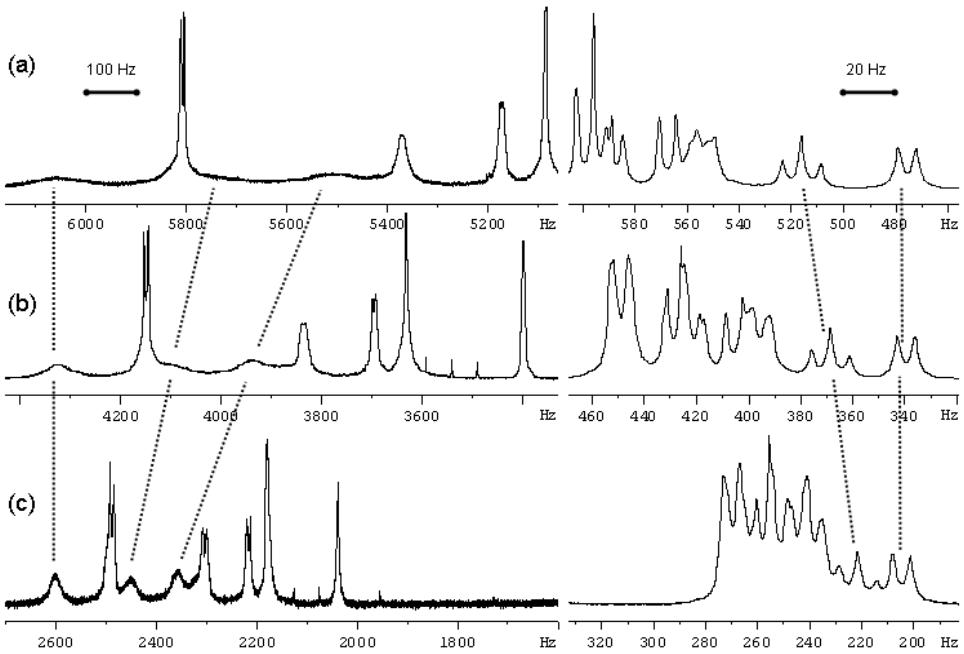

Figure 5.15: Pseudodesmin A ^{1}H spectra at 25℃ at field strengths of (a) 16.4 T (700.13 MHz), (b) 11.7 T (500.13 MHz) and (c) 7.0 T (300.13 MHz). As can be clearly seen from the H^{N} resonances (left part), the line widths increase as the magnetic field strength is increased, indicating a fast to intermediate exchange transition due to increased frequency differences between the two conformational states. As a comparison, the methyl resonance line widths (right part) do not change, as the frequency differences between the different states are inherently much smaller sot that the intermediate exchange regime is never reached.

acetonitrile (appendix E). There are also clear differences in the pattern of rOe contacts in DMSO measured at 323 K when compared to acetonitrile. Most notable are the absence of any correlations between the Leu7 and Val4 residues and the presence of correlations between the Ser6 H^{α} proton and Ile9 CH_2^{γ} and CH_3^{δ} protons. These observations cannot be explained from either the solution or crystal structure. Finally, a ^{1}H-^{2}H exchange experiment performed in DMSO at 310 K, confirms this as well. This was performed by adding 60 µl of methanol-d4 to a 550 µl *ca.* 2 mM pseudodesmin A solution. The resulting decay curves are provided in Figure 5.16. The most notable difference compared to the ^{1}H-^{2}H exchange experiment in acetonitrile is that the Val4 amide exchanges much slower when compared to the Leu1, Gln2, Thr3 and Ser6 amide protons, indicating that it is now significantly more shielded from the solvent.

The reason for this specific behaviour in DMSO solution can most likely be found in the strong propensity of DMSO molecules to form strong hydrogen bonds. The hydrogen bonding donor and acceptor capacity of organic functional groups can be expressed as generalised constants: the hydrogen bond donor constant α and the hydrogen bond acceptor constant β[17]. Some values are listed in Table 5.10[17, 18].

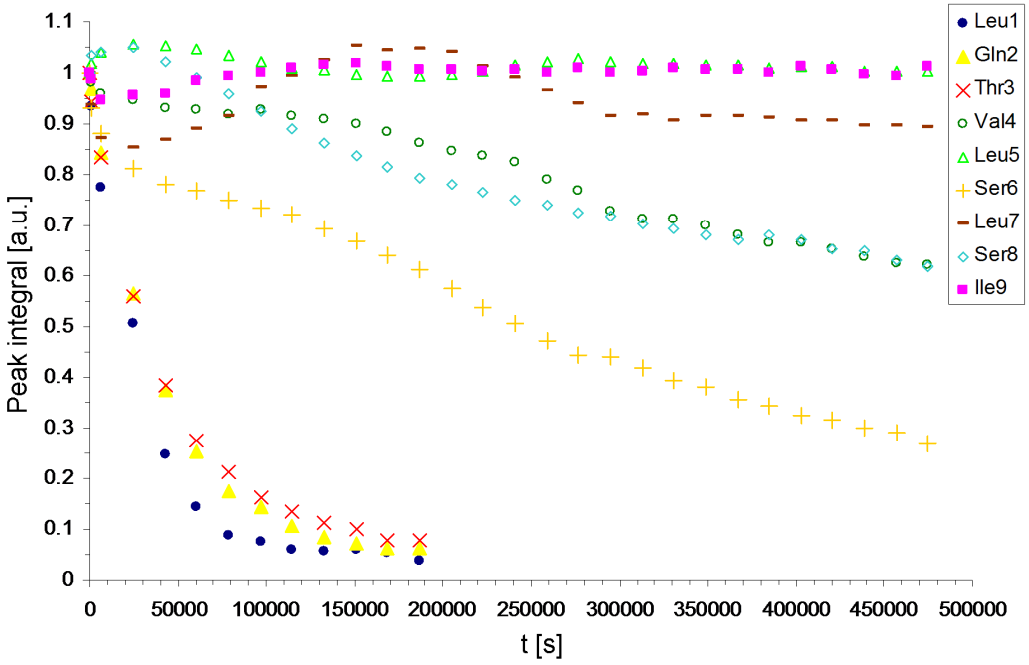

Figure 5.16: Peak integral evolution over time for the H^N protons during the ^1H-^2H exchange experiment in DMSO solution.

Table 5.10: Selected hydrogen bond donor and acceptor constant values

	α	β
amide	2.9	8.3
acetonitrile	1.7	4.7
acetone	1.5	5.8
water	2.8	4.5
DMSO	0.8	8.9
urea	3.0	8.3

The free enthalpy a hydrogen bond formation between two functional groups 1 and 2 is proportional to the product of the donor and acceptor constants of these groups:

$$\Delta G_{Hbond} \propto -\alpha_1 \beta_2 \tag{5.8}$$

The hydrogen bonding donor and acceptor capacities of both acetonitrile and acetone are below those of the amide group. This means that hydrogen bond formation between two amide groups is stronger and thus preferred over a hydrogen bond between an amide group and acetonitrile or acetone. DMSO is however a stronger hydrogen bond acceptor than amide carbonyl groups. Therefore, based on these numbers, it would be more favourable to form hydrogen bonds between an amide NH group and DMSO rather than between two amides. An explanation for the conformational heterogeneity of pseudodesmin A in DMSO could therefore reasonably be that intermolecular hydrogen bond formation with DMSO molecules strongly competes with the intramolecular hydrogen bonds that stabilize the

conformation, effectively causing an equilibrium between the folded and 'broken' structures. DMSO could thus be considered to act as a denaturant for pseudodesmin A. As a comparison, urea is a stronger hydrogen bond donor than amide NH groups based on the figures in Table 5.10 and is a very well known denaturant of protein structures. It should be mentioned that the constants in Table 5.10 are based on experimental or predicted values for simple 1:1 complexes formed by the donor and acceptor groups. These do not take into account any effects from conformational rearrangements, as would be the case in pseudodesmin A. They nevertheless do provide a useful qualitative picture.

Table 5.11: Comparison of scalar couplings between chloroform and acetonitirile

^3J	J_{CD3CN} [Hz]	J_{CDCl3} [Hz]	difference [Hz]	torsion angle difference[a] [°]
Leu1 H^NH^α	5.7	6	-0.4	--[b]
Gln2 H^NH^α	4	3.1	0.9	-7.6
Thr3 H^NH^α	7.5	6.2	1.3	-9.7
Val4 H^NH^α	6.3	4.9	1.4	-10.7
Leu5 H^NH^α	4.3	2.9	1.3	-11.4
Ser6 H^NH^α	8.5	8	0.5	-4.4
Leu7 H^NH^α	6.5	4.4	2.2	16.3
Ser8 H^NH^α	9.1	8.8	0.3	-3.1
Ile9 H^NH^α	10.7	9.8	0.9	--[c]
Thr3 $H^\alpha H^\beta$	10.7	10.9	-0.2	-1.3

[a] Torsion angles were calculated using equation (5.5) for H^NH^α couplings and equation (5.2) for the $H^\alpha H^\beta$ coupling.
[b] Not compared since the bond is assumed to be flexible in acetonitrile solution.
[c] Ile9 H^NH^α coupling constant in chloroform is out of range of the Karplus curve, most likely because the unusually attached ester group influences the correct parameterisation of the curve.

5.5 Conformation in chloroform

An important question is the extent to which the solution structure of pseudodesmin A in acetonitrile is maintained within the supramolecular structures formed through self-assembly in chloroform. This cannot be checked by a restrained molecular modelling as performed in acetonitrile solution due to the inability to distinguish intra- from intermolecular contacts in the 2D ROESY spectrum and the great amount of spin diffusion present in the 2D NOESY spectrum even at short mixing times. However, the $^3J_{HH}$ scalar couplings are a conformation sensitive parameter that, unlike the nOe, does not suffer from intra- or intermolecular ambiguity. The most relevant are of course the $^3J_{HNH\alpha}$ couplings reflecting the backbone φ torsion angles. The scalar couplings in chloroform solution where measured on a *ca*. 20 mM sample using an HNHA experiment (see appendix G). As seen in Table 5.11, neither their values nor the torsion angles derived from them change to an extent that would indicate major

local or global changes in the backbone conformation between the two solvents. Therefore, the solution structure of pseudodesmin A in acetonitrile is a valid model to explore the supramolecular assembly.

5.6 Conclusion

Both the crystal structure and the acetonitrile solution structure of pseudodesmin A were determined. They were found to be very similar to each other, with the main structural features being a left-handed α-helix comprising 5 to 6 residues (about 1.5 helical turns) followed by a loop of three residues (L-Leu7–D-Ser8–L-Ile9). The loop covalently connects the C-terminal end of the helix with its middle by ending in the lactone bond between the oligopeptide C-terminal carboxylate group and the Thr3 side chain hydroxyl group. The overall structure is amphipathic, with all hydrophilic and hydrophobic residues grouped along different sides of the molecule. This feature will be of importance in understanding the molecular mechanism of the self-association later on (section 6.5).

The main differences between the two structures are at the N-terminal end of the oligopeptide, where the Leu1 residue adopts different backbone torsion angles, and in the loop structure at the height of the Ile9 main chain torsion angles. These differences can be explained by the influence of intermolecular hydrogen bonds in the crystal structure. The solution structure appears to be quite rigid and well-defined, as a good convergence is found in the ensemble of conformations obtained by the restrained molecular modelling and very slow ^{1}H-^{2}H exchange rate constants are found for nearly all amide protons that are predicted to be solvent inaccessible. Only Leu1 and the HDA chain are suggested to possess a high conformational mobility in solution because of their low convergence in the ensemble of obtained conformations, which is not surprising given their position at the end of the exocyclic part of the oligopeptide chain. All of this contrasts the situation in DMSO solution where pseudodesmin A is found to exchange between multiple conformations. This is most likely due to the strong hydrogen bond acceptor capacity of the DMSO molecules, which can compete with the intramolecular amide hydrogen bonds.

In chloroform, where the pseudodesmin A molecules are self-associated in a supramolecular structure, the structure cannot be directly obtained by a restrained molecular modelling due to the inability to distinguish inter- and intramolecular ^{1}H-^{1}H contacts. However, comparing the $^{3}J_{HNH\alpha}$ scalar couplings measured in acetonitrile with those obtained in chloroform revealed that the acetonitrile solution structure is retained in the supramolecular assembly. With this information at hand, the focus of the study can now shift to the self-association phenomenon itself and to the

organisation of the individual pseudodesmin A molecules within the supramolecular structure.

5.7 References

[1] D. Sinnaeve, C. Michaux, J. Van hemel, J. Vandenkerckhove, E. Peys, F. A. M. Borremans, B. Sas, J. Wouters and J. C. Martins, "Structure and X-ray conformation of pseudodesmins A and B, two new cyclic lipodepsipeptides from *Pseudomonas* bacteria". *Tetrahedron*, **2009**, *65*(21) 4173-4181.

[2] D. Sinnaeve, Licentiaatsthesis, **2005**, "Gevorderde Structuuranalyse van een Recent Geïsoleerd Natuurproduct met Behulp van NMR Spectroscopie" Universiteit Gent (Gent).

[3] F. S. Han, R. J. Mortishire-Smith, P. B. Rainey and D. H. Williams, "Structure of the White-Line-Inducing Principle Isolated from *Pseudomonas Reactans*". *Acta Crystallographica Section C-Crystal Structure Communications*, **1992**, *48* 1965-1968.

[4] J. W. Quail, N. Ismail, M. S. C. Pedras and S. M. Boyetchko, "Pseudophomins A and B, a class of cyclic lipodepsipeptides isolated from a Pseudomonas species". *Acta Crystallographica Section C-Crystal Structure Communications*, **2002**, *58* o268-o271.

[5] R. J. Mortishire-Smith, J. C. Nutkins, L. C. Packman, C. L. Brodey, P. B. Rainey, K. Johnstone and D. H. Williams, "Determination of the Structure of an Extracellular Peptide Produced by the Mushroom Saprotroph Pseudomonas-Reactans". *Tetrahedron*, **1991**, *47*(22) 3645-3654.

[6] J. A. Smith and L. G. Pease, "Reverse Turns in Peptides and Proteins". *CRC Critical Reviews in Biochemistry*, **1980**, *8*(4) 315-399.

[7] D. Sorensen, T. H. Nielsen, C. Christophersen, J. Sorensen and M. Gajhede, "Cyclic lipoundecapeptide amphisin from Pseudomonas sp strain DSS73". *Acta Crystallographica Section C-Crystal Structure Communications*, **2001**, *57* 1123-1124.

[8] A. Henriksen, U. Anthoni, T. H. Nielsen, J. Sorensen, C. Christophersen and M. Gajhede, "Cyclic lipoundecapeptide tensin from Pseudomonas fluorescens strain 96.578". *Acta Crystallographica Section C-Crystal Structure Communications*, **2000**, *56* 113-115.

[9] W. F. Vranken, W. Boucher, T. J. Stevens, R. H. Fogh, A. Pajon, P. Llinas, E. L. Ulrich, J. L. Markley, J. Ionides and E. D. Laue, "The CCPN data model for NMR spectroscopy: Development of a software pipeline". *Proteins-Structure Function and Bioinformatics*, **2005**, *59*(4) 687-696.

[10] D. Neuhaus and M. P. Williamson, "The Nuclear Overhauser Effect in Structural and Conformational Analysis", 2nd ed., **2000**, New York, John Wiley and Sons Ltd.

[11] T. Facke and S. Berger, "SERF, a New Method for ^{1}H-^{1}H Spin-Coupling Measurement in Organic-Chemistry". *Journal of Magnetic Resonance Series A*, **1995**, *113*(1) 114-116.

[12] A. Demarco, M. Llinas and K. Wuthrich, "Analysis of ^{1}H-NMR Spectra of Ferrichrome Peptides .1. Non-Amide Protons". *Biopolymers*, **1978**, *17*(3) 617-636.

[13] K. Nagayama and K. Wuthrich, "Structural Interpretation of Vicinal Proton-Proton Coupling Constants $^{3}J_{H\alpha H\beta}$ in the Basic Pancreatic Trypsin Inhibitor Measured by Two-Dimensional J-Resolved NMR Spectroscopy". *European Journal of Biochemistry*, **1981**, *115*(3) 653-657.

[14] J. R. Maple, U. Dinur and A. T. Hagler, "Derivation of Force-Fields for Molecular Mechanics and Dynamics from Abinitio Energy Surfaces". *Proceedings of the National Academy of Sciences of the United States of America*, **1988**, *85*(15) 5350-5354.

[15] S. G. Hyberts, M. S. Goldberg, T. F. Havel and G. Wagner, "The Solution Structure of Eglin-C Based on Measurements of Many NOEs and Coupling-Constants and Its Comparison with X-Ray Structures". *Protein Science*, **1992**, *1*(6) 736-751.

[16] G. W. Vuister and A. Bax, "Quantitative J Correlation - a New Approach for Measuring Homonuclear 3-Bond J($H^N H^\alpha$) Coupling-Constants in ^{15}N-Enriched Proteins". *Journal of the American Chemical Society*, **1993**, *115*(17) 7772-7777.

[17] C. A. Hunter, "Quantifying intermolecular interactions: Guidelines for the molecular recognition toolbox". *Angewandte Chemie-International Edition*, **2004**, *43*(40) 5310-5324.

[18] J. L. Cook, C. A. Hunter, C. M. R. Low, A. Perez-Velasco and J. G. Vinter, "Solvent effects on hydrogen bonding". *Angewandte Chemie-International Edition*, **2007**, *46*(20) 3706-3709.

6 Self-association of pseudodesmin A

6.1 Introduction

In this chapter, the self-association properties of pseudodesmin A in chloroform solution will be investigated using both chemical shift and translational diffusion coefficient measurements. Translational diffusion coefficient measurements, the methodology of which has been described in Chapter 2, can provide insight into the average size of the supramolecular structures that are formed, as described in Chapter 1. The results of this study indicate that large supramolecular structures can indeed be formed with apparently no limit in size. Since the chemical shift is sensitive to the electronic environment of the nucleus, its variation with the degree of self-association can be used to map the regions in the pseudodesmin A molecule that are involved in intermolecular contacts. This is supplemented by intermolecular rOe data that can be identified as additional contacts observed at high concentration in chloroform when compared with the acetonitrile solution conformation. With all these results at hand and together with the monomer conformation, a model for the structure and organisation of the supramolecular assemblies is hypothesised which explains the self-association in non-polar solvents, its property to form oligomers of unlimited size and the suspected biological function of ion pore formation in cellular membranes. These results have been published as D. Sinnaeve et al, Chemistry-a European Journal, 2009, 15(46) 12653-12662.

6.2 Concentration dependent behaviour in chloroform solution

As discussed in Chapter 4, the line widths of the pseudodesmin A ^{1}H resonances increase significantly in chloroform or other non-polar solvents when compared to

acetonitrile. Line broadening due to conformational exchange was excluded as the effect is equally present on each resonance and no apparent change in line widths could be detected at different field strengths (data not shown). Therefore an increased rotational correlation time constant is the most likely explanation for this observation. Since solvent viscosity alone is insufficient to explain the drastic change in correlation time constant, it was hypothesised that pseudodesmin A self-associates to larger structures in non-polar environment. Since no significant exchange line broadening is observed and only one set of resonances is detected, it is therefore assumed that the association occurs with a rate that is fast on the NMR frequency time scale. In general under this condition, when oligomerisation occurs, the observed chemical shift δ and line widths are an average of the values expected for each possible oligomer size i, weighted by the molar fractions α_i present in the association equilibrium:

$$\delta_{av} = \sum_i \alpha_i \delta_i \tag{6.1}$$

Since the fractions α_i of the oligomers with size i are concentration dependent, the chemical shifts and the line widths should evolve towards the values of the monomer state at lower concentration. This is indeed observed, as for several resonances the chemical shift changes and the line widths sharpen when moving towards lower concentration in the range from 20.5 mM to 0.06 mM (Figure 6.1). This effectively proves that a self-association process is taking place. An interpretation of which particular resonances experience a chemical shift change with increased self-association is discussed in section 6.4. First, the self-association will be investigated through a determination of the translational diffusion coefficient.

The measurement of translational diffusion coefficients, which is directly linked to the size of the oligomers as described in section 1.4, can provide insight into the extent of the self-association. To this end, the translational diffusion coefficient was monitored as a function of the concentration at 25°C. The diffusion measurement used a convection compensated bipolar gradient PFG pulse sequence, applying 32 linearly sampled gradient increments values with the Δ and δ delays set in such a way that the signal decay was adequately sampled over the dynamic range of the gradient strength output. The concentration was measured using the ERETIC method (appendix H). A layer of water was put on top of the chloroform sample to avoid solvent evaporation over time, a technique known as ELISE[1]. The diffusion coefficient of internal TMS was monitored as well by performing a diffusion measurement with separately optimised Δ and δ values. The purpose of this was to use TMS as a crude internal indicator for viscosity changes that might occur as the pseudodesmin A concentration is increased. These can then be used to calculate a correction factor for the pseudodesmin A diffusion coefficients to remove the effects

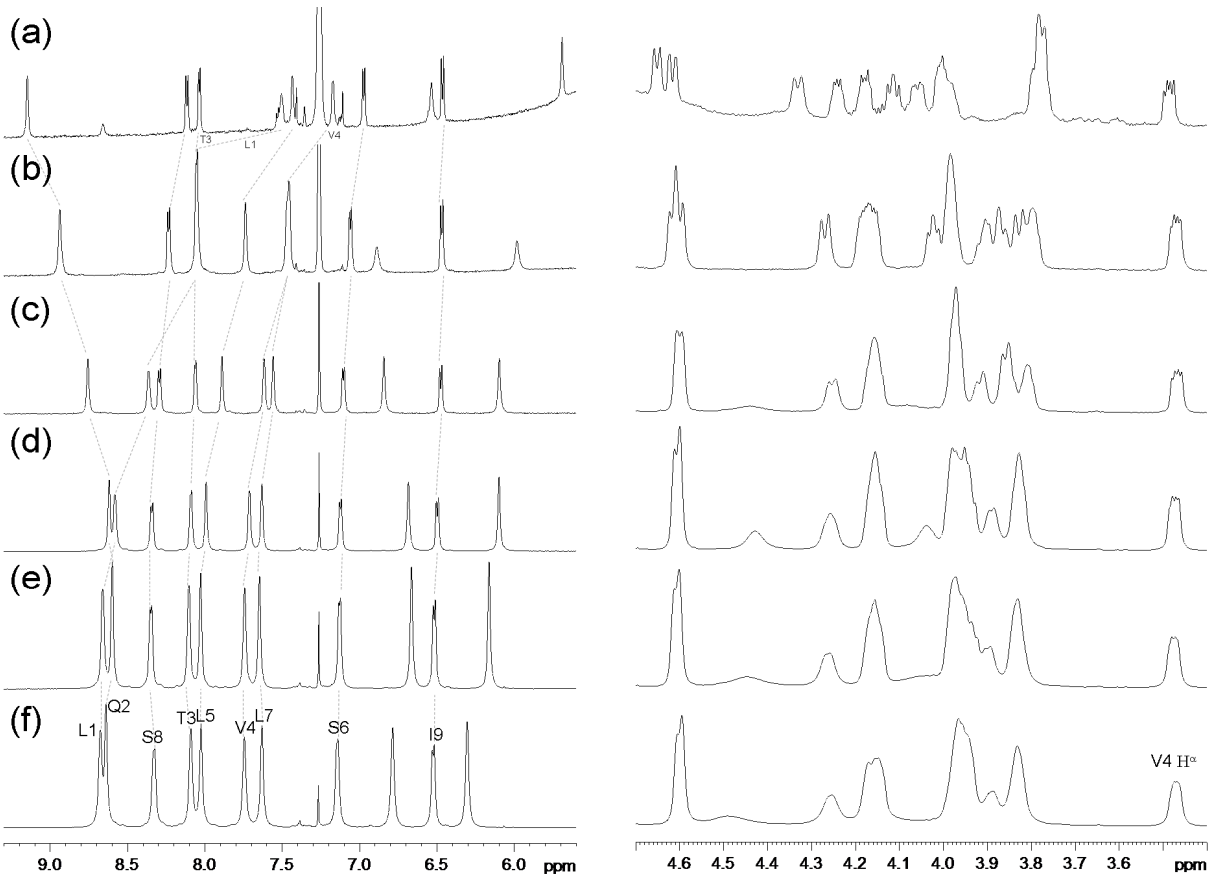

Figure 6.1: 1D ^{1}H spectra of pseudodesmin A in chloroform solution at 25℃ (left: H^N region, right: H^{α} region); All H^N protons are indicated by their corresponding amino acid one letter code and sequence position. (a) 0.06 mM; (b) 0.29 mM; (c) 1.13 mM; (d) 4.00 mM; (e) 9.97 mM; (f) 20.53 mM.

of the viscosity changes during the concentration study. A slight dependence of D_{TMS} with the pseudodesmin A concentration was found (Figure 6.2). Instead of using the D_{TMS} directly, the concentration dependence was first modelled by a linear regression analysis, the result of which was then used to calculate the viscosity correction factors (Figure 6.2). This is described in further detail in Figure 6.2 and Table 6.1.

A first important observation from the diffusion experiments is that the diffusion signal attenuation shows monoexponential behaviour at every concentration (Figure 6.3). The kinetics of the association is thus fast on the diffusion time scale. This implies that the apparent translational diffusion coefficient is a weighted average of the diffusion coefficients of each oligomer. This average manifests itself as follows[2]:

$$D_{av} = \frac{\sum_i i\alpha_i D_i}{\sum_i i\alpha_i} \tag{6.2}$$

Table 6.1: Translational diffusion measurement results on pseudodesmin A at various concentrations in chloroform and in acetonitrile

c [mM]	Δ [ms]	δ [ms]	D [µm^2/s][a]	D_{TMS} [µm^2/s][a]	Correction factor[b]	D_{corr} [µm^2/s][c]	R_H [Å][d]
20.53	450	1.50	106.7 ± 0.3	2102.5 ± 12.7	1.087	116.0 ± 0.3	35.1
18.32	450	1.50	108.8 ± 0.3	2147.5 ± 22.9	1.077	117.2 ± 0.3	34.7
16.29	450	1.50	109.2 ± 0.3	2137.7 ± 20.1	1.068	116.7 ± 0.3	34.9
13.33	200	2.00	126.8 ± 0.4	2160.3 ± 21.4	1.055	133.8 ± 0.4	30.4
11.90	450	1.35	132.5 ± 0.3	2179.5 ± 25.2	1.049	139.0 ± 0.3	29.3
10.86	450	1.20	137.2 ± 0.5	2156.0 ± 30.6	1.044	143.3 ± 0.6	28.4
10.30	450	1.10	149.3 ± 0.4	2203.7 ± 23.4	1.042	155.6 ± 0.4	26.1
9.97	450	1.20	146.7 ± 0.6	2196.3 ± 31.5	1.041	152.7 ± 0.6	26.6
9.46	450	1.10	150.4 ± 0.4	2191.5 ± 25.3	1.038	156.2 ± 0.4	26.0
7.86	450	1.05	163.1 ± 0.5	2229.4 ± 35.4	1.032	168.3 ± 0.5	24.2
6.88	450	1.05	167.8 ± 0.5	2215.1 ± 35.6	1.028	172.4 ± 0.5	23.6
6.15	450	1.10	178.8 ± 0.5	2245.2 ± 14.4	1.025	183.2 ± 0.5	22.2
4.58	450	1.00	195.1 ± 0.6	2233.8 ± 50.0	1.018	198.6 ± 0.7	20.5
4.00	450	0.95	202.0 ± 0.9	2239.2 ± 37.7	1.016	205.3 ± 0.9	19.8
3.06	450	0.95	220.6 ± 1.4	2252.6 ± 32.1	1.012	223.3 ± 1.4	18.2
1.93	450	0.90	252.7 ± 1.7	2266.9 ± 41.2	1.008	254.6 ± 1.7	16.0
1.59	450	0.85	256.6 ± 1.9	2250.1 ± 38.3	1.006	258.2 ± 1.9	15.8
1.13	450	0.80	277.3 ± 2.4	2287.8 ± 18.1	1.004	278.6 ± 2.5	14.6
0.72	450	0.80	293.2 ± 1.9	2288.3 ± 19.1	1.003	294.0 ± 1.9	13.8
0.53	450	0.80	312.1 ± 2.6	2282.1 ± 17.4	1.002	312.7 ± 2.6	13.0
0.45	450	0.75	318.0 ± 0.9	2268.4 ± 36.0	1.002	318.6 ± 0.9	12.8
0.29	450	0.70	341.3 ± 1.5	2256.9 ± 38.3	1.001	341.7 ± 1.5	11.9
0.14	450	0.60	414.3 ± 5.4	2262.2 ± 33.6	1.001	414.5 ± 5.4	9.8
0.10	450	0.60	431.9 ± 5.1	2291.8 ± 12.0	1.000	432.0 ± 5.1	9.4
0.08	450	0.60	454.6 ± 4.8	2283.6 ± 12.0	1.000	454.7 ± 4.8	8.9
0.07	450	0.60	455.4 ± 26.1	2290.2 ± 16.9	1.000	455.6 ±26.1	8.9
0.06	400	0.60	468.0 ± 13.5	2281.4 ± 14.5	1.000	468.1 ±13.5	8.7
CD_3CN	320	1.25	816.8 ± 4.4	3575.9 ± 70.3	--	--	7.2

[a] Error on diffusion coefficient calculated using a Monte Carlo procedure with 400 simulations (appendix C). Note that this error is based on the precision of the data points with respect to the fitted decay function and does not include uncertainties due to inaccuracies in the assumed experimental conditions, such as gradient calibration, temperature, etc. Therefore, the error may be somewhat underestimated, especially at higher concentrations.

[b] Viscosity correction factor calculated as $2281.5/(-8.9186 \times c + 2281.5)$, using the results shown in Figure 6.2.

[c] Pseudodesmin A diffusion coefficient multiplied with the correction factor.

[d] Hydrodynamic (or Stokes) radius based on D_{corr}, assuming a viscosity of 0.537 mPa·s for chloroform and 0.369 mPa·s for acetonitrile.

The weighting of the oligomer diffusion coefficients in the average occurs differently than was the case in equation (6.1). The reason for this is that the Brownian motions of the individual molecules do not occur independently when they are together in an oligomeric structure. The diffusion process is therefore coupled with the fast self-association equilibria. It can be shown that this results in an increased weighting of the larger oligomers[2]. The average and thus apparent diffusion coefficient D_{av} is an indicator for the degree of self-association, as it puts a lower limit on the maximum oligomer size that is present at that particular concentration. This size is represented by the hydrodynamic radius R_H, calculated from the average diffusion coefficient

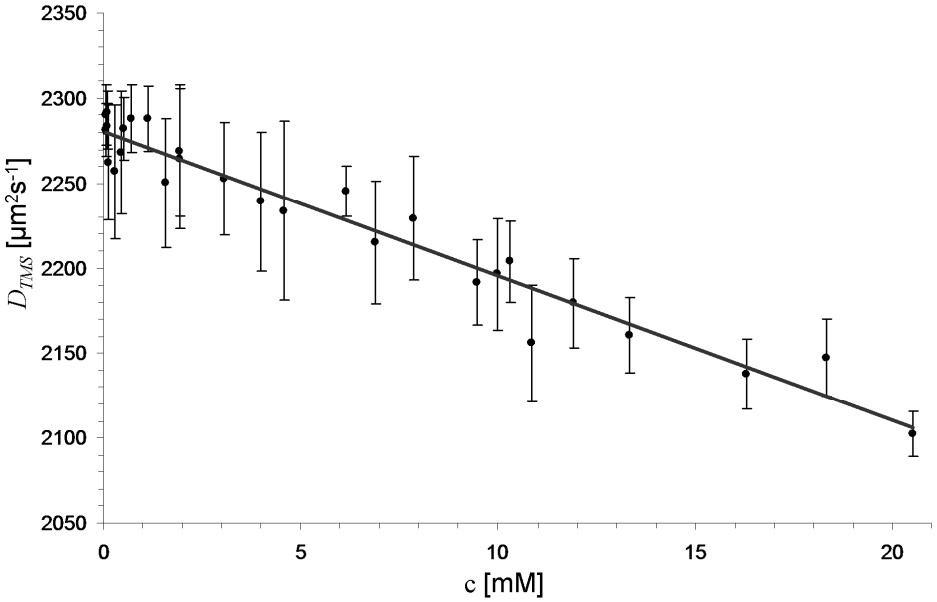

Figure 6.2: The TMS diffusion coefficient as a function of the pseudodesmin A concentration. A linear regression was performed, resulting in the relation $D_{TMS} = -8.9186 \times c + 2281.5$ ($R^2 = 0.91$). The viscosity correction factors that convert the pseudodesmin A diffusion coefficients to a concentration of zero can then be calculated as: $2281.5/(-8.9186 \times c + 2281.5)$ and are listed in Table 6.1.

using equation (1.39) (Table 6.1). Note that the hydrodynamic radius assumes a spherical shape. Although at this point nothing can be assumed about the shape of the supramolecular assembly, the hydrodynamic radius still provides a good qualitative picture on the degree of increase in average size.

The results in Table 6.1 show that the apparent diffusion coefficient changes strongly over the range of concentrations studied (Figure 6.4a). At the highest concentration, the average diffusion coefficient corresponds to a hydrodynamic radius of 35.1 Å, which is much larger than the dimensions of the molecule seen in the acetonitrile solution or crystal structures (*ca.* 5-8 Å radius). The diffusion coefficient drops continuously and increasingly with increasing concentration, until a value in agreement with the monomer structure dimensions is reached at 0.06 mM, the lowest concentration that could be probed here. The hydrodynamic radius of a single pseudodesmin A molecule derived from the diffusion coefficient measured in acetonitrile solution (Table 6.1) provides a similar value, further confirming that at the lowest concentration the association equilibrium is strongly shifted towards the monomer.

The apparent hydrodynamic radius thus increases fourfold over an increase in concentration with a factor 340. For a spherical object, a fourfold increase in radius corresponds to an increase of a factor 64 in volume. Although again the assumption of spherical objects was made, it is clear that the supramolecular structure formed at high concentration in chloroform must consist of many monomer units. In addition,

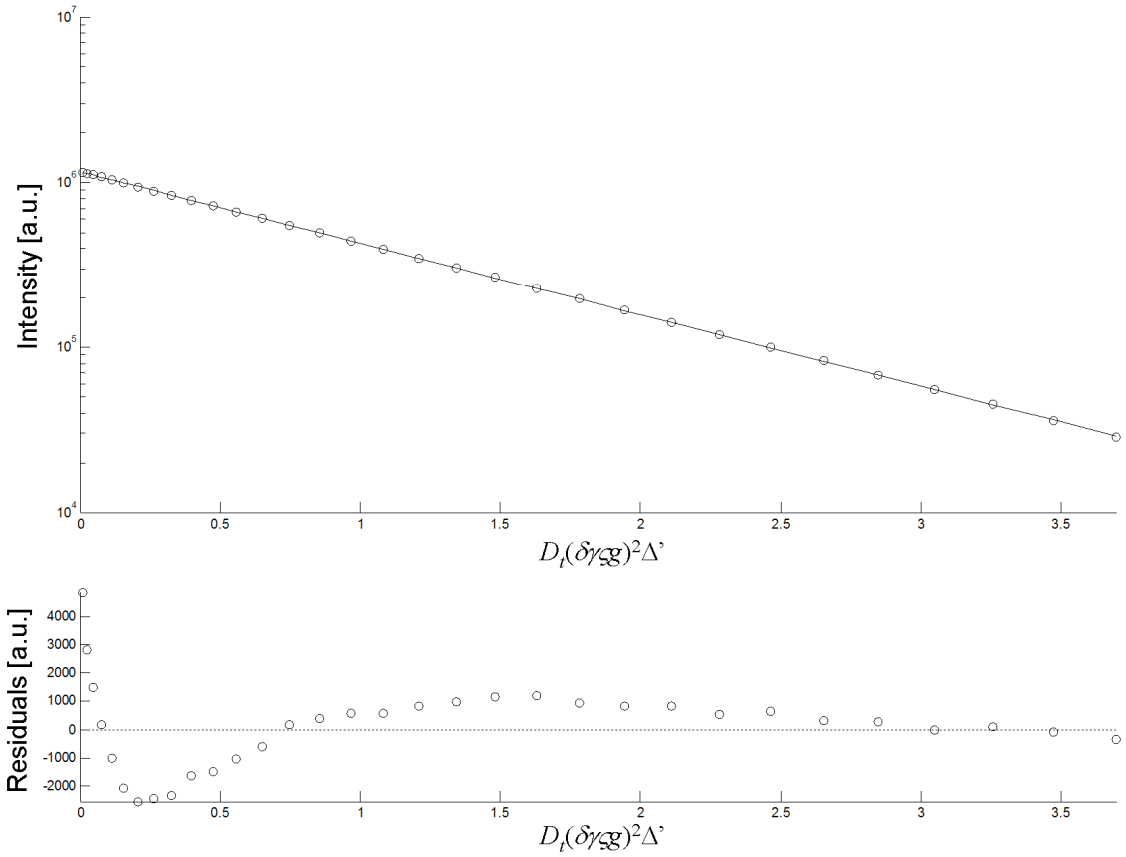

Figure 6.3: Methyl region signal intensity as a function of the gradient strength during the PFG experiment on a 20.53 mM solution of pseudodesmin A in chloroform. The decay is clearly monoexponential, resulting in the linear curve in the semilogarithmic plot. The small deviation from exponential behaviour as clearly seen in the residuals is most likely to be ascribed to magnetic gradient non-uniformity over the NMR sample.

there is no sign that a plateau value is reached. Taken all together, it is apparent that the self-association is indefinite, *i.e.* that there is no upper limit to the supramolecular size.

It is interesting to note the form of the concentration dependence of the diffusion coefficient and hydrodynamic radius. The apparent diffusion coefficient changes most rapidly at the lower concentrations measured, which might reflect a stronger increase in relative size of small oligomers than of larger ones at high concentration. The diffusion coefficient seems to be adequately described by a logarithmic relationship with the concentration (Figure 6.4b). Plotting the hydrodynamic radius (or the inverse of the diffusion coefficient) against the concentration also provides a quite linear behaviour (Figure 6.4c), except for the lowest concentrations (starting from *ca.* 1 mM downward) where a stronger concentration dependence is observed. This might already be interpreted with care as a preliminary indication that at lower concentrations the self-association mechanism is different from that at higher concentration.

6.3 Effect of solvent polarity

As discussed in Section 4.5, the behaviour of pseudodesmin A depends on the polarity of the solvent. To assess this effect on the self-association, a solvent titration was performed at 298 K by stepwise adding a *ca.* 2 mM solution of pseudodesmin A in acetonitrile to solution of pseudodesmin A of exactly equal concentration in chloroform. In this way, the acetonitrile volume percent is gradually increased from 0% to 13% without interference from the dependence on concentration which remains constant. The gradual increase of the acetonitrile content has a similar effect on the ^{1}H spectra as lowering the concentration in chloroform (Figure 6.5), gradually decreasing the line widths of the resonances. Figure 6.6 compares the degree and direction of the chemical shift changes of the H^{N} resonances with those observed by changing the concentration in chloroform, revealing the same trends to be present.

Table 6.2: Translational diffusion measurement results on pseudodesmin A during the chloroform to acetonitrile titration experiment.

v/v%	D [$\mu m^2 s^{-1}$][a]	R_H [Å][b]	D_{TMS} [$\mu m^2 s^{-1}$][a]
0.0	262.3 ± 1.8	15.5	1949.5 ±16.9
1.0	289.2 ± 2.4	14.1	1978.7 ±13.6
2.0	316.5 ± 1.7	12.9	1965.1 ±15.2
3.0	344.5 ± 2.1	11.8	1974.4 ±12.6
4.0	376.8 ± 2.0	10.8	1974.0 ±16.9
5.0	398.2 ± 1.6	10.2	1967.8 ±10.2
6.0	420.3 ± 2.8	9.7	1967.2 ±10.9
7.0	435.7 ± 2.2	9.3	1943.2 ±11.6
8.0	450.8 ± 2.9	9.0	1949.7 ±14.9
9.0	456.8 ± 2.6	8.9	1931.2 ±14.9
10.0	463.0 ± 1.8	8.8	1933.5 ±14.6
11.0	470.1 ± 2.0	8.7	1949.3 ±12.2
12.0	475.6 ± 2.2	8.6	1954.3 ± 9.6
13.0	484.7 ± 2.8	8.4	1963.6 ±16.1

[a] Error on diffusion coefficient calculated using a Monte Carlo procedure with 500 simulations (appendix C). Note that this error is based on the precision of the data points with respect to the fitted decay function and does not include uncertainties due to inaccuracies in the assumed experimental conditions, such as gradient calibration, temperature, etc. Therefore, the error may be somewhat underestimated.

[b] Hydrodynamic (or Stokes) radius assuming a viscosity of 0.537 mPa·s for chloroform.

The diffusion coefficient of both pseudodesmin A and internal TMS was followed as well (Table 6.2). For this, a monopolar gradient convection compensated PFG pulse sequence was used, applying 32 linearly sampled gradient increments values and using values for Δ and δ so that the signal decay was adequately sampled. The diffusion coefficient of TMS was monitored as a function of acetonitrile volume percent to check for any viscosity effects. It appears that no significant changes in TMS diffusion coefficient occur within the range of the experiment, thus excluding changes in viscosity (Figure 6.7). The pseudodesmin A diffusion coefficient increases

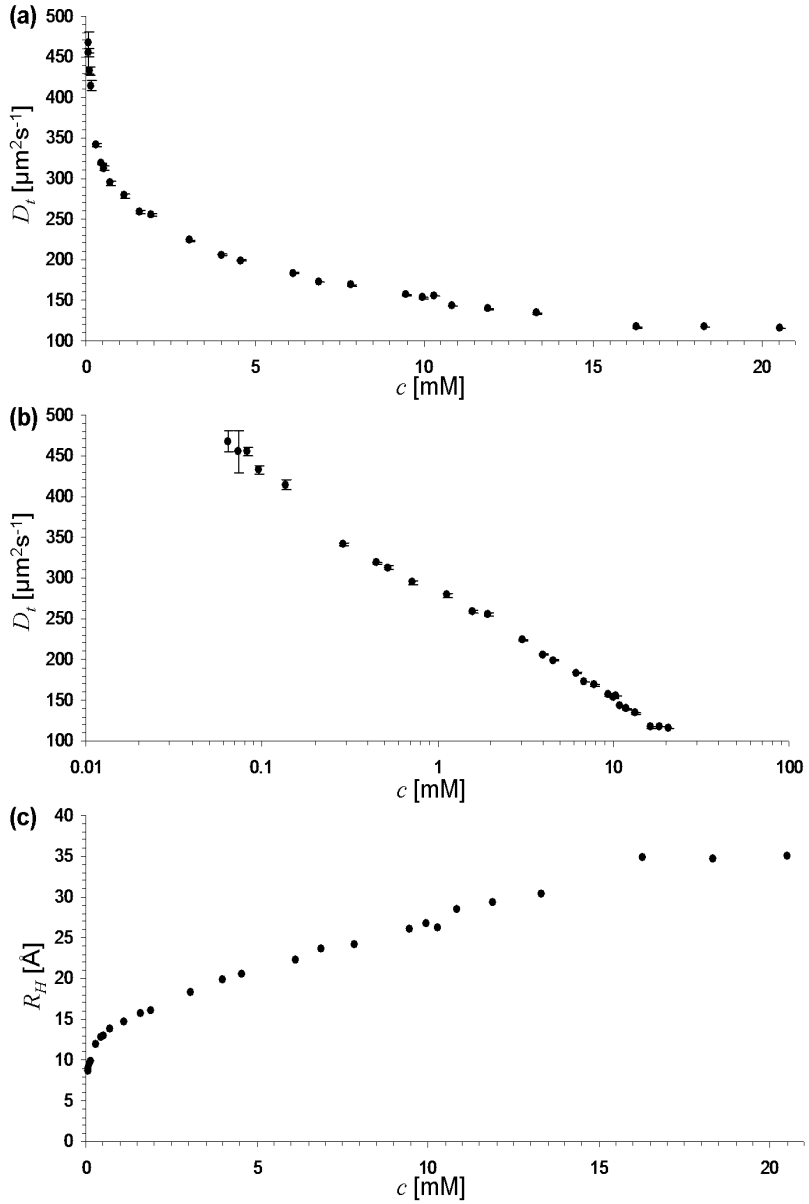

Figure 6.4: (a) Pseudodesmin A translational diffusion coefficient with 95% error bars, plotted against the concentration. (b) Same graph, but at semilogarithmic scale, revealing the apparent linear relation between the diffusion coefficient and the logarithm of the concentration. (c) Hydrodynamic radius plotted against the concentration.

steadily with the volume percent of acetonitrile (Figure 6.8), eventually reaching a value of 484.7 ± 2.8 $\mu m^2 s^{-1}$ at 13%. This is similar to the diffusion coefficient in chloroform solution at 0.06 mM, which was found to be 468.0 ± 13.5 $\mu m^2 s^{-1}$. All in all, gradually changing the polarity of the solvent environment has the same effect as lowering the concentration: shifting the self-association equilibria towards the monomeric state. This study confirms that the low polarity of the environment is the driving force of the self-association and that the size of the supramolecular structures formed can therefore be controlled by varying the overall polarity of the solvent.

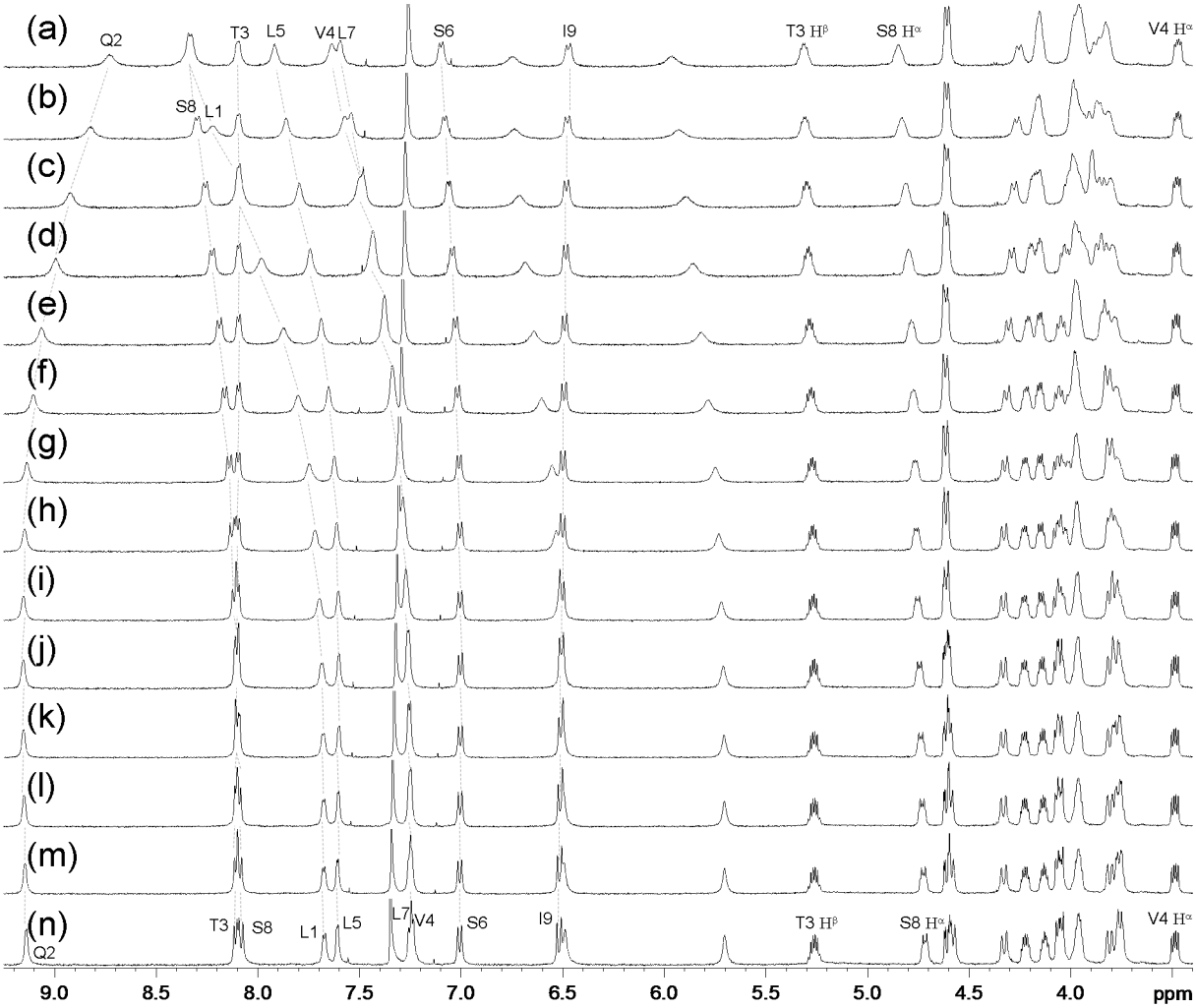

Figure 6.5: Evolution of the H^N and H^α regions of the 1D ^1H spectrum of pseudodesmin A during the chloroform to acetonitrile solvent titration. All H^N protons are indicated by their corresponding amino acid one letter code and sequence position. (a) 0% CD_3CN; (b) 1%; (c) 2%; (d) 3%; (e) 4%; (d) 5%; (g) 6%; (h) 7%; (i) 8%; (j) 9%; (k) 10%; (l) 11%; (m) 12%; (n) 13%.

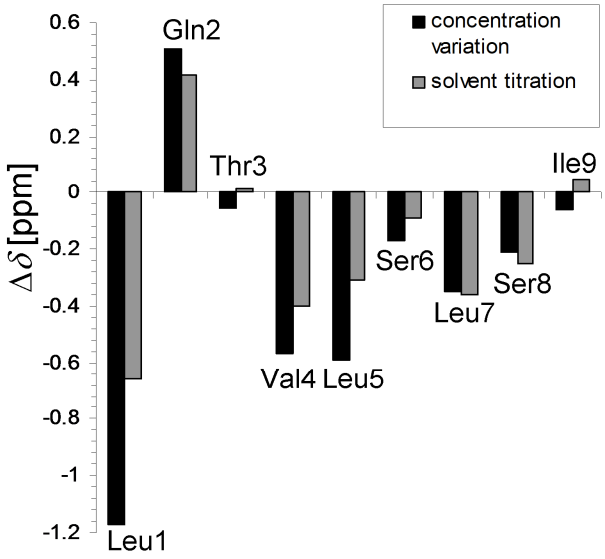

Figure 6.6: The difference between the ^1H chemical shift at the lowest and the highest concentration measured in chloroform, compared to the difference in ^1H chemical shift at the start and at the end of the chloroform to acetonitrile solvent titration.

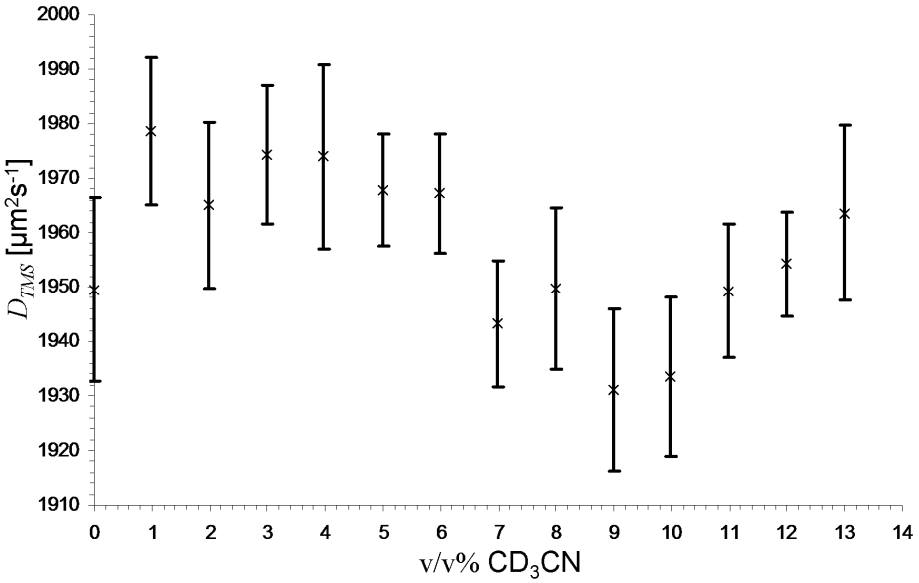

Figure 6.7: Variation of the TMS diffusion coefficient during the chloroform to acetonitrile titration experiment with 95% error bars.

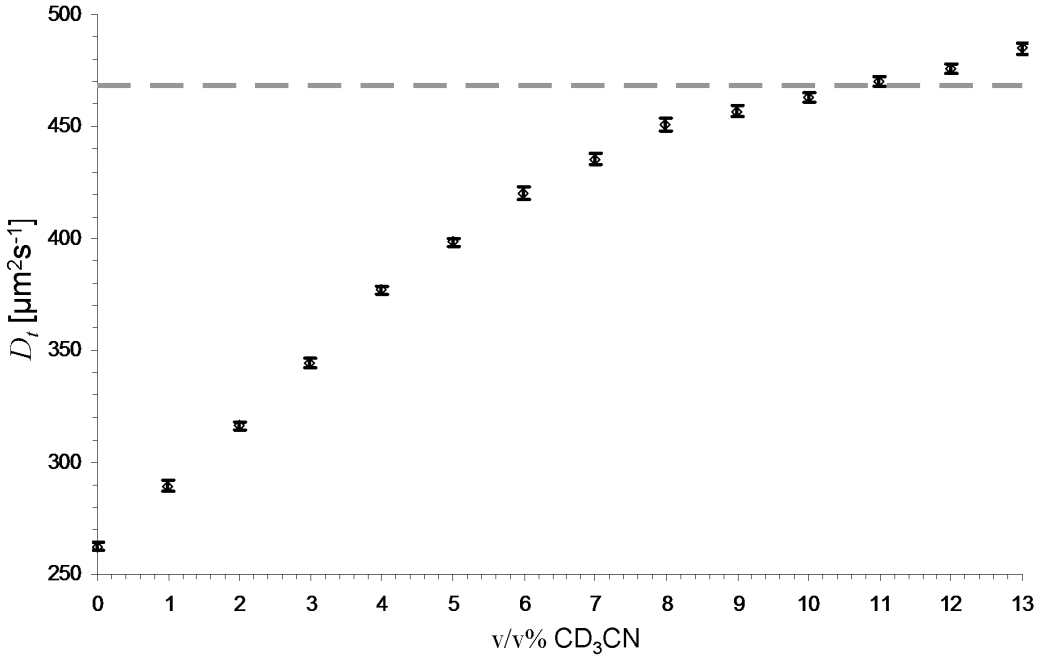

Figure 6.8: Pseudodesmin A diffusion coefficient during the chloroform to acetonitrile solvent titration experiment with 95% error bars. The dashed line at 468.1 µm^{2}s^{-1} represents the diffusion coefficient value of the lowest concentrations measured in chloroform (Table 6.1).

6.4 Identification of intermolecular contacts

What is the mechanism of the self-association of pseudodesmin A at the molecular level? To gain insight into this matter, it is important to identify which parts of the molecule are involved in the intermolecular contacts between monomer units. One

possible way of doing so would be to identify spatial proximities between the protons of different monomer units. Since the conformation of the monomer is known and has previously been shown to be retained within the supramolecular structure (section 5.5), all observed ^{1}H-^{1}H proximity correlations that cannot be explained by the monomer conformation can in principle be interpreted as intermolecular contacts. For this purpose, 2D NOESY spectra are not useful since the large size of the supramolecular structures leads to excessive spin diffusion (Figure 4.5), even at short mixing times. This makes the distinction between spin diffusion and intermolecular contacts impossible. However a 2D ROESY suffers less from these disadvantages. Indeed, spin diffusion develops inherently much slower during the spin lock mixing time[3]. In addition, any spin diffusion cross-peak that does get through will exhibit a sign inversion with respect to a regular rOe cross-peak due to the magnetisation experiencing a double negative rOe transfer step. The disadvantage of ROESY is a lower signal-to-noise ratio due to the faster $T_{1\rho}$ relaxation – which is a combination of T_1 and T_2 – during the spinlock when compared to the T_1 relaxation during the mixing time of a NOESY, although this did not pose any problems due to the high concentration of the pseudodesmin A sample used.

The experiment was performed on a *ca.* 20 mM chloroform solution at 700.13 MHz and at 283.0 K, using a 40 ms spinlock mixing time. After cataloguing all rOe correlations (Figure 6.9), they were confronted against the acetonitrile solution structure. In this way, several contacts were identified between protons that were far apart, both in the primary sequence (more than one residue apart) and spatially (more than 6 Å away in the solution structure). These rOes, listed in Table 6.3, mostly reflect contacts between backbone protons at the N-terminal (HDA, Leu1, Gln2) and the C-terminal (Ser6-Ile9) side of the structure. Typically, these contacts are between the H^N protons of Leu1 and Gln2 and between the H^α protons of Ser6, Leu7 and Ser8. These observations suggest that the contact between monomer units occur along these sides of the structure and at the level of the backbone. Since the amides at the helix N-terminus and carbonyls at the helix C-terminus and loop structure are not involved in any intramolecular hydrogen bonds, this contact is most likely mediated by intermolecular hydrogen bonds between these two groups. There are also several contacts between the hydrophilic residue side chains, mainly the Gln2 side chain amide group and both Ser side chains. This indicates that the side chains of the hydrophilic residues are close to each other. This contrasts with the side chains of the hydrophobic residues which, with the exception of the Ile9 H^β proton, are not involved in any intermolecular contacts. An HSQC-NOESY spectrum with mixing time 100 ms was recorded on a *ca.* 20 mM chloroform sample also did not reveal any nOes between the methyl resonances other than between those of the same side

chain (data not shown). It should be noted that the intermolecular contacts listed in Table 6.3 are limited to those that can impossibly be explained by intramolecular contacts. Therefore any intermolecular contacts that would exist between residues that are close intramolecularly will not be recognised in this analysis. For example, any intermolecular contacts between the side chains of the two Ser residues is confounded with the intramolecular contacts that already exist.

Table 6.3: Intermolecular rOe contacts between ^{1}H resonances in chloroform

resonance 1		resonance 2	d_{intra} [Å][a]	rOe[b]
HDA CH_2^{α}	-	Ser8 H^{α}	9.8	strong
HDA CH_2^{α}	-	Ser6/Ile9[c] H^{α}	9.8/6.6	weak
HDA CH_2^{γ}	-	Ser8 H^{α}	10.3	strong
Leu1 H^N	-	Ser6 CH_2^{β}	9.0	weak
Leu1 H^N	-	Leu7 H^{α}	12.5	strong
Leu1 H^N	-	Ser8 H^{α}	12.7	strong
Leu1 H^N	-	Ser8 OH	9.9	intermediate
Leu1 H^N	-	Ile9 H^{β}	9.3	strong
Leu1 H^N	-	Ser6/Ile9[c] H^{α}	10.7/10.0	intermediate
Gln2 H^N	-	Leu7 H^{α}	11.1	strong
Gln2 H^N	-	Ser8 H^{α}	11.6	strong
Gln2 H^N	-	Ser8 OH	8.3	intermediate
Gln2 H^N	-	Ser6/Ile9[c] H^{α}	8.5/9.9	weak
Gln2 H^N	-	Ile9 H^{β}	9.8	strong
Gln2 NH_2 E[d]	-	Ser6 CH_2^{β}	7.3	weak
Gln2 NH_2 Z[d]	-	Ser6 CH_2^{β}	8.4	weak
Gln2 NH_2 E	-	Ser6 OH	8.8	intermediate
Gln2 NH_2 Z	-	Ser6 OH	9.5	weak
Gln2 NH_2 E	-	Leu7/Leu5[c] H^{α}	13.5/10.5	intermediate
Gln2 NH_2 Z	-	Leu7/Leu5[c] H^{α}	14.3/11.0	intermediate
Gln2 NH_2 E	-	Ser8 H^{α}	13.1	strong
Gln2 NH_2 Z	-	Ser8 H^{α}	13.9	strong
Gln2 NH_2 E	-	Ser8 OH	9.4	weak
Gln2 NH_2 Z	-	Ser8 OH	10.3	weak
Gln2 NH_2 E	-	Ile9 H^{β}	12.7	weak
Gln2 NH_2 Z	-	Ile9 H^{β}	12.6	weak

[a] Intramolecular distance between the hydrogen atoms in the solution structure.
[b] rOe intensity in chloroform solution.
[c] Ambiguous assignment.
[d] Discrimination between E and Z protons based on Gln2 NH_2 – Gln2 CH_2^{γ} rOe intensities.

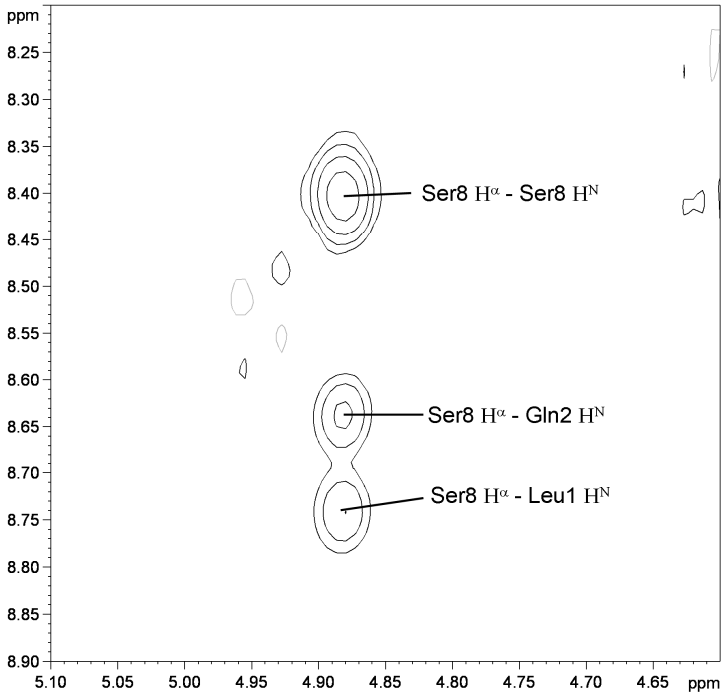

Figure 6.9: Example of two clear intermolecular rOe contacts visible in the 2D ROESY spectrum in chloroform.

Another parameter that can be used to screen the intermolecular contact surface is the chemical shift. As the degree of self-association varies, the very environment sensitive chemical shifts of the ^{1}H, ^{13}C and ^{15}N nuclei directly involved with the intermolecular contact surface should be the most affected. Since the monomeric state is only achieved at very low concentrations in chloroform (< 100 µM), it is not feasible to measure the ^{13}C and ^{15}N chemical shift by lowering the concentration. Therefore, a second chloroform to acetonitrile titration was performed at 283.0 K, this time measuring a ^{1}H-^{13}C gHSQC and a ^{1}H-^{15}N gHSQC spectrum at each step. Despite the lower sample temperature used, significant solvent evaporation took place during the titration study due to the long measuring time required at natural abundance. This creates a significant uncertainty on the effective acetonitrile volume percent. For this reason, the translational diffusion coefficient was measured as well and used as a quantitative descriptor of the degree of self-association. To obtain a relevant chemical-shift difference, the absolute value of the slope obtained through linear regression between the chemical shift and diffusion coefficient (ranging between 178.5 $\mu m^2 s^{-1}$ and 436.3 $\mu m^2 s^{-1}$) was multiplied with the difference in diffusion coefficient over the entire titration experiment (appendix I). The average chemical shift of each $^{1}H/^{15}N$[4] and $^{1}H/^{13}C$ HSQC cross-peak was calculated as:

$$\delta_{av}\left(^{1}H/^{15}N\right) = \delta\left(^{1}H\right) + \delta\left(^{15}N\right)/5$$
$$\delta_{av}\left(^{1}H/^{13}C\right) = \delta\left(^{1}H\right) + \delta\left(^{13}C\right)/2 \qquad (6.3)$$

The results are displayed in Figure 6.10 and are tabulated in appendix I. The most notable changes (> 0.3 ppm) in the $^{1}H/^{13}C$ chemical shifts occur mainly at those positions where intermolecular rOe contacts were detected as well (Leu7 CH^{α}, Ser8 CH^{α} and CH_2^{β}, HDA CH_2^{α}). Overall, no strong changes are detected at the level of the hydrophobic side chains, where the chemical shift perturbations of all methyl groups, except Thr3 CH_3^{γ}, lie between 0.02 ppm and 0.13 ppm. This is in agreement with the observation that no intermolecular rOe contacts were detected between these side chains. The larger perturbation of the Thr3 CH_3^{γ} group is not surprising, since it is directly attached to the macrocyclic structure and is oriented along the same side of the molecule as the hydrophilic residue side chains (*vide infra*, Figure 6.11)

In the $^{1}H/^{15}N$ chemical shift perturbations, important effects are seen for the Leu1 and Gln2 NH groups, which is in agreement with what was seen with the intermolecular rOe contacts. The same is true for the changes seen for the Leu7 and Ser8 NH groups, as their respective residues where also involved in intermolecular rOe contacts. However, the origin for the considerable changes at the level of the Val4 and Leu5 NH groups is less obvious. An explanation could be that the association process induces changes in the intramolecular hydrogen bond strengths, leading to the observed changes in the environment sensitive amide chemical shift. It is clear however from their location in the structure that they do not participate in the proposed interface. In the end, because of the limit size of the pseudodesmin A molecule, it is difficult to assume that only a limited region of the structure will be influenced by the association.

6.5 Proposal for the supramolecular structure

Pseudodesmin A is found to be soluble in most organic solvents, but very poorly soluble in water. Although a simple organic solvent such as chloroform should not be considered as a good mimic for a biological membrane environment, both share a non-polar nature and it is therefore likely that pseudodesmin A will favour an insertion into the membrane. Due to the nature and the stability of the monomer structure found in acetonitrile, it can be safely assumed that this structure will be adopted within the membrane as well. Given the non-polar environment, it is also very likely that the supramolecular structures will be formed in the membrane and could thus form the basis for the assumed ion pore formation (as discussed in Chapter 4). Indeed, due to its limited size (*ca.* 15 Å diameter), an individual pseudodesmin A molecule is incapable of spanning the membrane bilayer, with a diameter on the order of about 45 Å[5]. With all the data that have been gathered so far on the structure of pseudodesmin A and its self-association properties, it is possible to propose a model for the supramolecular structures. Such a model should explain why

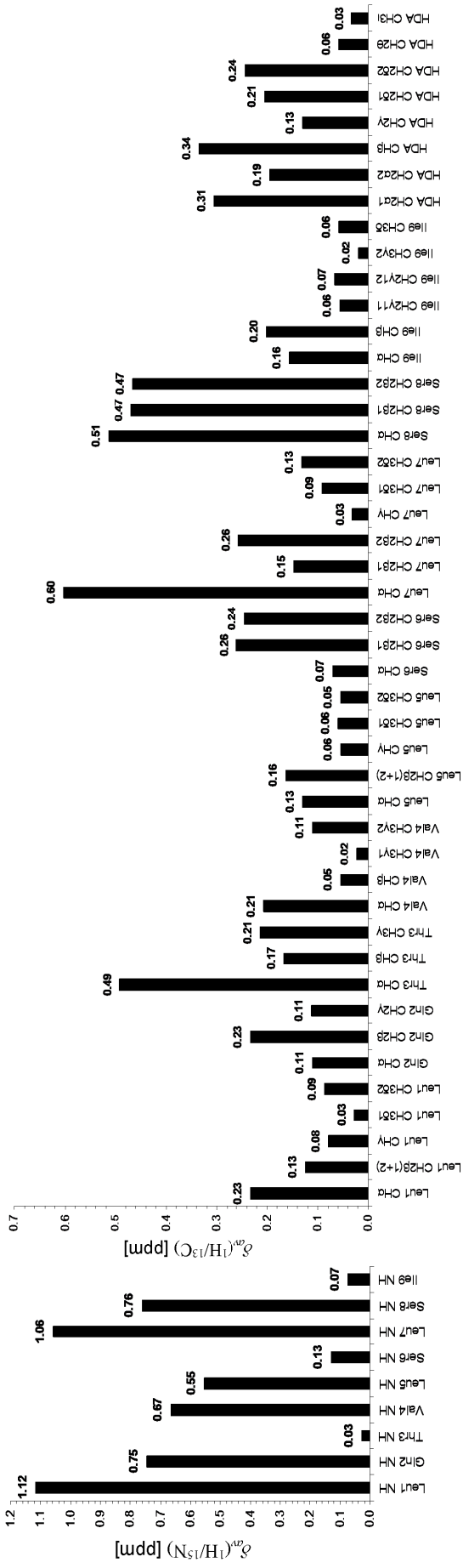

Figure 6.10: Average $^1H/^{13}C$ and $^1H/^{15}N$ chemical shift perturbations resulting from the second chloroform to acetonitrile solvent titration. These values are calculated and tabulated in appendix I.

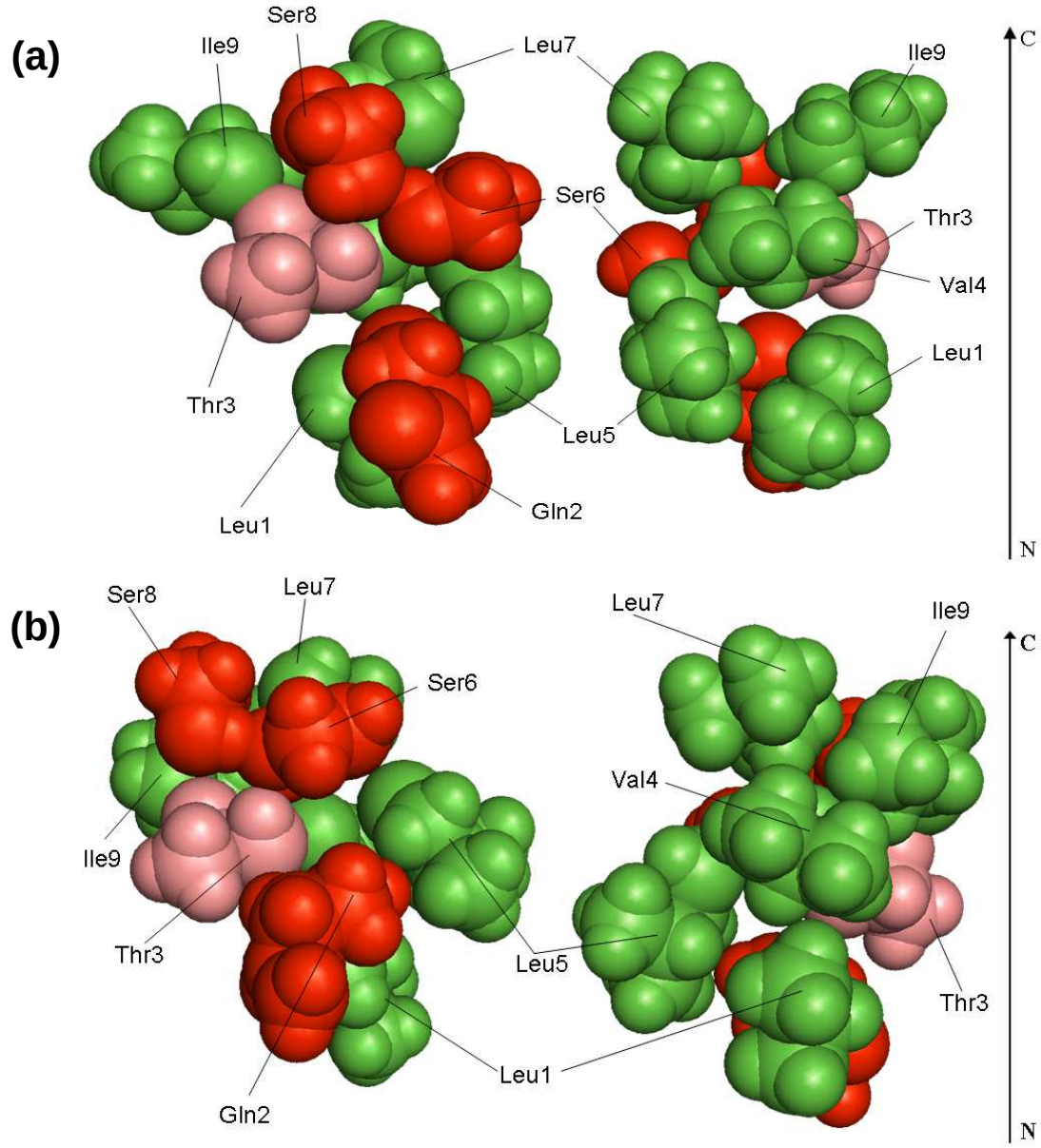

Figure 6.11: Sphere representation of the crystal (a) and solution (b) structures of pseudodesmin A to illustrate the amphipaticity, showing only the side chain atoms starting from CH^{α}. The hydrophobic and hydrophilic sides are shown separately, while the α-helix is aligned from bottom to top (N→C) as indicated by the arrow. Hydrophobic side chains are coloured green, hydrophilic side chains red and the Thr3 residue salmon. The HDA residue is left out for clarity.

the self-association occurs only in non-polar solvents, while in addition it can be related to the pore formation.

Two types of distinct monomer interactions are proposed to occur in the assembly of the supramolecular structures. Firstly, it is observed that the pseudodesmin A solution and crystal structures are amphipatic, *i.e.* the residues are positioned in the sequence so that all hydrophobic and hydrophilic side chains are divided in two groups along the molecular surface (Figure 6.11). This creates a large hydrophobic surface, comprised of all Leu, Ile and Val side chains. A smaller hydrophilic surface includes both the Ser and the Gln residue side chains. When inserted into a non-

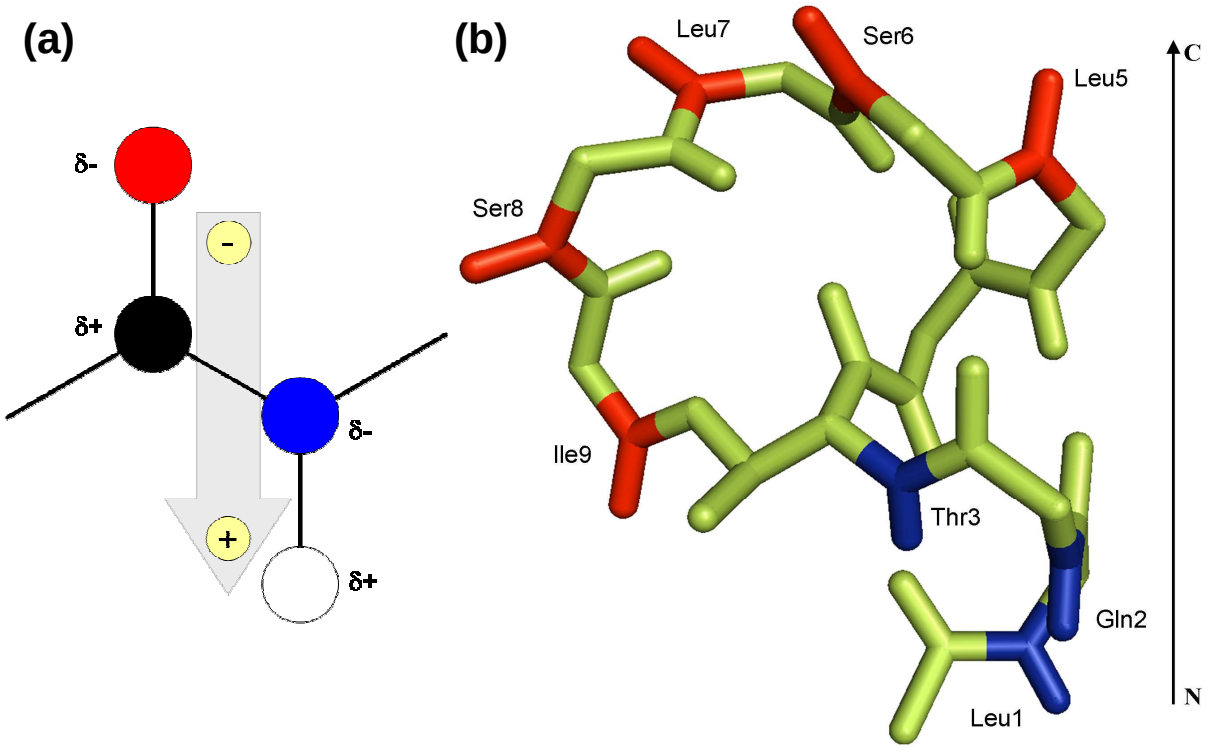

Figure 6.12: (a) Amide groups inherently possess a dipole moment due to the constructive addition of the dipole moments of the CO and NH bonds. In a helix structure motif, all amide groups are aligned, effectively creating a macrodipole. (b) The solution structure of pseudodesmin A showing only the main chain atoms. The α-helix, which thus creates a macrodipole, is aligned from bottom to top (N→C) as indicated by the arrow. All NH and CO groups available for intermolecular hydrogen bonding are coloured blue and red respectively, and are located at the ends of the helix and in the loop.

polar solvent or membrane environment, pseudodesmin A molecules can be expected to pack their hydrophilic surfaces together while extending the hydrophobic surfaces outward in order to minimise energetically unfavourable hydrophobic-hydrophilic contacts. This idea has been described previously for several AMPs[6, 7]. It finds additional support in the observation made before in section 4.3 that the hydrophobic and hydrophilic residue positions are strongly conserved within the viscosin group and thus appear to be essential for the biological function. The observed intermolecular contacts in section 6.4 between several hydrophilic side chains further confirm this hypothesis. However, such an aggregation would still be insufficient to create a structure that spans the membrane, and does not explain the huge apparent size observed in non-polar environments (section 6.2). Therefore, a second degree of assembly interactions is required.

Inherently, the helix structure possesses free CO and NH groups at its C- and N-terminal ends respectively, while in addition pseudodesmin A has more free CO groups in its loop structure. This creates a build-up of opposite charge at opposing sides of the molecule, effectively creating a macrodipole[8-10] (Figure 6.12). In a non-polar solvent or membrane, this can lead to an electrostatically driven alignment of molecules along a direction closely parallel with the helix, most likely with intermolecular NH-CO hydrogen bonds. This is supported by the observed strong

intermolecular rOe contacts of the Leu1 and Gln2 H^N with the Leu7 and Ser8 H^α. In this manner the 'length' necessary for the pore to span the cellular membrane is created. Such behaviour has also been previously been reported for the linear pentaibol antibiotic alamethicin[11]. This explains the observation of very large supramolecular structures at higher concentration in chloroform - larger than required for membrane spanning pores – since this interaction puts no limit on the length of the structures formed. In a membrane, the maximum size of such structures would be limited by the diameter of the bilayer, while in an organic solvent no such limitation is imposed. The formation of intermolecular amide hydrogen bonds gains further support by the results of a FT-infrared spectroscopy study combined with $^1H/^2H$ exchange of WLIP performed by Coraiola *et al*[12]. They detected the presence of non-hydrogen bonded amides in buffer solution, which seemed to decrease when dissolved in model membrane environment. As an alternative for a change in conformation of WLIP proposed by these authors, this could also be explained by intermolecular hydrogen bonding between the free NH groups of the N-terminal side of the helix of one molecular unit with the free CO groups of another unit.

With these two processes combined (Figure 6.13), a structure of sufficient size to span the membrane forms. Its interior is hydrophilic (Ser and Gln side chains), allowing positively charged ions to coordinate with alcohol or free carbonyl groups (perhaps also from the loop backbone), thus creating a channel through the membrane. The function of the HDA chain would then most likely be to increase membrane solubility or facilitate anchoring of the CLP into the membrane by tightly interacting with the lipid chains. The proposed model can of course be extended to the other CLPs with similar amphipatic structure as pseudodesmin A, such as WLIP, the pseudophomins, amphisin and tensin.

Finally, it would explain why the self-association is not observed in polar environment. It has been shown that the effective macrodipole μ_{eff} only manifests itself in an environment with low dielectric constant ε_r, as discussed by Sengupta *et al*[10]:

$$\mu_{eff} \propto \frac{1}{\varepsilon_r} \tag{6.4}$$

This is because the polar solvent molecules shield the macrodipole, therefore quenching the need for alignment of the pseudodesmin A molecules. In addition, the packing of the hydrophilic parts of the molecules will no longer occur, as the interaction between the hydrophilic side chains and the polar solvent is far less unfavourable compared to the non-polar solvents.

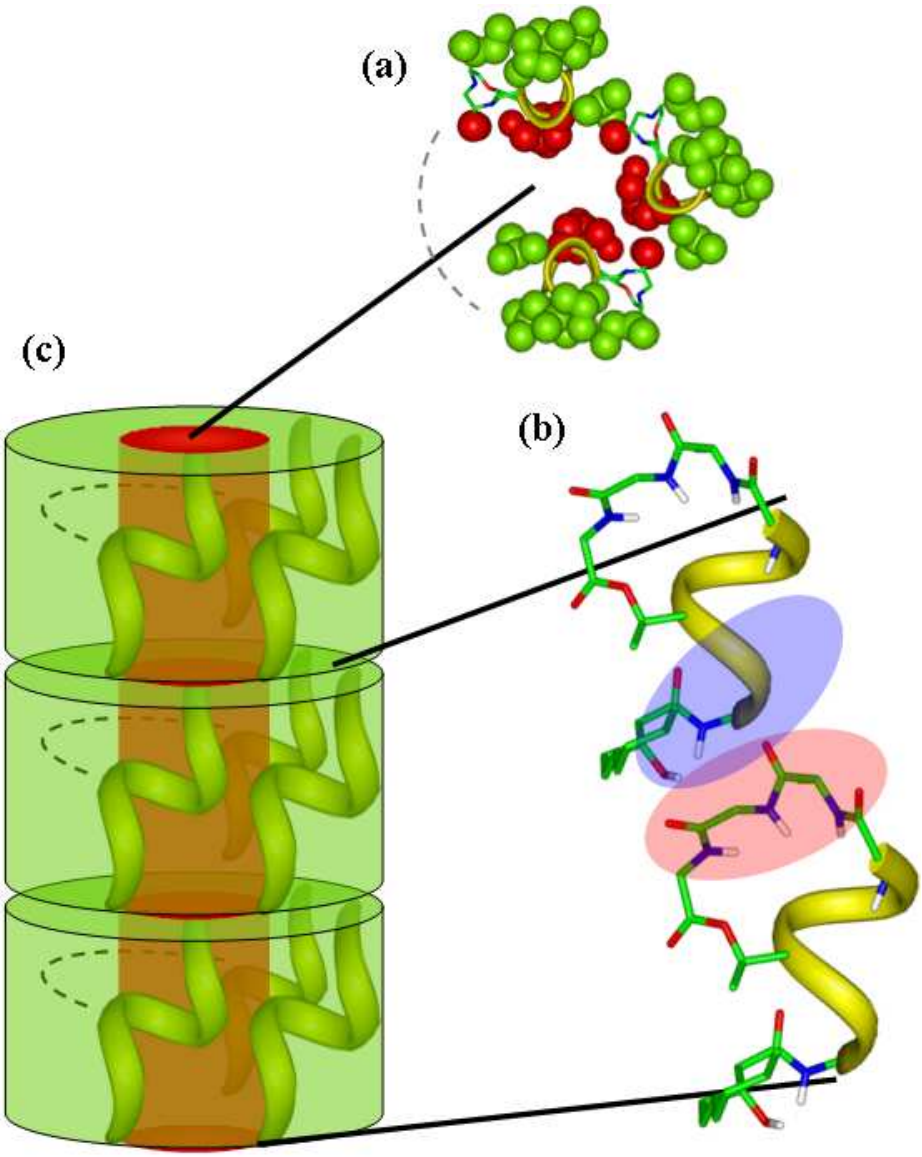

Figure 6.13: Illustration of the proposed model for the self-association. No actual residue specific intermolecular interactions or detailed arrangement of individual molecules are intended. (a) Top view of an undefined number of pseudodesmin A molecules aggregating their hydrophilic residue side chains (red) towards each other and directing the hydrophobic residue side chains (green) outward. (b) The free NH groups at the N-terminal end of the helix interact through electrostatic interaction with the free CO groups at the C-terminal end of the loop. (c) With both processes combined, a large supramolecular structure is formed with a hydrophilic interior and a hydrophobic exterior.

It should be emphasised that the number and exact arrangement of the monomer molecules within this structure cannot be specified. Only the type of interactions leading to the supramolecular structure and the concept of a hydrophilic inside and hydrophobic outside are specifically defined. The model also suggests that the structures are formed in two steps. First an aggregation of molecules by packing their hydrophilic sides against each other, and in a second step a stacking of these aggregates upon each other, leading to supramolecular structures that increase in length as the pseudodesmin A concentration is increased. It is possible that this two step mechanism is reflected within the observed different concentration dependence of the hydrodynamic radius at lower concentrations (section 6.2, Figure 6.4). At

higher concentrations, this mechanism should lead to structures of varying anisotropic dimensions. As discussed in Chapter 1, molecular anisotropy typically cannot be studied by using translational diffusion alone. Rotational diffusion, studied using heteronuclear relaxation (Chapter 3), should be able to provide more insight into this matter. This will be the subject of the following chapter.

6.6 References

[1] J. M. Wieruszeski, I. Landrieu, X. Hanoulle and G. Lippens, "ELISE NMR: Experimental liquid sealing of NMR samples". *Journal of Magnetic Resonance*, **2006**, *181*(2) 199-202.

[2] D. G. Leaist, "Diffusion in Associating Nonelectrolyte Mixtures - Stepwise Aggregation and Micelle Formation". *Canadian Journal of Chemistry-Revue Canadienne De Chimie*, **1988**, *66*(5) 1129-1134.

[3] D. Neuhaus and M. P. Williamson, "The Nuclear Overhauser Effect in Structural and Conformational Analysis", 2nd ed., **2000**, New York, John Wiley and Sons Ltd.

[4] B. Meyer and T. Peters, "NMR Spectroscopy techniques for screening and identifying ligand binding to protein receptors". *Angewandte Chemie-International Edition*, **2003**, *42*(8) 864-890.

[5] C. Brandon and J. Tooze, "Introduction to Protein Structure 2nd Edition", **1998**, New York, Garland Publishing Inc.

[6] S. R. Dennison, J. Wallace, F. Harris and D. A. Phoenix, "Amphiphilic α-helical antimicrobial peptides and their structure/function relationships". *Protein and Peptide Letters*, **2005**, *12*(1) 31-39.

[7] M. V. Prates, M. L. Sforca, W. C. B. Regis, J. R. S. A. Leite, L. P. Silva, T. A. Pertinhez, A. L. T. Araujo, R. B. Azevedo, A. Spisni and C. Bloch, "The NMR-derived solution structure of a new cationic antimicrobial peptide from the skin secretion of the anuran Hyla punctata". *Journal of Biological Chemistry*, **2004**, *279*(13) 13018-13026.

[8] W. G. J. Hol, L. M. Halie and C. Sander, "Dipoles of the Alpha-Helix and Beta-Sheet - Their Role in Protein Folding". *Nature*, **1981**, *294*(5841) 532-536.

[9] W. G. J. Hol, P. T. Vanduijnen and H. J. C. Berendsen, "Alpha-Helix Dipole and Properties of Proteins". *Nature*, **1978**, *273*(5662) 443-446.

[10] D. Sengupta, R. N. Behera, J. C. Smith and G. M. Ullmann, "The α helix dipole: Screened out?". *Structure*, **2005**, *13*(6) 849-855.

[11] A. D. Milov, M. I. Samoilova, Y. D. Tsvetkov, M. Jost, C. Peggion, F. Formaggio, M. Crisma, C. Toniolo, J. W. Handgraaf and J. Raap, "Supramolecular structure of self-assembling alamethicin analog studied by ESR and PELDOR". *Chemistry & Biodiversity*, **2007**, *4*(6) 1275-1298.

[12] M. Coraiola, P. Lo Cantore, S. Lazzaroni, A. Evidente, N. S. Lacobellis and M. Dalla Serra, "WLIP and tolaasin I, lipodepsipeptides from Pseudomonas reactans and Pseudomonas tolaasii, permeabilise model membranes". *Biochimica Et Biophysica Acta-Biomembranes*, **2006**, *1758*(11) 1713-1722.

7

Heteronuclear relaxation study of pseudodesmin A

7.1 Introduction

As discussed in Chapter 3, the relaxation rates of an NMR nucleus can be linked to the rotational diffusion properties of the molecule, assuming no contribution from internal motion or exchange processes. For this purpose, ^{13}C or ^{15}N nuclei that are covalently attached to at least one ^{1}H nucleus are most often used, as the relaxation mechanism due to dipole-dipole interaction with the ^{1}H nucleus is well defined (section 3.3) and is the dominating one. When a sufficient number of relaxation rate constants from different nuclei with various XH bond vector orientations within the molecule is obtained, the full rotational diffusion tensor can be determined, including the orientation of the tensor axes and the rotational diffusion coefficients. In turn, the diffusion coefficients can be used to estimate the dimensions of the molecule.

In the case of pseudodesmin A, the orientation of the CH and NH bond vectors are known within the monomer solution structure in acetonitrile. However, under self-association conditions, the bond orientation compared to the rotational diffusion tensor of the supramolecular structure needs to be known in order to evaluate the relaxation rate constants. Since the solution structure is maintained in chloroform (section 5.5), it is only the orientation of this structure within the supramolecular complex that remains an unknown factor. In this work, the experimental ^{13}C relaxation data of all backbone CH groups will be used to obtain both the orientation of the

monomer in the assembly and the rotational diffusion coefficients of the assembly. The former provides important information concerning the organisation of the supramolecular structure, while the latter allows an estimation of the dimensions of the structure. This analysis will be performed at several concentrations in chloroform, allowing the growth of the assemblies to be assessed along each dimension. If the model proposed in section 6.5 is indeed correct, one would expect at high concentration in chloroform that the increase in size occurs only along one direction.

In Table 7.1, an overview is given of the conditions and the different types of relaxation measurements that were performed at natural abundance in chloroform and acetonitrile solution. The results in acetonitrile solution, where pseudodesmin A is present in its monomer form, are discussed in section 7.2. Initial experiments in chloroform performed at 25℃ included ^{15}N relaxation measurements. It turned out that this nucleus was not the most informative for the study of anisotropy as most NH groups possess a similar orientation (see section 7.3.5) and the signal-to-noise ratio was quite low. The methyl ^{13}C relaxation rate measurements did not provide any results concerning this issue either (section 7.3.6). Measurements on the $^{13}C^{\alpha}$ nuclei were found to be the most useful to study the anisotropy of the supramolecular complex, and experiments were performed at multiple concentrations and multiple magnetic field strengths at a temperature of 283.0 K. The lower sample temperature was chosen to avoid evaporation of the volatile chloroform during the time intensive relaxation measurements, while in addition the ELISE[1] technique was used as well. The results are discussed in sections 7.3.2 and 7.3.3. The precise concentration of each chloroform sample was measured using the ERETIC method (appendix H). In chloroform at 16.4 mM and 6.6 mM, relaxation dispersion experiments were performed to assess the contribution of exchange to the R_2 relaxation rate constants, which will be discussed in section 7.3.4.1.

Table 7.1: Overview of the experimental relaxation data collected under several conditions

solvent	T [K]	c [mM]	$^{13}C^{\alpha}$, 11.7 T[a]			$^{13}C^{\alpha}$, 16.4 T[a]			$^{13}C^{\alpha}$, 16.4 T[a]	^{15}N, 16.4 T			$^{13}CH_3$, 16.4 T	
			R_1	R_2	nOe	R_1	R_2	nOe	relaxation dispersion	R_1	R_2	nOe	R_1	R_2
CD_3CN	298.2	*ca.* 7-9	×	×	×	✓	✓	✓	✓	✓	✓	✓	×	×
$CDCl_3$	298.2	15	×	×	×	×	×	×	×	✓	✓	×	✓	✓
$CDCl_3$	283.0	6.6	×	×	×	✓	✓	✓	✓	×	×	×	×	×
$CDCl_3$	283.0	16.4	✓	✓	✓	✓	✓	✓	✓	×	×	×	×	×
$CDCl_3$	283.0	44.8	×	×	×	✓	✓	✓	×	×	×	×	×	×

[a] $^{13}C^{\alpha}$ encompasses here all oligopeptide α-carbons and the Thr3 C^{β} and HDA C^{β} nuclei.

The outline of this chapter is as follows. In section 7.2, the acetonitrile results are presented and discussed, revealing the relaxation behaviour of the monomeric state. In section 7.3, the results of the measurements in chloroform are discussed. After an

overview of the experimental set-up and the results, it will be described how from the $^{13}C^{\alpha}$ relaxation data the degree and direction of anisotropy of the supramolecular structure can be assessed. This is first illustrated for only one concentration, 16.4 mM, and eventually applied to all concentrations. The ^{15}N and ^{13}C methyl results will be discussed afterwards. The chapter concludes (section 7.4) with a discussion on how the analysis of the results compares with the hypothesised model of the supramolecular structure.

7.2 Relaxation study in acetonitrile solution

7.2.1 Experimental set-up and results

7.2.1.1 $^{13}C^{\alpha}$ relaxation

The relaxation experiments in acetonitrile were performed at a magnetic field strength of 16.4 T and at 25℃ throughout. All $^{13}C^{\alpha}$ experiments (R_1, R_2 and steady state nOe, see section 3.7) were implemented with a spectral width of 4 ppm and 2048 complex time domain points in the direct ^{1}H dimension, while the indirect ^{13}C dimension was sampled with 64 complex time domain points and a spectral width of 24 ppm. The delay Δ in Figures 3.19, 3.21 and 3.22 was set to 3.45 ms, corresponding to an assumed $^{1}J_{CH}$ coupling of 145 Hz. For the R_1 and R_2 measurements, the interscan delay was set to 2 s. The delay between the 180° pulses in the CPMG sequences, τ_{cp} (Figure 3.21) was 900 µs. For the steady state nOe experiments, the interscan delay was 5 s, 4.13 s of which were used for ^{1}H irradiation in the saturation experiment. Prior to Fourier transform, all FIDs were multiplied with a squared cosine bell window function in both dimensions and subsequently zero filled to a 2048×128 real data matrix. The delay T (Figure 3.19) during the R_1 measurements was varied between 12.58 ms and 628.8 ms, while the total CPMG time during the R_2 measurements was varied between 5.91 ms and 591.36 ms, both randomly sampled over 14 experiments including one repeat. The R_1 and R_2 relaxation rate constants were fitted to the obtained data points (section 3.7), while a Monte Carlo error analysis was performed using 200 simulations to obtain 95% confidence intervals (appendix C). The nOe values were calculated using equation (3.10). The results are provided in Table 7.2 and displayed in Figure 7.1.

Table 7.2: Results of the $^{13}C^{\alpha}$ relaxation measurements in acetonitrile solution

	R_1 [s^{-1}][a]	R_2 [s^{-1}][a]	R_1/R_1[a]	nOe
Leu1 C^{α}	1.98 ± 0.04	3.72 ± 0.18	0.53 ± 0.03	1.25
Gln2 C^{α}	2.07 ± 0.04	2.74 ± 0.10	0.76 ± 0.03	1.35
Thr3 C^{α}	2.01 ± 0.05	2.43 ± 0.08	0.83 ± 0.03	1.40
Val4 C^{α}	2.02 ± 0.03	2.41 ± 0.08	0.84 ± 0.03	1.24
Leu5 C^{α}	1.96 ± 0.04	2.18 ± 0.07	0.90 ± 0.03	1.20
Ser6 C^{α}	2.03 ± 0.03	2.71 ± 0.07	0.75 ± 0.02	1.38
Leu7 C^{α}	2.03 ± 0.03	2.53 ± 0.08	0.80 ± 0.03	1.25
Ser8 C^{α}	2.07 ± 0.03	2.62 ± 0.06	0.79 ± 0.02	1.33
Ile9 C^{α}	1.84 ± 0.04	2.31 ± 0.07	0.79 ± 0.03	1.42
Thr3 C^{β}	2.06 ± 0.05	4.33 ± 0.41	0.47 ± 0.05	1.27
HDA C^{β}	1.34 ± 0.04	1.90 ± 0.12	0.70 ± 0.05	1.47

[a] Including the 95% error.

7.2.1.2 ^{15}N relaxation

For the ^{15}N relaxation experiments, the spectral width was set to 5 ppm in the direct ^{1}H dimension and to 7 ppm in the indirect ^{15}N dimension. The result of the low spectral width in the ^{15}N dimension was that the cross-peaks were folded back into the spectrum along the ^{15}N dimension, allowing a reduction in experiment time without loss of resolution. 1024 and 64 complex time domain points were measured along the direct and the indirect dimensions respectively. The delay Δ was set to 5.56 ms, corresponding to an assumed $^{1}J_{NH}$ coupling of 90 Hz. For the R_1 and R_2 measurements, the interscan delay was set to 2.5 s. The delay between the 180° pulses in the CPMG sequences τ_{cp} was 900 µs. For the steady state nOe experiments, the interscan delay was 5.74 s, 5.24 s of which were used for ^{1}H irradiation in the saturation experiment. Prior to Fourier transform, all FIDs were multiplied with a squared cosine bell window function in both dimensions and subsequently zero filled to a 2048×512 real data matrix. The delay T during the R_1 measurements was varied between 5 ms and 2 s, while the total CPMG time during the R_2 measurements was varied between 6 ms and 1.5 s, both randomly sampled over 14 experiments including one repeat. The R_1 and R_2 relaxation rate constants were fitted to the obtained data points, while a Monte Carlo error analysis was performed using 200 simulations to obtain 95% confidence intervals (appendix C). The nOe values were calculated using equation (3.10). The results are provided in Table 7.3 and displayed in Figure 7.1.

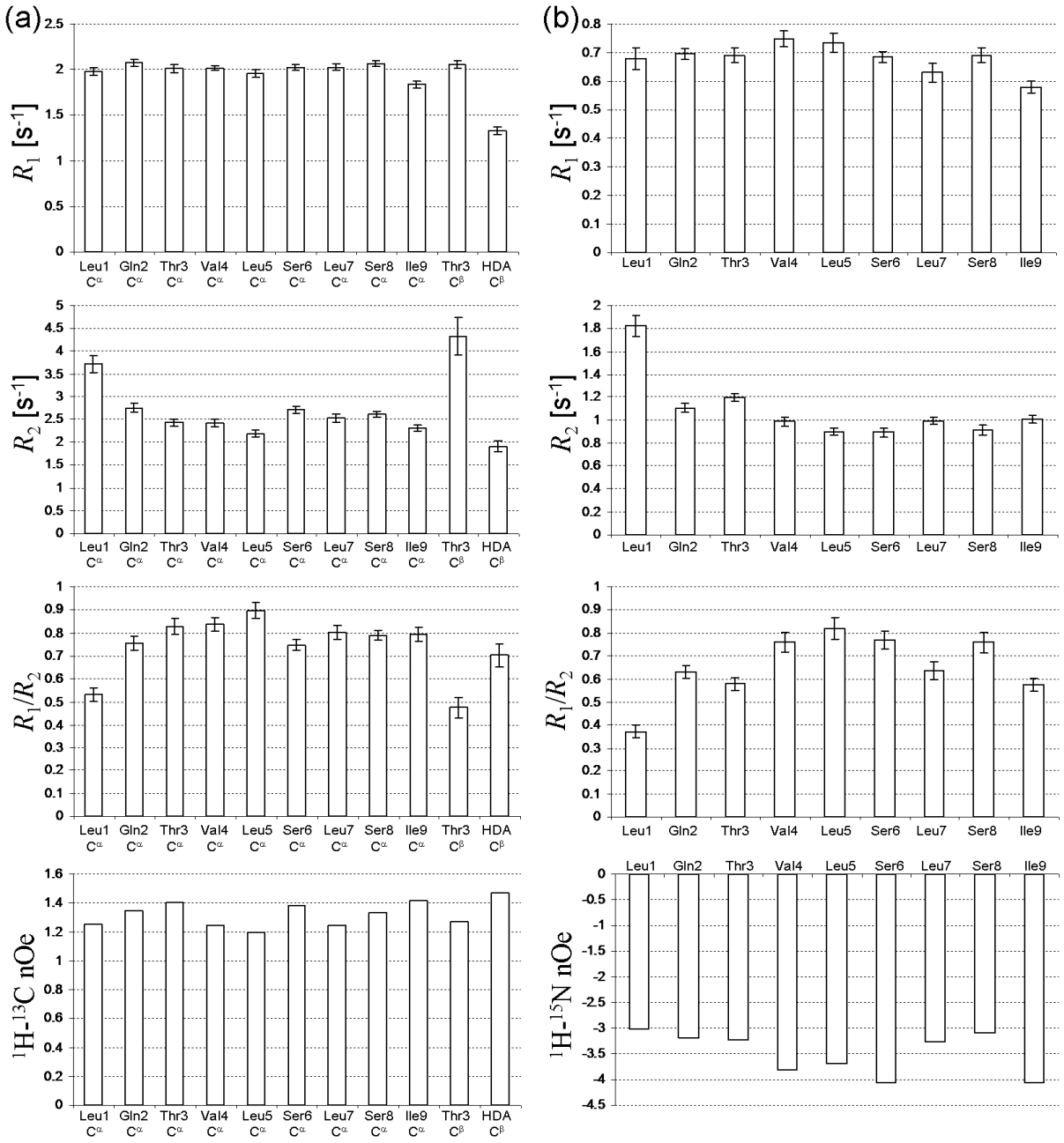

Figure 7.1: R_1 relaxation rate constants, R_2 relaxation rate constants, R_1/R_2 ratios and steady state nOe values of the (a) $^{13}C^{\alpha}$ nuclei and (b) ^{15}N nuclei, in acetonitrile at 25℃. Error bars repres ent 95% errors.

Table 7.3: Results of the ^{15}N relaxation measurements in acetonitrile solution

	R_1 [s^{-1}][a]	R_2 [s^{-1}][a]	R_1/R_1[a]	nOe
Leu1 N	0.680 ± 0.038	1.824 ± 0.091	0.37 ± 0.03	-3.03
Gln2 N	0.695 ± 0.020	1.102 ± 0.035	0.63 ± 0.03	-3.20
Thr3 N	0.691 ± 0.027	1.193 ± 0.037	0.58 ± 0.03	-3.24
Val4 N	0.748 ± 0.027	0.984 ± 0.041	0.76 ± 0.04	-3.80
Leu5 N	0.734 ± 0.035	0.894 ± 0.031	0.82 ± 0.05	-3.69
Ser6 N	0.685 ± 0.019	0.892 ± 0.038	0.77 ± 0.04	-4.06
Leu7 N	0.630 ± 0.033	0.991 ± 0.029	0.64 ± 0.04	-3.27
Ser8 N	0.691 ± 0.026	0.911 ± 0.040	0.76 ± 0.04	-3.09
Ile9 N	0.579 ± 0.021	1.005 ± 0.034	0.58 ± 0.03	-4.05

[a] Including the 95% error.

7.2.2 Discussion

Figure 7.1 plots the relaxation rate constants for each nucleus. At first glance, the values of the relaxation rate constants are in agreement with a small molecule in a low viscous solvent. For example, the nOe values of both ^{13}C and ^{15}N nuclei show that the relaxation regime lies closer to the extreme narrowing limit value (respectively 2.0 and –4.3) than to the spin diffusion limit value (respectively 0.15 and –1.5) (see Figure 3.14). Some variation can be seen between the different nuclei however. The HDA C^{β} R_1 and R_2 values are significantly lower than those of the other ^{13}C spins, which can be attributed to a higher degree of motional freedom at the alkyl chain. The Leu1 C^{α} and especially the Thr3 C^{β} R_2 values are higher than all other ^{13}C spin R_2 values. An increased R_2 value typically indicates a conformational exchange contribution, which appears a plausible conclusion for the N-terminal Leu1 C^{α}, but not for Thr3 C^{β}, which is part of the macrocyclic structure. The ^{15}N R_1 values show only limited variation over the different residues. The same is true for the R_2 values, except for Leu1, which could again be explained by conformational exchange processes at the N-terminal end of the exocyclic oligopeptide.

Each relaxation parameter can be used to estimate the global correlation time constant τ. This is done by minimising the squared difference between the experimental value and a calculated value obtained using an isotropic rotational diffusion model. For this, both dipole-dipole and chemical shift anisotropy relaxation effects are taken into account. The results are presented in Table 7.4, which also includes the hydrodynamic radii derived from the correlation time constant via the rotational diffusion coefficient (equations (1.27) and (1.43)). The first observation is that the calculated correlation time constants from the R_1/R_2 values are systematically higher than those calculated from either R_1, R_2 or the nOe. The reason for this can be found in the fact that for short correlation time constants (extreme narrowing regime) the R_1/R_2 ratio approaches asymptotically the value of 1. The estimated correlation time constant under these conditions thus becomes very sensitive to small deviations in R_1/R_2 caused by internal motion or exchange. In this case, the R_1/R_2 ratio is therefore an inappropriate parameter to estimate the correlation time constant. The nOe and the separate R_1 and R_2 relaxation rate constants are better alternatives, since these are more sensitive to the correlation time constant under these conditions. Other outliers include the HDA C^{β} spin, which for every relaxation parameter provide a lower correlation time constant. This can be explained by the strong contribution of internal motion to the relaxation, as a considerable degree of freedom (low S^2) for the conformational motion can be expected for this part of the molecule.

In the end, it is difficult to assess the isotropic correlation time constant of pseudodesmin A from Table 7.4 with good confidentiality, since the contributions from internal motions or, in the case of R_2, exchange can never be excluded. It is

however possible to derive a correlation time constant from the translational diffusion coefficient of pseudodesmin A, by first calculating the hydrodynamic radius using the Stokes-Einstein relation (1.39), then inserting this into the Debye-Einstein relation (1.43) and using the relation between rotational diffusion coefficient and the correlation time constant (equation (1.27)):

Table 7.4: Correlation time constants and hydrodynamic radii calculated from the measured relaxation parameters[a]

	R_1		R_2		nOe		R_1/R_2	
	τ [ns]	R_H [Å]	τ [ns]	R_H [Å]	τ [ns]	R_H [Å]	τ [ns]	R_H [Å]
Leu1 C^{α}	0.10	6.3	0.26	8.8	0.20	8.2	1.04	14.0
Gln2 C^{α}	0.10	6.5	0.14	7.3	0.18	7.9	0.56	11.4
Thr3 C^{α}	0.10	6.4	0.12	6.9	0.17	7.7	0.41	10.3
Val4 C^{α}	0.10	6.4	0.12	6.8	0.21	8.2	0.39	10.1
Leu5 C^{α}	0.09	6.3	0.10	6.5	0.22	8.3	0.25	8.7
Ser6 C^{α}	0.10	6.4	0.14	7.2	0.18	7.8	0.58	11.6
Leu7 C^{α}	0.10	6.4	0.13	7.0	0.21	8.2	0.47	10.7
Ser8 C^{α}	0.10	6.5	0.13	7.1	0.19	7.9	0.49	11.0
Ile9 C^{α}	0.09	6.1	0.11	6.7	0.17	7.6	0.48	10.9
Thr3 C^{β}	0.10	6.5	0.36	9.9	0.20	8.1	1.18	14.6
HDA C^{β}	0.06	5.4	0.09	6.2	0.16	7.5	0.68	12.2
Leu1 N	0.14	7.1	0.61	11.8	0.30	9.3	3.44	20.9
Gln2 N	0.14	7.2	0.27	9.0	0.28	9.0	1.85	17.0
Thr3 N	0.14	7.2	0.31	9.4	0.27	9.0	2.12	17.8
Val4 N	0.15	7.4	0.22	8.4	0.18	7.9	1.19	14.7
Leu5 N	0.15	7.4	0.19	8.0	0.20	8.1	0.87	13.2
Ser6 N	0.14	7.1	0.19	8.0	0.13	7.1	1.15	14.5
Leu7 N	0.12	6.9	0.23	8.5	0.26	8.9	1.82	16.9
Ser8 N	0.14	7.2	0.20	8.1	0.29	9.2	1.20	14.7
Ile9 N	0.11	6.6	0.23	8.5	0.13	7.1	2.14	17.9

[a] A viscosity of 0.369 mPa·s for acetonitrile at 25℃ is assumed

$$\tau = \frac{1}{6D_r} = \frac{4\pi\eta R_H^3}{3k_B T} = \frac{k_B^2 T^2}{162\pi^2\eta^2 D_t^3} \tag{7.1}$$

Assuming the diffusion coefficient from Table 6.1 and a viscosity of 0.369 mPa·s, the hydrodynamic radius is found to be 7.2 Å and the expected correlation time constant turns out to be 0.14 ns. This nicely falls in line with most of the values found in Table 7.4. In general, the results calculated from the R_1 values are about equal or lower than this, especially for the ^{15}N data. This validates the values obtained through D_t, as fast internal motion should qualitatively have the effect of lowering the calculated τ. The R_2 values then again provide either lower or higher correlation time constants, which can respectively be explained by again the effects of fast internal motion, or the effects of conformational exchange. For the latter, it should be noted that in this case even small exchange contributions can significantly contribute to the R_2 value, as these are inherently very low due to the very small correlation time constants. This

is in contrast to the situation in chloroform or for larger proteins, where similar exchange contributions would probably fall within the error bar of the R_2 value. The nOes provide values for τ which are typically higher than the one estimated from D_t. However, the nOe measurement using this experimental set-up might not be very precise (see section 7.3.2) and its deviation should therefore not be considered as an issue. Overall, it can be concluded from the analysis above and keeping in mind that the R_1/R_2 ratios are unsuitable reporters for the correlation time constant in this case, that the relaxation data are in fair agreement with the value of 0.14 ns for the isotropic correlation time constant τ, as derived from the translational diffusion coefficient.

When the results from the acetonitrile relaxation study need to be compared with those from the study in chloroform solution, the correlation time constant should be corrected for the difference in temperature and solvent viscosity. Assuming a viscosity for chloroform of 0.631 mPa·s at 10°C, the correlation time constant of the monomer in chloroform can be estimated as:

$$\tau_{CHCl_3} = \frac{\eta_{CHCl_3} T_{CH_3CN}}{\eta_{CH_3CN} T_{CHCl_3}} \tau_{CH_3CN} \qquad (7.2)$$

The result of this calculation is 0.25 ns.

7.3 Relaxation study in chloroform solution

7.3.1 Experimental set-up and results

7.3.1.1 $^{13}C^{\alpha}$ relaxation

$^{13}C^{\alpha}$ relaxation experiments (R_1, R_2 and steady state ^1H-^{13}C nOe) in chloroform were performed at three separate concentrations as determined by the ERETIC method: 6.6 mM, 16.4 mM and 44.8 mM. At the top of each sample a layer of water was placed to seal the solution and avoid evaporation (ELISE). Due to the limited material available, the 44.8 mM sample was prepared in a 3 mm tube but measured using a 5 mm probe head. The measurements were performed at 16.4 T. In addition experiments at 11.7 T were performed on the 16.4 mM sample. The temperature was set at 283.0 K throughout. Using the standard decp90 Bruker pulse sequence, the ^{13}C pulses were calibrated indirectly on the ^{13}C satellites in the ^1H spectrum of a 0.1 M ^{13}C enriched methanol solution in DMSO-d6 at 25°C in the case of the 6.6 mM and 16.4 mM measurements, or of a 20% $CHCl_3/CDCl_3$ mixture prepared in a 3 mm tube at 283.0 K. All spectra were recorded with a spectral width of 4 ppm in the direct ^1H

dimension and 24 ppm in the indirect ^{13}C dimension. The 6.6 mM and 44.8 mM sample were sampled by 1024 complex time domain points in the direct dimension and 64 complex time domain points in the indirect dimension. The 16.4 mM sample was sampled by 2048 complex time domain points in the direct dimension at both field strengths, while the number of indirect complex time domain points was 64 in the 16.4 T experiments and 12 in the 11.7 T experiments. The delay Δ in Figures 3.19, 3.21 and 3.22 was set to 2.94 ms, which is somewhat lower than the expected value for $^{1}J_{CH}$ coupling (145 Hz) in order to compensate for loss of signal due to the rapid R_2 relaxation. The interscan delay was set to 2 s for the R_1 and R_2 measurements. The delay between the 180° pulses in the CPMG sequences, τ_{cp} (Figure 3.21), was set to 900 µs. For the steady state nOe experiments at 16.4 T, the interscan delay was 5 s, 4.2 s of which were used for ^{1}H irradiation in the saturation experiment, while at 11.7 T this was 5.5 s with 3.1 s used for the ^{1}H irradiation. Prior to Fourier transform, only the first 512 complex time domain points in the direct dimension were retained to increase the signal-to-noise ratio. The FIDs were multiplied with a squared cosine bell window function in both dimensions. They were subsequently zero filled to a real data matrix size of 2048×256, 1024×512, 2048×512 and 2048×1024 for respectively the measurements at 6.6 mM, 44.8 mM, 16.4 mM at 16.4 T and the 16.4 mM sample at 11.7 T. The delay T (Figure 3.19) during the R_1 measurements was varied from 12.6 ms to 1.68 s, from 12.6 ms to 2.51 s, from 12.6 ms to 1.68 s and from 12.8 ms to 0.958 s for respectively the 6.6 mM, 44.8 mM, 16.4 mM samples at 16.4 T and 16.4 mM at 11.7 T. The total CPMG time during the R_2 measurements was varied between 5.92 ms and 118.3 ms, 0 ms and 59.0 ms, 5.91 ms and 65.05 ms and 5.85 ms and 64.4 ms for respectively 6.6 mM, 44.8 mM, 16.4 mM at 16.4 T and 16.4 mM at 11.7 T. The sampling always occurred randomly over 14 experiments, including at least one repeat experiment. The R_1 and R_2 relaxation rate constants were fitted to the obtained data points (section 3.7), while a Monte Carlo error analysis was performed using 200 simulations to obtain 95% confidence intervals (appendix C). The nOe values were calculated using equation (3.10). The results are provided in Tables 7.5 to 7.8 and displayed in Figures 7.2 to 7.4.

Table 7.5: Results of the $^{13}C^{\alpha}$ relaxation measurements on a 6.6 mM solution in chloroform at 16.4 T

	R_1 [s^{-1}][a]	R_2 [s^{-1}][a]	R_1/R_1[a]	nOe[b]
Leu1 C^{α}	1.39 ± 0.08	25.2 ± 2.8	0.055 ± 0.007	0.30 0.34
Gln2 C^{α}	1.51 ± 0.07	24.9 ± 1.6	0.061 ± 0.005	0.30 0.29
Thr3 C^{α}	1.45 ± 0.09	27.9 ± 1.1	0.052 ± 0.004	0.25 0.27
Val4 C^{α}	1.36 ± 0.08	26.0 ± 1.3	0.052 ± 0.004	0.28 0.31
Leu5 C^{α}	1.56 ± 0.11	23.7 ± 1.1	0.066 ± 0.006	0.30 0.33
Ser6 C^{α}	1.52 ± 0.06	24.7 ± 2.0	0.062 ± 0.006	0.26 0.29
Leu7 C^{α}	1.35 ± 0.10	30.8 ± 1.4	0.044 ± 0.004	0.28 0.25
Ser8 C^{α}	1.27 ± 0.12	34.6 ± 2.7	0.037 ± 0.004	0.26 0.25
Ile9 C^{α}	1.47 ± 0.05	23.5 ± 1.8	0.063 ± 0.005	0.27 0.36
Thr3 C^{β}	1.45 ± 0.06	32.0 ± 2.2	0.045 ± 0.004	0.31 0.27
HDA C^{β}	1.46 ± 0.05	31.5 ± 3.4	0.046 ± 0.005	0.43 0.33

[a] Including the 95% error.
[b] Two separate nOe measurements were performed.

Table 7.6: Results of the $^{13}C^{\alpha}$ relaxation measurements on a 16.4 mM solution in chloroform at 16.4 T

	R_1 [s^{-1}][a]	R_2 [s^{-1}][a]	R_1/R_1[a]	nOe
Leu1 C^{α}	1.23 ± 0.03	33.6 ± 2.1	0.037 ± 0.003	0.31
Gln2 C^{α}	1.40 ± 0.03	32.6 ± 1.7	0.043 ± 0.002	0.30
Thr3 C^{α}	1.25 ± 0.03	37.2 ± 1.1	0.034 ± 0.001	0.27
Val4 C^{α}	1.20 ± 0.04	39.4 ± 2.7	0.030 ± 0.002	0.28
Leu5 C^{α}	1.40 ± 0.04	31.6 ± 1.1	0.044 ± 0.002	0.29
Ser6 C^{α}	1.39 ± 0.05	33.0 ± 1.5	0.042 ± 0.002	0.34
Leu7 C^{α}	1.20 ± 0.05	43.3 ± 2.3	0.028 ± 0.002	0.25
Ser8 C^{α}	1.09 ± 0.06	50.2 ± 2.8	0.022 ± 0.002	0.29
Ile9 C^{α}	1.34 ± 0.03	31.2 ± 2.2	0.043 ± 0.003	0.34
Thr3 C^{β}	1.38 ± 0.05	39.6 ± 2.8	0.035 ± 0.003	0.35
HDA C^{β}	1.35 ± 0.05	38.7 ± 2.7	0.035 ± 0.003	0.38

[a] Including the 95% error.

Table 7.8: Results of the $^{13}C^{\alpha}$ relaxation measurements on a 16.4 mM solution in chloroform at 11.7 T

	R_1 [s^{-1}][a]	R_2 [s^{-1}][a]	R_1/R_1[a]	nOe[a]
Leu1 C^{α}	1.99 ± 0.14	45.6 ± 5.0	0.044 ± 0.006	0.32 0.38
Gln2 C^{α}	2.20 ± 0.12	34.7 ± 2.4	0.063 ± 0.006	0.33 0.37
Thr3 C^{α}	1.91 ± 0.11	40.3 ± 3.1	0.047 ± 0.005	0.33 0.34
Val4 C^{α}	1.96 ± 0.12	38.3 ± 3.4	0.051 ± 0.006	0.23 0.25
Leu5 C^{α}	2.20 ± 0.10	34.0 ± 2.0	0.065 ± 0.005	0.42 0.33
Ser6 C^{α}	2.12 ± 0.08	33.7 ± 3.1	0.063 ± 0.006	0.35 0.39
Leu7 C^{α}	1.91 ± 0.09	39.4 ± 2.1	0.049 ± 0.003	0.39 0.39
Ser8 C^{α}	2.01 ± 0.18	55.0 ± 8.5	0.037 ± 0.007	0.31 0.24
Ile9 C^{α}	2.13 ± 0.13	31.3 ± 2.2	0.068 ± 0.006	0.34 0.39
Thr3 C^{β}	2.11 ± 0.13	40.3 ± 3.3	0.052 ± 0.005	0.37 0.29
HDA C^{β}	1.92 ± 0.17	42.8 ± 4.3	0.045 ± 0.006	0.38 0.47

[a] Including the 95% error.
[b] Two separate nOe measurements were performed.

Table 7.7: Results of the $^{13}C^{\alpha}$ relaxation measurements on a 44.8 mM solution in chloroform at 16.4 T

	R_1 [s^{-1}][a]	R_2 [s^{-1}][a]	R_1/R_1[a]	nOe
Leu1 C^{α}	1.19 ± 0.11	43.4 ± 2.9	0.027 ± 0.003	0.41
Gln2 C^{α}	1.33 ± 0.10	45.8 ± 2.4	0.029 ± 0.003	0.30
Thr3 C^{α}	1.04 ± 0.08	49.1 ± 1.8	0.021 ± 0.002	0.32
Val4 C^{α}	1.05 ± 0.09	55.1 ± 3.5	0.019 ± 0.002	0.26
Leu5 C^{α}	1.38 ± 0.10	44.9 ± 3.3	0.031 ± 0.003	0.38
Ser6 C^{α}	1.23 ± 0.11	48.6 ± 4.3	0.025 ± 0.003	0.38
Leu7 C^{α}	0.98 ± 0.10	50.2 ± 7.2	0.019 ± 0.003	0.24
Ser8 C^{α}	0.92 ± 0.10	76.5 ± 7.2	0.012 ± 0.002	0.32
Ile9 C^{α}	1.25 ± 0.08	38.2 ± 3.5	0.033 ± 0.004	0.36
Thr3 C^{β}	1.19 ± 0.10	51.2 ± 2.6	0.023 ± 0.002	0.44
HDA C^{β}	1.21 ± 0.11	65.6 ± 5.1	0.018 ± 0.002	0.51

[a] Including the 95% error.

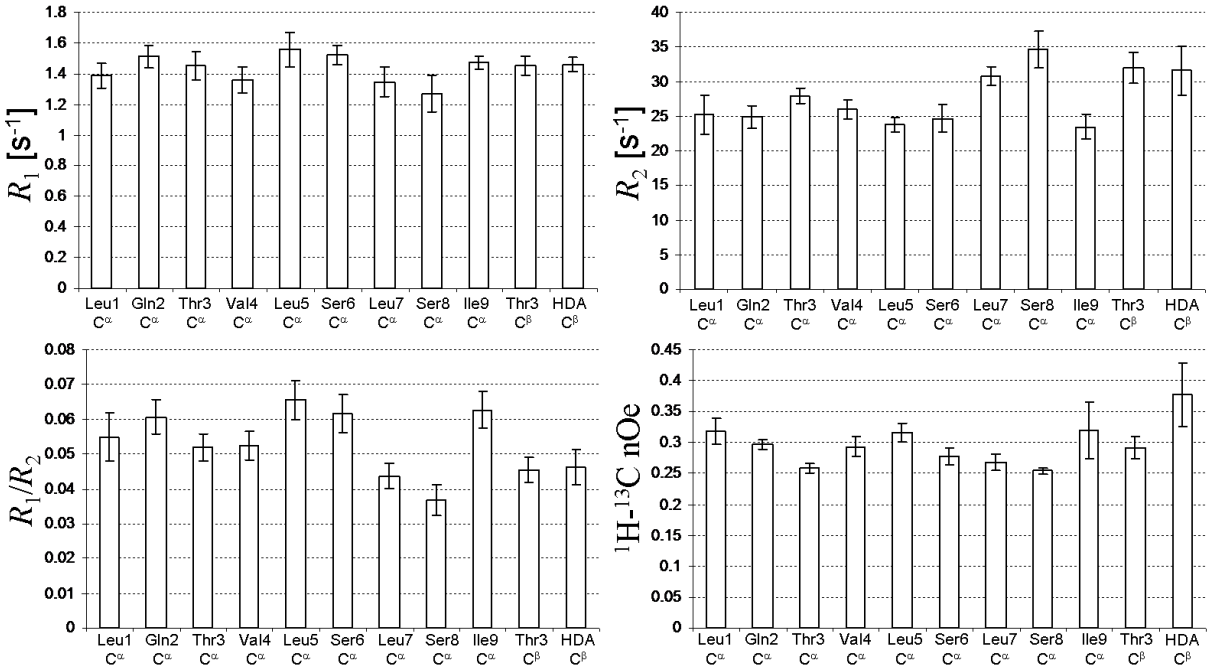

Figure 7.2: R_1 relaxation rate constants, R_2 relaxation rate constants, R_1/R_2 ratios and steady state nOe values of the $^{13}C^{\alpha}$ nuclei in a 6.6 mM chloroform solution at 10℃. The nOe value is the average between two repeated measurements with the upper and lower border of the error bars representing the two individual values. Error bars with the R_1, R_2 and R_1/R_2 represent 95% errors.

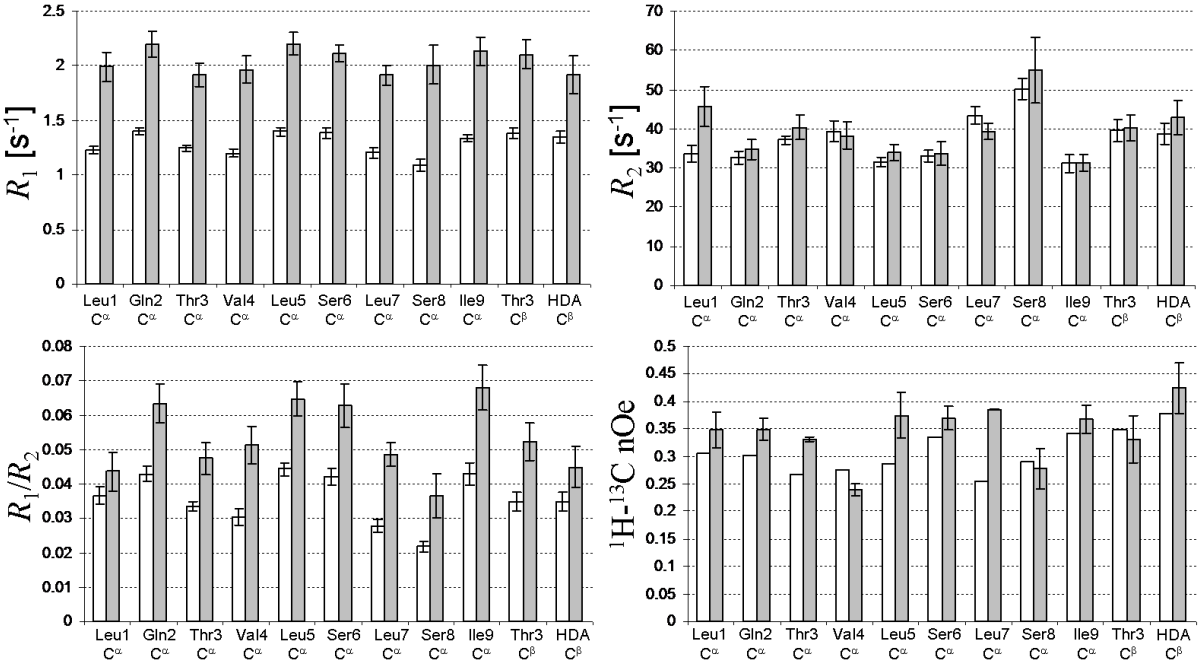

Figure 7.3: R_1 relaxation rate constants, R_2 relaxation rate constants, R_1/R_2 ratios and steady state nOe values of the $^{13}C^{\alpha}$ nuclei in a 16.4 mM solution in chloroform at 10℃. White bars represent data measured at 16.4 T, grey bars at 11.7 T. The nOe value at 11.7 T is the average between two repeated measurements with the upper and lower border of the error bars representing the two individual values. Error bars with the R_1, R_2 and R_1/R_2 represent 95% errors.

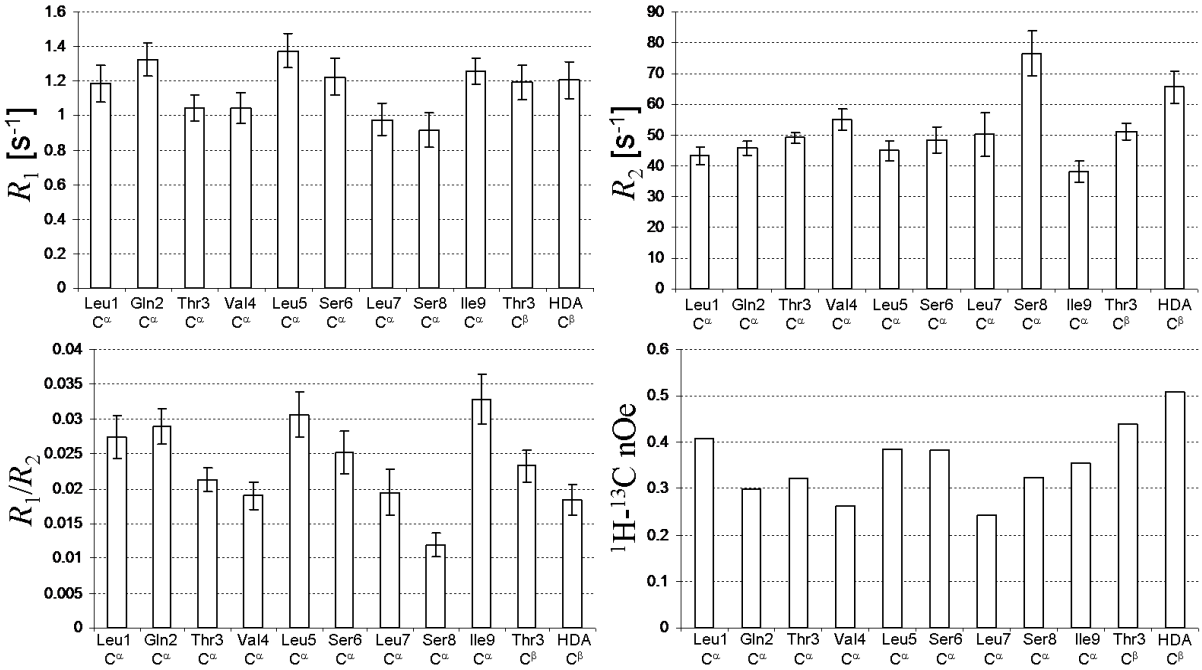

Figure 7.4: R_1 relaxation rate constants, R_2 relaxation rate constants, R_1/R_2 ratios and steady state nOe values of the $^{13}C^{\alpha}$ nuclei in a 44.8 mM chloroform solution at 10℃. Error bars represent 95% errors.

7.3.1.2 ^{15}N relaxation

The ^{15}N relaxation measurements (R_1 and R_2) in chloroform were performed on a 15 mM solution at 16.4 T and at 25°C. Using the standard decp90 Bruker pulse sequence, the ^{15}N pulses were calibrated indirectly on the ^{15}N satellites in the ^{1}H spectrum of a 0.1 M urea solution in DMSO-d6 at 25°C. The spectral width was set to 7.5 ppm in the direct ^{1}H dimension and to 6.6 ppm in the indirect ^{15}N dimension, resulting in spectral folding. 1024 and 64 complex time domain points were measured along the direct and the indirect dimensions respectively. The delay Δ was set to 4.90 ms, which is somewhat lower than the expected value for $^{1}J_{NH}$ coupling (90 Hz) in order to compensate for loss of signal due to the rapid R_2 relaxation. For the R_1 and R_2 measurements, the interscan delay was set to 2.5 s. The delay between the 180° pulses in the CPMG sequences τ_{cp} was 900 µs. Prior to Fourier transform, all FIDs were multiplied with a squared cosine bell window function in both dimensions and subsequently zero filled until a 2048×256 real data matrix was obtained. The delay T during the R_1 measurements was varied between 5 ms and 1.2 s, while the total CPMG time during the R_2 measurements was varied between 6 ms and 150 ms, both sampled over 14 experiments including one repeat. The R_1 and R_2 relaxation rate constants were fitted to the obtained decay data points (section 3.7), while a Monte Carlo error analysis was performed using 200 simulations to obtain 95% confidence intervals (appendix C). The results are provided in Table 7.9 and displayed in Figure 7.5.

Table 7.9: Results of the ^{15}N relaxation measurements on a 15 mM solution in chloroform at 16.4 T

	R_1 [s^{-1}][a]	R_2 [s^{-1}][a]	R_1/R_2[a]
Leu1 N	1.68 ± 0.10	10.29 ± 1.09	0.16 ± 0.02
Gln2 N	1.44 ± 0.10	9.58 ± 0.60	0.15 ± 0.01
Thr3 N	1.43 ± 0.08	10.49 ± 0.67	0.14 ± 0.01
Val4 N	1.44 ± 0.08	10.24 ± 0.89	0.14 ± 0.01
Leu5 N	1.58 ± 0.08	9.50 ± 0.73	0.17 ± 0.02
Ser6 N	1.44 ± 0.09	7.69 ± 0.55	0.19 ± 0.02
Leu7 N	1.76 ± 0.13	9.89 ± 0.80	0.18 ± 0.02
Ser8 N	1.35 ± 0.10	8.48 ± 0.83	0.16 ± 0.02
Ile9 N	1.47 ± 0.06	6.25 ± 0.47	0.24 ± 0.02

[a] Including the 95% error.

7.3.1.3 Methyl relaxation

The relaxation rate constants R_1 and R_2 of the methyl ^{13}C spins were measured using the pulse sequences described by Lewis Kay[2, 3]. They were performed on a 15 mM solution at 16.4 T and a temperature of 25°C. The spectral widths in the direct ^{1}H dimension and the indirect ^{13}C dimension were 4 ppm and 16 ppm respectively. A total of 2048 complex time domain points in the direct dimension and 64 time domain

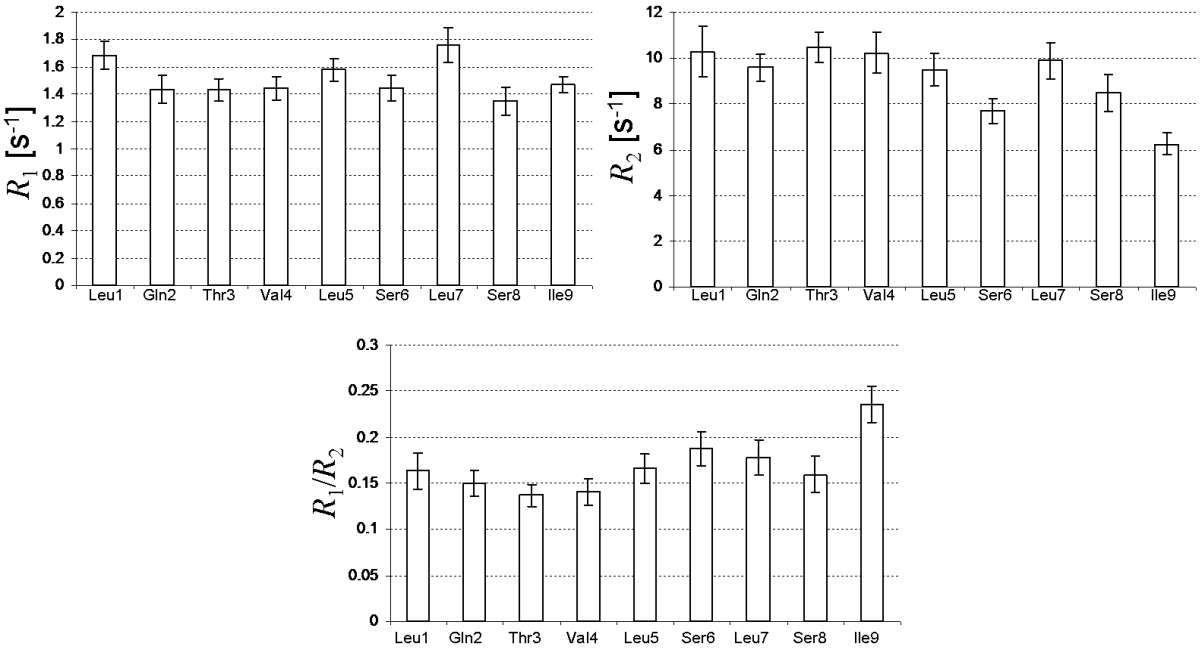

Figure 7.5: R_1 relaxation rate constants, R_2 relaxation rate constants and R_1/R_2 ratios of the ^{15}N nuclei in a 15 mM chloroform solution at 25℃. Erro r bars represent 95% errors.

points in the indirect dimension were sampled. The delay between subsequent scans was 1 s. The FIDs were multiplied with a squared cosine bell window function in both dimensions and afterwards zero filled to a 2048×128 real data matrix. For the R_1 measurements, the delay within the pulse sequence to allow for longitudinal ^{13}C relaxation was varied between 10.48 ms and 1.57 s over 14 experiments including one repeat. For the R_2 measurements, the time between the 180° pulses in the CPMG sequence, τ_{cp}, was 800 µs. The total duration of the CPMG sequence varied from 11.95 ms until 956.2 ms spread over 14 experiments, including one repeat experiment. Monoexponential decay curves were obtained, to which the R_1 and R_2 rate constants were fitted. A Monte Carlo error analysis was performed using 200 simulations to obtain 95% confidence intervals (appendix C). The results are provided in Table 7.10 and displayed in Figure 7.6.

Table 7.10: Results of the $^{13}CH_3$ relaxation measurements on a 15 mM solution in chloroform at 16.4 T

	R_1 [s^{-1}][a]	R_2 [s^{-1}][a]	R_1/R_2
HDA CH_3^{ι}	0.39 ± 0.05	0.43 ± 0.06	0.898 ± 0.163
Leu1 $CH_3^{\delta1}$	1.57 ± 0.05	3.31 ± 0.14	0.475 ± 0.024
Leu1 $CH_3^{\delta2}$	1.44 ± 0.05	2.90 ± 0.14	0.495 ± 0.028
Thr3 CH_3^{γ}	1.91 ± 0.10	5.82 ± 0.37	0.329 ± 0.027
Val4 $CH_3^{\gamma1}$	1.73 ± 0.08	5.43 ± 0.38	0.319 ± 0.026
Val4 $CH_3^{\gamma2}$	1.87 ± 0.09	5.61 ± 0.26	0.333 ± 0.022
Leu5 $CH_3^{\delta1}$	1.40 ± 0.05	2.87 ± 0.13	0.489 ± 0.028
Leu5 $CH_3^{\delta2}$	1.92 ± 0.07	3.65 ± 0.12	0.526 ± 0.026
Leu7 $CH_3^{\delta1}$	2.02 ± 0.09	3.83 ± 0.16	0.527 ± 0.032
Leu7 $CH_3^{\delta2}$	1.69 ± 0.09	3.60 ± 0.21	0.470 ± 0.037
Ile9 CH_3^{γ}	1.31 ± 0.08	4.73 ± 0.27	0.276 ± 0.023
Ile9 CH_3^{δ}	0.74 ± 0.06	3.12 ± 0.14	0.236 ± 0.022

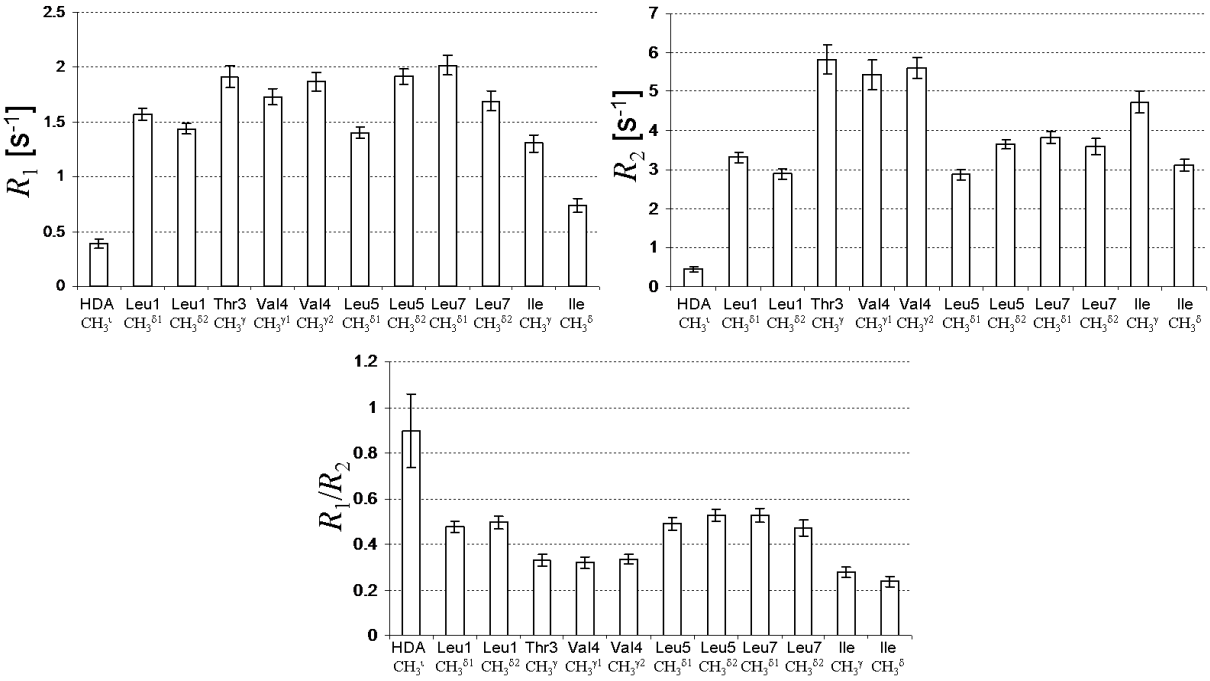

Figure 7.6: R_1 relaxation rate constants, R_2 relaxation rate constants and R_1/R_2 ratios of the ^{13}C methyl nuclei in a 15 mM chloroform solution at 25°C. Error bars represent 95% errors.

7.3.1.4 Relaxation dispersion

Relaxation dispersion experiments in chloroform (see section 3.7.5) were performed at two concentrations, 6.6 mM and 16.4 mM, to assess the possible contribution of exchange to the $^{13}C^{\alpha}$ R_2 relaxation rate constants. These were performed at 16.4 T and 283.0 K. The spectral widths were set to 4 ppm and 24 ppm in the ^{1}H and ^{13}C dimensions respectively. The number of complex time domain points sampled in both dimensions were 1024 and 64 respectively. The delay Δ in Figure 3.24 was set to 2.94 ms, while the interscan delay was 2 s. Prior to Fourier transform, only the first 512 complex time domain points in the direct dimension were retained to increase the signal-to-noise ratio. The FIDs were multiplied with a squared cosine bell window function in both dimensions and subsequently zero filled to a 1024×1024 real data matrix. The total duration of the CPMG sequences in the pulse sequence was 42.2 ms and 32.8 ms for the 6.6 mM and 16.4 mM experiments respectively, which allowed for sufficient reduction of the cross-peak intensity by R_2 relaxation. The value of n in the pulse sequence of Figure 3.24 was varied randomly between 1 (τ_{cp} = 2.59 ms) and 9 (τ_{cp} = 250 µs) in 10 steps including 1 repeat for the 6.6 mM series, while for the 16.4 mM experiments n varied between 1 (τ_{cp} = 2.01 ms) and 7 (τ_{cp} = 250 µs) in 9 steps including 2 repeats. The integral of each cross-peak was followed with τ_{cp} and is plotted in Figure 7.7.

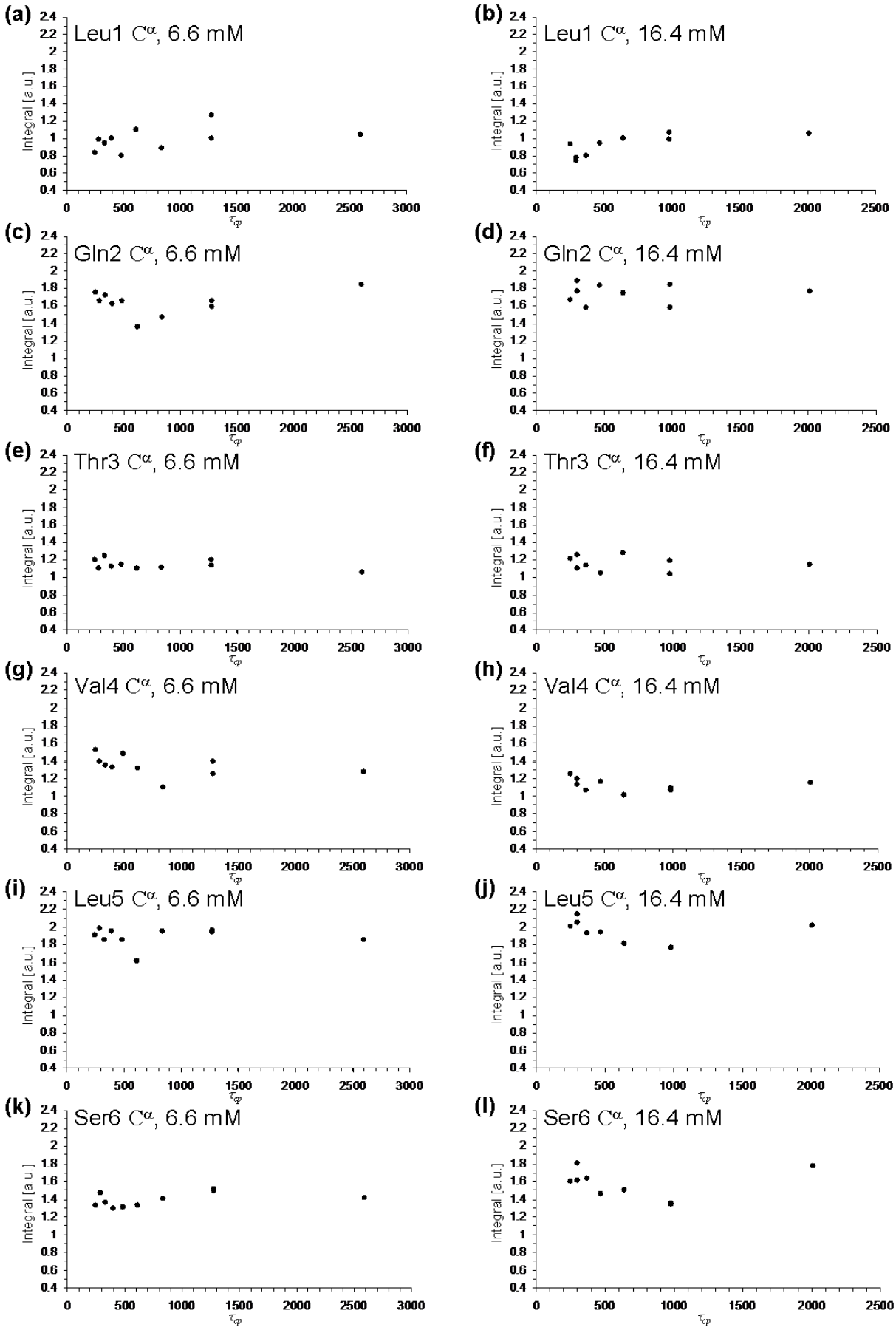

Figure 7.7a: Results of the relaxation dispersion experiments, part 1.

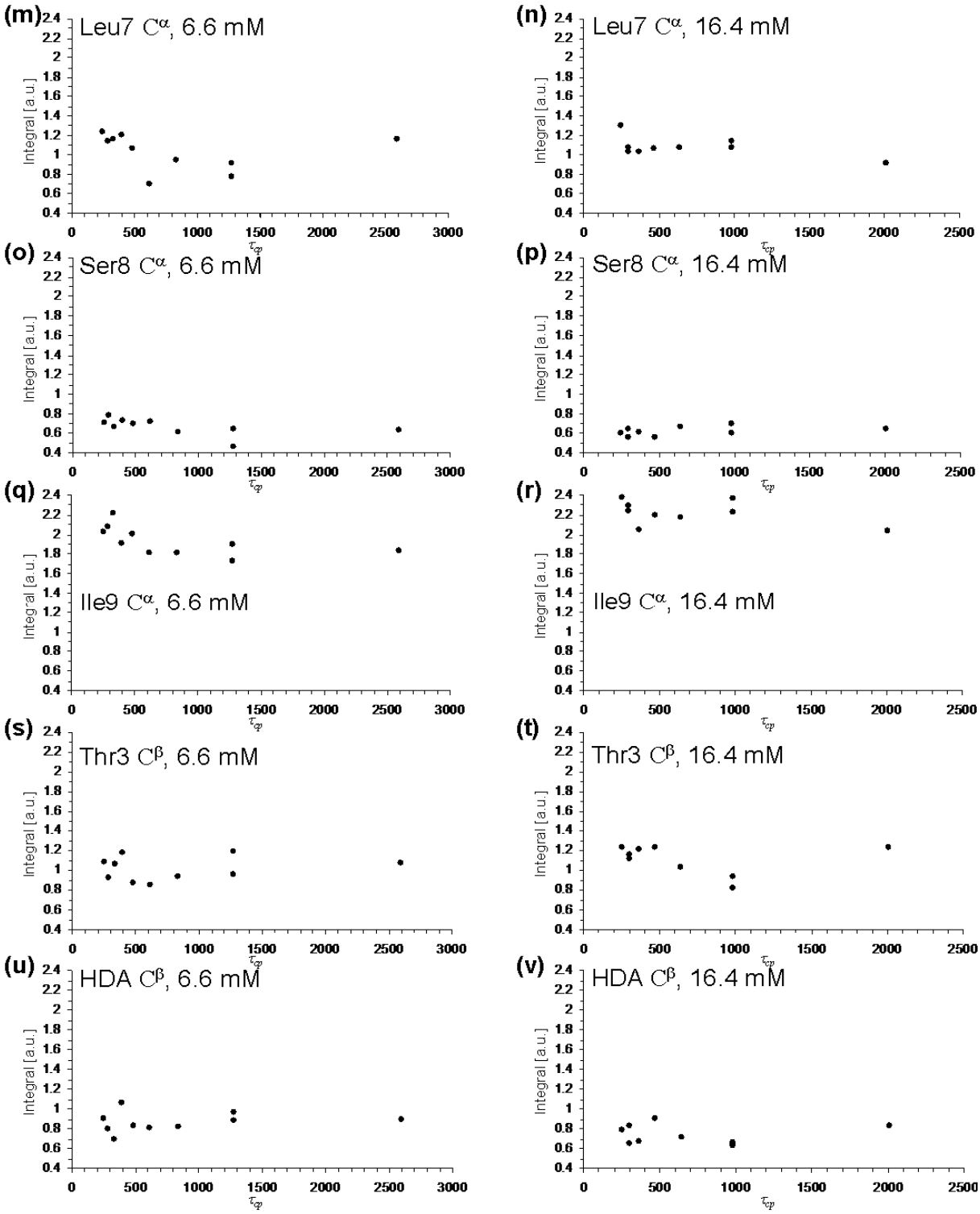

Figure 7.7b: Results of the relaxation dispersion experiments, part 2.

7.3.2 Discussion of $^{13}C^{\alpha}$ relaxation rate constants

The relaxation rate constants have a very different behaviour in chloroform than in acetonitrile. Firstly, the absolute values are now more in line with a large molecular entity: where the R_1 values in acetonitrile were around 2 s^{-1} (Table 7.2), they here

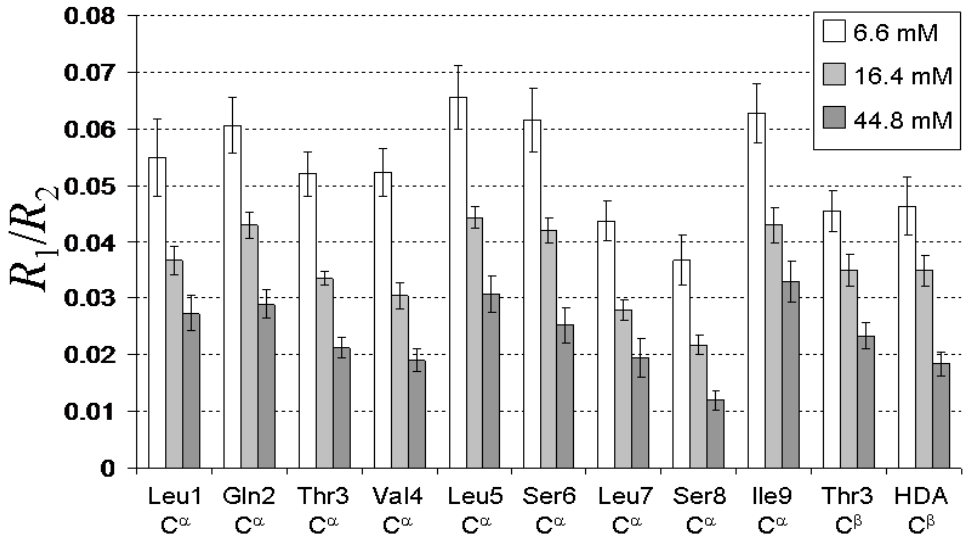

Figure 7.8: R_1/R_2 ratios $^{13}C^{\alpha}$ nuclei in chloroform at 10℃ at three different co ncentrations. Error bars represent 95% errors.

range between 1.0 s^{-1} and 1.5 s^{-1}. In Figure 3.13, where the R_1 rate constant was plotted against τ at 16.4 T field strength, it is seen that the former agrees with a correlation time on the order of 0.15 s, while the latter (assuming an increase of τ) is more in line with correlation time constants of 4.0 ns to 6.0 ns. A similar conclusion is reached from the R_2 values, which in chloroform have increased by a factor of 10, and the nOe values, which are now very close to the spin diffusion limit value of 0.15. The second observation is that the relaxation rate constants are concentration dependent. The R_2 values for example increase by about a factor of 2 from the low to the high concentration. All of these observations are of course in agreement with the self-assembly behaviour of pseudodesmin A in chloroform solution, with increasing average size of the assemblies upon increasing concentration.

In addition, a significant variation is observed in both R_1 and R_2 values over the different ^{13}C nuclei. In contrast with the results from the acetonitrile solution, these variations are consistent when comparing the R_1 and R_2 values with each other and when comparing the different concentrations (Figure 7.8) and field strengths (Figure 7.3). For instance, Leu7 C^{α} and Ser8 C^{α} both possess higher R_2 values and lower R_1 values. To a lesser extent, the same is true for Thr3 C^{α} and Val4 C^{α}. The contrast between the different nuclei becomes even clearer in the R_1/R_2 ratios, where the consistent variation in R_1 and R_2 strengthen each other. The Gln2, Leu5, Ser6 and Ile9 C^{α} nuclei provide higher R_1/R_2 ratios than the Thr3, Val4, Ser8 and Leu7 C^{α} nuclei. A possible explanation for this behaviour is the anisotropy of the supramolecular structure, which will be explored further in the next section. The nOe values do not show the same variation when compared to the R_1 and R_2 values and when compared amongst each other between the different concentrations. A reason for this could be that the relaxation regime is close to the spin diffusion limit, causing the possible effects of anisotropy to be very limited relative to the absolute value of

the nOe (see Figure 3.15). In addition, the accuracy of the nOe values is difficult to assess (*vide infra*), so it is therefore reasonable and prudent to assume that the variation observed is mainly due to experimental error or limited contributions of internal motion. Therefore, in the next sections only the anisotropy sensitive R_1/R_2 values will be considered further to investigate whether anisotropy is the cause of the observed variation.

As mentioned earlier, the nOe values do not show a very consistent behaviour when compared to R_1 and R_2. In addition, it is difficult to conclude whether the nOe remains relatively constant within the experimental error between the different concentrations and magnetic field strengths; something that would be expected for a large structure at the spin diffusion limit. The experiment was performed only once at 16.4 mM at 16.4 T and 44.8 mM and no Monte Carlo error assessment can be performed as with the R_1 and R_2 relaxation rates. At 6.6 mM and 16.4 mM at 11.7 T, the nOe experiments were repeated a second time (Tables 7.5 and 7.8), which showed for many nuclei quite a large relative difference in the measured nOe. This does suggest that the experimental error is quite high, in line with the seemingly random variation seen between the different datasets.

At 16.4 mM, the relaxation measurements were performed at both at 16.4 T and 11.7 T. The results are compared to those at 16.4 T in Figure 7.3. The R_1 values should theoretically be higher at lower field strength (since $R_1 \propto 1/B_0^2$ at the spin diffusion limit, see equation (3.97)), which is indeed the case. The R_2 values are practically constant for each nucleus, except for Leu1. The absence of field dependence is indeed expected at the spin diffusion limit (equation (3.100)) in the absence of exchange contributions. Leu1 C^α shows a significantly higher R_2 value at 11.7 T when compared to 16.4 T. This cannot be explained by conformational exchange, since the field dependence would then have been opposite. Since Leu1 C^α will be discarded during the anisotropic analysis (section 7.3.3.2), this discrepancy will not be investigated further.

7.3.3 Anisotropic analysis of $^{13}C^\alpha$ relaxation rate constants

7.3.3.1 Introduction

In section 7.3.2, it was noted that the $^{13}C^\alpha$ nuclei show a considerable variation in their R_1/R_2. In Figure 7.9, the solution structure is shown with the considered CH bonds explicitly visualised. When carefully studying the CH bonds over the molecule, an observable spread in their orientation can be observed. This variation appears to correlate with what was seen in the R_1/R_2 values. For example, the Ser8 and Leu7 CH bonds, both possessing low R_1/R_2 values, are roughly perpendicularly oriented

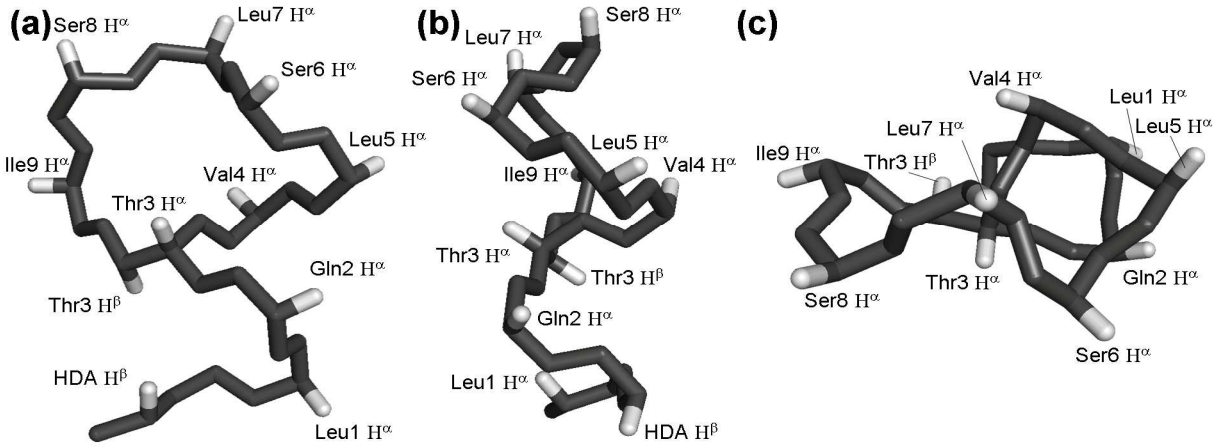

Figure 7.9: The solution structure of pseudodesmin A with only the main chain in black and the protons attached to the C^{α} nuclei in white. (a) Side view from the helix, N→C bottom to top, with the loop structure positioned to the left of the helix; (b) different side view from the helix, N→C bottom to top, with the loop structure positioned behind the helix; (c) Top view of the helix , N→C towards the reader, with the loop structure positioned to the left of the helix.

compared to the Ile9 and Leu5 CH bonds, which feature higher R_1/R_2 values. This already strongly hints that anisotropy is the cause of the observed R_1/R_2 variation. From the hypothetical model of the supramolecular assembly described in section 6.5, a prolate type structure is suspected. Theoretically, the minimum R_1/R_2 value is expected for a $^{13}C^{\alpha}$ nucleus of which the CH bond vector is positioned parallel to the long axis of the prolate structure (see Figure 3.15), corresponding with the main axis of the rotational diffusion tensor. At each concentration, the Ser8 C^{α} nucleus has the lowest experimental R_1/R_2 value and its CH bond vector can thus be assumed to make the smallest angle with the long axis of the supramolecular structure, being almost parallel with it.

To correlate the relaxation rate constants with the orientation of the CH bond vector in the solution structure, some assumptions first need to be made. The validity of each of these assumptions will be investigated after the anisotropy analysis in section 7.3.4. First, it is assumed that internal motions or exchange processes do not contribute to the relaxation. If this is indeed the case, the spectral density function and thus the values for R_1, R_2 and the nOe are only determined by the rotational diffusion coefficients and the orientation of the CH bond vector (see sections 3.3.5 and 3.4.2). It is therefore also preferred to work with the R_1/R_2 ratio, which is typically less prone to the effects of internal motion (section 3.6.4). The second assumption that will be made is that the rotational diffusion of the supramolecular complex is adequately described by an axial symmetric rotational diffusion tensor. Not only does this reduce the number of required rotational diffusion coefficients from 3 to 2 (sections 1.3 and 3.4.2), it also greatly decreases the dimensionality of the problem of determining the tensor frame's orientation. Indeed, the axially symmetric tensor requires only the three-dimensional orientation of one axis, while a fully anisotropic tensor would require two perpendicular axes to be oriented. The validity of this

assumption may already be suspected from the hypothesised model of the supramolecular complex, which suggests a cylindrical shaped structure. On the other hand, it is important because only a limited number of $^{13}C^{\alpha}$ type nuclei (probes) is available and it is desirable to keep the number of variables in the analysis to a minimum.

The strategy for the analysis of the anisotropy of the relaxation data occurs in two steps. First, the orientation of the main axis of the rotational diffusion tensor will be searched by use of a grid search. This means that for all possible orientations of this axis compared to the solution structure, the theoretical R_1/R_2 values will be calculated – using an educated guess of the rotational diffusion coefficients – and then compared to the experimental data. The orientation that is the most in agreement with the data will be chosen. In a second step the two rotational diffusion coefficients will be fitted to the experimental data.

In what follows, the practicalities of this analysis are described in detail and initially applied to the analysis of only one dataset (concentration 16.4 mM at a magnetic field strength of 16.4 T). Afterwards, the analysis will be applied to all datasets at once to obtain the final results.

7.3.3.2 Description of the analysis performed on the relaxation data at 16.4 mM and 16.4 T

Before the grid search can be performed, an initial estimation of the two rotational diffusion coefficients $D_r^{\parallel}$ and $D_r^{\perp}$ has to be made. Based on the expectation that the Ser8 CH bond is the most parallel with the rotational diffusion tensor frame's main axis and that the Ser6 CH bond is more or less perpendicular to the Ser8 CH bond as revealed from the monomer structure, their R_1/R_2 values will be used to obtain a very rough estimation the diffusion coefficients. Separately for both residues a correlation time constant τ_{iso} was calculated assuming isotropic rotational diffusion, in a similar fashion as was done before (section 7.2.2). It is assumed that this estimated τ_{iso} value is roughly a weighted average of the three correlation time constants associated with axial symmetric anisotropic relaxation, with the coefficients c_A, c_B and c_C determined by equations (3.78):

$$\begin{aligned}\tau_{iso} &= c_A\tau_A + c_B\tau_B + c_C\tau_C \\ &= \frac{1}{4}\left(3\cos^2\theta - 1\right)^2 \tau_A + 3\cos^2\theta\sin^2\theta\tau_B + \frac{3}{4}\sin^2\theta\tau_C\end{aligned} \tag{7.3}$$

Assuming that the Ser8 CH bond makes an angle $\theta = 0°$ with the main rotational diffusion axis and that the Ser6 CH makes an angle $\theta = 90°$, equation (7.3) can then be used to obtain estimations for τ_A and τ_C:

$$\tau_{iso}^{\text{Ser8}} \equiv \tau_A \tag{7.4}$$

$$\begin{aligned} \tau_{iso}^{\text{Ser6}} &\equiv \frac{1}{4}\tau_A + \frac{3}{4}\tau_C \\ \Leftrightarrow \tau_C &= \frac{4\tau_{iso}^{\text{Ser6}} - \tau_A}{3} \end{aligned} \tag{7.5}$$

From τ_A and τ_C, initial guesses for $D_r^{\parallel}$ and $D_r^{\perp}$ were then finally estimated using the relations (3.76), providing values of respectively 4.122×10^7 s^{-1} and 2.126×10^7 s^{-1}.

To mathematically describe the orientation of a CH bond, a normalised vector **CH** associated with this bond can be calculated using the x, y and z coordinates of the C and H atoms within the solution structure:

$$\mathbf{CH} = \frac{1}{\sqrt{\left(x_C - x_H\right)^2 + \left(y_C - y_H\right)^2 + \left(z_C - z_H\right)^2}} \begin{bmatrix} x_C - x_H \\ y_C - y_H \\ z_C - z_H \end{bmatrix} \tag{7.6}$$

The angle θ between the vector **CH** and any other vector **V** is then calculated as:

$$\theta = \arccos\left(\mathbf{V} \cdot \mathbf{CH}\right) \tag{7.7}$$

For calculation of the R_1 and R_2 values, the vector **V** needs to be the main axis of the axial symmetric rotational diffusion tensor frame. A grid search will be performed in which an initial vector $\mathbf{V_0}$ is rotated to a new vector $\mathbf{V_1}$ that may adopt all possible orientations. For each orientation of $\mathbf{V_1}$, the θ angles for every **CH** vector are determined (Figure 7.10) and inserted into the equations of the spectral density function of the axial symmetric anisotropic system (equations (3.77) and (3.78)), using estimated values of the three correlation times (*vide infra*). Using these θ angles, the theoretical R_1 and R_2 values are calculated for each C^{α} nucleus (equations (3.58) and (3.61), using both dipolar and CSA relaxation contributions). The theoretical R_1/R_2 values are calculated and compared to the experimental values by calculating the weighted sum of square difference SS:

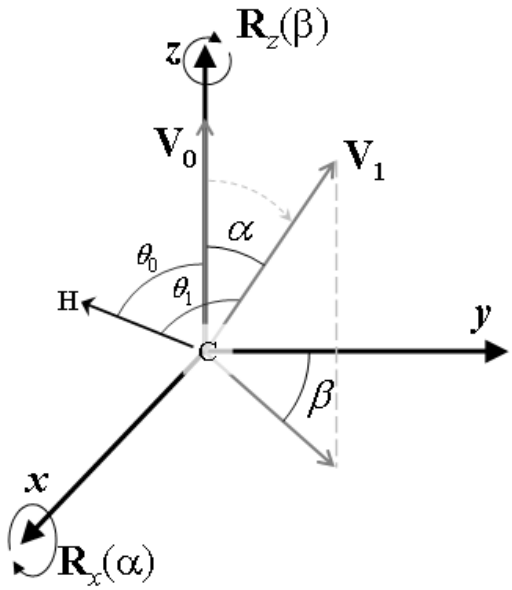

Figure 7.10: The CH bond vector makes an angle θ_0 with the initial vector $\mathbf{V}_0$, positioned parallel with the z-axis. The vector $\mathbf{V}_0$ can be rotated to a new vector $\mathbf{V}_1$ by a rotation first around the x-axis by an angle α and subsequently around the z-axis by an angle β. The CH bond vector makes an angle θ_1 with the $\mathbf{V}_1$ vector.

$$SS = \sum_i \left(\frac{\left(\frac{R_1^{th}}{R_2^{th}}\right)_i - \left(\frac{R_1^{\exp}}{R_2^{\exp}}\right)_i}{s_{R1/R2,i}} \right)^2 \tag{7.8}$$

in which $s_{R1/R2,i}$ is the experimental error on the i^{th} R_1/R_2 value. The SS value is thus a function of the orientation of the vector $\mathbf{V_1}$. The orientation which provides the minimal SS value is the direction that is most likely to be the main axis of the rotational diffusion tensor frame according to the experimental data.

At the start of the grid search, the solution structure was placed in a reference frame in which the Ser8 CH bond was positioned parallel to the z-axis. The initial vector $\mathbf{V_0}$ was then subsequently chosen to be oriented parallel to the z-axis as well. This is motivated not only by the expectation that the optimum orientation of $\mathbf{V_1}$ will be closely parallel to Ser8 CH, but also by the fact that the rotation from $\mathbf{V_0}$ to all possible orientations is more practically performed when it is parallel to one of the Cartesian axes. $\mathbf{V_1}$ was obtained from $\mathbf{V_0}$ using of two transformation matrices, one which first rotated the vector around the x-axis over an angle α, $\mathbf{R}_x(\alpha)$, and one around the z-axis over an angle β, $\mathbf{R}_z(\beta)$ (Figure 7.10), resulting in a new vector $\mathbf{V_1}$:

$$\mathbf{V_1} = \mathbf{R}_z(\beta)\mathbf{R}_x(\alpha)\mathbf{V} = \begin{bmatrix} \cos\beta & \sin\beta & 0 \\ -\sin\beta & \cos\beta & 0 \\ 0 & 0 & 1 \end{bmatrix} \begin{bmatrix} 1 & 0 & 0 \\ 0 & \cos\alpha & \sin\alpha \\ 0 & -\sin\alpha & \cos\alpha \end{bmatrix} \mathbf{V_0} \tag{7.9}$$

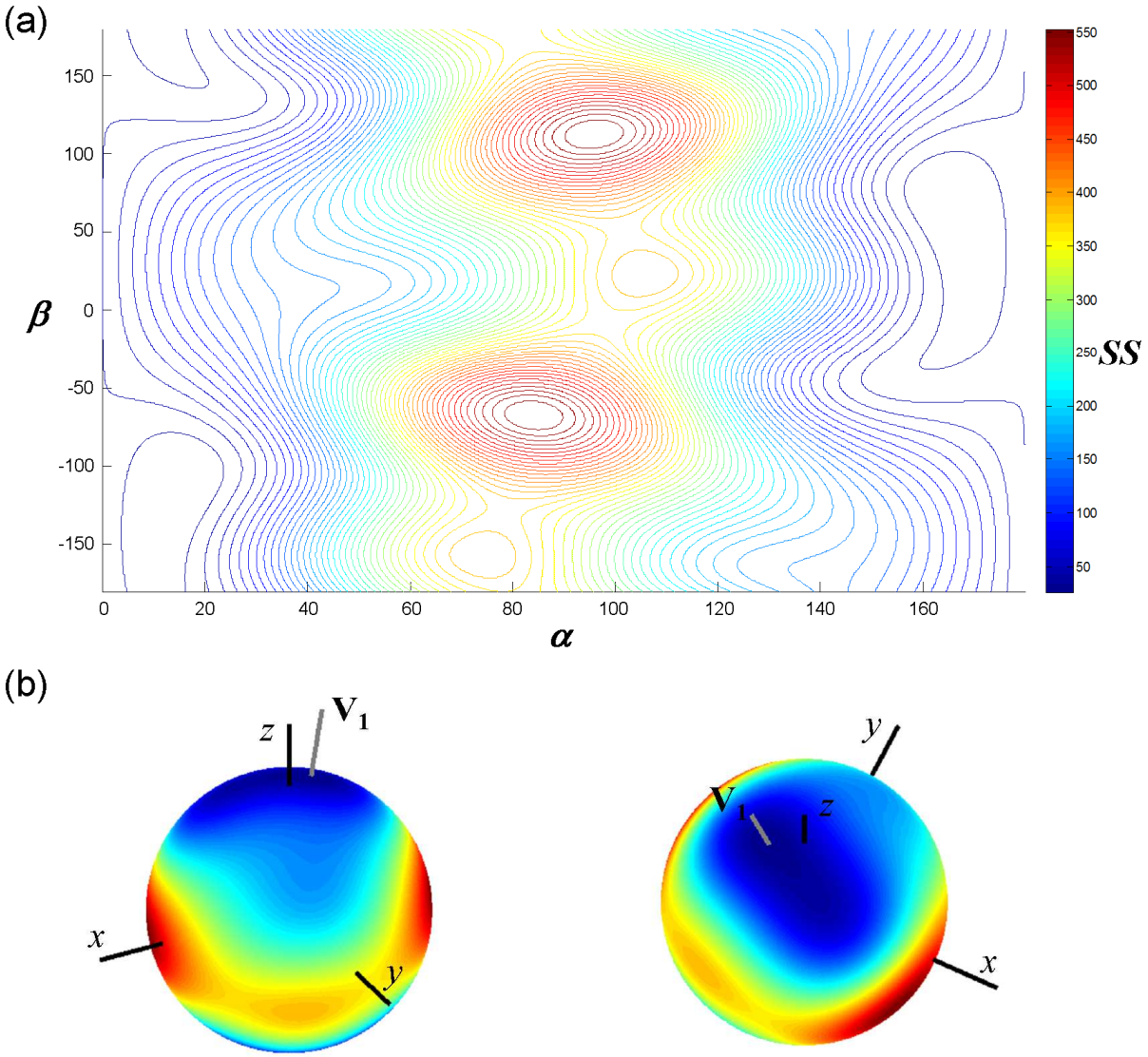

Figure 7.11: (a) Contour plot with the *SS* value as a function of α and β. (b) The *SS* value projected upon the surface of a sphere, viewed from two different angles. The *x*-, *y*- and *z*-axes are shown, as well as the $\mathbf{V}_1$ vector pointing in the direction of the minimum *SS* value.

The angle α was varied from 0° to 179.75° in steps of 0.25°, w hile β was varied from –180° to 179.5° in steps of 0.5°, resulting in a to tal of 518,400 orientations sampled in the grid search. The *SS* value for each combination of α and β, applied on the 16.4 mM at 16.4 T dataset, is plotted in Figure 7.11. The sum of square difference displays quite a strong dependence on the orientation of $\mathbf{V_1}$, its value ranging from 15.1 to 563.6. The minimum value is found at $\alpha = 14.25°$ and $\beta = -113.5°$, thus not far away from the initial orientation of $\mathbf{V_0}$ (Figure 7.11b). Although on the contour plot of Figure 7.11a the minimum in *SS* appears to be very broad along β, it should be reminded that α and β are in fact spherical coordinates and that the closer α is to 0° or 180°, the less effect the value of β has on the orientation of $\mathbf{V_1}$. This is best understood from Figure 7.11b, where the contour plot is projected on a sphere surface. A second important remark is that, due to the fact that the relaxation rate

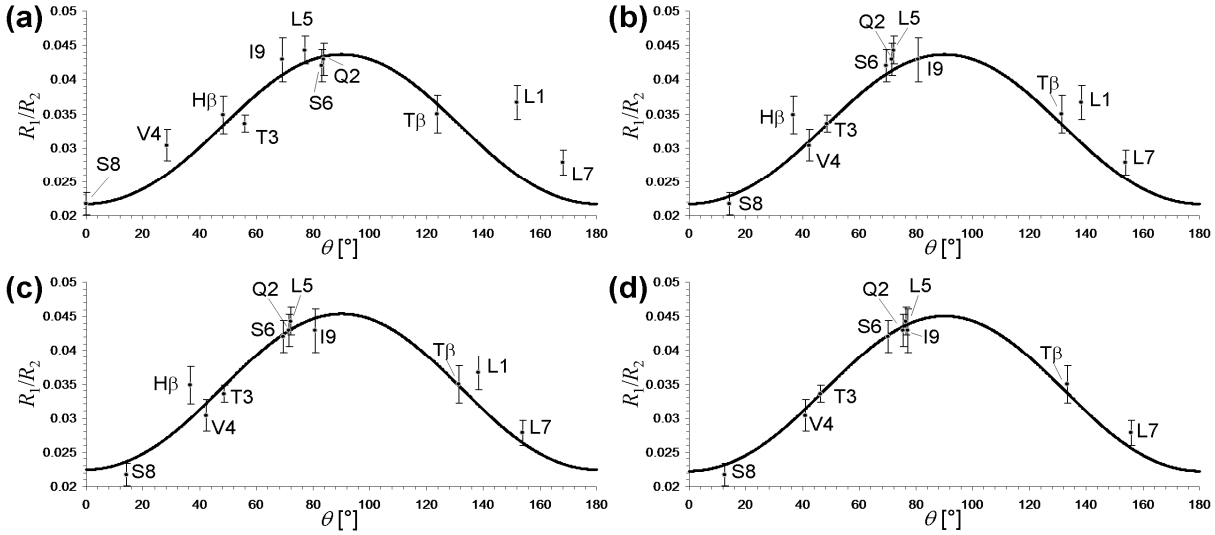

Figure 7.12: Theoretical R_1/R_2 ratios (solid line) and the experimental R_1/R_2 values (16.4 mM concentration, 16.4 T) versus θ. The data points are labelled using the one letter amino acid codes, with HDA C^{β} labelled as Hβ and Thr3 C^{β} labelled as Tβ. (a) Before the grid search, using initial estimated values for $D_r^{\parallel}$ and $D_r^{\perp}$ and calculating the data point θ angle relative to $\mathbf{V}_0$. (b) After the first grid search, using initial estimated values for $D_r^{\parallel}$ and $D_r^{\perp}$ and calculating the data point θ angle relative $\mathbf{V}_1$. (c) Same as in (b), but with newly fitted values for $D_r^{\parallel}$ and $D_r^{\perp}$. (d) After the second grid search (which excluded L1 and Hβ), θ angles calculated relative to $\mathbf{V}_2$' and newly fitted values for $D_r^{\parallel}$ and $D_r^{\perp}$.

constants in theory only depend on the cosine of θ, a form of symmetry exists in the *SS* contour plot. This effectively makes it only necessary to consider half of the plot.

In Figures 7.12a and 7.12b, the theoretical R_1/R_2 values are plotted against θ using the initial values of $D_r^{\parallel}$ and $D_r^{\perp}$. The experimental R_1/R_2 values are plotted against their θ values from both before and after the grid search. The fitting of the data points to the theoretical curve has notably improved after the grid search. Using the optimised orientation of $\mathbf{V_1}$ as the new assumed direction of the rotational diffusion tensor main axis, new $D_r^{\parallel}$ and $D_r^{\perp}$ values were fitted to the data points by searching the values that minimise the *SS*. This resulted in a reduced value of *SS* of 10.9, a value of 4.215×10^7 s^{-1} for $D_r^{\parallel}$ and 2.163×10^7 s^{-1} for $D_r^{\perp}$. The new theoretical curve is plotted in Figure 7.12c. From this curve, two outliers are detected: the HDA C^{β} and Leu1 C^{α}. Since these two nuclei are usual suspects in terms of a higher contribution of fast internal motion to the relaxation values, it would be reasonable to remove these data points from the study. Another plausible reason why these are outliers could be that the orientation of their respective CH bonds is not accurately represented by the acetonitrile solution structure, since the end of the exocyclic part was not well defined in this structure (section 5.3.2).

Because the optimisations of the orientation of the reference vector and the rotational diffusion coefficients were performed consecutively and two data points were removed, a second grid search should be performed using the fitted rotational

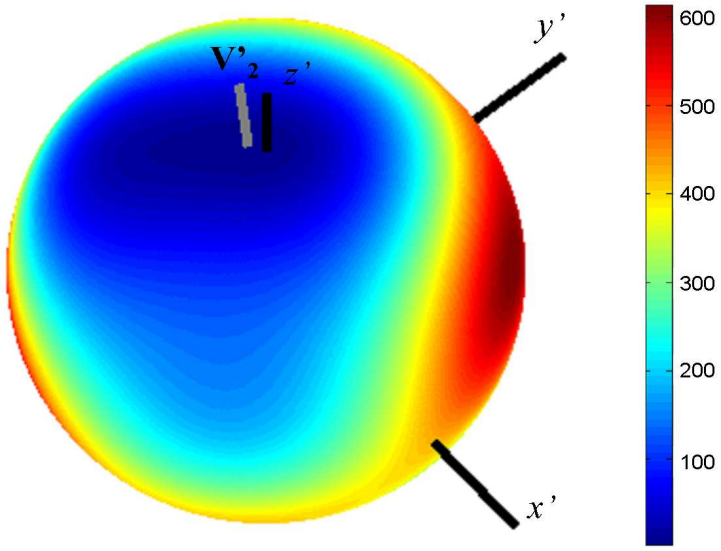

Figure 7.13: The *SS* value from the second grid search projected upon the surface of a sphere. The *x*'-, *y*'- and *z*'-axis are shown, as well as the $\mathbf{V'}_2$ vector pointing in the direction of the minimum *SS* value.

diffusion coefficients to obtain an even better optimised orientation. For this, the solution structure and $\mathbf{V_1}$ were placed into a new reference frame so that $\mathbf{V_1}$ was oriented parallel to the *z*'-axis of this new frame. During the second grid search, this 'new' vector $\mathbf{V_1'}$ was then rotated within this frame to a vector $\mathbf{V_2'}$, by using again the same transformation matrices as before:

$$\mathbf{V_2'} = \mathbf{R}_z(\beta')\mathbf{R}_x(\alpha')\mathbf{V_1'} \tag{7.10}$$

The *SS* value was calculated for each combination of α' and β', which were varied likewise as α and β during the first grid search (Figure 7.13). The *SS* during this second grid search varied between 3.1 and 612.7, and the values for α' and β' at its minimum value were 4.25° and –119.5° respectively. The rotational diffusion coefficients were optimised once more afterwards, resulting in the values of 4.202×10^7 s^{-1} and 2.153×10^7 s^{-1} for $D_r^{\parallel}$ and $D_r^{\perp}$ respectively and a final *SS* of 2.9. By applying equations (3.76), these rotational diffusion coefficients give rise to correlation time constants of τ_A = 7.74 ns, τ_B = 6.68 ns and τ_C = 4.74 ns. The resulting theoretical R_1/R_2 curve and experimental data points are plotted in Figure 7.12d. The θ angle of each CH bond is provided in Table 7.11, together with the resulting contribution of each correlation time constant to the spectral density function.

Table 7.11: Resulting θ angles and spectral density weighting coefficients of the CH bonds after the 2nd grid search at 16.4 mM

	Gln2 C^{α}	Thr3 C^{α}	Val4 C^{α}	Leu5 C^{α}	Ser6 C^{α}	Leu7 C^{α}	Ser8 C^{α}	Ile9 C^{α}	Thr3 C^{β}
θ [°]	75.3	46.2	41.1	76.4	70.3	155.7	12.7	77.0	133.5
c_A	0.16	0.05	0.12	0.17	0.11	0.56	0.86	0.18	0.04
c_B	0.18	0.75	0.74	0.16	0.30	0.42	0.14	0.14	0.75
c_C	0.66	0.20	0.14	0.67	0.59	0.02	0.00	0.68	0.21

7.3.3.3 Analysis performed at all concentrations and magnetic field strengths

An analysis similar to the one of the previous section was performed on all the $^{13}C^{\alpha}$ datasets at once. Since the R_1/R_2 patterns over all datasets are qualitatively the same, it is expected that each dataset provides a similar result in terms of the direction of the main axis of the rotational diffusion tensor. When the anisotropy analysis is performed on each dataset separately (results not shown), this is indeed found to be the case. It is however preferred to perform the analysis on all datasets simultaneously so that only a single set of θ values for the CH bonds is obtained. This is done by performing the grid search based on a total sum of square difference value SS_{tot}, which is the sum of all individual SS values. The rotational diffusion coefficients on the other hand are treated separately for each of the four datasets. Their initial values before the grid search were chosen from the anisotropy analyses performed on each dataset separately mentioned earlier. Otherwise the analysis was performed similarly as in the previous section, including two grid search steps and rotational diffusion coefficient fitting. The Leu1 C^{α} and the HDA C^{β} were discarded from the analysis before the first grid search. The results are presented in Tables 7.12 and 7.13 and Figure 7.14. The minimum total sum of square difference was 14.6 at the end of the analysis.

Table 7.12: Resulting θ angles and spectral density weighting coefficients of the CH bonds after the 2nd grid search using the R_1/R_2 data from all datasets

	θ [°]	c_A	c_B	c_C
Leu1 C^{α}	135.7 ± 1.8	0.07 ± 0.03	0.75 ± 0.002	0.18 ± 0.02
Gln2 C^{α}	71.3 ± 2.2	0.12 ± 0.02	0.28 ± 0.06	0.60 ± 0.03
Thr3 C^{α}	46.0 ± 1.5	0.05 ± 0.02	0.749 ± 0.003	0.20 ± 0.02
Val4 C^{α}	44.5 ± 1.9	0.07 ± 0.03	0.750 ± 0.002	0.18 ± 0.02
Leu5 C^{α}	73.7 ± 1.9	0.15 ± 0.02	0.22 ± 0.05	0.64 ± 0.03
Ser6 C^{α}	67.1 ± 1.8	0.07 ± 0.02	0.38 ± 0.05	0.54 ± 0.03
Leu7 C^{α}	152.2 ± 2.0	0.45 ± 0.06	0.51 ± 0.05	0.04 ± 0.01
Ser8 C^{α}	16.1 ± 1.9	0.78 ± 0.05	0.21 ± 0.05	0.004 ± 0.002
Ile9 C^{α}	81.1 ± 2.2	0.22 ± 0.02	0.07 ± 0.03	0.71 ± 0.02
Thr3 C^{β}	133.8 ± 1.4	0.05 ± 0.02	0.749 ± 0.003	0.20 ± 0.02
HDA C^{β}	34.1 ± 1.5	0.28 ± 0.04	0.65 ± 0.03	0.07 ± 0.01

Table 7.13: Resulting rotational diffusion coefficients after the 2nd grid search using the R_1/R_2 data

	6.6 mM 16.4 T	16.4 mM 16.4 T	44.8 mM 16.4 T	16.4 mM 11.7 T
$D_r^{\parallel}$ [μs^{-1}]	49.00 ± 3.17	43.25 ± 1.57	38.26 ± 2.56	34.61 ± 3.31
$D_r^{\perp}$ [μs^{-1}]	27.67 ± 1.21	21.08 ± 0.58	15.50 ± 0.85	20.64 ± 1.25

Following this analysis, a Monte Carlo error analysis was performed to assess the precision of the results. This was done by first obtaining a random noise value from a standard Normal distribution for each experimental R_1 and R_2 data point used in the

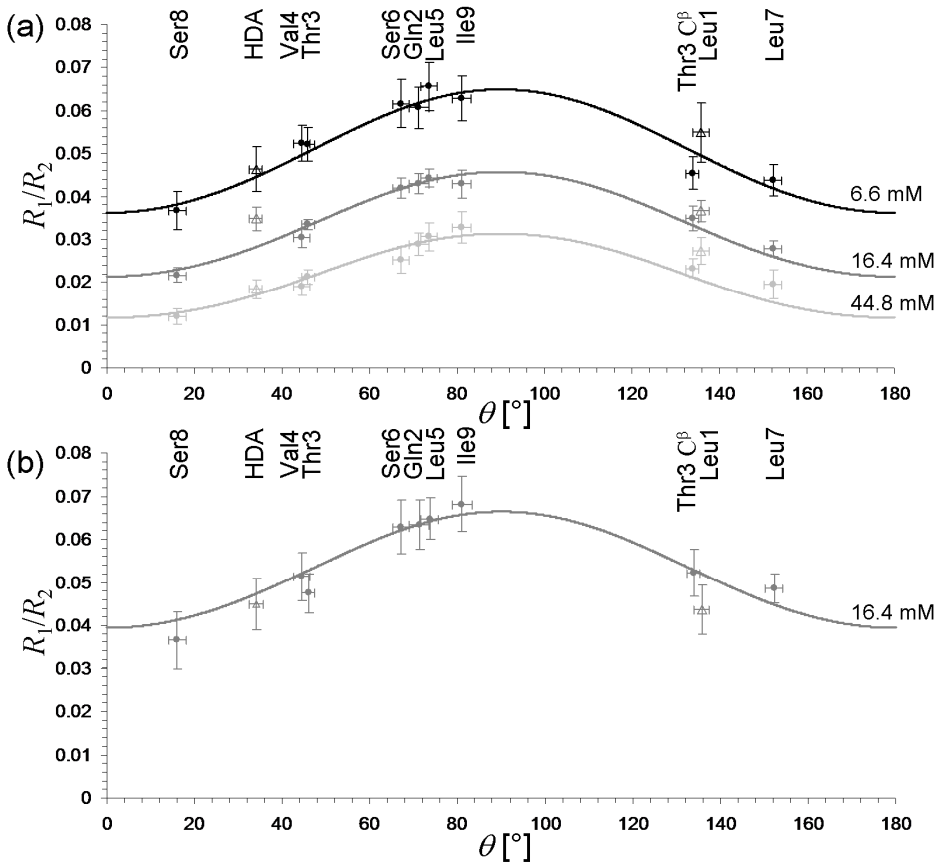

Figure 7.14: The final result after the two grid searches and rotational diffusion coefficient fitting in the analysis of all datasets simultaneously. The solid lines represent the theoretical R_1/R_2 values calculated using the fitted rotational diffusion coefficients for each dataset separately. The data points represented by a full dot were used during the grid search, while those represented by an empty triangle were not. The vertical error bars are the experimental R_1/R_2 95% errors, while the horizontal error bars are the 95% errors on the θ angle obtained from the Monte Carlo analysis. (a) Datasets measured at 16.4 T. (b) Datasets measured at 11.7 T.

grid search (9 nuclei for each of the four datasets, thus 72 independent noise values in total) using the Marsaglia polar method (see appendix C). These were then multiplied by the standard deviation of the respective (assumed Gaussian) error on R_1 or R_2 (95% error divided by 1.96) and added to the experimental value to create a new set of R_1/R_2 values. Using the results of the previous analysis as initial values, one grid search and one rotational diffusion coefficient fitting were performed using these new R_1/R_2 values. The grid search was limited to α values up to only 5°, which was afterwards found to be more than sufficient. This whole procedure was repeated 100 times. The standard deviations were calculated from the resulting 100 sets of rotational diffusion coefficients and CH bond θ values. The results are shown in Tables 7.12 and 7.13 and Figure 7.14. The variation on the orientation of the main rotational diffusion tensor direction is represented in Figure 7.15.

From this error analysis, it is revealed that the results of the anisotropy analysis are very robust. The 95% errors of the rotational diffusion coefficients are relatively small and show that the differences seen between the datasets are indeed statistically significant. Note that the relative errors (ratio between error and the value) on the $D_r^{\perp}$

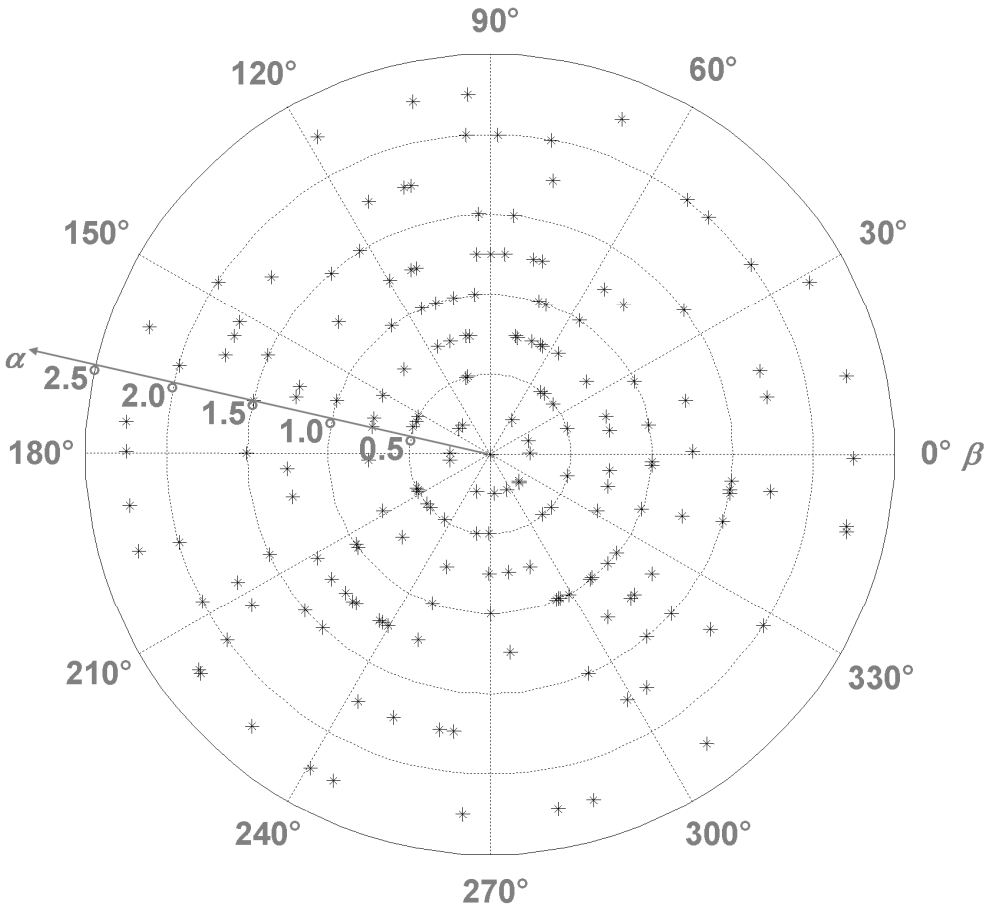

Figure 7.15: A polar plot representing the 100 α and β angle combinations obtained during the Monte Carlo error analysis. Each point represents the deviation of the newly optimised main axis direction during the Monte Carlo analysis from the optimal direction after the grid search using all datasets. The distance from the middle point represents the α coordinate while the polar position along the circle represents the β coordinate.

coefficients are always higher than those of the $D_r^{\parallel}$ values. This is not surprising, as the latter are mainly influenced by the degree of sampling at the top of the R_1/R_2 curve (around 90°), while the former is influenced more by the degree of sampling around 0°. Since there are more experimental data points situated at the top of the curve, this results in a higher robustness during the non-linear regression fitting for $D_r^{\parallel}$. The 95% errors on the θ values and Figure 7.15 show that the orientation of the main axis of the rotational diffusion coefficient axis is very robust as well, with maximum deviations of only 2.25° away from the optimal orientation found for the real experimental dataset.

7.3.4 Validation of the assumptions during the anisotropic analysis

7.3.4.1 Contributions of internal motions and exchange

When the nuclear spins exchange between multiple states with a rate not too different from the difference in resonance frequency of these states, this will result in

an additional contribution to the R_2 value (see section 3.5). These exchanging states could result here either from the oligomer and monomer states exchanging through self-association, or from molecular conformations that interconvert into each other. Given the rigidity of the solution structure, the latter is not expected. The effects of the self-association has already been established to be fast on the frequency time scale, which means that the exchange contribution to the R_2 relaxation rate constant, if present, should increase with the magnetic field. Since for large molecules R_2 should itself be practically field independent, the absence of field dependence of the experimental R_2 is a good argument in favour of absence of exchange contributions. This is indeed found for the ^{13}C R_2 values at 16.4 mM, which were measured at both 11.7 T and 16.4 T (Figure 7.3). The only exception appears to be Leu1 C^{α}. Its R_2 appears to decrease with the magnetic field strength however, ruling out exchange to be the cause.

Another experiment to assess the presence of exchange is relaxation dispersion. As described in detail in section 3.7.5, the degree of exchange contribution to R_2 depends on the delay τ_{cp} between the CPMG 180° pulses. It is thus possible to measure the exchange contribution R_{ex} by measuring the apparent R_2 for varying τ_{cp}. Because such a series of experiments would require a long measuring time, it was decided to follow the cross-peak integral as a function of τ_{cp} using a CMPG sequence of constant length. The length was chosen so that sufficient signal attenuation took place at short τ_{cp} value. If exchange processes at a similar time scale of τ_{cp} would contribute significantly to R_2, the signal intensity is expected to decrease upon increasing τ_{cp}. These experiments were performed at both 6.6 mM and 16.4 mM at a field strength of 16.4 T. The results were shown previously in Figure 7.7.

The data points are so scattered that it is impossible to detect a possible small decrease in signal intensity with increasing τ_{cp} values. For some τ_{cp} values the experiments were repeated once (1276 µs for 6.6 mM; 299 µs and 983 µs for 16.4 mM). As the difference in intensity between these repeat data points is often quite large, it seems that the scattering in data points as a function of τ_{cp} is a consequence of the precision of the experimental set-up. For none of the ^{13}C probes at any concentration, the signal intensity can thus be convincingly shown to decrease with increasing τ_{cp} values. This confirms the observation that no significant contributions to the relaxation rate constants arise from conformational exchange or exchange due to the self-association.

Conformational dynamics that occur with a correlation time constant of less than the global rotational motion correlation time constants have a different impact on the relaxation rate constants, as these will contribute to the spectral density functions themselves (see section 3.4.3). These internal motion contributions are of course

undesirable for properly correlating the relaxation rate constants to the rotational diffusion. The fact that the R_1/R_2 values can so nicely be correlated with the anisotropy of the supramolecular structure without any significant outliers (section 7.3.3) is in itself an indication that these internal motions are only minutely present, if at all. After all, since the squared order parameter S^2 and the internal motion correlation time constant τ_i in principle should vary from nucleus to nucleus, a large contribution from internal motions would lead to a much higher inconsistent scattering of the data points when compared to the theoretical curves and therefore muddle the correlation with the anisotropy.

It is however very difficult to perform a Lipari-Szabo type analysis to gain an idea of the values of the S^2 and τ_i. In macromolecular systems, these parameters are typically fitted from the combined R_1, R_2 and nOe data using the known global correlation time constants, or estimated using spectral density plotting[4, 5]. However, in this case the relaxation parameters are a concentration weighted average over all oligomer sizes and the monomer. As will be discussed in section 7.5 and in more detail in the next chapter, this leads to apparent discrepancies between the experimental values of R_1, R_2 and the nOe when compared to how they would need to relate to each other according to theory. This discrepancy cannot be explained by introducing a Lipari-Szabo type treatment. This does complicate matters. For example, the experimental nOe values of the ^{13}C nuclei, which for all concentrations range between 0.2 and about 0.4, are slightly higher when compared to the expected spin diffusion limit value of 0.15. As was discussed in section 3.6.4; the nOe can be quite sensitive to the presence of internal motion, pushing it to higher values. In this case, the apparent nOe can be considered as a weighted average of the high nOe values of the monomer state and the nOe value of the large oligomer states in the spin diffusion regime. This will thus always lead to a value somewhat higher than the spin diffusion limit nOe value and an assessment of the internal motions from the nOe value alone would therefore be confounded with this phenomenon. Including the R_1 and R_2 data in a so-called spectral density analysis then again provides values for S^2 higher than 1, which is physically meaningless.

In conclusion, the potential contributions of exchange can safely be excluded. However, the extent to which internal motions on the picosecond time scale contribute cannot readily be assessed. It is expected that the impact of such motions on the results are limited, taking into account the quality with which the data can be correlated with the anisotropy.

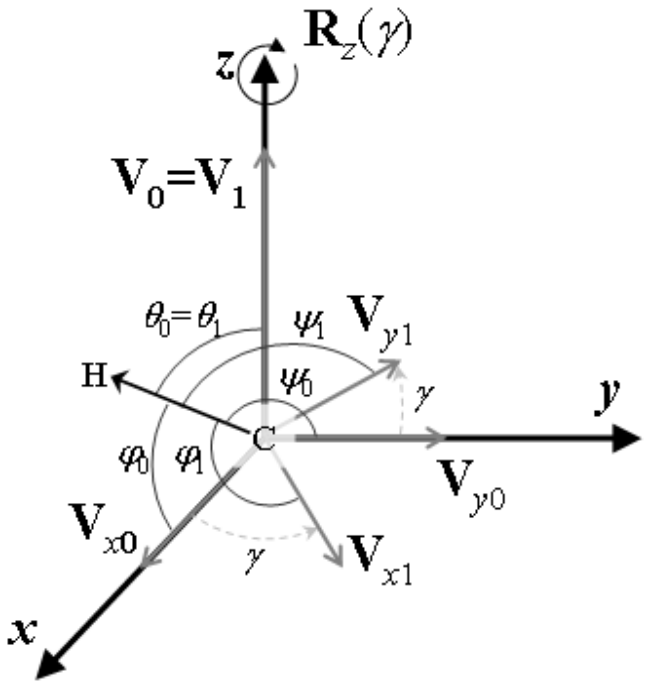

Figure 7.16: In the full anisotropic case, three angles between the CH bond vector and three perpendicular reference vectors (θ, φ and ψ) are required (section 3.4.2). The only rotation in the full anisotropic grid search that is performed here is around the z-axis by an angle γ.

7.3.4.2 Evaluation of the axial symmetry

The assumption of an axial symmetric rotational diffusion tensor was made above in order to limit the number of variables to be evaluated in the anisotropy analysis. However, a molecular object in principle is always fully anisotropic; axial symmetry is only an approximation to reality. The question addressed here is to what extent a fully anisotropic model can do a better job in explaining the variation in R_1/R_2 values.

The grid search provided a convincing orientation for the main axis of the rotational diffusion tensor. It is therefore assumed that this orientation remains the optimal one when a fully anisotropic grid search would be performed. Only the orientation of the two remaining axes of the diffusion tensor therefore need be optimised. This is done once again by means of a grid search, this time requiring the rotation along the main tensor axis. The three rotational diffusion coefficients will be fitted at every step of the grid search rather than afterwards.

As before, the R_1/R_2 values of Leu1 C^{α} and HDA C^{β} were discarded. The solution structure and the tensor main axis $\mathbf{V}_z$ were put in a reference frame so that the latter would be along the z-axis. The remaining two tensor axes $\mathbf{V}_{x0}$ and $\mathbf{V}_{y0}$ were then initially put along the x- and y-axes respectively. The grid search occurred by stepwise rotation aournd the z-axis with an angle γ using a transformation matrix $\mathbf{R}_z(\gamma)$,

effectively transforming $\mathbf{V}_{x0}$ and $\mathbf{V}_{y0}$ to $\mathbf{V}_{x1}$ and $\mathbf{V}_{y1}$, while $\mathbf{V}_z$ remains invariant under the rotation (Figure 7.16):

$$\mathbf{V}_{x1} = \mathbf{R}_z(\gamma)\mathbf{V}_{x0} = \begin{bmatrix} \cos\gamma & \sin\gamma & 0 \\ -\sin\gamma & \cos\gamma & 0 \\ 0 & 0 & 1 \end{bmatrix} \mathbf{V}_{x0} \tag{7.11}$$

$$\mathbf{V}_{y1} = \mathbf{R}_z(\gamma)\mathbf{V}_{y0} \tag{7.12}$$

The angles θ, φ, and ψ between the CH vectors and respectively the $\mathbf{V}_z$, $\mathbf{V}_{x1}$ and $\mathbf{V}_{y1}$ tensor axes were determined (equation (7.7)) and used in the equations of the fully anisotropic spectral density function (section 3.4.2) to allow calculation of the theoretical R_1/R_2 values. The angle γ was varied between 0° and 89.75° in steps of 0.25°. Further rotation is unnecessary since the spectral density only requires the cosines of the angles θ, φ, and ψ, thus making the sign of the angle irrelevant, while in addition a switch of the $\mathbf{V}_{x1}$ and $\mathbf{V}_{y1}$ directions will only permute the rotational diffusion coefficient D_r^x and D_r^y between the two directions. The three rotational diffusion coefficients were then fitted to the data for each value of γ by minimising the sum of square difference SS as defined by equation (7.8).

The minimised total sum of squares difference encompassing each dataset for each value of γ, $SS_{tot,min}$, is plotted in Figure 7.17. The maximum value of $SS_{tot,min}$ is 13.82, which is slightly lower than the minimum SS value after the final rotational diffusion coefficient fitting in section 7.3.3.3, which was 14.6. This is normal since the axial symmetry model is a special case of the fully anisotropic model, and therefore the $SS_{tot,min}$ value can never become higher than what was found in the axial symmetric case. The minimum $SS_{tot,min}$ value is 12.60, which is only a difference of 1.22 with the maximum value. Such a small difference is in sharp contrast with the large changes in sum of squares found during the axial symmetric anisotropy grid search.

The sum of square differences for each dataset separately are summarised in Table 7.14. Again the differences between the maximum and the minimum sum of square differences are very small. In addition, the γ angle at which the minima can be found are not consistent, differing strongly between datasets. The fitted rotational diffusion coefficients at this optimal γ angle are also listed in Table 7.14. The D_r^z, D_r^y and D_r^x rotational diffusion coefficients do not differ strongly from their corresponding axial symmetric counterparts ($D_r^z \rightarrow D_r^{\parallel}$ and D_r^x, $D_r^y \rightarrow D_r^{\perp}$; see Table 7.13). The difference between D_r^x and D_r^y reflects the deviation from the axial symmetric situation. This difference is compared in Table 7.14 with the 95% errors that were found for the $D_r^{\perp}$ diffusion coefficients. Both values are always of the same order of magnitude.

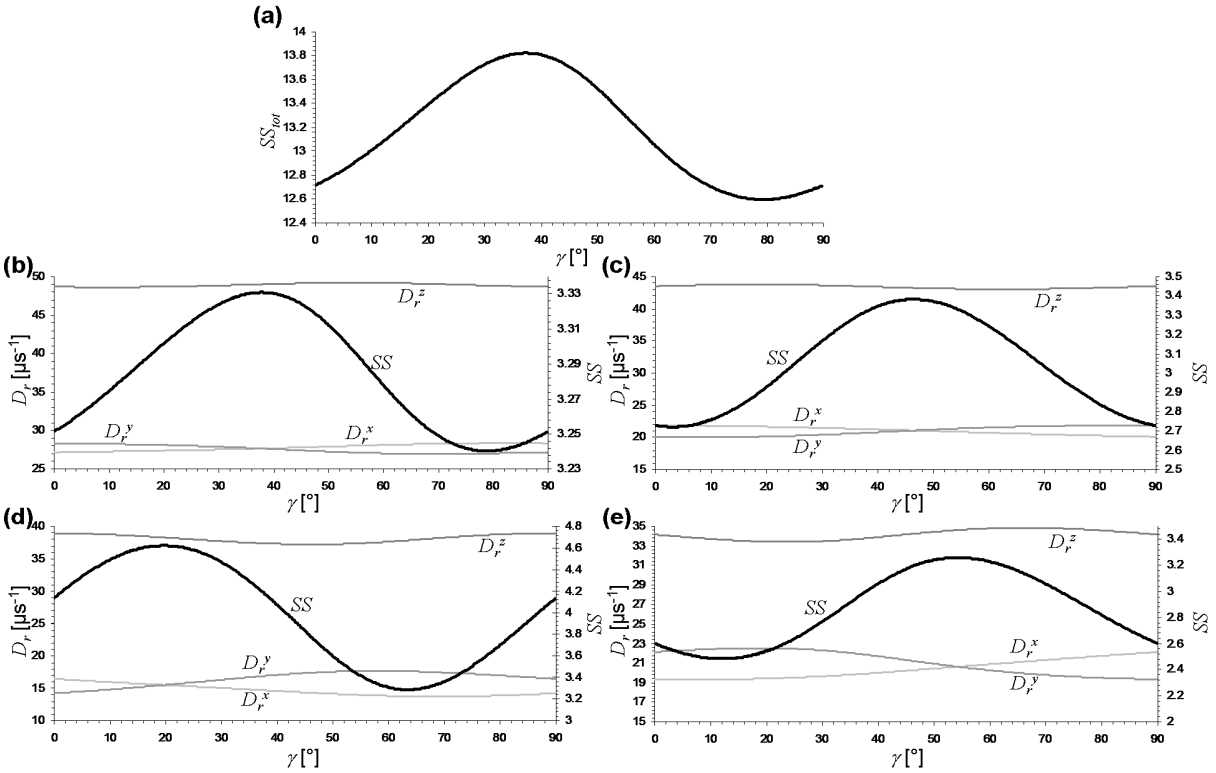

Figure 7.17: Results of the full anisotropic grid search. In (a), SS_{tot} is plotted as a function of γ. The other graphs show the SS value and fitted rotational diffusion coefficients as a function of γ for the individual datasets: (b) 6.6 mM 16.4 T; (c) 16.4 mM 16.4 T; (d) 44.8 mM 16.4 T; (e) 16.4 mM 11.7 T.

Therefore the deviation from the axial symmetric situation cannot be labelled as statistically significant.

Table 7.14: Overview of the results of the full anisotropic study for each dataset individually

	6.6 mM 16.4 T	16.4 mM 16.4 T	44.8 mM 16.4 T	16.4 mM 11.7 T
SS_{max}	3.33	3.38	4.62	3.26
SS_{min}	3.24	2.72	3.29	2.48
γ_{min}	78.75°	3.00°	63.50°	12.00°
D_r^z	4.88×10^7	4.36×10^7	3.78×10^7	3.36×10^7
D_r^x	2.83×10^7	2.18×10^7	1.38×10^7	1.93×10^7
D_r^y	2.70×10^7	2.01×10^7	1.77×10^7	2.25×10^7
$\lvert D_r^x - D_r^y \rvert$	1.32×10^6	1.77×10^6	3.89×10^6	3.13×10^6
$D_r^\perp$ 95% error	3.17×10^6	1.57×10^6	2.56×10^6	3.31×10^6

In conclusion, it can be stated with good confidence that the axial symmetric anisotropy approximation is sufficient to describe the relaxation data. This is a strong argument in favour of the formation of cylindrical shaped supramolecular structures.

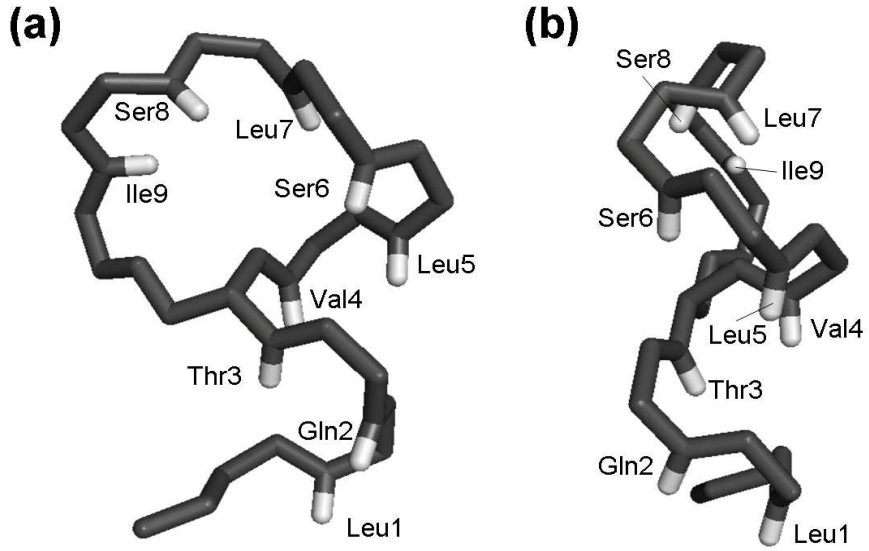

Figure 7.18: The solution structure of pseudodesmin A with only the main chain in black and the H^N nuclei in white, thereby emphasising the NH bond vectors. (a) Side view from the helix, N→C bottom to top, with the loop structure positioned to the left of the helix; (b) different side view from the helix, N→C bottom to top, with the loop structure positioned behind the helix.

7.3.5 Discussion of the ^{15}N relaxation rate constants

Just as with the ^{13}C relaxation data, the ^{15}N relaxation rate constants are very different in chloroform when compared to acetonitrile. Both the R_1 and R_2 relaxation rate constants (Table 7.9) have increased quite a bit, in agreement with a strong increase in correlation time constant. In principle, the ^{15}N relaxation data can be subjected to a similar anisotropy analysis as was performed on the ^{13}C relaxation data. However, when considering the solution structure, it is clear that the nine NH bonds are not as disperse in their orientation as the CH bonds (Figure 7.18). This results in a very limited sampling of the anisotropy. This is mainly due to the fact that a helix structure will inherently place all NH bonds along the helix direction, while in addition the NH bonds of Leu7 and Ser8 are also quite parallel to the helix. The only real exception is the Ile9 NH bond, which is positioned perpendicular to the helix structure. This is indeed reflected in the R_1/R_2 values (Figure 7.5) which show limited variation from Leu1 up to Ser8, but is significantly higher for Ile9. Given the orientation found for the main axis of the rotational diffusion tensor frame using the ^{13}C relaxation data, the θ angles can be calculated for the NH bonds as well. These are given in Table 7.15. The $D_r^{\parallel}$ and $D_r^{\perp}$ rotational diffusion coefficients can be fitted against these ^{15}N R_1/R_2 values, resulting in respectively 10.17×10^7 s^{-1} and 6.10×10^7 s^{-1}. The theoretical R_1/R_2 curve as a function of θ can then be calculated and is plotted in Figure 7.19a. The experimental data points are plotted as well. As expected, the Leu1 until Ser8 ^{15}N nuclei are all concentrated around the same region, while Ile9 is both an outlier in θ and R_1/R_2. Although the trend of the theoretical R_1/R_2 curve and the data points are in good agreement, the deviations from the curve are

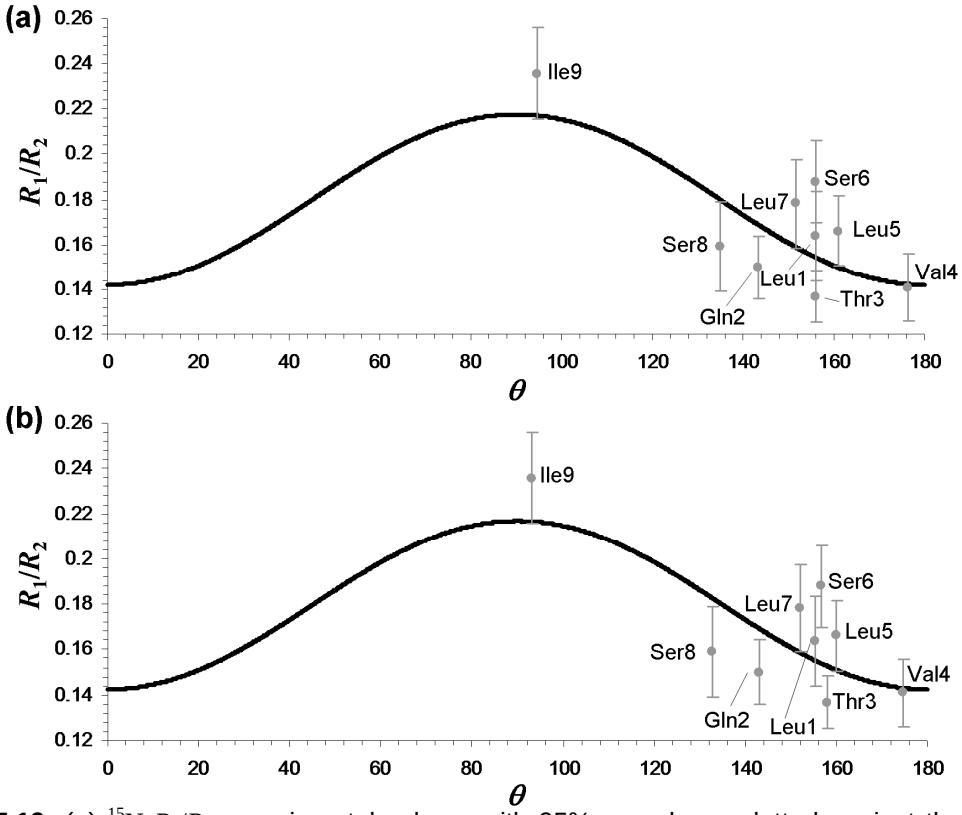

Figure 7.19: (a) ^{15}N R_1/R_2 experimental values, with 95% error bars, plotted against the angle θ between the NH bond vector and the main axis of the rotational diffusion tensor as obtained from the $^{13}C^{\alpha}$ relaxation data, and the theoretical R_1/R_2 curve based on the fitted rotational diffusion coefficients. (b) Same as in (a), but a grid search and rotational diffusion coefficient fitting based on the ^{15}N relaxation data was performed.

more extensive than in the case of the ^{13}C data. To check whether this is indeed the ideal orientation of the main axis of the rotational diffusion tensor for the ^{15}N data, a grid search was performed in a similar way as in section 7.3.3.2. The solution structure and the main tensor axis were put in a reference frame where the latter was along the z-axis. The grid search again rotated the main tensor axis so to sample all possible orientation using equation (7.9), with α varying from 0° to 179.75° in steps of 0.25° and β varying from –180° to 179.5° in steps of 0.5°. The minimum SS value was found at 2.00° and 48.5° for α and β respectively, which shows that the optimum orientation is practically the same as the one found for the ^{13}C data. The rotational diffusion coefficients were fitted to the newly calculated θ angles (Table 7.15), resulting in 10.10×10^7 s^{-1} and 6.11×10^7 s^{-1} for $D_r^{\parallel}$ and $D_r^{\perp}$ respectively. The new theoretical curve and data points are shown in Figure 7.19b, indeed showing barely any difference compared to the previous curve in Figure 7.19a. Note that the ^{15}N data were recorded at a higher temperature (25℃) and different concentration than the ^{13}C relaxation data, so that the rotational diffusion coefficients cannot be compared with previous results. In conclusion, the ^{15}N relaxation data, though itself not providing a very good dataset to perform the anisotropy analysis, is in agreement with the orientation of the rotational diffusion tensor found by the analysis of the ^{13}C relaxation data.

Table 7.15: θ angles and spectral density weighting coefficients of the NH bonds

	Leu1	Gln2	Thr3	Val4	Leu5	Ser6	Leu7	Ser8	Ile9
$\theta_{initial}$ [°] [a]	156.1°	143.3°	156.1°	176.3°	160.9°	155.9°	151.6°	13 4.9°	94.6°
c_A [a]	0.57	0.22	0.57	0.99	0.70	0.56	0.44	0.06	0.24
c_B [a]	0.41	0.69	0.41	0.01	0.29	0.42	0.52	0.75	0.02
c_C [a]	0.02	0.10	0.02	0.00	0.01	0.02	0.04	0.19	0.74
θ_{grid} [b]	155.5°	143.1°	158.1°	174.8°	160.2°	156.6°	152.1°	1 32.9°	93.3°

[a] θ angles calculated using the orientation of the rotational diffusion tensor main axis obtained from all $^{13}C^{\alpha}$ data

[b] θ angles calculated after the grid search on the ^{15}N R_1/R_2 data

7.3.6 Discussion of the methyl relaxation rate constants

The relaxation rate constants of the methyl ^{13}C nuclei of pseudodesmin A in chloroform were also measured at 25°C. The treatment of methyl ^{13}C relaxation is somewhat different from that of $^{13}C^{\alpha}$ relaxation, as for example the rotation around the methyl local threefold symmetry axis should be taken into account[2, 3]. A quantitative analysis of the methyl relaxation will not be performed here. Only one relevant qualitative conclusion can be made. The HDA methyl group has very low R_1 and R_2 rate constants compared to all other methyl groups (Figure 7.6). This indicates a strong contribution of internal motion at the end of the HDA chain. This is in agreement with the idea that the long hydrophobic alkyl chain protrudes from the supramolecular structure into the solvent. The hypothesised model also suggests that the hydrophobic side chains (and thus the methyl groups) of all residues stick out into the solvent as well. The long alkyl chain however has many more degrees of freedom for reorientation. This corresponds to a very low order parameter in terms of the Lipari-Szabo theory, thus making the impact of the fast internal motion correlation time constant much more significant when compared to the global rotational correlation time constants in the spectral density functions.

This observation is important as it is a good argument for stating that the alkyl chain is not anchored into a fixed orientation in the self-assembly.

7.4 Discussion and reflection on the proposed model of the supramolecular structure

In this study, the heteronuclear relaxation properties of both the monomer form in acetonitrile and the supramolecular form in chloroform have been studied. The relaxation rate constants in acetonitrile solution correspond to those of a small molecule in a low viscous solvent and allow to estimate the correlation time constant. In chloroform solution, the relaxation properties changed dramatically, now being in agreement with a large supramolecular structure, and were observed to be

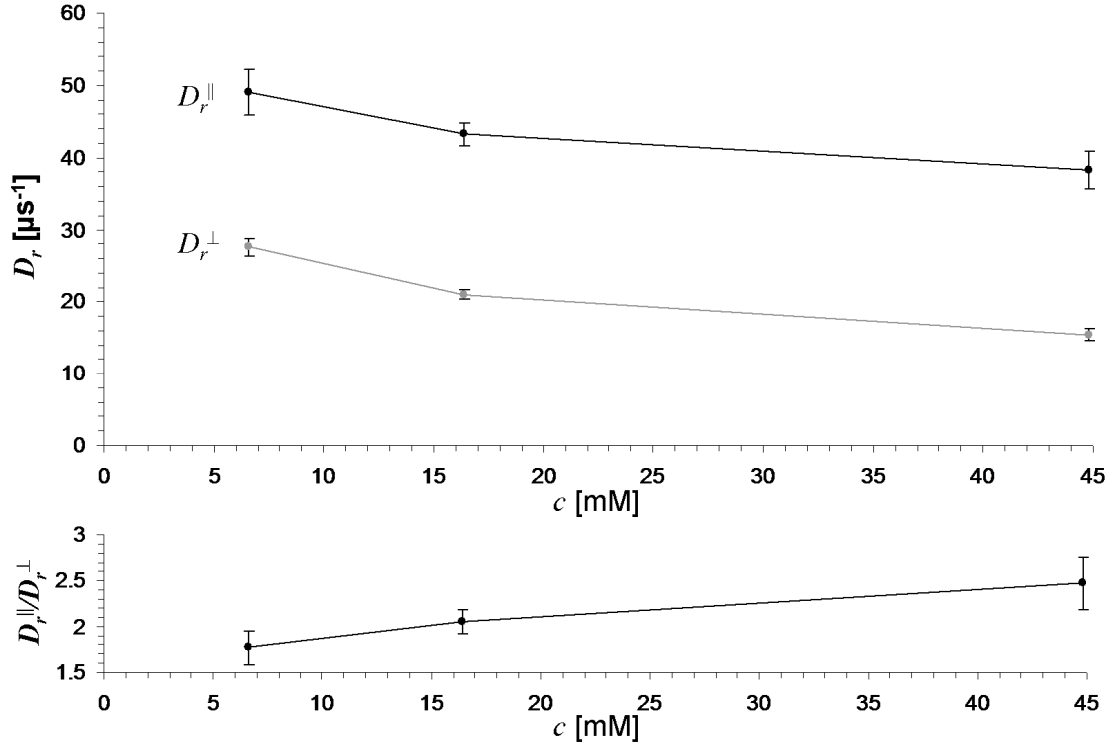

Figure 7.20: Rotational diffusion coefficients $D_r^{\parallel}$ and $D_r^{\perp}$ and their ratio as a function of concentration as obtained from the 16.4 T datasets, with 95% confidence intervals.

concentration dependent. It was found that the $^{13}C^{\alpha}$ and ^{15}N R_1/R_2 values could be convincingly correlated with the orientation of respectively the CH and NH bonds in the solution structure, proving the supramolecular structures to be anisotropic. Using $^{13}C^{\alpha}$ relaxation, the direction of this anisotropy was self-consistent for three concentrations measured at 16.4 T and one concentration at 11.7 T. An axial symmetric rotational diffusion tensor was assumed, which proved to be sufficient to describe the relaxation data.

The rotational diffusion coefficients that were fitted for each concentration are plotted in Figure 7.20. As the concentration increases, both rotational diffusion coefficients decrease as is expected for an increase of the average size of the supramolecular structure. The anisotropy is reflected by the $D_r^{\parallel}/D_r^{\perp}$ ratio (section 1.4), which is plotted in Figure 7.20. The anisotropy increases significantly with the concentration. The two rotational diffusion coefficients can be converted into the dimensions of an ellipsoid or a cylinder. For an ellipsoid, equations (1.44) until (1.48) should be used, which describe the rotational diffusion coefficients as a function of the semiaxes a and b of the ellipsoid. Since $D_r^{\parallel}$ is larger than $D_r^{\perp}$, the prolate ellipsoid equations should be used. For a cylinder, equations (1.51) until (1.54) are required, together with (3.76). Since all these equations cannot be analytically inverted, the dimensions were obtained by minimising the square of the difference between the obtained rotational diffusion coefficients and the ones calculated theoretically using the equations. The results are provided in Table 7.16 and in Figure 7.21.

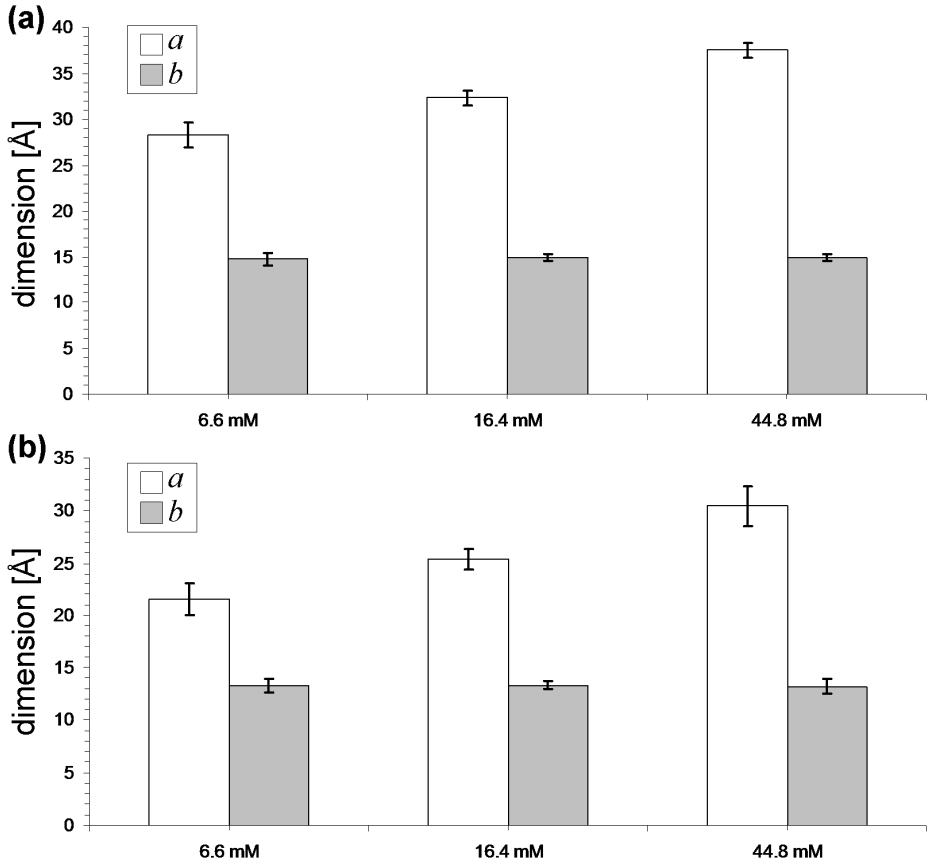

Figure 7.21: The semiaxes a and b, with 95% confidence intervals, obtained from the rotational diffusion coefficients from the datasets at 16.4 T and calculated using the (a) ellipsoid model and (b) cylinder model.

Table 7.16: Overview of the rotational diffusion coefficients and the corresponding ellipsoid and cylinder dimensions

	6.6 mM 16.4 T	16.4 mM 16.4 T	44.8 mM 16.4 T	16.4 mM 11.7 T
$D_r^{\parallel}$ [μs^{-1}]	49.00 ± 3.17	43.25 ± 1.57	38.26 ± 2.56	34.61 ± 3.31
$D_r^{\perp}$ [μs^{-1}]	27.67 ± 1.21	21.08 ± 0.58	15.50 ± 0.85	20.64 ± 1.25
$D_r^{\parallel}/D_r^{\perp}$ [a]	1.77 ± 0.19	2.05 ± 0.13	2.47 ± 0.28	1.68 ± 0.18
$cov(D_r^{\parallel} - D_r^{\perp})$ [μs^{-2}] [b]	-0.848	-0.194	-0.451	-0.856
$a_{ellipsoid}$ [Å] [a,c]	28.25 ± 1.35	32.31 ± 0.83	37.50 ± 0.83	30.59 ± 1.38
$b_{ellipsoid}$ [Å] [a,c]	14.78 ± 0.66	14.91 ± 0.37	14.93 ± 0.37	16.80 ± 0.70
$a_{cylinder}$ [Å] [a,c]	21.47 ± 1.53	25.36 ± 0.96	30.41 ± 1.87	22.96 ± 1.52
$b_{cylinder}$ [Å] [a,c]	13.27 ± 0.65	13.31 ± 0.37	13.22 ± 0.67	15.12 ± 0.69

[a] 95% error bar calculated by taking the standard deviation of each individual $D_r^{\parallel}/D_r^{\perp}$, a and b value calculated at each repetition during the Monte Carlo analysis (section 7.3.3.3). In the case of $D_r^{\parallel}/D_r^{\perp}$, it should be noted that the negative covariance between the $D_r^{\parallel}$ and $D_r^{\perp}$ values makes the error bar higher than what would be expected when assuming both parameters to be independent from each other.

[b] covariance between $D_r^{\parallel}$ and $D_r^{\perp}$

[c] A viscosity of 0.631 mPa·s for chloroform at 10℃ is assumed

The ellipsoid provides longer dimensions than the cylinder. This is not surprising, since an ellipsoid with the same dimensions as a cylinder has a lower surface area and volume when compared to the cylinder. It will therefore experience less friction with rotational motion and therefore have higher diffusion coefficients. The other way round, an ellipsoid with the same rotational diffusion coefficients as a cylinder will always have higher dimensions. It should be noted that based on the relaxation data, no statement can be made about which of the two objects approximate best the actual shape of the supramolecular structure. Given the hypothesised model, the cylinder shape would probably be the best choice. The diameter ($= 2\times b$) of the supramolecular structure of more than 26 Å remains constant with the concentration at 16.4 T and is about three times larger than the diameter of a single pseudodesmin A molecule (8-10 Å). The lengths ($= 2\times a$) vary between 40 Å and 60 Å, which correspond to respectively about 3 and 4.6 times the length of the solution structure measured from Leu1 H^N to the Leu7 carbonyl oxygen atom (13.0 Å).

The optimal direction of the reference vector $\mathbf{V}_2$' at the end of the second grid search corresponds to the main axis direction of the rotational diffusion tensor of the supramolecular structure relative to the individual pseudodesmin A molecule within the assembly. In other words, if the supramolecular structure is approximated to be shaped as a cylinder, the orientation of the individual molecules relative to its rotational axial symmetry axis can be obtained. This is displayed in Figure 7.22a, which shows the main chain of several monomer units that have been translated along this direction. The helix structure is not exactly parallel to the direction of growth, but makes an angle of about 25°. The free NH groups of Leu1 and Gln2 at the N-terminus of the helix are positioned near the free carbonyl groups of Ser6 and Leu7, suggesting that these are able to form hydrogen bond intermolecular contacts. This would be in agreement with the intermolecular contacts that were observed between the Leu1 H^N and Gln2 H^N protons and the Ser6, Leu7 and Ser8 H^α protons.

Although all molecules in the assembly should be making the same angle with the main axis, there still exists a degree of freedom in how they can be stacked upon each other. It is not excluded that each subsequent molecule has a slight rotation around the main axis when compared to the previous molecule, effectively creating a coiled arrangement. This means that in Figure 7.22 only one of the possible ways of stacking is represented. It is not feasible to make a judgement on this matter based on the most favourable arrangement for amide hydrogen bond formation between the molecules, since the structure is not accurately defined at its N-terminal end based on the data collected in acetonitrile solution. However, it can be excluded is that a rotation between subsequent molecules would be very large. This is illustrated by Figure 7.22b, where only the side chains are shown with a distinct colouring for the hydrophilic and hydrophobic chains. From the point of view of forming an ion-pore structure, the hydrophilic surfaces of successive molecules should border one

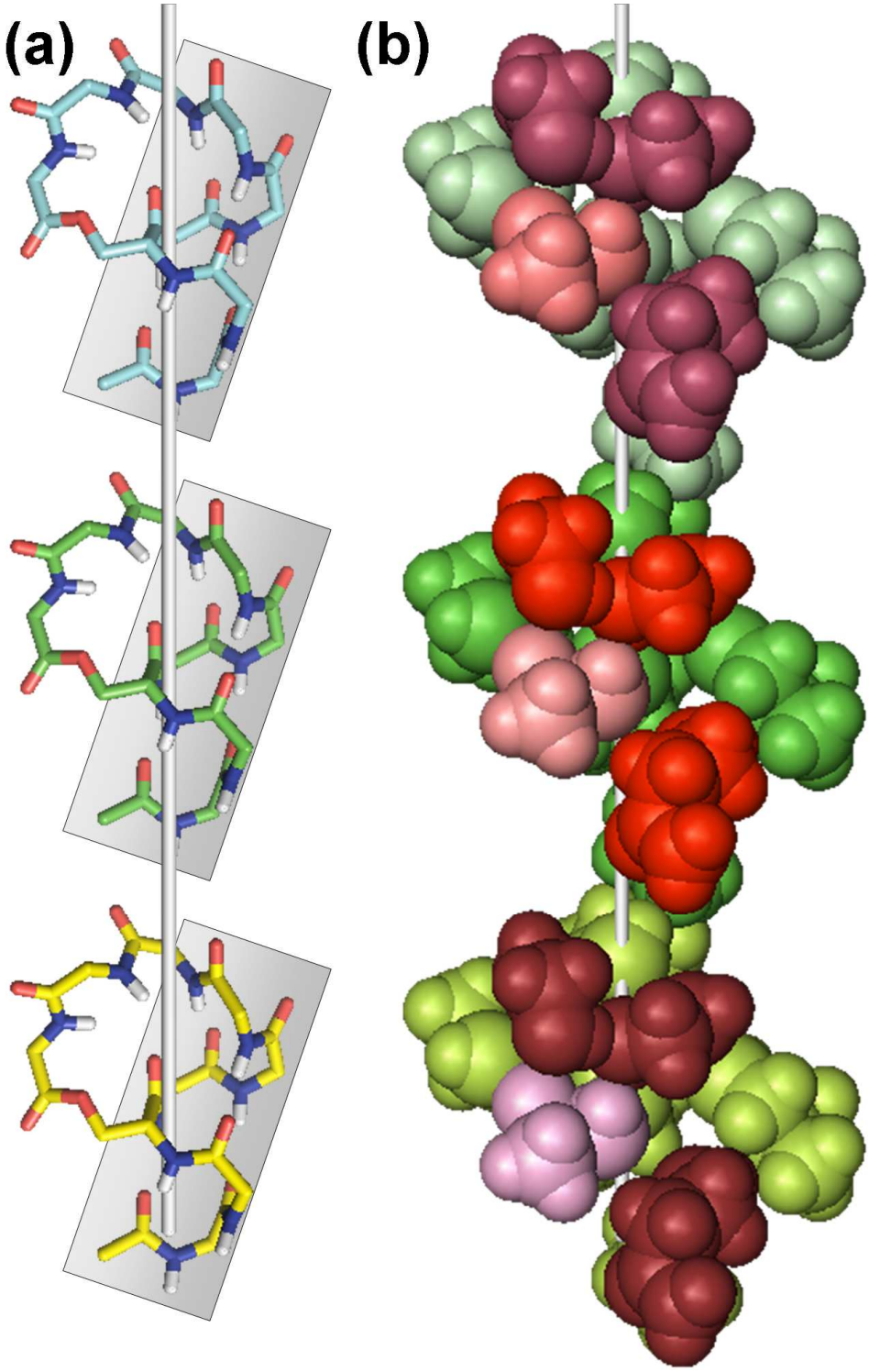

Figure 7.22: (a) Three copies of the solution structure translated by an arbitrary distance along the direction of the main axis of the rotational diffusion tensor, which is shown as a grey stick. Only the main chain of the structures is shown. The helix structure is accentuated by a rectangle. (b) Same as before, but with only the side chains shown as spheres. Hydrophobic side chains are shown in a green tint, the hydrophilic ones in a red tint and the Thr3 side chain in a pink tint.

another so as to be able to form a continuous hydrophilic tunnel. A coiled arrangement with a twist angle that is too large would interfere with this.

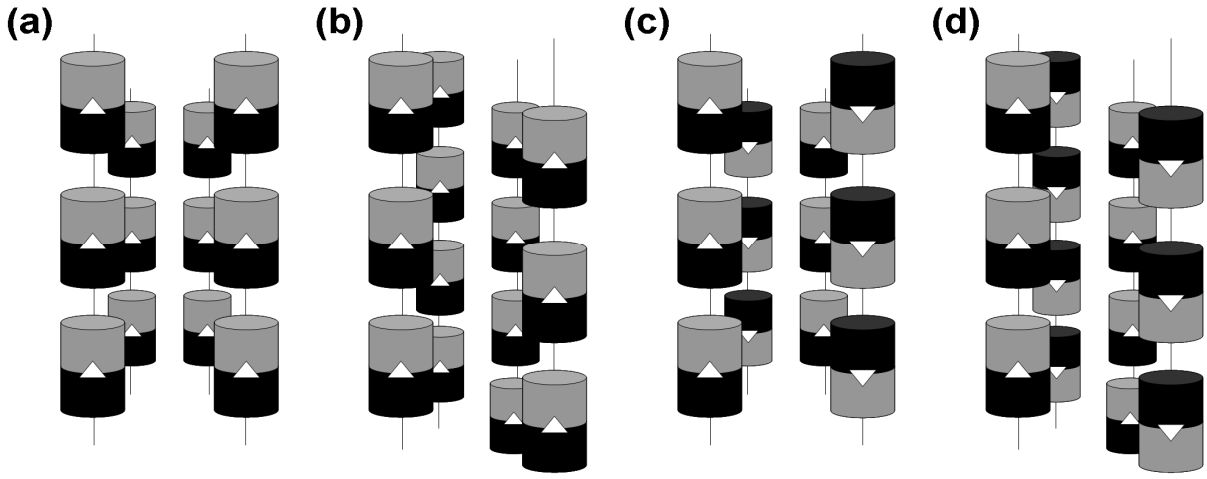

Figure 7.23: Multiple ways of stacking are possible. In this figure it is assumed that four strings are involved in the supramolecular assembly. (a) Each string points in the same direction (parallel) and the molecules in the string are positioned next to each other. (b) Each string points in the same direction (parallel), but the molecules possess a shift in their relative position between the strings. (c) The strings do not all point in the same direction (anti-parallel), but molecules in the string are positioned next to each other. (d) The strings do not all point in the same direction (anti-parallel) and the molecules possess a shift in their relative position between the strings

According to the proposed model, the strings of stacked molecules should be aligned with one another to form a cylindrical structure, with the hydrophilic sides packed to the inside. This is indeed confirmed from the estimated diameter of the supramolecular complex, which is of the order of several monomer molecules. The proposed model also suggests that the structures only grow in size along the direction of the end-to-end stacking. The fact that the estimated diameter of the complex appears to be independent of the concentration strongly supports this proposal. How exactly these strings of stacked structures are aligned, with or without a translation between the individual molecules, or in a parallel or anti-parallel arrangement (Figure 7.23), cannot be determined. An argument in favour for the alignment with a translation or in an anti-parallel fashion would be the intermolecular rOes observed between the Gln2 side chain NH_2 protons and the Ser side chains, as these chains can be positioned closely together in these spatial arrangements. However, an alternative explanation for these intermolecular contacts would be that the side chains from succeeding molecules within the string structure can be close to one another.

7.5 Conclusion

The analysis of the heteronuclear relaxation rate constants of pseudodesmin A have provided information concerning the shape (axial symmetry), the dimensions and the direction of growth of the supramolecular complexes. In addition, the orientation of the individual pseudodesmin A molecules within the complex is revealed, confirming that the complexes grow by a stacking mechanism mediated by interactions between

the free main chain NH groups and carbonyl groups. The success of the method used in this chapter owes to the spread of CH bond orientation within the fairly rigid pseudodesmin A monomer structure. This creates a sufficient spread in R_1/R_2 values measured over the molecule, providing a fitting with good confidence of the rotational diffusion coefficients.

It should be noted that the rotational diffusion coefficients and the dimensions that were obtained from relaxation rate constants are an average of the individual rate constants of the each oligomer size that is present in the self-association equilibrium. Though their values are very indicative of the degree of self-association and the way in which the distribution of sizes depends on the concentration, their absolute values should not be linked to a single supramolecular structure. In fact, the rotational diffusion coefficients obtained depend on whether the R_1, the R_2 or the R_1/R_2 ratio values were used in the anisotropic analysis (see chapter 8), although the direction of the main axis of the rotational diffusion tensor and the trend with concentration turns out to be constant. Even the magnetic field strength has an impact on the results. This is due to the fact that for the same distribution of oligomer sizes, the averaging of the R_1, R_2 and nOe values do not converge to values that would all suggest the same rotational diffusion coefficients, because of their different dependence on the correlation time constants and magnetic field strength through the spectral density functions. This will be explored in more detail in the final chapter.

7.6 References

[1] J. M. Wieruszeski, I. Landrieu, X. Hanoulle and G. Lippens, "ELISE NMR: Experimental liquid sealing of NMR samples". *Journal of Magnetic Resonance*, **2006**, *181*(2) 199-202.

[2] L. E. Kay, T. E. Bull, L. K. Nicholson, C. Griesinger, H. Schwalbe, A. Bax and D. A. Torchia, "The Measurement of Heteronuclear Transverse Relaxation-Times in AX_3 Spin Systems Via Polarization-Transfer Techniques". *Journal of Magnetic Resonance*, **1992**, *100*(3) 538-558.

[3] L. K. Nicholson, L. E. Kay, D. M. Baldisseri, J. Arango, P. E. Young, A. Bax and D. A. Torchia, "Dynamics of Methyl-Groups in Proteins as Studied by Proton-Detected ^{13}C NMR-Spectroscopy - Application to the Leucine Residues of Staphylococcal Nuclease". *Biochemistry*, **1992**, *31*(23) 5253-5263.

[4] M. Andrec, G. T. Montelione and R. M. Levy, "Lipari-Szabo mapping: A graphical approach to Lipari-Szabo analysis of NMR relaxation data using reduced spectral density mapping". *Journal of Biomolecular NMR*, **2000**, *18*(2) 83-100.

[5] R. A. Atkinson and B. Kieffer, "The role of protein motions in molecular recognition: insights from heteronuclear NMR relaxation measurements". *Progress in Nuclear Magnetic Resonance Spectroscopy*, **2004**, *44*(3-4) 141-187.

8

Relaxation rate constant behaviour under self-association conditions

8.1 The apparent disagreement between relaxation parameters

In Chapter 7, it was already noted that the rotational diffusion coefficients obtained from one concentration strongly depends on the particular relaxation parameter was used (R_1/R_2 ratio, R_1 or R_2 separately, different magnetic field strength). Thus, each relaxation parameter appears to suggest a different average size for the supramolecular complexes. In Figure 8.1, the theoretical $^{13}C^{\alpha}$ R_1 and $^{13}C^{\alpha}$ R_2 values for a rigid isotropic tumbling molecule with increasing correlation time constant are plotted against each other, taking both the dipole-dipole and $^{13}C^{\alpha}$ CSA relaxation mechanisms into account. The measured data points at each concentration are shown as well. The increasing variation in R_2 values with concentration can be interpreted as a consequence of the increasing anisotropy. Also, the data points are all clearly deviating from the theoretically expected R_1 vs. R_2 combinations, with an apparent too high R_1 value compared to R_2. This is observed at both 16.4 T and 11.7 T field strengths. Other deviations exist between the nOe and either the R_1 or the R_2 relaxation rate constants (Figures 8.2 and 8.3). The nOe is higher than the spin diffusion limit value that would have been expected given the R_1 and R_2 values. Finally, a discrepancy between the relaxation parameters at different field strengths is

observed as well (Figure 8.4). The R_1 values at 16.4 T are generally higher than what would have been expected from those at 11.7 T. The R_2 relaxation rate constants are practically field independent, as noted earlier in section 7.3.2. Between the nOe values, only a slight apparent discrepancy exists between the two field strengths, with the 16.4 T values being of the same magnitude as the 11.7 T values while the former should have been theoretically slightly lower than the latter. Of course, as noted before, the uncertainty of the nOe is quite significant (section 7.3.2), so the discrepancy between different field strengths might be an indirect consequence of this issue.

What is the origin of these apparent discrepancies? Exchange contributions to R_2 have been excluded earlier (section 7.3.4.1). The presence of fast internal motion on the other hand would (Figures 8.5 until 8.8) be able to explain the discrepancies seen for the nOes, but not those observed between R_1 and R_2, where increased internal motion contribution decreases both relaxation rate constants in the same way. Internal motion on a timescale higher than 100 ps, but lower than 1 ns, can theoretically provide an explanation for the R_1 vs. R_2 deviations (Figure 8.9). However, such an internal correlation time constant is physically unlikely, as this would be of the same order or larger than the correlation time constant of the pseudodesmin A monomer in chloroform conditions (0.25 ns, see section 7.2.2). What does become clear at this point is that the R_1 vs. R_2 deviations can only be explained by an 'averaging' of R_1 values near the top of the R_1 vs. R_2 curve and R_1 values further down the curve. Indeed, the Lipari-Szabo model can be regarded as an averaging of R_1 and R_2 values at a small correlation time constant (here τ_i) and large one (τ). When comparing Figures 8.5 and 8.9, it is clear that only when the small correlation time constant provides R_1 and R_2 values close enough to the maximum of the theoretical curve (here the $S^2 = 1$ curve), the averaged curve (here the $S^2 < 1$ curve) is able to cross the data points.

In what follows, it will be demonstrated that these deviations can be explained by the self-association process, where the apparent relaxation parameters are weighted averages of the values of the monomer and the supramolecular oligomers of each size present. Since each parameter varies differently with the correlation time constant, the weighted averages will each suggest a different apparent correlation time constant, resulting in the discrepancy. In section 8.2, this will be illustrated using a simple self-association model, qualitatively showing how all deviations observed in the experimental data can be explained. In section 8.3, these principles will be applied using indefinite self-association models after firstly discussing their theoretical basis. Finally, in section 8.4 an attempt will be made to find a model that quantitatively explains all the experimental data.

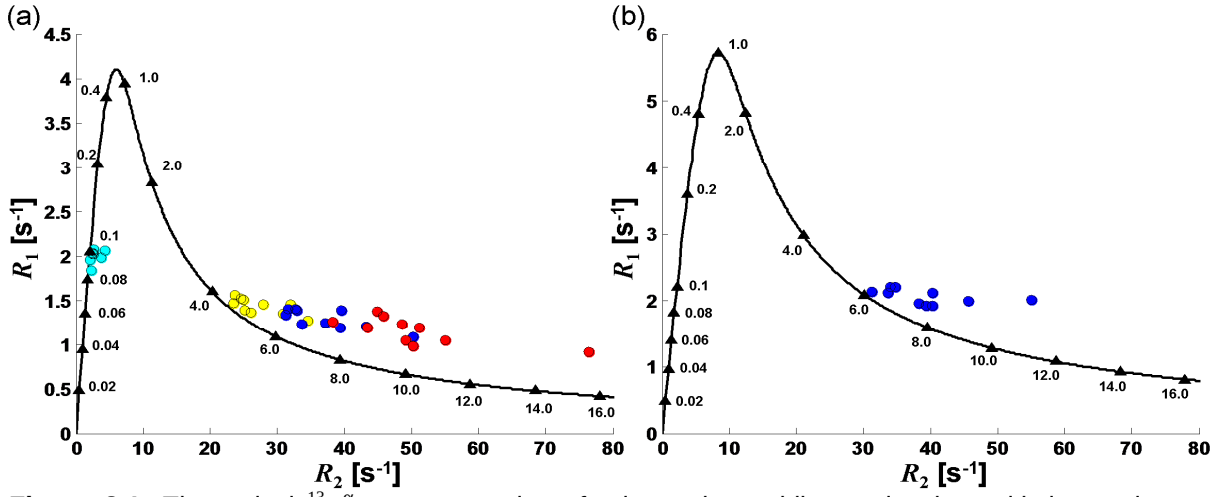

Figure 8.1: Theoretical $^{13}C^{\alpha}$ R_1 vs. R_2 values for isotropic tumbling molecules, with increasing τ (values in ns indicated on the curve), compared to the experimental relaxation data (6.6 mM yellow, 16.4 mM blue, 44.8 mM red and acetonitrile data cyan), at 16.4 T (a) and 11.7 T (b).

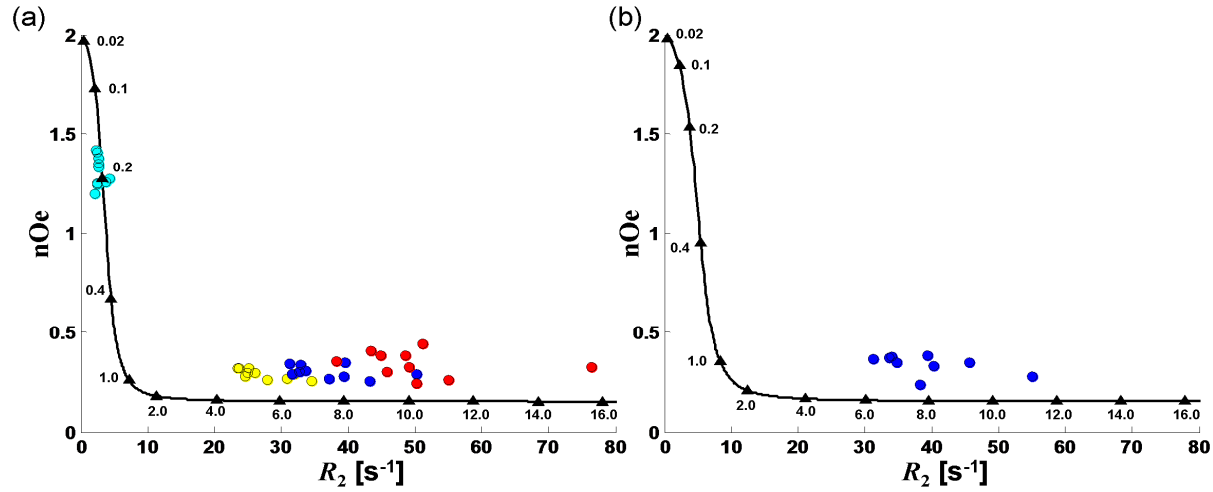

Figure 8.2: Theoretical $^{13}C^{\alpha}$ nOe vs. R_2 values for isotropic tumbling molecules, with increasing τ (values in ns indicated on the curve), compared to the experimental relaxation data (6.6 mM yellow, 16.4 mM blue, 44.8 mM red and acetonitrile data cyan), at 16.4 T (a) and 11.7 T (b).

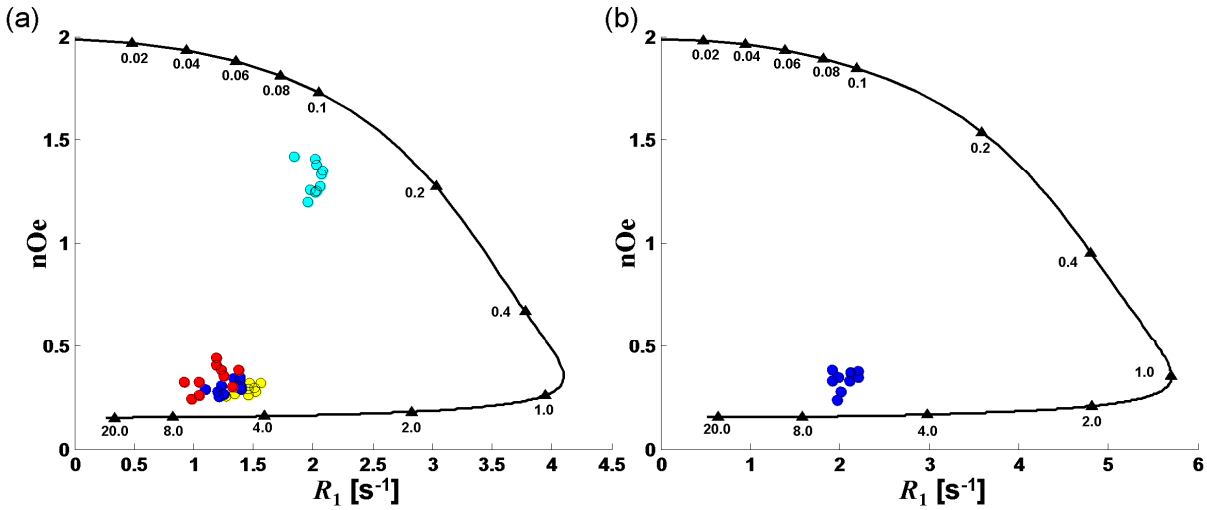

Figure 8.3: Theoretical $^{13}C^{\alpha}$ nOe vs. R_1 values for isotropic tumbling molecules, with increasing τ (values in ns indicated on the curve), compared to the experimental relaxation data (6.6 mM yellow, 16.4 mM blue, 44.8 mM red and acetonitrile data cyan), at 16.4 T (a) and 11.7 T (b).

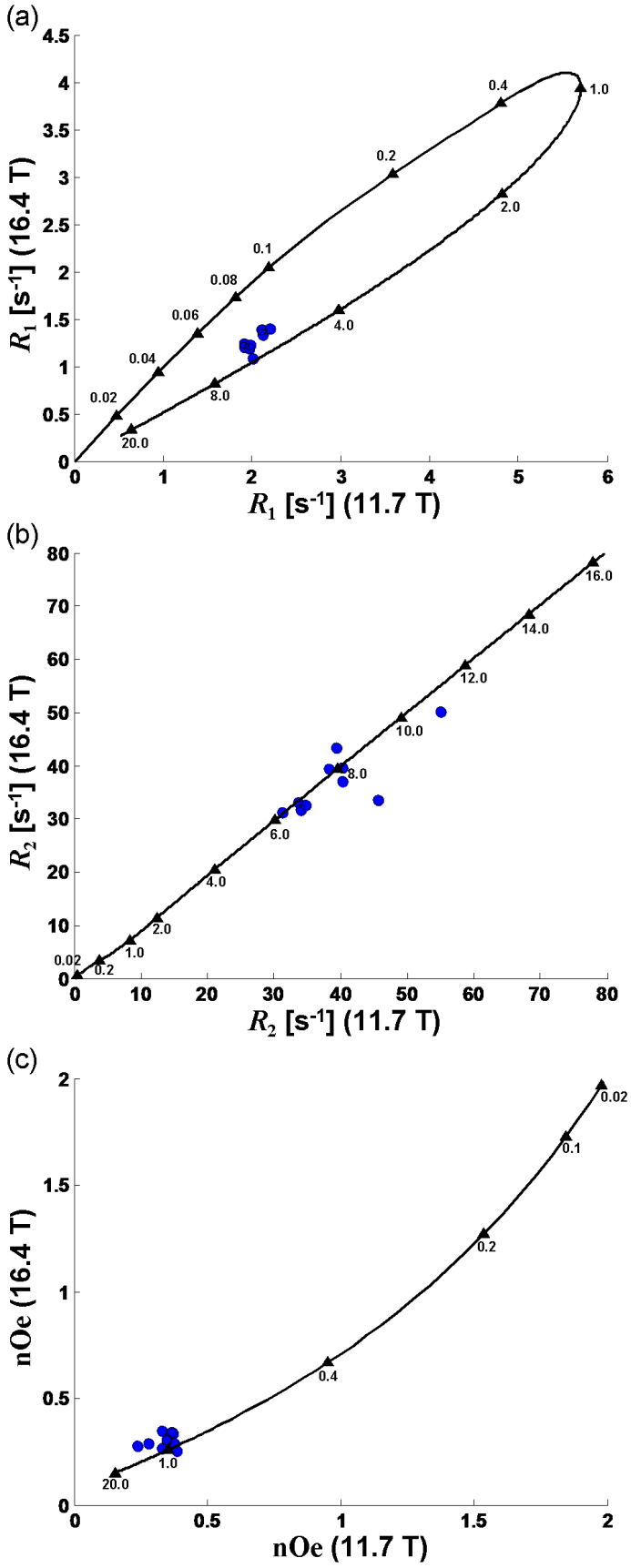

Figure 8.4: Theoretical $^{13}C^{\alpha}$ relaxation rate constants at 16.4 T vs. the same parameter at 11.7 T for isotropic tumbling molecules, with increasing τ (values in ns indicated on the curve), compared to the experimental relaxation data (16.4 mM; blue). (a) R_1; (b) R_2; (c) nOe.

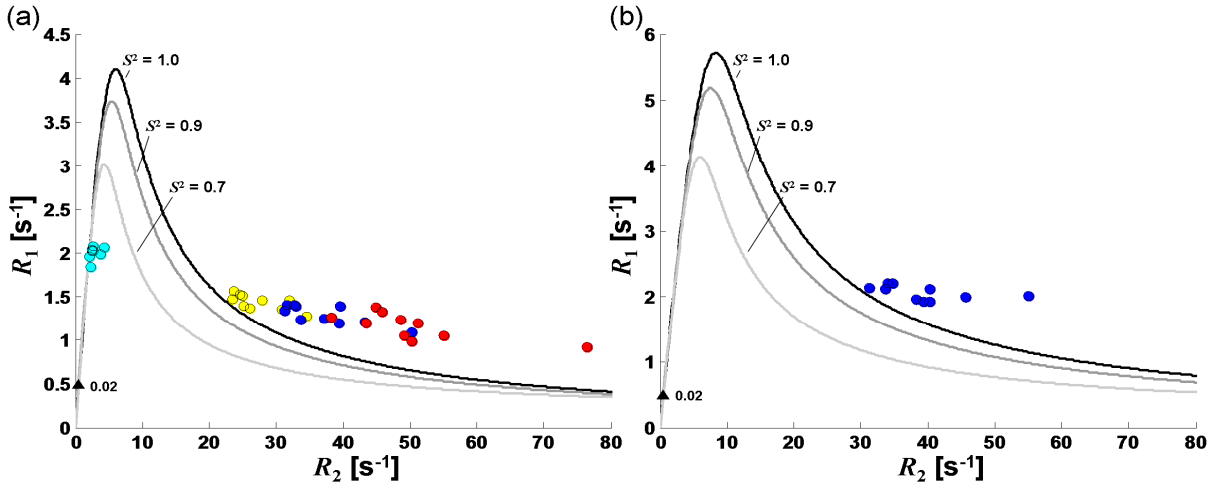

Figure 8.5: Same as in Figure 8.1, with theoretical curves now calculated from a Lipari-Szabo type spectral density function with internal correlation time constant of 0.02 ns and squared order parameter of 1.0, 0.9 and 0.7. (a) 16.4 T and (b) 11.7 T.

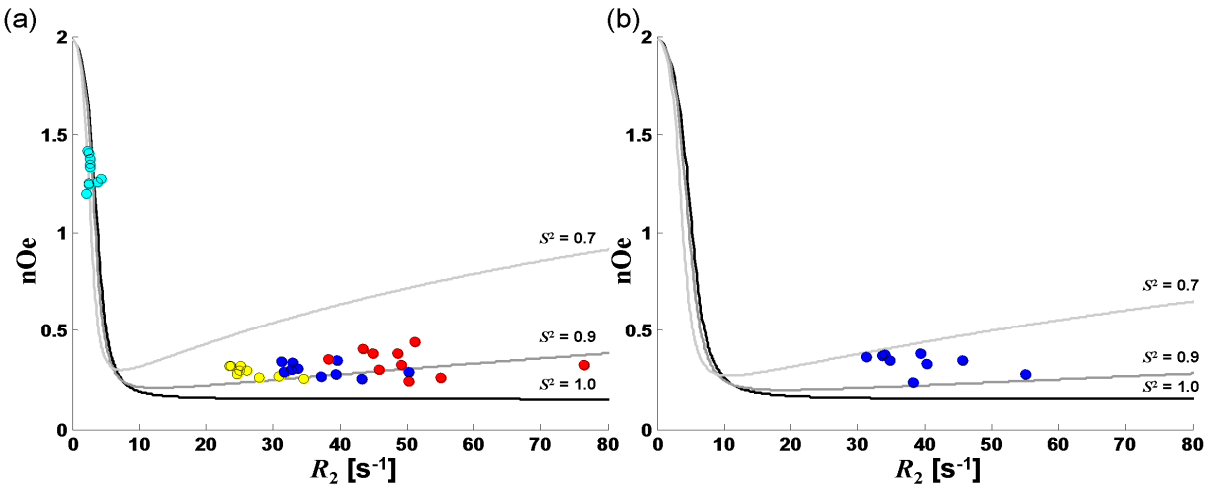

Figure 8.6: Same as in Figure 8.2, with theoretical curves now calculated from a Lipari-Szabo type spectral density function with internal correlation time constant of 0.02 ns and squared order parameter of 1.0, 0.9 and 0.7. (a) 16.4 T and (b) 11.7 T.

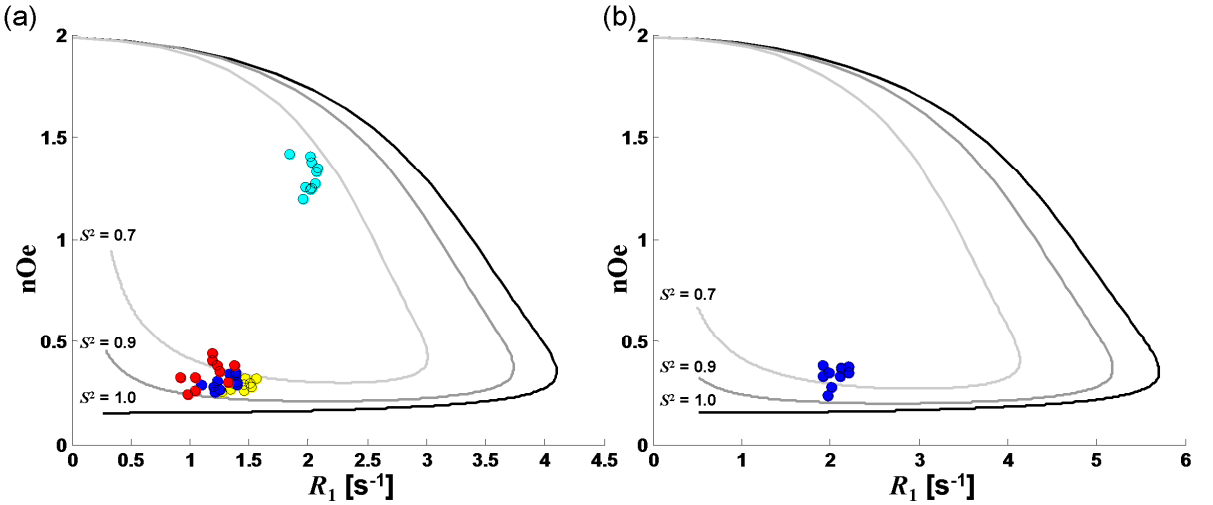

Figure 8.7: Same as in Figure 8.3, with theoretical curves now calculated from a Lipari-Szabo type spectral density function with internal correlation time constant of 0.02 ns and squared order parameter of 1.0, 0.9 and 0.7. (a) 16.4 T and (b) 11.7 T.

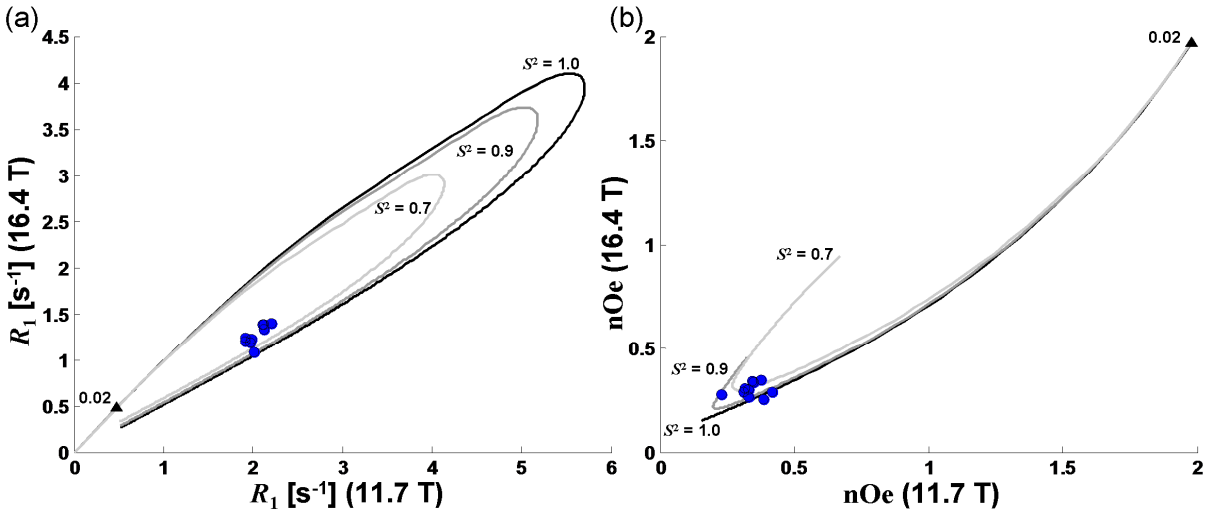

Figure 8.8: Same as in Figure 8.4, with theoretical curves now calculated from a Lipari-Szabo type spectral density function with internal correlation time constant of 0.02 ns and squared order parameter of 1.0, 0.9 and 0.7. (a) R_1; (b) nOe.

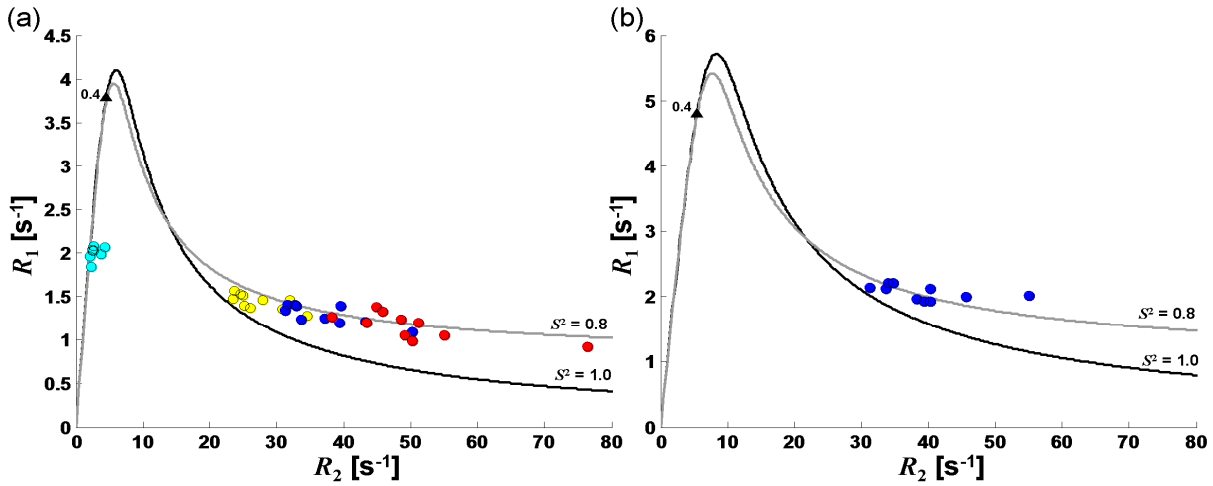

Figure 8.9: Same as in Figure 8.1, with theoretical curves now calculated from a Lipari-Szabo type spectral density function with internal correlation time constant of 0.4 ns and squared order parameter of 1.0 and 0.8. (a) 16.4 T and (b) 11.7 T.

8.2 Averaging of the relaxation parameters

A simple two state model will be considered to illustrate how self-association can affect the apparent relaxation parameters. A "monomer" state with a correlation time constant of τ_{mono} = 0.26 ns is assumed to be in fast exchange equilibrium with a "multimer" state with τ_{multi} = 10 ns. When the fraction of the monomer is α – varying between 1 (100% monomer) and 0 (100% multimer) – the average correlation time constant $\langle\tau\rangle$ is defined as:

$$\langle\tau\rangle = \alpha\tau_{mono} + (1-\alpha)\tau_{mono} \tag{8.1}$$

The average values of each relaxation parameter are similarly defined as:

$$\begin{aligned}\langle R_1\rangle &= \alpha R_1\left[\tau_{mono}\right] + (1-\alpha)\, R_1\left[\tau_{multi}\right] \\ \langle R_2\rangle &= \alpha R_2\left[\tau_{mono}\right] + (1-\alpha)\, R_2\left[\tau_{multi}\right] \\ \langle \mathrm{nOe}\rangle &= \alpha\,\mathrm{nOe}\left[\tau_{mono}\right] + (1-\alpha)\,\mathrm{nOe}\left[\tau_{multi}\right]\end{aligned} \tag{8.2}$$

The resulting combinations of $\langle R_1\rangle$, $\langle R_2\rangle$ and $\langle \mathrm{nOe}\rangle$ for each value of α are plotted in Figures 8.10 until 8.12. The average values sample new possible combinations that are able to qualitatively explain the behaviour of the experimental data points. For instance, the $\langle R_1\rangle$ values are higher than the theoretical R_1 values when comparing them at the same position on the R_2 axis. Similar conclusions can be made for the discrepancies of R_1 and the nOe at different field strengths (Figures 8.13).

To illustrate further the consequences of the averaging, an apparent average correlation time constant for both R_2 and R_1/R_2, $\langle\tau\rangle_{app,R2}$ and $\langle\tau\rangle_{app,R1/R2}$, is defined as the correlation time constant fitted from the individual $\langle R_2\rangle$ or $\langle R_1\rangle/\langle R_2\rangle$ values as if they were coming from a single isotropic molecule in solution. The reason why $\langle R_1\rangle/\langle R_2\rangle$ is chosen for this purpose rather than $\langle R_1\rangle$ is that there are always two theoretically possible correlation time constants that can be associated with the a single R_1 value. In Figure 8.14a, $\langle\tau\rangle_{app,R2}$ and $\langle\tau\rangle_{app,R1/R2}$ are plotted as a function of α together with the average correlation time constant $\langle\tau\rangle$. It is clear that when $0<\alpha<1$, the three different correlation time constants are not equal, with $\langle\tau\rangle_{app,R2}$ deviating slightly from $\langle\tau\rangle$ and $\langle\tau\rangle_{app,R1/R2}$ deviating quite strongly. It is thus clear that the result for the apparent correlation time constant depends on the choice of the parameter (R_2 or R_1/R_2) when calculating this from experimental values of self-associating system.

The reason for the different behaviour of the average relaxation parameters can be found in their different dependence on the correlation time constant. This is again illustrated for R_2 and R_1/R_2. For simplicity assume that both the monomer and multimer states are in the spin diffusion limit. As shown before in section 3.6.2, the relaxation rate constants are in this case proportional to:

$$\begin{aligned} R_1 &\propto 1/\tau \\ R_2 &\propto \tau \\ \Rightarrow R_1/R_2 &\propto 1/\tau^2 \end{aligned} \tag{8.3}$$

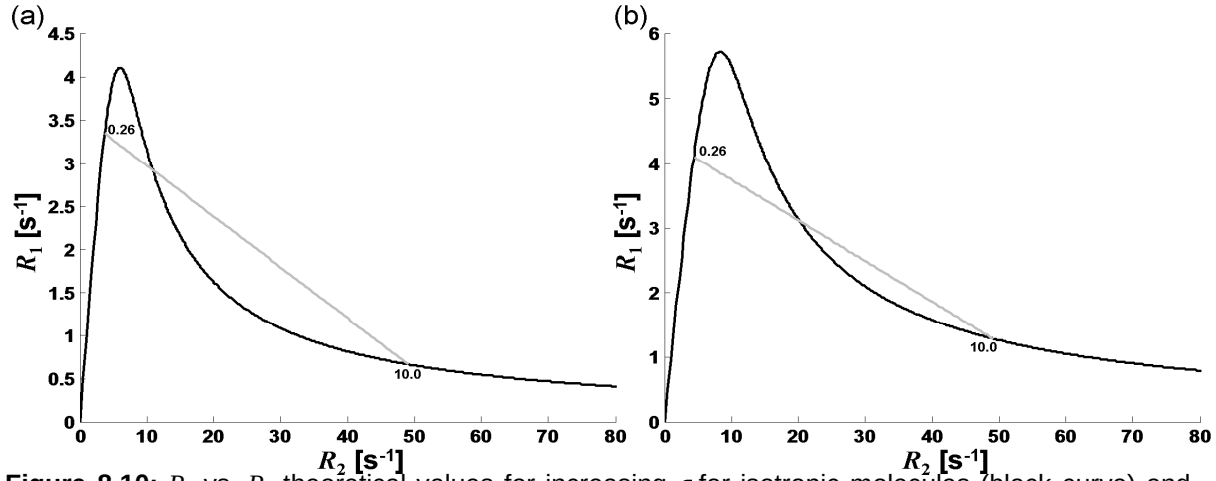

Figure 8.10: R_1 vs. R_2 theoretical values for increasing τ for isotropic molecules (black curve) and $\langle R_1 \rangle$ and $\langle R_2 \rangle$ values for increasing values of α (grey curve) using a simple two state model between monomer and multimer forms with respective correlation time constants of 0.26 ns and 10 ns (see equation (8.2)), at 16.4 T (a) and 11.7 T.

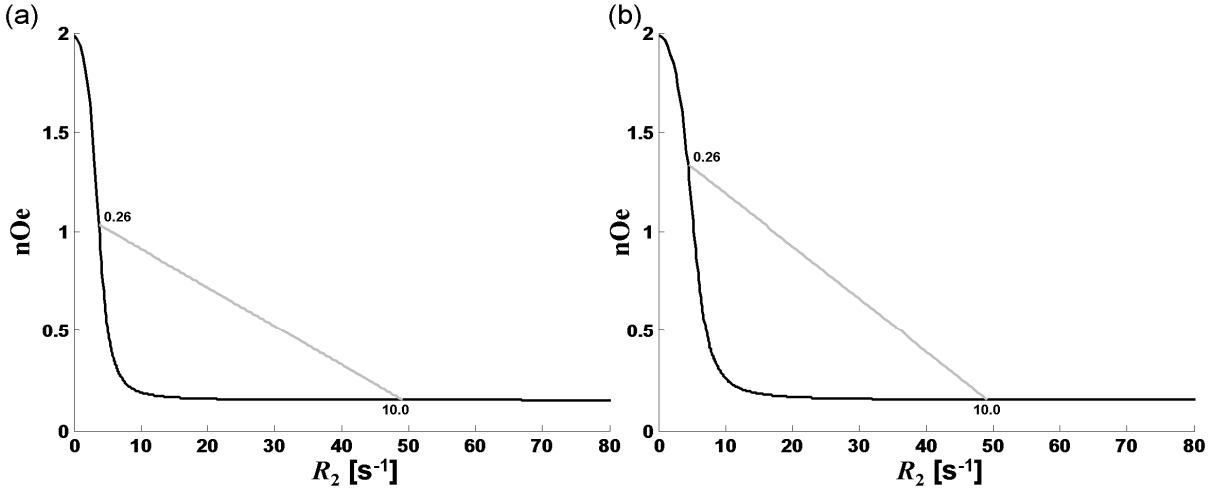

Figure 8.11: nOe vs. R_2 theoretical values for increasing τ for isotropic molecules (black curve) and $\langle$nOe$\rangle$ and $\langle R_2 \rangle$ values for increasing values of α (grey curve) using a simple two state model between monomer and multimer forms with respective correlation time constants of 0.26 ns and 10 ns (see equation (8.2)), at 16.4 T (a) and 11.7 T.

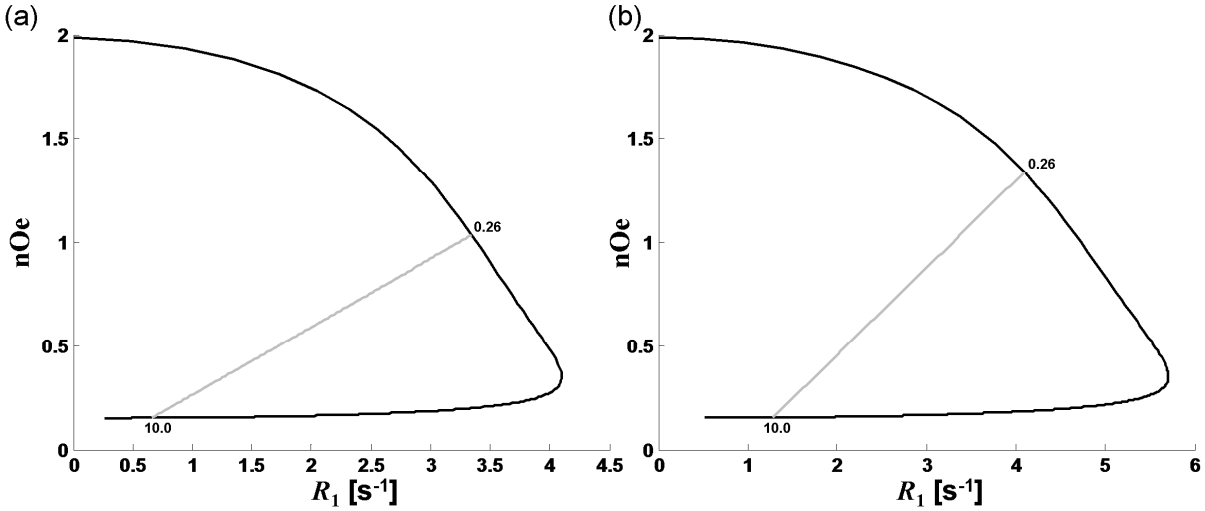

Figure 8.12: nOe vs. R_1 theoretical values for increasing τ for isotropic molecules (black curve) and $\langle$nOe$\rangle$ and $\langle R_1 \rangle$ values for increasing values of α (grey curve) using a simple two state model between monomer and multimer forms with respective correlation time constants of 0.26 ns and 10 ns (see equation (8.2)), at 16.4 T (a) and 11.7 T.

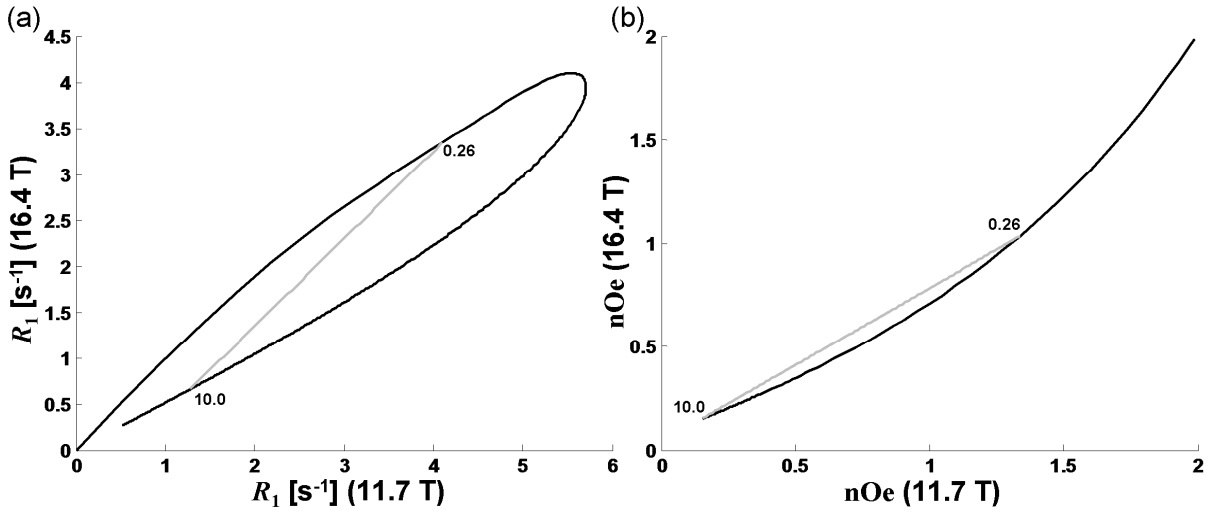

Figure 8.13: Relaxation parameters at 16.4 T vs. the same parameter 11.7 T, for increasing τ for isotropic molecules (black curve) and the average relaxation parameter for increasing values of α (grey curve) using a simple two state model between monomer and multimer forms with respective correlation time constants of 0.26 ns and 10 ns (see equation (8.2)). (a) R_1; (b) nOe.

The average relaxation rate constants will therefore be proportional to:

$$\begin{aligned} \langle R_1 \rangle &\propto \langle 1/\tau \rangle \\ \langle R_2 \rangle &\propto \langle \tau \rangle \\ \Rightarrow \langle R_1 \rangle / \langle R_2 \rangle &\propto \langle 1/\tau \rangle / \langle \tau \rangle \end{aligned} \tag{8.4}$$

with $\langle 1/\tau \rangle$ the average of the inverse of the correlation time constant; this is not the same as the inverse of its average. The calculation of the apparent correlation time constants assume the relations in (8.3) to hold however, so that:

$$\begin{aligned} \langle \tau \rangle_{app,R2} &\propto \langle R_2 \rangle \propto \langle \tau \rangle \\ \langle \tau \rangle_{app,R1/R2} &\propto \sqrt{\langle R_2 \rangle / \langle R_1 \rangle} \propto \sqrt{\langle \tau \rangle / \langle 1/\tau \rangle} \end{aligned} \tag{8.5}$$

Since $\langle \tau \rangle \neq \langle 1/\tau \rangle$, it can be concluded that the two apparent correlation time constants will not be equal to each other. The small discrepancy that can be seen between $\langle \tau \rangle$ and $\langle \tau \rangle_{app,R2}$ in Figure 8.14a, despite the above conclusion that both should be proportional to each other, is due to the fact that the monomer in this simulation is not in the spin diffusion limit as assumed in the above reasoning.

A similar reasoning applies for the magnetic field strength discrepancies in R_1 values. In this case, it is assumed that the exchange averaging encompasses multiple states (not necessarily all in the spin diffusion limit). The $\langle R_1 \rangle$ is then proportional to:

$$\langle R_1 \rangle \propto \left\langle \sum_k d_k \frac{\tau}{1+\left(B_0 \gamma_k \tau\right)^2} \right\rangle = \sum_i \alpha_i \sum_k d_k \frac{\tau_i}{1+\left(B_0 \gamma_k \tau_i\right)^2} \tag{8.6}$$

with the summation over k representing the sampling at different frequencies of the spectral density (see section 3.6.2), d_k representing spectral density weighting coefficients, γ_k being linear combinations of gyromagnetic ratios, and α_i and τ_i the fraction and the correlation time constant of state i. If all states above a certain index s are in the spin diffusion limit ($B_0\gamma_k\tau_i >> 1$), (8.6) can be rewritten as:

$$\langle R_1 \rangle \propto \left\{ \sum_{i \le s} \alpha_i \sum_k d_k \frac{\tau_i}{1+\left(B_0\gamma_k\tau_i\right)^2} \right\} + \left\{ \frac{\left(\sum_k \frac{d_k}{\gamma_k^2} \right)}{B_0^2} \sum_{i>s} \frac{\alpha_i}{\tau_i} \right\} \qquad (8.7)$$

From the above, it can be understood that the relative weight that each fraction α_i contributes to R_1 is independent of the magnetic field strength for states in the spin diffusion limit (B_0 can be placed outside the summation over i). For the states not in the spin diffusion limit however, the magnetic field strength does influence the relative weight each fraction contributes. Therefore, when the averaging of the R_1 relaxation rate constant involves small molecular size states, the relative degree with which each of these contribute to $\langle R_1 \rangle$ is field dependent, and therefore the apparent correlation time constant suggested by $\langle R_1 \rangle$ necessarily depends on the magnetic field strength. Similar reasoning applies for $\langle R_1 \rangle / \langle R_2 \rangle$. This is illustrated in Figure 8.14b for the simple two-state equilibrium model from above, where $\langle \tau \rangle_{app,R1/R2}$ values originating from $\langle R_1 \rangle / \langle R_2 \rangle$ values at two field strengths are compared with each other.

Figure 8.14c shows the apparent correlation time constant from the ^{1}H-^{13}C $\langle$nOe$\rangle$, $\langle \tau \rangle_{app,\mathrm{nOe}}$ at two field strengths together with $\langle \tau \rangle$. The $\langle \tau \rangle_{app,\mathrm{nOe}}$ stays closer to the monomer value even for low values of α. Only when the monomer is less than 10% present, the value starts to approach the multimer form. This behaviour is due to the nOe reaching a plateau value for a certain correlation time constant (section 3.6.2; *ca.* 2 ns for ^{13}C at 16.4 T), causing any deviation from this plateau value to immediately suggest a low correlation time constant. The nOe is thus very sensitive to the presence of small molecular size species in the averaging and will typically suggest an apparent correlation time constant that is very different from $\langle \tau \rangle$. The field strength has only a limited influence on $\langle \tau \rangle_{app,\mathrm{nOe}}$, since the nOe is only field dependent for the small molecular size species.

Now that the effects of self-association on the experimental relaxation rate constants and its consequences have been illustrated, the effects of an indefinite self-association situation, which is more realistic in the case of pseudodesmin A, can be investigated.

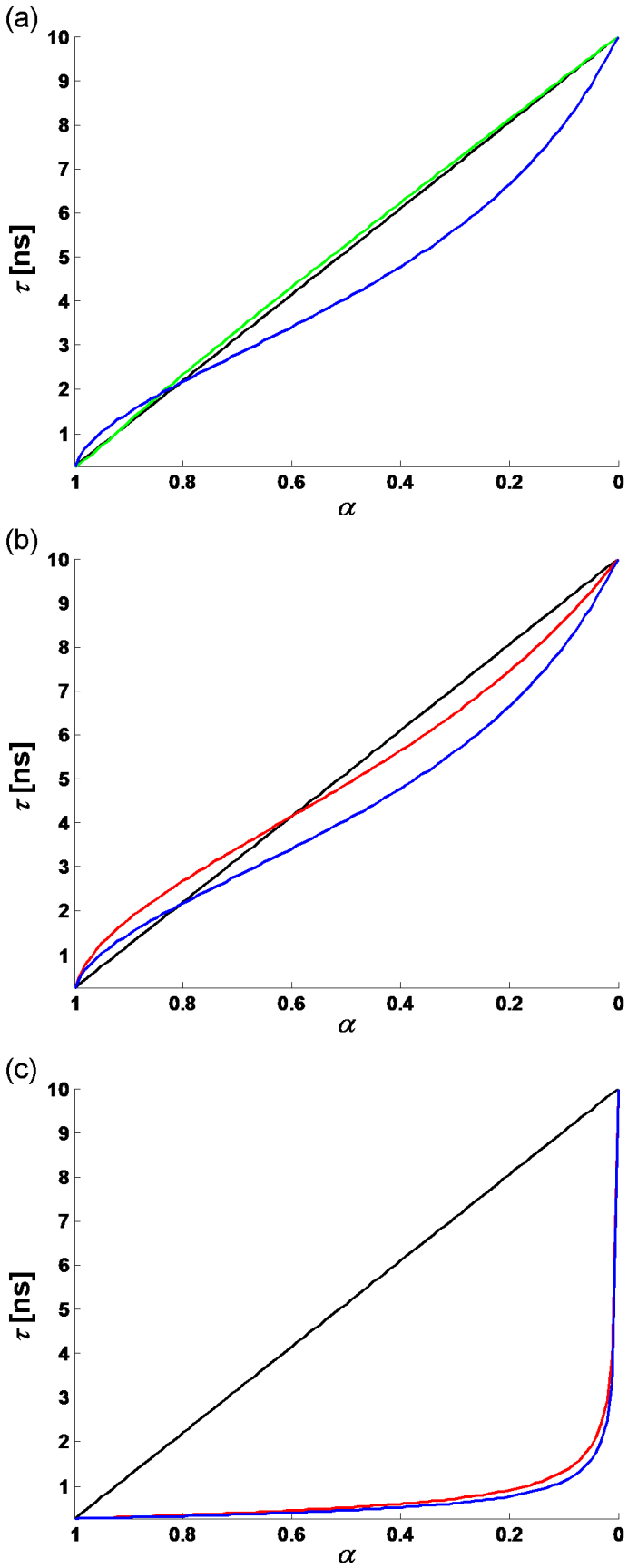

Figure 8.14: Fitted correlation time constant based on an averaged relaxation parameter vs. the monomer fraction α. In each plot, the black curve represents the average correlation time constant $\langle\tau\rangle$. (a) $\langle\tau\rangle_{app,R2}$ (green) and $\langle\tau\rangle_{app,R1/R2}$ (blue) at 16.4 T. (b) $\langle\tau\rangle_{app,R1/R2}$ at 16.4 T (blue) and 11.7 T (red). (c) $\langle\tau\rangle_{app,nOe}$ at 16.4 T (blue) and 11.7 T (red).

8.3 Averaging using indefinite self-association models

8.3.1 Thermodynamic models for indefinite self-associations

8.3.1.1 General principles of indefinite self-association models

Consider a molecule in monomeric form A that can self-associate to oligomers of any size i. The analytical concentration C of A is related to the equilibrium concentrations of all multimers A_i of size i by:

$$C = [A] + 2[A_2] + \ldots + i[A_i] + \ldots = \sum_i i[A_i] \tag{8.8}$$

The fraction α of the monomer and the fractions α_i of monomer within an oligomer of size i are then defined by:

$$\alpha = \frac{[A]}{C} \tag{8.9}$$

$$\alpha_i = \frac{i[A_i]}{C} \tag{8.10}$$

The chemical equilibria that describe the self-association are shown in Scheme 8.1.

$$2A \overset{K_2}{\rightleftharpoons} A_2$$

$$A + A_2 \overset{K_3}{\rightleftharpoons} A_3$$

$$\vdots$$

$$A + A_{(i-1)} \overset{K_i}{\rightleftharpoons} A_i$$

Scheme 8.1: Indefinite self-association equilibrium.

The fractions of the oligomers are determined by a system of an infinite number of equations:

$$
\begin{aligned}
K_2 &= \frac{[A_2]}{[A]^2} = \frac{\alpha_2}{2C\alpha^2} \Leftrightarrow \alpha_2 = 2CK_2\alpha^2 = 2C\beta_2\alpha^2 \\
K_3 &= \frac{[A_3]}{[A][A_2]} = \frac{2\alpha_3}{3C\alpha\alpha_2} \Leftrightarrow \alpha_3 = \frac{3}{2}CK_3\alpha\alpha_2 = 3C^2K_3K_2\alpha^3 = 3C^2\beta_3\alpha^3 \\
&\ldots \\
K_i &= \frac{[A_i]}{[A][A_{i-1}]} = \frac{(i-1)\alpha_i}{iC\alpha\alpha_{i-1}} \Leftrightarrow \alpha_i = \frac{i}{(i-1)}CK_i\alpha\alpha_{i-1} = iC^{i-1}K_i\ldots K_2\alpha^i = iC^{i-1}\beta_i\alpha^i
\end{aligned}
\tag{8.11}
$$

in which the cumulative equilibrium constants β_i are defined as:

$$
\beta_i = \begin{cases} 1 & i = 1 \\ \prod_{j=2}^{i} K_j & i \geq 2 \end{cases}
\tag{8.12}
$$

From the equations in (8.11) it becomes clear that each oligomer fraction can be calculated from the monomer fraction. Since all fractions have to sum up to 1, the value of the monomer fraction α is the one that fulfils the following equality:

$$
\begin{aligned}
1 &= \alpha + \sum_{i=2} \alpha_i \\
&= \sum_{i=1} iC^{i-1}\beta_i\alpha^i
\end{aligned}
\tag{8.13}
$$

When all equilibrium constants are defined, then the monomer fraction and subsequently all oligomer fractions can be obtained for a certain analytical concentration C. It is of course impossible to fit an infinite (or at least large) amount of equilibrium constants to a set of experimental data of finite size. For this reason, several models have been proposed in literature that provide a mathematical relation between all subsequent equilibrium constants, so they would all be determined by only one or two parameters.

8.3.1.2 The isodesmic model

In the isodesmic model[1], all equilibrium constants are assumed to be equal. This model, also called the 'equal K' or EK model, thus provides the simplest solution for a relation between the K_i values. In this case, the cumulative equilibrium constants become:

$$
\beta_i = K^{i-1}
\tag{8.14}
$$

with K the equilibrium constant of each reaction in scheme 8.1. Equation (8.13) simplifies to:

$$\begin{aligned} 1 &= \sum_{i=1} iC^{i-1}K^{i-1}\alpha^{i} \\ &= \alpha\sum_{i=1} i\left(CK\alpha\right)^{i-1} \end{aligned} \tag{8.15}$$

It is always true that $CK\alpha$ is smaller than 1, because otherwise the series in (8.15) would not converge. Because this condition is fulfilled, the following mathematical power series expansion can be used:

$$\frac{1}{\left(1-x\right)^{2}} = 1+2x+3x^{2}+4x^{3}+\ldots \qquad \forall\left|x\right|<1 \tag{8.16}$$

Equation (8.15) can then be rewritten as:

$$\begin{aligned} 1 &= \frac{\alpha}{\left(1-CK\alpha\right)^{2}} \\ \Leftrightarrow 0 &= C^{2}K^{2}\alpha^{2}-\left(2CK+1\right)\alpha+1 \\ \Leftrightarrow \alpha &= \frac{\left(2CK+1\right)-\sqrt{4CK+1}}{2C^{2}K^{2}} \end{aligned} \tag{8.17}$$

From this, and equation (8.11), the oligomer fractions are then calculated as:

$$\alpha_{i} = iC^{i-1}K^{i-1}\alpha^{i} \qquad \forall i \geq 2 \tag{8.18}$$

8.3.1.3 The isoenthalpic model

Another model was proposed by Chatelier[2], in which it is assumed that the enthalpy difference ΔH^{0} of each step in the self-association remains constant, but where the entropy difference ΔS^{0} is evaluated for each step. Here, this model will be referred to as the SK model. Only the translational and rotational entropies are considered, as the contributions from other sources of entropy differences (such as torsion and bending motions of the oligomers, or release of solvent molecules) are assumed to be relatively constant for each association step[2]. From molecular statistical principles, the translational entropy of oligomer i, $S_{t,i}$, and rotational entropy of oligomer i, $S_{r,i}$, can be written as:

$$S_{t,i} = R\left(\frac{3}{2}\ln i - \ln\left[A_i\right]\right) + \Upsilon_t \tag{8.19}$$

$$S_{r,i} = R\frac{1}{2}\ln I_i + \Upsilon_r \tag{8.20}$$

with R the universal gas constant and I_i the product of the moments of inertia around the three principle axes of oligomer i. Υ_t and Υ_r are constants independent of i and the concentration of the oligomer $[A_i]$ that will disappear during the following derivation. The ratio between the equilibrium constants K_i and K_2 can be related to the free enthalpy changes of their respective reactions, and since it assumed that only $S_{t,i}$ and $S_{r,i}$ vary between the different reactions, the following expression is found:

$$\begin{aligned}\ln\frac{K_i}{K_2} &= -\frac{\Delta G_i^0 - \Delta G_2^0}{RT} \\ &= \frac{\Delta S_i^0 - \Delta S_2^0}{R} \\ &= \frac{\left(S_{t,i} - S_{t,i-1} + S_{r,i} - S_{r,i-1}\right) - \left(S_{t,2} - S_{t,2} + S_{r,1} - S_{r,1}\right)}{R}\end{aligned} \tag{8.21}$$

Combining (8.21) with (8.19) and (8.20), subsequently using (8.11) and then rearranging, provides:

$$\begin{aligned}&\ln\frac{K_i}{K_2} = \frac{3}{2}\ln\frac{i}{2(i-1)} - \ln\frac{[A_i][A]}{[A_{i-1}][A_2]} + \frac{1}{2}\ln\frac{I_i I_1}{I_{i-1} I_2} \\ \Leftrightarrow\ &\frac{K_i}{K_2} = \left(\frac{i}{2(i-1)}\right)^{3/4}\left(\frac{I_i I_1}{I_{i-1} I_2}\right)^{1/4}\end{aligned} \tag{8.22}$$

If approximating each oligomer and the monomer as a cylinder object with semiaxes a_i and b_i as defined before (Figure 1.5), the product of the moments of inertia is given by:

$$\begin{aligned}I_i &= \frac{1}{2}m_i b_i^2\left(\frac{1}{4}m_i b_i^2 + \frac{1}{3}m_i a_i^2\right)^2 \\ &= \frac{1}{24}m_i^3 b_i^6\left(3 + 4\frac{a_i^2}{b_i^2}\right)^2\end{aligned} \tag{8.23}$$

where m_i is the mass of oligomer i. When assuming that an oligomer i is formed by the stacking the monomer cylinders – with semiaxes a and b and their ratio p – upon each other, then:

$$\begin{aligned} a_i &= ia \\ b_i &= b \\ m_i &= im_1 \end{aligned} \tag{8.24}$$

And (8.23) can be rewritten as:

$$I_i = \frac{1}{24} i^3 m_1^3 b^6 \left(3+4i^2p^2\right)^2 \tag{8.25}$$

Combining this expression with (8.22) provides an expression for K_i:

$$\begin{aligned} K_i &= K_2 \left(\frac{i}{2(i-1)}\right)^{3/4} \left(\frac{i^3\left(3+4i^2p^2\right)^2\left(3+4p^2\right)^2}{(i-1)^3\left(3+4(i-1)^2p^2\right)^2 8\left(3+16p^2\right)^2}\right)^{1/4} \\ &= K_2 \sqrt{\frac{i^3\left(3+4i^2p^2\right)\left(3+4p^2\right)}{8(i-1)^3\left(3+4(i-1)^2p^2\right)\left(3+16p^2\right)}} \end{aligned} \tag{8.26}$$

The equilibrium constants thus decrease with increasing oligomer size with a factor that is dependent only on the ratio between the monomer semiaxes. All equilibrium constants are thus defined from one single parameter, K_2. The equilibrium constants eventually converge to a constant value:

$$\lim_{i\to+\infty} K_i = K_2 \sqrt{\frac{\left(3+4p^2\right)}{8\left(3+16p^2\right)}} \tag{8.27}$$

This is illustrated in Figure 8.15 for different values of p. The cumulative equilibrium constants are given by:

$$\beta_i = K_2^{i-1} \sqrt{\left(\frac{i}{2^{i-1}}\right)^3 \left(\frac{3+4p^2}{3+16p^2}\right)^{i-1} \prod_{j=2}^{i} \frac{\left(3+4j^2p^2\right)}{\left(3+4(j-1)^2p^2\right)}} \tag{8.28}$$

The monomer fraction can then be found by numerically finding the value that corresponds to the following equality:

$$1=\alpha\left(1+\sum_{i=2}\left(CK_2\alpha\right)^{i-1}\sqrt{2^{3(1-i)}i^5\left(\frac{3+4p^2}{3+16p^2}\right)^{i-1}\prod_{j=2}^{i}\frac{\left(3+4j^2p^2\right)}{\left(3+4\left(j-1\right)^2p^2\right)}}\right) \tag{8.29}$$

8.3.1.4 Models assuming a preformed complex

In the case of the self-association of pseudodesmin A, a model was assumed with two levels of association. Besides the ever increasing stacking of molecules, a side-by-side packing of a certain number of molecules takes place as well. The thermodynamics of the side-by-side packing association will differs from that of the stacking association. The indefinite self-association models described above should therefore be modified to take this separate side-by-side association into account. As a crude approximation, it will be assumed that the individual molecules first associate to a complex of size N, without intermediates, with an equilibrium constant K_0, and that these complexes then further undergo the indefinite self-association. The chemical equilibria are shown in Scheme 8.2.

$$\begin{aligned} NA &\overset{K_0}{\rightleftharpoons} A_N \\ 2A_N &\overset{K_2}{\rightleftharpoons} A_{2N} \\ A_N + A_{2N} &\overset{K_3}{\rightleftharpoons} A_{3N} \\ &\vdots \\ A_N + A_{(i-1)N} &\overset{K_i}{\rightleftharpoons} A_{iN} \end{aligned}$$

Scheme 8.2: Indefinite self-association equilibrium of previously formed complex.

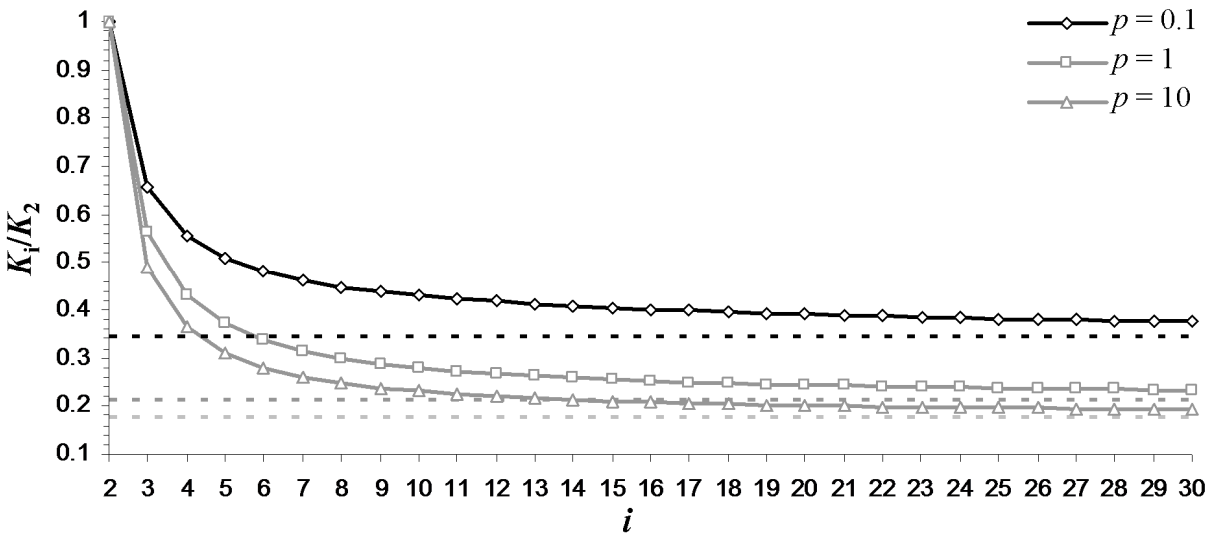

Figure 8.15: Indefinite self-association constants in the isoenthalpic model relative to K_2, assuming a fixed cylinder diameter and increasing length. Values are shown for three values of the monomer length/diameter ratio p. Dotted curves represent the equilibrium constant value at $i \to +\infty$

The fractions of the monomer molecules present in the oligomers can again be expressed in terms of the monomer fraction:

$$K_0 = \frac{[A_N]}{[A]^N} = \frac{\alpha_N}{NC^{N-1}\alpha^N} \Leftrightarrow \alpha_N = NC^{N-1}\beta_1 K_0 \alpha^N$$

$$K_2 = \frac{[A_2]}{[A_N]^2} = \frac{N\alpha_{2N}}{2C\alpha_N^2} \Leftrightarrow \alpha_{2N} = \frac{2}{N} CK_2 \alpha_N^2 = \frac{2}{N} C\beta_2 \alpha_N^2 = 2NC^{2N-1}\beta_2 K_0^2 \alpha^{2N}$$

$$K_3 = \frac{[A_{3N}]}{[A_N][A_{2N}]} = \frac{2N\alpha_{3N}}{3C\alpha\alpha_{2N}} \Leftrightarrow \alpha_{3N} = \frac{3}{2N} CK_3 \alpha_N \alpha_{2N} = 3NC^{3N-1}\beta_3 K_0^3 \alpha^{3N} \qquad (8.30)$$

...

$$K_i = \frac{[A_{iN}]}{[A_N]\left[A_{(i-1)N}\right]} = \frac{N(i-1)\alpha_{iN}}{iC\alpha\alpha_{(i-1)N}} \Leftrightarrow \alpha_{iN} = \frac{i}{(i-1)N} CK_{iN} \alpha_N \alpha_{(i-1)N} = iNC^{iN-1}\beta_i K_0^i \alpha^{iN}$$

with β_i defined as in (8.12). Similarly as before, the monomer fraction α itself can be obtained from the principle that all fractions need to sum up to 1:

$$1 = \alpha + N\sum_{i=1} iC^{iN-1}\beta_i K_0^i \alpha^{iN} \qquad (8.31)$$

In the isodesmic model (here designated as the EKN model), all equilibrium constants other than K_0 are assumed to be equal, so that equation (8.31) can be rewritten using (8.16):

$$\begin{aligned} 1 &= \alpha + N\sum_{i=1} iC^{iN-1}K^{i-1}K_0^i\alpha^{iN} \\ &= \alpha + NC^{N-1}\alpha^N K_0 \sum_{i=1} i\left(C^N K K_0 \alpha^N\right)^{i-1} \\ &= \alpha + \frac{NC^{N-1}\alpha^N K_0}{\left(1 - C^N K K_0 \alpha^N\right)^2} \end{aligned} \tag{8.32}$$

while the oligomer fractions are given by:

$$\alpha_{iN} = iNC^{iN-1}K^i K_0^i \alpha^{iN} \tag{8.33}$$

In the isoenthalpic model (SKN model), K_i was provided by equation (8.28), where p is now the ratio between the semiaxes of the preformed complex. To obtain α, the value that fits the following equation thus needs to be found:

$$1 = \alpha\left(1 + NK_0C^{N-1}\alpha^{N-1}\left(1 + \sum_{i=2}\left(C^N K_2 K_0 \alpha^N\right)^{i-1}\sqrt{2^{3(1-i)}i^5\left(\frac{3+4p^2}{3+16p^2}\right)^{i-1}\prod_{j=2}^{i}\frac{\left(3+4j^2p^2\right)}{\left(3+4(j-1)^2p^2\right)}}\right)\right) \tag{8.34}$$

8.3.2 Application to relaxation averaging

In this section, the effects of an indefinite self-association averaging will be illustrated by making some simple assumptions. The effective relaxation rate constants are calculated as an average over the monomer and each oligomer states, weighted by the fractions of each form. The indefinite self-association assumes an equilibrium between a theoretically infinite number of species. To be able to do practical calculations, the averaging is truncated at a finite size n for which the sum of all α_i with $i \leq n$ approaches sufficiently the value of 1 (*e.g.* no lower than 0.9999):

$$\begin{aligned} \langle R_1 \rangle &= \sum_{i=1}^{n} \alpha_i R_{1i} \\ \langle R_2 \rangle &= \sum_{i=1}^{n} \alpha_i R_{2i} \\ \langle \mathrm{nOe} \rangle &= \sum_{i=1}^{n} \alpha_i \mathrm{nOe}_i \\ 1 &\cong \sum_{i=1}^{n} \alpha_i \end{aligned} \tag{8.35}$$

The fractions α_i are calculated as described above, requiring the concentration, the necessary equilibrium constants and the nature of the self-association model as input. Here, the simple EK model will be assumed. The individual relaxation rate constants of each oligomer are calculated assuming an isotropic relaxation model with a correlation time constant that increases according to a linear increase of the volume with the oligomer size (see equations (1.27) and (1.43)):

$$\tau_i = \frac{\eta V_i}{k_B T} = \frac{\eta i V_{mono}}{k_B T} = i\tau_{mono} \tag{8.36}$$

The monomer correlation time constant τ_{mono} is assumed to be 0.25 ns. The results are shown in Figures 8.16 until 8.19, while Figure 8.20 plots the fractions for a number of selected KC values. The main difference with the simple two-state model in section 8.2 is that all curves have nearly the same shape as the theoretical ones instead of a straight line. In contrast with an association between a finite number of states, the indefinite self-association never converges to one single state at higher levels of association. Therefore the $\langle R_1 \rangle$ vs. $\langle R_2 \rangle$ curve never crosses the theoretical R_1 vs. R_2 curve, always hovering above the latter. This indeed is in agreement with how the experimental data points seem to behave with the concentration (Figure 8.1). The expected deviations between the nOe and R_2 values are now less strongly pronounced when compared to the two-state model of before, especially at higher concentrations. This is due to the significantly reduced contribution of oligomers that are not in the spin-diffusion regime. A similar conclusion can be made for the deviations between the R_1 relaxation rate constants at different field strengths, where the deviations are increasingly less strongly pronounced as the contribution of oligomers in the spin diffusion regime increases (see section 8.2).

Figure 8.21 shows the apparent correlation time constant from the $\langle R_1 \rangle / \langle R_2 \rangle$ and the $\langle R_2 \rangle$ values, $\langle \tau \rangle_{app,R1/R2}$ and $\langle \tau \rangle_{app,R2}$. Again the $\langle \tau \rangle_{app,R2}$ values are practically the same as the average correlation time constant $\langle \tau \rangle$, while the $\langle \tau \rangle_{app,R1/R2}$ values are consistently lower.

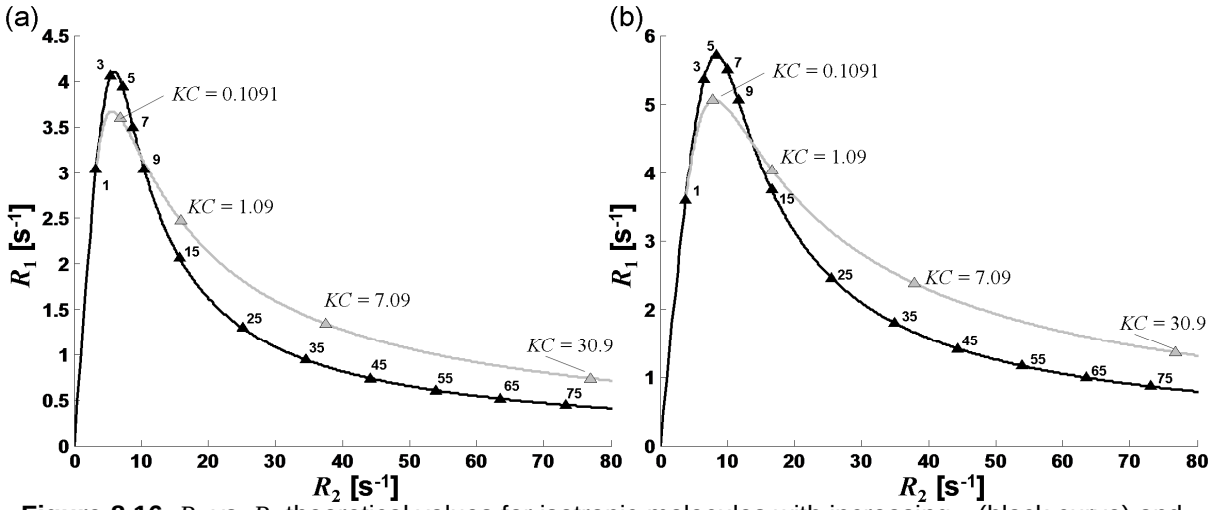

Figure 8.16: R_1 vs. R_2 theoretical values for isotropic molecules with increasing τ (black curve) and $\langle R_1 \rangle$ vs. $\langle R_2 \rangle$ values using the EK model (grey curve) for increasing KC values (see main text) at 16.4 T (a) and 11.7 T (b). The position of the R_1 and R_2 relaxation rate constants for selected number of oligomer sizes are indicated on the theoretical curve.

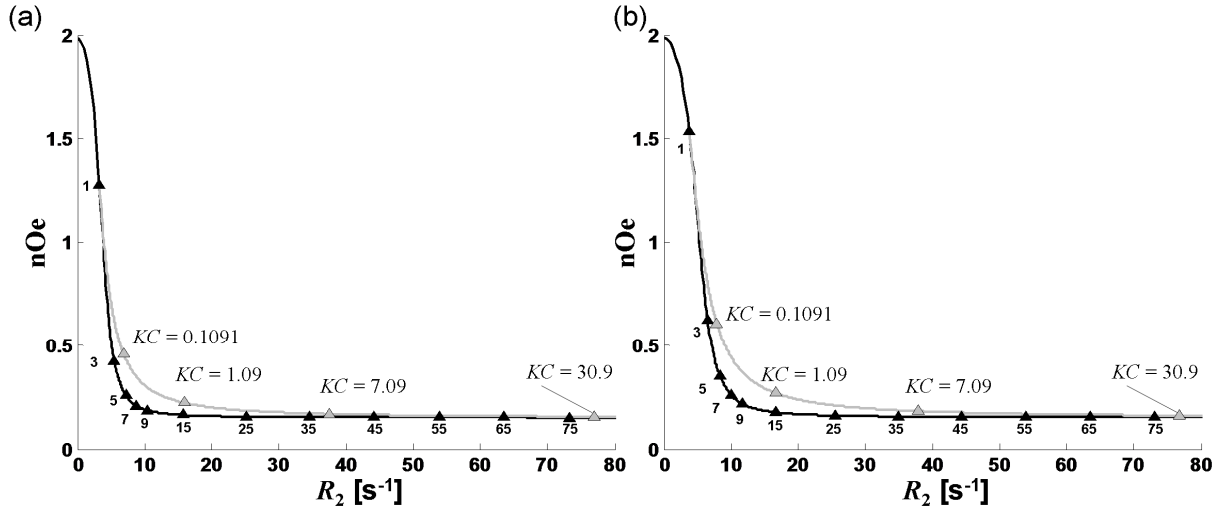

Figure 8.17: Same as Figure 8.16, but now for nOe vs. R_2 and $\langle$nOe$\rangle$ vs. $\langle R_2 \rangle$. (a) 16.4 T; (b) 11.7 T.

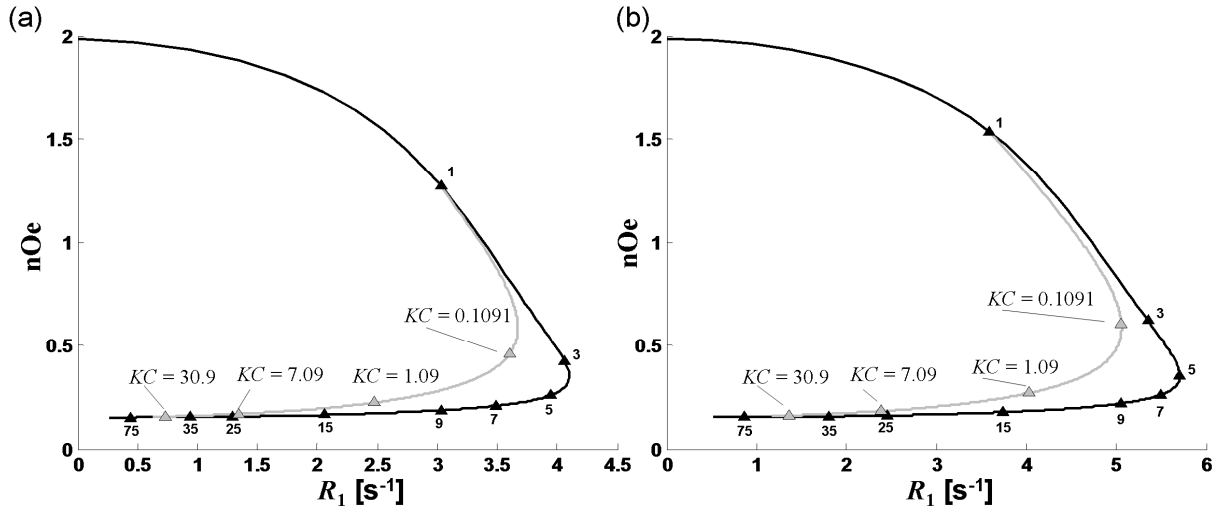

Figure 8.18: Same as Figure 8.16, but now for nOe vs. R_1 and $\langle$nOe$\rangle$ vs. $\langle R_1 \rangle$. (a) 16.4 T; (b) 11.7 T.

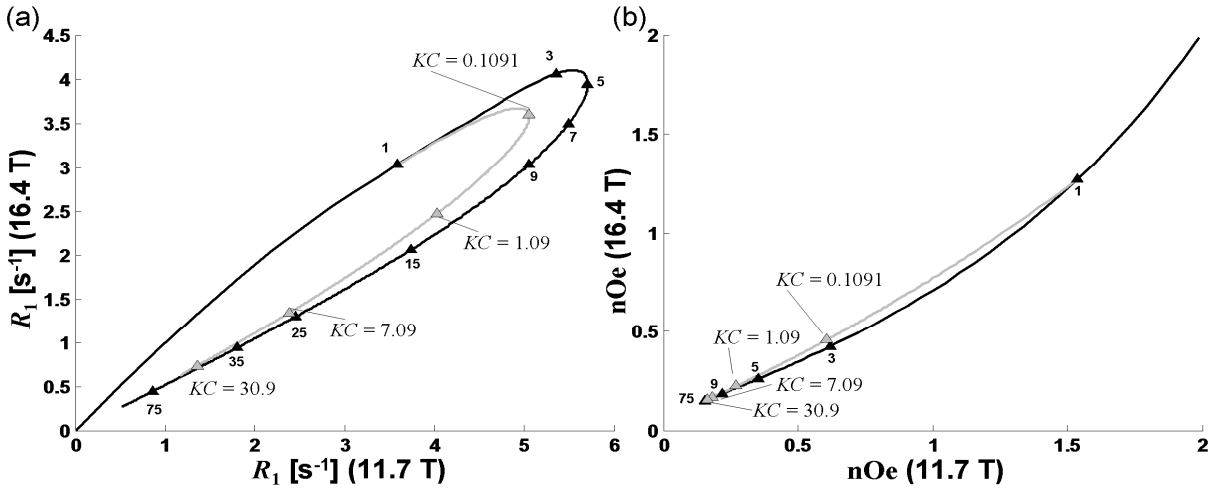

Figure 8.19: Relaxation parameters at 16.4 T vs. the same parameter at 11.7 T for isotropic tumbling molecules with increasing τ (black curve) and averaged relaxation values according to the EK model (grey curves) with increasing KC values (see main text). The positions of the R_1 and nOe relaxation rate constants for selected number of oligomer sizes are indicated on the theoretical curve. (a) R_1; (b) nOe.

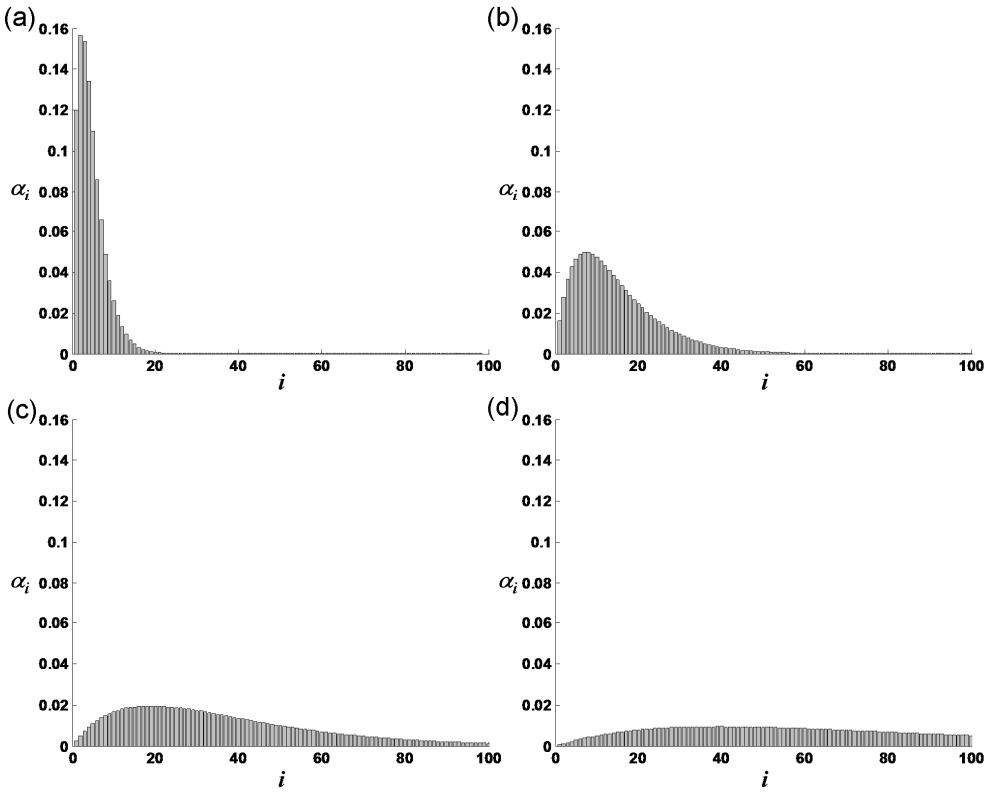

Figure 8.20: Distribution of the fractions of monomer molecules present in oligomers of size i in the EK model for KC values of (a) 0.1091, (b) 1.09, (c) 7.09 and (d) 30.9.

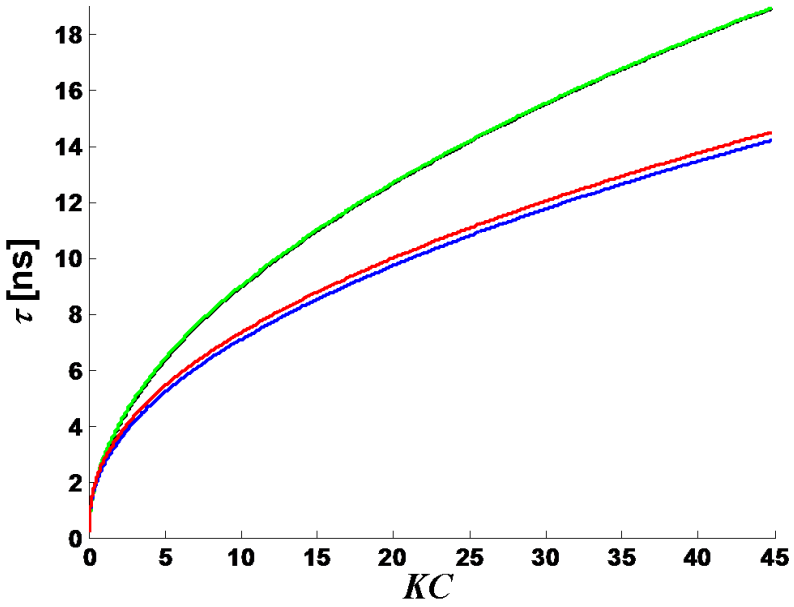

Figure 8.21: Apparent correlation time constants as a function of KC in the EK model (see main text): $\langle\tau\rangle_{app,R2}$ at 16.4 T (green curve), $\langle\tau\rangle_{app,R1/R2}$ at 16.4 T (blue curve) and 11.7 T (red curve). The average correlation time constant $\langle\tau\rangle$ is shown as a black curve, but it almost fully overlaps with the green curve.

8.4 Attempt to find a model to quantitatively explain the experimental data

Since all relaxation parameters are very sensitive to the degree and nature of the self-association, it should be possible to extract to a certain level the distribution of the different oligomer sizes out of the experimental data (Chapter 7). To do so however, several assumptions have to be made. First, a self-association model has to be chosen. From all models that were found in literature, the isoenthalpic model is the only one with a sound physical basis[2], *i.e.* the relation between the equilibrium constants is the result of physical considerations rather than being guided by a mathematically convenience[1]. As explained before (section 8.3.1.4), the self-association of pseudodesmin A is hypothesised to comprise two separate interactions. First, an initial complex of N molecules (labelled the π-state) is formed. The second interaction then encompasses the stacking of these π-states. The presence of these two separate processes in the self-association may find support in the behaviour with the concentration of the apparent hydrodynamic radius in chloroform (Figure 6.4c), which was found to be different at low concentrations when compared to high concentrations.

The π-state is assumed to possess a cylindrical shape with a radius of 13.3 Å (based on the results of the previous chapter) and a length of 14 Å (based on the dimensions of the acetonitrile solution structure). There is so far no strong argument favouring any particular value of the number of molecules N within the π-state. Any value that

would be reasonable considering the dimensions of the supramolecular complex found in Chapter 7 can be assumed. Here, a value of 6 will be chosen, based on the ratio between the volume of the cylindrical π-state (9896 Å^3) and the volume of the assumed spherical monomer with a hydrodynamic radius of 7.2 Å (1563 Å^3). These complexes then stack upon each other to form cylindrically shaped structures with constant radius but increasing length.

The maximum number of fractions that is considered during the averaging of relaxation parameters is 30, including the monomer fraction. The largest oligomer size that is considered during the calculations therefore exists out of $6 \times 29 = 174$ molecules. The monomer is assumed to behave isotropically with a correlation time constant τ_{mono} of 0.25 ns, based on what was found for pseudodesmin A in acetonitrile solution (section 7.2.2). The rotational diffusion coefficients and correlation time constants for the π-state and the first few oligomers are presented in Table 8.1, calculated using equations (1.51) until (1.54) and assuming a viscosity of 0.631 mPa·s for chloroform at 10℃.

Using the SKN model, no simulated curves matching satisfactory all data points could be obtained. Attempts to perform a fitting procedure of the model simulation to the experimental data all failed. The results presented here are obtained through a trial and error search that provided a simulated dataset that is in reasonable agreement with the experimental data behaviour. These results should therefore not be seen as the best fit to the data – since it is not – but rather as a proof of principle that it should be possible to find a model that describes the data quantitatively.

The simulated curves were generated using equilibrium constants K_0 and K_2, as defined for the SKN model in section 8.3.1.4, of respectively 1 mM^{-5} and 8 mM^{-1}. In Figure 8.22 until 8.25, the resulting averaged curves are shown. The averaged curves do not exactly follow the same trend as the experimental data points, as they do not cross the low concentration data points. Also, $\langle R_1 \rangle$ seems to decrease too fast with the concentration when compared to $\langle R_2 \rangle$. The $\langle \mathrm{nOe} \rangle$ values are lower than the experimental values for each dataset, except at 6.6 mM. Also, the experimental data points do not show any variation with concentration, while the averaged curves do show a significant variation (ranging from 0.25 to 0.17 at 16.4 T). The discrepancies between R_1 values at different field strength are also not quantitatively explained by the $\langle R_1 \rangle$ curves. It should be noted that, as shown in section 8.1, fast internal motion also can influence the nOe and R_1 values in a direction that explains the experimental data. It can therefore not be excluded that such effects are present.

In Figure 8.26, the R_1/R_2 values are plotted against the θ angle for each dataset. The $\langle R_1 \rangle / \langle R_2 \rangle$ curves do not agree with the curves obtained in the previous chapter, with

the exception of the 16.4 mM dataset at 16.4 T. When the rotational diffusion coefficients are fitted to the $\langle R_1 \rangle / \langle R_2 \rangle$ curves (Table 8.2), the obtained results are relatively close to those obtained from the experimental values (section 7.4). The trends seen are similar, with both rotational diffusion coefficients and cylinder average lengths that are decreasing with concentration, but with relatively constant cylinder diameters. The only exceptions are the results at 11.7 T, which provide similar rotational diffusion coefficients and dimensions when compared to the same concentration at 16.4 T. For the experimental values, strong deviations between the two magnetic fields were found (Table 7.16).

Table 8.1: Cylindrical semiaxes, calculated correlation time constants and rotational diffusion coefficients of the first 15 oligomers in the SKN simulation

fraction	size	a [Å]	b [Å]	τ_A [ns]	τ_B [ns]	τ_C [ns]	$D_r^{\parallel}$ [µs^{-1}]	$D_r^{\perp}$ [µs^{-1}]	$D_r^{\parallel} / D_r^{\perp}$
2 (π)	6	7	13.3	1.52	1.50	1.60	101.76	109.48	0.93
3	12	14	13.3	3.21	3.01	2.74	65.38	51.96	1.26
4	18	21	13.3	5.84	5.28	3.94	49.24	28.55	1.72
5	24	28	13.3	9.35	8.12	5.15	39.60	17.82	2.22
6	30	35	13.3	14.09	11.40	6.38	33.29	11.82	2.82
7	36	42	13.3	20.44	15.03	7.61	28.80	8.15	3.53
8	42	49	13.3	28.70	18.93	8.83	25.39	5.81	4.37
9	48	56	13.3	39.14	23.07	10.07	22.71	4.26	5.33
10	54	63	13.3	51.96	27.41	11.30	20.52	3.21	6.40
11	60	70	13.3	67.33	31.90	12.53	18.71	2.48	7.56
12	66	77	13.3	85.38	36.53	13.76	17.19	1.95	8.80
13	72	84	13.3	106.22	41.27	15.00	15.89	1.57	10.12
14	78	91	13.3	129.92	46.11	16.23	14.76	1.28	11.51
15	84	98	13.3	156.58	51.04	17.46	13.78	1.06	12.95
16	90	105	13.3	186.23	56.03	18.70	12.92	0.89	14.44

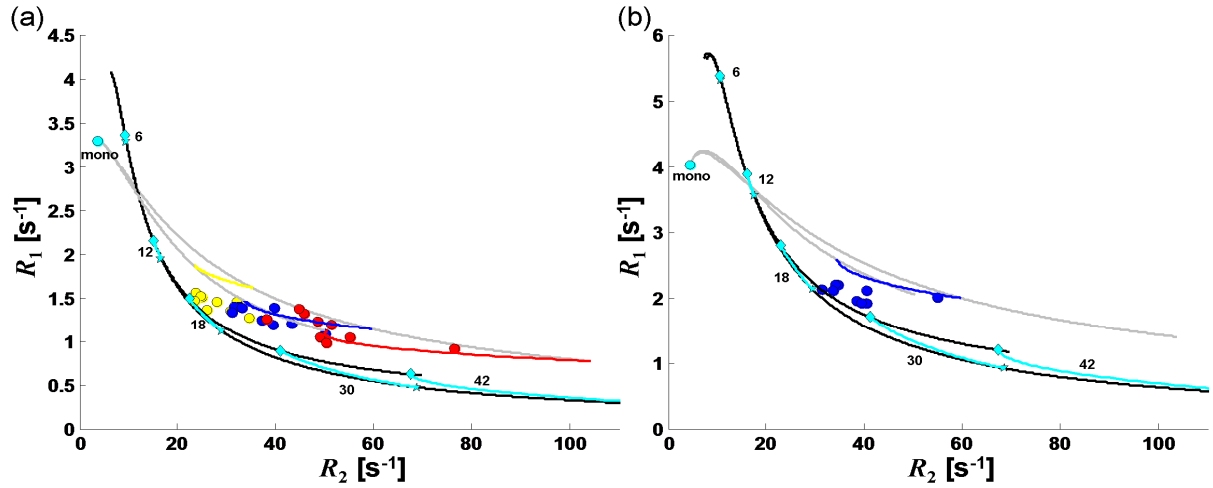

Figure 8.22: Results of the SKN model simulation averaging: R_1 vs. R_2, (a) 16.4 T; (b) 11.7 T. Black curves are the theoretical R_1-R_2 combinations for a cylindrical object with increasing length and constant radius of 13.3 Å, each curve representing the two extreme orientations in θ (0° and 90°). The cyan curves connect the cyan diamonds and pentagrams, each revealing the collection of R_1-R_2 combinations that belong to one particular oligomer size (size labelled in terms of number of monomer units). The cyan dot represents the monomer R_1-R_2 combination. The two grey curves are the $\langle R_1\rangle$-$\langle R_2\rangle$ combinations for increasing concentration, representing respectively the $\langle R_1\rangle_{\max}$ vs. $\langle R_2\rangle_{\min}$ and the $\langle R_1\rangle_{\min}$ vs. $\langle R_2\rangle_{\max}$ combinations. The coloured curves represent the $\langle R_1\rangle$-$\langle R_2\rangle$ combinations at each experimental concentration (6.6 mM yellow, 16.4 mM blue and 44.8 mM red), while the coloured dots are experimental data points.

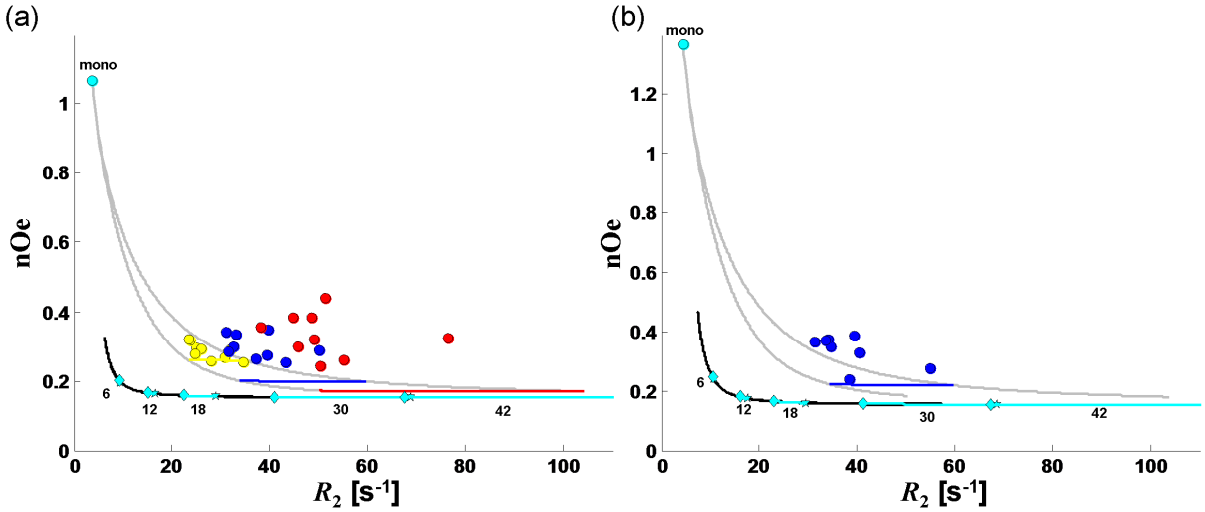

Figure 8.23: Results of the SKN model simulation averaging: nOe vs. R_2, (a) 16.4 T; (b) 11.7 T. Black curves are the theoretical nOe-R_2 combinations for a cylindrical object with increasing length and constant radius of 13.3 Å, each curve representing the two extreme orientations in θ (0° and 90°). The cyan curves connect the cyan diamonds and pentagrams, each revealing the collection of nOe-R_2 combinations that belong to one particular oligomer size (size labelled in terms of number of monomer units). The cyan dot represents the monomer nOe-R_2 combination. The two grey curves are the $\langle$nOe$\rangle$-$\langle R_2\rangle$ combinations for increasing concentration, representing respectively the $\langle$nOe $\rangle_{\max}$ vs. $\langle R_2\rangle_{\min}$ and the $\langle$nOe$\rangle_{\min}$ vs. $\langle R_2\rangle_{\max}$ combinations. The coloured curves represent the $\langle$nOe $\rangle$-$\langle R_2\rangle$ combinations at each experimental concentration (6.6 mM yellow, 16.4 mM blue and 44.8 mM red), while the coloured dots are experimental data points.

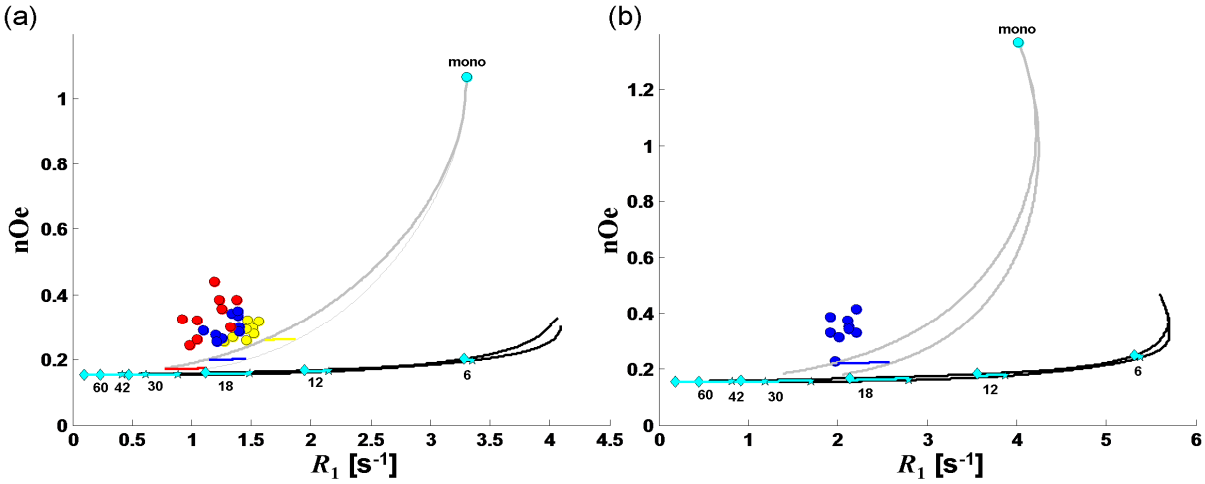

Figure 8.24: Results of the SKN model simulation averaging: nOe vs. R_1, (a) 16.4 T; (b) 11.7 T. Black curves are the theoretical nOe-R_1 combinations for a cylindrical object with increasing length and constant radius of 13.3 Å, each curve representing the two extreme orientations in θ (0° and 90°). The cyan curves connect the cyan diamonds and pentagrams, each revealing the collection of nOe-R_1 combinations that belong to one particular oligomer size (size labelled in terms of number of monomer units). The cyan dot represents the monomer nOe-R_1 combination. The two grey curves are the $\langle$nOe$\rangle$-$\langle R_1\rangle$ combinations for increasing concentration, representing respectively the $\langle$nOe$\rangle_{max}$ vs. $\langle R_1\rangle_{min}$ and the $\langle$nOe$\rangle_{min}$ vs. $\langle R_1\rangle_{max}$ combinations. The coloured curves represent the $\langle$nOe$\rangle$-$\langle R_1\rangle$ combinations at each experimental concentration (6.6 mM yellow, 16.4 mM blue and 44.8 mM red), while the coloured dots are experimental data points.

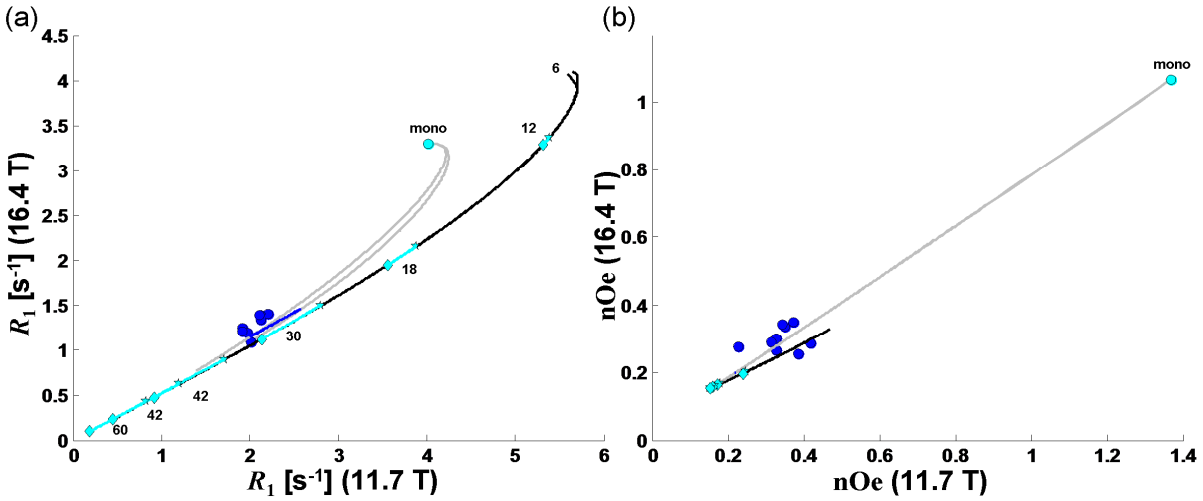

Figure 8.25: Results of the SKN model simulation averaging: R_1 (a) and nOe (b) at different magnetic fields. Black curves are the theoretical values for a cylindrical object with increasing length and constant radius of 13.3 Å, each curve representing the two extreme orientations in θ (0° and 90°). The cyan curves connect the cyan diamonds and pentagrams, each revealing the combinations that belong to one particular oligomer size (size labelled in terms of number of monomer units). The cyan dot represents the monomer relaxation parameter combination. The two grey curves are the averaged relaxation parameter combinations for increasing concentration, representing respectively the $\langle X_a\rangle_{max}$ vs. $\langle X_b\rangle_{min}$ (11.7 T) and the $\langle X_a\rangle_{min}$ vs. $\langle X_b\rangle_{max}$ combinations, with X_a and X_b either R_1 (a) or the nOe (b) at respectively 16.4 T and 11.7 T. The coloured curves represent the $\langle$nOe$\rangle$-$\langle R_1\rangle$ combinations at each experimental concentration (6.6 mM yellow, 16.4 mM blue and 44.8 mM red), while the coloured dots are experimental data points.

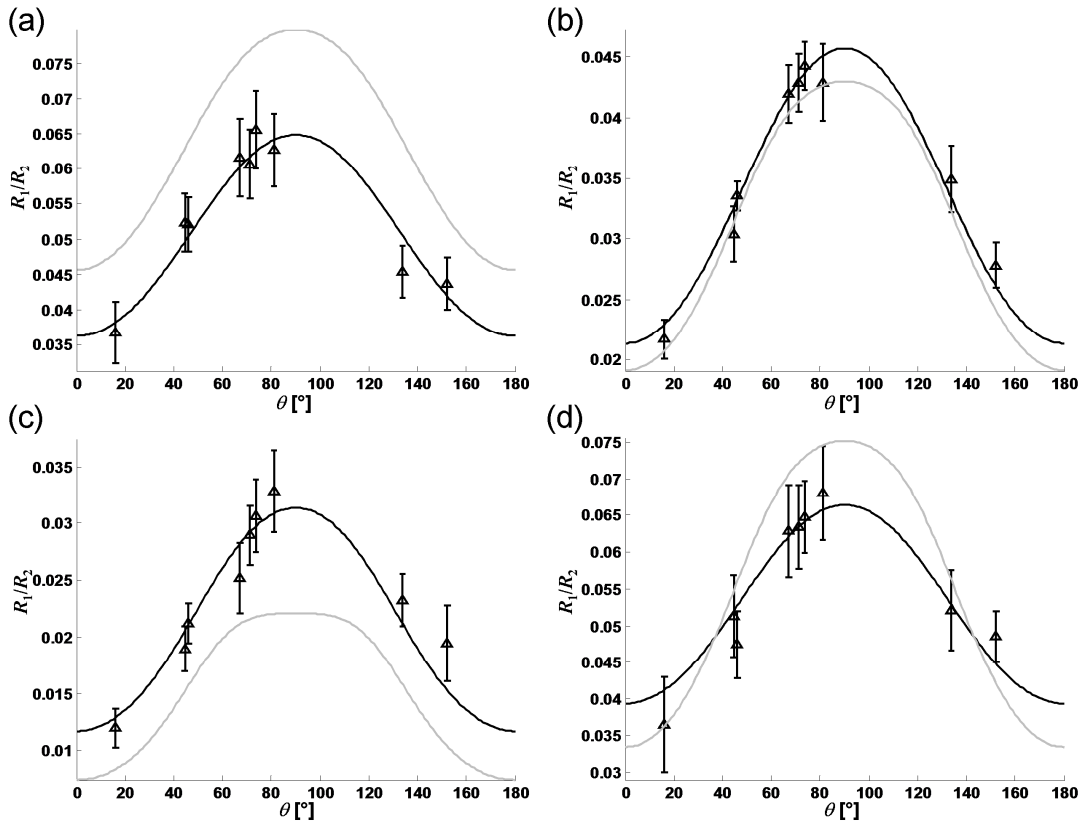

Figure 8.26: R_1/R_2 ratios plotted against the θ angles. The experimental data points (Gln2 C^{α} - Ile9 C^{α} and Thr3 C^{β}) are shown with 95% error bars, while the black curves are the R_1/R_2 values calculated using the obtained rotational diffusion coefficients for each dataset (Table 7.16). The grey curves are the $\langle R_1\rangle/\langle R_2\rangle$ values from the SKN model simulation at the same concentration and magnetic field strength as the experimental data points. (a) 6.6 mM, 16.4 T; (b) 16.4 mM, 16.4 T; (c) 44.8 mM, 16.4 T; (d) 16.4 mM, 11.7 T.

Table 8.2: Rotational diffusion coefficients, Correlation time constants and cylindrical semiaxes fitted from the $\langle R_1\rangle/\langle R_2\rangle$ curves.

C [mM]	B_0 [T]	a [Å]	b [Å]	τ_A [ns]	τ_B [ns]	τ_C [ns]	$D_r^{\parallel}$ [µs^{-1}]	$D_r^{\perp}$ [µs^{-1}]	$D_r^{\parallel}/D_r^{\perp}$
6.6	16.4	20.46	12.81	5.31	4.72	3.54	54.98	31.38	1.75
16.4	16.4	26.30	13.16	8.28	6.95	4.70	43.18	20.12	2.15
44.8	16.4	33.72	13.45	13.28	10.34	6.21	34.00	12.55	2.71
16.4	11.7	27.03	13.20	8.72	7.27	4.85	41.99	19.12	2.20

Finally, the distributions of fractions at the three experimental concentrations are shown Figure 8.27. The monomer fraction, the mean of the size distribution and its standard deviation are given in Table 8.3. As expected, the distribution shifts to oligomers with higher sizes at higher concentration. The distribution of oligomer sizes also becomes broader upon increasing concentration, which is inherent to any indefinite self-association thermodynamic model.

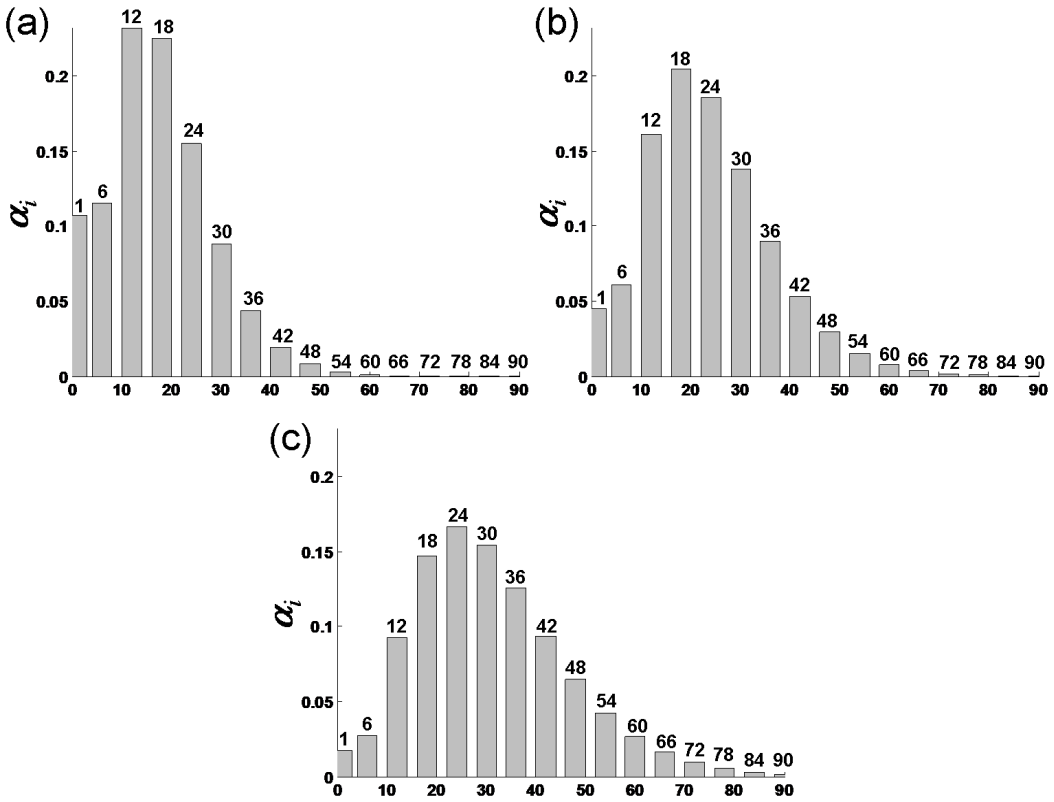

Figure 8.27: Distribution of α_i values in the SKN model simulation, with the size of each oligomer (number of monomer units) indicated above each bar. (a) 6.6 mM; (b) 16.4 mM; (c) 44.8 mM.

Table 8.3: Some properties for the α_i distributions obtained in the SKN model simulation

C [mM]	α[a]	Mean oligomer length[b]	Standard deviation[c]	mean size[d]
6.6	0.107	3.2	1.6	19.04
16.4	0.045	4.1	2.0	24.41
44.8	0.017	5.3	2.6	31.50

[a] Monomer fraction
[b] Mean length of the oligomers expressed as the number of π-states stacked upon each other
[c] Standard deviation of the oligomer length
[d] Mean size of the oligomers expressed as the number of monomer units per oligomer

8.5 Conclusion

It has been shown through simulation that a self-association process can indeed cause deviations observed between the experimental data and the theoretically expected relations between the different relaxation parameters. These deviations are most obvious between the R_1 and R_2 relaxation rate constants and cannot be reasonably explained by effects of sub nanosecond internal motion. The self-association will cause the nOe to a value to be higher than its spin diffusion limit value,

as expected from the other relaxation rate constants. This is due to an averaging involving the monomer and lower oligomer forms, which are not in the spin diffusion limit regime. As opposed to the discrepancies between R_1 and R_2, the deviations for the nOe can also be explained by internal motion. A similar conclusion can be formulated for discrepancies between the R_1 values at different magnetic field, where the magnetic field strength influences the weights for the low oligomer species in the averaging.

Simulations with indefinite self-association models, which assume that an association to oligomers of unlimited size is possible, explain the concentration dependent behaviour of the deviations between R_1 and R_2 values. This effectively confirms that the pseudodesmin A supramolecular complexes can indefinitely grow in size within the concentration range studied. Attempts were made to develop a model that quantitatively explains the behaviour of all experimental relaxation data. They were unsuccessful; however the preliminary results do show that it should be possible to find such a model. The reason why at the moment it is not feasible to achieve this goal is that too many required variables exist that now need to be roughly estimated. First, it is assumed that oligomers of only side-by-side packing of molecules are formed, which successively stack upon each other. Reality might prove to be somewhat more complex. Furthermore, the number of molecules that are present in this π-state complex cannot be confidently assessed from the results obtained until now. The dimensions of this complex are only approximations based on the results from the relaxation data analysis in Chapter 7 and the solution structure. In addition, the isoenthalpic thermodynamic model for the description of the stacking equilibria is in itself an assumption. Besides all this, the relaxation rate constants may also be influenced by the presence of internal motion.

To improve upon this issue, it will be necessary to study the behaviour of the relaxation rate constants at even lower concentration in chloroform to gain more insight into the size and anisotropy of the lowest oligomers. In addition, more insight into the molecular structure of the supramolecular complex will have to be obtained as to obtain a more detailed view in which steps the structures are formed.

8.6 References

[1] R. B. Martin, "Comparisons of indefinite self-association models". *Chemical Reviews*, **1996**, *96*(8) 3043-3064.

[2] R. C. Chatelier, "Indefinite Isoenthalpic Self-Association of Solute Molecules". *Biophysical Chemistry*, **1987**, *28*(2) 121-128.

General conclusion

In this work, considerable progress has been made on establishing the relation between the structure, self-association and function of pseudodesmin A. First, the conformation of pseudodesmin A was determined in acetonitrile solution and found to be principally identical to its crystal structure. In DMSO solution however, the pseudodesmin A structure is disrupted by the strong hydrogen bond acceptor capacity of the DMSO molecules, effectively creating an exchange between different conformations. These findings have important repercussions for a different member of the viscosin group, WLIP, which has been reported to adopt a dissimilar conformation in DMSO solution when compared to its crystal structure. The findings for pseudodesmin A, which contains only a Glu2 to Gln2 substitution in comparison to WLIP, effectively invalidate the reported WLIP solution conformation and take away any doubt that the conformation in the crystal structure would not be adopted under solution conditions.

The self-association was studied in chloroform by means of translational diffusion NMR measurements, which convincingly showed that large supramolecular structures of indefinite size can be formed at high pseudodesmin A concentrations. It was shown that the polarity of the solvent environment determines the extent of the self-association, demonstrating that the low polarity of the environment is the driving force of the self-association.

All the information extracted from the analysis of the conformation and the self-association behaviour allowed a model to be proposed for the organisation of the supramolecular assembly formed in the non-polar solvents. This is the first attempt to establish a relation between the structure and the biological properties of a CLP of the viscosin group. Since the viscosin group members belonging to the D-subgroup (WLIP, the pseudophomines and pseudodesmin B) possess nearly identical conformations when compared to pseudodesmin A, it can be assumed that the model applies to these compounds as well. For the members in the L-subgroup (viscosin, viscosinamide and the massetolides), the configuration of the main chain C^{α} is inversed when compared to pseudodesmin A. Since no conformational studies on one of these members have been reported so far, the impact on the conformation, the self-association and thus the biological mechanism can presently not be assessed.

Several aspects of the proposed model were confirmed independently by analysing the $^{13}C^{\alpha}$ relaxation rate constants in pseudodesmin A. From the data, average rotational diffusion coefficients could be obtained, which were in agreement with the cylindrical shape and the size that were expected from the proposed model. It was

shown that as the assembly grows in size, only the length of the cylindrical structure increases, while the diameter remains constant. By studying the relation between the orientation of the $^{13}C^{\alpha}–^{1}H$ bond vector and the R_1/R_2 ratios, the relative orientation of the individual monomer units with respect to the direction of growth of the supramolecular assembly could be established. This orientation is in agreement with the expected electrostatic interaction between both sides of the molecule. The latter result is one of the main advantages of this novel approach to study supramolecular assemblies. Where other techniques, such as AFM or SEM, would only be able to scan the surface of such structures, revealing their shape and size, the orientation of the individual molecules within the structures is usually not attainable. Another advantage over the aforementioned techniques is that the structures are studied free in solution; no adsorption to any surface is required.

This technique can in principle be applied to any system that self-assembles to anisotropic structures. The two main requirements are that the monomer conformation – which is preferably rigid – should be known and that the orientation of the $^{13}C^{\alpha}–^{1}H$ or $^{15}N–^{1}H$ bond vectors are sufficiently diverse so as to sample the anisotropic dependence of the relaxation rate constants. In addition, the size of the structures should also be controlled since too large structures will lead to high values for the relaxation rate constants R_2 and thus too low signal-to-noise ratios for experimental monitoring. The self-association should also be studied in free solution so that the rotational diffusion coefficients that are picked up are indeed determined by the dimensions of the assemblies themselves. For example, if pseudodesmin A were studied in bicelles instead of free solution, the rotational diffusion coefficients would be determined by the size and shape of the bicelles rather than that of the assembly. Experimental measuring time can also be an issue, as heteronuclear relaxation experiments (one HSQC type spectrum per data point – see section 3.7.2 – per relaxation rate constant and per concentration,) can become quite lengthy, especially at natural abundance.

In conclusion, it can be stated that this novel technique has possible applications for self-assembling systems in general and for self-assembling peptides in particular. The potential of this methodology will be further explored in the future.

Appendices

A

Spherical harmonic functions

The general expression for the spherical harmonic functions is given by:

$$\mathrm{Y}_m^l = \frac{1}{\sqrt{2\pi}} \Theta_m^l(\theta) e^{im\phi} \tag{A.1}$$

with l and m:

$$\begin{aligned} l &= 0,1,2,3,\ldots \\ m &= -l, -l+1, \ldots, l-1, l \end{aligned} \tag{A.2}$$

and with $\Theta_m^l(\theta)$ functions that are given by:

$$\Theta_m^l(\theta) = \begin{cases} (-1)^m \frac{1}{2^l l!} \sqrt{\frac{2l+1}{2} \frac{(l-m)!}{(l+m)!}} \sin^m\theta \frac{d^{l+m}}{d(\cos\theta)^{l+m}} \left(\cos^2\theta - 1\right)^l & \text{if } m \geq 0 \\ (-1)^m \Theta_{|m|}^l(\theta) & \text{if } m < 0 \end{cases} \tag{A.3}$$

The first few spherical harmonic functions are given by:

$$Y_0^0 = \frac{1}{\sqrt{4\pi}} \tag{A.4}$$

$$Y_1^1 = -\sqrt{\frac{3}{8\pi}} \sin\theta e^{i\phi} \tag{A.5}$$

$$Y_0^1 = \sqrt{\frac{3}{4\pi}} \cos\theta \tag{A.6}$$

$$Y_{-1}^1 = \sqrt{\frac{3}{8\pi}} \sin\theta e^{-i\phi} \tag{A.7}$$

$$Y_2^2 = \sqrt{\frac{15}{32\pi}} \sin^2\theta e^{2i\phi} \tag{A.8}$$

$$Y_1^2 = -\sqrt{\frac{15}{8\pi}} \cos\theta \sin\theta e^{i\phi} \tag{A.9}$$

$$Y_0^2 = \sqrt{\frac{5}{16\pi}} \left(3\cos^2\theta - 1\right) \tag{A.10}$$

$$Y_{-1}^2 = \sqrt{\frac{15}{8\pi}} \cos\theta \sin\theta e^{-i\phi} \tag{A.11}$$

$$Y_{-2}^2 = \sqrt{\frac{15}{32\pi}} \sin^2\theta e^{-2i\phi} \tag{A.12}$$

B

The Stejskal-Tanner equation for any pulse sequence

B.1 Solution to the Bloch-Torrey equations

The Bloch equations which include the effects of diffusion (2.8) and flow (2.29) will be solved here.

$$\frac{\partial}{\partial t}\begin{bmatrix} \mathrm{M}_z(t,z) \\ \mathrm{M}^+(t,z) \\ \mathrm{M}^-(t,z) \end{bmatrix} = \left(\omega_0 + \gamma G(t) z\right)\begin{bmatrix} 0 \\ -i\,\mathrm{M}^+(t,z) \\ i\,\mathrm{M}^-(t,z) \end{bmatrix} - R_2\begin{bmatrix} 0 \\ \mathrm{M}^+(t,z) \\ \mathrm{M}^-(t,z) \end{bmatrix} - R_1\begin{bmatrix} \mathrm{M}_z(t,z) - M_0 \\ 0 \\ 0 \end{bmatrix} + D_t\frac{\partial^2}{\partial z^2}\begin{bmatrix} \mathrm{M}_z(t,z) \\ \mathrm{M}^+(t,z) \\ \mathrm{M}^-(t,z) \end{bmatrix} - v_z\frac{\partial}{\partial z}\begin{bmatrix} \mathrm{M}_z(t,z) \\ \mathrm{M}^+(t,z) \\ \mathrm{M}^-(t,z) \end{bmatrix} \tag{B.1}$$

It is assumed that the gradient strength is time dependent, so that $\Omega(z) \equiv \Omega(z,t) = -\gamma G(t) z$. The evolution of the magnetisation due to chemical shift and relaxation is known and can therefore be filtered out of the above equations through the following substitutions:

$$\mathrm{M}_z(t,z) = M_0 - \left(M_0 - \Psi_z(t,z)\right)e^{-R_1 t} \tag{B.2}$$

$$\mathrm{M}^+(t,z) = \Psi^+(t,z)e^{-i\omega_0 t - R_2 t} \tag{B.3}$$

$$\mathrm{M}^-(t,z) = \Psi^-(t,z)e^{i\omega_0 t - R_2 t} \tag{B.4}$$

Inserting these equations into (B.1) lead to the following expressions:

$$\frac{\partial \Psi_z(t,z)}{\partial t} = D_t \frac{\partial^2 \Psi_z(t,z)}{\partial z^2} - v_z \frac{\partial \Psi_z(t,z)}{\partial z} \tag{B.5}$$

$$\frac{\partial \Psi^+(t,z)}{\partial t} = -i\gamma \mathrm{G}(t) z \Psi^+(t,z) + D_t \frac{\partial^2 \Psi^+(t,z)}{\partial z^2} - v_z \frac{\partial \Psi^+(t,z)}{\partial z} \tag{B.6}$$

$$\frac{\partial \Psi^-(t,z)}{\partial t} = i\gamma \mathrm{G}(t) z \Psi^-(t,z) + D_t \frac{\partial^2 \Psi^-(t,z)}{\partial z^2} - v_z \frac{\partial \Psi^-(t,z)}{\partial z} \tag{B.7}$$

The effects of the gradient can be filtered out by applying a substitution similar as for the chemical shift.

$$\Psi_z(t,z) = \Phi_z(t)e^{-i\,\mathrm{q}(t)z} \tag{B.8}$$

$$\Psi^+(t,z) = \Phi^+(t)e^{-i\,\mathrm{q}(t)z} \tag{B.9}$$

$$\Psi^-(t,z) = \Phi^-(t)e^{-i\,\mathrm{q}(t)z} \tag{B.10}$$

Here, the function $\mathrm{q}(t)$ is defined as:

$$\mathrm{q}(t) = \int_0^t \gamma p \,\mathrm{G}(t)\,dt \tag{B.11}$$

with p the coherence order (p = 0 for M_z magnetisation, $p = \pm 1$ for M^+ and M^- magnetisation). When substituting (B.11) into (B.5) to (B.7), the three resulting equations can be generalised into a single equation, with $\Phi_z(t) = \Phi^+(t) = \Phi^-(t) = \Phi(t)$:

$$\frac{\partial \Phi(t)}{\partial t} = \left(-D_t \mathrm{q}^2(t) + iv_z \mathrm{q}(t)\right)\Phi(t) \tag{B.12}$$

At this point it is assumed that only one type of magnetisation is present at one particular time (*cf*. only one unique CTP is selected by the phase cycling and spoil gradient scheme) and a function $\mathrm{p}(t)$ is defined that represents the coherence order of the CTP at time t. The effects of diffusion and flow on one type of magnetisation will simply be transferred to the other magnetisation by the rf-pulses (which were not taken into account in (B.1) for the sake of simplicity). The effects of relaxation and

chemical shift will be different for each type of magnetisation and are represented by equations (B.2), (B.3) and (B.4). The effects of diffusion and flow will be exactly the same on all the three magnetisation components and are described by the function $\Phi(t)$. The function $\mathrm{q}(t)$ is now redefined to take into account the changes in coherence order over time:

$$\mathrm{q}(t) = \int_0^t \gamma \mathrm{p}(t)\mathrm{G}(t)\,dt \tag{B.13}$$

The solution of the differential equation (B.12), assuming that $\Phi(0) = 1$, is:

$$\Phi(t) = e^{-D_t \int_0^t \mathrm{q}^2(t)dt} e^{iv_z \int_0^t \mathrm{q}(t)dt} \tag{B.14}$$

At the end of a pulse sequence, the signal intensity I that is measured will be weighted by this expression, with I_0 the collected contributions from the relaxation, chemical shift evolution and residual dephasing by the gradients:

$$I = I_0 e^{-D_t \int_0^t \mathrm{q}^2(t)dt} e^{iv_z \int_0^t \mathrm{q}(t)dt} \tag{B.15}$$

The evaluation of the integrals in (B.15) depends on the specific pulse sequence, the CTP and the gradient shapes used. In what follows, a number of generalised expressions will be derived for several pulse sequences (monopolar, bipolar, convection compensated) with varying gradient shapes.

B.2 Monopolar gradient pulse sequence

Figure B.1 shows how the product of the functions $\mathrm{p}(t)$ and $\mathrm{G}(t)$ vary over time during a monopolar gradient pulse sequence. This function is expressed as:

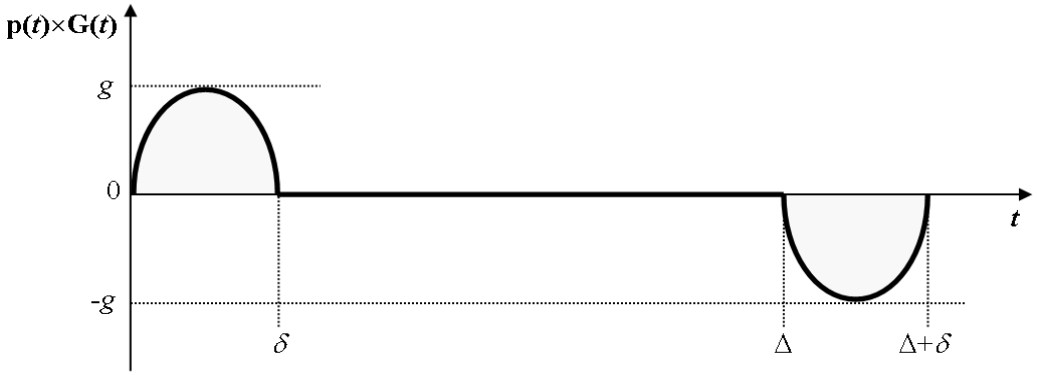

Figure B.1: The function $\mathrm{p}(t)\times\mathrm{G}(t)$ as a function of the time t (thick black line) for a monopolar gradient sequence.

$$\mathrm{p}(t)\mathrm{G}(t)=\begin{cases} g\,\mathrm{a}(t) & 0\le t\le\delta \\ 0 & \delta\le t\le\Delta \\ -g\,\mathrm{a}(t-\Delta) & \Delta\le t\le\Delta+\delta \end{cases} \tag{B.16}$$

With $a(t)$ the shape function of the gradient pulse. The function $\mathrm{q}(t)$ is then:

$$\mathrm{q}(t)=\begin{cases} \gamma g\,\mathrm{A}(t) & 0\le t\le\delta \\ \gamma g\,\mathrm{A}(\delta) & \delta\le t\le\Delta \\ \gamma g\,\mathrm{A}(\delta)-\gamma g\,\mathrm{A}(t-\Delta) & \Delta\le t\le\Delta+\delta \end{cases} \tag{B.17}$$

with:

$$\mathrm{A}(t)=\int_0^t a(t)\,dt \tag{B.18}$$

The squared of the function $\mathrm{q}(t)$ is:

$$\mathrm{q}^2(t)=\begin{cases} \gamma^2 g^2\,\mathrm{A}^2(t) & 0\le t\le\delta \\ \gamma^2 g^2\,\mathrm{A}^2(\delta) & \delta\le t\le\Delta \\ \gamma^2 g^2\left[\mathrm{A}^2(\delta)+\mathrm{A}^2(t-\Delta)-2\,\mathrm{A}(\delta)\,\mathrm{A}(t-\Delta)\right] & \Delta\le t\le\Delta+\delta \end{cases} \tag{B.19}$$

The integral to be evaluated to describe the effects of convection at the end of the monopolar pulse sequence is given by:

$$\begin{aligned} \int_0^{\Delta+\delta}\mathrm{q}(t)\,dt &= \gamma g\left[\int_0^{\delta}\mathrm{A}(t)\,dt+(\Delta-\delta)\,\mathrm{A}(\delta)+\delta\,\mathrm{A}(\delta)-\int_{\Delta}^{\Delta+\delta}\mathrm{A}(t-\Delta)\,dt\right] \\ &= \gamma g\Delta\,\mathrm{A}(\delta) \end{aligned} \tag{B.20}$$

The integral to be evaluated to describe the effects of diffusion at the end of the monopolar pulse sequence is given by:

$$\begin{aligned} \int_0^{\Delta+\delta}\mathrm{q}^2(t)\,dt &= \gamma^2 g^2\left[\int_0^{\delta}\mathrm{A}^2(t)\,dt+(\Delta-\delta)\,\mathrm{A}^2(\delta)+\delta\,\mathrm{A}^2(\delta)\right. \\ &\quad \left.+\int_{\Delta}^{\Delta+\delta}\mathrm{A}^2(t-\Delta)\,dt-2\,\mathrm{A}(\delta)\int_{\Delta}^{\Delta+\delta}\mathrm{A}(t-\Delta)\,dt\right] \\ &= \gamma^2 g^2\,\mathrm{A}^2(\delta)\left[\Delta+2\kappa-2\lambda\right] \end{aligned} \tag{B.21}$$

with:

$$\kappa = \frac{\int_0^{\delta} \mathrm{A}^2(t)\,dt}{\mathrm{A}^2(\delta)} \tag{B.22}$$

$$\lambda = \frac{\int_0^{\delta} \mathrm{A}(t)\,dt}{\mathrm{A}(\delta)} \tag{B.23}$$

B.3 Bipolar gradient pulse sequence

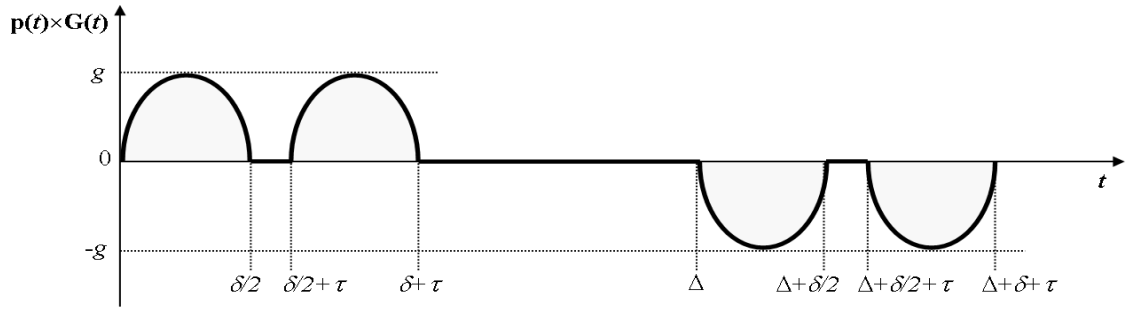

Figure B.2: The function $\mathrm{p}(t)\times\mathrm{G}(t)$ as a function of the time t (thick black line) for a bipolar gradient sequence.

Figure B.2 shows how the product of the functions $\mathrm{p}(t)$ and $\mathrm{G}(t)$ vary over time during a bipolar gradient pulse sequence. This function is expressed as:

$$\mathrm{p}(t)\mathrm{G}(t) = \begin{cases} g\,\mathrm{a}(t) & 0 \le t \le \delta/2 \\ 0 & \delta/2 \le t \le \delta/2+\tau \\ g\,\mathrm{a}(t-\delta/2-\tau) & \delta/2+\tau \le t \le \delta+\tau \\ 0 & \delta+\tau \le t \le \Delta \\ -g\,\mathrm{a}(t-\Delta) & \Delta \le t \le \Delta+\delta/2 \\ 0 & \Delta+\delta/2 \le t \le \Delta+\delta/2+\tau \\ -g\,\mathrm{a}(t-\Delta-\delta/2-\tau) & \Delta+\delta/2+\tau \le t \le \Delta+\delta+\tau \end{cases} \tag{B.24}$$

The function $q(t)$ is then:

$$\mathrm{q}(t)=\begin{cases}\gamma g\,\mathrm{A}(t) & 0\le t\le \delta/2\\ \gamma g\,\mathrm{A}(\delta/2) & \delta/2\le t\le \delta/2+\tau\\ \gamma g\left[\mathrm{A}(\delta/2)+\mathrm{A}(t-\delta/2-\tau)\right] & \delta/2+\tau\le t\le \delta+\tau\\ 2\gamma g\,\mathrm{A}(\delta/2) & \delta+\tau\le t\le \Delta\\ \gamma g\left[2\,\mathrm{A}(\delta/2)-\mathrm{A}(t-\Delta)\right] & \Delta\le t\le \Delta+\delta/2\\ \gamma g\,\mathrm{A}(\delta/2) & \Delta+\delta/2\le t\le \Delta+\delta/2+\tau\\ \gamma g\left[\mathrm{A}(\delta/2)-\mathrm{A}(t-\Delta-\delta/2-\tau)\right] & \Delta+\delta/2+\tau\le t\le \Delta+\delta+\tau\end{cases} \tag{B.25}$$

The squared of the function $q(t)$ is:

$$\mathrm{q}^2(t)=\begin{cases}\gamma^2 g^2\,\mathrm{A}^2(t) & 0\le t\le \delta/2\\ \gamma^2 g^2\,\mathrm{A}^2(\delta/2) & \delta/2+\tau\le t\le \delta+\tau\\ \gamma^2 g^2\left[\mathrm{A}^2(\delta/2)+\mathrm{A}^2(t-\delta/2-\tau)+2\,\mathrm{A}(\delta/2)\,\mathrm{A}(t-\delta/2-\tau)\right] & \delta/2+\tau\le t\le \delta+\tau\\ 4\gamma^2 g^2\,\mathrm{A}^2(\delta/2) & \delta+\tau\le t\le \Delta\\ \gamma^2 g^2\left[4\,\mathrm{A}^2(\delta/2)+\mathrm{A}^2(t-\Delta)-4\,\mathrm{A}(\delta/2)\,\mathrm{A}(t-\Delta)\right] & \Delta\le t\le \Delta+\delta/2\\ \gamma^2 g^2\,\mathrm{A}^2(\delta/2) & \Delta+\delta/2\le t\le \Delta+\delta/2+\tau\\ \gamma^2 g^2\left[\mathrm{A}^2(\delta/2)+\mathrm{A}^2(t-\Delta-\delta/2-\tau)-2\,\mathrm{A}(\delta/2)\,\mathrm{A}(t-\Delta-\delta/2-\tau)\right] & \Delta+\delta/2+\tau\le t\le \Delta+\delta+\tau\end{cases} \tag{B.26}$$

The integral to be evaluated to describe the effects of convection at the end of the bipolar pulse sequence is given by:

$$\begin{aligned}\int_0^{\Delta+\delta+\tau} \mathrm{q}(t)\,dt = \gamma g \Bigg[& \int_0^{\delta/2} \mathrm{A}(t)\,dt + \tau\,\mathrm{A}(\delta/2) + \frac{\delta}{2}\mathrm{A}(\delta/2) + \int_{\delta/2+\tau}^{\delta+\tau} \mathrm{A}(t-\delta/2-\tau)\,dt \\ & + 2(\Delta-\delta-\tau)\,\mathrm{A}(\delta/2) + \delta\,\mathrm{A}(\delta/2) - \int_{\Delta}^{\Delta+\delta/2} \mathrm{A}(t-\Delta)\,dt + \tau\,\mathrm{A}(\delta/2) \\ & + \frac{\delta}{2}\mathrm{A}(\delta/2) - \int_{\Delta+\delta/2+\tau}^{\Delta+\delta+\tau} \mathrm{A}(t-\Delta-\delta/2-\tau)\,dt \Bigg] \\ & = 2\gamma g \Delta\,\mathrm{A}(\delta/2)\end{aligned} \tag{B.27}$$

The result is exactly the same as found for monopolar gradients, given the fact that $\mathrm{A}(\delta)$ for monopolar gradients corresponds to $2\mathrm{A}(\delta/2)$ for bipolar gradients. The integral to be evaluated to describe the effects of diffusion at the end of the bipolar pulse sequence is given by:

$$\begin{aligned}\int_0^{\Delta+\delta+\tau} \mathrm{q}^2(t)\,dt = \gamma^2 g^2\,\mathrm{A}^2(\delta/2) \Bigg[& \kappa + \tau + \frac{\delta}{2} + \kappa + 2\lambda + 4(\Delta-\delta-\tau) \\ & 2\delta + \kappa - 4\lambda + \tau + \frac{\delta}{2} + \kappa - 2\lambda \Bigg] \\ & = \gamma^2 g^2\, 4\,\mathrm{A}^2(\delta/2) \left[\Delta + \kappa - \lambda - \frac{\delta}{4} - \frac{\tau}{2} \right]\end{aligned} \tag{B.28}$$

in which the notations κ and λ were already introduced:

$$\kappa = \frac{\int_0^{\delta/2} \mathrm{A}^2(t)\,dt}{\mathrm{A}^2(\delta/2)} \tag{B.29}$$

$$\lambda = \frac{\int_0^{\delta/2} \mathrm{A}(t)\,dt}{\mathrm{A}(\delta/2)} \tag{B.30}$$

B.4 Convection compensated pulse sequence

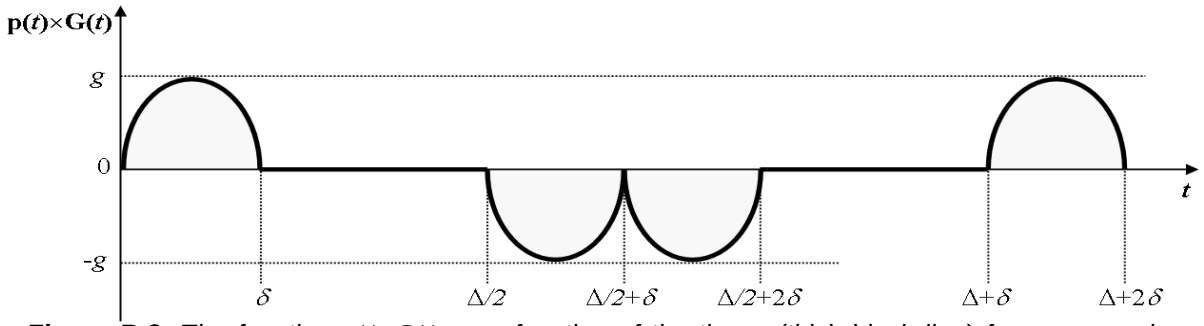

Figure B.3: The function $p(t)\times G(t)$ as a function of the time t (thick black line) for a monopolar convection compensated gradient sequence.

The convection compensated pulse sequence applying monopolar gradient pulses is shown in Figure B.3. As described in section 2.4.3, this sequence can be regarded as two monopolar non-convection compensated sequences placed after one another, but with opposite gradient strengths. As described in the same section, the two sequences cancel one another in term of the effects of convection. For the effects of diffusion, both sequences add up to each other, resulting in the following total value of the integral of the function $q^2(t)$, with κ and λ given by (B.22) and (B.23):

$$\begin{aligned}\int_0^{\Delta+2\delta} \mathrm{q}^2(t)\,dt &= \gamma^2 g^2 \mathrm{A}^2(\delta)\left[\frac{\Delta}{2}+2\kappa-2\lambda\right]+\gamma^2 g^2 \mathrm{A}^2(\delta)\left[\frac{\Delta}{2}+2\kappa-2\lambda\right] \\ &= \gamma^2 g^2 \mathrm{A}^2(\delta)\left[\Delta+4\kappa-4\lambda\right]\end{aligned} \tag{B.31}$$

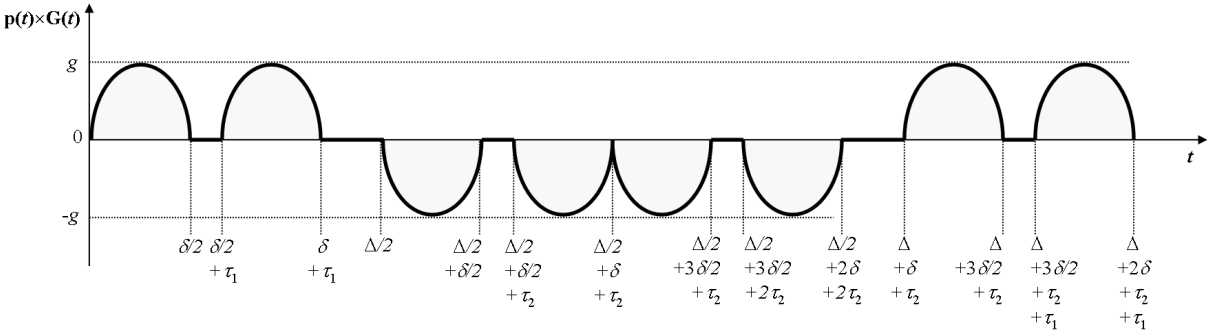

Figure B.4: The function $p(t)\times G(t)$ as a function of the time t (thick black line) for a bipolar convection compensated gradient sequence.

The convection compensated pulse sequence applying bipolar gradient pulses is shown in Figure B.4. Note the separately defined values of τ_1 and τ_2, which is done because in practice these have often slightly different values in standard pulse sequences. Similarly, the integral of the function $q^2(t)$ is the sum of the effects of each bipolar STE sequence separately, with κ and λ in this case given by (B.29) and (B.30):

$$\int_0^{\Delta+2\delta} \mathrm{q}^2(t)\,dt = \gamma^2 g^2 4\mathrm{A}^2(\delta/2)\left[\frac{\Delta}{2}+\kappa-\lambda-\frac{\delta}{4}-\frac{\tau_1}{2}\right]+\gamma^2 g^2 4\mathrm{A}^2(\delta/2)\left[\frac{\Delta}{2}+\kappa-\lambda-\frac{\delta}{4}-\frac{\tau_2}{2}\right]$$
$$= \gamma^2 g^2 4\mathrm{A}^2(\delta/2)\left[\Delta+2\kappa-2\lambda-\frac{\delta}{2}-\frac{\tau_1+\tau_2}{2}\right] \quad \text{(B.32)}$$

B.5 Gradient shapes

The three most common gradient shapes, rectangle, sine and smoothed rectangle, are illustrated in Figure 2.7. The functional forms of each of these shapes for either monopolar or bipolar gradient sequences are given here.

Monopolar

Rectangular (B.33)

$$a(t)=1 \quad 0\le t\le\delta$$

Sine (B.34)

$$a(t)=\sin\left(\frac{\pi}{\delta}t\right) \quad 0\le t\le\delta$$

Smoothed Rectangle (B.35)

$$a(t)=\begin{cases}\sin^2\left(\frac{5\pi}{\delta}t\right) & 0\le t\le\frac{\delta}{10}\\ 1 & \frac{\delta}{10}\le t\le\frac{9\delta}{10}\\ \cos^2\left(\frac{5\pi}{\delta}\left(t-\frac{9}{10}\delta\right)\right) & \frac{9\delta}{10}\le t\le\delta\end{cases}$$

Bipolar

Rectangular (B.36)

$$a(t)=1 \quad 0\le t\le\delta/2$$

Sine (B.37)

$$a(t)=\sin\left(\frac{2\pi}{\delta}t\right) \quad 0\le t\le\delta/2$$

Smoothed Rectangle (B.38)

$$a(t)=\begin{cases}\sin^2\left(\frac{10\pi}{\delta}t\right) & 0\le t\le\frac{\delta}{20}\\ 1 & \frac{\delta}{20}\le t\le\frac{9\delta}{20}\\ \cos^2\left(\frac{10\pi}{\delta}\left(t-\frac{9}{20}\delta\right)\right) & \frac{9\delta}{20}\le t\le\frac{\delta}{2}\end{cases}$$

B.6 Overview of the different forms of the Stejskal-Tanner equation

The resulting from of the Stesjkal-Tanner equation is found by inserting the expression of the integral over the squared of the function $\mathrm{q}(t)$ into equation (B.15). The general expression of the monopolar sequences (including convection compensated) is given by:

$$I = I_0 e^{-D_t\gamma^2\delta^2\varsigma^2 g^2(\Delta-b\delta)} \quad \text{(B.39)}$$

For bipolar non-convection compensated sequences this is:

$$I = I_0 e^{-D_t \gamma^2 \delta^2 \varsigma^2 g^2 \left(\Delta - b\delta - \frac{\tau}{2}\right)} \tag{B.40}$$

and for bipolar convection compensated sequences:

$$I = I_0 e^{-D_t \gamma^2 \delta^2 \varsigma^2 g^2 \left(\Delta - b\delta - \frac{\tau_1 + \tau_2}{2}\right)} \tag{B.41}$$

The factor ς^2 is a shape factor depending only on the gradient shape, while b is a constant that depends on both the gradient shape and the pulse sequence used. Their values for each gradient shape/pulse sequence combination are listed in Table B.1.

Table B.1: Overview of gradient shape factors ς^2 and coefficients b

Gradient shape	ς^2	b			
		Non-convection monopolar	Non-convection bipolar	Convection monopolar	Convection bipolar
Rectangular	1	$\frac{1}{3}$	$\frac{1}{3}$	$\frac{2}{3}$	$\frac{2}{3}$
Sine	$\frac{4}{\pi^2}$	$\frac{1}{4}$	$\frac{5}{16}$	$\frac{1}{2}$	$\frac{5}{8}$
Smoothed Rectangular	$\frac{81}{100}$	$\frac{1484\pi^2 - 207}{4860\pi^2}$	$\frac{6344\pi^2 - 207}{19440\pi^2}$	$\frac{1484\pi^2 - 207}{2430\pi^2}$	$\frac{6344\pi^2 - 207}{9720\pi^2}$

C

Error analysis by Monte Carlo

All Monte Carlo analyses were performed in MATLAB version 7.5 (The MathWorks Inc.) using in house written scripts. In a first step, a number of standard normally distributed numbers need to be generated. For this, the polar Marsaglia method is used to obtain these from the standard MATLAB random number generator, which generates uniformly distributed numbers. Two numbers u_1 and u_2 uniformly distributed between –1 and 1 are continuously drawn until they agree to the following condition:

$$u_1^2 + u_2^2 < 1 \tag{C.1}$$

From these two numbers, a standard normally distributed random number n_1 can be obtained:

$$n_1 = u_1 \sqrt{-2 \frac{\ln\left(u_1^2 + u_2^2\right)}{u_1^2 + u_2^2}} \tag{C.2}$$

As many random numbers are generated as there are data points. In the case of translational diffusion analysis, these numbers are multiplied with the residual sum of square difference between the data points and the fitted curve. They are subsequently added to the data points, effectively creating a new, simulated dataset. The fitting procedure is then performed again on this dataset, providing new fitted values for the diffusion coefficient D_t and the pre-exponential factor I_0. This whole procedure is repeated many times (see main text for each individual case), and the errors on the fitted parameters are then calculated as the standard deviations of all

simulated D_t and I_0 parameters. The 95% errors are calculated as 1.96 times the standard deviation, assuming a Gaussian distribution of the simulated parameters.

For the Monte Carlo analysis on the anisotropic relaxation study (section 7.3.3.3), the data points already have an error available. The standard normally distributed numbers are therefore multiplied with these errors and subsequently added to the respective data point. From these, errors were calculated on the rotational diffusion coefficients, dimensions and XH vector orientations, as described in Chapter 7.

D

Derivation of the expressions for the relaxation rate constants

The derivation of the expressions of the relaxation rate constants in terms of the spectral density functions is done using equation (3.45) and the expressions of the Hamiltonians for both dipolar and CSA relaxation mechanisms in terms of random functions and base operators. The relaxation rate constants are a linear combination of values of the spectral density function at several frequencies. The contribution of each of these values will be derived here for the dipolar contribution to the transverse autorelaxation rate constant of spin I (represented by the operator I^{+}) to illustrate how this is done. Taking into account the considerations of section 3.3.4 concerning the spectral density function, the expression that needs to be evaluated is given by:

$$R_{2,I}^{DD} = \frac{K_{DD}^2}{2} \sum_{m=-2}^{2} \sum_{p} \frac{\left\langle \mathrm{I}^{+} \left| [\mathrm{B}_p^{-m}, [\mathrm{B}_p^{m}, \mathrm{I}^{+}]] \right\rangle}{\left\langle \mathrm{I}^{+} \left| \mathrm{I}^{+} \right\rangle \right.} (-1)^{m} a_p^{m} a_p^{-m} \mathrm{J}\left(\omega_p^{m}\right) \qquad \text{(D.1)}$$

The operators B_p^m and the coefficients a_p^m are given in Table 3.2. For every combination of m and p that is given in this table, the double commutator needs to be evaluated. Expressions for the base operators are found in section 3.3.1. Some handy rules can be derived for these expressions (with X denoting any operator):

$$[\mathrm{I}^-,\mathrm{I}^+] = -2\mathrm{I}_z \quad [\mathrm{S}^-,\mathrm{S}^+] = -2\mathrm{S}_z \tag{D.2}$$

$$[\mathrm{I}^-,\mathrm{I}_z] = \mathrm{I}^- \quad [\mathrm{S}^-,\mathrm{S}_z] = \mathrm{S}^- \tag{D.3}$$

$$[\mathrm{I}^+,\mathrm{I}_z] = -\mathrm{I}^+ \quad [\mathrm{S}^+,\mathrm{S}_z] = -\mathrm{S}^+ \tag{D.4}$$

$$\mathrm{I}_z\mathrm{I}_z = \mathrm{S}_z\mathrm{S}_z = \frac{1}{4}\mathrm{E} \tag{D.5}$$

$$\mathrm{EX} = \mathrm{X} \tag{D.6}$$

<u>$m = 0$, $p = -1$</u>

$$\begin{aligned}[\mathrm{I}^+\mathrm{S}^-,[\mathrm{I}^-\mathrm{S}^+,\mathrm{I}^+]] &= [\mathrm{I}^+\mathrm{S}^-,[\mathrm{I}^-,\mathrm{I}^+]\mathrm{S}^+] \\ &= -2[\mathrm{I}^+\mathrm{S}^-,\mathrm{I}_z\mathrm{S}^+] \\ &= \mathrm{I}^+\end{aligned} \tag{D.7}$$

<u>$m = 0$, $p = 0$</u>

$$\begin{aligned}[\mathrm{I}_z\mathrm{S}_z,[\mathrm{I}_z\mathrm{S}_z,\mathrm{I}^+]] &= [\mathrm{I}_z\mathrm{S}_z,[\mathrm{I}_z,\mathrm{I}^+]\mathrm{S}_z] \\ &= [\mathrm{I}_z\mathrm{S}_z,\mathrm{I}^+\mathrm{S}_z] \\ &= [\mathrm{I}_z,\mathrm{I}^+]\mathrm{S}_z\mathrm{S}_z \\ &= \frac{1}{4}\mathrm{I}^+\mathrm{E} \\ &= \frac{1}{4}\mathrm{I}^+\end{aligned} \tag{D.8}$$

<u>$m = 0$, $p = +1$</u>

$$\begin{aligned}[\mathrm{I}^-\mathrm{S}^+,[\mathrm{I}^+\mathrm{S}^-,\mathrm{I}^+]] &= [\mathrm{I}^-\mathrm{S}^+,[\mathrm{I}^+,\mathrm{I}^+]\mathrm{S}^-] \\ &= 0\end{aligned} \tag{D.9}$$

<u>$m = -1$, $p = 0$</u>

$$\begin{aligned}[\mathrm{I}_z\mathrm{S}^+,[\mathrm{I}_z\mathrm{S}^-,\mathrm{I}^+]] &= [\mathrm{I}_z\mathrm{S}^+,[\mathrm{I}_z,\mathrm{I}^+]\mathrm{S}^-] \\ &= [\mathrm{I}_z\mathrm{S}^+,\mathrm{I}^+\mathrm{S}^-] \\ &= \frac{1}{2}\mathrm{I}^+\end{aligned} \tag{D.10}$$

$\underline{m = -1,\ p = +1}$

$$\begin{aligned}[I^+S_z,[I^-S_z,I^+]] &= [I^+S_z,[I^-,I^+]S_z] \\ &= -2[I^+S_z,I_zS_z] \\ &= -2S_zS_z[I^+,I_z] \\ &= 2\frac{1}{4}E\,I^+ \\ &= \frac{1}{2}I^+\end{aligned} \tag{D.11}$$

$\underline{m = +1,\ p = 0}$

$$\begin{aligned}[I_zS^-,[I_zS^+,I^+]] &= [I_zS^-,[I_z,I^+]S^+] \\ &= [I_zS^-,I^+S^+] \\ &= \frac{1}{2}I^+\end{aligned} \tag{D.12}$$

$\underline{m = +1,\ p = +1}$

$$\begin{aligned}[I^-S_z,[I^+S_z,I^+]] &= [I^-S_z,[I^+,I^+]S_z] \\ &= 0\end{aligned} \tag{D.13}$$

$\underline{m = -2,\ p = 0}$

$$\begin{aligned}[I^+S^+,[I^-S^-,I^+]] &= [I^+S^+,[I^-,I^+]S^-] \\ &= -2[I^+S^+,I_zS^-] \\ &= I^+\end{aligned} \tag{D.14}$$

$\underline{m = +2,\ p = 0}$

$$\begin{aligned}[I^-S^-,[I^+S^+,I^+]] &= [I^-S^-,[I^+,I^+]S^+] \\ &= 0\end{aligned} \tag{D.15}$$

In the next step, these operators need to be left-bracketed with $\langle I^+|$. Every result from above is proportional to I^+, so the following expression only has to be evaluated once:

$$\begin{aligned}\left\langle I^+ \middle| I^+ \right\rangle &= \left\langle I^- I^+ \right\rangle \\ &= \left\langle |\beta\alpha\rangle\langle\beta\alpha| + |\beta\beta\rangle\langle\beta\beta| \right\rangle \\ &= \langle\alpha\alpha|\beta\alpha\rangle\langle\beta\alpha|\alpha\alpha\rangle + \langle\alpha\alpha|\beta\beta\rangle\langle\beta\beta|\alpha\alpha\rangle + \langle\alpha\beta|\beta\alpha\rangle\langle\beta\alpha|\alpha\beta\rangle + \langle\alpha\beta|\beta\beta\rangle\langle\beta\beta|\alpha\beta\rangle \\ &\quad + \langle\beta\alpha|\beta\alpha\rangle\langle\beta\alpha|\beta\alpha\rangle + \langle\beta\alpha|\beta\beta\rangle\langle\beta\beta|\beta\alpha\rangle + \langle\beta\beta|\beta\alpha\rangle\langle\beta\alpha|\beta\beta\rangle + \langle\beta\beta|\beta\beta\rangle\langle\beta\beta|\beta\beta\rangle \\ &= 0+0+0+0+1+0+0+1 \\ &= 2\end{aligned} \tag{D.16}$$

This is also the value of the normalisation factor in the denominator of (3.45). For every combination of m and p for which the result was not zero, the frequency of the base operator can be identified and the coefficients from Table 3.2 are gathered.

$\underline{m = 0, p = -1}$

$$\left|\omega_{-1}^{0}\right| = \left|\omega_I - \omega_S\right| \qquad (-1)^0 a_{-1}^0 a_{-1}^0 = \frac{1}{4} \tag{D.17}$$

$\underline{m = 0, p = 0}$

$$\left|\omega_{0}^{0}\right| = 0 \qquad (-1)^0 a_0^0 a_0^0 = 4 \tag{D.18}$$

$\underline{m = -1, p = 0}$

$$\left|\omega_{0}^{-1}\right| = \left|\omega_S\right| \qquad (-1)^{-1} a_0^{-1} a_0^1 = \frac{3}{2} \tag{D.19}$$

$\underline{m = -1, p = +1}$

$$\left|\omega_{1}^{-1}\right| = \left|\omega_I\right| \qquad (-1)^{-1} a_1^{-1} a_1^1 = \frac{3}{2} \tag{D.20}$$

$\underline{m = +1, p = 0}$

$$\left|\omega_{0}^{1}\right| = \left|\omega_S\right| \qquad (-1)^{1} a_0^{1} a_0^{-1} = \frac{3}{2} \tag{D.21}$$

$\underline{m = -2, p = 0}$

$$\left|\omega_{0}^{-2}\right| = \left|\omega_I + \omega_S\right| \qquad (-1)^{-2} a_0^{-2} a_0^2 = \frac{3}{2} \tag{D.22}$$

Combining all these results into equation (3.45) provides the final result:

$$\begin{aligned} R_{2,I}^{DD} &= \frac{K_{DD}^2}{2}\left[\frac{1}{4}\mathrm{J}(\omega_I - \omega_S) + \mathrm{J}(0) + \frac{3}{4}\mathrm{J}(\omega_S) + \frac{3}{4}\mathrm{J}(\omega_I) + \frac{3}{4}\mathrm{J}(\omega_S) + \frac{3}{2}\mathrm{J}(\omega_I + \omega_S)\right] \\ &= \frac{K_{DD}^2}{8}\left[4\,\mathrm{J}(0) + \mathrm{J}(\omega_I - \omega_S) + 3\,\mathrm{J}(\omega_I) + 6\,\mathrm{J}(\omega_S) + 6\,\mathrm{J}(\omega_I + \omega_S)\right] \end{aligned} \tag{D.23}$$

E

Pseudodesmin A spectra, chemical shift assignments and scalar couplings

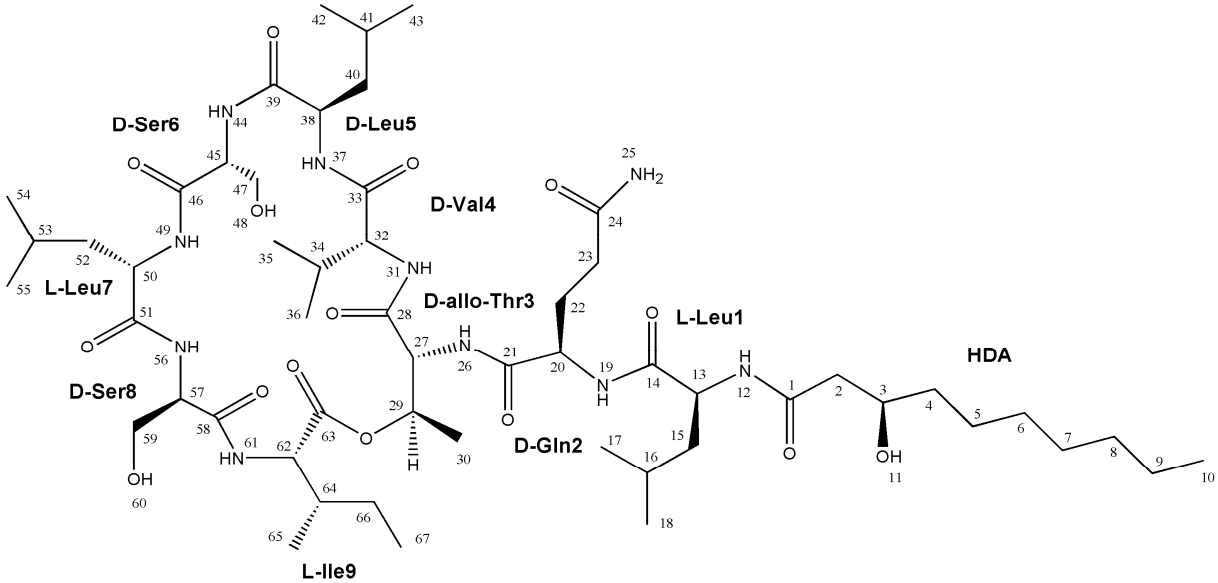

Figure E.1: The chemical structure of pseudodesmin A, with number labelling for the chemical shift assignment tables.

E.1 Acetonitrile

Table E.1: Chemical shift assignments and ^{1}H-^{1}H scalar couplings of pseudodesmin A in acetonitrile solution (298.0 K, 16.4 T)

		^{1}H δ [ppm]	^{13}C δ [ppm]	^{15}N δ [ppm]
HDA				
	CO 1		175.27	
	$CH_2\alpha$ 2	2.34 / 2.43	44.81	
	CHβ 3	3.97	69.53	
	$CH_2\gamma$ 4	1.47	38.27	
	$CH_2\delta$ 5	1.31 / 1.41	26.36	
	$CH_2\varepsilon$ 6	1.29	30.20	
	$CH_2\zeta$ 7	1.29	30.20	
	$CH_2\eta$ 8	1.27	32.63	
	$CH_2\theta$ 9	1.29	23.44	
	$CH_3\iota$ 10	0.88	14.44	
	OH 11	4.40		
Leu1				
$^{3}J_{HNH\alpha}$ 5.67 Hz	NH 12	7.73		-253.87
	CHα 13	3.87	53.92	
	CO 14		175.34	
	$CH_2\beta$ 15	1.65 / 1.74	39.46	
	CHγ 16	1.67	25.46	
	$CH_3\delta$ 17	0.90	22.16	
	$CH_3\delta$ 18	0.94	23.21	
Gln2				
$^{3}J_{HNH\alpha}$ 3.99 Hz	NH 19	8.76		-260.90
	CHα 20	3.98	57.58	
	CO 21		176.63	
	$CH_2\beta$ 22	2.02	26.35	
	$CH_2\gamma$ 23	2.38	32.01	
	COδ 24		176.15	
	NH_2 25	5.81 / 6.36		-275.54
Thr3				
$^{3}J_{HNH\alpha}$ 7.45 Hz	NH 26	8.15		-266.17
$^{3}J_{H\alpha H\beta}$ 10.71 Hz	CHα 27	3.99	61.77	
	CO 28		174.33	
	CHβ 29	5.33	70.33	
	$CH_3\gamma$ 30	1.30	18.58	

Table E.1: Chemical shift assignments and ^{1}H-^{1}H scalar couplings of pseudodesmin A in acetonitrile solution (298.0 K, 16.4 T) (*continued*)

		^{1}H δ [ppm]	^{13}C δ [ppm]	^{15}N δ [ppm]
Val4				
$^{3}J_{HNH\alpha}$ 6.30 Hz	NH 31	7.33		-259.73
	CHα 32	3.49	65.08	
	CO 33		174.63	
	CHβ 34	2.17	30.02	
	CH_3γ 35	0.92	19.56	
	CH_3γ 36	0.95	21.12	
Leu5				
$^{3}J_{HNH\alpha}$ 4.25 Hz	NH 37	7.72		-266.48
	CHα 38	3.97	55.74	
	CO 39		173.62	
	CH_2β 40	1.51 / 1.66	40.71	
	CHγ 41	1.77	25.53	
	CH_3δ 42	0.87	23.36	
	CH_3δ 43	0.88	21.34	
Ser6				
$^{3}J_{HNH\alpha}$ 8.47 Hz	NH 44	7.11		-276.91
	CHα 45	4.32	56.45	
	CO 46		171.93	
	CH_2β 47	3.81 / 4.15	64.80	
	OHγ 48	4.98		
Leu7				
$^{3}J_{HNH\alpha}$ 6.53 Hz	NH 49	7.10		-260.63
	CHα 50	4.13	54.90	
	CO 51		173.80	
	CH_2β 52	1.58 / 1.88	42.11	
	CHγ 53	1.89	25.55	
	CH_3δ 54	0.90	21.42	
	CH_3δ 55	0.99	23.53	
Ser8				
$^{3}J_{HNH\alpha}$ 9.10 Hz	NH 56	7.94		-273.98
	CHα 57	4.43	57.02	
	CO 58		171.86	
	CH_2β 59	3.66 / 3.86	63.25	
	OHγ 60	3.80		
Ile9				
$^{3}J_{HNH\alpha}$ 10.70 Hz	NH 61	6.68		-270.70
	CHα 62	4.56	57.17	
	CO 63		170.12	
	CHβ 64	1.97	36.97	
	CH_3γ 65	0.82	16.28	
	CH_2γ 66	0.97 / 1.15	25.31	
	CH_3δ 67	0.86	12.36	

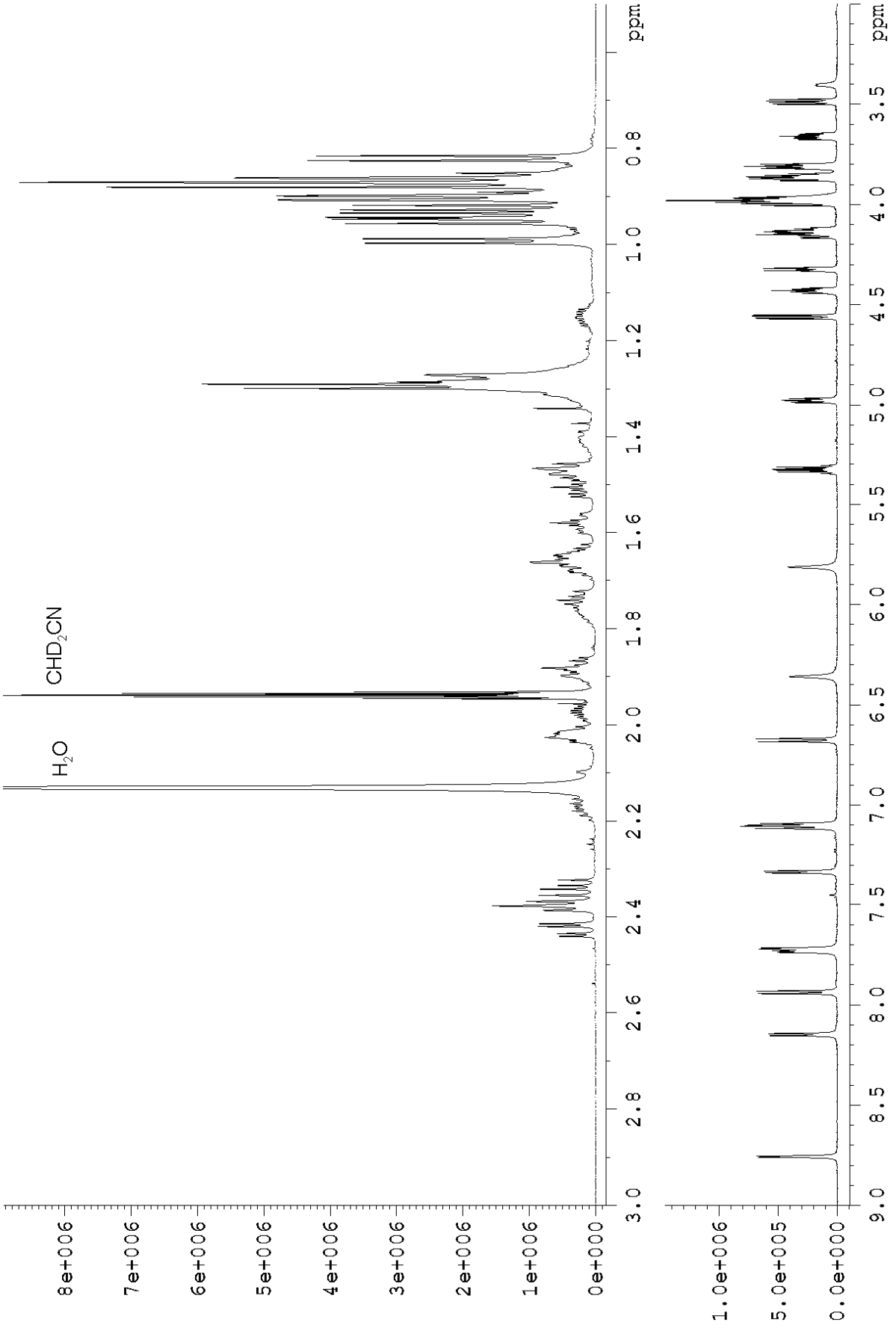

Figure E.2: 1D ^{1}H spectrum of pseudodesmin A in acetonitrile solution, recorded at 16.4 T, 298.0 K.

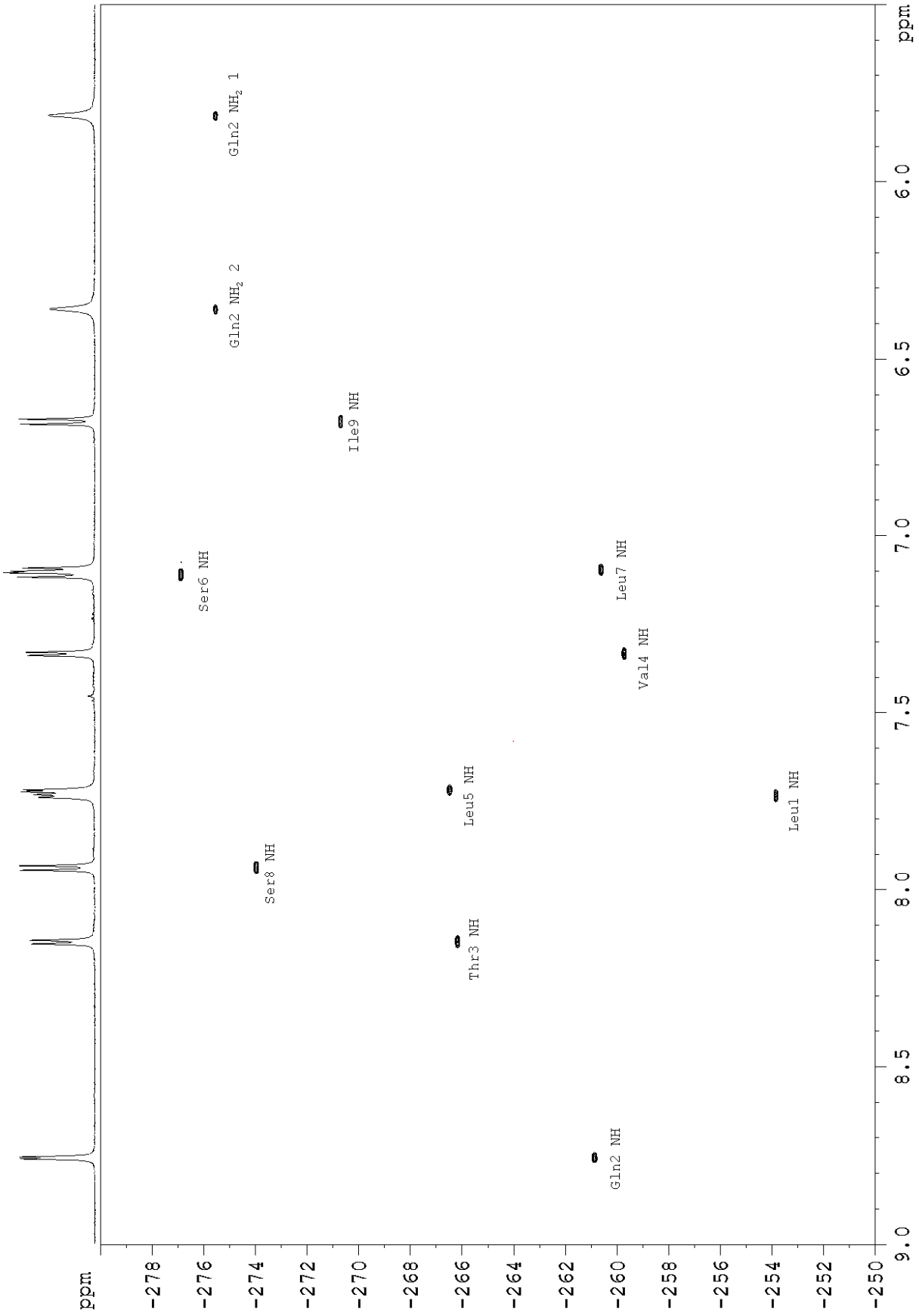

Figure E.3: 2D ^{1}H-^{15}N HSQC spectrum of pseudodesmin A in acetonitrile solution, recorded at 16.4 T, 298.0 K.

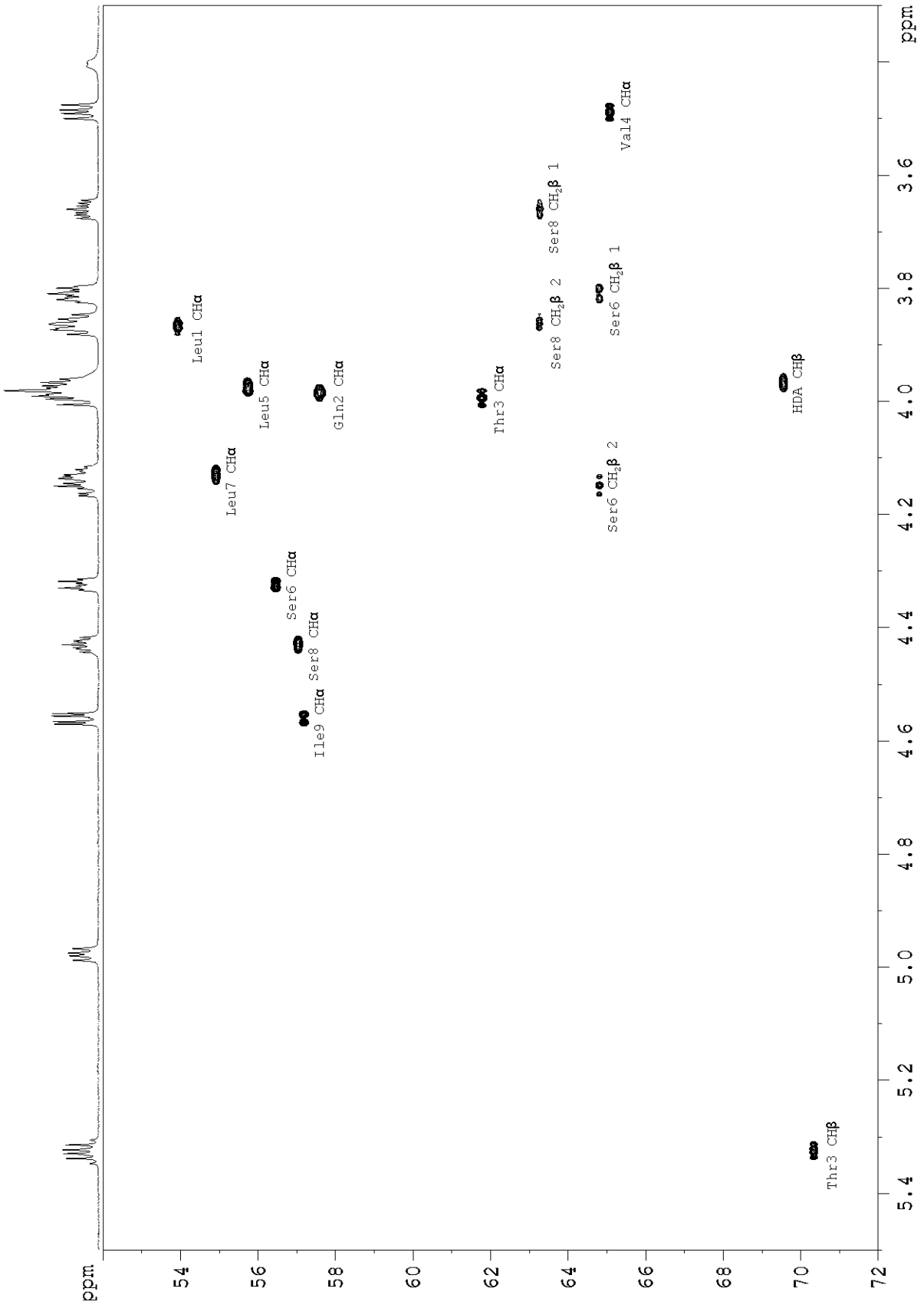

Figure E.4a: 2D ^{1}H-^{13}C HSQC spectrum of pseudodesmin A in acetonitrile solution, recorded at 16.4 T, 298.0 K, CH^{α} region.

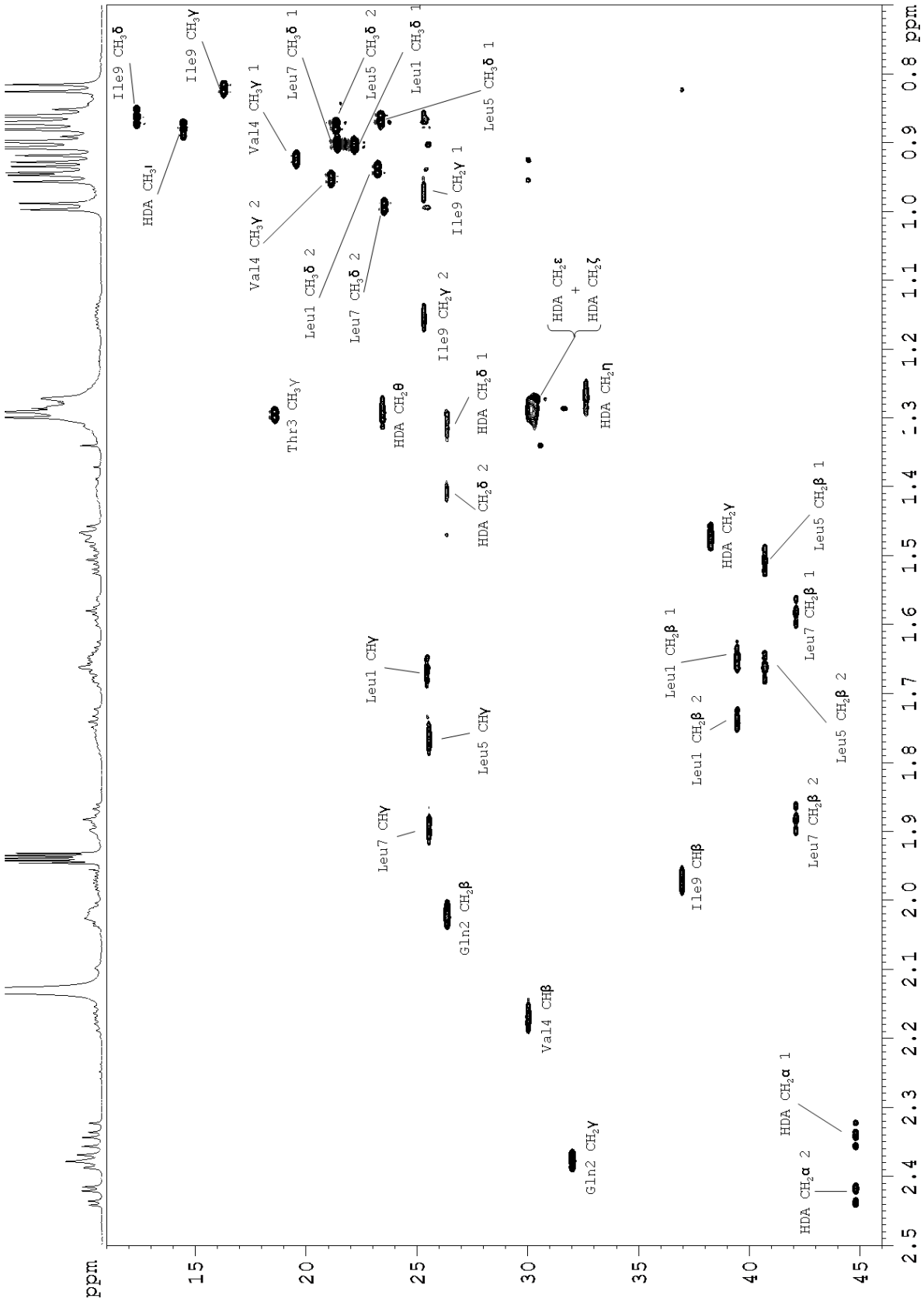

Figure E.4b: 2D ^{1}H-^{13}C HSQC spectrum of pseudodesmin A in acetonitrile solution, recorded at 16.4 T, 298.0 K, methylene and methyl regions.

E.2 DMSO

Table E.2: Chemical shift assignments of pseudodesmin A in DMSO solution (298.0 K, 11.7 T)

	^{1}H δ [ppm]	^{13}C δ [ppm]	^{15}N δ [ppm]
HDA			
CO 1		172.08	
$CH_2\alpha$ 2	2.27	43.30	
CHβ 3	3.85	67.41	
$CH_2\gamma$ 4	1.36	37.03	
$CH_2\delta$ 5	1.24 / 1.36	24.88	
$CH_2\varepsilon$ 6	1.23	28.79	
$CH_2\zeta$ 7	1.23	28.79	
$CH_2\eta$ 8	1.23	31.11	
$CH_2\theta$ 9	1.26	21.96	
$CH_3\iota$ 10	0.85	13.80	
OH 11	4.59		
Leu1			
NH 12	8.31		-259.59
CHα 13	4.14	51.81	
CO 14		173.41	
$CH_2\beta$ 15	1.49	39.82	
CHγ 16	1.59	24.01	
$CH_3\delta$ 17	0.86	21.89	
$CH_3\delta$ 18	0.90	22.57	
Gln2			
NH 19	8.65		-253.24
CHα 20	4.01	54.05	
CO 21		172.95	
$CH_2\beta$ 22	1.83 / 1.90	26.61	
$CH_2\gamma$ 23	2.16	31.18	
COδ 24		173.27	
NH_2 25	6.79 / 7.26		-272.15
Thr3			
NH 26	8.29		-267.23
CHα 27	4.25	58.28	
CO 28		ND	
CHβ 29	5.16	68.65	
$CH_3\gamma$ 30	1.18	17.27	
Val4			
NH 31	7.86		-262.11
CHα 32	3.81	60.27	
CO 33		170.66	
CHβ 34	2.06	29.85	
$CH_3\gamma$ 35	0.81	19.06	
$CH_3\gamma$ 36	0.81	18.47	
Leu5			
NH 37	7.39		-265.50
CHα 38	4.28	51.89	
CO 39		ND	
$CH_2\beta$ 40	1.43 / 1.67	39.77	
CHγ 41	1.70	23.91	
$CH_3\delta$ 42	0.84	20.53	
$CH_3\delta$ 43	0.89	22.94	
Ser6			
NH 44	8.19		-269.89
CHα 45	4.07	56.70	
CO 46		170.04	
$CH_2\beta$ 47	3.68 / 3.77	61.27	
OHγ 48	5.03		
Leu7			
NH 49	7.75		-260.71
CHα 50	4.24	50.98	
CO 51		ND	
$CH_2\beta$ 52	1.60	39.35	
CHγ 53	1.70	23.91	
$CH_3\delta$ 54	0.82	20.80	
$CH_3\delta$ 55	0.90	23.08	
Ser8			
NH 56	7.67		-270.52
CHα 57	4.29	56.87	
CO 58		170.21	
$CH_2\beta$ 59	3.59 / 3.72	61.60	
OHγ 60	4.83		
Ile9			
NH 61	7.26		-268.77
CHα 62	ND	ND	
CO 63		168.88	
CHβ 64	1.62	35.60	
$CH_3\gamma$ 65	0.69	14.84	
$CH_2\gamma$ 66	0.90 / 1.27	24.55	
$CH_3\delta$ 67	0.75	11.24	

ND = not determined; ^{15}N assignments at 323.0 K and 16.4 T.

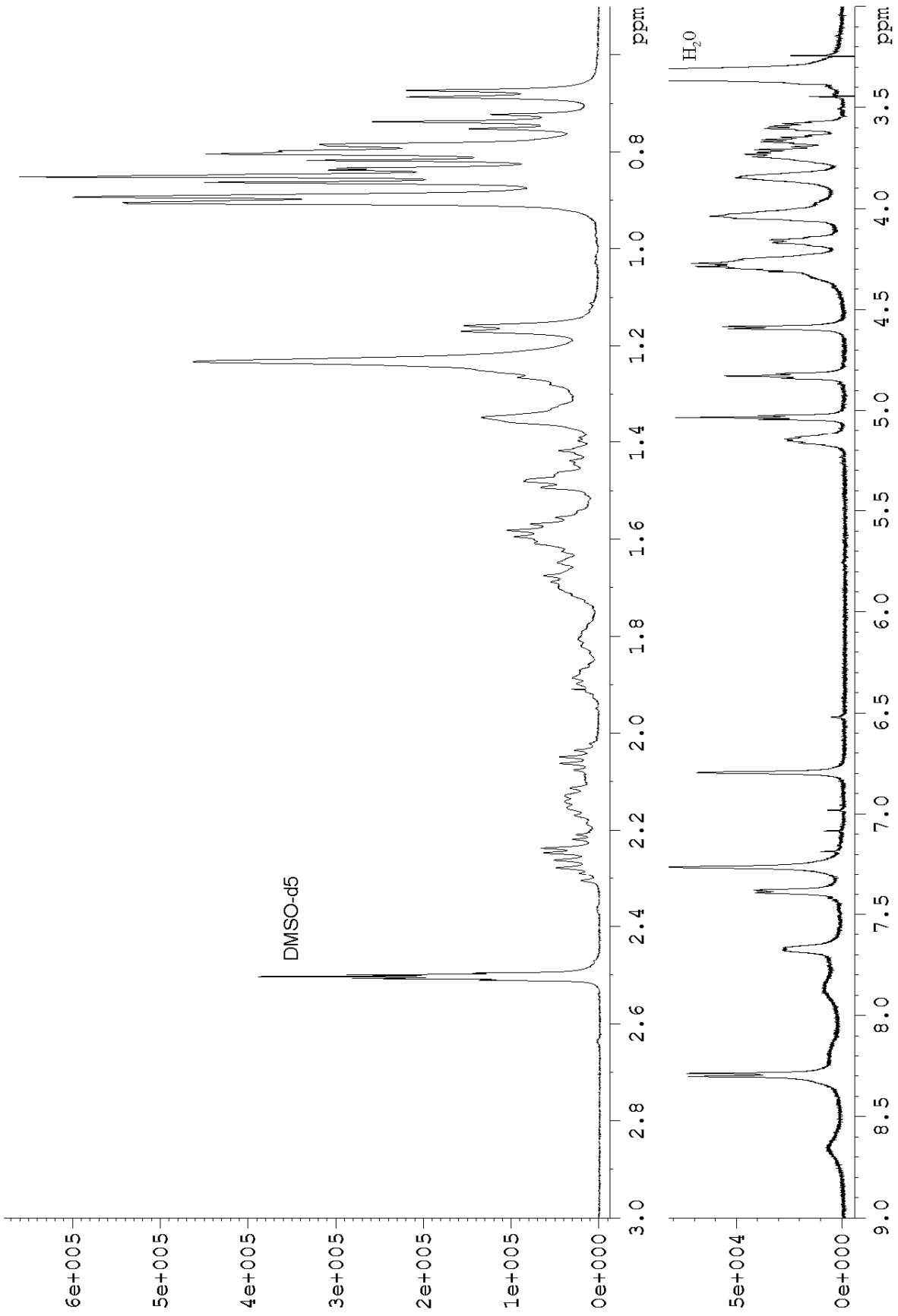

Figure E.5: 1D ^{1}H spectrum of pseudodesmin A in DMSO solution, recorded at 11.7 T, 298.0 K.

E.3 Chloroform

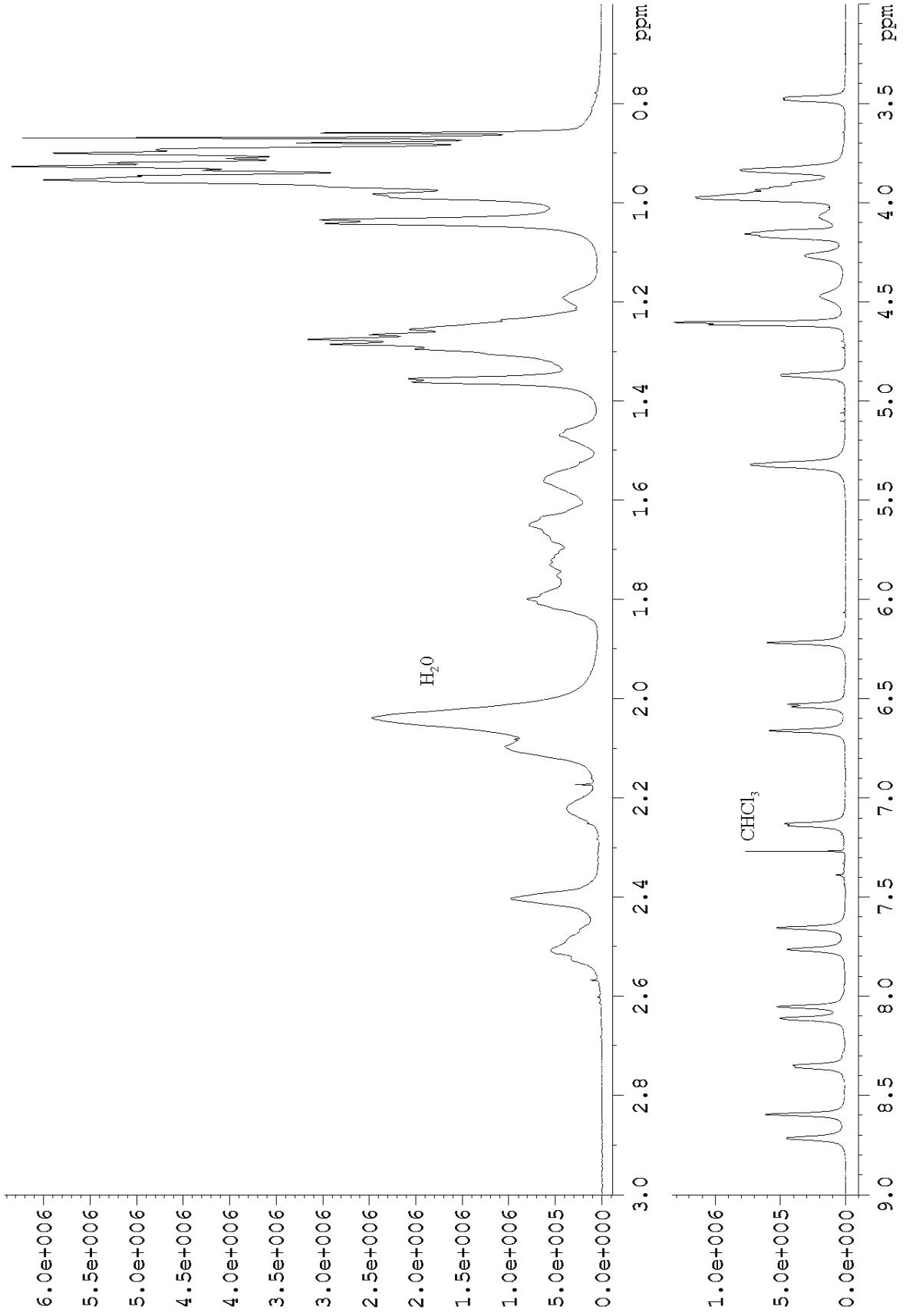

Figure E.6: 1D ^{1}H spectrum of pseudodesmin A in chloroform solution, recorded at 16.4 T, 25.0℃, ca 20 mM.

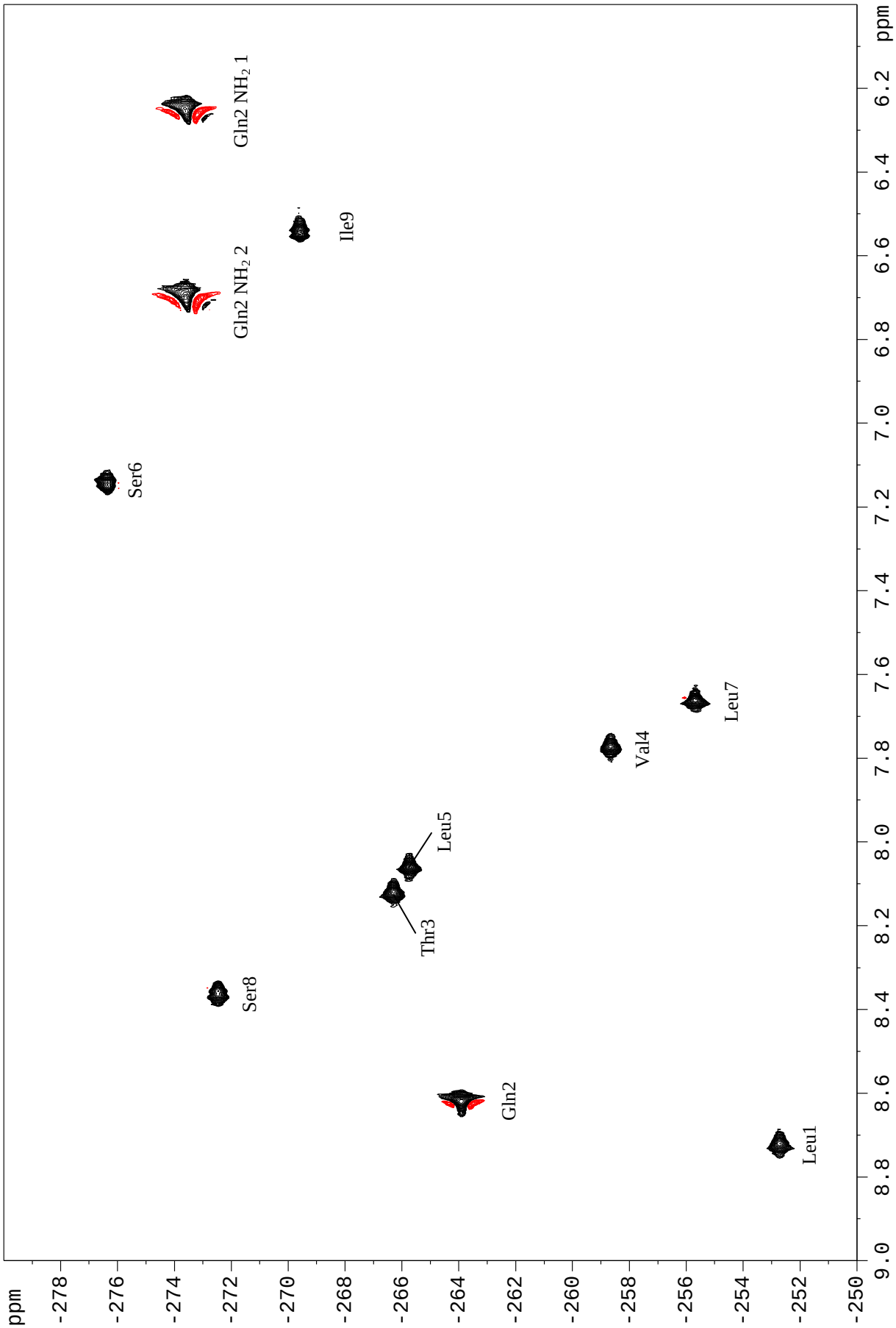

Figure E.7: 2D ^{1}H-^{15}N HSQC spectrum of pseudodesmin A in chloroform solution, recorded at 16.4 T, 25.0℃.

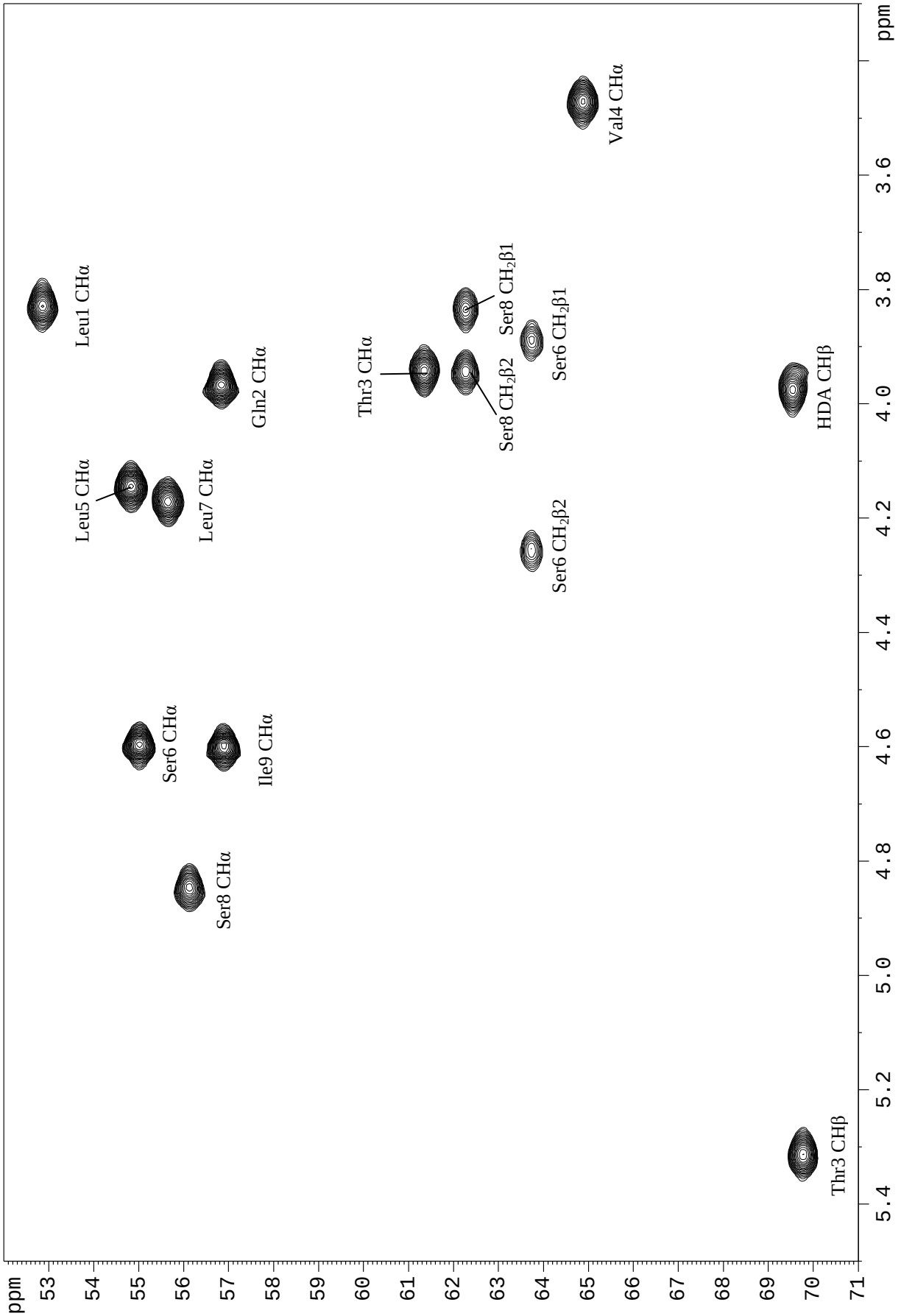

Figure E.8a: 2D ^{1}H-^{13}C HSQC spectrum of pseudodesmin A in chloroform solution, recorded at 16.4 T, 25.0℃, CH^{α} region.

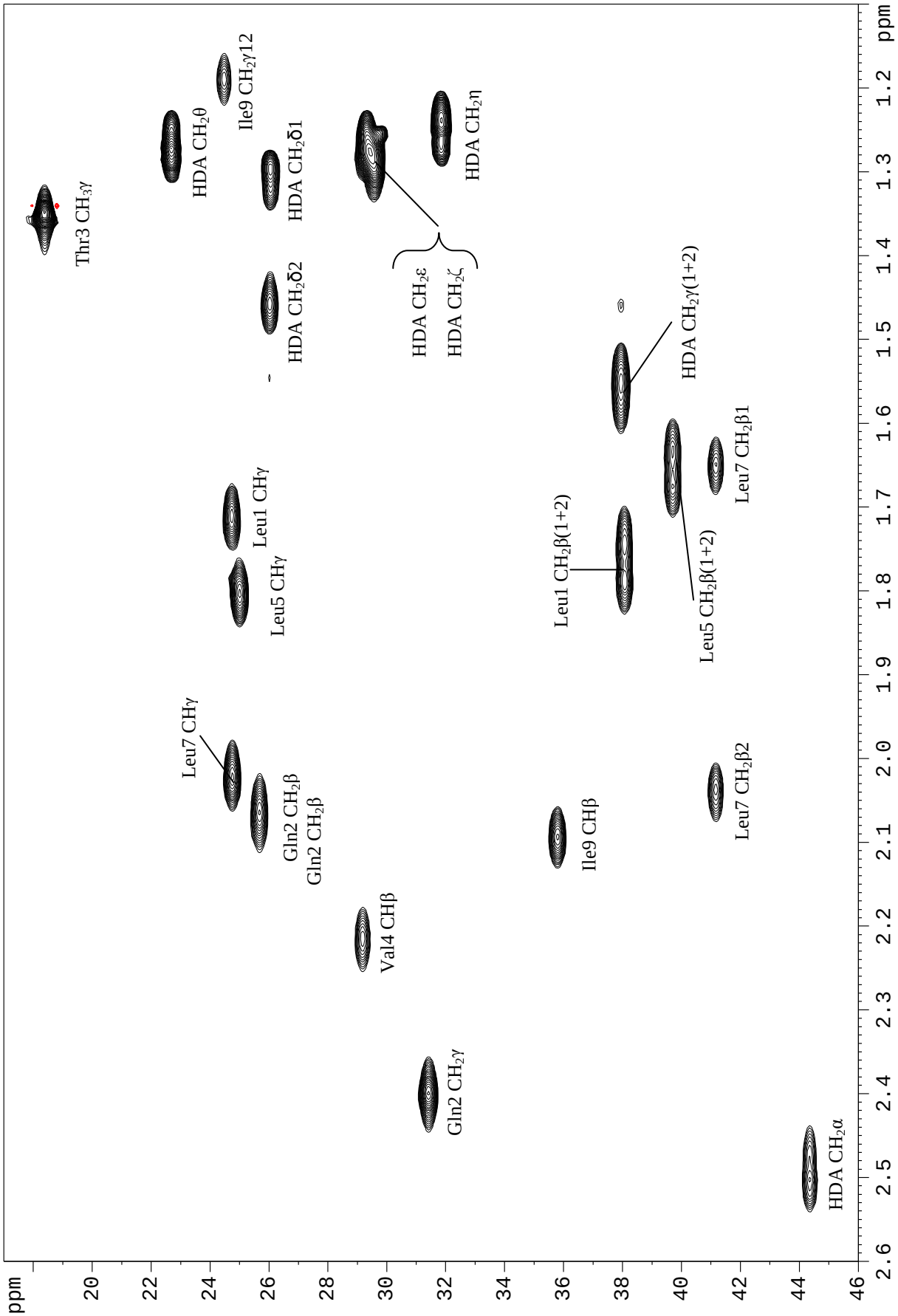

Figure E.8b: 2D ^{1}H-^{13}C HSQC spectrum of pseudodesmin A in chloroform solution, recorded at 16.4 T, 25.0℃, methylene region.

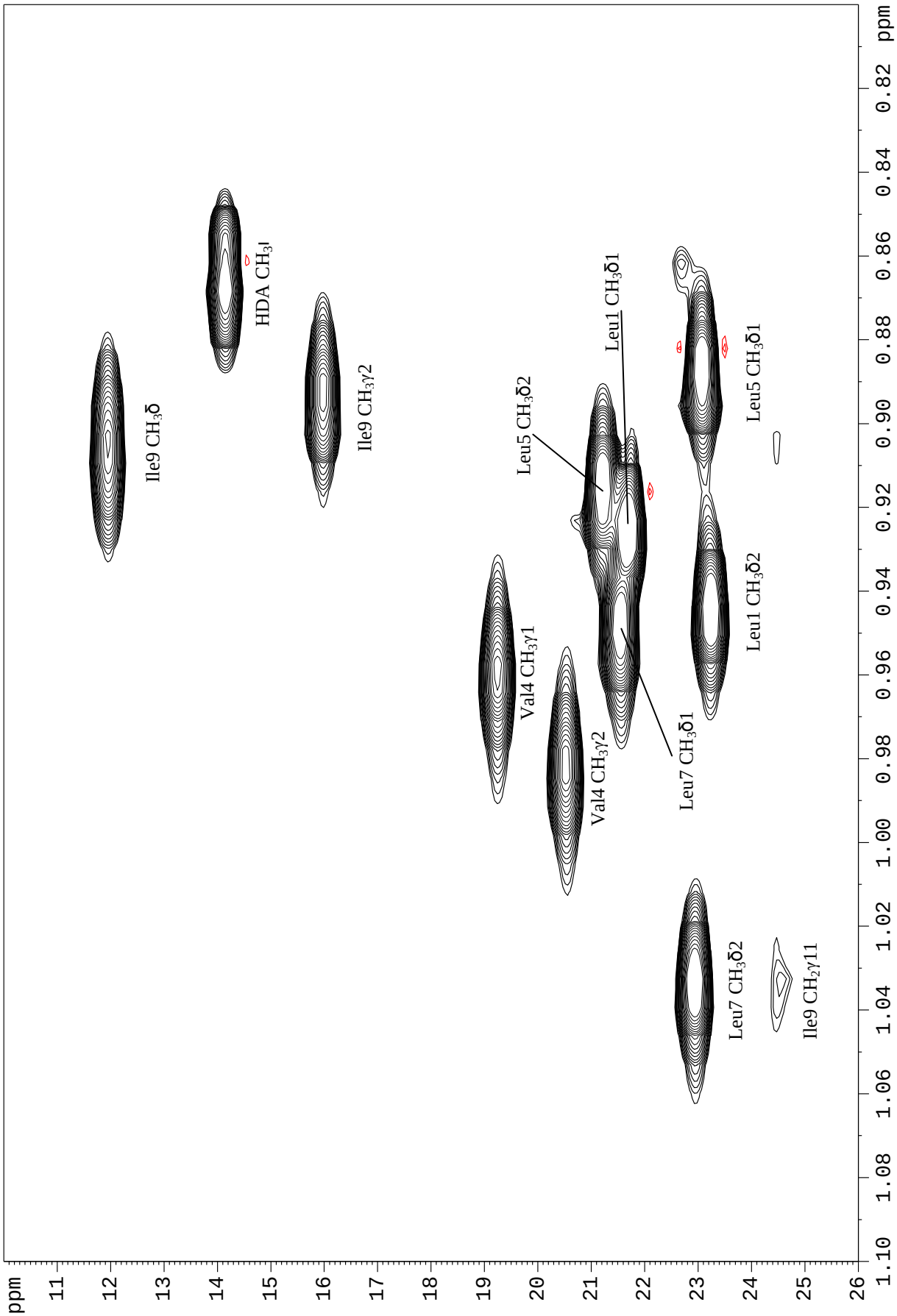

Figure E.8c: 2D ^{1}H-^{13}C HSQC spectrum of pseudodesmin A in chloroform solution, recorded at 16.4 T, 25.0℃, methyl region.

F

Experiments for the measurement of scalar couplings: SERF and HNHA

The SERF (SElective ReFocusing) experiment was used to measure the $^{3}J_{H\alpha H\beta}$ couplings in acetonitrile (Leu1, Thr3, Leu5, Ser6, Leu7 and Ser8) and in chloroform (Thr3) (Chapter 5). The experiment, described by Fäcke and Berger[1], selectively excites one of the ^{1}H resonances (E-BURP2 pulse) and performs a spin echo type experiment with the refocusing occurring selectively and simultaneously on both the ^{1}H resonances (REBURP pulses). The duration of the spin echo experiment is varied to obtain a 2D spectrum similar as a 2D J-resolved spectrum, but where only the scalar coupling information between the two ^{1}H spins involved is retained. Typically 4096 direct complex time domain points and 32 indirect time domain points were sampled. Prior to Fourier transform, the direct dimension was multiplied with a squared cosine bell window function, while the indirect dimension was multiplied with a squared cosine bell or Gaussian resolution enhancing window function. The scalar coupling was measured along the F1 dimension as the distance between the maxima of the two resulting peaks.

Due to the broad line width in chloroform solution, it is not possible to just read the $^{3}J_{HNH\alpha}$ couplings directly from the 1D ^{1}H spectrum. Instead, the HNHA experiment proposed by Vuister and Bax[2] was used. It is a 3D experiment consisting out of two

^{1}H dimensions and one ^{15}N dimension. Between the two proton dimensions, diagonal peaks are visible at the H^{N} proton frequency and cross-peaks between the H^{N} and H^{α} frequencies. All these peaks are correlated along the third ^{15}N dimension according to the amide ^{15}N chemical shift. The experiment is set up in such way that the ratio between a cross-peak and its corresponding diagonal peak of opposite sign can be related to the $^{3}J_{HNH\alpha}$ coupling by the relation:

$$\frac{I_{cross}}{I_{diag}} = -\tan^{2}\left(2\pi\,{}^{3}J_{HNH\alpha}\,\zeta\right) \qquad \text{(F.1)}$$

with ζ a delay in the pulse sequence here set to 13.05 ms. The experiment was performed at 16.4 T, with 2048 time domain points sampled in the direct dimension (F3), 32 time domain points in the indirect ^{1}H dimension (F2) and 16 time domain points in the indirect ^{15}N dimension (F1). The spectral widths were set to 7.0 ppm for the ^{1}H dimensions and 6.6 ppm for the ^{15}N dimension. The low spectral width set for ^{15}N folded the spectrum in this dimension, allowing the peaks to be sufficiently resolved with the limited number of indirect time domain points measured. Resolution in F2 and F1 was improved via one order of forward linear prediction. Zero filling was performed until a 2048×256×256 matrix was obtained, which was Fourier transformed using squared cosine bell window functions and afterwards baseline corrected with 5th degree polynomials in each dimension.

[1] T. Facke and S. Berger, "SERF, a New Method for ^{1}H-^{1}H Spin-Coupling Measurement in Organic-Chemistry". *Journal of Magnetic Resonance Series A*, **1995**, 113(1) 114-116.

[2] G.W. Vuister and A. Bax, "Quantitative J Correlation - a New Approach for Measuring Homonuclear 3-Bond J($H^{N}H^{\alpha}$) Coupling-Constants in ^{15}N-Enriched Proteins". *Journal of the American Chemical Society*, **1993**, 115(17) 7772-7777.

G

Restraint file for molecular modelling of the solution structure

The restraint file used to obtain the solution structure is provided on the following pages, containing chirality, distance and dihedral restraints.

```
!BIOSYM restraint 1
!
#chiral
1:LEU_1:CA S
1:GLN_1B:CA R
1:THR_1C:CA R
1:THR_1C:CB R
1:VAL_1D:CA R
1:LEU_1E:CA R
1:SER_1F:CA R
1:LEU_1G:CA S
1:SER_1H:CA R
1:ILE_1I:CA S
1:ILE_1I:CB S
1:ALHD_1J:C2 R
!
#distance
1:ILE_1I:HN        1:ILE_1I:HA         0.000  3.167  10.00  10.00 1000.000
1:ILE_1I:HN        1:ILE_1I:HB         0.000  3.770  10.00  10.00 1000.000
1:ILE_1I:HN        1:ILE_1I:HG1*       0.000  3.583  10.00  10.00 1000.000
1:ILE_1I:HN        1:THR_1C:HA         0.000  4.044  10.00  10.00 1000.000
```

```
1:ILE_1I:HN         1:THR_1C:HB         0.000  4.933  10.00  10.00 1000.000
1:ILE_1I:HN         1:THR_1C:HG*        0.000  6.453  10.00  10.00 1000.000
1:ILE_1I:HN         1:VAL_1D:HA         0.000  3.958  10.00  10.00 1000.000
1:ILE_1I:HN         1:SER_1F:HG         0.000  4.697  10.00  10.00 1000.000
1:ILE_1I:HN         1:LEU_1G:HB1        0.000  3.699  10.00  10.00 1000.000
1:ILE_1I:HN         1:LEU_1G:HB2        0.000  3.356  10.00  10.00 1000.000
1:ILE_1I:HN         1:SER_1H:HN         0.000  2.469  10.00  10.00 1000.000
1:ILE_1I:HN         1:SER_1H:HA         0.000  3.520  10.00  10.00 1000.000
1:ILE_1I:HA         1:ILE_1I:HB         0.000  2.685  10.00  10.00 1000.000
1:ILE_1I:HA         1:ILE_1I:HG1*       0.000  4.447  10.00  10.00 1000.000
1:ILE_1I:HA         1:THR_1C:HG*        0.000  5.181  10.00  10.00 1000.000
1:ILE_1I:HB         1:ILE_1I:HG1*       0.000  3.656  10.00  10.00 1000.000
1:ILE_1I:HB         1:ILE_1I:HG2*       0.000  3.201  10.00  10.00 1000.000
1:ILE_1I:HD1*       1:ILE_1I:HN         0.000  5.041  10.00  10.00 1000.000
1:ILE_1I:HD1*       1:ILE_1I:HA         0.000  5.405  10.00  10.00 1000.000
1:ILE_1I:HD1*       1:ILE_1I:HB         0.000  3.875  10.00  10.00 1000.000
1:ILE_1I:HG1*       1:THR_1C:HB         0.000  3.902  10.00  10.00 1000.000
1:ILE_1I:HG1*       1:VAL_1D:HA         0.000  3.538  10.00  10.00 1000.000
1:ILE_1I:HG2*       1:ILE_1I:HN         0.000  4.202  10.00  10.00 1000.000
1:ILE_1I:HG2*       1:ILE_1I:HA         0.000  3.710  10.00  10.00 1000.000
1:LEU_1:HN          1:LEU_1:HA          0.000  2.536  10.00  10.00 1000.000
1:LEU_1:HN          1:GLN_1B:HN         0.000  3.240  10.00  10.00 1000.000
1:LEU_1:HN          1:ALHD_1J:HC*       0.000  3.421  10.00  10.00 1000.000
1:LEU_1:HN          1:ALHD_1J:H2        0.000  3.600  10.00  10.00 1000.000
1:LEU_1:HA          1:LEU_1:HD*         0.000  5.240  10.00  10.00 1000.000
1:LEU_1:HA          1:GLN_1B:HN         0.000  2.587  10.00  10.00 1000.000
1:LEU_1:HA          1:THR_1C:HN         0.000  4.562  10.00  10.00 1000.000
1:LEU_1:HB*         1:LEU_1:HA          0.000  3.472  10.00  10.00 1000.000
1:LEU_1:HB*         1:VAL_1D:HN         0.000  4.463  10.00  10.00 1000.000
1:LEU_1:HB*         1:VAL_1D:HB         0.000  3.477  10.00  10.00 1000.000
1:LEU_1:HB*         1:LEU_1:HD*         0.000  5.512  10.00  10.00 1000.000
1:LEU_1:HB*         1:GLN_1B:HN         0.000  5.074  10.00  10.00 1000.000
1:LEU_1:HD*         1:LEU_1:HN          0.000  5.710  10.00  10.00 1000.000
1:GLN_1B:HN         1:GLN_1B:HA         0.000  2.966  10.00  10.00 1000.000
1:GLN_1B:HN         1:GLN_1B:HB*        0.000  3.567  10.00  10.00 1000.000
1:GLN_1B:HN         1:GLN_1B:HG*        0.000  4.026  10.00  10.00 1000.000
1:GLN_1B:HN         1:THR_1C:HN         0.000  2.890  10.00  10.00 1000.000
1:GLN_1B:HA         1:GLN_1B:HB*        0.000  3.388  10.00  10.00 1000.000
1:GLN_1B:HB*        1:GLN_1B:HG*        0.000  4.301  10.00  10.00 1000.000
1:GLN_1B:HB*        1:THR_1C:HN         0.000  4.579  10.00  10.00 1000.000
1:GLN_1B:HG*        1:THR_1C:HN         0.000  4.216  10.00  10.00 1000.000
1:GLN_1B:HG*        1:GLN_1B:HA         0.000  3.950  10.00  10.00 1000.000
1:THR_1C:HN         1:THR_1C:HB         0.000  2.670  10.00  10.00 1000.000
1:THR_1C:HN         1:THR_1C:HG*        0.000  3.648  10.00  10.00 1000.000
1:THR_1C:HN         1:VAL_1D:HN         0.000  2.627  10.00  10.00 1000.000
1:THR_1C:HA         1:VAL_1D:HN         0.000  3.515  10.00  10.00 1000.000
1:THR_1C:HA         1:SER_1F:HG         0.000  2.606  10.00  10.00 1000.000
1:THR_1C:HA         1:SER_1H:HN         0.000  3.563  10.00  10.00 1000.000
1:THR_1C:HB         1:VAL_1D:HN         0.000  2.923  10.00  10.00 1000.000
1:THR_1C:HB         1:VAL_1D:HG1*       0.000  4.618  10.00  10.00 1000.000
1:THR_1C:HB         1:ALHD_1J:HC*       0.000  4.560  10.00  10.00 1000.000
1:THR_1C:HG*        1:THR_1C:HA         0.000  3.342  10.00  10.00 1000.000
1:THR_1C:HG*        1:VAL_1D:HN         0.000  5.780  10.00  10.00 1000.000
1:VAL_1D:HN         1:ILE_1I:HG1*       0.000  5.633  10.00  10.00 1000.000
1:VAL_1D:HN         1:VAL_1D:HA         0.000  3.063  10.00  10.00 1000.000
1:VAL_1D:HN         1:VAL_1D:HB         0.000  2.547  10.00  10.00 1000.000
1:VAL_1D:HN         1:LEU_1E:HN         0.000  2.762  10.00  10.00 1000.000
1:VAL_1D:HA         1:VAL_1D:HB         0.000  3.255  10.00  10.00 1000.000
1:VAL_1D:HA         1:LEU_1E:HN         0.000  3.933  10.00  10.00 1000.000
1:VAL_1D:HA         1:LEU_1G:HN         0.000  3.530  10.00  10.00 1000.000
1:VAL_1D:HA         1:LEU_1G:HB1        0.000  3.905  10.00  10.00 1000.000
```

```
1:VAL_1D:HA       1:SER_1H:HN        0.000  4.650  10.00  10.00 1000.000
1:VAL_1D:HB       1:LEU_1E:HN        0.000  2.834  10.00  10.00 1000.000
1:VAL_1D:HG2*     1:VAL_1D:HN        0.000  4.674  10.00  10.00 1000.000
1:VAL_1D:HG2*     1:VAL_1D:HA        0.000  3.722  10.00  10.00 1000.000
1:VAL_1D:HG1*     1:VAL_1D:HN        0.000  3.553  10.00  10.00 1000.000
1:VAL_1D:HG1*     1:VAL_1D:HA        0.000  3.566  10.00  10.00 1000.000
1:LEU_1E:HD*      1:LEU_1E:HN        0.000  6.274  10.00  10.00 1000.000
1:LEU_1E:HD*      1:LEU_1E:HA        0.000  4.762  10.00  10.00 1000.000
1:LEU_1E:HD*      1:LEU_1E:HB2       0.000  4.627  10.00  10.00 1000.000
1:LEU_1E:HD*      1:LEU_1E:HB1       0.000  4.774  10.00  10.00 1000.000
1:LEU_1E:HN       1:LEU_1E:HA        0.000  3.035  10.00  10.00 1000.000
1:LEU_1E:HN       1:LEU_1E:HG        0.000  2.626  10.00  10.00 1000.000
1:LEU_1E:HA       1:LEU_1E:HB2       0.000  2.899  10.00  10.00 1000.000
1:LEU_1E:HA       1:LEU_1E:HB1       0.000  2.591  10.00  10.00 1000.000
1:LEU_1E:HA       1:LEU_1E:HG        0.000  3.021  10.00  10.00 1000.000
1:LEU_1E:HA       1:SER_1F:HN        0.000  3.091  10.00  10.00 1000.000
1:LEU_1E:HB2      1:LEU_1E:HN        0.000  3.623  10.00  10.00 1000.000
1:LEU_1E:HB2      1:LEU_1E:HG        0.000  2.838  10.00  10.00 1000.000
1:LEU_1E:HB2      1:SER_1F:HN        0.000  3.425  10.00  10.00 1000.000
1:LEU_1E:HB1      1:SER_1F:HN        0.000  3.179  10.00  10.00 1000.000
1:SER_1F:HN       1:LEU_1E:HN        0.000  3.050  10.00  10.00 1000.000
1:SER_1F:HN       1:SER_1F:HB1       0.000  2.875  10.00  10.00 1000.000
1:SER_1F:HN       1:SER_1F:HB2       0.000  3.617  10.00  10.00 1000.000
1:SER_1F:HN       1:SER_1F:HG        0.000  2.522  10.00  10.00 1000.000
1:SER_1F:HN       1:SER_1H:HN        0.000  3.939  10.00  10.00 1000.000
1:SER_1F:HA       1:SER_1F:HB1       0.000  2.573  10.00  10.00 1000.000
1:SER_1F:HA       1:SER_1F:HB2       0.000  2.583  10.00  10.00 1000.000
1:SER_1F:HA       1:SER_1F:HG        0.000  4.053  10.00  10.00 1000.000
1:SER_1F:HB1      1:THR_1C:HG*       0.000  5.129  10.00  10.00 1000.000
1:SER_1F:HB1      1:SER_1F:HG        0.000  2.526  10.00  10.00 1000.000
1:SER_1F:HB2      1:SER_1F:HG        0.000  2.982  10.00  10.00 1000.000
1:SER_1F:HG       1:THR_1C:HG*       0.000  6.268  10.00  10.00 1000.000
1:SER_1F:HG       1:SER_1H:HN        0.000  3.381  10.00  10.00 1000.000
1:LEU_1G:HN       1:LEU_1E:HN        0.000  4.421  10.00  10.00 1000.000
1:LEU_1G:HN       1:LEU_1G:HA        0.000  3.150  10.00  10.00 1000.000
1:LEU_1G:HN       1:LEU_1G:HB1       0.000  3.435  10.00  10.00 1000.000
1:LEU_1G:HN       1:LEU_1G:HD*       0.000  6.457  10.00  10.00 1000.000
1:LEU_1G:HN       1:SER_1H:HN        0.000  2.786  10.00  10.00 1000.000
1:LEU_1G:HA       1:LEU_1G:HB1       0.000  2.800  10.00  10.00 1000.000
1:LEU_1G:HA       1:LEU_1G:HD*       0.000  4.861  10.00  10.00 1000.000
1:LEU_1G:HB1      1:LEU_1G:HD*       0.000  4.375  10.00  10.00 1000.000
1:LEU_1G:HB1      1:SER_1H:HN        0.000  3.942  10.00  10.00 1000.000
1:LEU_1G:HB2      1:SER_1H:HN        0.000  3.441  10.00  10.00 1000.000
1:LEU_1G:HD*      1:VAL_1D:HA        0.000  5.376  10.00  10.00 1000.000
1:ALHD_1J:HC*     1:ALHD_1J:H2       0.000  3.666  10.00  10.00 1000.000
1:ALHD_1J:H3*     1:LEU_1:HN         0.000  5.102  10.00  10.00 1000.000
1:ALHD_1J:H3*     1:ALHD_1J:HC*      0.000  4.510  10.00  10.00 1000.000
1:ALHD_1J:H3*     1:ALHD_1J:H2       0.000  3.652  10.00  10.00 1000.000
1:ALHD_1J:H4*     1:ALHD_1J:H2       0.000  3.924  10.00  10.00 1000.000
1:ALHD_1J:HH      1:LEU_1:HN         0.000  4.619  10.00  10.00 1000.000
1:ALHD_1J:HH      1:GLN_1B:HN        0.000  4.430  10.00  10.00 1000.000
1:SER_1H:HN       1:LEU_1G:HA        0.000  3.394  10.00  10.00 1000.000
1:SER_1H:HN       1:SER_1H:HA        0.000  3.126  10.00  10.00 1000.000
1:SER_1H:HN       1:SER_1H:HB2       0.000  3.264  10.00  10.00 1000.000
1:SER_1H:HA       1:SER_1H:HB2       0.000  2.598  10.00  10.00 1000.000
1:SER_1H:HA       1:SER_1H:HB1       0.000  2.771  10.00  10.00 1000.000
1:SER_1H:HA       1:SER_1H:HG        0.000  3.495  10.00  10.00 1000.000
1:SER_1H:HB1      1:ILE_1I:HN        0.000  3.725  10.00  10.00 1000.000
1:SER_1H:HB1      1:SER_1H:HN        0.000  2.972  10.00  10.00 1000.000
1:SER_1H:HG       1:ILE_1I:HN        0.000  3.989  10.00  10.00 1000.000
1:SER_1H:HG       1:SER_1H:HN        0.000  2.741  10.00  10.00 1000.000
```

```
1:SER_1H:HG        1:SER_1H:HB2        0.000  2.341  10.00  10.00 1000.000
!
#NMR_dihedral
1:ALHD_1J:C    1:ALHD_1J:C1    1:LEU_1:N       1:LEU_1:CA    175 -175 100 100 1000
1:LEU_1:CA     1:LEU_1:C       1:GLN_1B:N      1:GLN_1B:CA   175 -175 100 100 1000
1:GLN_1B:CA    1:GLN_1B:C      1:THR_1C:N      1:THR_1C:CA   175 -175 100 100 1000
1:THR_1C:CA    1:THR_1C:C      1:VAL_1D:N      1:VAL_1D:CA   175 -175 100 100 1000
1:VAL_1D:CA    1:VAL_1D:C      1:LEU_1E:N      1:LEU_1E:CA   175 -175 100 100 1000
1:LEU_1E:CA    1:LEU_1E:C      1:SER_1F:N      1:SER_1F:CA   175 -175 100 100 1000
1:SER_1F:CA    1:SER_1F:C      1:LEU_1G:N      1:LEU_1G:CA   175 -175 100 100 1000
1:LEU_1G:CA    1:LEU_1G:C      1:SER_1H:N      1:SER_1H:CA   175 -175 100 100 1000
1:SER_1H:CA    1:SER_1H:C      1:ILE_1I:N      1:ILE_1I:CA   175 -175 100 100 1000
```

H Concentration measurements using ERETIC

To determine the concentration of pseudodesmin A in chloroform solution, the ERETIC[1] (Electronic Reference To access In vivo Concentrations) method was applied. In this method, an rf-signal that exponentially decreases in amplitude is transmitted by the outer coil in the probe during the acquisition of the FID. This signal is picked up by the inner detection coil and leads to an artificial Lorentzian shaped resonance in the spectrum. The intensity, frequency and phase of this peak can all be set at will. The idea of the method is that the integral of this signal relative to the 'real' signals in the spectrum remains constant between different samples. This condition holds provided the properties of these samples are indeed similar (*i.e.* same solvent conditions) and if a sufficiently long interscan delay is chosen between scans to remove the effects of T_1-relaxation on the integrals.

The reference samples prepared for the calibration of the ERETIC signals were a solution of (±)-menthol in chloroform. For the concentration study of pseudodesmin A in chloroform (section 6.1), four samples with different concentration were prepared. Both the menthol and the chloroform were weighed in the NMR tube to calculate the concentration. For each sample, four ERETIC experiments were performed successively. The ratio between the integrals of the menthol signal at ca 3.4 ppm and the ERETIC signal was determined (Figure H.1). The slope of the linear regression curve with the intercept fixed at the origin (intercept equals zero with a statistical p-value of 0.05) was taken as calibration value. The concentration of pseudodesmin A

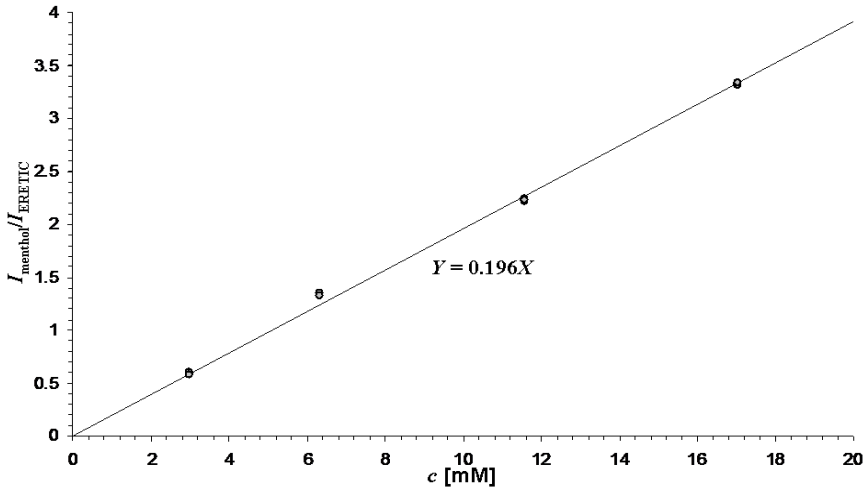

Figure H.1: Concentration calibration curve for the ERETIC signal integral.

is then calculated as, with n_H the number of $^1\mathrm{H}$ spins that is represented by the integral $I_{pseudoA}$:

$$c_{pseudoA} = 0.196 \frac{I_{pseudoA}}{n_H I_{ERETIC}} \tag{H.1}$$

The concentrations of the chloroform solutions prepared for the relaxation studies (Chapter 7) where determined in a similar fashion.

[1] S. Akoka, L. Barantin, and M. Trierweiler, "Concentration measurement by proton NMR using the ERETIC method". *Analytical Chemistry*, **1999**, 71(13) 2554-2557.

I

Solvent titration data

Tabulated data for second solvent titration performed to assess the ^{1}H, ^{13}C and ^{15}N chemical shift changes (see Figure 6.10).

Table I.1: Diffusion coefficients and ^{1}H, ^{13}C and ^{15}N chemical shifts measured during the second solvent titration, and converted into an average $^{1}H/^{n}X$ chemical shift change

point			1	2	3	4	5	6	7	8	9	10	11				
			Diffusion coefficients [µm²/s]											ΔD			
$D_{pseudodesmin\ A}$			178.5	202.7	222.1	239.6	265.4	299.3	327.9	348.7	373.4	405.7	436.3	257.8			
error[a]			0.7	1.0	1.4	0.8	1.8	1.6	1.2	1.5	1.7	2.0	2.1				
D_{TMS}			1880.8	1885.5	1862.6	1862.6	1861.3	1857.2	1849.1	1843.4	1859.3	1825.5	1858.9				
error[a]			4.9	10.3	2.9	5.1	2.5	4.2	4.3	3.5	13.0	3.2	3.1				
			$^{1}H/^{13}C$ Chemical shifts [ppm]											Slope[b]	R^2	|Slope|×ΔD	average[c]
Leu1	CHα	^{1}H	3.84	3.83	3.82	3.81	3.80	3.79	3.78	3.77	3.77	3.77	3.77	-2.95E-04	-0.96	0.08	0.23
		^{13}C	52.74	52.80	52.82	52.84	52.90	52.94	52.96	52.98	53.02	53.04	53.05	1.21E-03	0.99	0.31	
Leu1	CH_2β(1+2)	^{1}H	1.77	1.77	1.77	1.77	1.77	1.76	1.76	1.75	1.75	1.74	1.73	-1.54E-04	-0.99	0.04	0.13
		^{13}C	37.88	37.90	37.89	37.90	37.91	37.93	37.94	37.96	37.97	38.02	38.08	6.65E-04	0.94	0.17	
Leu1	CHγ	^{1}H	1.72	1.72	1.71	1.71	1.70	1.69	1.68	1.68	1.67	1.67	1.66	-2.52E-04	-1.00	0.06	0.08
		^{13}C	24.61	24.62	24.61	24.61	24.61	24.62	24.61	24.62	24.62	24.64	24.66	1.19E-04	0.74	0.03	
Leu1	CH_3δ1	^{1}H	0.94	0.93	0.93	0.93	0.93	0.93	0.93	0.92	0.92	0.92	0.92	-8.33E-05	-0.98	0.02	0.03
		^{13}C	21.53	21.55	21.54	21.53	21.53	21.54	21.53	21.53	21.54	21.53	21.57	4.98E-05	0.38	0.01	
Leu1	CH_3δ2	^{1}H	0.95	0.95	0.95	0.95	0.95	0.95	0.95	0.95	0.95	0.95	0.95	-5.60E-06	-0.53	0.00	0.09
		^{13}C	23.26	23.23	23.20	23.18	23.18	23.18	23.14	23.12	23.12	23.08	23.08	-6.64E-04	-0.97	0.17	
Gln2	CHα	^{1}H	3.99	3.98	3.98	3.98	3.97	3.97	3.96	3.96	3.96	3.95	3.94	-1.73E-04	-1.00	0.04	0.11
		^{13}C	56.61	56.63	56.64	56.60	56.63	56.64	56.65	56.67	56.67	56.72	56.77	5.13E-04	0.87	0.13	
Gln2	CH_2β	^{1}H	2.07	2.08	2.07	2.07	2.07	2.07	2.07	2.07	2.06	2.06	2.05	-9.00E-05	-0.93	0.02	0.23
		^{13}C	25.65	25.56	25.50	25.46	25.39	25.32	25.26	25.24	25.19	25.21	25.29	-1.63E-03	-0.90	0.42	
Gln2	CH_2γ	^{1}H	2.41	2.42	2.42	2.42	2.43	2.43	2.43	2.43	2.43	2.43	2.42	4.77E-05	0.54	0.01	0.11
		^{13}C	31.21	31.26	31.27	31.25	31.29	31.32	31.32	31.36	31.36	31.40	31.44	7.78E-04	0.98	0.20	
Thr3	CHα	^{1}H	3.92	3.94	3.96	3.97	3.99	4.01	4.02	4.03	4.04	4.03	4.02	4.36E-04	0.92	0.11	0.49
		^{13}C	61.38	61.24	61.13	61.08	60.95	60.83	60.74	60.70	60.64	60.62	60.67	-2.95E-03	-0.95	0.76	
Thr3	CHβ	^{1}H	5.32	5.31	5.31	5.30	5.30	5.29	5.28	5.27	5.27	5.27	5.26	-2.35E-04	-0.99	0.06	0.17
		^{13}C	69.71	69.69	69.66	69.65	69.64	69.61	69.57	69.56	69.52	69.51	69.52	-8.24E-04	-0.98	0.21	
Thr3	CH_3γ	^{1}H	1.36	1.35	1.35	1.34	1.34	1.34	1.33	1.33	1.32	1.32	1.31	-1.56E-04	-0.99	0.04	0.21
		^{13}C	18.38	18.29	18.23	18.19	18.19	18.14	18.08	18.04	18.03	18.00	18.05	-1.35E-03	-0.94	0.35	
Val4	CHα	^{1}H	3.47	3.47	3.48	3.47	3.47	3.47	3.48	3.47	3.48	3.48	3.47	1.34E-05	0.56	0.00	0.21
		^{13}C	64.84	64.78	64.72	64.69	64.63	64.58	64.52	64.51	64.46	64.45	64.46	-1.57E-03	-0.97	0.41	
Val4	CHβ	^{1}H	2.22	2.21	2.21	2.20	2.20	2.19	2.18	2.18	2.17	2.17	2.17	-1.99E-04	-0.98	0.05	0.05
		^{13}C	29.13	29.14	29.14	29.12	29.13	29.13	29.12	29.13	29.13	29.13	29.15	2.66E-05	0.28	0.01	
Val4	CH_3γ1	^{1}H	0.97	0.97	0.97	0.97	0.97	0.97	0.97	0.97	0.97	0.97	0.96	-1.35E-05	-0.48	0.00	0.02
		^{13}C	19.24	19.23	19.22	19.22	19.22	19.24	19.25	19.23	19.25	19.25	19.28	1.44E-04	0.70	0.04	
Val4	CH_3γ2	^{1}H	0.99	0.98	0.98	0.98	0.98	0.98	0.98	0.98	0.97	0.97	0.97	-6.79E-05	-0.97	0.02	0.11
		^{13}C	20.44	20.47	20.47	20.48	20.48	20.51	20.54	20.54	20.58	20.58	20.64	7.20E-04	0.98	0.19	

Leu5	CHα	^{1}H	4.15	4.15	4.14	4.15	4.14	4.14	4.14	4.13	4.13	4.12	4.10	-1.45E-04	-0.86	0.04	0.13
		^{13}C	54.79	54.73	54.68	54.65	54.62	54.58	54.55	54.55	54.53	54.56	54.64	-7.18E-04	-0.76	0.19	
Leu5	CH_2β(1+2)	^{1}H	1.65	1.65	1.65	1.65	1.64	1.64	1.64	1.64	1.64	1.63	1.62	-9.25E-05	-0.98	0.02	0.16
		^{13}C	39.63	39.66	39.65	39.67	39.71	39.75	39.77	39.80	39.82	39.86	39.91	1.08E-03	0.99	0.28	
Leu5	CHγ	^{1}H	1.80	1.80	1.80	1.80	1.80	1.79	1.79	1.79	1.79	1.79	1.78	-7.19E-05	-0.99	0.02	0.06
		^{13}C	24.94	24.93	24.90	24.89	24.90	24.90	24.87	24.87	24.86	24.86	24.87	-2.91E-04	-0.90	0.08	
Leu5	CH_3δ1	^{1}H	0.90	0.89	0.89	0.89	0.89	0.88	0.88	0.88	0.87	0.87	0.87	-9.51E-05	-0.98	0.02	0.06
		^{13}C	23.00	23.02	23.02	23.02	23.02	23.05	23.06	23.05	23.07	23.07	23.07	2.81E-04	0.97	0.07	
Leu5	CH_3δ2	^{1}H	0.92	0.92	0.92	0.92	0.92	0.92	0.91	0.91	0.91	0.91	0.90	-7.45E-05	-0.99	0.02	0.05
		^{13}C	21.22	21.19	21.17	21.15	21.15	21.16	21.13	21.11	21.14	21.11	21.16	-2.76E-04	-0.71	0.07	
Ser6	CHα	^{1}H	4.61	4.61	4.61	4.61	4.61	4.61	4.61	4.60	4.60	4.57	4.54	-2.10E-04	-0.77	0.05	0.07
		^{13}C	54.86	54.82	54.80	54.78	54.76	54.76	54.75	54.77	54.77	54.83	54.94	1.28E-04	0.19	0.03	
Ser6	CH_2β1	^{1}H	3.90	3.89	3.89	3.87	3.86	3.85	3.84	3.83	3.83	3.83	3.83	-3.13E-04	-0.96	0.08	0.26
		^{13}C	63.73	63.78	63.82	63.84	63.91	63.95	63.98	64.01	64.04	64.06	64.09	1.40E-03	0.99	0.36	
Ser6	CH_2β2	^{1}H	4.26	4.27	4.28	4.28	4.29	4.30	4.31	4.32	4.32	4.32	4.31	2.23E-04	0.91	0.06	0.24
		^{13}C	63.70	63.79	63.81	63.85	63.90	63.96	63.98	64.01	64.04	64.07	64.09	1.45E-03	0.98	0.37	
Leu7	CHα	^{1}H	4.15	4.17	4.18	4.18	4.19	4.20	4.21	4.21	4.21	4.21	4.20	2.16E-04	0.89	0.06	0.60
		^{13}C	55.86	55.70	55.58	55.52	55.40	55.25	55.13	55.05	54.95	54.84	54.75	-4.24E-03	-1.00	1.09	
Leu7	CH_2β1	^{1}H	1.66	1.66	1.66	1.66	1.66	1.66	1.66	1.66	1.66	1.65	1.65	-2.41E-05	-0.62	0.01	0.15
		^{13}C	41.04	41.09	41.12	41.12	41.17	41.21	41.23	41.26	41.27	41.31	41.33	1.09E-03	0.99	0.28	
Leu7	CH_2β2	^{1}H	2.06	2.04	2.03	2.03	2.01	1.99	1.98	1.97	1.96	1.95	1.94	-4.70E-04	-0.99	0.12	0.26
		^{13}C	41.06	41.11	41.12	41.14	41.18	41.21	41.23	41.27	41.28	41.31	41.34	1.05E-03	1.00	0.27	
Leu7	CHγ	^{1}H	2.03	2.03	2.03	2.03	2.03	2.03	2.03	2.02	2.02	2.02	2.01	-5.89E-05	-0.76	0.02	0.03
		^{13}C	24.68	24.67	24.66	24.66	24.66	24.66	24.65	24.66	24.67	24.69	24.73	1.26E-04	0.49	0.03	
Leu7	CH_3δ1	^{1}H		0.95	0.95	0.95	0.95	0.95	0.95	0.95	0.95	0.95	0.94	-3.04E-05	-0.81	0.01	0.09
		^{13}C		21.49	21.45	21.44	21.44	21.42	21.39	21.36	21.36	21.34	21.33	-6.57E-04	-0.98	0.17	
Leu7	CH_3δ2	^{1}H	1.04	1.04	1.04	1.04	1.04	1.04	1.03	1.03	1.03	1.03	1.02	-5.81E-05	-0.96	0.01	0.13
		^{13}C	22.90	22.93	22.93	22.95	22.95	22.99	23.02	23.04	23.07	23.08	23.15	9.13E-04	0.98	0.24	
Ser8	CHα	^{1}H	4.89	4.88	4.86	4.85	4.83	4.82	4.80	4.79	4.77	4.74	4.69	-7.16E-04	-0.99	0.18	0.51
		^{13}C	56.13	56.04	55.96	55.94	55.85	55.75	55.66	55.59	55.54	55.50	55.54	-2.56E-03	-0.98	0.66	
Ser8	CH_2β1	^{1}H	3.81	3.84	3.86	3.87	3.90	3.94	3.97	3.98	4.01	4.02	4.02	8.80E-04	0.98	0.23	0.47
		^{13}C	62.15	62.18	62.19	62.23	62.27	62.34	62.38	62.45	62.49	62.57	62.61	1.88E-03	1.00	0.48	
Ser8	CH_2β2	^{1}H	3.98	3.96	3.93	3.93	3.90	3.88	3.85	3.83	3.81	3.78	3.76	-8.79E-04	-1.00	0.23	0.47
		^{13}C	62.16	62.20	62.20	62.21	62.27	62.35	62.39	62.46	62.49	62.57	62.62	1.86E-03	0.99	0.48	
Ile9	CHα	^{1}H	4.61	4.61	4.60	4.61	4.61	4.61	4.61	4.61	4.61	4.60	4.60	-3.01E-05	-0.56	0.01	0.16
		^{13}C	56.87	56.83	56.79	56.78	56.75	56.71	56.66	56.65	56.61	56.59	56.58	-1.16E-03	-0.99	0.30	
Ile9	CHβ	^{1}H	2.12	2.11	2.10	2.10	2.09	2.09	2.08	2.07	2.07	2.06	2.05	-2.62E-04	-1.00	0.07	0.20
		^{13}C	35.59	35.62	35.63	35.62	35.65	35.68	35.71	35.74	35.76	35.81	35.88	1.04E-03	0.98	0.27	
Ile9	CH_2γ11	^{1}H	1.03	1.03	1.03	1.03	1.03	1.04	1.04	1.04	1.04	1.04	1.03	3.54E-05	0.49	0.01	0.06
		^{13}C	24.35	24.36	24.36	24.34	24.37	24.39	24.37	24.39	24.39	24.43	24.45	3.72E-04	0.91	0.10	
Ile9	CH_2γ12	^{1}H	1.18	1.18	1.17	1.17	1.17	1.17	1.16	1.16	1.16	1.16	1.16	-8.80E-05	-0.96	0.02	0.07
		^{13}C	24.36	24.37	24.36	24.35	24.37	24.38	24.38	24.39	24.40	24.43	24.45	3.43E-04	0.92	0.09	
Ile9	CH_3γ2	^{1}H	0.90	0.90	0.90	0.90	0.90	0.90	0.90	0.89	0.89	0.89	0.88	-6.90E-05	-0.90	0.02	0.02
		^{13}C	15.96	15.96	15.94	15.94	15.94	15.95	15.95	15.93	15.95	15.94	15.96	3.85E-06	0.03	0.00	
Ile9	CH_3δ	^{1}H	0.91	0.91	0.91	0.91	0.91	0.90	0.90	0.90	0.90	0.89	0.89	-8.92E-05	-0.99	0.02	0.06
		^{13}C	11.94	11.94	11.93	11.93	11.93	11.95	11.96	11.96	11.98	11.97	12.02	2.85E-04	0.87	0.07	
HDA	CH_2α1	^{1}H	2.51	2.51	2.46	2.46	2.43	2.42	2.40	2.39	2.38	2.36	2.35	-6.50E-04	-0.98	0.17	0.31
		^{13}C	44.45	44.43	44.39	44.40	44.37	44.34	44.29	44.27	44.25	44.20	44.17	-1.07E-03	-0.99	0.28	
HDA	CH_2α2	^{1}H	2.51	2.51	2.50	2.50	2.50	2.49	2.48	2.48	2.47	2.47	2.46	-2.16E-04	-1.00	0.06	0.19
		^{13}C	44.45	44.43	44.39	44.38	44.37	44.33	44.30	44.27	44.25	44.20	44.16	-1.07E-03	-1.00	0.28	
HDA	CHβ	^{1}H	3.95	3.95	3.96	3.96	3.96	3.96	3.96	3.96	3.96	3.96	3.96	4.71E-05	0.96	0.01	0.34
		^{13}C	69.58	69.45	69.37	69.31	69.23	69.14	69.06	69.04	68.98	68.94	68.93	-2.51E-03	-0.97	0.65	
HDA	CH_2γ	^{1}H	1.56	1.55	1.55	1.55	1.54	1.54	1.53	1.53	1.53	1.52	1.51	-1.53E-04	-1.00	0.04	0.13
		^{13}C	38.03	37.99	37.96	37.94	37.94	37.91	37.89	37.88	37.86	37.85	37.83	-7.02E-04	-0.98	0.18	
HDA	CH_2δ1	^{1}H	1.29	1.30	1.30	1.30	1.30	1.30	1.30	1.30	1.30	1.30	1.30	1.40E-05	0.74	0.00	0.21
		^{13}C	26.07	26.01	25.95	25.92	25.88	25.82	25.76	25.75	25.70	25.68	25.69	-1.56E-03	-0.97	0.40	
HDA	CH_2δ2	^{1}H	1.47	1.47	1.47	1.46	1.46	1.45	1.45	1.45	1.44	1.44	1.43	-1.52E-04	-1.00	0.04	0.24
		^{13}C	26.05	25.98	25.94	25.92	25.87	25.80	25.74	25.72	25.68	25.65	25.67	-1.59E-03	-0.98	0.41	
HDA	CH_2θ	^{1}H	1.27	1.27	1.28	1.28	1.28	1.28	1.28	1.28	1.28	1.29	1.29	5.29E-05	0.97	0.01	0.06
		^{13}C	22.66	22.65	22.64	22.64	22.67	22.66	22.66	22.69	22.68	22.71	22.76	3.50E-04	0.84	0.09	
HDA	CH_3ι	^{1}H	0.87	0.87	0.87	0.87	0.87	0.87	0.88	0.88	0.88	0.88	0.88	4.73E-05	0.99	0.01	0.03
		^{13}C	14.14	14.13	14.12	14.12	14.12	14.14	14.14	14.14	14.15	14.14	14.18	1.59E-04	0.72	0.04	

			^{1}H/^{15}N Chemical shifts [ppm]											Slope[b]	R²	|Slope|×ΔD	average[c]
Leu1	NH	^{1}H		8.54	8.47	8.41	8.31	8.19	8.11	8.05	7.96	7.89	7.86	-3.04E-03	-0.99	0.78	1.12
		^{15}N		-253.08	-253.19	-253.35	-253.71	-253.95	-254.19	-254.27	-254.45	-254.49	-254.39	-6.46E-03	-0.95	1.67	
Gln2	NH	^{1}H			8.73	8.78	8.87	8.94	9.00	9.03	9.08	9.10	9.08	1.74E-03	0.95	0.45	0.75
		^{15}N			-263.58	-263.53	-263.31	-263.14	-263.00	-262.90	-262.73	-262.55	-262.32	5.79E-03	1.00	1.49	
Thr3	NH	^{1}H	8.12	8.11	8.11	8.11	8.11	8.11	8.11	8.11	8.11	8.11	8.13	1.07E-05	0.15	0.00	0.03
		^{15}N	-266.15	-266.17	-266.13	-266.13	-266.09	-266.08	-266.07	-266.05	-266.04	-266.05	-266.04	5.01E-04	0.94	0.13	
Val4	NH	^{1}H	7.78	7.72	7.68	7.64	7.58	7.52	7.47	7.44	7.39	7.36	7.35	-1.74E-03	-0.99	0.45	0.67
		^{15}N	-258.56	-258.79	-258.88	-258.97	-259.09	-259.23	-259.35	-259.46	-259.55	-259.64	-259.64	-4.20E-03	-0.98	1.08	
Leu5	NH	^{1}H	8.08	8.04	8.01	7.98	7.92	7.88	7.84	7.81	7.78	7.76	7.76	-1.33E-03	-0.98	0.34	0.55
		^{15}N	-265.65	-265.79	-265.91	-265.97	-266.18	-266.33	-266.44	-266.52	-266.61	-266.64	-266.60	-4.05E-03	-0.97	1.04	
Ser6	NH	^{1}H	7.14	7.12	7.11	7.10	7.09	7.06	7.06	7.05	7.04	7.03	7.04	-4.07E-04	-0.96	0.10	0.13
		^{15}N	-276.52	-276.57	-276.53	-276.59	-276.58	-276.57	-276.56	-276.58	-276.64	-276.64	-276.69	-4.79E-04	-0.85	0.12	
Leu7	NH	^{1}H	7.70	7.64	7.60	7.58	7.52	7.46	7.42	7.39	7.35	7.31	7.28	-1.64E-03	-1.00	0.42	1.06
		^{15}N	-255.34	-255.76	-256.04	-256.22	-256.62	-256.98	-257.32	-257.59	-257.86	-258.24	-258.58	-1.23E-02	-1.00	3.17	
Ser8	NH	^{1}H	8.43	8.38	8.36	8.34	8.30	8.27	8.24	8.21	8.19	8.15	8.12	-1.14E-03	-1.00	0.30	0.76
		^{15}N	-272.52	-272.73	-272.88	-273.03	-273.30	-273.64	-273.88	-274.13	-274.35	-274.62	-274.71	-9.04E-03	-1.00	2.33	
Ile9	NH	^{1}H	6.48	6.50	6.50	6.49	6.49	6.50	6.50	6.51	6.51	6.52	6.54	1.61E-04	0.91	0.04	0.07
		^{15}N	-269.99	-270.07	-270.06	-270.15	-270.19	-270.17	-270.19	-270.19	-270.20	-270.19	-270.16	-6.09E-04	-0.76	0.16	

[a] 95% error calculated as 1.96 times the standard deviation of 500 diffusion coefficients obtained using a Monte Carlo procedure

[b] Slope obtained by linear regression between chemical shift and pseudodesmin A diffusion coefficients

[c] Average chemical shift change calculated as $\delta_{av} = \delta(^1\mathrm{H}) + \delta(\mathrm{X})/n$ with n=2 for X=^{13}C and n=5 for X=^{15}N

J

Published papers concerning pseudodesmin A

The following pages contain two papers that have been published concerning pseudodesmin A:

1. D. Sinnaeve, C. Michaux, J. Van hemel, J. Vandenkerckhove, E. Peys, F.A.M. Borremans, B. Sas, J. Wouters, and J.C. Martins
   "Structure and X-ray conformation of pseudodesmins A and B, two new cyclic lipodepsipeptides from *Pseudomonas* bacteria".
   Tetrahedron, **2009**, 65(21) 4173-4181.

2. D. Sinnaeve, P.M.S. Hendrickx, J. Van hemel, E. Peys, B. Kieffer, and J.C. Martins,
   "The Solution Structure and Self-Association Properties of the Cyclic Lipodepsipeptide Pseudodesmin A Support Its Pore-Forming Potential".
   Chemistry-a European Journal, **2009**, 15(46) 12653-12662.

Summary

Pseudodesmin A is a cyclic lipodepsipeptide (CLP) that consists of an oligopeptide chain of nine amino acid residues of both D and L configuration (L-Leu1-D-Gln2-D-allo-Thr3-D-Val4-D-Leu5-D-Ser6-L-Leu7-D-Ser8-L-Ile9) and a fatty acid chain moiety ((3R)-3-hydroxydecanoic acid) bonded to the N-terminus of the oligopeptide. The C-terminus of the oligopeptide is involved in a lactone bond with the hydroxyl group of the Thr3 residue, effectively forming a cyclic structure of seven residues. The molecule was isolated from *Pseudomonas* bacteria living in the mucus layer on the skin of the black belly salamander (*Desmognathus quadramaculatus*) and was found to possess promising antimicrobial activity, mainly against Gram positive bacteria. It is a member of the viscosin group of CLPs, which are produced by a diversity of *Pseudomonas* bacteria.

For several CLPs, including some of the viscosin group, it has been hypothesised that they can insert themselves into the phospholipid bilayer of the cellular membrane and form hydrophilic pores allowing migration of ions, which is most likely the origin of the biological activity. Pseudodesmin A was found to be able to self-assemble in non-polar organic solvents (most notably chloroform) by observing changes in the properties of the NMR spectra when compared to those observed in polar organic solvents (most notably acetonitrile). This self-assembly into large supramolecular structures is reminiscent of its expected ability to form ion pore structures in the non-polar environment of the cellular membrane. Since these molecules are too small to span the membrane, an assembly into larger structures would be a feasible mechanism. The study of the self-assembly in organic solvents may therefore provide insight into the pore forming mechanism of this group of CLPs. In addition, because only a limited amount of pseudodesmin A is available, organic solvents have the unique advantage of allowing the recuperation of the product, which would not be possible when studying the interaction with model membranes or bicelles.

The goal of this dissertation was to investigate the self-assembly in organic solvents by means of NMR spectroscopy in general and translational diffusion and heteronuclear relaxation measurements in particular. The study occurred in three distinct steps. First, the conformation of pseudodesmin A was determined. Both the X-ray diffraction crystal structure and the NMR acetonitrile solution structure were obtained. These structures are nearly identical and feature a left-handed α-helix of 5 to 6 residues (*ca.* 1.5 helical turns). It is followed by a three residue loop (L-Leu7-D-Ser8-L-Ile9) that covalently connects the C-terminal end of the helix with its middle through the lactone bond with the Thr3 side chain. The structure is amphipathic, *i.e.* the hydrophilic and hydrophobic side chains are clustered into two areas of the molecular surface. This appears to be of importance for the biological function of this

group of CLPs, since the position of the hydrophilic and hydrophobic residues are conserved between the viscosin group members. The conformation was obtained in acetonitrile solution, where no self-association occurs. A direct determination of the monomer structure within the supramolecular assembly formed in chloroform solution is not feasible however, mainly because no distinction can be made between intra- and intermolecular contact information that would be obtained through NMR. However, the acetonitrile solution conformation of pseudodesmin A can be shown to be mostly retained within the supramolecular assembly by comparing the NMR scalar couplings obtained in chloroform and acetonitrile solution, which are determined by the main chain φ torsion angles.

As a side note, it is found that in DMSO solution the pseudodesmin A conformation is no longer stable and an exchange between multiple different conformations exists. This is most likely due to the ability of DMSO to act as a very strong hydrogen bond acceptor. It will therefore be a strong competitor with the amide carbonyl CO group to form a hydrogen bond with the amide NH groups, effectively disturbing the intramolecular hydrogen bond network. This result is important for the viscosin group member WLIP, since the conformation of this compound in DMSO solution has been reported in literature. The results found for pseudodesmin A in this dissertation effectively invalidate the WLIP solution structure, as the latter is obtained by attempting to find a single conformation based on experimental restraints that are in reality the result of multiple conformations.

In a second step, the self-association was studied by means of translational diffusion NMR. This method measures the translational diffusion coefficient of the components in solution by means of magnetic field gradient methods. The translational diffusion coefficient is a measure of the size of an object. When an exchange between multiple states occurs on a time scale faster than the diffusion NMR experiment (*e.g.* the pseudodesmin A molecules are in equilibrium between their monomer state and multiple sizes of oligomers), an average diffusion coefficient is obtained reflecting the average oligomer size. By monitoring the diffusion coefficient of pseudodesmin A as a function of concentration in chloroform, it was proven that a self-association effectively occurs, with increasing concentrations pushing the self-association equilibria towards oligomers of larger sizes. It is found that large supramolecular assemblies of the order of tens of units can be formed without an apparent limit to the maximum size. Monitoring the diffusion coefficient as a function of the solvent polarity (chloroform/acetonitrile mixtures), it is observed that the degree with which the self-association occurs is indeed very dependent on the solvent polarity. The size of the supramolecular structures formed can thus be controlled by the solvent polarity. This study also confirms that the non-polar environment is the driving force of the self-association.

Using the information obtained in these first two steps, a model for the supramolecular structures can be hypothesised that takes into account the pseudodesmin A conformation, the solvent polarity as a driving force, the ability to form oligomers of unlimited size and the suspected function of these structures as ion pores. This model assumes two distinct levels of interaction within the supramolecular structure. First, the pseudodesmin A molecules aggregate by packing their hydrophilic side chains against each other while their hydrophobic surface are located at the outside of the structure. This minimises the contact that the hydrophilic surface makes with the non-polar solvent (or membrane) environment. At a second level, the molecules can stack upon one another in a direction that is more or less parallel to the helix structure. This is mediated by free carbonyl CO and amide NH groups at respectively the C-terminal and the N-terminal ends of the helix structure. This direction of interaction finds support by intermolecular contacts observed between ^{1}H nuclei located in these two areas of the molecule. In principle, this stacking can continue without limitation. Taken together, these two interactions create a large, cylindrical structure that can grow in one direction, with a hydrophilic inside and a hydrophobic outside. The hydrophobic outside makes the structure soluble in the non-polar membrane environment, while the hydrophilic inside can mediate transport of ions from one side of the structure to the other. Because of its large size, this structure would easily be able to span the membrane bilayer, effectively creating an ion pore.

In a third step, heteronuclear $^{13}C^{\alpha}$ relaxation is used to gain more insight into the organisation of the supramolecular structure and to confirm some aspects of the proposed model. The longitudinal and transverse relaxation rate constants, R_1 and R_2 respectively, of the $^{13}C^{\alpha}$ spins are found to be dependent on the orientation of the CH bond vector within the pseudodesmin A conformation. Such dependence is typical for an object that possesses anisotropic rotational diffusion properties, which would confirm that the supramolecular structures have an anisotropic shape. The orientation of the pseudodesmin A monomer within the supramolecular structure and the average values for the rotational diffusion coefficients of the oligomers can be optimised to fit the experimental data. It is found that the experimental data are adequately described by a prolate axial symmetric molecular shape, which confirms the idea of cylindrically shaped structures. The orientation of the monomer is such that the long axis of the supramolecular assembly is nearly parallel to the helix structure. This is in agreement with the proposed model where the direction of stacking would be between the N-terminal free NH groups and the C-terminal free CO groups. When these experiments are repeated at different concentrations, reproducible results for the monomer orientation are found. The fitted rotational diffusion coefficients – which just as in the case of the translational diffusion coefficients can be seen as an average of all oligomer sizes – suggest an increasing average size and anisotropy of the supramolecular structures according to

concentration. When these rotational diffusion coefficients are converted into dimensions of a cylindrical object, it is found that the average length of the structures increases with concentration while the average diameter remains constant. This is again in good agreement with the model proposed above.

The conclusion in the end is thus that much insight has been gained into both the nature of the self-association and the structure of the supramolecular assembly. A model has been proposed that provides a relation between the conformation, the self-association and ultimately the biological function of pseudodesmin A. These results are not only expected to be valid for pseudodesmin A, but can also be applied to other members of the viscosin group that have been shown to possess a similar conformation. Most notably, these are WLIP, pseudophomin A and B and pseudodesmin B, which all possess an identical sequence in stereochemistry. In addition, in the case of WLIP and pseudophomin A, crystal structures have been reported that are identical to the one determined for pseudodesmin A. The other members of the viscosin group (viscosin itself, viscosinamide and the massetolides) all have a very similar amino acid sequence, but have an inversed configuration of the stereo centre in the main chain at the position of Leu5 (D-Leu5 to L-Leu5 substitution). Since no conformations of any of these compounds have been reported in literature, the impact of this structural change on the ability to self-associate can so far not be assessed.

In addition to these results specific for pseudodesmin A, the use of heteronuclear relaxation is a novel methodology to study supramolecular assemblies by NMR. The method allows the orientation of the monomer within the assembly and the dimensions of the assembly to be obtained, given that certain conditions are satisfied. The success of this method depends on the spread of orientation of CH bond vectors in the monomer structure, which creates a sufficient variation in relaxation rate constants to allow the anisotropy to be detected and quantitatively described.

The fact that the relaxation rate constants measured are averages of the individual oligomer values, leads to deviations from the behaviour expected for the relaxation rate constants relative to one another. This is demonstrated by simulations. The results from these simulations confirm that the pseudodesmin A molecules are involved in an indefinite self-association, *i.e.* they can form assemblies of unlimited size. In addition, it should be possible to obtain an idea of the distribution of different oligomer sizes from these average relaxation rate constants measured at different concentrations and magnetic field strengths. However, this does require some assumptions to be made on the formation and the structure of the supramolecular assemblies. Further experiments will have to be performed at low concentration to allow progress to be made in this issue

Samenvatting

Pseudodesmine A is een cyclisch lipodepsipeptide (CLP), bestaande uit een oligopeptide keten van negen aminozuren van zowel L als D configuratie (L-Leu1-D-Gln2-D-allo-Thr3-D-Val4-D-Leu5-D-Ser6-L-Leu7-D-Ser8-L-Ile9) en een vetzure keten ((3R)-3-hydroxydecaanzuur) dat gebonden is aan het N-terminale uiteinde van de oligopeptide keten. Het C-terminale uiteinde van het oligopeptide is verbonden met de hydroxyl groep van het Thr3 residu via een lacton binding, waardoor een cyclisch heptapeptide structuur wordt gevormd. Het molecuul, dat werd geïsoleerd uit *Pseudomonas* bacteriën die leven in de slijmlaag op de huid van de Amerikaanse black belly salamander, bezit beloftevolle antimicrobiële activiteit, vooral tegen Gram positieve bacteriën. Het is een lid van de viscosinegroep van CLP's die allen worden geproduceerd door diverse *Pseudomonas* bacteriën.

Voor meerdere CLP's, onder andere enkele uit de viscosinegroep, werd de hypothese vooropgesteld dat ze zich kunnen invoegen in de fosfolipide dubbellaag van cellulaire membranen en daar hydrofiele poriën vormen. Deze zouden dan instaan voor het passieve transport van ionen doorheen dit membraan, wat hoogstwaarschijnlijk aan de basis ligt van de biologische activiteit. Voor pseudosdesmine A werd vastgesteld dat het zich kan zelfassembleren in niet-polaire organische solventen (in het bijzonder chloroform). Dit valt te besluiten uit de vergelijking van de waargenomen NMR spectrale eigenschappen in niet-polaire solventen met deze waargenomen in polaire solventen (in het bijzonder acetonitrille). Deze zelfassemblage tot grote supramoleculaire structuren kan in verband worden gebracht met de verwachte eigenschap om ionporiën te vormen in de niet-polaire cellulaire membraanomgeving. Aangezien deze moleculen te klein zijn om het membraan te kunnen overspannen, zou een assemblage tot grotere structuren een denkbaar mechanisme zijn. De studie van de zelfassemblage in organische solventen kan daardoor dus inzicht verschaffen in het porievormend mechanisme van deze groep CLP's. Daarbovenop bezitten organische solventen het unieke voordeel dat het product gerecupereerd kan worden, in tegenstelling tot studies waar interactie met modelmembranen of bicellen centraal staan. Dit is van groot belang bij het onderzoek dat hier wordt uitgevoerd, aangezien slechts een beperkte hoeveelheid pseudodesmine A beschikbaar is.

Het doel van dit doctoraatswerk is het onderzoek van deze zelfassemblage in organische solventen met behulp van NMR spectroscopische methoden in het algemeen en translationele diffusie en heteronucleaire relaxatiemetingen in het bijzonder. Het onderzoek werd in drie onderscheidbare stappen uitgevoerd. Ten eerste moest de conformatie van pseudodesmine A worden achterhaald. Zowel de X-stralen diffractie kristalstructuur als de NMR structuur in acetonitrille oplossing

werden bepaald. Deze twee structuren zijn quasi identiek en bevatten een linksdraaiende α-helix van 5 tot 6 residuen (*ca.* 1.5 helicale draaiingen). De helix wordt gevolgd door een lus bestaande uit drie residuen (L-Leu7-D-Ser8-L-Ile9), die het C-terminale uiteinde van de helix covalent met het midden ervan verbindt via de lacton binding ter hoogte van de Thr3 zijketen. De structuur is amfipatisch, d.w.z. dat de hydrofiele en hydrofobe zijketens gegroepeerd liggen langs twee verschillende zijden van het moleculair oppervlak. Dit blijkt van belang te zijn voor de biologische functie van deze groep CLP's, daar de positie van de hydrofiele en hydrofobe residuen wordt behouden tussen de leden van de viscosinegroep. De conformatie werd bekomen in acetonitrile oplossing, waarin geen zelfassociatie optreedt. Een directe bepaling van de monomere conformatie in de supramoleculaire assemblages die in chloroform oplossing gevormd worden, is echter niet haalbaar, voornamelijk omdat er geen onderscheid kan worden gemaakt tussen de intra- en intermoleculaire contactinformatie dat met NMR kan worden bekomen. Echter, het kan worden aangetoond dat de pseudodesmine A conformatie in acetonitrile oplossing grotendeels wordt behouden binnen de supramoleculaire assemblage. Dit gebeurt door het vergelijken van de NMR scalaire koppelingen die werden bekomen in chloroform en acetonitrile oplossing, waarvan de waarde wordt bepaald door de φ torsiehoeken in de hoofdketen.

Terloops werd ook ontdekt dat de conformatie van pseudodesmine A in DMSO oplossing niet stabiel is en dat er een uitwisseling tussen meerdere verschillende conformaties bestaat. Dit is hoogstwaarschijnlijk omwille van de zeer sterke waterstofbrugontvangereigenschap van DMSO. Op deze manier treedt het in competitie met de amide carbonyl CO groep bij het vormen van waterstofbruggen met de amide NH groepen en verstoort het dus het intramoleculaire waterstofbruggennetwerk. Deze bevinding is ook belangrijk voor WLIP, een lid van de viscosinegroep, aangezien een conformatie in DMSO oplossing van dit product werd gerapporteerd in de literatuur. De resultaten met betrekking tot pseudodesmine A invalideren de conformatie in oplossing van WLIP, aangezien deze laatste werd bekomen door één enkele conformatie te berekenen gebaseerd op experimentele restricties die in realiteit het resultaat zijn van meerdere conformaties.

In een tweede stap werd de zelfassociatie bestudeerd met behulp van translationele diffusie NMR. Deze methode meet de translationele diffusiecoëfficiënt van de producten in oplossing met behulp van methodes gebaseerd op magnetische veldgradiënten. De translationele diffusiecoëfficiënt is een maat voor de grootte van een object. Wanneer een uitwisseling tussen verscheidene vormen optreedt op een tijdschaal sneller dan het diffusie NMR experiment (dit betekent, er bestaat een evenwicht tussen de monomere en de verscheidene oligomeervormen van de pseudodesmine A moleculen), dan zal een uitgemiddelde waarde voor de diffusiecoëfficiënt worden waargenomen dat ook een gemiddelde grootte reflecteert.

Het volgen van de pseudodesmine A diffusiecoëfficiënt in functie van de concentratie in chloroform levert het bewijs dat de zelfassociatie effectief plaatsgrijpt, daar toenemende concentratie de zelfassociatie-evenwichten naar grotere oligomeren drijven. Grote supramoleculaire structuren worden gevormd, in de grootteorde van tientallen eenheden, zonder een schijnbare grens in maximale grootte. Wanneer de diffusiecoëfficiënt in functie van de polariteit van het solvent wordt gevolgd (chloroform/acetonitrile mengsels), wordt er geobserveerd dat de mate waarmee de zelfassociatie plaatsgrijpt zeer sterk afhankelijk is van de polariteit. De grootte van de supramoleculaire structuren kan dus worden gecontroleerd met behulp van de polariteit van het solvent. Dit bevestigd ook dat de niet-polaire omgeving de drijvende kracht is van de zelfassociatie.

Gebruikmakende van de informatie dat werd bekomen in deze eerste twee stappen, kan er een model voor de structuur van de supramoleculaire assemblages als hypothese voorop gesteld worden. De gegevens die dit model in rekening neemt zijn de pseudodesmine A conformatie, de polariteit van het solvent dat als drijvende kracht, de mogelijkheid om oligomeren van onbeperkte grootte te vormen en de verwachte functie van de supramoleculaire structuren als ionporiën. Dit model veronderstelt twee onderscheidbare niveaus van interactie binnen de supramoleculaire structuur. Op het eerste niveau kunnen de pseudodesmine A moleculen aggregeren via een pakking van hun hydrofiele zijketens aan de binnenkant van deze aggregatie, terwijl de hydrofobe zijketens zich aan het buitenoppervlak bevinden. Dit minimaliseert het contact dat het hydrofiele oppervlak maakt met de niet-polaire solvent (of membraan) omgeving. Het tweede niveau houdt in dat de moleculen kunnen stapelen in een richting dat min of meer parallel is met de helix structuur. Dit wordt bewerkstelligd door vrije carbonyl CO en amine NH groepen aan de respectievelijk C-terminale en N-terminale uiteinden van de helixstructuur. Deze richting van interactie wordt bevestigd door waargenomen intermoleculaire contacten tussen ^{1}H kernen die zich in beide gebieden van het molecule bevinden. In principe kan deze opeenstapeling steeds verder gaan zonder beperking. Alles samen genomen creëren deze twee interacties een grote, cilindrische structuur dat slechts in één richting groeit, met een hydrofiele binnenkant en een hydrofobe buitenkant. De hydrofobe buitenkant zorgt ervoor dat de structuur oplosbaar is in de niet-polaire membraanomgeving, terwijl de hydrofiele binnenkant het transport van ionen van het ene naar het andere uiteinde van de structuur kan bemiddelen. Gezien zijn grootte kan deze structuur met gemak de dubbellaag van het membraan overspannen en aldus een ionporie vormen.

In een derde stap werden heteronucleaire $^{13}C^{\alpha}$ relaxatiemetingen gebruikt om meer inzicht in de organisatie van de supramoleculaire structuur te verkrijgen en om enkele aspecten van het vooropgesteld model te bevestigen. De longitudinale en transversale $^{13}C^{\alpha}$ relaxatiesnelheidsconstanten, respectievelijk R_1 en R_2, blijken

afhankelijk te zijn van de oriëntatie van de CH bindingsvector in de pseudodesmine A conformatie. Een dergelijke afhankelijkheid is typerend voor een object dat anisotrope rotationele diffusie-eigenschappen bezit. Dit bevestigt dat de supramoleculaire structuren een anisotrope vorm bezitten. De oriëntatie van het pseudodesmin A monomeer binnenin de supramoleculaire structuur, alsook de gemiddelde waarden voor de rotationele diffusiecoëfficiënten van de oligomeren kunnen worden geoptimaliseerd met behulp van de experimentele data. Er wordt vastgesteld dat de experimentele data voldoende worden beschreven door een prolaat axiaal symmetrische moleculaire vorm, dat het idee van een cilindrische structuur bevestigd. De oriëntatie van het monomeer is zodanig dat de lange as van de supramoleculaire assemblage bijna parallel is met de helix structuur. Dit is in overeenstemming met het vooropgesteld model waarbij de richting van de opeenstapeling zou gebeuren tussen de vrije N-terminale NH en de C-terminale CO groepen. Bij herhaling van deze experimenten bij verschillende concentraties worden reproduceerbare resultaten gevonden voor de monomeeroriëntatie. De gefitte rotationele diffusiecoëfficiënten – die net zoals in het geval van de translationele diffusiecoëfficiënten kunnen worden gezien als uitgemiddelde waarden voor alle oligomeergroottes – tonen een toenemende gemiddelde grootte en anisotropie aan voor de supramoleculaire structuren met toenemende concentratie. Wanneer deze rotationele diffusiecoëfficiënten worden omgezet naar de dimensies van een cilindrisch object, wordt er waargenomen dat de gemiddelde lengte van de structuren toeneemt met de concentratie, terwijl de gemiddelde diameter constant blijft. Dit is opnieuw in overeenstemming met het vooropgestelde model.

De eindconclusie is dus dat een grote hoeveelheid inzicht werd verworven in zowel de aard van de zelfassociatie als de structuur van de supramoleculaire assemblages. Een model werd vooropgesteld dat een verband legt tussen de conformatie, de zelfassociatie en uiteindelijk de biologische functie van pseudodesmine A. Het kan verwacht worden dat deze resultaten niet enkel opgaan voor pseudodesmine A, maar ook voor andere leden van de viscosinegroep waarvan een gelijkaardige conformatie werd aangetoond. In het bijzonder zijn dit WLIP, pseudophomine A en B en pseudodesmine B, die allen een identieke sequentie in stereochemie bezitten. Daarbovenop werden voor WLIP en pseudophomine A kristalstructuren gerapporteerd die identiek zijn aan dat van pseudodesmine A. De andere leden van de viscosinegroep (viscosine zelf, visosinamide en de massetoliden) bezitten allen een gelijkaardige aminozuursequentie, doch hebben een geïnverteerde configuratie van het stereocentrum in de hoofdketen ter hoogte van Leu5 (D-Leu5 naar L-Leu5 substitutie). Aangezien er nog geen conformationele studies werden uitgevoerd van deze verbindingen, kan de impact van deze structurele verandering op de zelfassociatie voorlopig nog niet worden beoordeeld.

Naast deze resultaten specifiek voor pseudodesmine A, kan het gebruik van heteronucleaire relaxatie als een nieuwe methodologie worden beschouwd om supramoleculaire assemblages te bestuderen met NMR. De methode laat toe om de oriëntatie van het monomeer binnenin de assemblage te bepalen, alsook de dimensies van het assemblage. Het succes van deze methode wordt bepaald door de spreiding in oriëntatie van de CH bindingsvectoren in de monomere structuur dat een voldoende grote variatie veroorzaakt in relaxatiesnelheidsconstanten en dus toelaat om de anisotropie te detecteren en kwantitatief te beschrijven.

Het feit dat de relaxatiesnelheidsconstanten worden gemeten als gemiddeldes van de individuele oligomeerwaarden, zorgt voor afwijkingen van het verwachte gedrag van de relaxatiesnelheidsconstanten relatief ten opzichte van elkaar. Dit wordt aangetoond met behulp van simulaties. Het resultaat van deze simulaties bevestigen dat de pseudodesmine A molecules betrokken zijn in een onbegrensde zelfassociatie, d.w.z. dat ze assemblages kunnen vormen van onbeperkte grootte. Daarnaast zou het mogelijk moeten zijn om een idee te bekomen van de distributie aan verschillende oligomeergroottes, gebaseerd op de gemiddelde waarden van de relaxatiesnelheidsconstanten gemeten bij verschillende concentraties en magnetische veldsterktes. Om dit te doen moeten er echter meerdere veronderstellingen worden gemaakt over de vorming en de structuur van de supramoleculaire assemblages. Verdere experimenten zullen moeten worden uitgevoerd bij lage concentraties om hierin vordering te kunnen maken.